JANUARY 2022

AJNR

VOLUME 43 • PP 1–157

AJNR
AMERICAN JOURNAL OF NEURORADIOLOGY

JANUARY 2022
VOLUME 43
NUMBER 1
WWW.AJNR.ORG

THE JOURNAL OF DIAGNOSTIC AND INTERVENTIONAL NEURORADIOLOGY

Petrobasal vein: A previously unrecognized vein

Diagnostic accuracy of transcranial Doppler and angiographic vasospasm

Thrombectomy for venous sinus thrombosis in vaccine-induced thrombotic thrombocytopenia

Official Journal ASNR • ASFNR • ASHNR • ASPNR • ASSR

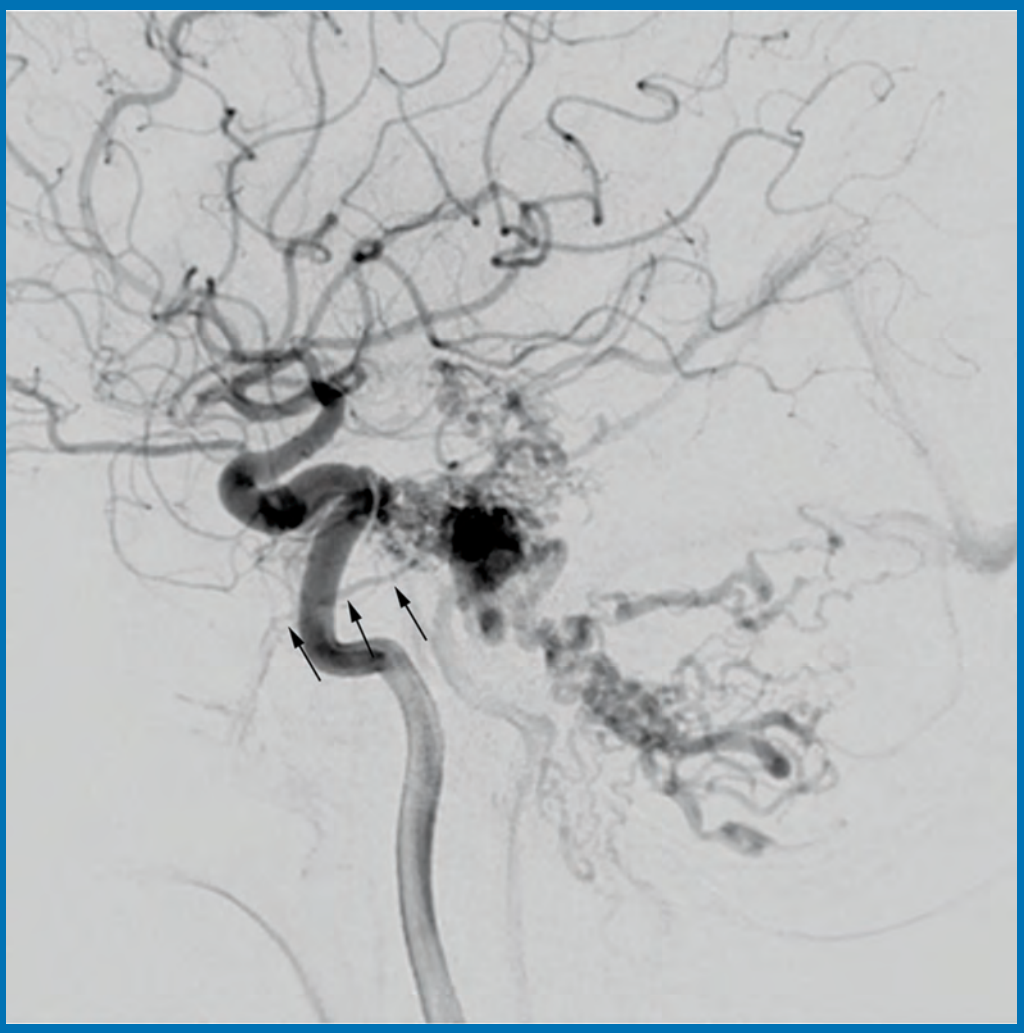

WEB™ Embolization: **Clinically Proven**

12,000 +
Patients Treated

100 +
Publications

10 Years
of Continuous Innovation

MicroVention™
TERUMO

microvention.com

WEB™ 17

Aneurysm Embolization System

LOWER PROFILE

NEW SIZES

MORE ACCESS OPTIONS

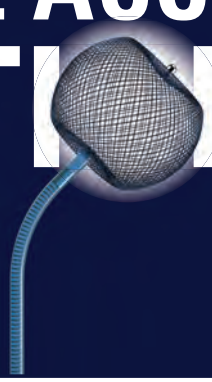

INDICATIONS FOR USE:
The WEB Aneurysm Embolization System is intended for the endovascular embolization of ruptured and unruptured intracranial aneurysms and other neurovascular abnormalities such as arteriovenous fistulae (AVF). The WEB Aneurysm Embolization System is also intended for vascular occlusion of blood vessels within the neurovascular system to permanently obstruct blood flow to an aneurysm or other vascular malformation

POTENTIAL COMPLICATIONS:
Potential complications include but are not limited to the following: hematoma at the site of entry, aneurysm rupture, emboli, vessel perforation, parent artery occlusion, hemorrhage, ischemia, vasospasm, clot formation, device migration or misplacement, premature or difficult device detachment, non-detachment, incomplete aneurysm filling, revascularization, post-embolization syndrome, and neurological deficits including stroke and death. For complete indications, potential complications, warnings, precautions, and instructions, see instructions for use (IFU provided with the device).

VIA 21, 27, 33 - The VIA Microcatheter is intended for the introduction of interventional devices (such as the WEB device/stents/flow diverters) and infusion of diagnostic agents (such as contrast media) into the neuro, peripheral, and coronary vasculature.

VIA 17,17 Preshaped - The VIA Microcatheter is intended for the introduction of interventional devices (such as the WEB device/stents/flow diverters) and infusion of diagnostic agents (such as contrast media) into the neuro, peripheral, and coronary vasculature.

The VIA Microcatheter is contraindicated for use with liquid embolic materials, such as n-butyl 2-cyanoacrylate or ethylene vinyl alcohol & DMSO (dimethyl sulfoxide).

The device should only be used by physicians who have undergone training in all aspects of the WEB Aneurysm Embolization System procedure as prescribed by the manufacturer.

RX Only: Federal law restricts this device to sale by or on the order of a physician.

For healthcare professional intended use only.

MicroVention™
TERUMO

MicroVention Worldwide Innovaton Center — PH +1.714.247.8000

35 Enterprise
Aliso Viejo, CA 92656 USA

MicroVention UK Limited — PH +44 (0) 191 258 6777
MicroVention Europe, S.A.R.L. — PH +33 (1) 39 21 77 46
MicroVention Deutschland GmbH — PH +49 211 210 798-0
Website — microvention.com

CE 0297

AJNR
AMERICAN JOURNAL OF NEURORADIOLOGY

CALL FOR AJNR EDITORIAL FELLOWSHIP CANDIDATES

2022 Candidate Information and Requirements

ASNR and AJNR are pleased once again to join efforts with other imaging-related journals that have training programs on editorial aspects of publishing for trainees or junior staff (<5 years on staff), including Radiology (Olmsted fellowship), AJR (Figley and Rogers fellowships), JACR (Bruce J. Hillman fellowship), and Radiologia.

GOALS

- Increase interest in editorial and publication-related activities in younger individuals.
- Increase understanding and participation in the AJNR review process.
- Incorporate into AJNR's Editorial Board younger individuals who have previous experience in the review and publication process.
- Fill a specific need in neuroradiology not offered by other similar fellowships.
- Increase the relationship between "new" generation of neuroradiologists and more established individuals.
- Increase visibility of AJNR among younger neuroradiologists.

ACTIVITIES OF THE FELLOWSHIP

- Serve as Editorial Fellow for one year. This individual will be listed on the masthead as such.
- Review at least one manuscript per month for 12 months. Evaluate all review articles submitted to AJNR.
- Learn how electronic manuscript review systems work.
- Be involved in the final decision of selected manuscripts together with the Editor-in-Chief.
- Participate in all monthly Senior Editor telephone conference calls.
- Participate in all meetings of the Editors during the annual meetings of ASNR and RSNA and the Radiology Editors Forum as per candidate's availability. The Foundation of the ASNR will provide $2000 funding for this activity.
- Evaluate progress and adjust program to specific needs in annual meeting or telephone conference with the Editor-in-Chief.
- Embark on an editorial scientific or bibliometric project that will lead to the submission of an article to AJNR or another appropriate journal as determined by the Editor-in-Chief. This project will be presented by the Editorial Fellow at the ASNR annual meeting.
- Recruit trainees as reviewers as determined by the Editor-in-Chief.
- Organize and host a Fellows' Journal Club podcast.
- Serve as Guest Editor for an issue of AJNR's News Digest with a timely topic.

QUALIFICATIONS

- Be a fellow in neuroradiology from North America, including Canada (this may be extended to include other countries).
- Be a junior faculty neuroradiology member (< 5 years) in either an academic or private environment.
- Be an "in-training" or member of ASNR in any other category.

APPLICATION

- Include a short letter of intent with statement of goals and desired research project. CV must be included.
- Include a letter of recommendation from the Division Chief or fellowship program director. A statement of protected time to perform the functions outlined is desirable.
- Applications will be evaluated by AJNR's Senior Editors prior to the ASNR annual meeting. The name of the selected individual will be announced at the meeting.
- Applications should be received by March 1, 2022 and sent to Ms. Karen Halm, AJNR Managing Editor, electronically at khalm@asnr.org.

AJNR go green

AJNR urges American Society of Neuroradiology members to reduce their environmental footprint by voluntarily suspending their print subscription.

The savings in paper, printing, transportation, and postage directly fund new electronic enhancements and expanded content.

The digital edition of *AJNR* presents the print version in its entirety, along with extra features including:

- **Publication Preview**
- **Case Collection**
- **Podcasts**
- **The *AJNR* News Digest**
- **The *AJNR* Blog**

It also reaches subscribers much faster than print. An electronic table of contents will be sent directly to your mailbox to notify you as soon as it publishes.

Readers can search, reference, and bookmark current and archived content 24 hours a day on www.ajnr.org.

ASNR members who wish to opt out of print can do so by using the AJNR Go Green link on the *AJNR* Website (http://www.ajnr.org/content/subscriber-help-and-services). Just type your name in the email form to stop print and spare our ecosystem.

MIDRC

MEDICAL IMAGING AND DATA RESOURCE CENTER.

Medical Imaging in the Fight against COVID-19
Call for Contributions

The Medical Imaging and Data Resource Center (MIDRC) is a multi-organizational initiative in the fight against the ongoing worldwide pandemic co-led by the ACR®, the RSNA, and the AAPM and is hosted at the University of Chicago.

The primary goal is to accelerate machine learning research by creating a high quality COVID-19 image commons linked to relevant clinical data made available as a public resource.

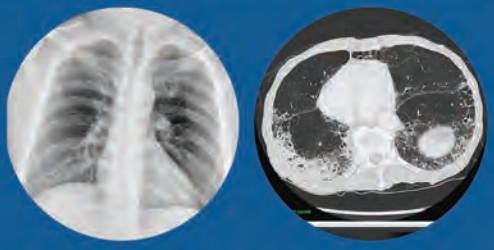

ASNR has teamed up with MIDRC to advance the understanding of the neuroimaging manifestations of COVID-19 and to enhance the MIDRC image commons.

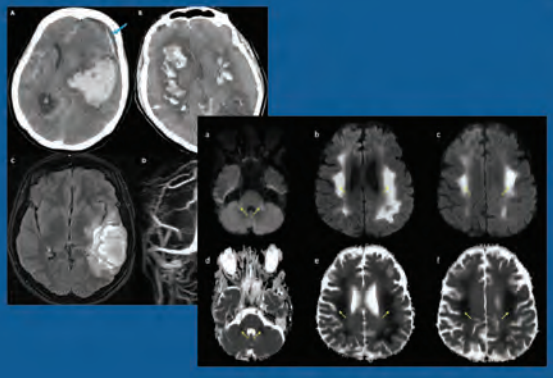

- To ensure success, MIDRC encourages all institutions and hospitals, both small and large, to donate their COVID-19 medical images and data to the cause.
- MIDRC provides a HIPAA-compliant mechanism to securely submit medical images and clinical metadata, and is committed to helping institutions throughout the submission process.

Visit midrc.org for more information

ACR American College of Radiology

RSNA Radiological Society of North America

AAPM American Association of Physicists in Medicine

The University of Chicago

NIH National Institute of Biomedical Imaging and Bioengineering

Creating Biomedical Technologies to Improve Health

Explore the New ASNR Career Center

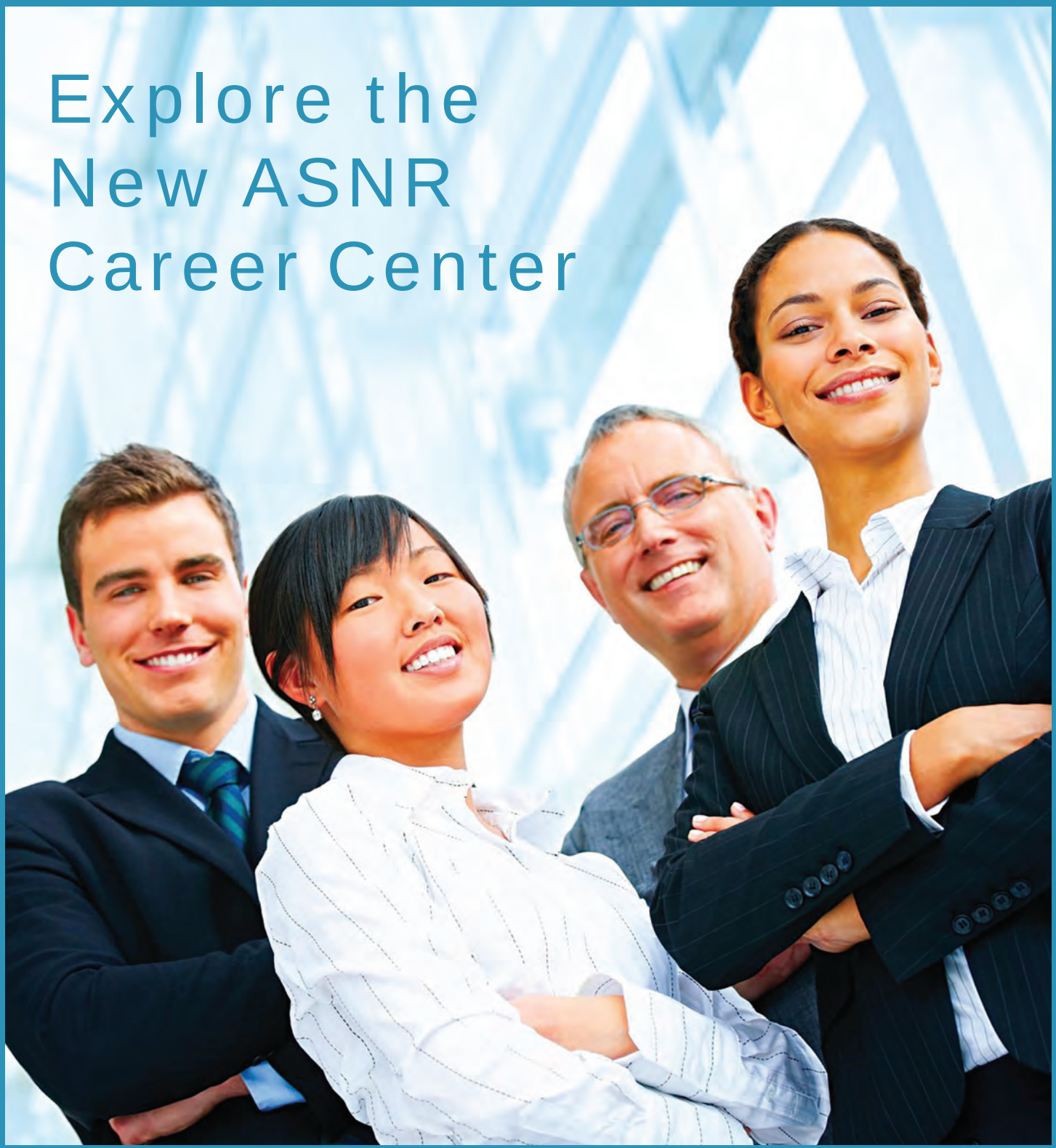

Your Premier Resource for Professional Development

- Access to jobs in the National Healthcare Career Network
- Confidential resume posting
- One-time free resume review
- Professional online profile
- Saved jobs capability

Start here: careers.asnr.org

ASNR
American Society of Neuroradiology

AJNR

AMERICAN JOURNAL OF NEURORADIOLOGY

JANUARY 2022
VOLUME 43
NUMBER 1
WWW.AJNR.ORG

Publication Preview at www.ajnr.org features articles released in advance of print. Visit www.ajnrblog.org to comment on AJNR content and chat with colleagues and AJNR's News Digest at http://ajnrdigest.org to read the stories behind the latest research in neuroimaging.

AJNR (Am J Neuroradiol ISSN 0195–6108) is a journal published monthly, owned and published by the American Society of Neuroradiology (ASNR), 800 Enterprise Drive, Suite 205, Oak Brook, IL 60523. Annual dues for the ASNR include approximately 21% for a journal subscription. The journal is printed by Intellicor Communications, 330 Eden Road, Lancaster, PA 17601; Periodicals postage paid at Oak Brook, IL and additional mailing offices. Printed in the U.S.A. POSTMASTER: Please send address changes to American Journal of Neuroradiology, P.O. Box 3000, Denville, NJ 07834, U.S.A. Subscription rates: nonmember $430 ($505 foreign) print and online, $320 online only; institutions $495 ($565 foreign) print and basic online, $980 ($1050 foreign) print and extended online, $380 online only (basic), $825 online only (extended); single copies are $35 each ($40 foreign). Indexed by PubMed/MEDLINE, BIOSIS Previews, Current Contents (Clinical Medicine and Life Sciences), EMBASE, Google Scholar, HighWire Press, Q-Sensei, RefSeek, Science Citation Index, SCI Expanded, ReadCube, and Semantic Scholar.

BOOK REVIEWS *R.M. Quencer, Section Editor*

Please visit www.ajnrblog.org to read and comment on Book Reviews.

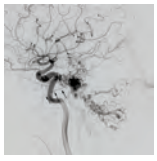

Lateral view on right internal carotid angiography shows a dAVF fed by multiple feeders from the meningohypophyseal trunk. In addition to the dAVF draining retrogradely via the various petrosal veins into the cerebellar cortical veins and lateral mesencephalic vein, there is another drainage route via the PBV into the emissary vein of the foramen rotundum.

Indicates Editor's Choices selection
Indicates Fellows' Journal Club selection
Indicates open access to non-subscribers at www.ajnr.org
Indicates article with supplemental online data
Indicates article with supplemental online video
Evidence-Based Medicine Level 1
Evidence-Based Medicine Level 2

AJNR

AMERICAN JOURNAL OF NEURORADIOLOGY

Publication Preview at www.ajnr.org features articles released in advance of print. Visit www.ajnrblog.org to comment on AJNR content and chat with colleagues and AJNR's News Digest at http://ajnrdigest.org to read the stories behind the latest research in neuroimaging.

JANUARY 2022 • VOLUME 43 • NUMBER 1 • WWW.AJNR.ORG

Title: Arthur Ravenel Jr Bridge. This bridge spans the Cooper River, connecting Charleston and Mount Pleasant, South Carolina. A cable-stayed bridge, it has won multiple awards for aesthetics and functionality, a tall order since the history of Charleston and the bridge's predecessors mandated it withstand earthquakes, hurricanes, ship collisions, increasing traffic loads, and the passage of the largest of ships in this major port. The pedestrian walkway has an extended curved approach providing spectacular cross-sectional views prior to the exhilarating walk across the bridge. Its design and operation are ecologically praiseworthy. The wattage, height, and operating hours of the bridge lights, and the use of reflective rather than electric road signs, are intended to minimize adverse impacts on migratory birds and loggerhead hatchling turtles.

Manfred Hauben, MD, MPH, Pfizer Inc and NYU Langone Health, New York City

Spectrum of Neuroradiologic Findings Associated with Monogenic Interferonopathies

P. Benjamin, S. Sudhakar, F. D'Arco, U. Löbel, O. Carney, C.-J. Roux, N. Boddaert, C. Hemingway, D. Eleftheriou, and K. Mankad

ABSTRACT

SUMMARY: The genetic interferonopathies are a heterogeneous group of disorders thought to be caused by the dysregulated expression of interferons and are now commonly considered in the differential diagnosis of children presenting with recurrent or persistent inflammatory phenotypes. With emerging therapeutic options, recognition of these disorders is increasingly important, and neuroimaging plays a vital role. In this article, we discuss the wide spectrum of neuroradiologic features associated with monogenic interferonopathies by reviewing the literature and illustrate these with cases from our institutions. These cases include intracerebral calcifications, white matter T2 hyperintensities, deep WM cysts, cerebral atrophy, large cerebral artery disease, bilateral striatal necrosis, and masslike lesions. A better understanding of the breadth of the neuroimaging phenotypes in conjunction with clinical and laboratory findings will enable earlier diagnosis and direct therapeutic strategies.

ABBREVIATIONS: AGS = Aicardi-Goutières syndrome; ICC = intracranial calcifications; IFN = interferon; SLE = systemic lupus erythematosus; SAVI = *STING*-associated vasculopathy of infancy; WMH = white matter hyperintensities

Interferons (IFNs) are a family of cytokines that are induced through the stimulation of pattern-recognition receptors that sense pathogen-derived nucleic acids.[1-3] They exert their activity through a complex network of regulatory pathways (Fig 1) for modulating innate/acquired immunity and resistance to viral infections.[2-4] These tightly regulated mechanisms protect against inappropriate immune activation triggered by endogenous nucleic acids while maintaining a rapid and effective response to exogenous nucleic acids derived from pathogens.[3,4] The interferonopathies are an expanding group of disorders that are thought to disrupt this delicate equipoise by overactivation of the IFN response, resulting in pathology from chronic inflammation.[2-5] In their most distinctive form, these diseases are monogenic neuroinflammatory disorders of infancy.[3-5]

In 1984, Aicardi and Goutières[6] described a disorder with progressive encephalopathy, CSF lymphocytosis, and neuroradiologic findings that mimic transplacental infection but test serologically negative. We now know that this disorder, which we refer to as Aicardi-Goutières syndrome (AGS), is characterized by genetic mutations that disrupt mechanisms that protect against inappropriate immune activation triggered by endogenous nucleic acids.[1,3,4] The subsequent dysregulated expression of IFNs is thought to promote unwanted inflammatory responses through their pleiotropic effects.[2-4] This interferonopathy hypothesis is supported by the fact that elevated IFN levels in the CSF and blood have long been described in patients with AGS.[1,7] More recently, upregulation of interferon-stimulated genes, an "interferon signature," which can be detected in peripheral blood, has been reported to be present in most patients with AGS and other interferonopathies.[1,3,4] As more mutations in these genes are described, a broad spectrum of phenotypes with considerable overlap has been revealed, many of which have prominent systemic manifestations, including inflammatory vasculopathy and systemic autoimmune disease.[3,4,8-10] Recognition of these diseases has become increasingly important not only for more reliable genetic counseling but because of the emergence of promising therapeutic strategies.[3,11,12] Neuroimaging often provides a valuable clue to the diagnosis of this expanding group of disorders[3,5,11,13-15] and will be the focus of this article.

Search Strategy

MEDLINE and EMBASE were searched from inception to week 1 of 2021 using the Ovid online portal. We used the following

Received April 7, 2021; accepted after revision June 29.

From the Department of Radiology (P.B., S.S., F.D., U.L., O.C., K.M.), Great Ormond Street Hospital for Children National Health Service Foundation Trust, London, UK; Department of Paediatric Radiology (C.-J.R., N.B.), Hôpital Necker–Enfants Malades, Paris, France; Institut Imagine (N.B.), Institut National de la Santé et de la Recherche Médicale Union Mutualiste Retraite 1163, Paris, France; Department of Paediatric Neurology (C.H.), Great Ormond Street Hospital, London, UK; and Infection, Inflammation, and Immunology Section (D.E.), University College London Great Ormond Street Institute of Child Health, London, UK.

Please address correspondence to Philip Benjamin, MD, Great Ormond St Hospital for Children NHS Foundation Trust, Great Ormond St, London, WCIN 3JH, United Kingdom; e-mail: philip.benjamin@nhs.net

Indicates open access to non-subscribers at www.ajnr.org

Indicates article with online supplemental data.

http://dx.doi.org/10.3174/ajnr.A7362

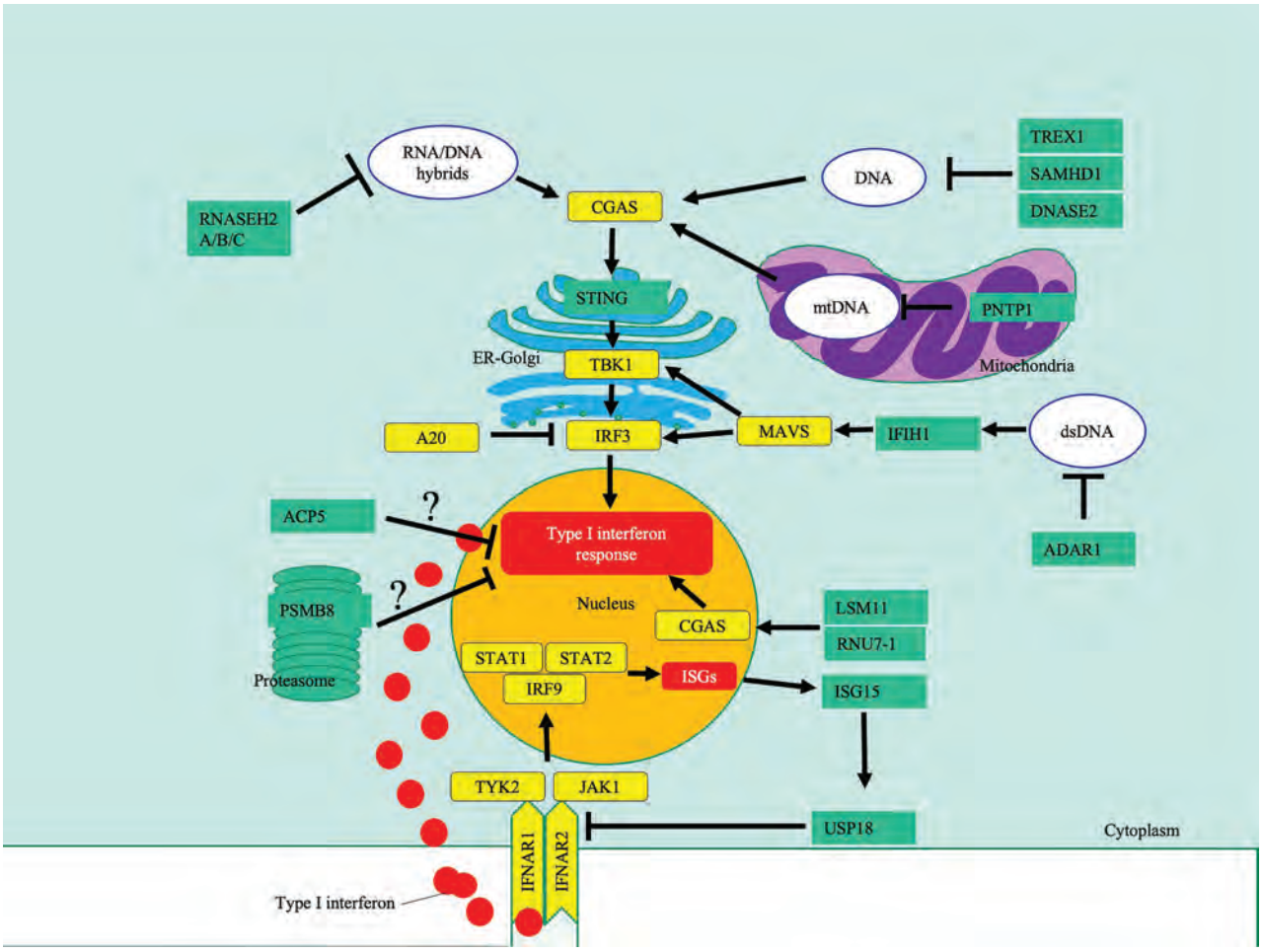

FIG 1. A highly simplified diagram highlighting key pathways affected in type 1 interferonopathies, in which neuroimaging findings have been described. The *black bars* indicate inhibition, and the *arrows*, activation. ? indicates that the mechanism of IFN induction is unclear. *CGAS* indicates cyclic GMP-AMP synthase; *TBK1*, TANK-binding kinase 1; *IRF3*, IFN regulatory factor 3; *MAVS*, mitochondrial antiviral-signaling protein; *IFNAR*, IFN α/β receptor; *JAK1*, Janus kinase 1; *TYK2*, tyrosine kinase 2; *PSMB8*, proteasome subunit β type-8; *TREX1*, three prime repair exonuclease 1; *RNASE H*, ribonuclease H; *SAMHD1*, SAM And HD domain-containing deoxynucleoside triphosphate triphosphohydrolase 1; *IFIH1*, interferon induced with helicase C domain 1; *PNPT1*, polyribonucleotide nucleotidyltransferase 1; *DNASE2*, deoxyribonuclease 2; *ACP5*, acid phosphatase 5; *ISG15*, interferon-stimulated gene 15; *RNU7-1*, RNA, U7 small nuclear 1; *USP18*, ubiquitin-specific peptidase 18; *STAT2*, signal transducer and activator of transcription 2; ER, endoplasmic reticulum; mtDNA, mitochondrial DNA.

keywords: 1) "interferonopathy" ($n = 245$), 2) "Aicardi-Goutières syndrome" ($n = 501$), 3) 1 and "intracranial calcification" ($n = 10$), 4) 1 and "brain" ($n = 34$), 5) 1 and "neuroimaging", 5) 2 and "neuroimaging" ($n = 5$), and 6) 1 and 2 ($n = 79$). The abstracts were reviewed to determine whether the article should be included. The search was supplemented by searching the bibliographies of relevant articles.

Monogenic Interferonopathies and Neuroimaging

The Online Supplemental Data provide a list of interferonopathies in which neuroimaging findings have been described; Fig 1 illustrates the key pathways involved. Common neuroimaging findings across the interferonopathies include intracerebral calcifications and T2 white matter hyperintensities (WMH) (Online Supplemental Data).

AGS, the best-described group of interferonopathies, is characterized by mutations in any of several genes (including *TREX1, RNASEH2A/B/C, SAMHD1, ADAR1, IFIH1*),[3] which are involved in the metabolism of nucleic acids or their recognition.[1] Recent additions to this are *LSM11* and *RNU7-1*, which encode small nuclear ribonucleoproteins, which are key components of the U7 replication-dependent histone pre-messenger RNA–processing complex, which is thought to help maintain the structure of nucleosomes, preventing activation of cyclic GMP-AMP synthase by nuclear DNA.[16]

TREX1 mutations are associated with a true neonatal presentation (Figs 2 and 3) and, therefore, mimic transplacental infection.[17] Most patients, however, present a little later, with the most frequent mutations occurring in *RNASEH2B* (Fig 4).[7,18] The neuroimaging phenotypes continue to expand as these mutations are better described and more are discovered. For example, intracranial vasculopathy has been described with *SAMHD1* mutations,[19] and bilateral striatal necrosis, with *ADAR1* mutations (Online Supplemental Data).[20]

Similar destructive neuroinflammatory conditions have been documented in genetic disorders in which other components of the

IFN signaling pathway are affected (Online Supplemental Data).[1,3,13] For example, loss-of-function mutations in ubiquitin-specific peptidase 18 (*USP18*), which is a negative regulator of type I IFN signaling, is also associated with intracerebral calcification and WMH (Online Supplemental Data).[13,21]

In some interferonopathies, systemic findings are a more prominent feature, such as interstitial lung disease in *STING*-associated vasculopathy of infancy (SAVI) or skin lesions in proteasome-associated autoinflammatory syndromes (Online Supplemental Data). Intracranial calcifications have also been described in a few of these cases and can, on occasion, provide an important clue to the diagnosis.

Due to the considerable overlap in the neuroimaging phenotypes, it is seldom possible to make a diagnosis on the basis of neuroradiologic findings alone, and these should always be considered in conjunction with clinical and laboratory findings (Fig 5). Indeed, neuroimaging can sometimes have normal findings, and the lack of neuroimaging findings, like intracranial calcifications, does not exclude an interferonopathy, certainly early on in the disease. In the rest of this article, we describe both characteristic and more unusual neuroradiologic features associated with interferonopathies, including findings that could lead one to suspect certain mutations. These include intracerebral calcifications, WMH, deep WM cysts, cerebral atrophy, large cerebral artery disease, bilateral striatal necrosis, and masslike lesions.

Intracerebral Calcification

Intracerebral calcifications (ICC) have been reported to be present in >90% of subjects with AGS.[18] ICC are also described in most other interferonopathies, even when systemic features predominate such as proteasome-associated autoinflammatory syndromes and SAVI (Online Supplemental Data).[3] Calcifications tend to be punctate or linear, reflecting their relationship to microvascular structures. Often sagittal or coronal reconstructions make it easier to appreciate the relationship with the deep, perforating vessels or deep medullary veins/arteries (Fig 6). The calcifications (Figs 2 and 3) are most commonly symmetric and seen in the basal ganglia and deep WM and dentate nuclei of the cerebellum[18] but can be seen throughout the brain. The morphology of the calcifications varies from fine/punctate to larger conglomerates. *TREX1* mutations are usually associated with more severe calcifications.[18] Neuropathologic studies

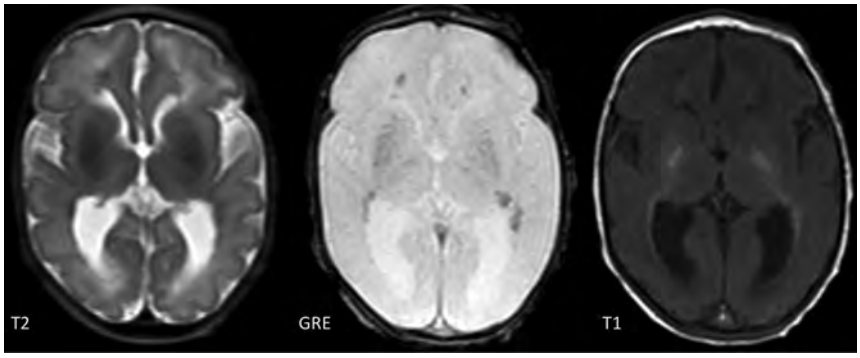

FIG 2. T2, gradient recalled-echo (GRE) and T1-weighted images of a 9-day-old boy with a *TREX1* mutation demonstrating basal ganglia and periventricular calcifications.

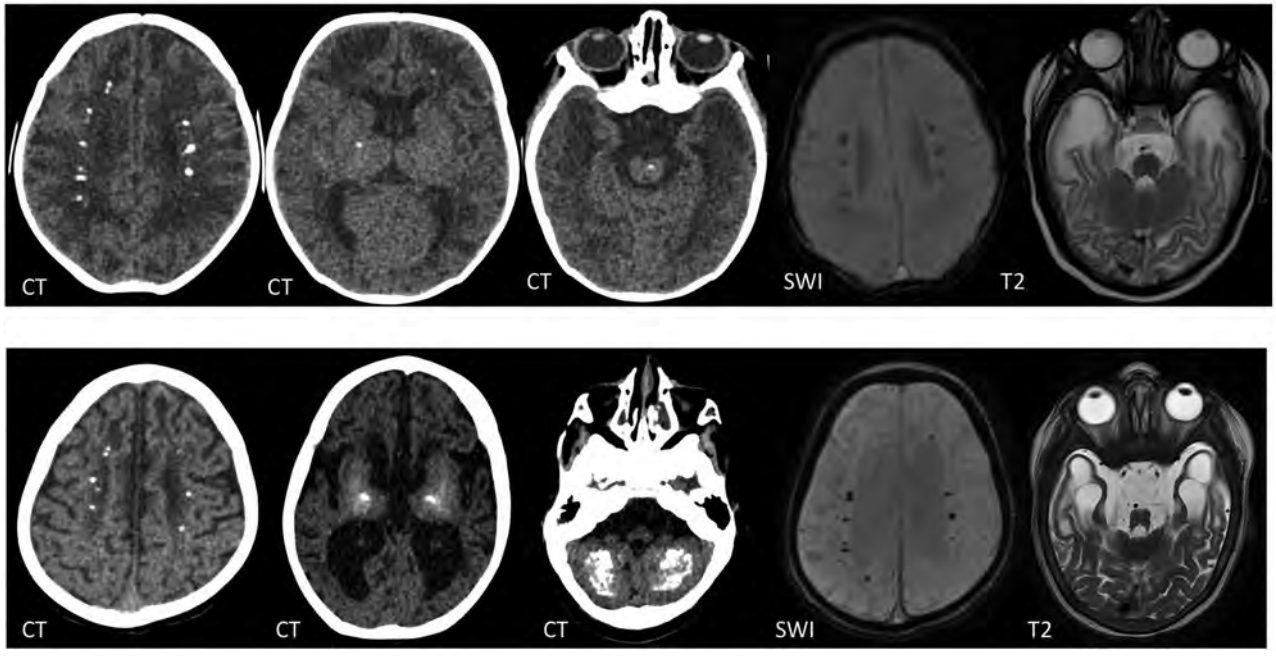

FIG 3. CT, SWI, and T2-weighted images of a boy with a *TREX1* mutation. The upper row shows imaging at 2 months of age, and the lower row, at 2 years of age. There are periventricular, basal ganglia, brainstem, and cerebellar WM calcifications, which progress with time. Note the interval volume loss with WM rarefaction, most marked in the anterior temporal lobes.

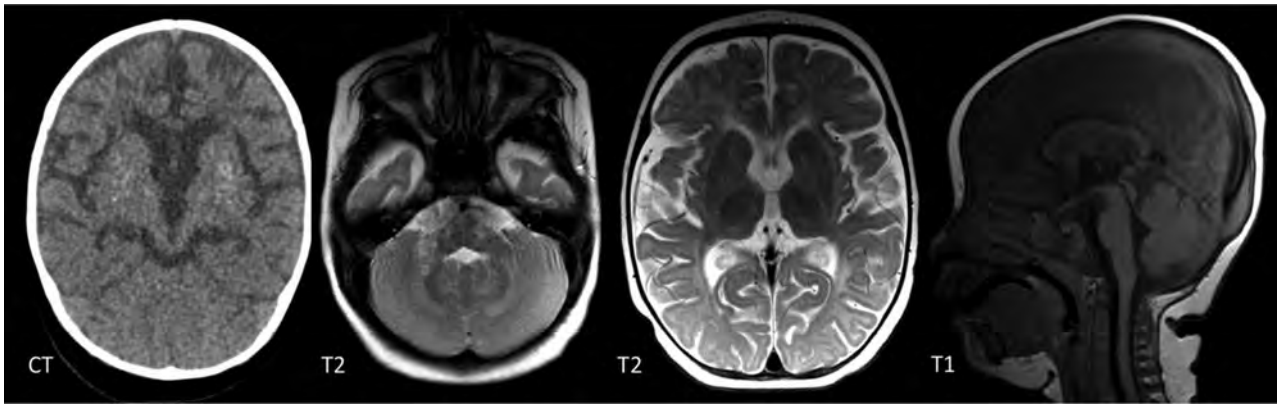

FIG 4. A 1-year-old girl with a *RNASEH2B* mutation. There are patchy WMH throughout the brain. Symmetric T2-signal abnormality is noted in the globus pallidus, thalamus, and dentate nucleus. There is global cerebral volume loss. CT confirms basal ganglia calcifications.

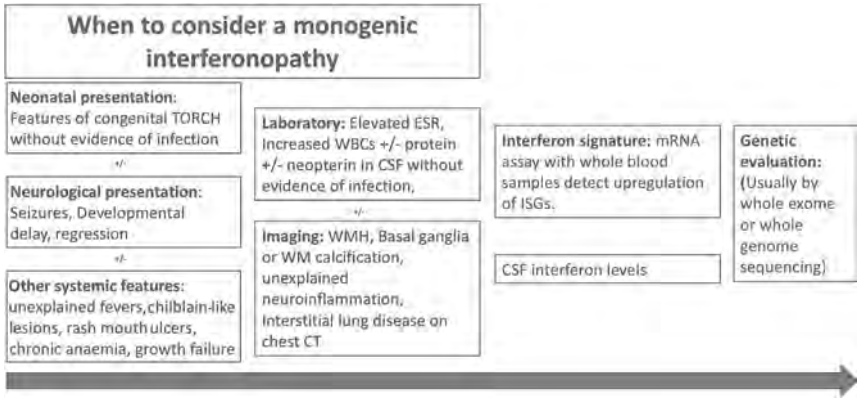

FIG 5. A potential route to the diagnosis of monogenic type 1 interferonopathies. The *red boxes* contain clinical, laboratory, and imaging findings that lead one to suspect an interferonopathy. The *green boxes* contain diagnostic tests performed when a monogenic type 1 interferonopathy is strongly suspected. ESR indicates erythrocyte sedimentation rate; WBC, white blood cells; ISG, interferon-stimulated genes; TORCH, (T)oxoplasmosis, (O)ther Agents, (R)ubella (also known as German Measles), (C)ytomegalovirus, and (H)erpes Simplex; mRNA, messenger RNA.

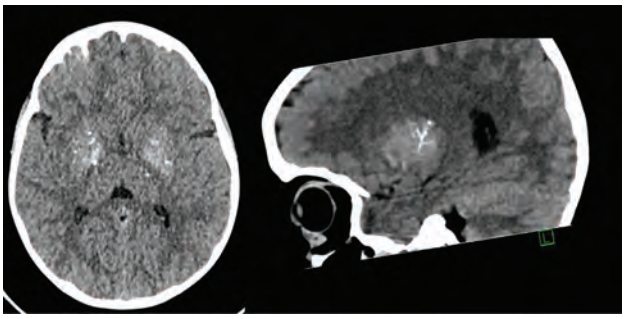

FIG 6. A CT study in axial and sagittal reconstructions shows punctate and linear branching calcifications along the deep perforators in a 7-year-old boy with a *SAMHD1* mutation.

show calcifications in the walls of medium/small vessels and perivascular spaces.[22-24] One study has suggested that IFNs act directly on vascular smooth-muscle cells, inducing a calcifying microangiopathy.[24] The increasing use of MR imaging as the first imaging technique in clinical practice may reduce the identification or recognition of intracranial calcifications, but the sensitivity can be improved by using gradient-echo or susceptibility-weighted sequences. CT is recommended in patients in whom interferonopathies are suspected and no calcifications are seen on MR imaging.[18]

WM Abnormalities

WMH have been described in most interferonopathies (Online Supplemental Data) and appear to be the most common finding in those with a later disease onset when ICC are less common.[25] Neuropathologic studies in AGS show inhomogeneous demyelination and astrogliosis, which is, again, supportive of a microangiopathy.[22,23] WM involvement is most commonly diffuse or with a frontotemporal predominance, but involvement can also be periventricular or patchy.[18] *TREX1* mutations are associated with more severe involvement, causing WM rarefaction in the anterior frontal and temporal lobes and deep WM cysts.[15,18,26] Delayed myelination can be associated with *RNASEH2B* mutations (Fig 7) but progresses with time because it is not a primary disorder of myelination.[18] Interferonopathies should also be considered in patients with MR imaging findings interpreted as periventricular leukomalacia.[18,23]

Brain Volume Loss

The degree of brain volume loss (Figs 3 and 7) depends on when the patient presents during the course of the disease, and it can be progressive. It is likely to be due to a combination of gray and WM volume loss. Although not always obvious on imaging, the neocortex and cerebellar cortex can be involved with numerous microinfarcts seen on some neuropathologic studies, which are likely to contribute to brain volume loss.[23,24] Pontocerebellar hypoplasia has also been reported, but this is relatively infrequent and is likely subsequent to the supratentorial brain volume loss.[15,18,26,27]

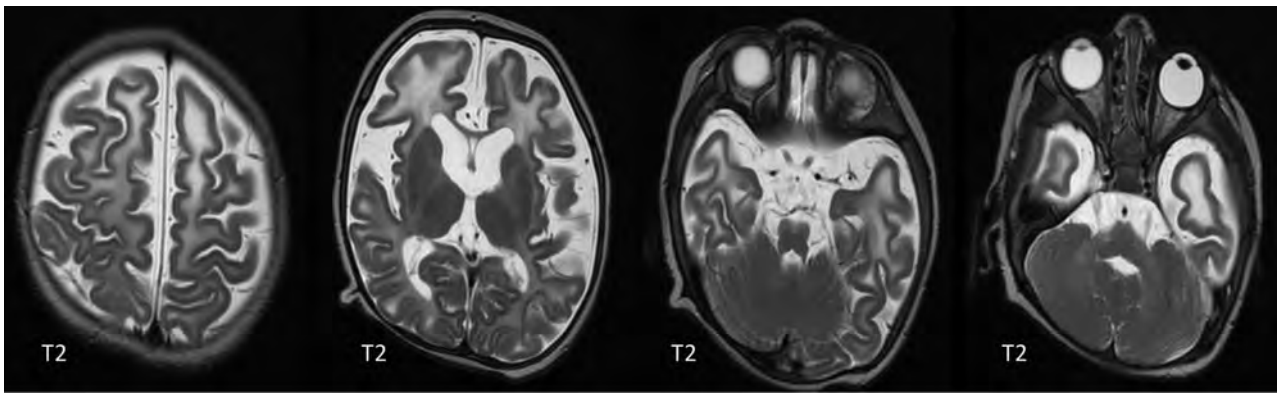

FIG 7. A 24-week-old boy with a *RNASEH2C* mutation with WM abnormalities in the frontal and temporal lobes and generalized volume loss.

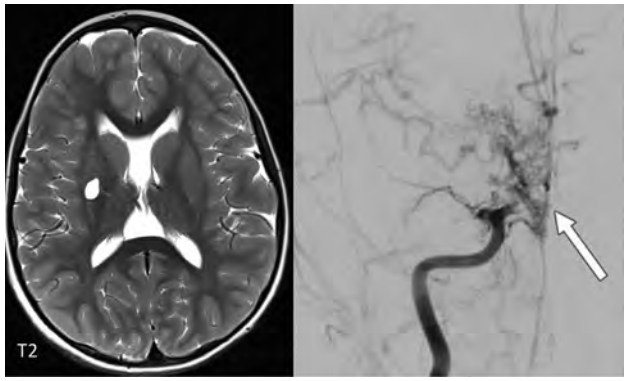

FIG 8. Lacunar infarct in the right putamen in a 7-year-old boy with a *SAMDH1* mutation. The angiogram on the right demonstrates a Moyamoya-type vasculopathy with occlusion of the right M1 and A1 (*arrow*).

Large Cerebral Artery Disease

Intracerebral large-artery involvement, including stroke, Moyamoya-type vasculopathy, aneurysms, and stenosis of single vessels, has most often been reported with *SAMHD1* mutations (Fig 8)[18,19] and less frequently with *TREX1* mutations.[28] Neuropathology in a patient with a *SAMHD1* mutation also showed calcifying microangiopathy,[24] which suggests a disease process similar to the that in other interferonopathies (Fig 6). The reason for the increased frequency of large-vessel disease in these mutations, however, is uncertain.

Bilateral Striatal Necrosis

Bilateral striatal necrosis has been reported in the context of *ADAR1* (Fig 9) and *PNPT1* (Fig 10) mutations in addition to WMH and ICC.[20,29,30] Imaging can show bilateral striatal swelling and signal abnormality with cavitation/atrophy on follow-up imaging. Globus pallidus swelling and signal abnormality can also be seen (Fig 11). The mechanism remains unclear, and metabolic disorders should be ruled out. These findings can sometimes be seen in a para-/postinfectious setting, and it has been hypothesized that local neuroinflammation may contribute to synaptic dysfunction and excitotoxicity.[31] Freckle-like skin lesions are characteristic of *ADAR1* mutations.[29]

Masslike Lesions

Masslike or ring-enhancing lesions have been described in heterozygous C-terminal frameshift mutations in *TREX1* (causing a disorder called retinal vasculopathy with cerebral leukodystrophy), which occur in conjunction with ICC and scattered WMH, though this disorder tends to present later in life.[32] These lesions are often misdiagnosed as tumors or as other inflammatory diseases such as sarcoidosis. Neuropathology can show necrotizing granulomatous inflammation.[11] The presence of coexistent neuroimaging features such as ICC should alert the clinician to the potential diagnosis of interferonopathy.

Hemorrhage

Deep GM, cerebellar, and intraventricular hemorrhage has been described in patients with *USP18* deficiency[11,33] and *TREX1* mutations.[18] Although these patients had coexistent coagulopathies, the location of the hemorrhage is reminiscent of that seen with *COL4A1* mutations and could conceivably be due to an underlying vasculopathy. Subdural and subarachnoid hemorrhage has also been reported in patients with a *STAT2* mutation, which disrupts *STAT2* interaction with *USP18,* a key negative regulator of IFN signaling.[34]

Some Differential Diagnoses to Consider

Due to the nonspecific nature of the neuroradiologic findings, the differential diagnosis is wide, including other inflammatory and neurogenetic disorders. In cases of neonatal presentation, congenital infections should first be ruled out. It has been suggested that "true periventricular" calcification in the ependymal/subependymal regions is more suggestive of infection.[35] Other features that make infection more likely include malformations of cortical development and anterior temporal cysts as seen in congenital cytomegalovirus (Fig 12).[35]

Other conditions known to be associated with an increased expression of IFN-regulated genes include systemic lupus erythematosus (SLE)[36] and juvenile dermatomyositis.[37] These, however, tend to present later in life, and systemic features usually predominate. The most common neuroimaging findings described with SLE are also of a microangiopathy, including nonspecific focal WMH,[38] brain atrophy, intracranial calcifications, and hemorrhage,[39] though other inflammatory findings such as

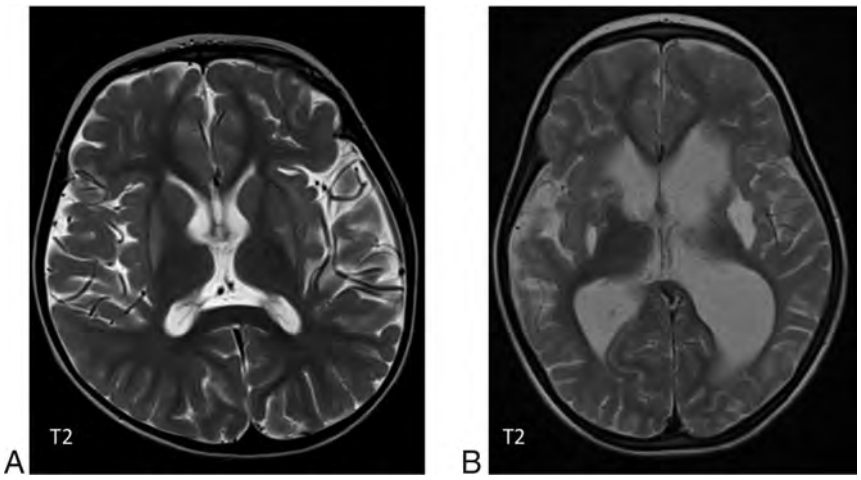

FIG 9. *A*, Bilateral putaminal signal abnormality in a 4-year-old boy with a confirmed *ADAR1* mutation. There was no diffusion restriction. *B*, A different patient also with an *ADAR1* mutation showing cavitation in both putamina.

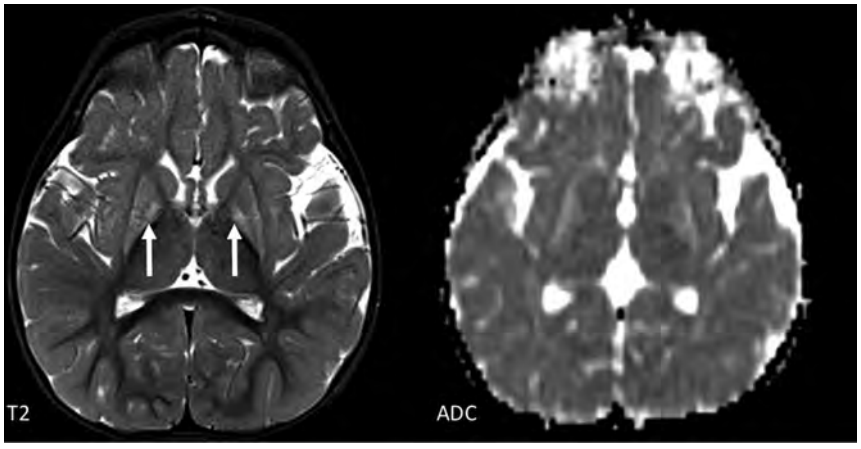

FIG 10. An 18-month-old girl with a *PNTP1* mutation with signal abnormality and decreased volume of both the putamina and globi pallidi. Diffusion restriction is seen in the globi pallidi.

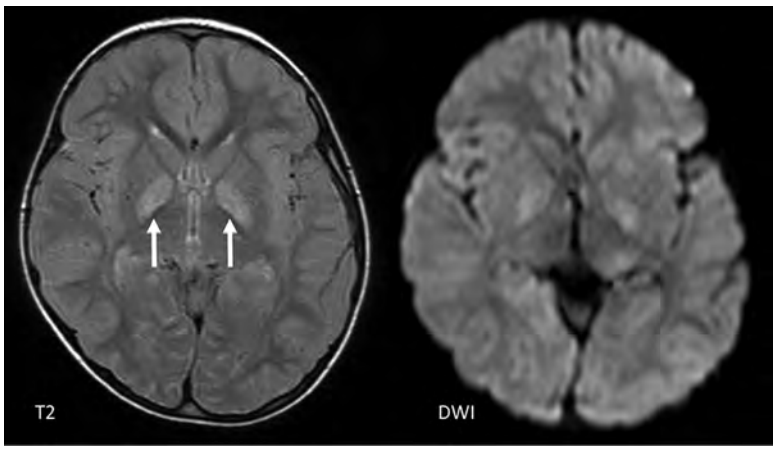

FIG 11. Atypical imaging features in a 4-year-old girl with an *ADAR1* mutation showing a T2 signal abnormality and mild diffusion restriction in the globi pallidi bilaterally (*arrows*), but not in the putamina.

leptomeningeal enhancement, large-vessel vasculitis, and masslike lesions have also been described.[40]

Hyperinflammatory clinical syndromes like hemophagocytic lymphohistiocytosis should also be considered. Hemophagocytic lymphohistiocytosis can be primary, resulting from genetic defects or secondary to infection, malignancy, immunosuppression, or autoimmune diseases such as SLE. CNS involvement is common, and the neuroimaging findings are variable, including focal/diffuse WMH, perivascular enhancement (particularly in the posterior fossa), meningeal enhancement, masslike lesions, and hemorrhage (Fig 13).[41]

Some leukodystrophies, like Cockayne syndrome, can have a very similar appearance with diffuse WMH and ICC. Unlike AGS, there is a severe delay or an arrest in myelination, and the calcifications can be cortical/leptomeningeal (Fig 14).[42]

Genetic microangiopathies such as collagen IV (*COL4A1/A2*) related disease can also show similar imaging findings.[35] They are characteristically associated with porencephalic cysts or periventricular leukomalacia.[43] It has been suggested that the calcification is more subtle, involving subependymal/periventricular regions (Fig 15).[43]

Calcifications of the cerebral microvessels are also seen in primary familial brain calcification, a group of neurogenetic disorders associated with diverse motor, cognitive, and psychiatric symptoms.[44] Calcifications are typically symmetric, commonly involving the deep GM structures. The autosomal dominant form can be caused by mutations in genes encoding phosphate transporters (*SLC20A2, XPR1*) or platelet-derived growth factor B and its receptor (*PDGFB, PDGFRB*). An autosomal recessive form has been described with mutations in encoding junctional adhesional molecules (*JAM2, JAM3*), myogenesis-regulating glycosidase (*MYORG*), and occludin (*OCLN*).[45] Calcification is more severe in the autosomal recessive form involving the subcortical WM. Brainstem calcification may be more common with *MYORG* mutations.[44]

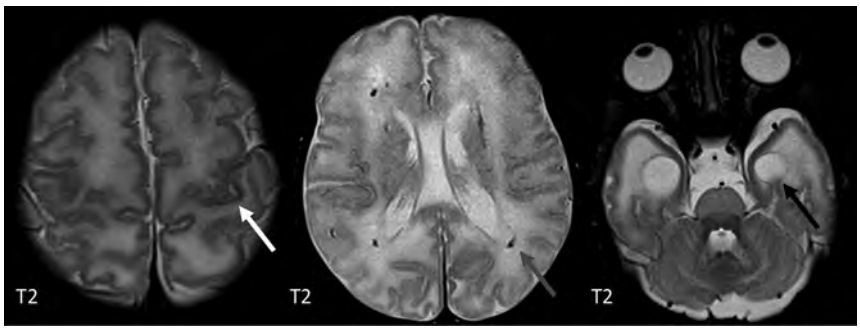

FIG 12. T2-weighted MR imaging of a 9-day-old girl with congenital cytomegalovirus infection showing polymicrogyria (*white arrow*), periventricular calcifications (*gray arrow*), and anterior temporal lobe cysts (*black arrow*).

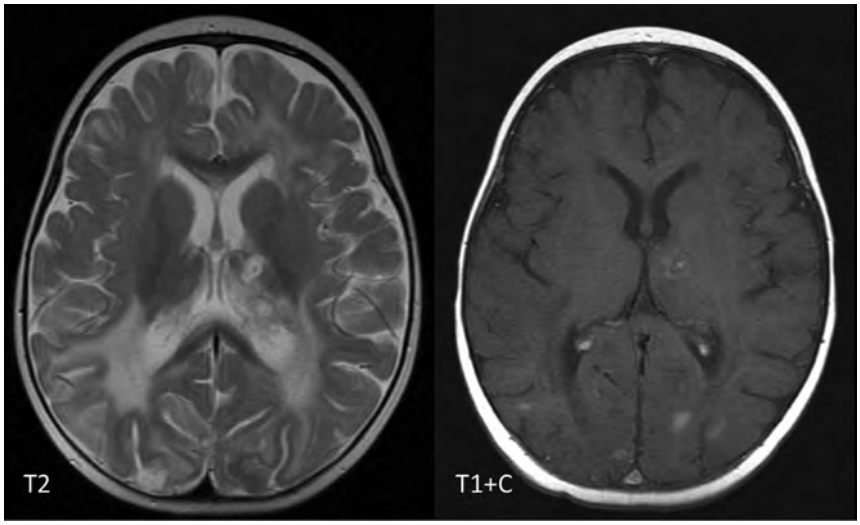

FIG 13. A 6 month-old girl with perforin-deficient hemophagocytic lymphohistiocytosis. There is diffuse WM signal abnormality seen on the T2-weighted image and multiple enhancing pseudotumoural lesions seen on the T1 postcontrast image (T1 + C) in the left thalamus and posterior temporal and occipital lobes bilaterally.

Some conditions with clinical and imaging overlap to transplacental infection may ultimately turn out to be interferonopathies. One such example is *RNaseT2* mutations, which result in loss of ribonuclease T2 protein function, causing accumulation of ribosomal RNA.[46] *RNaseT2* mutation causes cystic leukoencephalopathy without megalencephaly. The imaging findings are very similar to those of congenital cytomegalovirus infection and are characterized by anterior temporal lobe cysts and extensive WM hyperintensities in a normal-sized brain.

CONCLUSIONS

Neuroimaging is essential in interferonopathies, in which neuroinflammation is a predominant feature, as in AGS. Even when systemic features predominate, neuroimaging can often provide an important clue to the diagnosis. However, the spectrum of findings is wide and should always be considered in conjunction with clinical and laboratory findings. A common feature on neuroimaging seems to be evidence of calcifying microangiopathy characterized by WMH and ICC, which is best picked up on susceptibility-weighted MR imaging sequences or CT, though large-vessel disease, bilateral striatal necrosis, hemorrhage, and masslike lesions are also seen with some

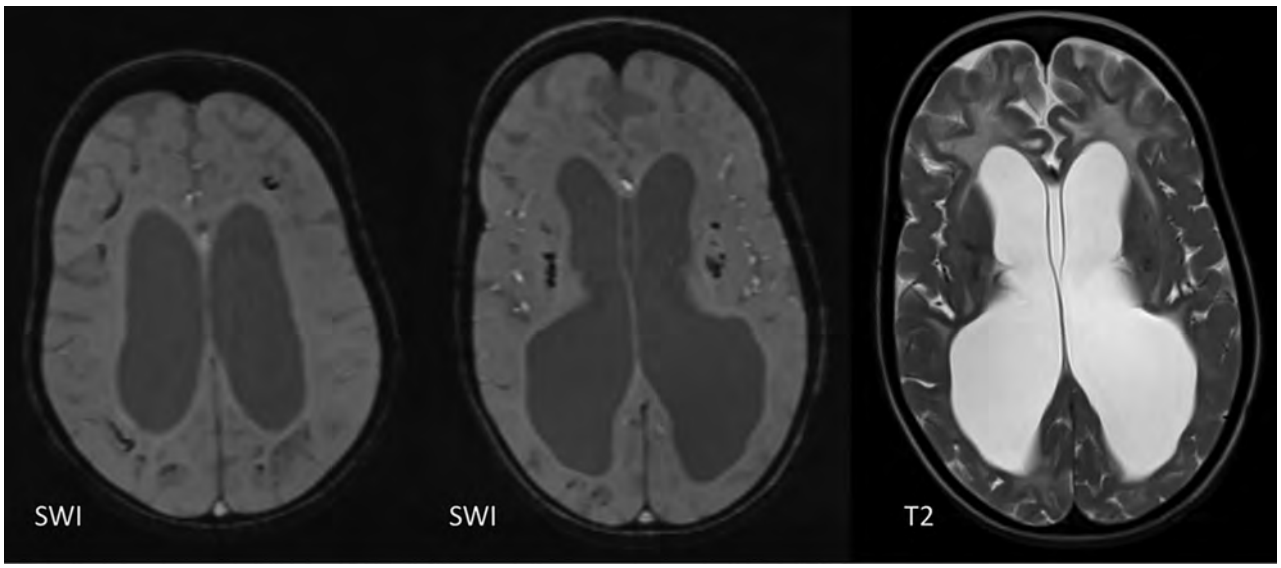

FIG 14. A 6-year-old boy with Cockayne syndrome showing subcortical and basal ganglia calcifications on SWI and diffuse WM signal abnormality seen on the T2-weighted image. There is marked WM volume loss.

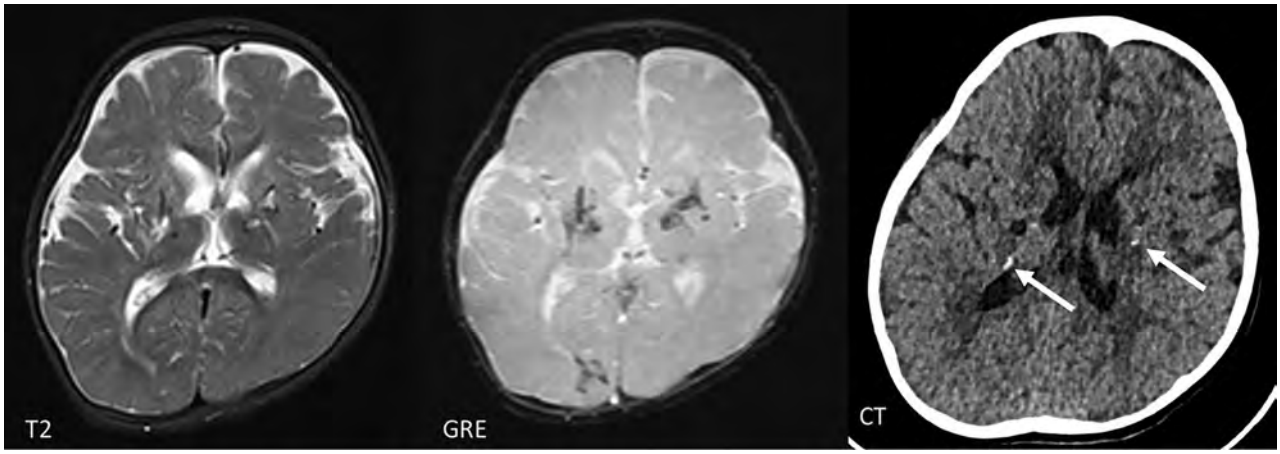

FIG 15. Hemosiderin-lined cavities in the basal ganglia and thalamus and subtle periventricular calcification on CT (*white arrows*) in a 3-year-old boy with a *COL4A1* mutation.

mutations. A CT scan is recommended when type 1 interferonopathies are suspected and no calcifications are seen on MR imaging. The list of interferonopathies and associated neuroimaging findings will, no doubt, continue to grow as more genotype-phenotype correlations are identified.

As a common feature, all interferons activate the Janus kinase signal transducers of activation and the transcription signaling pathway (Fig 1).[47] There are now several encouraging reports, with Janus kinase inhibitor therapy resulting in a prompt and sustained recovery, sometimes with an improvement or stabilization in imaging appearance.[11,33,34] Reverse-transcriptase inhibitors have also been shown to reduce interferon signaling in patients with AGS.[48] Clinical trials are currently underway. These promising new therapeutic strategies make recognition of these disorders all the more important. As this field continues to grow, neuroimaging is likely to play an increasing role in diagnosis, monitoring, and prognostication.

Disclosures: Felice D'Arco—*UNRELATED*: *Expert Testimony*: expert witness in UK and Ireland; *Payment for Lectures Including Service on Speakers Bureaus*: European Society of Neuroradiology, *Comments*: honoraria for lectures in the European courses of neuroradiology. Cheryl Hemingway—*UNRELATED*: *Consultancy*: pharmaceutical companies, *Comments*: I have provided expert advice on steering groups for the following companies: Roche, Biogen, UCB, Viela Bio, Novartis; *Grants/Grants Pending*: Medical Research Council, *Comments*: I have a research grant for pediatric MS research for some of my salary; *Payment for Lectures Including Service on Speakers Bureaus*: pharmaceutical, *Comments*: I have received money from Novartis for delivering a lecture on Pediatric MS. Kshitij Mankad—*UNRELATED*: *Employment*: Great Ormond Street Hospital, *Comments*: regular post; *Expert Testimony*: medicolegal reporting in the UK; *Payment for Lectures Including Service on Speakers Bureaus*: speaker honoraria, *Comments*: Novartis, Siemens.

REFERENCES

1. Crow YJ, Manel N. **Aicardi–Goutières syndrome and the type I interferonopathies.** *Nat Rev Immunol* 2015;15:429–40 CrossRef Medline
2. Lee-Kirsch MA. **The type I interferonopathies.** *Annu Rev Med* 2017;68:297–315 CrossRef Medline
3. Eleftheriou D, Brogan PA. **Genetic interferonopathies: an overview.** *Best Pract Res Clin Rheumatol* 2017;31:441–59 CrossRef Medline
4. Volpi S, Picco P, Caorsi R, et al. **Type I interferonopathies in pediatric rheumatology.** *Pediatr Rheumatol Online* 2016;14:35 CrossRef Medline
5. McGlasson S, Jury A, Jackson A, et al. **Type I interferon dysregulation and neurological disease.** *Nat Rev Neurol* 2015;11:515–23 CrossRef Medline
6. Aicardi J, Goutières F. **A progressive familial encephalopathy in infancy with calcifications of the basal ganglia and chronic cerebrospinal fluid lymphocytosis.** *Ann Neurol* 1984;15:49–54 CrossRef Medline
7. Crow YJ, Chase DS, Schmidt JL, et al. **Characterization of human disease phenotypes associated with mutations in TREX1, RNASEH2A, RNASEH2B, RNASEH2C, SAMHD1, ADAR, and IFIH1.** *Am J Med Genet* 2015;167:296–312 CrossRef Medline
8. Clarke SL, Robertson L, Rice GI, et al. **Type 1 interferonopathy presenting as juvenile idiopathic arthritis with interstitial lung disease: report of a new phenotype.** *Pediatr Rheumatol Online* 2020;18:37 CrossRef Medline
9. Clarke SL, Pellowe EJ, de Jesus AA, et al. **Interstitial lung disease caused by STING-associated vasculopathy with onset in infancy.** *Am J Respir Crit Care Med* 2016;194:639–42 CrossRef Medline
10. Li J, An S, Du Z. **Familial interstitial lung disease caused by mutation of the STING1 gene.** *Front Pediatr* 2020;8:543 CrossRef Medline
11. Mulhern CM, Hong Y, Omoyinmi E, et al. **Janus kinase 1/2 inhibition for the treatment of autoinflammation associated with heterozygous TNFAIP3 mutation.** *J Allergy Clin Immunol* 2019;144:863–66.e5 CrossRef Medline
12. Schwartz DM, Blackstone SA, Sampaio-Moura N, et al. **Type I interferon signature predicts response to Janus kinase inhibition in haploinsufficiency of A20.** *Ann Rheum Dis* 2020;79:429–31 CrossRef Medline
13. Meuwissen ME, Schot R, Buta S, et al. **Human USP18 deficiency underlies type 1 interferonopathy leading to severe pseudo-TORCH syndrome.** *J Exp Med* 2016;213:1163–74 CrossRef Medline
14. Uzgil B, Scherr EH. **Neuroimaging in Aicardi-Goutieres syndrome.** *Neurology* 2016;86:15–16 CrossRef Medline
15. Uggetti C, Piana RL, Orcesi S, et al. **Aicardi-Goutières syndrome: neuroradiologic findings and follow-up.** *AJNR Am J Neuroradiol* 2009;30:1971–76 CrossRef Medline
16. Uggenti C, Lepelley A, Depp M, et al. **cGAS-mediated induction of type I interferon due to inborn errors of histone pre-mRNA processing.** *Nat Genet* 2020;52:1364–72 CrossRef Medline
17. Livingston J, Crow Y. **Neurologic phenotypes associated with mutations in TREX1, RNASEH2A, RNASEH2B, RNASEH2C, SAMHD1, ADAR1, and IFIH1: Aicard-Goutières syndrome and beyond.** *Neuropediatrics* 2016;47:355–60 CrossRef Medline
18. La Piana R, Uggetti C, Roncarolo F, et al. **Neuroradiologic patterns and novel imaging findings in Aicardi-Goutières syndrome.** *Neurology* 2016;86:28–35 CrossRef Medline
19. Ramesh V, Bernardi B, Stafa A, et al. **Intracerebral large artery disease in Aicardi-Goutières syndrome implicates SAMHD1 in vascular homeostasis: SAMHD1 and intracerebral large**

artery disease. *Dev Med Child Neurol* 2010;52:725–32 CrossRef Medline
20. Livingston JH, Lin JP, Dale RC, et al. **A type I interferon signature identifies bilateral striatal necrosis due to mutations in ADAR1.** *J Med Genet* 2014;51:76–82 CrossRef Medline
21. Ma L, Zhou Y, Zhang Y, et al. **Role of A20 in interferon-α-mediated functional restoration of myeloid dendritic cells in patients with chronic hepatitis C.** *Immunology* 2014;143:670–78 CrossRef Medline
22. Gilani A, Adang LA, Vanderver A, et al. **Neuropathological findings in a case of IFIH1-related Aicardi-Goutières syndrome.** *Pediatr Dev Pathol* 2019;22:566–70 CrossRef Medline
23. Barth PG. **The neuropathology of Aicardi-Goutières syndrome.** *Eur J Paediatr Neurol* 2002;6(Suppl A):A27–31; discussion A37–39, A77–86 CrossRef Medline
24. Klok MD, Bakels HS, Postma NL, et al. **Interferon-α and the calcifying microangiopathy in Aicardi-Goutières syndrome.** *Ann Clin Transl Neurol* 2015;2:774–79 CrossRef Medline
25. Piccoli C, Bronner N, Gavazzi F, et al. **Late-onset Aicardi Goutières syndrome: a characterization of presenting clinical features.** *Pediatr Neurol* 2021;115:1–6 CrossRef Medline
26. Vanderver A, Prust M, Kadom N, et al. **Early-onset Aicardi-Goutières Syndrome: magnetic resonance imaging (MRI) pattern recognition.** *J Child Neurol* 2015;30:1343–48 CrossRef Medline
27. Abdel-Salam GM, Abdel-Hamid MS, Mohammad SA, et al. **Aicardi-Goutières syndrome: unusual neuro-radiological manifestations.** *Metab Brain Dis* 2017;32:679–83 CrossRef Medline
28. Wu CC, Peng SS, Lee WT. **Intracerebral large artery disease in Aicardi-Goutières syndrome with TREX1 mutation: a case report.** *Neurol Sci* 2020;41:3353–56 CrossRef Medline
29. La Piana R, Uggetti C, Olivieri I, et al. **Bilateral striatal necrosis in two subjects with Aicardi-Goutières syndrome due to mutations in ADAR1 (AGS6).** *Am J Med Genet A* 2014;164A:815–19 CrossRef Medline
30. Vedrenne V, Gowher A, De Lonlay P, et al. **Mutation in PNPT1, which encodes a polyribonucleotide nucleotidyltransferase, impairs RNA import into mitochondria and causes respiratory-chain deficiency.** *Am J Hum Genet* 2012;91:912–18 CrossRef Medline
31. Cirillo G, Cirillo M, Panetsos F, et al. **Selective vulnerability of basal ganglia: insights into the mechanisms of bilateral striatal necrosis.** *J Neuropathol Exp Neurol* 2019;78:123–19 CrossRef Medline
32. Weerasekare J, Kassa R, Keegan BM. **Retinal vasculopathy with cerebral leukoencephalopathy due to TREX-1 mutation: an important mimicker of CNS inflammatory disease.** *Mult Scler Relat Disord* 2021;47:102639 CrossRef Medline
33. Alsohime F, Martin-Fernandez M, Temsah MH, et al. **Janus kinase inhibitor therapy in a child with inherited USP18 deficiency.** *N Engl J Med* 2020;382:256–65 CrossRef Medline
34. Duncan CJ, Thompson B, Chen R, et al. **Severe type I interferonopathy and unrestrained interferon signaling due to a homozygous germline mutation in STAT2.** *Sci Immunol* 2019;4:eaav7501 CrossRef Medline
35. Livingston JH, Stivaros S, Warren D, et al. **Intracranial calcification in childhood: a review of aetiologies and recognizable phenotypes.** *Dev Med Child Neurol* 2014;56:612–26 CrossRef Medline
36. Rönnblom L, Leonard D. **Interferon pathway in SLE: one key to unlocking the mystery of the disease.** *Lupus Sci Med* 2019;6:e000270 CrossRef Medline
37. Kim H, Gunter-Rahman F, McGrath JA, et al. **Expression of interferon-regulated genes in juvenile dermatomyositis versus Mendelian autoinflammatory interferonopathies.** *Arthritis Res Ther* 2020;22:69 CrossRef Medline
38. Al-Obaidi M, Saunders D, Brown S, et al. **Evaluation of magnetic resonance imaging abnormalities in juvenile onset neuropsychiatric systemic lupus erythematosus.** *Clin Rheumatol* 2016;35:2449–56 CrossRef Medline
39. Lalani TA, Kanne JP, Hatfield GA, et al. **Imaging findings in systemic lupus erythematosus.** *Radiographics* 2004;24:1069–86 CrossRef Medline
40. Panagopoulos D, Themistocleous M. **Central nervous system manifestation of lupus erythematosus resembling brain abscess.** *Int J Pediatr Adolesc Med* 2019;6:29–37 CrossRef Medline
41. Klein C, Kleinschmidt-DeMasters BK, Liang X, et al. **A review of neuropathological features of familial and adult hemophagocytic lymphohistiocytosis.** *J Neuropathol Exp Neurol* 2019;78:197–208 CrossRef Medline
42. Koob M, Laugel V, Durand M, et al. **Neuroimaging in Cockayne syndrome.** *AJNR Am J Neuroradiol* 2010;31:1623–30 CrossRef Medline
43. Livingston J, Doherty D, Orcesi S, et al. **COL4A1 mutations associated with a characteristic pattern of intracranial calcification.** *Neuropediatrics* 2011;42:227–33 CrossRef Medline
44. Grangeon L, Wallon D, Charbonnier C, et al; French PFBC study group. **Biallelic MYORG mutation carriers exhibit primary brain calcification with a distinct phenotype.** *Brain* 2019;142:1573–86 CrossRef Medline
45. LeBlanc MA, Penney LS, Gaston D, et al. **A novel rearrangement of occludin causes brain calcification and renal dysfunction.** *Hum Genet* 2013;132:1223–34 CrossRef Medline
46. Tonduti D, Orcesi S, Jenkinson EM, et al. **Clinical, radiological and possible pathological overlap of cystic leukoencephalopathy without megalencephaly and Aicardi-Goutières syndrome.** *Eur J Paediatr Neurol* 2016;20:604–10 CrossRef Medline
47. Prinz M, Knobeloch KP. **Type I interferons as ambiguous modulators of chronic inflammation in the central nervous system.** *Front Immun* 2012;3:67 CrossRef Medline
48. Rice GI, Meyzer C, Bouazza N, et al. **Reverse-transcriptase inhibitors in the Aicardi–Goutières syndrome.** *N Engl J Med* 2018;379:2275–77 CrossRef

Glutamine Imaging: A New Avenue for Glioma Management

S. Ekici, J.A. Nye, S.G. Neill, J.W. Allen, H.-K. Shu, and C.C. Fleischer

ABSTRACT

SUMMARY: The glutamine pathway is emerging as an important marker of cancer prognosis and a target for new treatments. In gliomas, the most common type of brain tumors, metabolic reprogramming leads to abnormal consumption of glutamine as an energy source, and increased glutamine concentrations are associated with treatment resistance and proliferation. A key challenge in the development of glutamine-based biomarkers and therapies is the limited number of in vivo tools to noninvasively assess local glutamine metabolism and monitor its changes. In this review, we describe the importance of glutamine metabolism in gliomas and review the current landscape of translational and emerging imaging techniques to measure glutamine in the brain. These techniques include MRS, PET, SPECT, and preclinical methods such as fluorescence and mass spectrometry imaging. Finally, we discuss the roadblocks that must be overcome before incorporating glutamine into a personalized approach for glioma management.

ABBREVIATIONS: ASCT2 = alanine, serine, cysteine transporter 2; ^{11}C-Gln = 5-^{11}C-(2S)-glutamine; DMI = deuterium metabolic imaging; [^{18}F]-FGln = 4-[^{18}F]-(2S,4R)-fluoroglutamine; 2-HG = 2-hydroxyglutarate; *IDH* = *isocitrate dehydrogenase*; MSI = mass spectrometry imaging; mTOR = mechanistic target of rapamycin; NMR = nuclear MR; PRESS = point-resolved spectroscopy; TCA = tricarboxylic acid

Abnormal Glutamine Metabolism in Gliomas

Gliomas are one of the most common types of brain tumors, and accurate diagnosis relies on imaging and histology.[1] While histology can identify the tumor grade, *isocitrate dehydrogenase* (*IDH*) mutation status, and other pathologic markers, it requires invasive tissue sampling and is impractical for treatment monitoring. The recent emergence of treatments targeting cancer metabolism in clinical trials, combined with poor prognosis particularly for high-grade gliomas, necessitates new noninvasive metabolic imaging strategies capable of stratifying patients, monitoring treatment response, and prognostication. Here, we describe the importance of glutamine in glioma progression and management, followed by a review of imaging techniques capable of quantifying glutamine concentrations.

A hallmark of many cancers, including gliomas, is metabolic reprogramming that enables cancer cells to divide quickly and evade clearance by remodeling the tumor microenvironment.[2] One of the most common examples of reprogramming is the Warburg effect, evidenced by high rates of glycolysis and lactate production, even in the presence of oxygen. In addition to high glucose consumption, gliomas also have increased rates of glutamine intake and require larger stores of glutamine for survival compared with healthy cells.[3] Glutamine is an important energy substrate and carbon source for cancer cells, and glutamine "addiction" is emerging as a hallmark of many cancers.[4] Glutamine is catabolized to several by-products that aid in cancer proliferation, including glutamate via glutaminolysis and α-ketoglutarate as an intermediate of the tricarboxylic acid (TCA) cycle.[5] Most primary World Health Organization grade II and III infiltrating gliomas and secondary glioblastomas (World Health Organization grade IV) exhibit *IDH* mutations that produce 2-hydroxyglutarate (2-HG) rather than α-ketoglutarate.[5] Glutamine is also a vital nitrogen source for the production of amino acids, nucleotides, fatty acids, and polyamines necessary for proliferation. Cancer cells have an increased demand for nitrogen, and large stores of glutamine enable high rates of synthetic biomass generation and TCA cycle anaplerosis.[4]

The intake of nutrients including glutamine by noncancerous cells is limited by growth factors. In cancer cells, increased consumption of glutamine is, in part, facilitated by oncogenic drivers including Myc and the mechanistic target of rapamycin (mTOR). Myc increases expression of glutamine transporters, modulates expression of glutaminase, and activates enzymes involved in

Received May 5, 2021; accepted after revision August 4.

From the Departments of Radiology and Imaging Sciences (S.E., J.A.N., J.W.A., C.C.F.), Pathology and Laboratory Medicine (S.G.N.), Radiation Oncology (H.-K.S.), and Neurology (J.W.A.), Emory University School of Medicine, Atlanta, Georgia; and Wallace H. Coulter Department of Biomedical Engineering (C.C.F.), Georgia Institute of Technology and Emory University, Atlanta, Georgia.

Please address correspondence to Candace Fleischer, PhD, 1841 Clifton Rd NE, Rm 290, Atlanta, GA 30029; e-mail: candace.fleischer@emory.edu; @fleischer_lab

Indicates open access to non-subscribers at www.ajnr.org

http://dx.doi.org/10.3174/ajnr.A7333

purine and pyrimidine synthesis.[2,4] Myc-induced metabolic reprogramming even precedes MR imaging–observable tumor growth.[6] Mice with Myc-activated hepatocytes display increased expression of genes related to glutamine transport and breakdown in the pretumor state, including glutaminase and glutamine dehydrogenase.[6] Increased mTOR signaling is commonly associated with cancer proliferation and can be activated in cancers with high concentrations of intracellular glutamine mediated through the alanine, serine, cysteine transporter 2 (ASCT2).[7] mTOR stimulates glutaminolysis in cancer cells by increasing the activity of glutamine dehydrogenase and promoting the breakdown of glutamine into TCA cycle intermediates.[4]

Glutamine use in cancer cells varies within and between tumors due to dynamic interactions among the tumor microenvironment, oncogenes, tissue type, and nutrient availability.[5,8] Myc-induced differences in glutamine transporters and glutaminase concentrations result in some gliomas accumulating large stores of glutamine, while others readily catabolize glutamine.[9,10] Gliomas with high rates of glutamine catabolism exhibit metabolic plasticity, resistance to treatment, and a mesenchymal phenotype.[11] Mesenchymal gliomas in mice have increased glutamine concentrations compared with healthy brain tissue and nonmesenchymal glioma subtypes.[12] These results have been demonstrated in patients with gliomas using glutamine-based PET, with high glutamine concentrations observed in progressing gliomas compared with the surrounding brain tissue or clinically stable tumors.[13] Because mesenchymal subtypes are generally associated with worse outcomes, glutamine concentrations may indicate prognosis. Mice treated with chemotherapy show a significant decrease in tumoral glutamine concentrations, supporting the importance of in vivo glutamine quantification after treatment.[13] Increases in glutamine flux, ie, conversion of glutamine to glutamate, have been observed in glioma-bearing mice treated with temozolomide, a potential explanation for glutamine decreases following chemotherapy.[14] Because inhibiting glutamine metabolism limits cancer growth and promotes antitumor immunity in the microenvironment,[15] the glutamine pathway has been identified as a potential marker for progression and treatment response as highlighted in depth in recent reviews.[16,17]

Glutamine as an Emerging Pharmacologic Target

Due to the demonstrated role of glutamine in gliomas, glutamine metabolism is an emerging pharmacologic target, and several compounds targeting glutamine intake or enzymes involved in glutamine catabolism are currently being evaluated in preclinical and early-stage clinical trials.[16] Glutaminase, the primary enzyme that catabolizes glutamine in cells, is the target of both telaglenastat or CB-839 and the small-molecule inhibitor compound 968, both of which have been shown to decrease glioma growth, though CB-839 is more specific to glutaminase.[11] In vitro studies of glutaminase inhibition show depletion of treatment-resistant glioblastoma cells and subsequent reduction of glutamine for downstream use in the TCA cycle.[11] Because these inhibitors are not as effective against gliomas that exhibit a glycolytic phenotype,[10] identifying patients with high levels of tumoral glutamine may aid in the prognostication and stratification of patients, particularly for emerging treatments such as glutamine pathway inhibitors. CB-839 is currently being evaluated in a Phase Ib clinical trial in combination with chemotherapy and radiation for treatment of *IDH*-mutant astrocytomas and anaplastic astrocytomas.[18] A promising glutamine antagonist, 6-diazo-5-oxo-L-norleucin, has also shown efficacy in inhibiting glutaminolysis in humans.[16] While these treatments hold promise, the standard of care treatment for gliomas is maximal surgical excision followed by radiation therapy with concurrent and adjuvant chemotherapy.

Characterizing and Quantifying Glutamine Metabolism

Quantifying glutamine in vivo using translational imaging techniques may be useful in identifying glutamine as a biomarker, stratifying patients for novel therapies particularly inhibitors of glutamine metabolism, and accelerating translation of emerging treatments to the clinic. While in vitro experiments are the first step in validating novel treatments targeting glutamine metabolism, they do not fully capture the heterogeneity and complexity of the local tumor environment.[19] Metabolic phenotypes depend on dynamic interactions between cancer cells and surrounding cells, tissue type, nutrient availability, inflammatory cells, and genetic landscape; in vivo glutamine monitoring is necessary to fully understand its role as a potential prognostic biomarker. Advances in metabolic imaging modalities including MRS, PET, SPECT, and emerging preclinical techniques such as mass spectrometry imaging (MSI) and fluorescence imaging facilitate in vivo measurements of glutamine metabolism in gliomas. Advantages and limitations of imaging techniques capable of measuring glutamine are reviewed below within the context of glioma management.

Glutamine Imaging Techniques

^{1}H-MRS. MR imaging is a key diagnostic method for gliomas and provides anatomic information on tumor size and location. MRS is a complementary but less used method capable of noninvasively quantifying multiple metabolites simultaneously using the same MR imaging hardware.[20] MRS does not require an exogeneous contrast agent with the exception of hyperpolarized MRS (see "Hyperpolarized ^{13}C-MRS") and relies most commonly on endogenous ^{1}H nuclei. Current MRS research in gliomas is largely focused on detection of 2-HG as a marker for *IDH* mutations along with decreased NAA and increased choline, lactate, and lipids.[20] Metabolites related to glutamine metabolism can also be detected using MRS, including glutamine, glutamate, alanine, and glutathione.[20] One advantage of MRS is the ability to use its ex vivo and in vitro analog, nuclear MR (NMR) spectroscopy, to identify and evaluate promising biomarkers before clinical translation. NMR spectroscopy can detect low metabolite concentrations and overlapping peaks not possible with in vivo MRS and has been used to show that increases in alanine, glutamate, and lactate correlate with lower survival and higher tumor grade in intact glioma tissue.[21]

In vivo, MRS is capable of quantifying localized metabolite concentrations as low as ~1 mM on the minute timescale (Fig 1*A*–*C*).[22] Tumor concentrations of glutamine measured at 7T as high as 5.5 mM have been reported in patients with gliomas.[23] Glutamine concentrations measured with MRS in normal-appearing contralateral white matter in patients with glioblastoma have been reported to be ~3.4 mM, significantly higher than in healthy

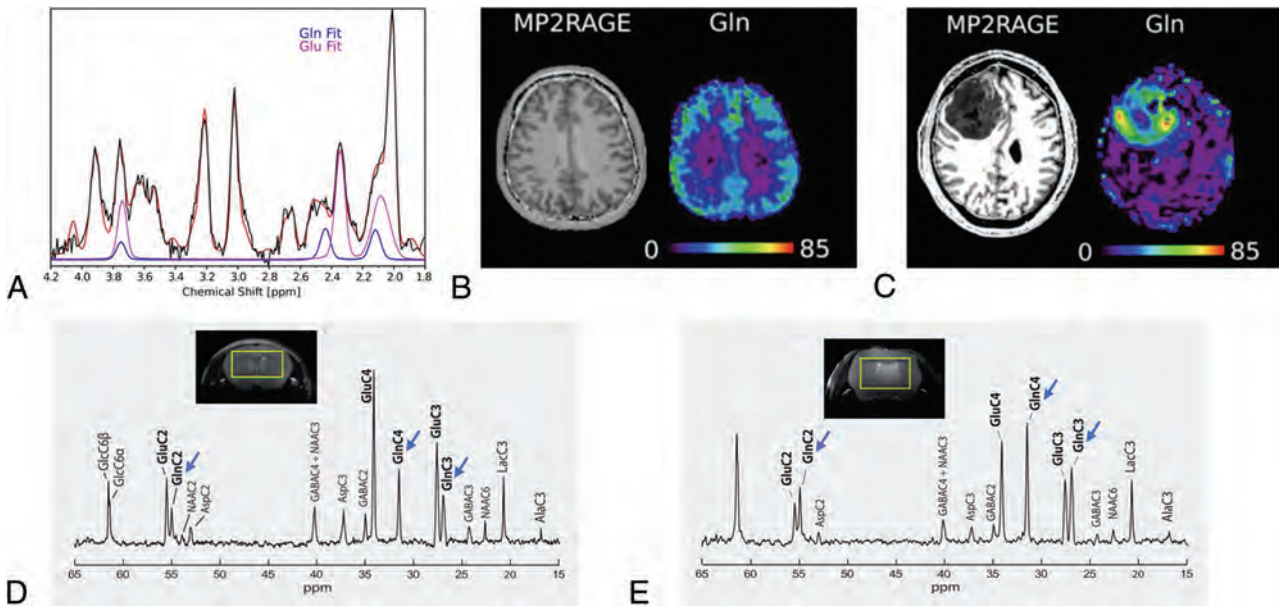

FIG 1. ^{1}H- and ^{13}C-MR spectra of healthy brain and glioma tissue. *A*, ^{1}H-MR spectrum acquired at 7T using a 3D MR spectroscopic imaging sequence in a healthy human volunteer. Glutamine and glutamate peak fits are shown in blue and pink, respectively, demonstrating separation at 7T. *B*, Structural MP2RAGE image and glutamine metabolite map acquired in the same subject as in *A*. The *Color bar* shows metabolite concentrations in arbitrary units. *C*, Structural MP2RAGE image and a glutamine metabolite map acquired in a male patient with glioblastoma (51 years of age). The *Color bar* shows metabolite concentrations in arbitrary units. Glutamine concentrations are increased in the tumor region, indicated by the *dark mass* in the MP2RAGE image, relative to the rest of the brain. *A–C* adapted and reprinted with permission from Hingerl et al.[22] *D*, ^{13}C-MR spectrum acquired in a healthy mouse brain at 14.1T after 3 hours of infusion with [1,6-^{13}C]-glucose. *E*, ^{13}C-MR spectrum acquired from a tumor-bearing mouse brain after 3 hours of infusion of [1,6-^{13}C]-glucose. Decreased glutamate peak intensities (carbon [C]2, C3, and C4) and glutamine peak intensities (C2, C3, and C4) are observed compared with healthy brain without tumor (*blue arrows*). *D* and *E* adapted and reprinted with permission from Lai et al.[30] Ala indicates alanine; Asp, aspartate; GABA, γ-aminobutyric acid; Glc, glucose; Gln, glutamine; Glu, glutamate; Lac, lactate; NAA, *N*-acetylaspartate.

controls (2.7 mM) or patients with low-grade gliomas (2.4 mM), suggesting the ability of MRS to detect early infiltration in normal-appearing regions.[24] Single-voxel MRS (~8 cm^3) and multivoxel MRS are the most common clinical implementations available on many MR imaging scanners, but whole-brain MRS has also been demonstrated in gliomas.[25] MRS has been used to quantify changes in metabolites as a result of metabolic reprogramming, differentiate proliferative gliomas from brain metastasis, and predict tumor grade.[25,26] Longitudinal ^{1}H-MRS studies in patients with glioblastomas showed that pretreatment increases in glutamine plus glutamate were correlated with tumor proliferation and poor prognosis.[27]

While MRS has the benefits of repeatability, lack of ionizing radiation, and availability at many clinical sites, separating overlapping glutamine and glutamate resonances in ^{1}H-MR spectra acquired at typical clinical field strengths (1.5T or 3T) can be challenging.[20] The commonly used point-resolved spectroscopy (PRESS) sequence with a TE of 20 ms at 3T has been shown to detect both glutamine and glutamate with quantification comparable with that of spectra acquired on 7T MR imaging scanners;[28] however, higher-field-strength scanners facilitate improved signal-to-noise ratios and better peak separation.[29] In vivo studies using high-field MR imaging scanners have demonstrated significantly higher glutamine levels in glioma-bearing mice at the onset of neurologic symptoms compared with presymptomatic mice.[30] With recent FDA approval of both Siemens (Magnetom Terra) and GE (Signa) 7T MR scanners, MRS has the potential to become a viable method for routine glutamine imaging.

Further advances in ^{1}H-MRS methods have improved the detection of glutamine and separation from glutamate peaks. Chemical exchange saturation transfer, which measures chemical exchange between bulk water and metabolites, has been shown to facilitate quantification of glutamate in response to CB-839 treatment in breast cancer,[31] and glutamine chemical exchange saturation transfer has been used for pH monitoring in animal models of brain tumors.[32] Spectral editing techniques can separate overlapping peak resonances in 1D spectra and have been used to detect γ-aminobutyric acid, 2-HG, and glutathione.[33-35] Most spectral editing techniques use *J*-difference editing to isolate the signal of interest. For example, a *J*-modulated spectroscopy method was shown to separate glutamine from glutamate in spectra acquired at 3T in healthy adult brains.[35] Emerging single-step spectral editing methods have been demonstrated for simultaneous quantification of glutamine, glutamate, and glutathione at 7T in healthy adults.[34] Because increased glutamine and glutamate in gliomas correlate with increased proliferation and glutathione is implicated in treatment resistance, further evaluation in patients with gliomas undergoing treatment is warranted.[34,36] While 2D techniques, including localized correlational spectroscopy and *J*-PRESS, have also enabled separation of glutamine from glutamate,[37] long scan times have relegated many 2D sequences to research applications.

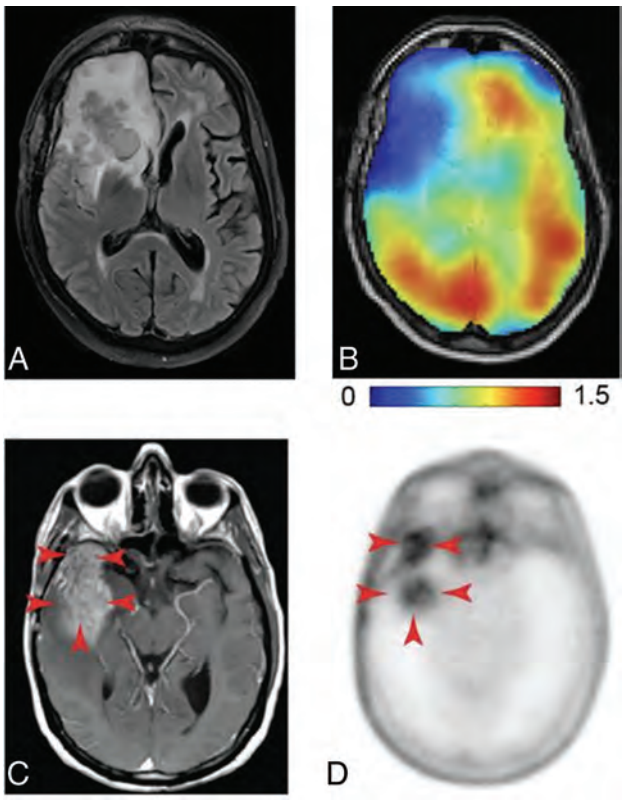

FIG 2. DMI and PET images of glutamine metabolism in gliomas. *A*, T2-weighted FLAIR MR image acquired in a patient with a glioblastoma with a tumor in the right frontal lobe. *B*, DMI maps of the same section position as in *A* showing ^{2}H-labeled glutamine + glutamate, with lower concentrations in the tumor region compared with normal-appearing brain tissue. *Color bar* is in millimolar units. *A* and *B* reprinted with permission from DeFeyter et al[41] and used under the CC BY-NC license 4.0. *C*, TI-weighted MR image with contrast enhancement acquired in a patient with glioblastoma. The tumor region is indicated with *red arrows*. *D*, 4-[^{18}F]-FGln PET image acquired in the same patient as in *C*, with high uptake in the tumor region (*red arrows*) and minimal background uptake. *C* and *D* reprinted from Venneti et al,[13] with permission from AAAS.

Hyperpolarized ^{13}C-MRS. ^{13}C-MRS has been used to study the brain; however, due to low sensitivity from limited natural abundance and a low gyromagnetic ratio, hyperpolarized ^{13}C is required in vivo. Hyperpolarization increases ^{13}C-signal temporarily via dynamic nuclear polarization.[38] After infusion with a hyperpolarized ^{13}C-labeled substrate, the flux of the labeled substrate to its metabolic products can be measured (Fig 1*D*, *-E*).[30] One of the most commonly studied ^{13}C metabolites is [1-^{13}C]-pyruvate, which is catabolized into lactate, alanine, and bicarbonate in cells and provides a useful tool to monitor the by-products of glycolysis.[38] [1-^{13}C]-pyruvate has been used in patients with gliomas to measure the conversion of pyruvate to lactate, with high rates of lactate production observed in recurrent tumors.[39] Hyperpolarized ^{13}C tracers have been developed for glucose, acetate, α-ketoglutarate, and glutamine, all of which have demonstrated blood-brain barrier permeability necessary for hyperpolarized MRS experiments.[38] ^{13}C-MRS has been used to assess changes in glutamine metabolism in response to treatments. Subramani et al[14] showed that glioma-bearing mice injected with [3–^{13}C]-glutamine convert glutamine to glutamate at higher rates after treatment with temozolomide. This increase in glutamate was also observed using ^{1}H-MRS on the same mice.[14] Similarly, Molloy et al[40] used [3–^{13}C]-glutamine and demonstrated an increase in conversion of glutamine to glutamate in glioma cells in response to a downstream inhibitor of glutamine metabolism. These studies highlight the potential of hyperpolarized ^{13}C-MRS studies to monitor glutamine metabolites both for validating ^{1}H-MRS findings and evaluating the response to treatment. While an on-site hyperpolarizer is required and short T1 relaxation times require rapid imaging for most ^{13}C tracers, ^{13}C-MRS facilitates direct measurement of glutamine metabolism without the use of an ionizing tracer.

Deuterium Metabolic Imaging. In vivo deuterium metabolic imaging (DMI) is an emerging MRS technique that measures ^{2}H-labeled substrates. ^{2}H-MRS has been primarily demonstrated to detect labeled glucose and its metabolic products including glutamine, glutamate, and lactate (Fig 2*A*, *-B*).[41] In rats and humans, DMI has revealed metabolic differences between gliomas and healthy tissue, with glioma tissue exhibiting lower levels of glutamine plus glutamate and higher levels of lactate and glucose due to the Warburg effect.[41] While DMI has been used in vivo to image and quantify glucose metabolism and flux through the TCA cycle, separation of glutamine and glutamate, even at high magnetic field strengths, is challenging. Moreover, the gyromagnetic ratio of ^{2}H is ~7 times lower than ^{1}H and requires ingestion or injection of a ^{2}H-labeled substrate. DMI technology is improving quickly and provides a noninvasive method of quantifying active metabolism in vivo.[42]

MRS Limitations and Considerations. MRS, while not standard clinical practice, is frequently used in patients with gliomas. Currently, it is most often ordered by clinicians to characterize increasing enhancement after previous radiation therapy and to distinguish radiation-induced necrosis from recurrent tumor. Limitations of MRS include nonstandardized analysis, challenges with reproducibility, the need for input by the radiologist for voxel placement, low signal-to-noise ratios, and long acquisition times. Optimization of in vivo glutamine quantification with MRS, combined with improved postprocessing methods, is an immediate goal.[43,44] Fast, whole-brain MRS to generate spatial glutamine maps is likely necessary before incorporation of MRS into routine clinical workflow. Most important, MRS, while FDA-approved, is still considered investigational by most insurance companies, and lack of reimbursement has limited widespread clinical implementation. As more data emerge regarding the value of quantifying glutamine for gliomas, MRS will be increasingly recognized and recommended by clinicians and radiologists, possibly working to counter this issue. For a comprehensive review of clinical MRS, we direct readers to de Graaf et al[42] and Wilson et al.[43]

Glutamine PET. FDG-PET has been used clinically for tumor grading, determining tumor boundaries, and guiding biopsies.[45] PET has high sensitivity and spatial and temporal resolution (3–5 mm on the second timescale); however, specificity is limited by uptake of FDG in healthy brain as well as tumors.[45] A recently developed glutamine fluoro-analog, 4-[^{18}F]-(2S,4R)-fluoroglutamine ([^{18}F]-FGln) has enabled noninvasive imaging of glutamine in gliomas

(Fig 2*C*, *-D*).[13] Mice and humans with gliomas show high [^{18}F]-FGln uptake in tumors, and [^{18}F]-FGln PET may distinguish actively growing gliomas from stable tumors.[13] In a study of mice with gliomas, tumor-to-background ratios of 3.6 were observed, indicating increased [^{18}F]-FGln in tumor compared with healthy tissue.[46] A study of 14 patients with cancer metastasis to the brain showed significantly higher [^{18}F]-FGln PET activity in the tumor relative to healthy brain tissue compared with FDG-PET, indicating the potential utility of glutamine PET.[47] In a Phase I clinical trial, [^{18}F]-FGln PET was able to identify tumors with genetic precursors to glutamine addiction, including *IDH* and *tumor protein 53* mutations in several cancers including gliomas.[48]

Glutamine PET tracers may be advantageous for identifying gliomas exhibiting glutamine addiction and stratifying patients for treatment. In mice, gliomas treated with chemotherapy exhibited significantly decreased [^{18}F]-FGln uptake compared with pretreatment tumors.[13] Similar results were also observed in mice with breast, colorectal, and lung cancer treated with the V-9302, an inhibitor of glutamine transporter ASCT2.[49] However, pharmacokinetic studies indicate that [^{18}F]-FGln is defluorinated and metabolized quickly.[46] [^{18}F]-FGln derivatives have been developed to improve the stability of the tracers in vivo to address this limitation. [^{18}F]-fluoroboronoglutamine has improved stability in mice, though the efficacy in glioma models is yet to be determined.[50]

In addition to [^{18}F]-FGln, two dipeptide glutamine PET tracers, [^{18}F]-Gly-(2*S*,4*R*)4-fluoroglutamine and [^{18}F]-Ala-(2*S*,4*R*)4-fluoroglutamine, have been developed with improved in vivo stability. After injection of the tracers in mice with gliosarcomas, tracers were localized in the tumors and [^{18}F]Ala-(2*S*,4*R*)4-fluoroglutamine displayed a similar distribution and tumor-to-background ratio compared with [^{18}F]-FGln. [^{18}F]-Ala-(2*S*,4*R*)4-fluoroglutamine may be comparable with the [^{18}F]-FGln PET tracer; however, further validation in clinical trials is necessary.[51] In addition to [^{18}F]-FGln, the ^{11}C-glutamine PET tracer 5-^{11}C-(2*S*)-glutamine (^{11}C-Gln) has also been developed. In the first in-human study, Cohen et al[52] evaluated the utility of ^{11}C-Gln in tracking treatment response to CB-839 as part of a clinical trial evaluating glutamine inhibitors for treatment of colorectal cancer. Preliminary results revealed the utility of ^{11}C-Gln in identifying heterogeneous glutamine uptake by lesions; however, the intrinsically shorter half-life of ^{11}C-Gln compared with [^{18}F]-FGln may limit its utility. Further comparisons of the in vivo kinetics of [^{18}F]-FGln and ^{11}C-Gln tracers in patients with gliomas will be important for determining the utility of ^{11}C-Gln.

PET Limitations and Considerations. While PET may be useful in different stages of glioma care because it provides direct and quantitative information about glutamine metabolism, limitations include the short half-life of labeling isotopes (eg, ^{11}C) requiring an on-site cyclotron, exposure to ionizing radiation, and analysis possibly requiring measurements of labeled glucose or glutamine levels in arterial blood. Many of these limitations can be overcome by development of glutamine analogues labeled with longer-lived isotopes (eg, [^{18}F]) and by using internal reference regions or image-derived input functions to negate the need for arterial blood in the analysis. With the advent of large-FOV PET systems, the increased quantitative sensitivity offered by a full kinetic analysis will become more accessible in the clinical environment.[53] While [^{18}F]-FGln and ^{11}C-Gln tracers are not yet approved by the FDA, FDA approval of amino acid–based PET tracers support the potential and feasibility of glutamine PET,[54] and preliminary work has shown that these agents can discern low- from high-grade gliomas.[55] Ongoing clinical trials will continue to elucidate the safety and efficacy of glutamine PET for gliomas. Further development and validation studies will be increasingly important as glutamine continues to emerge as a marker of prognosis and treatment response.

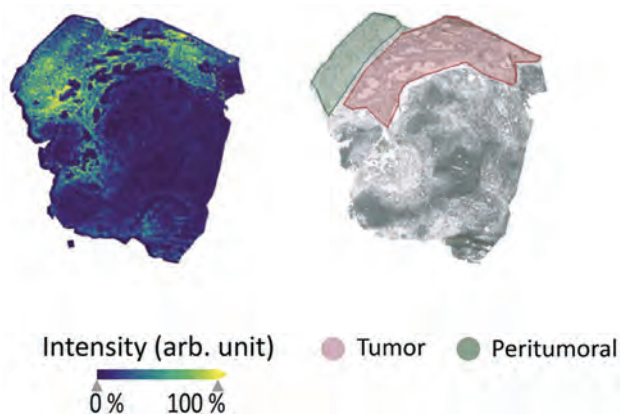

FIG 3. MSI to image glutamine metabolism. Matrix-assisted laser desorption/ionization TOF MSI of glutamine distribution in an ex vivo human glioma sample (*left*), with an annotated brightfield image of the same sample showing the tumor and peritumoral regions (*right*). The MSI map shows increased intensity of glutamine in the tumor regions compared with both peritumoral and nontumoral regions and is a promising emerging method for imaging glutamine. Arb. unit indicates arbitrary unit. Reprinted with permission from Kampa et al[56] and used under the CC BY license 4.0.

Emerging Methods

Emerging methods for glutamine detection, including MSI, fluorescence imaging, and glutamine SPECT, have shown utility in characterizing glutamine metabolism in animal models and may complement clinically integrated methods such as MR imaging and PET. MSI quantifies the spatial distribution of metabolites including glutamine by conducting mass spectrometry experiments of thin tissue slices (Fig 3).[56] MSI of human glioblastoma samples shows significant increases in glutamine, glutamate, and lactate in the tumor region compared with peritumoral and nontumoral regions.[56] Advanced MSI methods including ultra-high-resolution MSI based on Fourier-transform mass spectrometry also reveal heterogeneous distributions of metabolites related to both the TCA cycle and glutamine metabolism in mouse glioblastoma tissue.[57] Another application of MSI is identifying differences in the energetics of glioma molecular subtypes in patient-derived xenografts, which reveal that *IDH*-mutated gliomas have abnormal mitochondrial metabolism compared with *IDH* wild-type gliomas yet do not have significantly different glutamine or glutamate levels.[58] MSI has high molecular specificity and spatial resolution (submillimeter); however, it is currently performed only on ex vivo samples, and acquisition times are long (minutes to hours). While quantifying glutamine in excised tissue is a

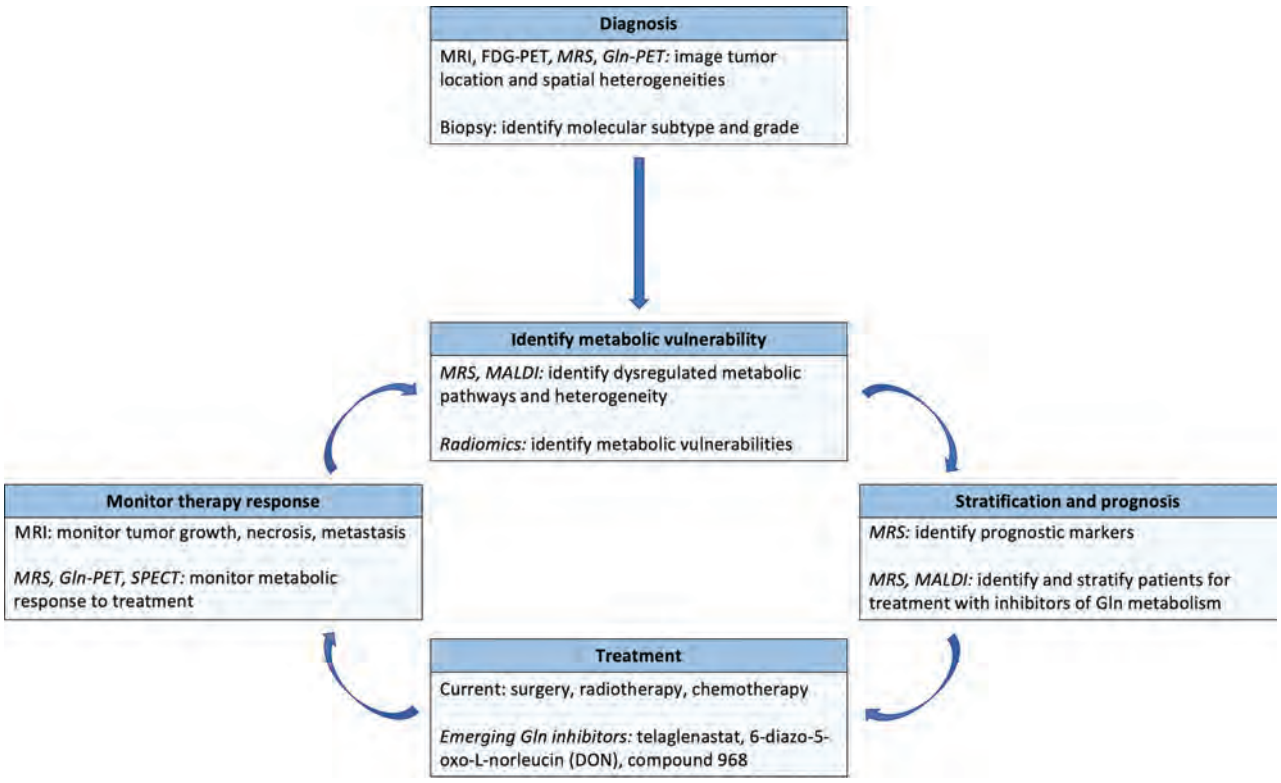

FIG 4. Framework for using glutamine imaging techniques in glioma management. Imaging methods to quantify and measure local glutamine changes may be useful for diagnosis, identification of metabolic vulnerabilities, patient stratification, and improved treatment monitoring. Methods currently not integrated into clinical workflows are indicated with *italics*. MALDI indicates matrix-assisted laser desorption/ionization.

limitation of MSI compared with MR imaging and PET because excised tissue may undergo degradation before metabolite quantification,[59] its high specificity may be used to validate results from MR imaging and PET studies. Furthermore, analysis of excised tissue may also aid pathologists and cancer biologists in characterizing the considerable intratumoral heterogeneity of glioblastoma.[60]

Fluorescence imaging of glutamine and glutamine transporters using optical microscopy and spectroscopy is an emerging method with high spatial resolution (submicron), currently limited to in vitro studies.[61,62] Quantification of glutamine uptake and energy flux has been demonstrated in brain cancer cells in response to epidermal growth factor receptor treatment.[63] Although this technology currently analyzes a small number of cells, proof-of-concept studies to characterize the glutamine response to new treatments are an important first step to motivate larger in vivo studies. Last, new glutamine SPECT tracers have been developed and show promise as clinical tools. Ghoreishi et al[64] conjugated glutamine to technetium Tc99m, a commonly used isotope for SPECT. Mice injected with the nanoconjugate tracer showed significantly higher radioactivity in lung tumors compared with other organs and high stability in human serum. While SPECT is clinically integrated and both fluorescence imaging of glutamine transport and SPECT glutamine tracers are promising, evaluation of these emerging methods in humans is unexplored.

Discussion and Outlook

Targeting glutamine metabolism for improved outcomes in patients with gliomas holds clinical promise, particularly as emerging pharmacologic treatments targeting glutamine catabolism and transport have shown efficacy in vivo (Fig 4).[8] In vivo glutamine quantification is clinically achievable due to advances in noninvasive image acquisition and analysis. Previous studies have shown that glutamine imaging with ^{1}H-MRS, ^{13}C-MRS, and PET has potential prognostic value because concentrations of glutamine and its related metabolites are correlated with decreased survival.[12,13,30] Emerging techniques including MSI and fluorescence imaging may validate MR imaging and PET findings at the single-cell level.[57,62]

In the future, multiple strategies may facilitate evaluation of glutamine as a prognostic marker. The first and most straightforward strategy is the continued standardization and development of MRS and PET for glutamine quantification because both modalities are frequently used in clinical cancer imaging. The second is the use of multiparametric approaches, including radiomics, to use existing clinical data to improve prediction and stratification.[65] Incorporation of metabolic information, including glutamine into radiomics analyses, has been limited; however, radiomics may facilitate the use of the large amount of imaging data often untouched in radiologic practice. The final strategy is advancement of emerging molecular-scale methods, including those outlined here. Given the high cost and limited availability of clinical imaging systems particularly in rural areas, development of low-cost methods is an important goal for the future.

Although glutamine imaging is still largely in the research and development stage, monitoring changes in glutamine metabolism may provide insight into tumor heterogeneity and response to new therapies, enabling stratification for personalized treatment

plans. The development of new treatment strategies, particularly pharmacologic compounds targeting the glutamine pathway, will likely benefit from longitudinal metabolic imaging that includes quantification of local glutamine concentrations. While outstanding challenges in glutamine imaging must be addressed, including standardization and, in some cases, FDA approval, there is clear motivation for the continued investigation and evaluation of glutamine as a promising imaging biomarker of glioma progression, treatment selection and stratification, and prognosis.

Disclosures: Selin Ekici—*UNRELATED*: *Travel/Accommodations/Meeting Expenses Unrelated to Activities Listed*: International Society for Magnetic Resonance in Medicine annual conferences, *Comments*: awarded a waived registration and trainee (educational) stipend for the 2019 and 2020 annual meetings. Jonathon A. Nye—*UNRELATED*: *Employment*: Emory University School of Medicine.

REFERENCES

1. Reni M, Mazza E, Zanon S, et al. **Central nervous system gliomas.** *Crit Rev Oncol Hematol* 2017;113:213–34 CrossRef Medline
2. Pavlova NN, Thompson CB. **The emerging hallmarks of cancer metabolism.** *Cell Metab* 2016;23:27–47 CrossRef Medline
3. Hensley CT, Wasti AT, DeBerardinis RJ. **Glutamine and cancer: cell biology, physiology, and clinical opportunities.** *J Clin Invest* 2013;123:3678–84 CrossRef Medline
4. Márquez J, Alonso FJ, Matés JM, et al. **Glutamine addiction in gliomas.** *Neurochem Res* 2017;42:1735–46 CrossRef Medline
5. Vander Heiden MG, DeBerardinis RJ. **Understanding the intersections between metabolism and cancer biology.** *Cell* 2017;168:657–69 CrossRef Medline
6. Hu S, Balakrishnan A, Bok RA, et al. **13C-pyruvate imaging reveals alterations in glycolysis that precede c-Myc-induced tumor formation and regression.** *Cell Metab* 2011;14:131–42 CrossRef Medline
7. Nicklin P, Bergman P, Zhang B, et al. **Bidirectional transport of amino acids regulates mTOR and autophagy.** *Cell* 2009;136:521–34 CrossRef Medline
8. Li T, Copeland C, Le A. **Glutamine metabolism in cancer.** In: Le A, ed. *The Heterogeneity of Cancer Metabolism*. Springer-Verlag International Publishing; 2021:17–38
9. Cluntun AA, Lukey MJ, Cerione RA, et al. **Glutamine metabolism in cancer: understanding the heterogeneity.** *Trends Cancer* 2017;3:169–80 CrossRef Medline
10. Oizel K, Chauvin C, Oliver L, et al. **Efficient mitochondrial glutamine targeting prevails over glioblastoma metabolic plasticity.** *Clin Cancer Res* 2017;23:6292–6304 CrossRef Medline
11. Koch K, Hartmann R, Tsiampali J, et al. **A comparative pharmacometabolomic study of glutaminase inhibitors in glioma stem-like cells confirms biological effectiveness but reveals differences in target-specificity.** *Cell Death Discov* 2020;6:20 CrossRef Medline
12. Oizel K, Yang C, Renoult O, et al. **Glutamine uptake and utilization of human mesenchymal glioblastoma in orthotopic mouse model.** *Cancer Metab* 2020;8:9 CrossRef Medline
13. Venneti S, Dunphy MP, Zhang H, et al. **Glutamine-based PET imaging facilitates enhanced metabolic evaluation of gliomas in vivo.** *Sci Transl Med* 2015;7:274ra17 CrossRef Medline
14. Subramani E, Radoul M, Najac C, et al. **Glutamate is a noninvasive metabolic biomarker of IDH1-mutant glioma response to temozolomide treatment.** *Cancer Res* 2020;80:5098–5108 CrossRef Medline
15. Byun JK, Park M, Lee S, et al. **Inhibition of glutamine utilization synergizes with immune checkpoint inhibitor to promote antitumor immunity.** *Mol Cell* 2020;80:592–606.e8 CrossRef Medline
16. Choi YK, Park KG. **Targeting glutamine metabolism for cancer treatment.** *Biomol Ther (Seoul)* 2018;26:19–28 CrossRef Medline
17. Altman BJ, Stine ZE, Dang CV. **From Krebs to clinic: glutamine metabolism to cancer therapy.** *Nat Rev Cancer* 2016;16:619–34 CrossRef Medline
18. Kizilbash SH, McBrayer S, Port J, et al. **A phase Ib trial of CB-839 (telaglenastat) in combination with radiation therapy and temozolomide in patients with IDH-mutated diffuse astrocytoma and anaplastic astrocytoma (NCT03528642).** *J Clin Oncol* 2019;37:TPS2075 CrossRef
19. Lenting K, Verhaak R, Ter Laan M, et al. **Glioma: experimental models and reality.** *Acta Neuropathol* 2017;133:263–82 CrossRef Medline
20. Öz G, Alger JR, Barker PB, et al; MRS Consensus Group. **Clinical proton MRS in central nervous system disorders.** *Radiology* 2014;270:658–79 CrossRef Medline
21. Ekici S, Risk BB, Neill SG, et al. **Characterization of dysregulated glutamine metabolism in human glioma tissue with 1H NMR.** *Sci Rep* 2020;10:20435 CrossRef Medline
22. Hingerl L, Strasser B, Moser P, et al. **Clinical high-resolution 3D-MR spectroscopic imaging of the human brain at 7 T.** *Invest Radiol* 2020;55:239–48 CrossRef Medline
23. Ganji SK, An Z, Tiwari V, et al. **In vivo detection of 2-hydroxyglutarate in brain tumors by optimized point-resolved spectroscopy (PRESS) at 7T.** *Magn Reson Med* 2017;77:936–44 CrossRef Medline
24. Kallenberg K, Bock HC, Helms G, et al. **Untreated glioblastoma multiforme: increased myo-inositol and glutamine levels in the contralateral cerebral hemisphere at proton MRS.** *Radiology* 2009;253:805–12 CrossRef Medline
25. Cordova JS, Shu HK, Liang Z, et al. **Whole-brain spectroscopic MRI biomarkers identify infiltrating margins in glioblastoma patients.** *Neuro Oncol* 2016;18:1180–89 CrossRef Medline
26. Ohba S, Murayama K, Abe M, et al. **Magnetic resonance imaging and proton magnetic resonance spectroscopy for differentiating between enhanced gliomas and malignant lymphomas.** *World Neurosurg* 2019;127:e779–87 CrossRef Medline
27. Heintz A, Chombar J, Boussida S, et al. **P14.92 study of glutaminergic and glutamatergic metabolism in 1H-MRS monovoxel in the most aggressive part of 62 glioblastoma before and after 18 months treatment.** *Neuro Oncol* 2019;21(Suppl 3):iii89 CrossRef
28. Bell T, Goerzen D, Near J, et al. **Examination of methods to optimize glutamate-glutamine separation at 3T.** In: *Proceedings of the International Society for Magnetic Resonance in Medicine*, Virtual. August 8–14, 2020
29. Pradhan S, Bonekamp S, Gillen JS, et al. **Comparison of single voxel brain MRS at 3T and 7T using 32-channel head coils.** *Magn Reson Imaging* 2015;33:1013–18 CrossRef Medline
30. Lai M, Vassallo I, Lanz B, et al. **In vivo characterization of brain metabolism by 1H MRS, 13C MRS and 18FDG PET reveals significant glucose oxidation of invasively growing glioma cells.** *Int J Cancer* 2018;143:127–38 CrossRef Medline
31. Zhou R, Bagga P, Nath K, et al. **Glutamate-weighted chemical exchange saturation transfer magnetic resonance imaging detects glutaminase inhibition in a mouse model of triple-negative breast cancer.** *Cancer Res* 2018;78:5521–26 CrossRef Medline
32. Harris RJ, Cloughesy TF, Liau LM, et al. **pH-weighted molecular imaging of gliomas using amine chemical exchange saturation transfer MRI.** *Neuro Oncol* 2015;17:1514–24 CrossRef Medline
33. An L, Araneta MF, Johnson C, et al. **Simultaneous measurement of glutamate, glutamine, GABA, and glutathione by spectral editing without subtraction.** *Magn Reson Med* 2018;80:1776–86 CrossRef Medline
34. An L, Araneta MF, Victorino M, et al. **Signal enhancement of glutamine and glutathione by single-step spectral editing.** *J Magn Reson* 2020;316:106756 CrossRef Medline
35. Zhang Y, Shen J. **Simultaneous quantification of glutamate and glutamine by J-modulated spectroscopy at 3 Tesla.** *Magn Reson Med* 2016;76:725–32 CrossRef Medline
36. Olivier C, Oliver L, Lalier L, et al. **Drug resistance in glioblastoma: the two faces of oxidative stress.** *Front Mol Biosci* 2020;7:620677 Medline

37. Arm J, Al-Iedani O, Quadrelli S, et al. **Reliability of neurometabolite detection with two-dimensional localized correlation spectroscopy at 3T.** *J Magn Reson Imaging* 2018;48:1559–69 CrossRef Medline
38. Wang ZJ, Ohliger MA, Larson PE, et al. **Hyperpolarized 13C MRI: state of the art and future directions.** *Radiology* 2019;291:273–84 CrossRef Medline
39. Miloushev VZ, Granlund KL, Boltyanskiy R, et al. **Metabolic imaging of the human brain with hyperpolarized 13C pyruvate demonstrates 13C lactate production in brain tumor patients.** *Cancer Res* 2018;78:3755–60 CrossRef Medline
40. Molloy AR, Najac C, Viswanath P, et al. **MR-detectable metabolic biomarkers of response to mutant IDH inhibition in low-grade glioma.** *Theranostics* 2020;10:8757–70 CrossRef Medline
41. De Feyter HM, Behar KL, Corbin ZA, et al. **Deuterium metabolic imaging (DMI) for MRI-based 3D mapping of metabolism in vivo.** *Sci Adv* 2018;4:eaat7314 CrossRef Medline
42. de Graaf RA, Hendriks AD, Klomp DW, et al. **On the magnetic field dependence of deuterium metabolic imaging.** *NMR Biomed* 2020;33: e4235 CrossRef Medline
43. Wilson M, Andronesi O, Barker PB, et al. **Methodological consensus on clinical proton MRS of the brain: review and recommendations.** *Magn Reson Med* 2019;82:527–50 CrossRef Medline
44. Sung D, Risk BB, Owusu-Ansah M, et al. **Optimized truncation to integrate multi-channel MRS data using rank-R singular value decomposition.** *NMR Biomed* 2020;33:e4297 CrossRef Medline
45. Albert NL, Weller M, Suchorska B, et al. **Response Assessment in Neuro-Oncology Working Group and European Association for Neuro-Oncology recommendations for the clinical use of PET imaging in gliomas.** *Neuro Oncol* 2016;18:1199–208 CrossRef Medline
46. Miner MW, Liljenbäck H, Virta J, et al. **(2S, 4R)-4-[(18)F] fluoroglutamine for on vivo PET imaging of glioma xenografts in mice: an evaluation of multiple pharmacokinetic models.** *Mol Imaging Biol* 2020;22:969–78 CrossRef Medline
47. Xu X, Zhu H, Liu F, et al. **Imaging brain metastasis patients with 18F-(2S,4R)-4-fluoroglutamine.** *Clin Nucl Med* 2018;43:e392–99 CrossRef Medline
48. Dunphy MPS, Harding JJ, Venneti S, et al. **In vivo PET assay of tumor glutamine flux and metabolism: in-human trial of (18)F-(2S,4R)-4-fluoroglutamine.** *Radiology* 2018;287:667–75 CrossRef Medline
49. Schulte ML, Fu A, Zhao P, et al. **Pharmacological blockade of ASCT2-dependent glutamine transport leads to antitumor efficacy in preclinical models.** *Nat Med* 2018;24:194–202 CrossRef Medline
50. Li C, Liu H, Duan D, et al. **Preclinical study of an 18F-labeled glutamine derivative for cancer imaging.** *Nucl Med Biol* 2018;64-65:34–40 CrossRef Medline
51. Zha Z, Ploessl K, Lieberman BP, et al. **Alanine and glycine conjugates of (2S,4R)-4-[18F]fluoroglutamine for tumor imaging.** *Nucl Med Biol* 2018;60:19–28 CrossRef Medline
52. Cohen AS, Grudzinski J, Smith GT, et al. **First-in-human PET imaging and estimated radiation dosimetry of L-[5-^{11}C]-glutamine in patients with metastatic colorectal cancer.** *J Nucl Med* 2021 April 30. [Epub ahead of print] CrossRef Medline
53. Dimitrakopoulou-Strauss A, Pan L, Sachpekidis C. **Kinetic modeling and parametric imaging with dynamic PET for oncological applications: general considerations, current clinical applications, and future perspectives.** *Eur J Nucl Med Mol Imaging* 2021;48:21–39 CrossRef Medline
54. Galldiks N, Langen K-J. **Amino acid PET: an imaging option to identify treatment response, posttherapeutic effects, and tumor recurrence?** *Front Neurol* 2016;7:120 CrossRef Medline
55. Albano D, Tomasini D, Bonù M, et al. **^{18}F-fluciclovine (^{18}F-FACBC) PET/CT or PET/MRI in gliomas/glioblastomas.** *Ann Nucl Med* 2020;34:81–86 CrossRef Medline
56. Kampa JM, Kellner U, Marsching C, et al. **Glioblastoma multiforme: metabolic differences to peritumoral tissue and IDH-mutated gliomas revealed by mass spectrometry imaging.** *Neuropathology* 2020;40:546–58 CrossRef Medline
57. Dilillo M, Ait-Belkacem R, Esteve C, et al. **Ultra-high mass resolution MALDI imaging mass spectrometry of proteins and metabolites in a mouse model of glioblastoma.** *Sci Rep* 2017;7:603 CrossRef Medline
58. Fack F, Tardito S, Hochart G, et al. **Altered metabolic landscape in IDH-mutant gliomas affects phospholipid, energy, and oxidative stress pathways.** *EMBO Mol Med* 2017;9:1681–95 CrossRef Medline
59. Esteve C, Tolner EA, Shyti R, et al. **Mass spectrometry imaging of amino neurotransmitters: a comparison of derivatization methods and application in mouse brain tissue.** *Metabolomics* 2016;12:30 CrossRef Medline
60. Bernstock JD, Mooney JH, Ilyas A, et al. **Molecular and cellular intratumoral heterogeneity in primary glioblastoma: clinical and translational implications.** *J Neurosurg* 2019 Aug 23 [Epub ahead of print] CrossRef Medline
61. Besnard J, Okumoto S. **Glutamine flux imaging using genetically encoded sensors.** *J Vis Exp* 2014;e51657 CrossRef Medline
62. Gruenwald K, Holland JT, Stromberg V, et al. **Visualization of glutamine transporter activities in living cells using genetically encoded glutamine sensors.** *PLoS One* 2012;7:e38591 CrossRef Medline
63. Xue M, Wei W, Su Y, et al. **Supramolecular probes for assessing glutamine uptake enable semi-quantitative metabolic models in single cells.** *J Am Chem Soc* 2016;138:3085–93 CrossRef Medline
64. Ghoreishi SM, Khalaj A, Sabzevari O, et al. **Technetium-99m chelator-free radiolabeling of specific glutamine tumor imaging nanoprobe: in vitro and in vivo evaluations.** *Int J Nanomedicine* 2018;13:4671–83 CrossRef Medline
65. Jang K, Russo C, Di Ieva A. **Radiomics in gliomas: clinical implications of computational modeling and fractal-based analysis.** *Neuroradiology* 2020;62:771–90 CrossRef Medline

Cavernous Sinus Vascular Venous Malformation

J.C. Benson, K.L Eschbacher, A. Raghunathan, D. Johnson, D.K. Kim, and J. Van Gompel

ABSTRACT

SUMMARY: Vascular venous malformations of the cavernous sinus have multiple imaging features that can be used to distinguish them from other entities in the region. Accurate identification of these lesions is essential: Vascular venous malformation lesions carry considerable risk of intraoperative hemorrhage, so preoperative recognition of vascular venous malformations can greatly impact the treatment strategies used. Nevertheless, because of their scarcity, many radiologists are unfamiliar with the radiologic and clinical features of cavernous sinus vascular venous malformations. This article will describe a case of an asymptomatic vascular venous malformation; outline its imaging, clinical, and pathologic features; and review the relevant literature regarding this diagnosis.

ABBREVIATIONS: CCM = cerebral cavernous malformation; ISSVA = International Society for the Study of Vascular Anomalies; RBC = red blood cell; VM = vascular venous malformation

A 50-year-old man with no notable medical history presented to our institution with a 2-year history of bilateral nonpulsatile tinnitus. The patient's work-up included an audiogram that demonstrated asymmetric left-sided hearing loss. This prompted evaluation with internal auditory canal MR imaging, which incidentally discovered a mass in the left cavernous sinus.

Imaging and Biopsy

The initial MR imaging noted a well-circumscribed mass centered in the left cavernous sinus, which encroached on the left aspect of the sella. The mass encased the left ICA, which was deviated medially. Intralesional signal was hyperintense on FLAIR and isointense to gray matter on T1WI. On T2 sampling perfection with application-optimized contrasts by using different flip angle evolution (SPACE sequence; Siemens), the lesion was notably heterogeneous, with a somewhat coarsened texture. Intralesional enhancement was also heterogeneous (Fig 1).

Initially, the differential for this lesion included meningioma, schwannoma, and cavernous sinus hemangioma. However, there was also some concern that this represented a chondroid lesion, such as a chondrosarcoma. The neurosurgical team was consulted, and they planned to resect the mass via a craniotomy with cavernous sinus exploration. The preoperative stereotactic CTA revealed findings extremely atypical of chondrosarcoma. First, the mass lacked an intralesional chondroid matrix. Also, the adjacent osseous structures appeared remodeled rather than eroded, suggestive of a benign and long-standing process (Fig 2).

Two additional imaging examinations were then performed to evaluate the mass for features of a vascular venous malformation (VM). First, a technetium Tc99m-tagged red blood cell (RBC) scan was completed, which demonstrated avid radiotracer accumulation within the mass on delayed images. Then, a dynamic contrast-enhanced MR imaging was performed, which demonstrated progressive enhancement of the mass on sequential images (Fig 3). Altogether, the imaging was highly suggestive of a VM. The patient ultimately underwent a biopsy of the mass for pathologic confirmation. Complete resection was not attempted due to the patient's preoperative lack of symptoms and the known favorable response of such lesions to focal treatment with stereotactic radiation.

Pathology

The biopsy from the left cavernous sinus showed a collection of predominantly thin-walled, large-caliber, anastomosing vessels within collagenous stroma. Occasional thick-walled vessels were present, showing a relatively prominent smooth-muscle layer and lacking an internal elastic lamina. All vessels were lined by bland endothelial cells, and no mitotic activity or cytologic atypia was present (Fig 4). No proliferation of meningothelial cells was

Received August 2, 2021; accepted after revision September 9.

From the Departments of Radiology (J.C.B., D.J., D.K.K.), Laboratory Medicine and Pathology (K.L.E., A.R.), and Neurologic Surgery (J.V.G.), Mayo Clinic, Rochester, Minnesota.

Please address correspondence to John C. Benson, MD, Department of Radiology, Mayo Clinic, 200 1st St SW, Rochester, MN 55901; e-mail: benson.john3@mayo.edu

http://dx.doi.org/10.3174/ajnr.A7343

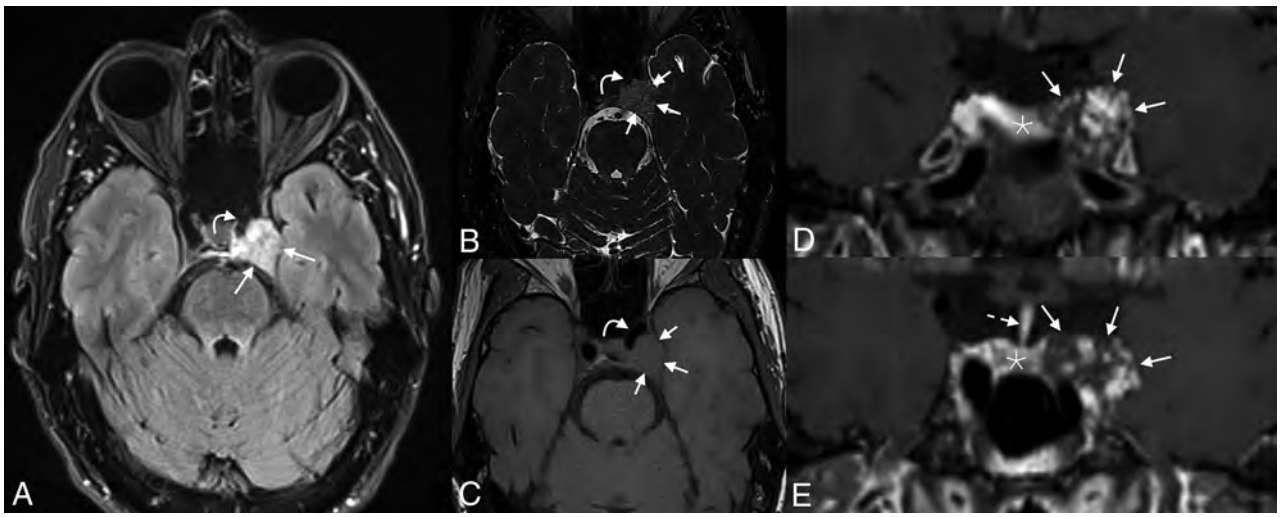

FIG 1. Initial MR imaging of the lesion demonstrates a well-circumscribed mass (*straight arrows*) in the left cavernous sinus with hyperintense signal on FLAIR (*A*). The left ICA is medialized and encased by the mass (*curved arrows*). Intralesional signal is notably heterogeneous and coarsened on T2 SPACE (*B*); enhancement is also heterogeneous (*C–E*). Coronal postcontrast images delineate encroachment of the mass into the sella, with mild mass effect on the pituitary (*asterisks*); the infundibulum (*dashed arrow*) has slightly deviated to the right.

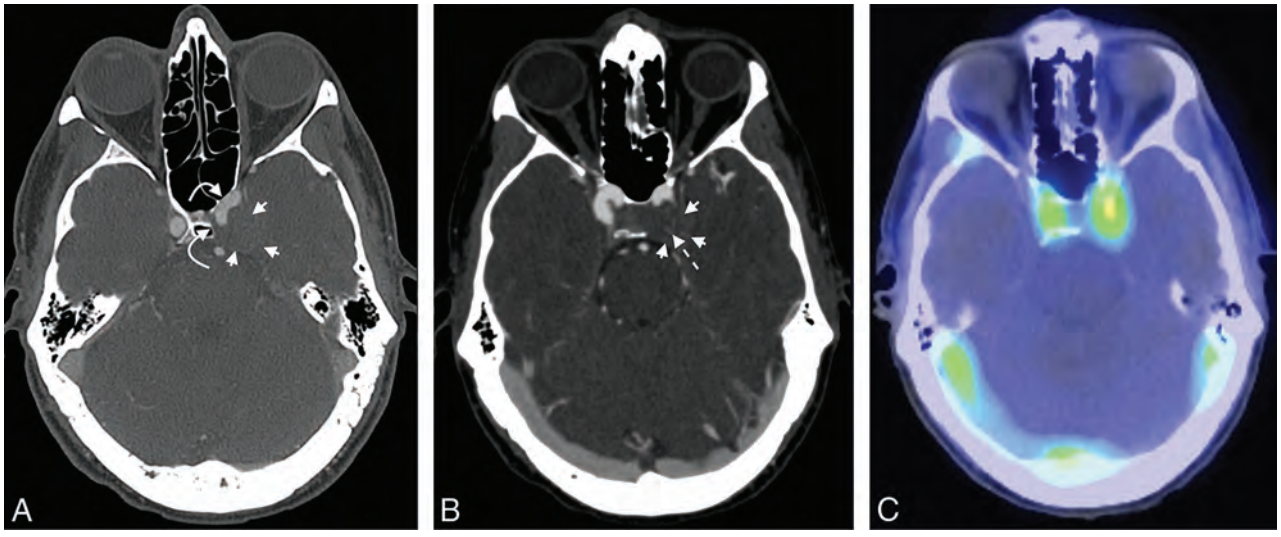

FIG 2. Preoperative CTA (*A* and *B*) demonstrates prominent bony remodeling about the margins of the mass (*curved arrows*). The mass itself is essentially isodense to the parenchyma (between the *short straight arrows*). Its inferior border is close to but does not appear to originate from the petroclival fissure (not shown). Small enhancing intralesional vessels are appreciated (*dashed arrow*). A subsequent technetium Tc-99m-tagged RBC SPECT scan (*C*) shows intense radiotracer accumulation within the mass on delayed images.

present to suggest the presence of a meningioma. There was no evidence of cartilaginous material or a proliferation of spindle cells to support the diagnosis of a chondrosarcoma or schwannoma. Overall, the histopathologic features were diagnostic of a cavernous venous malformation.[1,2] The diagnosis was cavernous sinus VM.

Discussion

Cavernous sinus VMs represent rare non-neoplastic entities and account for 3% of all cavernous sinus lesions.[3] The lesions overwhelming occur in women, accounting for up to 94% of cases. The mean age at the time of diagnosis is 44 years.[3] Because the masses tend to be slow-growing, symptom onset is often insidious, with gradually progressive headaches, cranial nerve palsies, hypopituitarism, and proptosis.[4,5] The masses may enlarge during pregnancy, resulting in symptom exacerbation that improves after delivery.[6]

Imaging features of cavernous sinus VMs have been extensively described and largely match those noted in this case. The masses are well-circumscribed and cause a local mass effect on adjacent structures. As they enlarge, VMs first displace and later encase the ICA; the vessel lumen is usually preserved (a schematic is shown in Fig 5).[7] CT often shows remodeling of the adjacent bone, while CTA may show small arterially enhancing intralesional vessels. On MR imaging, the lesions are markedly T2 hyperintense, with intralesional signal approaching that of CSF.[3]

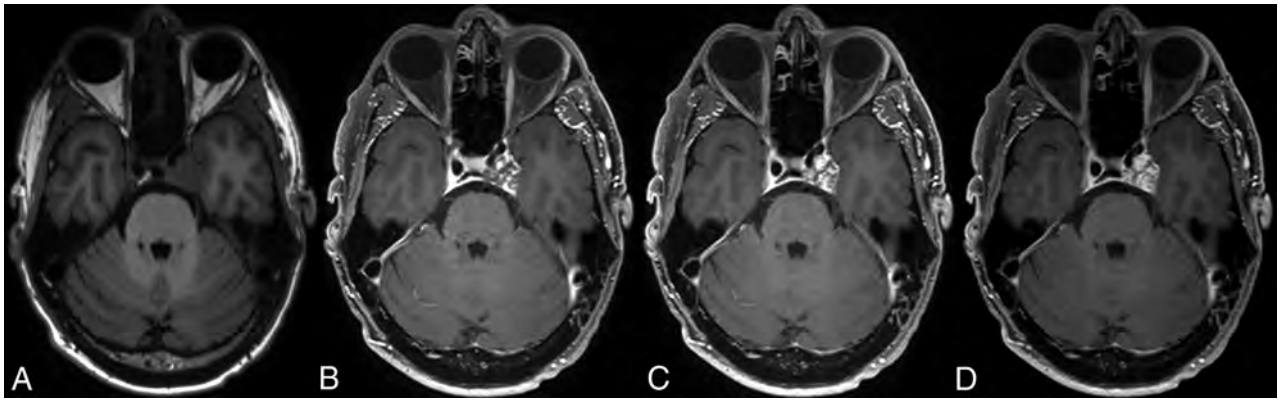

FIG 3. Dynamic contrast imaging. On precontrast (*A*) image, the mass is slightly isointense to nearby gray matter. Sequential postcontrast images (*B–D*) show progressive filling-in with contrast preferentially going to the periphery of the mass.

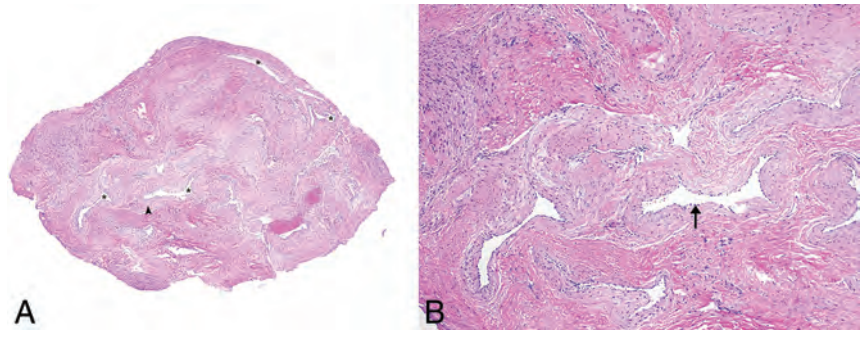

FIG 4. Histopathologic examination reveals that the mass is composed of numerous, predominantly thin-walled, anastomosing vascular channels (*asterisk*) embedded within delicate collagenous stroma. The vessels are predominantly thin-walled, with few vessels showing thickened muscular walls (*arrowhead*) (*A*, original magnification, ×40). Higher-power magnification shows that these abnormal vascular channels are lined with cytologically bland endothelial cells (*arrow*) and lack internal elastic laminae (*B*, original magnification, ×100). The specimen is stained with H&E.

Dural tails have also been reported in some lesions, though they seem to be rare.[8] He et al,[9] in an assessment of 133 cavernous sinus lesions (24 were cavernous sinus VMs), found 4 imaging biomarkers suggestive of VMs: ultra-high intralesional T2 signal, signal uniformity, infiltration of the sellar region, and dumbbell-shape. If all 4 characteristics were present, the sensitivity and specificity of the findings were 87.5% and 96.3%, respectively

Nevertheless, even with these features present, it can be difficult to confidently distinguish VMs from their closest mimickers: meningiomas and schwannomas.[10] Schwannomas, in particular, are also often dumbbell in shape.[11] When large, schwannomas typically follow the path of the nerves from which they arise. Schwannomas along the trigeminal nerve, for example, might extend posteriorly into the adjacent Meckel cave or inferiorly through the foramen ovale. Meningiomas are usually hypointense to gray matter on T2—not markedly hyperintense like hemangiomas—and often have an associated dural tail that extends along the ipsilateral tentorium.[11]

In such cases, dynamic MR imaging can help confirm the diagnosis. Like their hepatic counterparts, cavernous sinus VMs demonstrate characteristic centripetal "filling in" of enhancement on dynamic contrast imaging.[12,13] This is thought to represent a gradual influx of contrast into the large slow-flow vascular regions.[14] Still, centripetal enhancement is not universally present. Some authors have posited that 3 pathologic subtypes of VMs exist, with notable differences in their vascular makeups.[15,16] Per the classification by Yao et al,[15] type A lesions are spongelike with an intact pseudocapsule, largely composed of thin-walled sinusoids; type B lesions have incomplete or absent pseudocapsules and contain well-formed vasculatures; and type C lesions have features of both. Regardless of the recognition of such classifications, histologic differences may certainly play a role in imaging differences. For example, lesions with greater numbers of thin-walled vessels may fill with contrast earlier, thereby leading to early homogeneous enhancement that is present on all phases. Smaller lesions, too, may lack centripetal enhancement.[12]

If diagnostic uncertainty exists, a nuclear medicine–tagged RBC scan using technetium Tc99m–labeled RBCs may be used. Classically, such examinations are used to detect VMs within the liver. However, prior studies have shown similar accumulation of technetium Tc99m when used in cavernous sinus VMs.[17] Labeled RBC studies typically show photopenia during initial dynamic phase images. Subsequent slow accumulation of tracer results in marked intralesional uptake on 30-minute and 3-hour delayed images.[4]

The terminology of cavernous sinus VMs deserves explanation. Ever since Virchow first categorized vascular anomalies in the mid-19th century, the classification of vascular anomalies has undergone numerous adjustments. Today, the 2014 classification created by the International Society for the Study of Vascular Anomalies (ISSVA) is considered the mainstay resource for vascular anomaly classification.[18] Unfortunately, however, terminology from prior classification attempts has been passed on, often

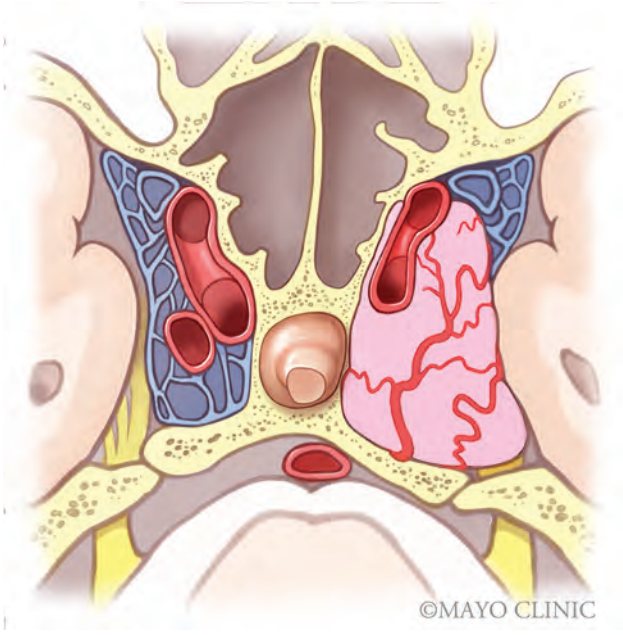

FIG 5. Illustration of a cavernous sinus vascular venous malformation with typical lesion characteristics. The mass has multiple benign characteristics, including remodeling of the adjacent bone and displacement—or encasement—of the ICA without high-grade luminal narrowing. Reproduced with permission from the Mayo Foundation for Medical Education and Research, all rights reserved.

as colloquial descriptors of various anomalies. VMs such as the one seen in this case are often still called "hemangiomas," both in the literature and clinical contexts. However, it is more precise to label such lesions vascular venous malformations.[19]

Thus, cavernous sinus VMs should not be confused with intraaxial cerebral cavernous malformations (CCMs) (often imprecisely referred to as cavernous hemangiomas or cavernomas). Per the ISSVA nomenclature, the cavernous sinus VM seen in this case is a common type of venous malformation and is morphologically distinct from other subtypes of venous malformations including CCMs. CCMs are specifically located within the parenchyma of the brain or spinal cord and have characteristic imaging findings that are distinct from common venous malformations.[18,20]

Histologically, the closest comparison with the cavernous VM in this case would be an AVM. An AVM is composed of variably sized veins, as well as arteries characterized by identifiable internal elastic lamina—a finding that was absent in our case.[1] In addition, some authors suggest that cavernous VMs may have an associated capsule or pseudocapsule, which may differentiate these lesions from CCMs.[20] However, this finding may represent reactive changes in the tissue surrounding the malformation rather than originating from the lesion itself, so it may not be a reliable indicator of these distinct pathologic entities. Also, as mentioned above, some authors have noted that not all proposed subtypes of VMs have a pseudocapsule.

Identification of cavernous sinus VMs on imaging is of utmost importance because surgical management of the lesions carries a considerable risk. The lesions are highly prone to hemorrhage and are in close anatomic proximity to the ICA and multiple cranial nerves.[3] Perioperative mortality from uncontrolled bleeding reached 12%–36% in older studies, though recent series have reported better success.[21–23] The lesions can also recur.[24] Thus, many physicians opt to treat VMs with stereotactic radiosurgery, either as a primary treatment strategy or as adjuvant therapy following surgery.[25,26] This has been shown to be successful: Lee et al,[27] in a study of 31 patients treated with stereotactic radiosurgery, showed that all patients had >50% lesion-volume reduction at 6 months. A meta-analysis by Wang et al[28] found that most patients have lesion regression after stereotactic radiosurgery.

The patient reported here recovered well from his biopsy, with only minimal double vision when looking downward. He elected to undergo gamma knife radiosurgery, which was completed 2 months after the biopsy. The patient will be followed with serial imaging to monitor the treatment response.

Case Summary

1. Cavernous sinus vascular venous malformations have multiple characteristic imaging features, including marked T2 hyperintensity and centripetal filling-in on dynamic contrast-enhanced MRI. Use of the latter, in suspected cases, can help avoid a potentially dangerous biopsy.
2. Technetium Tc99m–tagged RBC scans typically demonstrate intralesional radiotracer accumulation on delayed images.
3. Histologically, cavernous VMs are characterized as a mass-forming aggregate of venous-type vessels that lack an internal elastic lamina.
4. Cavernous sinus VMs are notoriously difficult to resect due to their propensity to hemorrhage. Radiosurgery is a viable alternative and is effective at decreasing lesion volume.

Disclosure forms provided by the authors are available with the full text and PDF of this article at www.ajnr.org.

REFERENCES

1. Bruder E, Perez-Atayde AR, Jundt G, et al. **Vascular lesions of bone in children, adolescents, and young adults: a clinicopathologic reappraisal and application of the ISSVA classification.** *Virchows Arch Int Arch* 2009;454:161–79 CrossRef Medline
2. Brahmbhatt AN, Skalski KA, Bhatt AA. **Vascular lesions of the head and neck: an update on classification and imaging review.** *Insights Imaging* 2020;11:19 CrossRef Medline
3. Linskey ME, Sekhar LN. **Cavernous sinus hemangiomas: a series, a review, and an hypothesis.** *Neurosurgery* 1992;30:101–08 CrossRef Medline
4. Salanitri GC, Stuckey SL, Murphy M. **Extracerebral cavernous hemangioma of the cavernous sinus: diagnosis with MR imaging and labeled red cell blood pool scintigraphy.** *AJNR Am J Neuroradiol* 2004;25:280–84 Medline
5. Yadav RR, Boruah DK, Yadav G, et al. **Imaging characteristics of cavernous sinus cavernous hemangiomas.** *Neuroradiol J* 2012;25:515–24 CrossRef Medline
6. Shi J, Hang C, Pan Y, et al. **Cavernous hemangiomas in the cavernous sinus.** *Neurosurgery* 1999;45:1308–13; discussion 1313–14 CrossRef Medline
7. Suri A, Ahmad FU, Mahapatra AK. **Extradural transcavernous approach to cavernous sinus hemangiomas.** *Neurosurgery* 2007;60:483–88; discussion 488–89 CrossRef Medline
8. Montoya F, Vidal A, Sepulveda F, et al. **Cavernous sinus hemangioma: imaging diagnosis and surgical considerations.** *World Neurosurg* 2021;146:e30–37 CrossRef Medline

9. He K, Chen L, Zhu W, et al. **Magnetic resonance standard for cavernous sinus hemangiomas: proposal for a diagnostic test.** *Eur Neurol* 2014;72:116–24 CrossRef Medline
10. Korchi AM, Cuvinciuc V, Caetano J, et al. **Imaging of the cavernous sinus lesions.** *Diagn Interv Imaging* 2014;95:849–59 CrossRef Medline
11. Abdel Razek AA, Castillo M. **Imaging lesions of the cavernous sinus.** *AJNR Am J Neuroradiol* 2009;30:444–52 CrossRef Medline
12. Jinhu Y, Jianping D, Xin L, et al. **Dynamic enhancement features of cavernous sinus cavernous hemangiomas on conventional contrast-enhanced MR imaging.** *AJNR Am J Neuroradiol* 2008;29:577–81 CrossRef Medline
13. Sohn CH, Kim SP, Kim IM, et al. **Characteristic MR imaging findings of cavernous hemangiomas in the cavernous sinus.** *AJNR Am J Neuroradiol* 2003;24:1148–51 Medline
14. Munawar K, Nayak G, Fatterpekar GM, et al. **Cavernous sinus lesions.** *Clin Imaging* 2020;68:71–89 CrossRef Medline
15. Yao Z, Feng X, Chen X, et al. **Magnetic resonance imaging characteristics with pathological correlation of cavernous malformation in cavernous sinus.** *J Comput Assist Tomogr* 2006;30:975–79 CrossRef Medline
16. Zhou LF, Mao Y, Chen L. **Diagnosis and surgical treatment of cavernous sinus hemangiomas: an experience of 20 cases.** *Surg Neurol* 2003;60:31–36; discussion 36–37 CrossRef Medline
17. Noblett DA, Chang J, Toussi A, et al. **Hemangioma of the cavernous sinus: a case series.** *J Neurol Surg Rep* 2018;79:e26–30 CrossRef Medline
18. Steiner JE, Drolet BA. **Classification of vascular anomalies: an update.** *Semin Intervent Radiol* 2017;34:225–32 CrossRef Medline
19. Weinberg BD, Goff RD, Soares BP, et al. **Primary vascular lesions of the cavernous sinus: beyond "hemangioma."** *Neurographics* 2018;8:317–26 CrossRef
20. Gonzalez LF, Lekovic GP, Eschbacher J, et al. **Are cavernous sinus hemangiomas and cavernous malformations different entities?** *Neurosurg Focus* 2006;21:e6 CrossRef CrossRef
21. Ohata K, El-Naggar A, Takami T, et al. **Efficacy of induced hypotension in the surgical treatment of large cavernous sinus cavernomas.** *J Neurosurg* 1999;90:702–08 CrossRef Medline
22. Bansal S, Suri A, Singh M, et al. **Cavernous sinus hemangioma: a fourteen year single institution experience.** *J Clin Neurosci* 2014;21:968–74 CrossRef Medline
23. Yihe D, Qinghai M, Zhiyong Y, et al. **Diagnosis and microsurgical treatment of cavernous sinus hemangioma.** *Artif Cells Blood Substit Immobil Biotechnol* 2010;38:109–12 CrossRef Medline
24. Nishimura F, Park YS, Nakagawa I, et al. **Hemorrhagic cavernous sinus hemangioma with sudden-onset abducens palsy.** *World Neurosurg* 2018;112:1–5 CrossRef Medline
25. Schwyzer L, Tuleasca C, Borruat FX, et al. **Gamma knife surgery for a hemangioma of the cavernous sinus in an adult: case report and short review of the literature.** *Neurochirurgie* 2017;63:320–22 CrossRef Medline
26. Cho JM, Sung KS, Jung IH, et al. **Temporal volume change of cavernous sinus cavernous hemangiomas after gamma knife surgery.** *Yonsei Med J* 2020;61:976–80 CrossRef Medline
27. Lee C-C, Sheehan JP, Kano H, et al. **Gamma knife radiosurgery for hemangioma of the cavernous sinus.** *J Neurosurg* 2017;126:1498–1505 CrossRef Medline
28. Wang X, Mei G, Liu X, et al. **The role of stereotactic radiosurgery in cavernous sinus hemangiomas: a systematic review and meta-analysis.** *J Neurooncol* 2012;107:239–45 CrossRef Medline

Development and Practical Implementation of a Deep Learning–Based Pipeline for Automated Pre- and Postoperative Glioma Segmentation

E. Lotan, B. Zhang, S. Dogra, W.D. Wang, D. Carbone, G. Fatterpekar, E.K. Oermann, and Y.W. Lui

ABSTRACT

BACKGROUND AND PURPOSE: Quantitative volumetric segmentation of gliomas has important implications for diagnosis, treatment, and prognosis. We present a deep-learning model that accommodates automated preoperative and postoperative glioma segmentation with a pipeline for clinical implementation. Developed and engineered in concert, the work seeks to accelerate clinical realization of such tools.

MATERIALS AND METHODS: A deep learning model, autoencoder regularization–cascaded anisotropic, was developed, trained, and tested fusing key elements of autoencoder regularization with a cascaded anisotropic convolutional neural network. We constructed a dataset consisting of 437 cases with 40 cases reserved as a held-out test and the remainder split 80:20 for training and validation. We performed data augmentation and hyperparameter optimization and used a mean Dice score to evaluate against baseline models. To facilitate clinical adoption, we developed the model with an end-to-end pipeline including routing, preprocessing, and end-user interaction.

RESULTS: The autoencoder regularization–cascaded anisotropic model achieved median and mean Dice scores of 0.88/0.83 (SD, 0.09), 0.89/0.84 (SD, 0.08), and 0.81/0.72 (SD, 0.1) for whole-tumor, tumor core/resection cavity, and enhancing tumor subregions, respectively, including both preoperative and postoperative follow-up cases. The overall total processing time per case was ~10 minutes, including data routing (~1 minute), preprocessing (~6 minute), segmentation (~1–2 minute), and postprocessing (~1 minute). Implementation challenges were discussed.

CONCLUSIONS: We show the feasibility and advantages of building a coordinated model with a clinical pipeline for the rapid and accurate deep learning segmentation of both preoperative and postoperative gliomas. The ability of the model to accommodate cases of postoperative glioma is clinically important for follow-up. An end-to-end approach, such as used here, may lead us toward successful clinical translation of tools for quantitative volume measures for glioma.

ABBREVIATIONS: AR = autoencoder regularization; BraTS = Brain Tumor Segmentation; CA = cascaded anisotropic; CNN = convolutional neural network; DL = deep learning; ET = enhancing tumor; HGG = high-grade glioma; LGG = low-grade glioma; NC = necrotic core; RC = resection cavity; T1ce = T1 postcontrast; TC = tumor core; WT = whole tumor

There is a growing body of literature suggesting that machine learning may revolutionize the diagnosis, treatment, and follow-up of patients with gliomas, some of the most difficult malignancies to manage.[1-3] In the near-term, deep learning (DL) promises to facilitate rapid and user-independent quantitative tumor segmentation.[4] There is evidence that accurate delineation of tumor subregions of enhancement and edema can form the basis for individualized, precision medicine such as predicting a response to therapy and survival,[5] as well as aiding in streamlining radiation therapy planning.[6]

Thus far, the literature demonstrates proof of concept, showing state-of-the-art DL models using convolutional neural networks (CNNs) with moderately good median and mean Dice scores with respect to ground truth manual segmentations in the range of 0.74–0.85 and 0.61–0.77, respectively, for enhancing tumor.[7-9] Despite promising initial results, multisequence DL-based automatic glioma segmentation methods have yet to reach clinical practice, and several barriers to implementation exist.[1,10-12] Besides

Received May 5, 2021; accepted after revision September 22.

From the Departments of Radiology (E.L., B.Z., S.D., D.C., G.F., E.K.O., Y.W.L.), Population Health (W.D.W.), and Neurosurgery, School of Medicine (E.K.O.), NYU Langone Health, New York, New York.

E. Lotan and B. Zhang contributed equally to this work.

This work was supported in part by NSF Award #1928614.

Please address correspondence to Yvonne W. Lui, MD, NYU Langone Health, Department of Radiology, 660 1st Ave, Room 336, NY, NY 10016; e-mail: yvonne.lui@nyumc.org

Indicates article with online supplemental data.

http://dx.doi.org/10.3174/ajnr.A7363

the requisite testing of models for accuracy and generalizability to local data,[13] clinical implementation requires end-to-end solutions with streamlined preprocessing[14] and integrated user interfaces as well as the ability to accommodate postoperative cases.[7]

All too often, machine learning models are developed isolated from the intended clinical environment, making it difficult to later engineer a clinical translation. Here, we present an end-to-end pipeline for development and implementation of an automatic segmentation tool for both preoperative and postoperative cases and discuss the strength and challenges of such an approach to development.

MATERIALS AND METHODS

Data Description

The study was approved by our institutional research ethics committee. Ground truth MR imaging data of manually segmented brain gliomas included 335 (259 high-grade glioma [HGG] and 76 low-grade glioma (LGG) preoperative cases from the Brain Tumor Segmentation (BraTS) 2019 open-access repository and an additional 102 cases from our local medical center, which included 62 postoperative (52 HGGs, 10 LGGs) and 40 preoperative (30 HGGs, 10 LGGs) cases. The postoperative cases consist of follow-up MRIs beginning typically at and beyond 3 months after initial resection that serve clinically as postoperative baselines and that are used to track disease progression/recurrence, respectively. Any scans performed in the immediate postsurgical (within 48 hours of surgery) period were not included. Since its inception in 2012, the BraTS, organized in conjunction with the Medical Image Computing and Computer-Assisted Interventions conferences, has been evaluating machine learning models for volumetric segmentation of gliomas on brain MRIs. The BraTS multi-institutional, international dataset, including data from 19 independent institutions, is widely used as a benchmark, containing manually segmented preoperative HGG and LGG across multiple vendors and machines.[7,15,16] The dataset from our local institution does not overlap the BraTS data (our institution was not among the sites that originally contributed to the BraTS dataset) and is composed of histologically confirmed grade II–IV gliomas according to World Health Organization criteria (2007 or 2016 criteria, depending on whether the case occurred before or after 2016). Because these data are separate from the original BraTS data, we refer here to these data as the local dataset. Each glioma case consists of 4 different sequences (T1 precontrast, T1 postcontrast [T1ce], T2, and T2-FLAIR). Twenty preoperative and 20 postoperative cases were randomly selected from the local dataset for testing. The remainder of 397 cases were randomly split between training and validation datasets using an 80:20 ratio.

MR Imaging Protocol

Data belonging to the local dataset consisted of imaging performed on 3T scanners from 3 different scanner types (Magnetom Skyra, Magnetom Vida, and Magnetom Prisma; Siemens) and 5 imaging sites from a single vendor (Siemens) using our local, standard clinical brain tumor preoperative and postoperative MR imaging protocols consisting of the following pulse sequence parameters: 1) axial precontrast 2D T1-weighted: TE = 12 ms, TR = 715 ms, FOV = 256 × 256 mm^2, flip angle = 8°, resolution = 1 × 1 mm, section thickness = 5 mm; 2) postcontrast 3D MPRAGE (~5-minute interval between contrast injection and postcontrast acquisition): TE = 4 ms, TR = 2200 ms, FOV = 256 × 256 mm^2, flip angle = 15°, isotropic resolution = 1 × 1 × 1 mm; 3) 3D T2 FLAIR sampling perfection with application-optimized contrasts by using different flip angle evolution (SPACE sequence; Siemens): TE = 325 ms, TR = 6000 ms, FOV = 256 × 232 mm^2, flip angle = 120° using isotropic 1 × 1 × 1 mm voxels; and 4) T2-weighted imaging, preoperative studies including a 3D T2 SPACE: TE = 420 ms, TR = 3200 ms, FOV = 256 × 232 mm^2, flip angle = 120°, isotropic 1 × 1 × 1 mm resolution. For postoperative, follow-up cases, we performed an axial 2D T2-weighted series: TE = 81 ms, TR = 5460 ms, FOV = 320 × 260 mm^2, and flip angle = 120° using a nonisotropic voxel size of 1 × 1 × 5 mm. This difference was to practically accommodate existing clinical follow-up brain tumor protocols.

Manual Segmentation

Ground truth manual segmentation data from BraTS were established and verified by clinical experts and are described elsewhere.[7,15,16] Ground truth manual segmentation of the 102 cases comprising the local dataset was performed using ITK-SNAP, Version 3.6.0 (http://itksnap.org).[17] For manual segmentation, the following subregions were outlined following the established BraTS protocol: whole tumor (WT), tumor core (TC, which includes enhancing and nonenhancing portions of tumor as well as central cystic or necrotic regions), and enhancing tumor (ET).[7] Note that for regions defined above, each subsequent region is a subregion of the previous one, with the following relationships: WT–TC = volume of peritumoral edema; TC–ET = the sum of nonenhancing tumor and any necrotic or cystic core (NC). In addition, we adapted this previously published BraTS segmentation paradigm to accommodate postoperative scans illustrated by the equation: TC–ET = nonenhancing tumor + NC + resection cavity (RC). Thus, the model was trained to derive the following 3 segments: WT, TC, and ET from which peritumoral edema, TC–ET, and ET can be calculated and presented to the end user. For manual segmentation, T1 MPRAGE was used for ET, and T2-FLAIR sequences were used for peritumoral edema as was done for the BraTS data. Coregistered T1 and T1ce images are used to differentiate ET from nonenhancing subacute blood products. Manual segmentations from all 102 cases were reviewed in consensus by 2 board-certified neuroradiologists with Certificates of Added Qualification and having 10 and 15 years of experience. The average time for manual segmentation of the tumor subregions per each case was approximately 1 hour.

Data Preprocessing

MR imaging volumes were converted to NIfTI format using "dcm2niix" (https://github.com/rordenlab/dcm2niix).[18] DICOM is not typically used directly in machine learning training and conversion to a NIfTI format is a fairly standard and accepted method for handling image data because the conversion is lossless and there are good existing Python libraries for handling NIfTI. Precontrast T1, T2, and FLAIR MR images were coregistered to

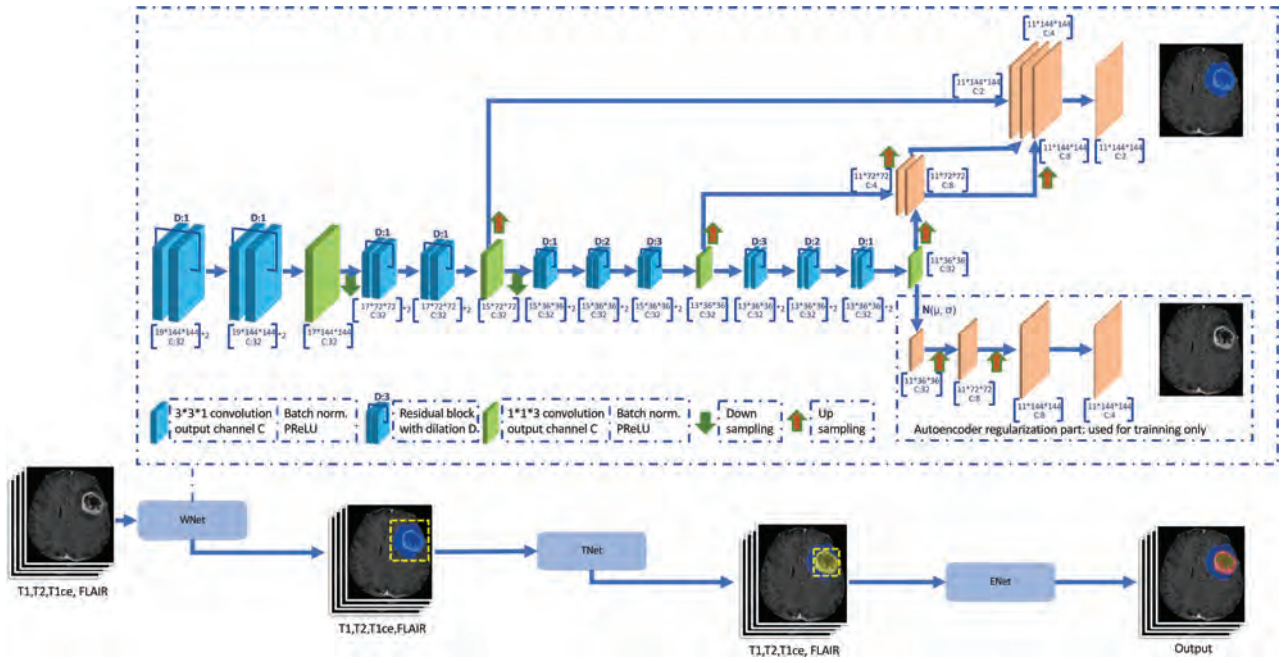

FIG 1. Summary of network architecture showing the combined use of triple CA-CNN[8] and autoencoder regularization.[9] Three networks hierarchically segment whole tumor (WNet), tumor core (TNet), and enhancing tumor (ENet) sequentially. These are structurally similar, and each network has a dilated ResNetlike block with the GroupNorm normalization, multiscale fusion, downsampling, and upsampling. ENet uses only 1 downsampling layer. The output of the segmentation decoder has 2 channels followed by a sigmoid for segmentation maps. The AC branch reconstructs the input image into itself and is used only during training to regularize the shared encoder.

T1ce volume via rigid transformation with 6 *df* from FMRIB's Linear Image Registration Tool (FLIRT; http://www.fmrib.ox.ac.uk/fsl/fslwiki/FLIRT). When 3D T2 SPACE was not available, we used only 2D T2. Skull-stripping in the patient's space was performed using the Advanced Normalization Tools software package (ANTS; http://stnava.github.io/ANTs/) with a template from the LONI Probabilistic Brain Atlas (LPBA40) to eliminate superfluous data.[19] The LPBA40 two dataset is composed of 40 healthy subjects and their corresponding manually labeled brain masks.[20] Image intensities were normalized to a standard normal distribution ($\mu = 0, \sigma = 1$).

Model Architecture and Postprocessing

Our model architecture fuses key elements from 2 of the top-ranked BraTS models that have made their source code publicly available: 1) a cascaded anisotropic CNN (CA-CNN), ranked number 2 in the 2017 BraTS Challenge;[8] and 2) an autoencoder regularization (AR), ranked number 1 in the 2018 BraTS Challenge.[9] These works are attributed originally to research groups from University College London, United Kingdom, and NVIDIA Corporation, respectively. We fused the autoencoder regularization with the cascaded CNN (AR-CA); a summary overview of the architecture is shown in Fig 1.

The first step in the fused model involves using a framework combining CA-CNN and an additional branch of variational autoencoder to reconstruct the input image of a brain glioma for regularization consistent with the architecture described by Myronenko.[9] In addition to the CA-CNN encoder backbone, there are 2 decoders: 1) a segmentation decoder that generates the segmentation maps for the 3 subregions: WT, TC, and ET; and 2) a variation decoder trained to reconstruct the input MR image used only during the training step. The encoder backbone is composed of 10 residual blocks with different dilations and 4 fused blocks. Each of these blocks contains 2 intraslice convolution layers with an intraslice $3 \times 3 \times 1$ kernel. The input of a residual block is directly added to the output, encouraging the block to learn residual functions with reference to the input.[8] The fused block has an interslice $1 \times 1 \times 3$ kernel. Convolution layers with either of these kernels have C output channels, and each is followed by a batch normalization layer and a Parametric Rectified Linear Unit activation layer. The segmentation decoder upsamples the previous fused blocks, concatenates them, and produces a final block with 2 channels to generate the final binary prediction. The WT is first segmented (WNet); then the bounding box including the WT, which directly combines the 4 sequences (T1, T1ce, T2, and FLAIR), is used as multiview fusion input for the TC segmentation (TNet). On the basis of the obtained bounding box of the TC, the ET (ENet) is finally segmented. The segmentation results from 3 different orthogonal views (axial, coronal, and sagittal) are fused by averaging the softmax output to achieve higher accuracy for each individual network. Once the glioma was segmented, postprocessing steps for hole filling and island removal were performed followed by reconversion to DICOM. Hole filling fills holes smaller than 3 mm^3 inside predicted tumors, while the island removal keeps only tumor components with volumes larger than 1/10 for WT, TC, and ET in each of the cascaded segmentation steps performed (WNet, TNet, and Enet, respectively). Reconversion to DICOM is performed on T1ce and FLAIR volumes in the axial plane using SimpleITK (https://simpleitk.org/). DICOM metadata are copied from the original corresponding series section by section.

Median and mean Dice scores for AR-CA model and 2 baseline models compared against expert manual segmentations for preoperative and postoperative test glioma cases

Model	Dice Score, Preoperative Cases (Median/Mean [SD])			Dice Score, Postoperative Cases (Median/Mean [SD])		
	WT	TC	ET	WT	TC	ET
AR-CA	0.91/0.88/0.09[a]	0.91/0.79/0.23[a]	0.87/0.75/0.27[a]	0.84/0.83/0.08[a]	0.86/0.84/0.06[a]	0.74/0.72/0.12[a]
CA-CNN[8]	0.90/0.85/0.11	0.91/0.83/0.17	0.84/0.70/0.31	0.80/0.80/0.14	0.84/0.81/0.07	0.69/0.67/0.14
AR[9]	0.87/0.84/0.09	0.82/0.72/0.12	0.71/0.68/0.21	0.82/0.75/0.14	0.63/0.63/0.2	0.66/0.61/0.16

Note:—TC indicates tumor core, including nonenhancing tumor, necrotic or cystic central regions and, in the case of postoperative cases, the resection cavity.
[a] Best-performing model in terms of median Dice scores.

Learning

All models, AR-CA and individual baseline models, were trained and tested using the same datasets as described above. We applied data augmentation by flipping and randomly applying volume center shifting and scaling (factor within 0.9–1.1). We tuned and optimized network hyperparameters: learning rate, optimization function, drop-out rate, batch size (number of images simultaneously processed during training), number of epochs (full training cycles), Adam optimizer for gradient descent optimization,[21] and Δ and patience of the early stop. The early stop is a mechanism to preemptively stop training when the increase in performance on the validation set (Δ) becomes too small for a certain time (patience). To prevent overfitting, we applied the Parametric Rectified Linear Units activation function. All calculations were done on a single NVIDIA Tesla V100 SXM2 32 GB of memory (https://www.nvidia.com/en-gb/data-center/tesla-v100/). A hyperparameter tuning loop typically took ~18 hours and was performed using the validation data. Three hundred epochs were trained by setting the learning rate to 0.001 and the decay rate to 0.01, with a 3-epoch interval to derive the optimal validation Dice scores. The code was implemented in Python 3.6 with Pytorch 1.2 (https://pypi.org/project/pytorch-pipeline/).

Model Assessment

The accuracy of the output of the DL segmentation model was compared with expert manual segmentation of subregions using the Dice score and the Jaccard index, and all cases were visually inspected. The Dice score and Jaccard index are mathematically related similarity indices [Jaccard index = Dice/(2-Dice)] ranging between 0 and 1, where 1 corresponds to perfect agreement. The distributions of the preoperative and postoperative tumor volumes are given in the Online Supplemental Data. Comparison is made of the AR-CA model performance on the test dataset against both original implementations of the CA-CNN and AR as baseline models.

Pipeline Implementation

For clinical implementation of automatic tumor segmentation, an end-to-end pipeline was constructed to identify and route the MR imaging DICOM of patients with glioma, perform the file conversion and necessary preprocessing steps, run the DL-based model, and push quantitative results to clinical viewing.

RESULTS

The Table and the Online Supplemental Data outline mean and median Dice scores and Jaccard indices, respectively, in 40 test cases for the fusion model, AR-CA, and the baseline models CA-CNN and AR, compared against the expert manual segmentations for WT, TC, and ET subregions. Preoperative and postoperative cases are reported separately. In general, there is an overlap in performance among these approaches in terms of Dice scores for both pre- and postoperative cases, with the highest mean and median values achieved using the combination approach in the fusion model compared with the 2 individual baseline models, which inform its main architecture (Table).[8,9] Most important, our results were achieved across different machines across multiple imaging sites (Online Supplemental Data). Segmentation labels computed by baseline and AR-CA models compared against ground truth manual segmentation are shown on representative preoperative and postoperative test cases in Fig 2.

Pipeline Implementation

An overview of the implementation pipeline framework is shown in Fig 3. The pipeline operates by using 2 servers: one for data transmission and the other for inference. The former is responsible for routing of images to the inference server and pushing its output back to the PACS. The inference server contains 3 modules: 1) the preprocessor for image conversion to NIfTI, skull-stripping, and coregistration among series; 2) segmentation using the fusion model, AR-CA, to produce segmentation for ET, TC, and WT;[7] and 3) the postprocessor for tumor ROI volume quantification including island removal and hole-filling operations, followed by reverse conversion back to DICOM. The overall total processing time for 1 case was ~10 minutes including data routing (~1 minute), preprocessing (~6 minutes), segmentation (~1–2 minutes), and postprocessing (~1 minute).

DISCUSSION

We present an open source, end-to-end pipeline for fully automatic volumetric segmentation of both pre- and postoperative gliomas and describe the required measures for practical integrated implementation to routine clinical workflow. The AR-CA model described here is inspired by a fusion of key model elements from 2 publicly available top-ranked BraTS models that were designed to segment preoperative gliomas. We retrained on an enlarged cohort that also included postoperative follow-up imaging, achieving high performance on both preoperative and postoperative cases. In fact, this fused model enhanced via hyperparameter optimization and data augmentation resulted in higher Dice scores overall compared with results obtained by individual original top-ranked BraTS models.[8,9]

An automatic volumetric approach to measuring tumor burden may offer notable advantages over 1D and 2D methods

commonly used for glioma measurement and ultimately may even achieve better performance than manual segmentations. Indeed, a recent randomized and blinded comparison study using a data base of 741 glioma cases reported a better qualitative performance of the DL-based segmentation algorithm compared with human raters, with a mean Dice score of 0.87 for the whole tumor.[22] There is evidence that volumetric measures provide more accurate and consistent estimation with better prediction of overall survival, especially for HGGs in light of their often complex shape.[23-26] Specifically, postoperative contrast-enhancing tumor volume is strongly associated with overall survival and progression-free survival in patients with glioblastoma.[23,27]

Until to now, there have been few attempts to use DL to segment postoperative MR images of patients with gliomas.[10-12,15] Most of these works do not address identification of the surgical cavity and achieve maximal Dice scores of 0.65–0.7 for postoperative cases. More recently, Ermiş et al,[6] developed a dedicated DL-based model for automatic segmentation of the RC in a cohort of 30 postoperative patients with HGGs. They noted that the model may be helpful for postoperative radiation therapy with effective time-savings, though the results were still suboptimal compared with human raters. Chang et al[10] developed a DL automatic algorithm based on 3D U-Net architecture for volumetric segmentation of brain gliomas, which includes 2 subregions: FLAIR hyperintensity and T1 contrast-enhancing, omitting NC and RC subregions. They used a cohort of preoperative ($n = 293$) and postoperative ($n = 54$) patients with gliomas and found high agreement between manual raters and automatic volumetric segmentation with reported Dice scores of 0.696 and 0.701 for the enhancing tumor and peritumoral edema, respectively. In that work, the surgical cavity was not segmented. The results of our AR-CA model outperformed these previously reported Dice scores and further provide labeled segmentation of the NC/RC subregions, which are important for radiation therapy planning.[6] Zeng et al[11] used a hybrid generative-discriminative model (GLISTRboost) for segmentation of pre- and postoperative

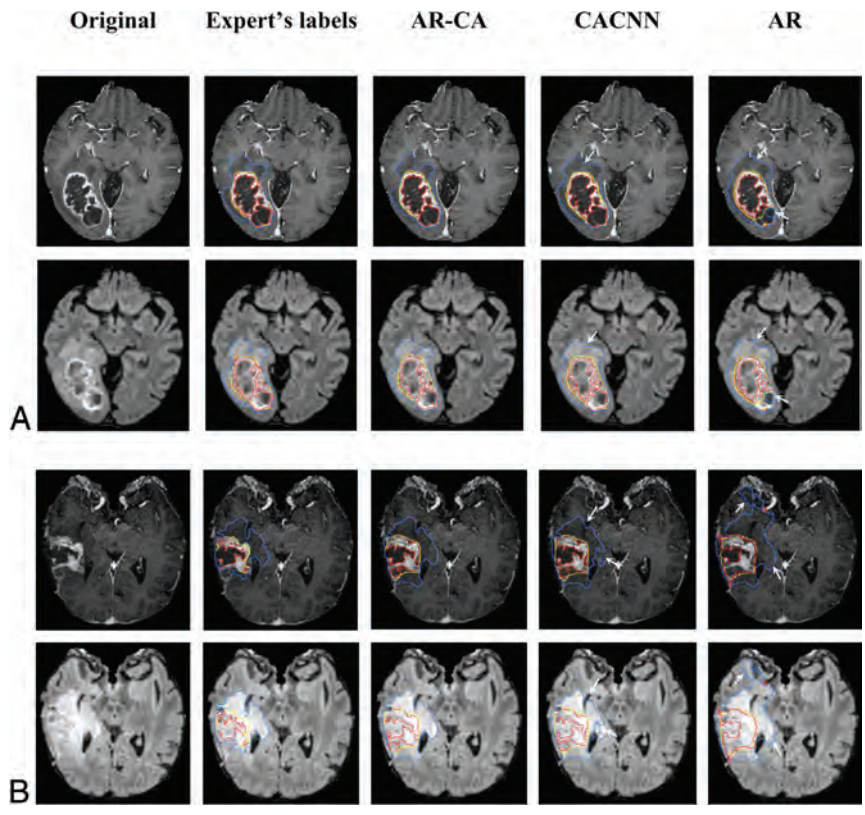

FIG 2. Segmentation labels computed using the AR-CA model and 2 baseline models for comparison, shown here with the ground truth expert manual segmentation on representative preoperative (*A*) and postoperative (*B*) glioma (at 5-months' follow-up) test cases. Segmented tumor regions overlaid on postcontrast 3D MPRAGE and 3D SPACE FLAIR. The *blue mask* denotes the whole tumor (peritumoral edema and tumor core); the *yellow mask* denotes the tumor core (nonenhancing, necrotic tumor/resection cavity, and enhancing portions of the tumor); and the *red mask* denotes the enhancing tumor. *Arrows* mark areas of overestimation or underestimation of peritumoral edema by the baseline models compared with the AR-CA model and the ground truth segmentations.

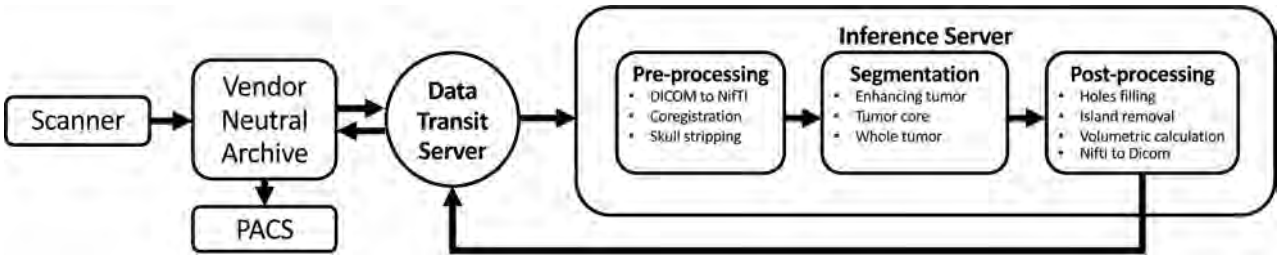

FIG 3. Schematic visualization of the implementation pipeline. An end-to-end pipeline was built to automate routing of relevant DICOM series from the MR imaging scanner through a vendor-neutral archive server to the inference server where preprocessing, automatic segmentation, and postprocessing tasks are executed. Thereafter, output results are sent back to the PACS for viewing using the data-transmit server again. Overall total processing time for 1 case is about 10 minutes including data routing (~1 minute), preprocessing (~6 minutes), segmentation (~1–2 minutes), and postprocessing (~1 minute).

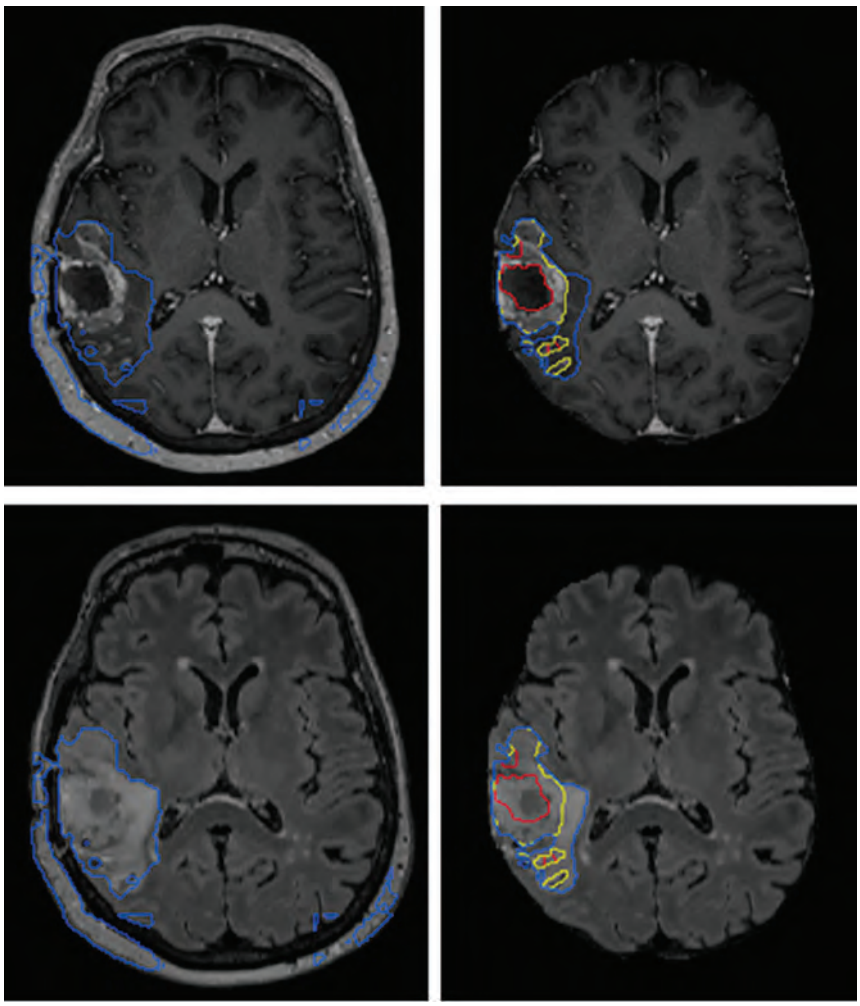

FIG 4. AR-CA segmentation model performance for high-grade gliomas with (*right*) and without (*left*) skull-stripping. T1 MPRAGE postcontrast (*upper*) and FLAIR (*lower*) images are shown. This example demonstrates how preprocessing steps are necessary to facilitate proper segmentation with obvious errors in estimating the whole tumor and entirely failing to segment the tumor core and enhancing tumor subregions.

MR images of patients with gliomas (186 preoperative and 32 postoperative MR images were included). Their results showed median Dice scores of 0.75 and 0.65 for the preoperative and postoperative cases, respectively, compared with the reference segmentation.

Meier et al[12] aimed to evaluate the use of a fully automatic segmentation method, Brain Tumor Image Analysis (BraTumIA; http://mia-software.artorg.unibe.ch/BraTumIA/) for estimating the extent of resection and residual tumor volume of contrast-enhancing tumor after an operation, reporting the segmentation of the enhancing component without segmentation of the RC. Although our results overall are promising, we did observe a few postoperative segmentations with low accuracy, perhaps as a result of limited resilience of the model to operative artifacts, such as brain distortion, blood products, and air in the RC. There were also some cases of periventricular tumors in which portions of the ventricular system and choroid plexus were mislabelled as TC and ET, respectively.

Once a pipeline is fully integrated into the PACS and clinical workflows, any model improvements and updates can be made quite readily on the server without requiring changes in other components of the pipeline.

Challenges of Model Development

Preprocessing steps exactly analogous to how data from the BraTS datasets are processed are used here because the model is inspired from top performers on prior BraTS Challenges and the BraTS dataset in model development. In addition, preprocessing of DICOM is almost always necessary for input into machine learning models because the current common software libraries accommodate different image formats, though generally not DICOM. Such preprocessing steps are, of course, not part of any routine clinical image handling. Such preprocessing steps are nontrivial, typically rule-based, and account for ~60% of the total processing time, given the relative speed of inference. Model performance is also dependent on meticulously reproducing these steps or their equivalent (Fig 4).

Another challenge is that publicly available code repositories variably include optimization parameters. The lack of optimization parameters certainly limits cross-institution adoption. As we move forward, sharing of optimization parameters is also critical to facilitate effective sharing of models.

While the BraTS Challenge has contributed significantly to moving the field forward, ultimately for clinical use, a model is needed that can handle both preoperative and postoperative cases because longitudinal follow-up and assessment of postoperative residua are desired. Thus, training models to handle postoperative cases is necessary to achieve higher clinical relevance. For postoperative cases, to the best of our knowledge, there are no publicly available ground truth datasets. In performing our own manual segmentations, we also found inherent difficulties in discrimination between NC versus RC and ET versus postoperative enhancement. For consistency, our approach was to label the RC and NC together and also label the ET and postoperative enhancement together, a method that has been used previously.[1] While clearly incompletely precise, these pairs of areas have overlapping intensity characteristics and are simply not reproducibly segmented manually or otherwise; similar observations have also been noted by others in the field.[11,28,29]

Not only is it important to test and potentially retrain on local data due to differences in sequence parameters, in attempting to

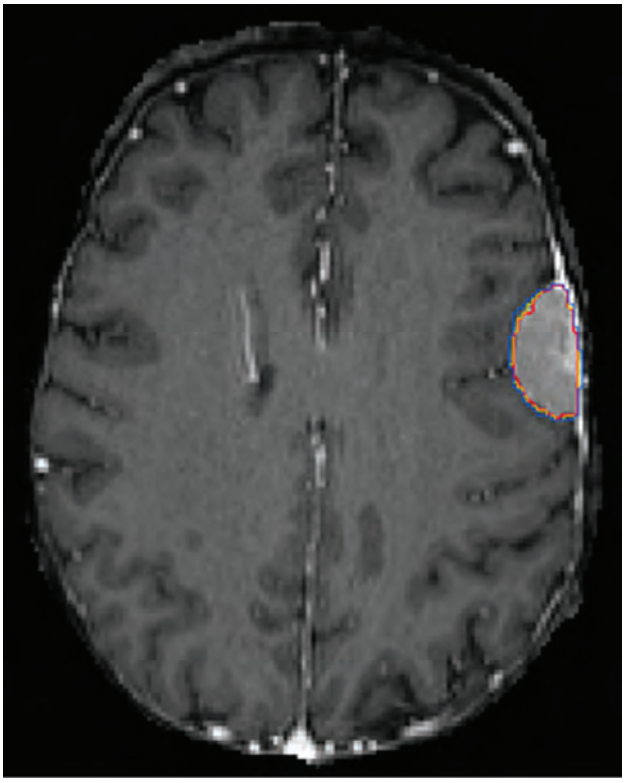

FIG 5. AR-CN segmentation model performance in a patient with left convexity meningioma. Despite reasonably good performance of the model is this case, the model has not been trained or tested on this type of pathology and would not be reliably expected to perform on such cases.

do so, we also found that sequences used for our local clinical MR imaging protocols (and likely also true for other imaging centers) do not necessarily match BraTS imaging sequences. For example, at our institution, it is not customary to acquire all three 3D pulse sequences (T1-weighted, T2-weighted, and T2 FLAIR) in every follow-up tumor case due to the long acquisition times associated with such a protocol, mainly reserved for operative cases for stereotaxis. Thus, effective clinical segmentation models need be able to handle differences in preoperative and postoperative protocols. The model performance may well have been higher for postoperative cases if we had access to 3D T2 SPACE for training in all cases; however, with the aim of developing a tool adaptive to its clinical environment rather than the other way around, we retrained using our existing clinical protocols achieving 4%–6% improvement in Dice scores for the different subregions. Most important, once the pipeline is worked out, model improvements or substitutions or both are easy to implement. Therefore, continued clinical evaluations of segmentation models should be performed.

Challenges of Implementation

A number of practical challenges were present when mapping out implementation. Correct routing of studies and series to the model is required, necessitating mapping from multiple scanners and sites. Studies were routed on the basis of the type of protocol. Unfortunately, we have a single protocol for preoperative neurosurgical cases that include pathologies different from gliomas (eg, meningioma, metastasis, arteriovenous malformation). When these were input into the model, some of the output was reasonable (Fig 5), though the model is not reliable for these other pathologies because it has not been trained or tested on any such examples. To address this issue, we had to create a discrete protocol for presurgical MR imaging with glioma segmentation. Of note, there is a clinical precedent for specialized protocols such as this, for example, for the indication of dementia and referrer requests for quantitative volumetrics of the brain. For series routing, filtering rules were set up on the basis of series description, though due to description drift with time and inconsistent naming convention, this currently requires manual periodic evaluation for updating of rules, and irregularities were encountered more frequently initially.

Left/right mirror-image flipping occurred in some cases with one of the 3D sequences. This may have resulted from scanner differences in terms of setup, defaults, and direction of scanning. This occasionally prevented proper coregistration, resulting in nonsense output. Another barrier encountered was sudden failure of the pipeline, resulting in no studies being processed. After investigation, it appeared that the mount between the data transit server and the storage space disconnected due to a reboot of one of the servers. Thus, we set up a notification mechanism when the mount/server was down. Finally, in ~5% of cases, we encountered inconsistent delays in routing to the inference node because there was no notification of completion of image routing and, thus, no clear trigger for the model to run. Typically, routing to the inference node took 1–2 minutes; however, in about 20% of the cases typically due to delays on the scanner itself, the delay could be as much as 15–30 minutes. We set a wait-time window on the inference node of 2 minutes for a new study, looping over all previously received studies during that day. In aggregate, across all modes of failure described, approximately 90% of cases yielded useful segmentation masks. Most important, routing solutions are likely to benefit from machine learning, possibly DL.[30]

Toward successful deployment, the need to educate end users including radiologists, neurosurgeons, and neuro-oncologists about the strengths and limitations of the tool is paramount. Tumor segmentations must be reviewed and volume calculations must not be blindly followed. Over- and underestimation of tumor will occur, and the calculation of a 95% confidence interval for all measurements is further recommended. One should consider what the output looks like, whether to output directly to the clinical PACS environment or a separate application. For workflow purposes, more often than not, viewing in the PACS is preferred by clinical radiologists and obviates the need for navigating complex additional software; however, not all PACS vendors can accommodate specific output (color, overlays, and so forth), and sending too many unnecessary, additional series to the PACS can overwhelm and possibly confuse viewers. In this case, we sent output segmentations directly to the PACS superimposed on SPACE FLAIR and MPRAGE postcontrast in the axial plane. We avoided complex interactions between the end user and the segmentation, though a templated macro is added to the report regarding the accuracy of the segmentation and poor segmentations can be marked in the PACS as such.

Limitations

The postoperative segmentation definitions used here are defined on the basis of imaging characteristics and do not necessarily imply that these should dictate specific treatments. We realize that postsurgical tumors are challenging to detect and parse. Ground truth manual segmentations are generally considered the criterion standard for this task; however, they are also known to have interobserver variability.[31] This tool is not intended as a classification tool for recurrent tumor and notably does not incorporate information from diffusion and perfusion MR imaging. We believe that a tool such as the one described here can help inform follow-up in patients with gliomas by providing quantitative 3D measures based on the standard imaging pulse sequences described, though clearly these must be interpreted in conjunction with the images themselves in addition to any other available pulse sequences, prior imaging, and, as always, by a trained radiologist and oncologic care team with knowledge of the clinical history, treatment regimen, and current presentation. In addition, postoperative cases are not represented in the BraTS dataset, so these are derived exclusively from our local dataset, which is relatively small. Although there are images obtained from 3 different scanner types (Magnetom Skyra, Magnetom Prisma, and Magnetom Vida) and 5 imaging sites, these are from a single institution, represent images from a single vendor, and are all acquired at 3T. Adoption for use in a different institution would require testing and possible fine-tuning the model on local data. In the future, the model would likely benefit from a greater number of training datasets.

CONCLUSIONS

This study serves as proof of concept of model development coordinated with pipeline implementation for a DL-based model for automatic volumetric segmentation that can handle both pre- and postoperative gliomas. Such a unified approach facilitates model design and training compatible with routine clinical workflow. We present a model that most importantly accommodates postoperative cases that are clinically important to assess for disease progression and recurrence. The model fuses key innovations from available top-ranked source codes with favorable performance achieved after hyperparameter optimization and discusses the challenges and limitations of the tool. Such a tool may help finally realize clinical translation of quantitative measures for brain tumors.

Source code can be found at https://github.com/abenpy/ARCNet.

Disclosures: Eric K. Oermann—*UNRELATED*: *Consultancy*: Google Inc; *Employment*: Merck & Co; *Stock/Stock Options:* Artisight LLC. Yvonne W. Lui—*UNRELATED*: *Grants/Grants Pending*: National Institutes of Health, The Leon Lowenstein Foundation, Department of Defense, National Science Foundation.* *Money paid to the institution.

REFERENCES

1. Meier R, Knecht U, Loosli T, et al. **Clinical evaluation of a fully-automatic segmentation method for longitudinal brain tumor volumetry.** *Sci Rep* 2016;6:23376 CrossRef Medline
2. Sotoudeh H, Shafaat O, Bernstock JD, et al. **Artificial intelligence in the management of glioma: era of personalized medicine.** *Front Oncol* 2019;9:768 CrossRef Medline
3. Kickingereder P, Neuberger U, Bonekamp D, et al. **Radiomic subtyping improves disease stratification beyond key molecular, clinical, and standard imaging characteristics in patients with glioblastoma.** *Neuro Oncol* 2018;20:848–57 CrossRef Medline
4. Lotan E, Jain R, Razavian N, et al. **State of the art: machine learning applications in glioma imaging.** *AJR Am J Roentgenol* 2019;212:26–37 CrossRef Medline
5. Pei L, Vidyaratne L, Rahman MM, et al. **Context aware deep learning for brain tumor segmentation, subtype classification, and survival prediction using radiology images.** *Sci Rep* 2020;10:19726 CrossRef Medline
6. Ermiş E, Jungo A, Poel R, et al. **Fully automatic brain resection cavity delineation for radiation target volume definition in glioblastoma patients using deep learning.** *Radiat Oncol* 2020;15:100 CrossRef Medline
7. Bakas S, Reyes M, Jakab A, et al. **Identifying the best machine learning algorithms for brain tumor segmentation, progression assessment, and overall survival prediction in the BRATS challenge.** *arXiv* 2019. 1811.02629; https://arxiv.org/abs/1811.02629. Accessed November 15, 2021
8. Wang G, Li W, Ourselin S, et al. **Automatic brain tumor segmentation using cascaded anisotropic convolutional neural networks.** *arXiv* 2017. 1709.00382; https://arxiv.org/abs/1709.00382. Accessed November 15, 2021
9. Myronenko A. **3D MRI brain tumor segmentation using autoencoder regularization.** *arXiv* 2018. 1810.11654; https://arxiv.org/abs/1810.11654. Accessed November 15, 2021
10. Chang K, Beers AL, Bai HX, et al. **Automatic assessment of glioma burden: a deep learning algorithm for fully automatic volumetric and bidimensional measurement.** *Neuro Oncol* 2019;21:1412–22 CrossRef Medline
11. Zeng K, Bakas S, Sotiras A, et al. **Segmentation of gliomas in pre-operative and post-operative multimodal magnetic resonance imaging volumes based on a hybrid generative-discriminative framework.** *Brainlesion* 2016;10154:184–94 CrossRef Medline
12. Meier R, Porz N, Knecht U, et al. **Automatic estimation of extent of resection and residual tumor volume of patients with glioblastoma.** *J Neurosurg* 2017;127:798–806 CrossRef Medline
13. Srivastava N, Hinton GE, Krizhevsky A, et al. **Dropout: a simple way to prevent neural networks from overfitting.** *J Mach Learn Res* 2014;15:1929–58
14. Acosta-Cabronero J, Williams GB, Pereira JMS, et al. **The impact of skull-stripping and radio-frequency bias correction on grey-matter segmentation for voxel-based morphometry.** *Neuroimage* 2008;39:1654–65 CrossRef Medline
15. Menze BH, Jakab A, Bauer S, et al. **The multimodal brain tumor image segmentation benchmark (BRATS).** *IEEE Trans Med Imaging* 2015;34:1993–2024 CrossRef Medline
16. Bakas S, Akbari H, Sotiras A, et al. **Advancing the cancer genome atlas glioma MRI collections with expert segmentation labels and radiomic features.** *Sci Data* 2017;4:170117 CrossRef Medline
17. Yushkevich PA, Pashchinskiy A, Oguz I, et al. **User-guided segmentation of multi-modality medical imaging datasets with ITK-SNAP.** *Neuroinformatics* 2019;17:83–102 CrossRef Medline
18. Li X, Morgan PS, Ashburner J, et al. **The first step for neuroimaging data analysis: DICOM to NIfTI conversion.** *J Neurosci Methods* 2016;264:47–56 CrossRef Medline
19. Avants BB, Tustison NJ, Song G, et al. **A reproducible evaluation of ANTs similarity metric performance in brain image registration.** *Neuroimage* 2011;54:2033–44 CrossRef Medline
20. Shattuck DW, Mirza M, Adisetiyo V, et al. **Construction of a 3D probabilistic atlas of human cortical structures.** *Neuroimage* 2008;39:1064–80 CrossRef Medline
21. CBICA's image processing portal. https://ipp.cbica.upenn.edu/. Accessed April 7, 2021
22. Mitchell JR, Kamnitsas K, Singleton KW, et al. **Deep neural network to locate and segment brain tumors outperformed the expert**

technicians who created the training data. *J Med Imaging (Bellingham)* 2020;7:055501 CrossRef Medline
23. Sales AHA, Bette S, Barz M, et al. **Role of postoperative tumor volume in patients with MGMT-unmethylated glioblastoma.** *J Neurooncol* 2019;142:529–36 CrossRef Medline
24. D'Arco F, O'Hare P, Dashti F, et al. **Volumetric assessment of tumor size changes in pediatric low-grade gliomas: feasibility and comparison with linear measurements.** *Neuroradiology* 2018;60:427–36 CrossRef Medline
25. Gilligan LA, DeWire-Schottmiller MD, Fouladi M, et al. **Tumor response assessment in diffuse intrinsic pontine glioma: comparison of semiautomatic volumetric, semiautomatic linear, and manual linear tumor measurement strategies.** *AJNR Am J Neuroradiol* 2020;41:866– 73 CrossRef Medline
26. Dempsey MF, Condon BR, Hadley DM. **Measurement of tumor "size" in recurrent malignant glioma: 1D, 2D, or 3D?** *AJNR Am J Neuroradiol* 2005;26:770–76 Medline
27. Orringer D, Lau D, Khatri S, et al. **Extent of resection in patients with glioblastoma: limiting factors, perception of resectability, and effect on survival.** *J Neurosurg* 2012;117:851–59 CrossRef Medline
28. Visser M, Müller DM, van Duijn RJ, et al. **Inter-rater agreement in glioma segmentations on longitudinal MRI.** *Neuroimage Clin* 2019;22:101727 CrossRef Medline
29. Kubben PL, Postma AA, Kessels AG, et al. **Intraobserver and interobserver agreement in volumetric assessment of glioblastoma multiforme resection.** *Neurosurgery* 2010;67:1329–34 CrossRef Medline
30. Grøvik E, Yi D, Iv M, et al. **Handling missing MRI sequences in deep learning segmentation of brain metastases: a multicenter study.** *NPJ Digit Med* 2021;4:33 CrossRef Medline
31. Growcott S, Dembrey T, Patel R, et al. **Inter-observer variability in target volume delineations of benign and metastatic brain tumours for stereotactic radiosurgery: results of a national quality assurance programme.** *Clin Oncol (R Coll Radiol)* 2020;32:13–25 CrossRef Medline

Quantifying T2-FLAIR Mismatch Using Geographically Weighted Regression and Predicting Molecular Status in Lower-Grade Gliomas

S. Mohammed, V. Ravikumar, E. Warner, S.H. Patel, S. Bakas, A. Rao, and R. Jain

ABSTRACT

BACKGROUND AND PURPOSE: The T2-FLAIR mismatch sign is a validated imaging sign of *isocitrate dehydrogenase*–mutant 1p/19q noncodeleted gliomas. It is identified by radiologists through visual inspection of preoperative MR imaging scans and has been shown to identify *isocitrate dehydrogenase*–mutant 1p/19q noncodeleted gliomas with a high positive predictive value. We have developed an approach to quantify the T2-FLAIR mismatch signature and use it to predict the molecular status of lower-grade gliomas.

MATERIALS AND METHODS: We used multiparametric MR imaging scans and segmentation labels of 108 preoperative lower-grade glioma tumors from The Cancer Imaging Archive. Clinical information and T2-FLAIR mismatch sign labels were obtained from supplementary material of relevant publications. We adopted an objective analytic approach to estimate this sign through a geographically weighted regression and used the residuals for each case to construct a probability density function (serving as a residual signature). These functions were then analyzed using an appropriate statistical framework.

RESULTS: We observed statistically significant (*P* value = .05) differences between the averages of residual signatures for an *isocitrate dehydrogenase*–mutant 1p/19q noncodeleted class of tumors versus other categories. Our classifier predicts these cases with area under the curve of 0.98 and high specificity and sensitivity. It also predicts the T2-FLAIR mismatch sign within these cases with an under the curve of 0.93.

CONCLUSIONS: On the basis of this retrospective study, we show that geographically weighted regression–based residual signatures are highly informative of the T2-FLAIR mismatch sign and can identify *isocitrate dehydrogenase*–mutation and 1p/19q codeletion status with high predictive power. The utility of the proposed quantification of the T2-FLAIR mismatch sign can be potentially validated through a prospective multi-institutional study.

ABBREVIATIONS: GWR = geographically weighted regression; *IDH* = *isocitrate dehydrogenase*; LGG = lower-grade glioma; PDF = probability density function

Diffuse gliomas are rare-but-life-threatening neoplasms characterized by infiltrative tumor growth in the brain. They have traditionally been classified according to phenotypic subtypes, including astrocytomas, oligodendrogliomas, and glioblastomas.[1,2] The incidence of gliomas has steadily increased with time, with currently 5.9 cases per 100,000.[3] Among diffuse gliomas, the World Health Organization characterizes low-grade gliomas as grade II tumors, while grade III are anaplastic tumors and grade IV are glioblastomas.[4] However, research based on the The Cancer Genome Atlas often groups tumors from grades II and III together as lower-grade to distinguish them from the phenotypically distinct grade IV glioblastomas.[5-7]

Received March 29, 2021; accepted after revision September 3.

From the Departments of Biostatistics (S.M., A.R.), Computational Medicine & Bioinformatics (S.M., V.R., E.W., A.R.), and Radiation Oncology (A.R.), Michigan Institute for Data Sciences (A.R.), and Department of Biomedical Engineering (A.R.), University of Michigan, Ann Arbor, Michigan; Department of Radiology & Medical Imaging (S.H.P.), University of Virginia School of Medicine, Charlottesville, Virginia; Departments of Radiology (S.B.) and Pathology & Laboratory Medicine (S.B.), University of Pennsylvania, Philadelphia, Pennsylvania; and Departments of Radiology (R.J.) and Neurosurgery (R.J.), New York University Grossman School of Medicine, New York, New York.

V. Ravikumar and E. Warner contributed equally to this work.

The content of this publication is solely the responsibility of the authors and does not represent the official views of the National Institutes of Health.

S. Mohammed and A. Rao acknowledge support from the National Institutes of Health–National Cancer Institute grants R37-CA214955 and CCSG P30 CA046592, the University of Michigan Institutional Research Funds, and ACS RSG-16-005-01. S. Mohammed was partially supported by Precision Health at the University of Michigan. S.H. Patel was supported by the National Institutes of Health–National Cancer Institute grant GI15673. S. Bakas was supported by the National Institutes of Health–National Cancer Institute grants U01CA242871 and U24CA189523, and the National Institutes of Health–National Institute of Neurological Disorders and Stroke grant R01NS042645.

Please address correspondence to Arvind Rao, PhD, University of Michigan, Department of Computational Medicine & Bioinformatics, 100 Washtenaw Ave, Ann Arbor, MI 48109-1382; e-mail: ukarvind@umich.edu

Indicates open access to non-subscribers at www.ajnr.org

Indicates article with online supplemental data.

http://dx.doi.org/10.3174/ajnr.A7341

Recent genomic studies have resulted in lower-grade gliomas (LGGs) being categorized on the basis of molecular biomarkers that are associated with differing prognoses and responses to treatment.[1,6] LGGs are currently classified by the presence/absence of a mutation in the *isocitrate dehydrogenase* (*IDH*)*1*/*IDH2* genes, as well as the presence/absence of codeletion of the 1p and 19q chromosomes (1p/19q).[1,4,6] *IDH* mutations are known to confer improved survival in patients with LGG and potentially better treatment outcomes.[1,6] The presence of the 1p/19q codeletion also indicates better survival outcomes as well as increased sensitivity to specific forms of treatment.[1,6]

An imaging phenotype known as the T2-FLAIR mismatch sign in LGGs has drawn interest as a robust diagnostic tool to identify a specific molecular subtype of LGGs, namely *IDH*-mutant 1p/19q noncodeleted astrocytomas.[6-8] This sign is characterized by the presence of complete/near-complete hyperintense signal on T2 TSE (referred to as T2 from here on) and a relatively hypointense signal on T2-weighted FLAIR (referred to as FLAIR from here on) except for a hyperintense peripheral rim. The T2-FLAIR mismatch sign was initially reported by Patel et al[6] to be a highly specific marker for *IDH*-mutant, noncodeleted gliomas with a positive predictive value of 100% in both the test and validation sets. These results have been validated by multiple research groups with high specificity,[7,9-14] and the T2-FLAIR mismatch sign is now considered a useful and robust imaging sign.[8] However, we emphasize that the 100% positive predictive value studies were all based on retrospective studies,[6,7,9-14] and the results cannot be directly assumed for a general population. For example, Johnson et al[12] found that T2-FLAIR mismatch elicits false-positives for *IDH*-mutant, noncodeleted astrocytomas in pediatric glioma cases. Additionally, as discussed in Foltyn et al,[14] looser definitions of "mismatch" that do not require complete or near-complete hypointense T2 signal and a hyperintense peripheral rim on FLAIR may also elicit false-positives.

Analyses of distinct histopathologic and radiologic features of the brain have been conducted to better understand the physiologic context of the T2-FLAIR mismatch. For example, ADC values computed from diffusion-weighted images were shown to identify *IDH*-mutant noncodeleted LGGs with high specificity, capturing cases in which a T2-FLAIR mismatch was not apparent, in addition to those in which a mismatch was present.[15] This study suggests that T2-FLAIR mismatch is also involved in the pathways that enable the *IDH*-mutated noncodeleted gliomas to exhibit increased ADC values compared with other subtypes.[15] Aliotta et al[15] added that the T2-FLAIR mismatch has substantially higher ADC values and lower relative CBV values compared with other *IDH*-mutant noncodeleted cases that do not have a mismatch. These values are considered well-known prognostic factors for glioma cases, and ADC has been implicated as a possible proxy for differences in tumor microenvironment.[15] Therefore, although specific molecular pathway information must be investigated to better understand the mechanism for the T2-FLAIR mismatch, there is marked evidence that a mismatch emerges as a special case of *IDH* mutation and 1p19/q noncodeletion and confers possible tumor differences, which could have potential prognostic or predictive implications in the future. Our discussion of ADC here is to provide some background on the biologic motivations of our work, and we would like to emphasize that our proposed approach uses only T2 and FLAIR imaging sequences.

Although several studies analyzing the T2-FLAIR mismatch are available, to our knowledge, this is a first attempt to develop a statistical framework to detect the T2-FLAIR mismatch from MR images alone. We hypothesized that a statistical framework should be able to discriminate among different molecular subtypes of LGGs, including between *IDH*-mutant tumors with and without 1p/19q codeletion as well as the presence of a T2-FLAIR mismatch, even when the characteristic peripheral ring is not visible. Such a framework should allow the robust analysis of image characteristics that confer discriminative power that is not easily achieved by human reviewers.

Our proposed statistical framework builds a quantification of the T2-FLAIR mismatch using patients' MRIs to build a classifier for tumor subtypes on the basis of features extracted from the mismatch quantification. The proposed workflow of our approach is provided in Fig 1. We use a spatial analysis technique called geographically weighted regression (GWR)[16] in combination with tools from geometric functional data analysis to quantify the mismatch between T2 and FLAIR. We refer to our quantification as a residual signature to differentiate it from T2-FLAIR mismatch. Using appropriate statistical frameworks (further details in the Materials and Methods section and the Online Supplemental Data), we devised permutation-based hypothesis tests to investigate differences among groups of residual signatures (eg, *IDH*-mutated versus *IDH* wild-type) and built classification models to predict the molecular status of the subjects. This framework of permutation tests and classification models has also been successfully used for the analysis of imaging data in the context of diabetic retinopathy.[17,18]

MATERIALS AND METHODS

Data

The multimodal MR imaging scans used in this study were obtained from The Cancer Imaging Archive[19] and comprise baseline preoperative scans from 108 LGG tumors with segmentation labels generated by an automated algorithm and revised by an expert board-certified neuroradiologist.[20,21] The tumor segmentation masks were matched across all MR imaging modalities. Clinical information including *IDH* status and the 1p/19q codeletion status was obtained from supplementary information provided with the 2016 pan-glioma article.[22] The T2-FLAIR mismatch sign labels for these cases were used from the original publication,[6] which was evaluated by 2 independent neuroradiologists. For these 108 subjects with LGGs, the sample composition for the molecular characteristics and mismatch signatures are shown in Table 1.

Image Preprocessing

The voxel intensity values for the MR imaging scans are difficult to compare across subjects due to variation in scanner configurations. We preprocessed the scans to normalize the intensity values using a biologically motivated normalization technique called WhiteStripe (https://cran.r-project.org/web/packages/WhiteStripe/index.html).[23] White Stripe normalization applies a z score transformation to the whole brain using parameters that are estimated from the distribution of normal-appearing white matter.[23] It is shown to satisfy a set of 7 statistical principles for image normalization such as the following: 1) having a common interpretation across

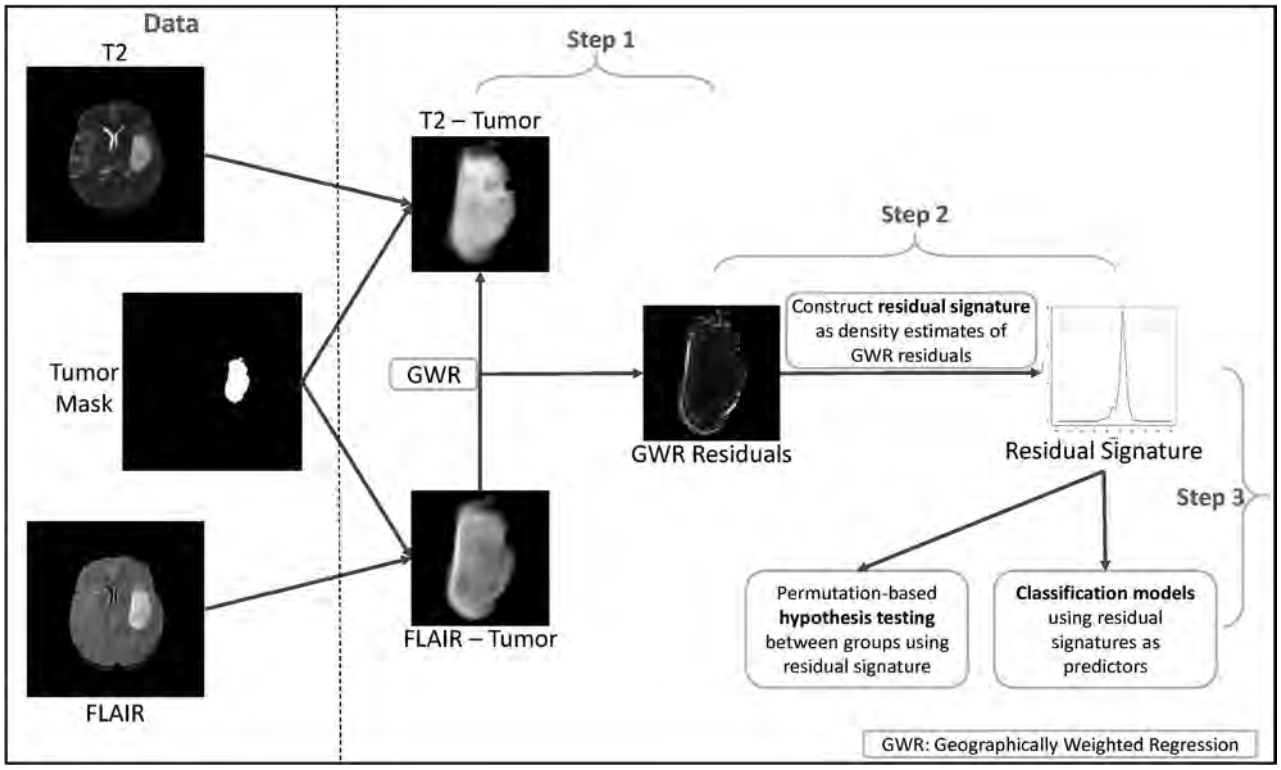

FIG 1. Workflow of our proposed approach. We obtained the tumor region from T2 and FLAIR scans using the tumor-segmentation mask. In step 1, we performed GWR with pixel values from the tumor region in T2 and FLAIR as the response and predictor, respectively. In step 2, a residual signature (ie, probability density function) was constructed using residuals from GWR. In step 3, we used residual signature–based features for hypothesis testing and classification models.

Table 1: Sample composition for different molecular characteristics and mismatch signatures[a]

Groupings	Group 1	Group 2
(A) *IDH*-mutation status	Mutated ($n = 83$)	Wild-type ($n = 22$)
(B) 1p/19q codeletion status	Noncodeleted ($n = 56$)	Codeleted ($n = 27$)
(C) *IDH* mutant and 1p/19q noncodeleted *v*ersus others	Noncodeleted ($n = 56$)	Others ($n = 49$)
T2-FLAIR mismatch type		
(D) In all LGGs	Mismatch ($n = 11$)	No mismatch ($n = 94$)
(E) In *IDH*-mutant LGGs	Mismatch ($n = 11$)	No mismatch ($n = 72$)
(F) In *IDH* -mutant and 1p/19q noncodeleted LGGs	Mismatch ($n = 11$)	No mismatch ($n = 45$)

[a] Three subjects were excluded due to missing data. The 6 groupings based on the molecular status and mismatch indicators are indicated as (A)–(F).

locations within the same tissue type, 2) being replicable, 3) preserving the rank of intensities, 4) having similar distributions for the same tissues of interest within and across patients, 5) not being influenced by biologic abnormality or population heterogeneity, 6) being minimally sensitive to noise and artifacts, and 7) not resulting in loss of information associated with pathology or other phenomena.[23] This normalization is done for both T2 and FLAIR images. In our analysis, for each subject, we considered only 1 axial section of the MR imaging scan that had the largest connected component of tumor from the whole tumor region.

Geographically Weighted Regression

GWR is a spatial-analysis technique to study the spatially varying relationships between the response and covariates in a regression model.[16] It is a statistical modeling approach similar to locally weighted regression used in curve-fitting and smoothing applications. The local regression parameters in a GWR are estimated by using subsets of data by appropriately weighting them (on the basis of proximity) with respect to the location at which the model is being estimated.

GWR Model. We will explain the GWR model in the context of our analysis. Consider the T2 and FLAIR MR imaging scans for an axial section and the corresponding tumor segmentation mask. We perform GWR within the segmented tumor region with the pixel intensity values of T2 as the response and of FLAIR as predictors. For each tumor pixel, s = 1,...,n (where n is the total number of tumor pixels in the MR imaging), the GWR model is given as $y_s = \beta_{so} + x_s\beta_s + \varepsilon_s$, with y_s and x_s being the intensity values of the tumor pixel s from T2 and FLAIR MR imaging scans, respectively. Here, β_{so} is the intercept, β_s is the regression coefficient, and ε_s is the random error. The spatial location of a tumor pixel is identified by its corresponding grid coordinates from the axial section. We can compute the distance between any pair of tumor pixels as the Euclidean distance between the corresponding grid coordinates. These distances are used as input to a kernel function

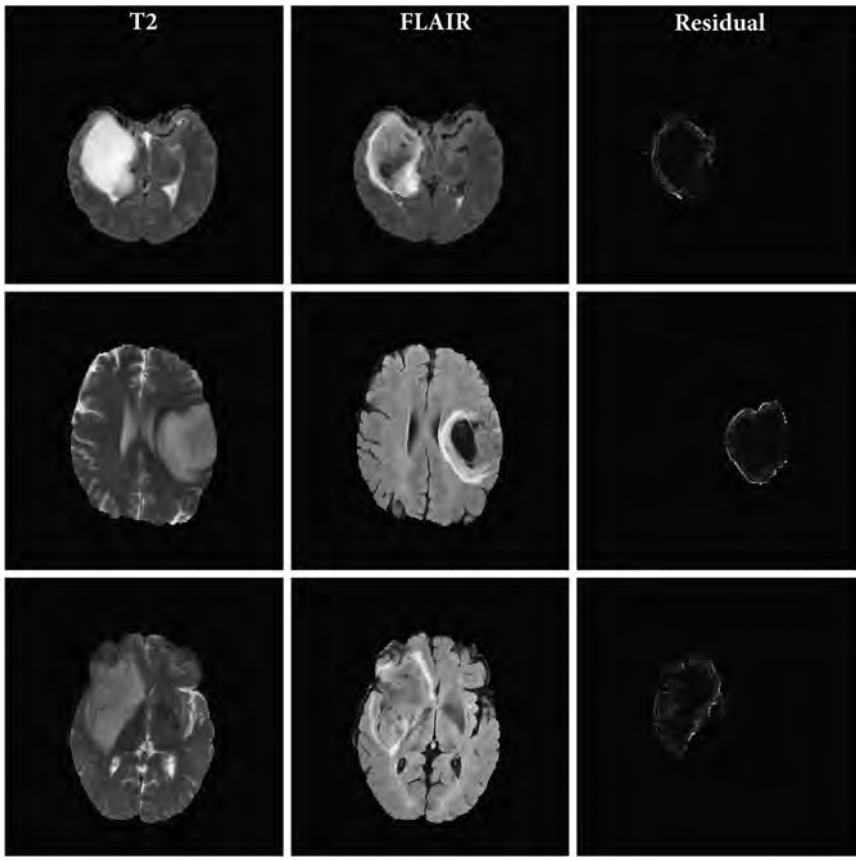

FIG 2. T2 TSE and FLAIR MR images and the magnitude of the residual signatures corresponding to T2-FLAIR mismatch LGGs. Each row corresponds to an axial section from a patient tumor. The 3 columns represent the T2, FLAIR, and magnitude of the GWR residual for each tumor pixel, respectively.

to compute weights that capture spatial dependence between the tumor pixels. For example, the weight corresponding to 2 tumor pixels in close proximity will be higher compared with the weight for pixels farther away from each other. These weights are then used to estimate the GWR model parameters at each tumor pixel s. Further details about the model formulation and estimation are provided in the Online Supplemental Data.

GWR Residuals. As an illustration, we consider $\hat{\varepsilon}_s$ to be the residual from the GWR model described above. Here, $\hat{\varepsilon}_s$ can be interpreted as the amount of T2 pixel intensity not explained by the FLAIR pixel intensity through GWR. To quantitatively assess the mismatch between T2 and FLAIR images, we consider $\hat{\varepsilon}_s$ for all the tumor pixels $s = 1,...,n$ and create a representation of the mismatch. We construct a probability density function (PDF) using these GWR residuals to quantify the mismatch. This PDF (referred to as the residual signature) acts as a surrogate for the mismatch and can be used for subsequent statistical analysis.

Probability Density Functions

The residual signature in our framework is an object of the space of PDFs. We wanted to have a metric (distance) that measures the dissimilarity between any 2 PDFs. There are multiple approaches to construct such a metric; however, they pose various computational challenges.[24] We considered an equivalent representation of the PDFs via a square root transformation,[25] which allows a simple computation of the distance between any 2 PDFs using the geometry of the space of square root transformations. This transformation also facilitates computation of an average (or mean) PDF, which provides efficient summarization and visualization, for the sample of PDFs. Details about the computation of the distance and average are provided in the Online Supplemental Data.

Permutation-Based Hypothesis Test. We devised a permutation-based hypothesis test to investigate any differences in the average PDFs of the 2 groups (eg, *IDH*-mutated versus wild-type). Thus, we first computed the average PDFs of the 2 groups and used the distance between 2 average PDFs as the test statistic. We created the null distribution for the test statistic by randomly permuting the group labels between the subjects. A P value was constructed by comparing the test statistic with the null distribution (details in the Online Supplemental Data).

Classification. Standard classification algorithms (eg, logistic regression, probit regression) can be used when the predictors belong to the Euclidean space. However, in our case, the data object corresponding to each subject is a PDF (ie, the residual signature). Hence, we used a geometric framework that maps each PDF to a vector of values via a principal component analysis for the sample of PDFs (details in the Online Supplemental Data). Using these Euclidean representations of PDFs (ie, the principal component scores), we constructed a probit regression model, a generalized linear model that models a binary categoric variable using numeric and/or categoric predictors.

RESULTS

For the 108 subjects with LGGs, we defined 6 different combinations of groups based on their molecular status and the T2-FLAIR mismatch sign.[6] The 6 groupings and the corresponding sample size for each category are shown in Table 1. Three subjects were excluded due to missing data. The residual signature for each subject was constructed by computing the kernel density estimate from the GWR residuals.

Figures 2 and 3 show the T2 TSE and FLAIR images and the pixel-wise GWR residual magnitudes from the tumor region for 3 sample cases with and without mismatch, respectively. We can see that the GWR residuals in Fig 2 clearly capture the

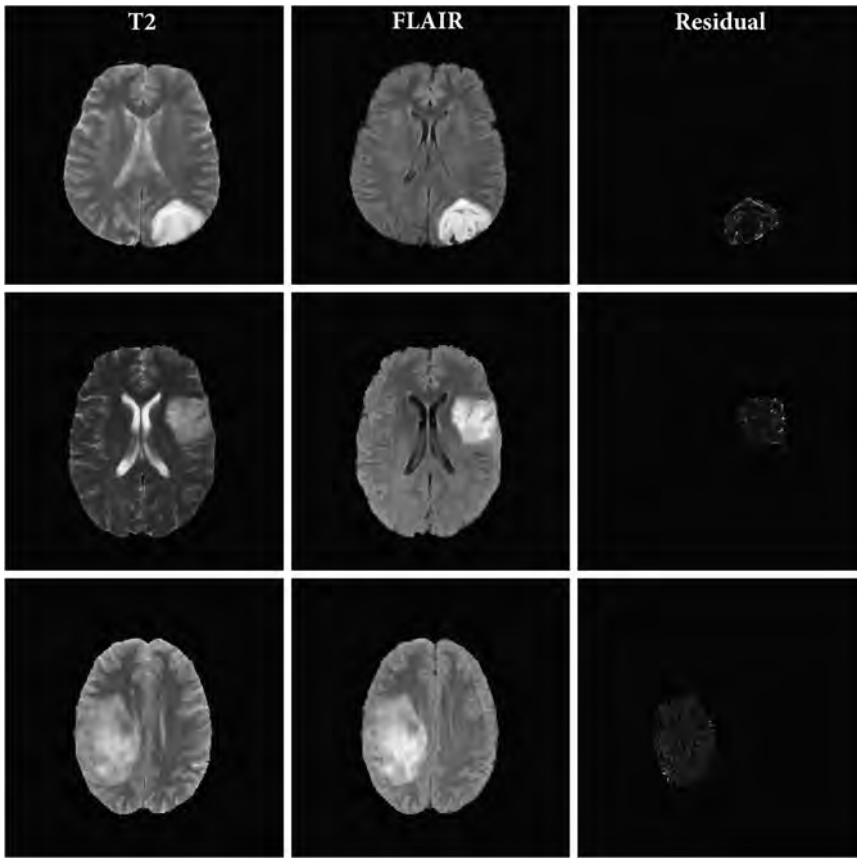

FIG 3. T2 TSE and FLAIR MR images and the magnitude of the residual signatures corresponding to no-mismatch LGGs. Each row corresponds to an axial scan from a patient's tumor. The 3 columns represent the T2, FLAIR, and magnitude of the GWR residual for each tumor pixel, respectively.

Table 2: *P* values (and adjusted *P* values) from permutation-based hypothesis tests to test for differences between the group averages of the PDFs[a]

Comparison	*P* Value	*P* Value (adjusted)
(A) *IDH*-mutation status	.46	.46
(B) 1p/19q codeletion status	.03	.05
(C) *IDH* mutant and 1p/19q noncodeleted versus others T2-FLAIR mismatch type	.02	.05
(D) In all LGGs	.03	.05
(E) In *IDH*-mutant LGGs	.04	.05
(F) In *IDH*-mutant and 1p/19q noncodeleted LGGs	.06	.08

[a] The *P* values adjusted for multiple comparisons are also presented.

Table 3: Classification results based on leave-one-out cross-validation approach for each of the 6 groupings[a]

Comparison	AUC and 95% CI	Sensitivity	Specificity
(A)	0.96 (0.91–1)	0.88	0.96
(B)	0.98 (0.94–1)	1.00	0.98
(C)	0.98 (0.94-1)	0.98	1.00
(D)	0.81 (0.54–1)	0.82	0.94
(E)	0.82 (0.58–1)	0.82	0.93
(F)	0.93 (0.84–1)	0.91	0.91

Note:—AUC indicates area under the curve.
[a] These include the AUCs with the corresponding 95% CIs, sensitivity, and specificity. The groupings and comparisons indicated as (A)-(F) are described in Table 1.

hyperintense rim structure that is characteristic of a mismatch, whereas in Fig 3, there is no specific pattern to the GWR residuals but rather just a noisy distribution of pixel values over the tumor area. These images indicate that in cases with the mismatch, there is a clear difference in the axial rim along the boundary of the tumor between the T2 and FLAIR sequences.

Hypothesis Test Results

For each grouping, we computed the group averages of the PDFs as described in the Materials and Methods section. These group-wise average PDFs are shown as a figure in the Online Supplemental Data for each of the 6 groupings (A)–(F). Differences in the group averages are visually evident (through the differences in the peaks and tails) for the groupings (B)–(F) but not for (A). We performed the permutation-based hypothesis test to evaluate these differences in the groups and compute *P* values as described in the Materials and Methods section. We considered 100,000 random permutations for each test, and the corresponding *P* values are presented in the second column of Table 2. We also present the false discovery rate–adjusted *P* values to account for multiple comparisons (ie, multiple hypotheses tests). From these results, we see that the average residual signature (or the average PDF) among the groups for the groupings (B)–(F) has a small *P* value (close to .05). This provides reasonable evidence against the null hypothesis that the average PDFs between the 2 groups are the same. This is in agreement with the visual differences in the average PDFs of these groupings (Online Supplemental Data).

Classification Results

We considered the residual signature for each subject as the predictor and built classification models (as described in the Materials and Methods section) with the corresponding group label as the response for each of the 6 groupings. We used a leave-one-out cross-validation approach for prediction, and the results are presented in Table 3. For example, we considered the grouping (A) for *IDH* status, ie, *IDH*-mutated and *IDH* wild-type, and obtained the vector representation of the PDFs by leaving 1 subject out and predicting the group label for the left-out subject. This process was repeated across all the subjects by leaving 1 subject out each time.

We report the area under the curve, its Bonferroni-adjusted 95% confidence interval, sensitivity, and specificity. The confidence intervals are Wald-type, which are computed using the DeLong variance estimator[26] using the pROC[27] package in R statistical and computing software (http://www.r-project.org/). Using our residual signatures as predictors, we saw a strong predictive performance for the groupings (A)–(C) and (F). Specifically, our residual signatures have strong sensitivity and specificity for the 1p/19q codeletion status in *IDH*-mutant LGGs.

DISCUSSION

The T2-FLAIR mismatch sign is a well-validated indicator of *IDH*-mutant 1p/19q noncodeleted LGGs. In this study, we quantified the mismatch as a PDF constructed using the residuals from a locally (geographically) weighted regression of the T2 pixel intensities on the corresponding FLAIR image. Furthermore, we evaluated the utility of this residual signature in identifying various molecular subtypes of LGGs. We devised a permutation-based hypothesis test to detect significant differences among the average PDFs of groups on the basis of molecular subtypes of glioma and a classification algorithm to predict subtype labels of the tumor.

Figures 2 and 3 capture the hyperintense rim structure that is characteristic of the T2-FLAIR mismatch signature. The visually observed differences in rim intensity are summarized in a figure in the Online Supplemental Data; cases having the T2-FLAIR mismatch have wider tails in their average PDFs than those without. This could be indicative of the high magnitude of residuals coming from the tumor rim. Given the high specificity of the mismatch signature to the *IDH*-mutant 1p/19q noncodeleted class of gliomas, we compared the residual signature of these cases with other classes. Most interesting, we observed significant differences in the average profile of this class of gliomas compared with other subtypes, regardless of their mismatch labels. Results from the permutation-based hypothesis test agree with visual differences in mean signatures. Specifically, comparisons (B) and (C) indicate significant differences in mean residual profiles of the *IDH*-mutated 1p/19q noncodeleted class of tumors. This result combined with the comparison (F) about differences within this subclass with and without mismatch indicate the utility of our approach. Our GWR-based approach is able to learn subtle features from the images that are difficult to discern visually. These features could potentially serve as sensitive markers for the *IDH*-mutant noncodeleted subtype of gliomas. To validate this hypothesis, we devised a classification algorithm using Euclidean representations (ie, principal component scores) of the T2-FLAIR GWR residual signatures.

The features extracted from GWR residuals are highly predictive of major glioma subtypes. Our classifier identifies *IDH*-mutated 1p/19q noncodeleted cases with near certainty in comparisons (B) and (C), which is better than its performance in identifying the mismatch within these cases in comparisons (D) and (E). Our classification model has high sensitivity and specificity to discriminate the 1p/19q codeletion status in *IDH*-mutant LGGs. This observation supports the findings of Patel et al[6] that report a 100% positive predictive value in predicting *IDH*-mutated astrocytomas by visual inspection in a retrospective study. Our work, however, builds on this result in several important ways. First, our results demonstrate that *IDH*-mutated 1p/19q codeletion status can be identified in gliomas from the residual signatures computed using GWR with high areas under the curve and specificity. Second, our work is not influenced by any of the inter- and intra-observer variability that is inherent in visual inspection of the mismatch sign from the MR images. Our framework is built on quantitative image analysis and rigorous statistical theory and provides a potentially powerful radiogenomic tool for identifying various molecular subtypes of gliomas. Our results indicate that radiomic features based on a T2-FLAIR mismatch are highly predictive of the *IDH*-mutant noncodeleted glioma subtype and provide a comprehensive quantitative alternative to the visually observed mismatch signature.

Furthermore, our statistical framework does not require advanced computing resources. The GWR model estimation is the only computationally intensive step in our framework, which, on average, took about 22.5 seconds per subject to execute. This time varies with the number of tumor pixels (ie, varying tumor sizes). Further details about the computation time are provided in the Online Supplemental Data. Software to implement our approach can be made available on reasonable request and with appropriate permissions from the University of Michigan.

CONCLUSIONS

Inspired by the value of the T2-FLAIR mismatch in identifying molecular subgroups of gliomas, we have developed a fully automated algorithm for quantifying the extent of mismatch between T2 and FLAIR scans, given tumor segmentation masks and extracted features from the T2-FLAIR residual signature that are strongly predictive of the glioma subtypes. We have shown that the residual signatures computed from performing GWR can be used to build classifiers that are potentially highly specific as well as sensitive to the *IDH*-mutant 1p/19q noncodeleted class of gliomas but need to be tested in a real-world environment through a prospective multi-institutional study. Visual identification of the T2-FLAIR mismatch sign is challenging due to its qualitative definition and readout, as well as the low sensitivity in identifying the *IDH*-mutant noncodeleted class of gliomas.[14] Our approach builds highly accurate classifiers on the basis of statistically informed features of the T2-FLAIR mismatch and may be a useful tool in predicting the molecular subtypes in LGGs.

Disclosures: Shariq Mohammed—*RELATED*: *Grant*: National Institutes of Health.* Visweswaran Ravikumar—*RELATED: Grant*: National Institutes of Health–National Cancer Institute grants R37-CA214955, CCSG P30 CA046592, ACS RSG-16-005-01.* Elisa Warner—*RELATED*: *Grant*: National Institutes of Health/American Cancer Society, *Comments*: paid by the National Cancer Institute and American Cancer Society, respectively, to the University of Michigan, Ann Arbor.* Sohil Patel—*UNRELATED*: *Grants/Grants Pending*: National Institutes of Health, *Comments*: National Cancer Institute, award No. GI15673.* Spyridon Bakas—*RELATED*: *Grant*: National Institutes of Health, *Comments*: Research reported in this publication was partly supported by the National Cancer Institute and the National Institute of Neurological Disorders and Stroke of the National Institutes of Health under award numbers NCI:U01CA242871, NCI:U24CA189523, and NINDS:R01NS042645. Arvind Rao—*RELATED*: *Grant*: National Institutes of Health–National Cancer Institute, American Cancer Society*; *UNRELATED*: *Consultancy*: Voxel Analytics, LLC; *Employment*: University of Michigan, Ann Arbor; *Payment for Lectures Including Service on Speakers Bureaus*: Cambridge Healthtech Institute. Rajan Jain—*UNRELATED*: *Royalties*: Thieme. *Money paid to the institution.

REFERENCES

1. Claus EB, Walsh KM, Wiencke JK, et al. **Survival and low-grade glioma: the emergence of genetic information.** *Neurosurg Focus* 2015;38:E6 CrossRef Medline
2. Wesseling P, Capper D. **WHO 2016 classification of gliomas.** *Neuropathol Appl Neurobiol* 2018;44:139–50 CrossRef Medline
3. Ho VKY, Reijneveld JC, Enting RH, et al. **Changing incidence and improved survival of gliomas.** *Eur J Cancer* 2014;50:2309–18 CrossRef Medline
4. Louis DN, Perry A, Reifenberger G, et al. **The 2016 World Health Organization classification of tumors of the central nervous system: a summary.** *Acta Neuropathol* 2016;131:803–20 CrossRef Medline
5. Brat DJ, Verhaak GW, Aldape KD, et al; Cancer Genome Atlas Research Network. **Comprehensive, integrative genomic analysis of diffuse lower-grade gliomas.** *N Engl J Med* 2015;372:2481–98 CrossRef Medline
6. Patel SH, Poisson LM, Brat DJ, et al. **T2-FLAIR mismatch, an imaging biomarker for IDH and 1p/19q status in lower-grade gliomas: a TCGA/TCIA project.** *Clin Cancer Res* 2017;23:6078–85 CrossRef Medline
7. Broen MP, Smits M, Wijnenga MM, et al. **The T2-FLAIR mismatch sign as an imaging marker for non-enhancing IDH-mutant, 1p/19q-intact lower-grade glioma: a validation study.** *Neuro Oncol* 2018;20:1393–99 CrossRef Medline
8. Jain R, Johnson DR, Patel SH, et al. **"Real world" use of a highly reliable imaging sign: "T2-FLAIR mismatch" for identification of IDH mutant astrocytomas.** *Neuro Oncol* 2020;22:936–43 CrossRef Medline
9. Lasocki A, Gaillard F, Gorelik A, et al. **MRI features can predict 1p/19q status in intracranial gliomas.** *AJNR Am J Neuroradiol* 2018;39:687–92 CrossRef Medline
10. Niemeyer B, Muniz B, Marchiori E. **T2-FLAIR mismatch sign as an imaging biomarker in lower-grade gliomas.** *Eur Neurol* 2018;79:317–18 CrossRef Medline
11. Batchala PP, Muttikkal TJE, Donahue JH, et al. **Neuroimaging-based classification algorithm for predicting 1p/19q-codeletion status in IDH-mutant lower-grade gliomas.** *AJNR Am J Neuroradiol* 2019;40:426–32 CrossRef Medline
12. Johnson DR, Kaufmann TJ, Patel SH, et al. **There is an exception to every rule: T2-FLAIR mismatch sign in gliomas.** *Neuroradiology* 2019;61:225–27 CrossRef Medline
13. Juratli TA, Tummala SS, Riedl A, et al. **Radiographic assessment of contrast enhancement and T2/FLAIR mismatch sign in lower-grade gliomas: correlation with molecular groups.** *J Neurooncol* 2019;141:327–35 CrossRef Medline
14. Foltyn M, Taborda KN, Neuberger U, et al. **T2/FLAIR-mismatch sign for noninvasive detection of IDH-mutant 1p/19q non-codeleted gliomas: validity and pathophysiology.** *Neurooncol Adv* 2020;2:vdaa004 CrossRef Medline
15. Aliotta E, Dutta SW, Feng X, et al. **Automated apparent diffusion coefficient analysis for genotype prediction in lower-grade glioma: association with the T2-FLAIR mismatch sign.** *J Neurooncol* 2020;149:325–35 CrossRef Medline
16. Brunsdon C, Fotheringham AS, Charlton ME. **Geographically weighted regression: a method for exploring spatial nonstationarity.** *Geographical Analysis* 2010;28:281–98 CrossRef
17. Mohammed S, Li T, Chen XD, et al. **Density-based classification in diabetic retinopathy through thickness of retinal layers from optical coherence tomography.** *Sci Rep* 2020;10:1–13 CrossRef Medline
18. Matuk J, Mohammed S, Kurtek S, et al. **Biomedical applications of geometric functional data analysis.** In: Grohs P, Holler M, Weinmann A. *Handbook of Variational Methods for Nonlinear Geometric Data*. Springer-Verlag; 2020:675–701
19. Clark K, Vendt B, Smith K, et al. **The Cancer Imaging Archive (TCIA): maintaining and operating a public information repository.** *J Digit Imaging* 2013;26:1045–57 CrossRef Medline
20. Bakas S, Akbari H, Sotiras A, et al. **Advancing the Cancer Genome Atlas glioma MRI collections with expert segmentation labels and radiomic features.** *Sci Data* 2017;4:170117 CrossRef Medline
21. Bakas S, Akbari H, Sotiras A, et al. **Segmentation labels and radiomic features for the pre-operative scans of the TCGA-LGG collection [BraTS-TCGA-LCC].** *Cancer Imaging Archive* 2017 CrossRef
22. Ceccarelli M, Barthel FP, Malta TM, et al; TCGA Research Network. **Molecular profiling reveals biologically discrete subsets and pathways of progression in diffuse glioma.** *Cell* 2016;164:550–63 CrossRef Medline
23. Shinohara RT, Sweeney EM, Goldsmith J, et al. **Statistical normalization techniques for magnetic resonance imaging.** *Neuroimage Clin* 2014;6:9–19 CrossRef Medline
24. Klassen EP, Srivastava A. *Functional and Shape Data Analysis*. Springer-Verlag; 2016
25. Bhattacharyya A. **On a measure of divergence between two statistical populations defined by their probability distributions.** *Bulletin of the Calcutta Mathematical Society* 1943;35:99–109
26. DeLong ER, DeLong DM, Clarke-Pearson DL. **Comparing the areas under two or more correlated receiver operating characteristic curves: a nonparametric approach.** *Biometrics* 1988;44:837–45 CrossRef Medline
27. Robin X, Turck N, Hainard A, et al. **pROC: an open-source package for R and S+ to analyze and compare ROC curves**. *BMC Bioinformatics* 2011;12:77 CrossRef Medline

Hypovascular Cellular Tumor in Primary Central Nervous System Lymphoma is Associated with Treatment Resistance: Tumor Habitat Analysis Using Physiologic MRI

S.Y. Jeong, J.E. Park, N. Kim, and H.S. Kim

ABSTRACT

BACKGROUND AND PURPOSE: The microenvironment of lymphomas is known to be highly variable and closely associated with treatment resistance and survival. We tried to develop a physiologic MR imaging–based spatial habitat analysis to identify regions associated with treatment resistance to facilitate the prediction of tumor response after initial chemotherapy in patients with primary central nervous system lymphoma.

MATERIALS AND METHODS: Eighty-one patients with pathologically confirmed primary central nervous system lymphoma were enrolled. Pretreatment physiologic MR imaging was performed, and K-means clustering was used to separate voxels into 3 spatial habitats according to ADC and CBV values. Associations of spatial habitats and clinical and conventional imaging predictors with time to progression were analyzed using Cox proportional hazards modeling. The performance of statistically significant predictors for time to progression was assessed using the concordance probability index.

RESULTS: The 3 spatial habitats of hypervascular cellular tumor, hypovascular cellular tumor, and hypovascular hypocellular tumor were identified. A large hypovascular cellular habitat was most significantly associated with short time to progression (hazard ratio, 2.83; $P = .017$). The presence of an atypical finding (hazard ratio, 4.41; $P = .016$), high performance score (hazard ratio, 5.82; $P = .04$), and high serum lactate dehydrogenase level (hazard ratio, 1.01; $P = .013$) was significantly associated with time to progression. A predictive model constructed using the habitat score and other imaging parameters showed a concordance probability index for prediction of time to progression of 0.70 (95% CI, 0.54–0.87).

CONCLUSIONS: A hypovascular cellular tumor habitat is associated with treatment resistance in primary central nervous system lymphoma, and its assessment may refine prechemotherapy imaging–based response prediction for patients with primary central nervous system lymphoma.

ABBREVIATIONS: CE = contrast-enhanced; C-index = concordance probability index; ECOG = Eastern Cooperative Oncology Group; LDH = lactate dehydrogenase; MTX = methotrexate; nCBV = normalized cerebral blood volume; PCNSL = primary central nervous system lymphoma; TTP = time to progression

Primary central nervous system lymphoma (PCNSL) represents a histologically and immunohistochemically homogeneous type of lymphoma.[1] However, the microenvironment of B-cell lymphomas was recently shown to be highly variable[2] with regard to both the spatial arrangement and composition of cells, including immune and inflammatory cells, blood and lymphatic vascular networks, and the extracellular matrix. The tumor microenvironment is closely associated with treatment resistance and survival[2-4] and partly reflects the tumor cell content and genetic aberrations. The mainstay of treatment for PCNSL is high-dose methotrexate (MTX) in combination with other chemotherapeutic agents.[5,6] Because drug delivery, distribution, and interaction with the tumor are determined by the tumor microenvironment,[7,8] depiction of the spatial arrangement of tumor cellularity and vascularity may provide valuable information for predicting treatment response.

The tumor microenvironment can be depicted using imaging parameters derived from physiologic MR imaging such as ADC mapping, CBV mapping, and permeability parameters.[9,10] In PCNSL, high cellularity with a low ADC is associated with poor

Received May 10, 2021; accepted after revision September 20.

From the Department of Radiology and Research Institute of Radiology (S.Y.J., J.E.P., H.S.K.), University of Ulsan College of Medicine, Asan Medical Center, Seoul, Korea; and DYNAPEX LLC (N.K.), Seoul, Korea.

This work was supported by the Basic Science Research Program through the National Research Foundation of Korea (NRF) funded by the Ministry of Education, Science and Technology (grant number: NRF-2020R1A2B5B01001707 and NRF-2020R1A2C4001748) and by a grant (2020IP0097) from the Asan Institute for Life Sciences, Asan Medical Center, Seoul, Korea.

Please address correspondence to Ji Eun Park, MD, PhD, Department of Radiology and Research Institute of Radiology, University of Ulsan College of Medicine, Asan Medical Center, 88 Olympic-ro 43-gil, Songpa-Gu, Seoul 05505, Korea; e-mail: jieunp@gmail.com

Indicates article with online supplemental data.

http://dx.doi.org/10.3174/ajnr.A7351

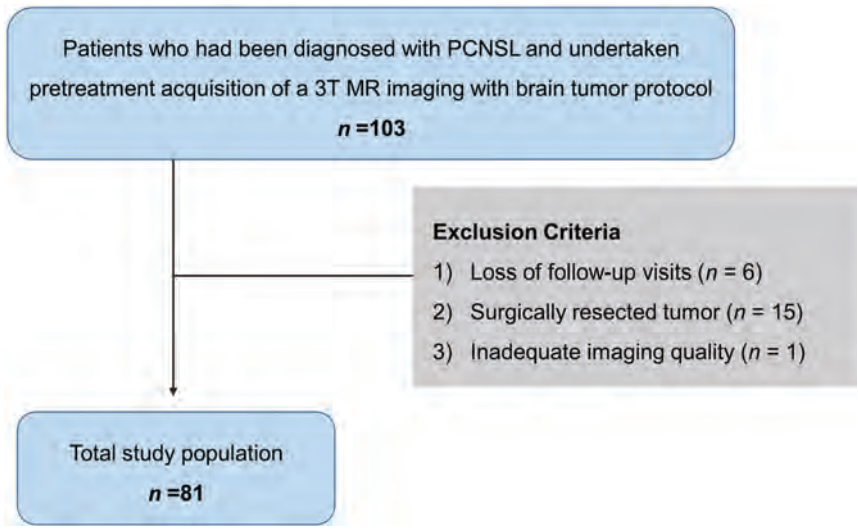

FIG 1. Flow chart of patient recruitment.

prognosis,[11] whereas a low permeability pattern [7,8] is associated with shorter progression-free survival. However, these previous studies were limited in their depiction of the spatial arrangement, with a single parameter providing unidirectional information on high or low parametric values. Physiologic MR imaging–based spatial habitat analysis refers to the parcellation of voxels on the basis of imaging parameters obtained from physiologic MR imaging of ADC and CBV to explain the habitat-based tumor environment. The parcellation of voxels using physiologic parameters enables depiction of regions of relative hyper- or hypocellularity and relative hyper- or hypovascularity. The combined spatial information from cellularity- and vascularity-reflecting physiologic MR imaging parameters will enable more precise prediction of treatment response,[12] especially identification of any tumor fraction with treatment resistance, which may exhibit high cellularity and low vascularity.

Clustering methods can be applied to measurements of multiple parameters to separate different tumor habitats through parcellation.[12] We hypothesized that physiologic MR imaging–based tumor parcellation could potentially provide spatial information on pretreatment PCNSL and identify regions of treatment resistance in patients with PCNSL. The purpose of this study was to develop spatial habitat analysis based on multiparametric physiologic MR imaging and identify regions associated with treatment resistance to facilitate the prediction of tumor response after initial chemotherapy in patients with PCNSL.

MATERIALS AND METHODS

Study Population

This retrospective study was reviewed and approved by the institutional review board of Asan Medical Center (institutional review board No. 2021–0265), and the requirement for informed consent was waived. A review of the database of Asan Medical Center identified 103 patients who were diagnosed with PCNSL between July 2011 and September 2018. The inclusion criteria were as follows: 1) pretreatment acquisition of 3T MR imaging with a brain tumor protocol including anatomic MR imaging and physiologic MR imaging (DWI and DSC perfusion imaging); 2) histopathologic confirmation of PCNSL by stereotactic biopsy; and 3) adequate follow-up examinations (no longer than 2 weeks after completion of all planned therapy) to determine the treatment response according to clinicoradiologic consensus after MTX-based chemotherapy. Patients were excluded if they were lost to follow-up visits ($n = 6$), the tumor was surgically resected ($n = 15$), or any imaging was unreadable (because of artifacts, $n = 1$). Therefore, 81 patients were included in this study (age range, 29–80 years; mean age, 61.6 [SD, 11.8] years; 43 women). A flow chart of patient selection is shown in Fig 1.

Clinical Variables and Treatment

Clinical and pathologic data were retrieved from the medical records. Baseline characteristics including age, sex, Eastern Cooperative Oncology Group (ECOG) performance status at diagnosis,[13] initial tumor volume, mean serum lactate dehydrogenase (LDH) level, mean CSF total protein, pretreatment imaging characteristics (location and presence of atypical findings), and initial posttreatment response based on a clinicoradiologic examination were collected.

All included patients had a pathologic diagnosis of diffuse large B-cell PCNSL and received MTX-based induction chemotherapy following 1 of 3 protocols: 1) MTX only (3–8 g/m^2/day; $n = 54$); 2) a combination therapy with MTX and procarbazine, lomustine (CCNU), and vincristine regimen (PCV): procarbazine (0.1–0.2 g/m^2/day)/vincristine (1.4 mg/m^2/week; $n = 15$); or 3) a combination therapy with MTX, PCV, and rituximab (375 mg/m^2/week; $n = 12$). After the patient was diagnosed with diffuse large B-cell PCNSL, dexamethasone was used in all patients for supportive care to minimize symptoms due to vasogenic edema or tumor mass effect.

Response Assessment and Outcome Definition

The posttreatment tumor response was assessed according to the International Primary CNS Lymphoma Collaborative Group criteria[14] based on MR imaging, corticosteroid use, CSF cytology, and slit lamp examination. A complete response was defined as resolution of contrast-enhancing lesions on follow-up MR imaging and, if indicated, by CSF cytologic analysis (performed if CSF cytology was positive for malignant cells at the time of diagnostic staging). A partial response was defined as an interval decrease in contrast-enhancing lesion volume, and progressive disease was defined as an interval increase in contrast-enhancing lesion volume or development of new enhancing lesions on follow-up contrast-enhanced MR imaging or involvement of the eye or CSF. All follow-up imaging to assess the overall treatment response was performed within 2 weeks after completion of all planned chemotherapy of the first or second cycle. Clinicoradiologic diagnoses of posttreatment responses were made by consensus between a neurooncologist (Shin-kyo Yoon, with 10 years of experience in neuro-oncology practice) and a neuroradiologist (Ho Sung Kim,

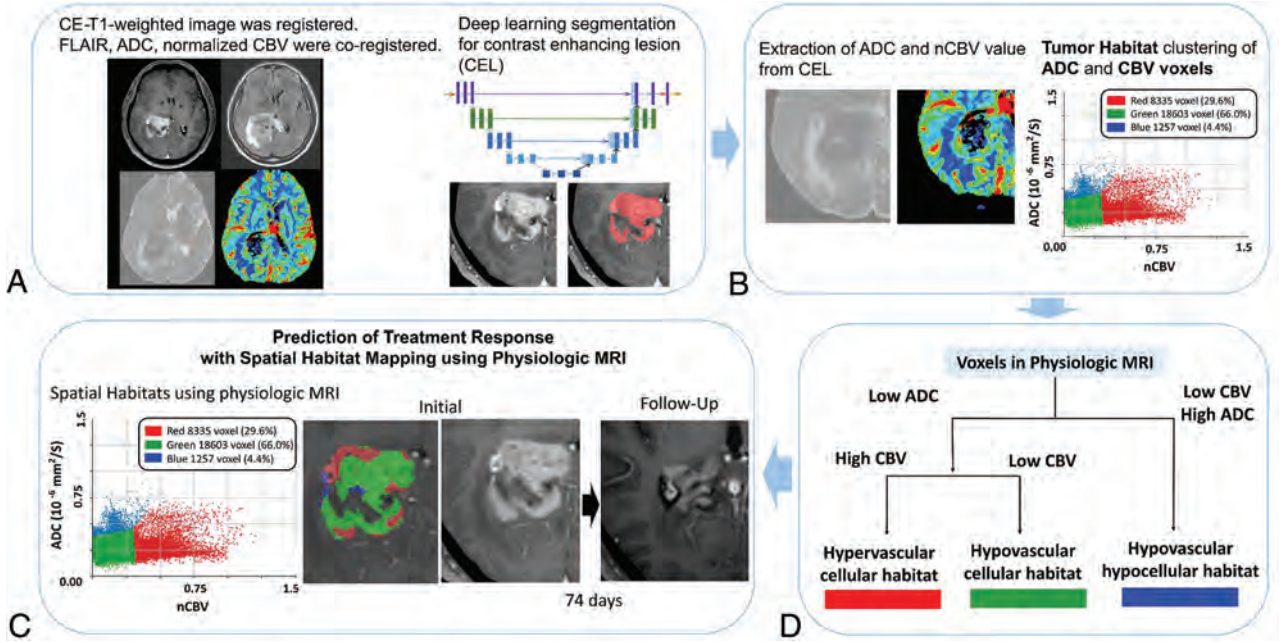

FIG 2. The overall process of the deep learning segmentation and tumor habitat analysis. *A*, Image acquisition, registration, and deep learning segmentation for a contrast-enhancing lesion (CEL). *B*, Extraction of ADC and nCBV values from the CEL and voxel classifications based on ADC and nCBV values. The individual voxels in each cluster are grouped according to their similarities and differences using a K-means clustering algorithm. *C*, The cluster number is set to 3 to depict 3 different habitats according to the combinations of ADC and nCBV parameters: hypervascular cellular, hypovascular cellular, and hypovascular hypocellular. *D*, Voxels are shown as spatial habitats in the original image space. Associations of pretreatment tumor habitats with TTP were analyzed.

with 18 years of experience in neuro-oncologic imaging) after complete imaging and medical chart review.[15] Both complete response and partial response were used as a composite end point to define "treatment response," and both stable disease and progressive disease were used as a composite end point to define "treatment resistance." Time to progression (TTP) was defined[5] as the interval between the initiation of induction therapy until documentation of resistance to induction therapy (MR imaging after 6 cycles or stable disease after at least 2 cycles and progression or death from any cause), relapse, or death from any cause after having achieved a partial or complete response.

MR Imaging Acquisitions

The brain tumor imaging protocol was acquired on a 3T scanner (Ingenia 3.0 CX; Philips Healthcare) and included conventional and advanced sequences, including T2WI, T2-weighted FLAIR, T1WI, DWI, DSC perfusion imaging, and contrast-enhanced (CE)-T1WI. The detailed imaging protocols are provided in the Online Supplemental Data, and the preprocessing procedures for the DWI and DSC imaging are summarized in the Online Supplemental Data.

Conventional Image Analysis

All MR images were read by an experienced neuroradiologist (S.Y. Jeong with 6 years of experience) who was blinded to the clinical outcomes. Conventional MR imaging parameters included deep or superficial location and the presence of atypical features of necrosis or a hemorrhagic component.[16,17] A deep location meant involvement of the basal ganglia, corpus callosum, periventricular areas, brainstem, and cerebellum. A superficial location meant involvement of the cerebral hemisphere with the exception of deep brain structures. The Online Supplemental Data show cases demonstrating atypical findings of PCNSL on conventional imaging.

Deep Learning Segmentation

The overall process of the deep learning segmentation and tumor habitat analysis is shown in Fig 2. The 3D CE-T1WI of each patient was registered and resampled into $1 \times 1 \times 1$ mm isometric voxel sizes. T2WI, ADC, and normalized CBV (nCBV) maps were then coregistered and resampled to the isovoxel 3D enhanced T1WI using rigid transformations with 6 *df* in the SPM package (Version 12; http://www.fil.ion.ucl.ac.uk/spm/).

Deep learning segmentation was performed using an implementation of a 3D UNet-based method (https://github.com/MIC-DKFZ/nnUNet)[18] applied to the FLAIR and 3D CE-T1WI using the PyTorch package, Version 1.1 in Python 3.7 (http://www.python.org). This deep learning segmentation package is optimized for processing heterogeneous MR imaging results with various pathologic characteristics. The segmentation process included identification of contrast-enhancing lesions, necrosis, and peritumoral edema, with the contrast-enhancing lesions being chosen for subsequent investigation.

Tumor Habitat Analysis

The final voxel classifications based on ADC and nCBV values were implemented using a K-means clustering module in the scikit-learn Python package (https://scikit-learn.org/stable/index.html). The individual voxels in each cluster were grouped according to their similarities and differences using a K-means clustering algorithm with squared Euclidean distances between voxel

Table 1: Patients and imaging characteristics of the PCNSLs included in this study

Clinical Characteristics (n = 81)	
Mean age (yr)	61.6 (SD, 11.8)
Sex	
Male/female	38/43 (46.9%/53.1%)
ECOG performance status at diagnosis (case No) (%)	
1	71 (87.7%)
2	2 (2.5%)
3	6 (7.4%)
4	2 (2.5%)
Mean serum LDH level	225.9 (SD, 59.9)
Mean CSF-total protein	107.0 (SD, 103.0)
Initial treatment response (case No) (%)	
Treatment response (CR and PR)	64 (79.0%)
Treatment failure (SD and PD)	17 (21.0%)
Imaging characteristics (case No) (%)	
Location	
Deep[a]	69 (85.2%)
Hemisphere	12 (14.8%)
Atypical findings[b] (case No) (%)	
Positive	14 (17.3%)
Negative	67 (82.7%)

Note:—CR, complete response; PR, partial response; PD, progressive disease; SD, stable disease.
[a] Deep location: thalamus, basal ganglia, corpus callosum, periventricular area, cerebellum.
[b] Atypical findings: presence of hemorrhage or necrosis.

intensities as the similarity metric. The cluster number was set to 3 to depict 3 different habitats according to the combinations of ADC and nCBV parameters, with the intention of avoiding overparameterized models[19] and producing a model that was easily explainable. For example, low or high ADC and CBV values reflected "hyper-/hypovascularity" and "cellularity/hypocellularity," respectively, and 3 clusters was the lowest number to demonstrate the biologic differences.

Population-Level Clustering. Three clusters were set using ADC and nCBV values: Cluster 1 represented hypervascular cellular tumor with high CBV values and low ADC values; cluster 2 represented hypovascular cellular tumor with low CBV values and low ADC values; and cluster 3 represented hypovascular hypocellular tumor with low CBV values and high ADC values. All voxels were allocated to 1 of the 3 clusters and were displayed as spatial habitats in the original image space. The parameter value ranges for the boundary of the spatial habitats were $4.37–4.9\times10^{-6}$ mm^2/s for nCBV and $103–121\times10^{-6}$ mm^2/s for ADC.

Statistical Analysis

All results are reported as median with range or 95% CI for continuous variables and as frequency or percentage for categoric variables. All statistical tests were 2-sided, and a P value $< .05$ was considered to indicate statistical significance. Statistical analyses were performed by using R software, Version 3.4.3 (https://www.r-project.org).

The associations between TTP and clinical and conventional imaging predictors were determined by univariable Cox analysis. Univariate analyses were performed to analyze the associations of tumor habitats with TTP using Cox regression or the Kaplan-Meier method (log-rank test). Hazard ratios indicate the relative change in hazard incurred by a unit increase in each parameter, and 20,000 voxels were considered as 1 U in this study.

The Pearson correlation was used to further analyze the correlation of each tumor habitat with the overall tumor burden of the contrast-enhancing lesion.

To compare clinical predictors, conventional imaging findings, and tumor habitats, random survival forest analysis was performed. The variable importance of predictors for TTP was calculated with 10-fold cross-validation using the randomForestSRC (https://cran.r-project.org/web/packages/randomForestSRC/index.html) module in R.

Habitat Risk Score. For the significant predictors identified in the univariate Cox regression, an optimal cutoff for stratifying high- and low-risk groups was estimated using the maxstat algorithm in R with 10-fold cross-validation, which ensured unbiased prediction within the sample.[20] Using this cutoff from the exploratory analysis, we developed a habitat risk score to stratify patients according to risk, with each predictor being assigned a discrete score of 1 if it was above its cutoff and zero if it was below it.

Prediction Performance for TTP. A model combining the habitat risk score and clinical and conventional imaging predictors was created, and its concordance probability index (C-index) was calculated. The performance of the model was quantified with respect to discrimination and calibration.[21] Discrimination was measured with the Harrell C-index, and calibration was tested using the version of the Hosmer-Lemeshow test by D'Agostino and Nam.[22]

RESULTS

Patient and Imaging Characteristics of the Study Population

The baseline demographics, clinical characteristics, and conventional imaging characteristics of the study patients and tumors are summarized in Table 1. All the study patients underwent initial treatment with MTX-based chemotherapy. The mean duration between pretreatment MR imaging and the initial chemotherapy was 4.8 (SD, 5.1) days. The mean follow-up duration between pretreatment MR imaging and the first posttreatment MR imaging was 50.8 (SD, 27.1) days. No patient died from treatment-related toxicity.

Clinical and Conventional Imaging Predictors for TTP

The results of the univariate analysis to evaluate clinical and conventional imaging predictors are summarized in Table 2. Among the potential clinical and imaging predictors, the presence of an atypical finding (hazard ratio, 4.41; 95% CI, 1.32–14.71; $P = .016$), a high ECOG score of 3 or 4 (hazard ratio, 5.82; 95% CI, 1.07–31.66; $P = .04$), and a high serum LDH level (hazard ratio, 1.01; 95% CI, 1.00–1.02; $P = .013$) were significantly associated with TTP in PCNSL.

Tumor Habitats Associated with TTP

The results of the univariate analysis to evaluate the associations of the 3 tumor habitats with TTP are summarized in Table 3. Among the tumor habitats, a large hypovascular cellular habitat

Table 2: Clinical and imaging predictors associated with TTP in PCNSL

Variable	Hazard Ratio	95% CI	*P* Value
Age	0.98	0.94–1.03	.55
Atypical finding[a]	4.41	1.32–14.71	.016
CSF-total protein	1.00	0.99–1.00	.70
ECOG			
2 (reference)			
3 or 4	5.82	1.07–31.66	.04
Serum LDH level	1.01	1.00–1.02	.013
Deep location[b]	1.75	0.33–9.08	.50

[a] Atypical findings: presence of hemorrhage or necrosis.
[b] Deep location: thalamus, basal ganglia, corpus callosum, periventricular area, cerebellum.

Table 3: Exploratory analysis of spatial habitats for predicting TTP in patients with PCNSL

	TTP		
Spatial Tumor Habitats	Hazard Ratio[a]	95% CI	*P* Value
No. of voxels (20,000 voxels)			
Hypervascular cellular habitat	1.39	0.29–6.44	.29
Hypovascular cellular habitat	2.83	1.20–6.65	.017
Hypovascular hypocelluar habitat	2.03	0.58–7.15	.27
Voxel fraction (%)			
Hypervascular cellular habitat	0.88	0.04–20.97	.83
Hypovascular cellular habitat	2.07	0.29–14.83	.46
Hypovascular hypocelluar habitat	0.46	0.05–4.01	.48
ADC	0.98	0.95–1.01	.16
CBV	0.80	0.45–1.32	.38

[a] Hazard ratios reported here indicate the relative change in hazard that a 10-unit (20,000 voxels) increase in each imaging parameter incurs.

(20,000 voxels) was significantly associated with a short TTP (hazard ratio, 2.83; 95% CI, 1.20–6.65; $P = .017$; Fig 3). No other tumor habitats or percentages of the tumor habitats were associated with TTP.

The single physiologic parameters of ADC and CBV showed no significant association with TTP ($P > .05$).

The correlations between the overall tumor burden and each habitat were moderate (hypervascular cellular habitat, $r = 0.51$, $P < .001$; and hypovascular hypocellular habitat, $r = 0.55$, $P < .001$) to strong (hypovascular cellular habitat, $r = 0.81$; $P < .001$).

The variable importance values of the clinical predictors, conventional imaging findings, and tumor habitats are shown in the Online Supplemental Data. The variable importance of tumor habitats of the hypovascular cellular habitat (variable importance, 0.0049) was higher than that of age (variable importance, 0.0037) and lower than that of atypical findings (variable importance, 0.0185).

Risk Stratification Using the Tumor Habitat Score

The optimal tumor habitat cutoff for stratifying patients according to treatment response and treatment resistance was >9000 voxels in the hypovascular cellular habitat. This cutoff value stratified patients according to treatment response and treatment resistance with a significant difference in the log-rank test ($P = .001$). Figure 4 shows the Kaplan-Meier survival curve and the risk table generated on the basis of the hypovascular cellular habitat. A habitat risk score based on discrete increments in the hypovascular cellular habitat was assigned for the patients.

Performance of the Prediction Model for TTP

The results of the prediction of TTP in PCNSL using tumor habitat and single physiologic MR imaging parameters are summarized in Table 4. The C-index for prediction of TTP using tumor habitats was 0.65 (95% CI, 0.52–0.78), which was significantly higher than that of the single physiologic MR imaging parameters.

A predictive model was constructed using the habitat score, the presence of an atypical finding, the ECOG score, and the serum LDH level. The C-index of this model combining selected clinical predictors, conventional imaging predictors, and tumor habitat for predicting TTP was 0.73 (95% CI, 0.67–0.80), which was higher than that of models based on clinical predictors only (C-index, 0.68; 95% CI, 0.54–0.82) or conventional imaging predictors only (C-index, 0.63; 95% CI, 0.50–0.76). The Hosmer-Lemeshow test indicated that the model had good calibration ($P > .5$). The C-index of the combined model of clinical predictors and conventional imaging predictors for predicting TTP was 0.71 (95% CI, 0.54–0.78), which was slightly lower than the combined habitat score model, but it did not reach statistical significance ($P = .10$).

DISCUSSION

In this study, we demonstrated that in PCNSL, the TTP after initial chemotherapy could be predicted by physiologic MR imaging–based tumor habitat analysis. A hypovascular cellular habitat with both low CBV and ADC values was significantly associated with treatment resistance, with a large extent of hypovascular cellular habitat being associated with a short TTP. Furthermore, a model combining selected clinical parameters, conventional imaging predictors, and tumor habitat analysis had great predictive power for identifying treatment resistance to initial chemotherapy.

The tumor microenvironment is composed of both cellular and molecular components that continuously interact. The tumor microenvironments in lymphomas are highly variable with regard to both the spatial arrangement and composition of cells. The tumor microenvironment plays critical roles in the regulation of tumor cell survival, proliferation, and immune escape, which leads to treatment resistance.[2,4,8] Imaging techniques such as texture analysis, fractal analysis, and habitat analysis can quantify these spatial heterogeneities of microenvironments within tumors,[12] and in this study, we used tumor habitat analysis to identify tumor subregions and then used them to predict treatment resistance. Tumor habitat analysis, which parcellates similar voxels using a clustering method, can reflect the heterogeneity of tumor cellularity and vascularity and identify subregions that can be used to predict the response to chemotherapy in PCNSL.

A significant inverse correlation exists between tumor cellularity and ADC values,[23] suggesting that ADC values can be used as a surrogate marker of tumor proliferation.[24-26] ADC values have shown potential as a prognostic imaging biomarker for the response to treatment of non-Hodgkin lymphoma.[27] In our study,

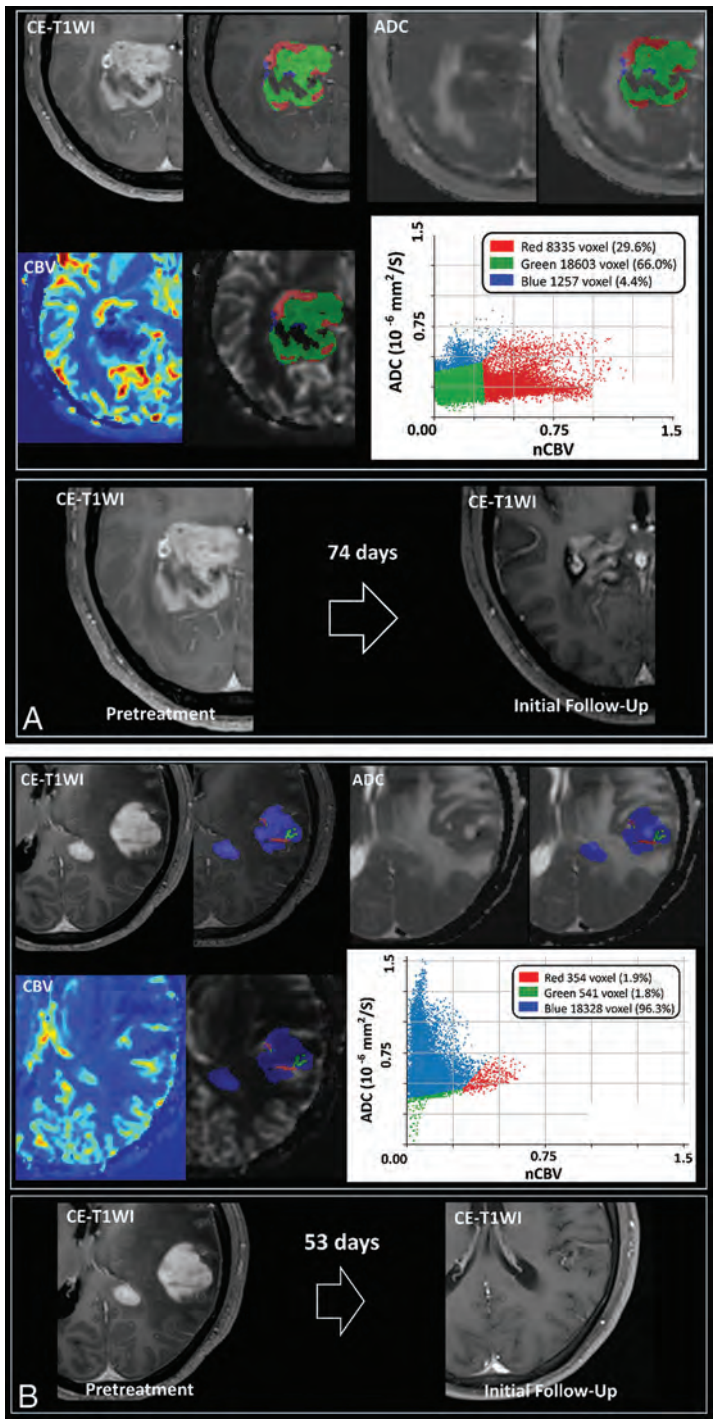

FIG 3. *A*, Demonstration of the 3 spatial habitats defined by clustering of voxels using normalized ADC and nCBV maps in a 53-year-old male patient. The hypervascular cellular habitat (red) shows high nCBV and low ADC, the hypovascular cellular habitat (green) shows low nCBV and low ADC, and the hypovascular hypocellular habitat (blue) shows low nCBV and high ADC. The tumor exhibits a large hypovascular cellular habitat (green), and a persistent enhancing mass was associated with a short TTP after initial chemotherapy. *B*, Demonstration of the 3 spatial habitats defined by clustering of voxels using normalized ADC and nCBV maps in a 57-year-old male patient. The hypervascular cellular habitat (red) shows high nCBV and low ADC, the hypovascular cellular habitat (green) shows low nCBV and low ADC, and the hypovascular hypocellular habitat (blue) shows low nCBV and high ADC. The tumor has a small hypovascular cellular habitat (green) and showed a complete response at 53 days after initial chemotherapy.

low ADC values in PCNSL with a cellular habitat indicating a high tumor burden correlated with adverse clinical outcomes.

CBV measurements obtained using DSC MR imaging are one of the indirect modalities used to evaluate the functional vascularity of the tumor and its oxygenation status,[28,29] which are closely related to the response to chemotherapy or radiation therapy.[30] The hypovascular habitat identified in our study may reflect a hypoxic microenvironment that is resistant to treatment, with changes in gene and molecular expression and evolution toward increased malignancy and an increasingly aggressive phenotype.[30] Furthermore, low CBV values may represent a decrease in the patent vessels that deliver the chemotherapeutic agent to the tumor bed, which, therefore, induces resistance to treatment. This is supported in a previous study[31] that found that high CBV values were associated with a good prognosis with longer overall survival and progression-free survival in PCNSL. The hypovascular cellular habitat showed the strongest correlation with overall tumor burden, and it may indicate the region of tumor core to be treated rather than the region responding well to therapy.

Five clinical parameters are well-known to correlate with a worse prognosis in PCNSL: elevated LDH, age older than 60 years, poor performance status, elevated CSF protein, and location of tumor within the deep regions of the brain such as periventricular regions, basal ganglia, brainstem, and/or cerebellum.[16] The presence of atypical imaging findings that reflect necrosis or a hemorrhagic component is associated with short TTP.[16,17] These findings also indicate poor tumor perfusion and decreased perfusion-related drug delivery because of necrosis and hemorrhage within the tumor.[32,33]

This study has several limitations. The first is the small sample size resulting from the rarity of the disease and the lack of external validation. Second, the chemotherapy regimens

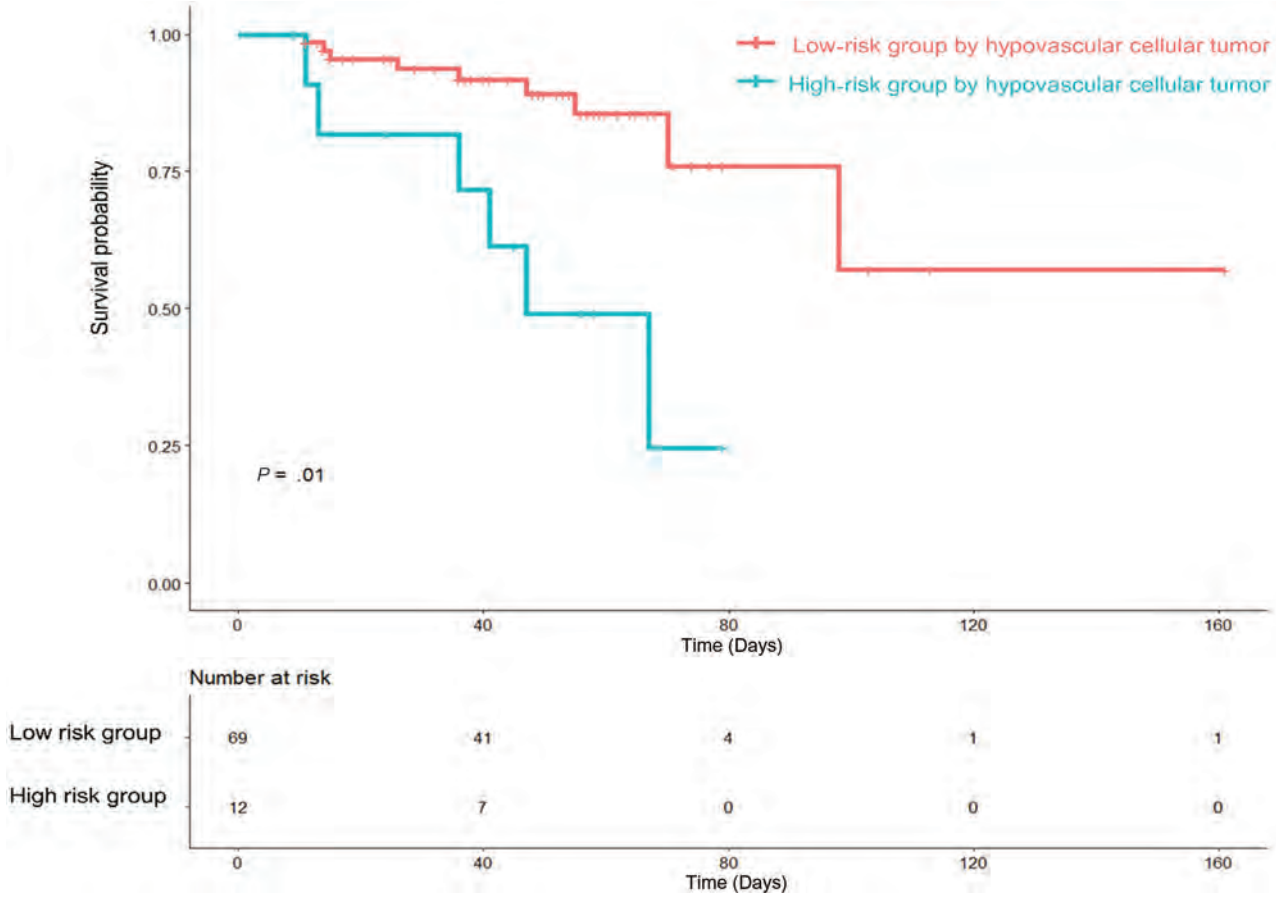

FIG 4. Kaplan-Meier analysis of TTP in patients with PCNSL stratified by hypovascular cellular habitat (log-rank, $P = .01$).

Table 4: Prediction of TTP in PCNSLs according to tumor habitat, ADC, and CBV[a]

	Combination of Clinical, Conventional Imaging Predictors, and Tumor Habitats	Combined Clinical and Conventional Predictors	Tumor Habitats	Clinical Predictors Only	Conventional Imaging Predictors Only
C-index	0.73	0.71	0.65	0.68	0.63
95% CI	0.67–0.80	0.54–0.78	0.52–0.78	0.54–0.82	0.50–0.76
P value	Reference	.01	.012	.81	.62

[a] Combined clinical predictors were age, ECOG score, and mean serum LDH level; the conventional imaging predictor was the presence of atypical image findings. *P* value refers to the significance in the difference of the C-indices between the combined model and the single model assessed using "CompareC" (https://cran.r-project.org/web/packages/compareC/index.html) in the R statistical and computing software.

used in this study were not unified. Because there is no consensus regarding the other agents to be used in combination with MTX, several combinations of MTX-based chemotherapy were tried. We did not perform subgroup analysis per regimen because there were only a small number of patients in each combination regimen. Also, although high-dose radiation therapy plus consolidation chemotherapy or radiation therapy or both are used, there is no consensus on their combination with MTX.[34] Our results should be confirmed by other studies with strict control of the chemotherapy regimen. Finally, the prediction performance was not high, with a C-index of only 0.70. Nonetheless, our study may be meaningful because it demonstrates the heterogeneity of PCNSL using physiologic MR imaging and the possibility of a future imaging biomarker–directed therapeutic plan. A well-designed prospective study is warranted.

CONCLUSIONS

The analysis of spatial habitats derived from multiparametric physiologic MR imaging may provide added value for predicting treatment response after initial chemotherapy. A hypovascular cellular tumor habitat was associated with treatment resistance in PCNSL and may be useful for refining imaging-based prediction for patients with PCNSL before they undergo chemotherapy.

ACKNOWLEDGMENT

We would like to thank Shin-Kyo Yoon, MD, for helping us in assessment of treatment response in this study.

Disclosure forms provided by the authors are available with the full text and PDF of this article at www.ajnr.org.

REFERENCES

1. Cai Q, Fang Y, Young KH. **Primary central nervous system lymphoma: molecular pathogenesis and advances in treatment.** *Transl Oncol* 2019;12:523–38 CrossRef Medline
2. Fowler NH, Cheah CY, Gascoyne RD, et al. **Role of the tumor microenvironment in mature B-cell lymphoid malignancies.** *Haematologica* 2016;101:531–40 CrossRef Medline
3. Alame M, Pirel M, Costes-Martineau V, et al. **Characterisation of tumour microenvironment and immune checkpoints in primary central nervous system diffuse large B cell lymphomas.** *Virchows Arch* 2020;476:891–902 CrossRef Medline
4. Scott DW, Gascoyne RD. **The tumour microenvironment in B cell lymphomas.** *Nat Rev Cancer* 2014;14:517–34 CrossRef Medline
5. Lenz G, Dreyling M, Hoster E, et al. **Immunochemotherapy with rituximab and cyclophosphamide, doxorubicin, vincristine, and prednisone significantly improves response and time to treatment failure, but not long-term outcome in patients with previously untreated mantle cell lymphoma: results of a prospective randomized trial of the German Low Grade Lymphoma Study Group (GLSG).** *J Clin Oncol* 2005;23:1984–92 CrossRef Medline
6. Nayak L, Batchelor TT. **Recent advances in treatment of primary central nervous system lymphoma.** *Curr Treat Options Oncol* 2013;14:539–52 CrossRef Medline
7. Chung SR, Choi YJ, Kim HS, et al. **Tumor vascular permeability pattern is associated with complete response in immunocompetent patients with newly diagnosed primary central nervous system lymphoma: retrospective cohort study.** *Medicine* 2016;95:e2624 CrossRef Medline
8. Hatzoglou V, Oh JH, Buck O, et al. **Pretreatment dynamic contrast-enhanced MRI biomarkers correlate with progression-free survival in primary central nervous system lymphoma.** *J Neurooncol* 2018;140:351–58 CrossRef Medline
9. Kim M, Kim HS. **Emerging techniques in brain tumor imaging: what radiologists need to know.** *Korean J Radiol* 2016;17:598–619 CrossRef Medline
10. Provenzale JM, Mukundan S, Barboriak DP. **Diffusion-weighted and perfusion MR imaging for brain tumor characterization and assessment of treatment response.** *Radiology* 2006;239:632–49 CrossRef Medline
11. Barajas RF Jr, Rubenstein JL, Chang JS, et al. **Diffusion-weighted MR imaging derived apparent diffusion coefficient is predictive of clinical outcome in primary central nervous system lymphoma.** *AJNR Am J Neuroradiol* 2010;31:60–66 CrossRef Medline
12. O'Connor JP, Rose CJ, Waterton JC, et al. **Imaging intratumor heterogeneity: role in therapy response, resistance, and clinical outcome.** *Clin Cancer Res* 2015;21:249–57 CrossRef Medline
13. Oken MM, Creech RH, Tormey DC, et al. **Toxicity and response criteria of the Eastern Cooperative Oncology Group.** *Am J Clin Oncol* 1982;5:649–55 CrossRef Medline
14. Abrey LE, Batchelor TT, Ferreri AJ, et al; International Primary CNS Lymphoma Collaborative Group. **Report of an international workshop to standardize baseline evaluation and response criteria for primary CNS lymphoma.** *J Clin Oncol* 2005;23:5034–43 CrossRef Medline
15. Wen PY, Macdonald DR, Reardon DA, et al. **Updated response assessment criteria for high-grade gliomas: Response Assessment in Neuro-Oncology Working Group.** *J Clin Oncol* 2010;28:1963–72 CrossRef Medline
16. Ferreri AJ, Blay JY, Reni M, et al. **Prognostic scoring system for primary CNS lymphomas: the International Extranodal Lymphoma Study Group experience.** *J Clin Oncol* 2003;21:266–72 CrossRef Medline
17. Thurnher MM, Rieger A, Kleibl-Popov C, et al. **Primary central nervous system lymphoma in AIDS: a wider spectrum of CT and MRI findings.** *Neuroradiology* 2001;43:29–35 CrossRef Medline
18. Isensee F, Jaeger PF, Kohl SA, et al. **nnU-Net: a self-configuring method for deep learning-based biomedical image segmentation.** *Nat Methods* 2021;18:203–11 CrossRef Medline
19. Gull SF. **Bayesian inductive inference and maximum entropy.** In: Erickson GJ, Smith CR, eds. *Maximum-Entropy and Bayesian Methods in Science and Engineering: Fundamental Theories of Physics* (An International Book Series on The Fundamental Theories of Physics: Their Clarification, Development and Application), vol 31-32. Springer-Verlag Netherlands; 1988:53–74
20. Ingrisch M, Schneider MJ, Norenberg D, et al. **Radiomic analysis reveals prognostic information in T1-weighted baseline magnetic resonance imaging in patients with glioblastoma.** *Invest Radiol* 2017;52:360–66 CrossRef Medline
21. Han K, Song K, Choi BW. **How to develop, validate, and compare clinical prediction models involving radiological parameters: study design and statistical methods.** *Korean J Radiol* 2016;17:339–50 CrossRef Medline
22. D'agostino RB, Nam BH. **Evaluation of the performance of survival analysis models: discrimination and calibration measures.** *Advances in Survival Analysis* 2003;23:1–25
23. Africa E, Pauciulo A, Vadalà R, et al. **Primary central nervous system lymphoma: role of DWI in the differential diagnosis.** *Rays* 2005;30:221–26 Medline
24. Guo AC, Cummings TJ, Dash RC, et al. **Lymphomas and high-grade astrocytomas: comparison of water diffusibility and histologic characteristics.** *Radiology* 2002;224:177–83 CrossRef Medline
25. Herneth AM, Guccione S, Bednarski M. **Apparent diffusion coefficient: a quantitative parameter for in vivo tumor characterization.** *Eur J Radiol* 2003;45:208–13 CrossRef Medline
26. Khayal IS, Vandenberg SR, Smith KJ, et al. **MRI apparent diffusion coefficient reflects histopathologic subtype, axonal disruption, and tumor fraction in diffuse-type grade II gliomas.** *Neuro Oncol* 2011;13:1192–201 CrossRef Medline
27. Wu X, Kellokumpu-Lehtinen PL, Pertovaara H, et al. **Diffusion-weighted MRI in early chemotherapy response evaluation of patients with diffuse large B-cell lymphoma–a pilot study: comparison with 2-deoxy-2-fluoro- D-glucose-positron emission tomography/computed tomography.** *NMR Biomed* 2011;24:1181–90 CrossRef Medline
28. Yetkin FZ, Mendelsohn D. **Hypoxia imaging in brain tumors.** *Neuroimaging Clin N Am* 2002;12:537–52 CrossRef Medline
29. Le Duc G, Péoc'h M, Rémy C, et al. **Use of T(2)-weighted susceptibility contrast MRI for mapping the blood volume in the glioma-bearing rat brain.** *Magn Reson Med* 1999;42:754–61 CrossRef Medline
30. Knisely JP, Rockwell S. **Importance of hypoxia in the biology and treatment of brain tumors.** *Neuroimaging Clin N Am* 2002;12:525–36 CrossRef Medline
31. Valles FE, Perez-Valles CL, Regalado S, et al. **Combined diffusion and perfusion MR imaging as biomarkers of prognosis in immunocompetent patients with primary central nervous system lymphoma.** *AJNR Am J Neuroradiol* 2013;34:35–40 CrossRef Medline
32. Buttini M, Appel K, Sauter A, et al. **Expression of tumor necrosis factor alpha after focal cerebral ischaemia in the rat.** *Neuroscience* 1996;71:1–16 CrossRef Medline
33. Zazulia AR, Diringer MN, Videen TO, et al. **Hypoperfusion without ischemia surrounding acute intracerebral hemorrhage.** *J Cereb Blood Flow Metab* 2001;21:804–10 CrossRef Medline
34. Kim SK, Park JE, Kim KH, KSNO Guideline Working Group, et al. **A national consensus survey for current practice in brain tumor management, III: brain metastasis and primary central nervous system lymphoma.** *Brain Tumor Res Treat* 2020;8:20–28 CrossRef Medline

An Investigation of Water Diffusivity Changes along the Perivascular Space in Elderly Subjects with Hypertension

J. Kikuta, K. Kamagata, K. Takabayashi, T. Taoka, H. Yokota, C. Andica, A. Wada, Y. Someya, Y. Tamura, R. Kawamori, H. Watada, S. Naganawa, and S. Aoki

ABSTRACT

BACKGROUND AND PURPOSE: Hypertension may be related to alterations of the glymphatic system, a waste metabolite drainage system in the brain. We aimed to investigate analysis along the perivascular space index changes in elderly subjects with hypertension.

MATERIALS AND METHODS: Diffusion-weighted images were acquired from 126 subjects, including 63 subjects with hypertension (25 men and 38 women; mean age, 72.45 years) and 63 age- and sex-matched controls (25 men and 38 women; mean age, 72.16 years). We calculated the analysis along the perivascular space index as a ratio of the mean of x-axis diffusivities in the projection and association areas to the mean of y-axis diffusivity in the projection area and z-axis diffusivity in the association area. The left, right, and mean analysis along the perivascular space indices of both hemispheres were compared between the hypertension and control groups using a Mann-Whitney *U* test. The Spearman correlation coefficient was used to assess the correlation between the left, right, and mean ALPS indices and blood pressure and pulse pressure.

RESULTS: The left ($P = .011$) and mean ($P = .024$) analysis along the perivascular space indices of the hypertension group were significantly lower than that of the control group. The left, right, and mean analysis along the perivascular space indices of all subjects were significantly negatively correlated with blood pressure values ($r = -0.200$ to -0.278, $P = .002$–0.046) and pulse pressure values ($r = -0.221$ to -0.245, $P = .006$–0.013).

CONCLUSIONS: Our results are consistent with a model in which hypertension causes glymphatic dysfunction.

ABBREVIATIONS: ALPS = analysis along the perivascular space; HT = hypertension; ISF = interstitial fluid

The glymphatic system is a waste metabolite drainage system in the brain.[1-3] It consists of four sequential anatomic segments. First, the cerebrospinal fluid (CSF) flows along the perivascular space surrounding the penetrating arteries. Second, the CSF disperses into the interstitial space and transfers waste metabolites into the interstitial fluid (ISF) facilitated by aquaporin-4 water channels, which form the outer wall of the perivascular space. Third, the ISF-containing waste metabolites flow out of the large-caliber draining vein.[2] Finally, interstitial solutes exit the brain through meningeal lymphatic vessels, together with the venous sinuses.[4] Glymphatic dysfunction leads to the deposition of toxic waste products, such as amyloid β and tau proteins, which contribute to the pathogenesis of Alzheimer disease.[5-7] Toxic solute accumulation due to drainage dysfunction has been demonstrated in normal aging,[8] traumatic brain injury,[9] and stroke.[10]

Hypertension (HT) is a risk factor for Alzheimer disease in the elderly.[11,12] HT involves pathologic alterations of small cerebral blood vessels and capillaries.[13,14] Mestre et al[13] found that the perivascular pump is less efficient in hypertensive mice due to dynamic changes in the vessel wall. Moreover, Mortensen et al[14] demonstrated suppression of glymphatic activity in spontaneously hypertensive rats, which reduced parenchymal waste transport.

On the basis of these findings, we hypothesized that patients with HT have an impairment of the glymphatic system. Alterations in glymphatic function due to HT in living human brains have not been reported to date because of the challenges

Received April 6, 2021; accepted after revision September 6.

From the Department of Radiology (J.K., K.K., K.T., C.A., A.W., S.A.), Sportology Center (Y.S., Y.T., R.K., H.W.), and Department of Metabolism & Endocrinology (Y.T., R.K., H.W.), Juntendo University Graduate School of Medicine, Tokyo, Japan; Department of Innovative Biomedical Visualization (T.T.), Graduate School of Medicine, Nagoya University, Aichi, Japan; Department of Diagnostic Radiology and Radiation Oncology (H.Y.), Graduate School of Medicine, Chiba University, Chiba, Japan; and Department of Radiology (S.N.), Nagoya University Graduate School of Medicine, Aichi, Japan.

This work was supported, in part, by the Japan Society for the Promotion of Science Grants-in-Aid for Scientific Research, grant Nos. 18H02772 and 20K16737, and a Grant-in-Aid for Special Research in Subsidies for ordinary expenses of private schools from the Juntendo Research Branding Project.

Please address correspondence to Junko Kikuta, MD, PhD, Department of Radiology, Juntendo, University of Medicine, 2-1-1 Hongo, Bunkyo-ku, Tokyo 113-8421, Japan; e-mail: j.kikuta.hy@juntendo.ac.jp

http://dx.doi.org/10.3174/ajnr.A7334

Table 1: Demographic characteristics of the participants[a]

	Control Group ($n = 63$)	HT Group ($n = 63$)	*P* Values
Age	72.16 (SD, 5.11)	72.45 (SD, 5.26)	1
Sex (male/female)	25/38	25/38	1
Systolic blood pressure (mm Hg)	123.55 (SD, 10.09)	143.63 (SD, 14.51)	<.001
Diastolic blood pressure (mm Hg)	80.30 (SD, 6.85)	88.60 (SD, 9.30)	<.001
Average blood pressure (mm Hg)	98.86 (SD, 7.96)	113.76 (SD, 11.37)	<.001
Pulse pressure (mm Hg)	67.56 (SD, 12.28)	82.13 (SD, 13.86)	<.001
Body mass index (kg/m^2)	21.56 (SD, 2.72)	23.76 (SD, 2.55)	<.001
Hemoglobin A1c (%)	5.83 (SD, 0.67)	5.76 (SD, 0.40)	.654
Total cholesterol (mg/dL)	216.73 (SD, 49.08)	203.68 (SD, 33.92)	.093
High-density lipoprotein (mg/dL)	63.98 (SD, 13.31)	64.89 (SD, 15.45)	.988
Low-density lipoprotein (mg/dL)	129.89 (SD, 31.54)	119.33 (SD, 30.01)	.043
Triglyceride (mg/dL)	94.46 (SD, 65.70)	97.17 (SD, 46.48)	.415
Deep white matter hyperintensities Fazekas scale	1.16 (SD, 0.48)	1.41 (SD, 0.64)	.013

[a] Data are presented as means (SDs).

encountered during in vivo tracer studies. Taoka et al[15] introduced the analysis along the perivascular space (ALPS) method, which is calculated using DWI as a noninvasive tool to evaluate the glymphatic system of living humans. This method assumes that diffusion plays an essential role in fluid transport in the brain parenchyma. We assessed ALPS index differences between elderly subjects with and without HT and evaluated the association between the ALPS index and blood pressure and pulse pressure.

MATERIALS AND METHODS

This study was approved by the ethics committee of Juntendo University in November 2015 and was conducted according to the principles outlined in the Declaration of Helsinki.

Study Participants

The Bunkyo Health Study is a prospective cohort study that has been running for >10 years.[16] We recruited elderly subjects 65–84 years of age who were living in Bunkyo-ku, an urban area in Tokyo. Our cohort comprised 1629 elderly people. Of these, 160 participants underwent both FLAIR imaging and DWI. All subjects were right-handed and had no history of diabetes (hemoglobin A1c < 6.5%), hyperlipidemia (total cholesterol < 240 mg/dL, low-density lipoprotein < 140 mg/dL, high-density lipoprotein > 40 mg/dL, and triglyceride < 150 mg/dL), or obesity (body mass index < 25 kg/m^2; Table 1). Subjects with systolic/diastolic blood pressure of ≥135/85 mm Hg during their first visit or those who had a history of using antihypertensive drugs were included in the HT group. We included 126 elderly participants, including 63 subjects with HT (25 men and 38 women; mean age, 72.45 [SD, 5.26] years) and 63 age- and sex-matched subjects without HT (controls; 25 men and 38 women; mean age, 72.16 [SD, 5.11] years) in this study. The demographic characteristics of the study subjects are presented in Table 1.

MR Imaging Acquisition

We performed FLAIR imaging (TR = 11,000 ms; TE = 100 ms; TI = 2000 ms; section thickness = 5 mm) on a 3T MR imaging scanner (Airis Vento; Hitachi) in all participants. Deep white hyperintensity evaluation using the Fazekas scale based on axial FLAIR imaging was performed by an experienced neuroradiologist. DWI data were acquired on a 3T MR imaging scanner (Magnetom Prisma; Siemens) with a 64-channel head coil. Echo-planar imaging was acquired using a b-value of 1000 s/mm^2 along 64 isotropic diffusion gradients in the anterior–posterior phase-encoding direction with the following parameters: TR = 3300 ms; TE = 70 ms; FOV = 229 × 229 mm; matrix size = 130 × 130; resolution = 1.8 × 1.8 mm; section thickness = 1.8 mm; acquisition time = 7 minutes 29 seconds. Each DWI acquisition was completed with a $b = 0$ image. We also acquired standard and reverse phase-encoded blipped images with no diffusion weighting (blip-up and blip-down) to correct for magnetic susceptibility–induced distortions related to echo-planar imaging acquisitions.

DWI Processing

DWI data were processed using the FMRIB Software Library,[17] Version 6.0 (FSL; www.fmrib.ox.ac.uk/fsl). Diffusion-weighted data were corrected for susceptibility-induced geometric distortions, eddy current distortions, and intervolume subject motion using the eddy and topup toolboxes. Diffusivity maps of each subject were acquired in the directions of the x- (right-left, *Dxx*), y- (anterior-posterior, *Dyy*), and z-axes (inferior-superior, *Dzz*).[18] *Dxx* corresponds to the direction of the deep white matter vessels in the periventricular white matter. Considering that the glymphatic system runs along these deep white matter vessels, the *Dxx* is assumed to partly reflect water diffusivity along the glymphatic system. Fractional anisotropy maps of all study participants were also generated and registered to the FMRIB58_FA standard space (https://fsl.fmrib.ox.ac.uk/fsl/fslwiki/FMRIB58_FA) using FSL's Linear Image Registration Tool (FLIRT; http://www.fmrib.ox.ac.uk/fsl/fslwiki/FLIRT) and nonlinear registration tool (FNIRT; http://fsl.fmrib.ox.ac.uk/fsl/fslwiki/FNIRT).

ROI Placement

For ROI placement, 1 subject (68-year-old female control participant) with minimal head movement (ie, with the smallest sum of squared difference) was selected. Using this subject's color-coded fractional anisotropy map, we manually placed 5-mm-diameter square ROIs in the projection and association areas at the level of the ventricle bodies of the left and right hemispheres (Fig 1). In the projection area, dominant fibers run in the z-axis direction, perpendicular to both the x- and y-axes, whereas in the association area, dominant fibers run in the y-axis direction, perpendicular to both the x- and z-axes. The resulting ROIs were then registered to the same fractional anisotropy template. Finally, we manually checked the positions of the ROIs on each participant's fractional anisotropy image. Manual corrections were not performed because all ROIs were correctly placed.

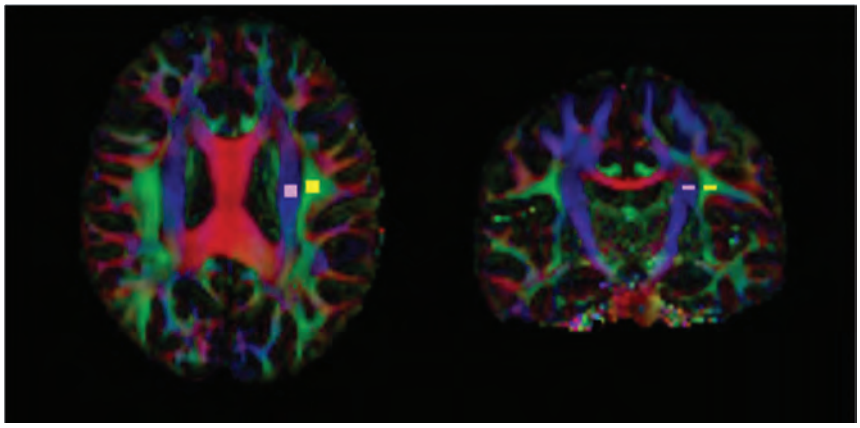

FIG 1. ROI placement for the calculation of the ALPS index. *Square ROIs* of $5 \times 5\,mm^2$ were placed in the projection (pink) and association (yellow) areas.

Table 2: The values of the left, right, and mean ALPS indices in the HT and control groups[a]

	HT Group	Control Group	*P* Value
Left ALPS index	1.30 (SD, 0.22)	1.40 (SD, 0.19)	.011
Right ALPS index	1.32 (SD, 0.18)	1.37 (SD, 0.21)	.094
Mean ALPS index	1.31 (SD, 0.19)	1.39 (SD, 0.19)	.024

[a] Data are presented as means (SDs).

ALPS Index Calculation

The diffusivity values of the x-, y-, and z-axes within the ROIs were obtained for each participant. The ALPS index was calculated as a ratio of the mean of the x-axis diffusivity in the projection area (*Dxxproj*) and x-axis diffusivity in the association area (*Dxxassoc*) to the mean of the y-axis diffusivity in the projection area (*Dyyproj*) and the z-axis diffusivity in the association area (*Dzzassoc*) as follows:

$$ALPS\ index = \frac{Dxxproj + Dxxassoc}{Dyyproj + Dzzassoc}.$$

An ALPS index close to 1.0 reflects minimal diffusion along the perivascular space, whereas higher values indicate greater diffusivity. The left and right ALPS indices and the mean ALPS index of the left and right hemispheres were calculated.

Statistical Analysis

Statistical analysis was performed using SPSS Statistics, Version 27.0 (IBM). The left, right, and mean ALPS indices of the control and HT groups were compared using a nonparametric Mann-Whitney *U* test. The associations between the left, right, and mean ALPS indices of all subjects and the values of systolic blood pressure, diastolic blood pressure, average blood pressure, and pulse pressure were evaluated using Spearman correlation coefficients. A *P* value $<.05$ was considered statistically significant.

RESULTS

The features of the control and HT groups are summarized in Table 1. The control and HT groups did not differ significantly in age, sex, hemoglobin A1c, total cholesterol, high-density lipoprotein, or triglyceride values. As expected, the HT group had significantly higher ($P < .001$) systolic, diastolic, and average blood pressures and pulse pressures than the control group. Furthermore, the HT group had significantly higher body mass index ($P < .001$) and Fazekas scale scores ($P < .013$) than the control group. In contrast, the low-density lipoprotein value of the control group was significantly higher than that of the HT group ($P < .043$). Nevertheless, all subjects were without obesity or hyper-low-density lipoprotein cholesterolemia. Moreover, we confirmed no white matter hyperintensities in the ROIs.

The left ($P = .011$) and mean ALPS ($P = .024$) indices of the HT group were significantly lower than those of the control group. However, the right ALPS index did not differ significantly between the HT and control groups ($P = .094$). Table 2 shows the left, right, and mean ALPS index values of the HT and control groups. Figure 2 shows the box plots of the left, right, and mean ALPS indices between the HT and control groups. Furthermore, the left, right, and mean ALPS indices of all subjects were significantly negatively correlated with systolic blood pressure values ($r = -0.202$ to -0.263, $P = .003$–$.023$), diastolic blood pressure values ($r = -0.200$ to -0.218, $P = .014$–$.046$), average blood pressure values ($r = -0.231$ to -0.278, $P = .002$–$.009$), and pulse pressure values ($r = -0.221$ to -0.245, $P = .006$–$.013$). The scatterplots in Fig 3 show the correlation between the left, right, and mean ALPS indices and systolic blood pressure, diastolic blood pressure, average blood pressure, and pulse pressure values.

DISCUSSION

We evaluated elderly subjects with HT using the ALPS index, which is a potential biomarker for the assessment of glymphatic activity in the living human brain. Our results demonstrated that left and mean ALPS indices in the subjects with HT were significantly lower relative to controls, though no significant difference was observed between the HT and control groups for the right ALPS index. Our study also found negative correlations between the left, right, and mean ALPS indices and blood pressure, and the left, right, and mean ALPS indices and pulse pressure, which suggest that glymphatic dysfunction is related to HT.

HT increases the risk of cognitive impairment, vascular dementia, and Alzheimer disease in the elderly.[11,12,19,20] The accumulation of toxic solutes such as amyloid β and tau protein in the brain was shown to be an important neuropathologic mechanism of cognitive dysfunction in elderly subjects with HT.[5-7] Previous studies have indicated that the accumulation of waste metabolites causes glymphatic dysfunction, which leads to further deposition.[1-3] HT and arteriosclerosis have been shown to lead to pathologic changes in small cerebral blood vessels and capillaries.[13,14] Such abnormalities contribute to reductions in cerebral blood flow and volume, which cause white matter hypoperfusion. Moreover, endothelial cell abnormalities and blood-brain barrier dysfunction may contribute

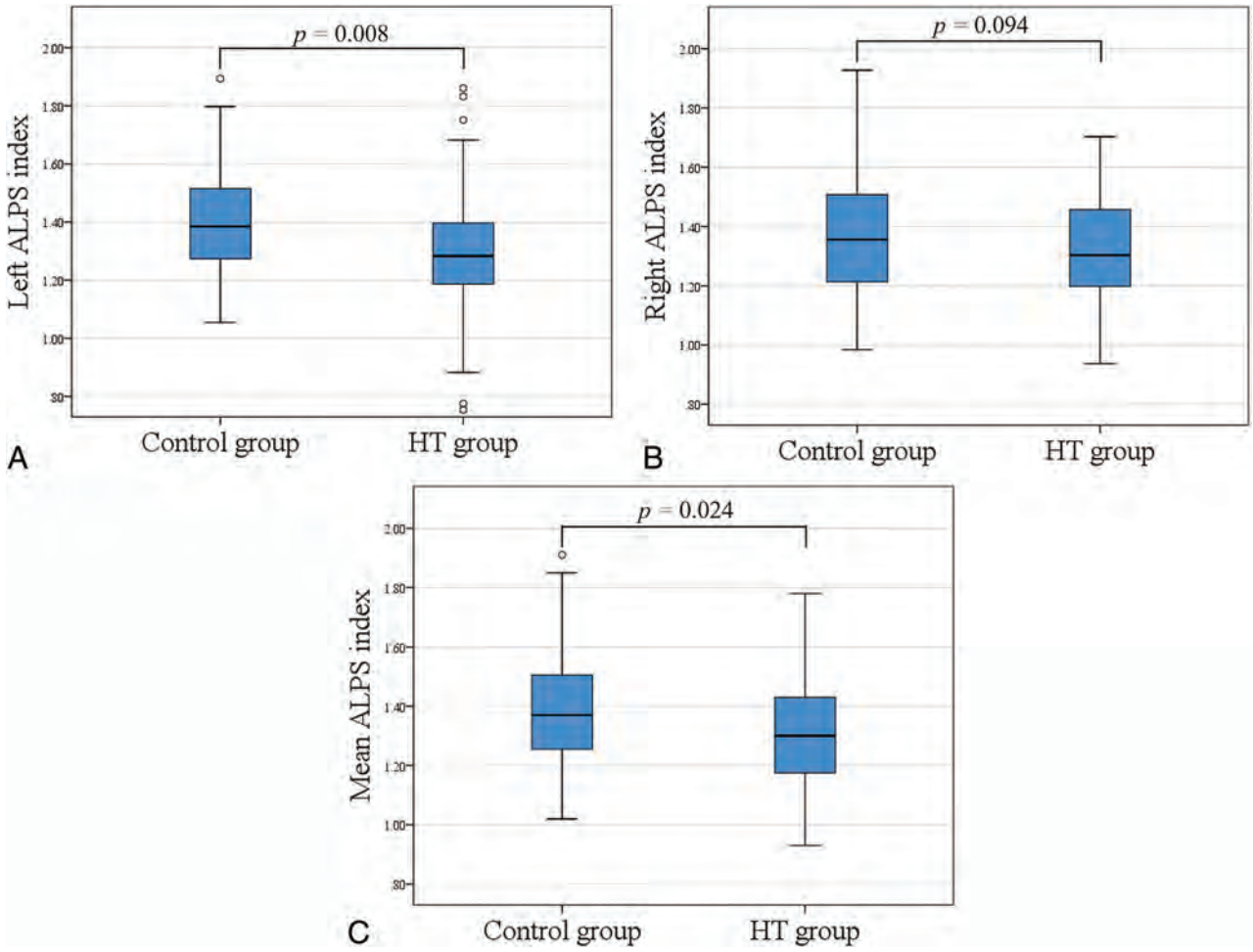

FIG 2. Boxplots of the left, right, and mean ALPS indices in the HT and control groups.

to white matter impairment. In the present study, although we did not detect any white matter hyperintensities in the ROIs, the HT group had more advanced white matter impairment than the control group. Adler et al[21] demonstrated that blood-brain barrier disruption increases the permeability of the vessel wall and mobilizes inflammatory factors such as macrophages, lymphocytes, and complementary components, which may lead to myelin damage. Yamamoto et al[22] also reported dilation of the perivascular space, accompanied by myelin degeneration and defects in ISF drainage in cerebral autosomal dominant arteriopathy, with subcortical infarcts and leukoencephalopathy associated with extensive small-vessel disease. In addition, Kamagata et al[23] reported an association between arterial stiffness and white matter demyelination using magnetization transfer saturation imaging. Notably, myelin-rich tissue, such as white matter, has been shown to be more sensitive to ISF flow obstruction.[24] Therefore, small-vessel diseases may be associated with alterations of both white matter microstructure and drainage function. Furthermore, in small-vessel disease, because of the difference in the anatomic bifurcation of the left and right carotid arteries, the left carotid artery is considered more susceptible to strong pulse pressure directly from the aortic arch, which increases the likelihood of plaque formations and intima damage becoming more severe.[25] Thus, microangiopathy due to HT in the left cerebral hemisphere may be more marked than that in the right cerebral hemisphere. This possibility may explain why the ALPS indices of the left hemisphere showed a significant difference between the HT and control groups, which was not observed in the right hemisphere.

To the best of our knowledge, this is the first study to show changes in water diffusivity along the perivascular space in living patients with HT. Previously, the suppression of glymphatic function has been observed in spontaneously hypertensive rats using dynamic contrast-enhanced MR imaging,[14] which suggested that hypertensive conditions reduce the effectiveness of arterial pulsation as a driver of CSF-ISF exchange and impair glymphatic activity. Using ex vivo fluorescence imaging, Mestre et al[13] also demonstrated that the perivascular pump is less efficient in hypertensive mice due to changes in vessel wall dynamics. The perivascular pump driven by arterial pulsation is a powerful mechanism for fluid transport within the brain.[26] Therefore, the decreased function of the perivascular pump could lead to a reduction in glymphatic activity. In line with previous studies in hypertensive animals, our findings demonstrated the effect of HT on human glymphatic dysfunction. Our study observed weak correlations between the ALPS index and blood pressure and the ALPS index and pulse pressure. Bewick et al[27] reported that a weak correlation with a low *R*-value can be statistically significant in a large sample size. We used a relatively large sample size; thus, a weak correlation

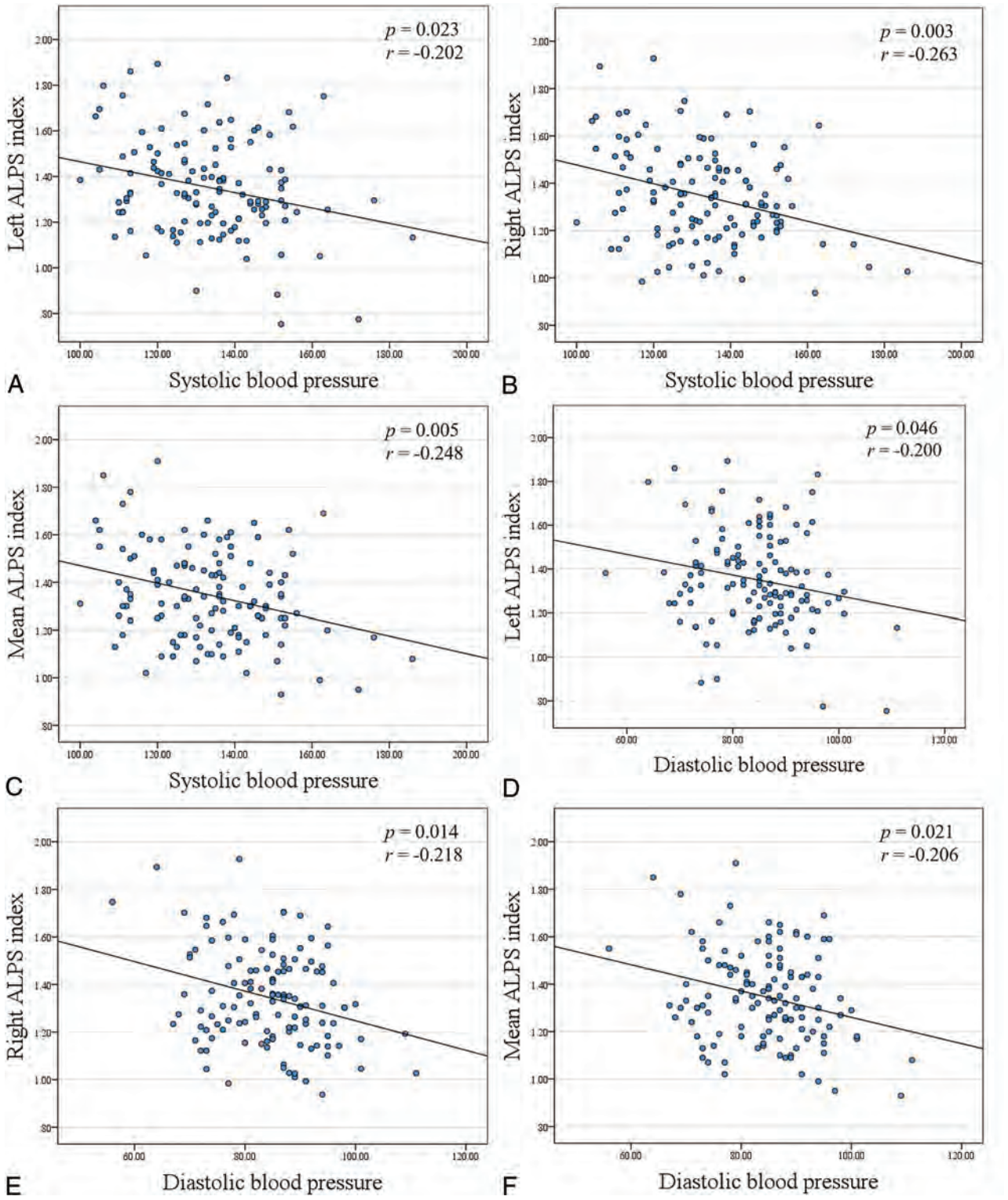

FIG 3. Scatterplots. *A–C*, Correlations between the left, right, and mean ALPS indices and the systolic blood pressure values. *D–F*, Correlations between the left, right, and mean ALPS indices and the diastolic blood pressure values. *G–I*, Correlations between the left, right, and mean ALPS indices and the average blood pressure values. *J–L*, Correlations between the left, right, and mean ALPS indices and the pulse pressure values in all subjects.

is still considered clinically relevant. High pulse pressure reflects an estimate of the stiffness of the large central arteries, and high blood pressure results from arteriosclerosis in the peripheral arteries.[28] Such arterial damage may lead to glymphatic dysfunction due to arterial pulsation and perivascular pump changes.[1,29,30]

The clearance of waste metabolites is essential for tissue homeostasis and is mediated by the blood-brain barrier and the CSF-ISF exchange pathway.[31] The glymphatic system is a clearance mechanism associated with CSF and ISF dynamics, as observed in many tracing studies. Iliff et al[1] showed that CSF

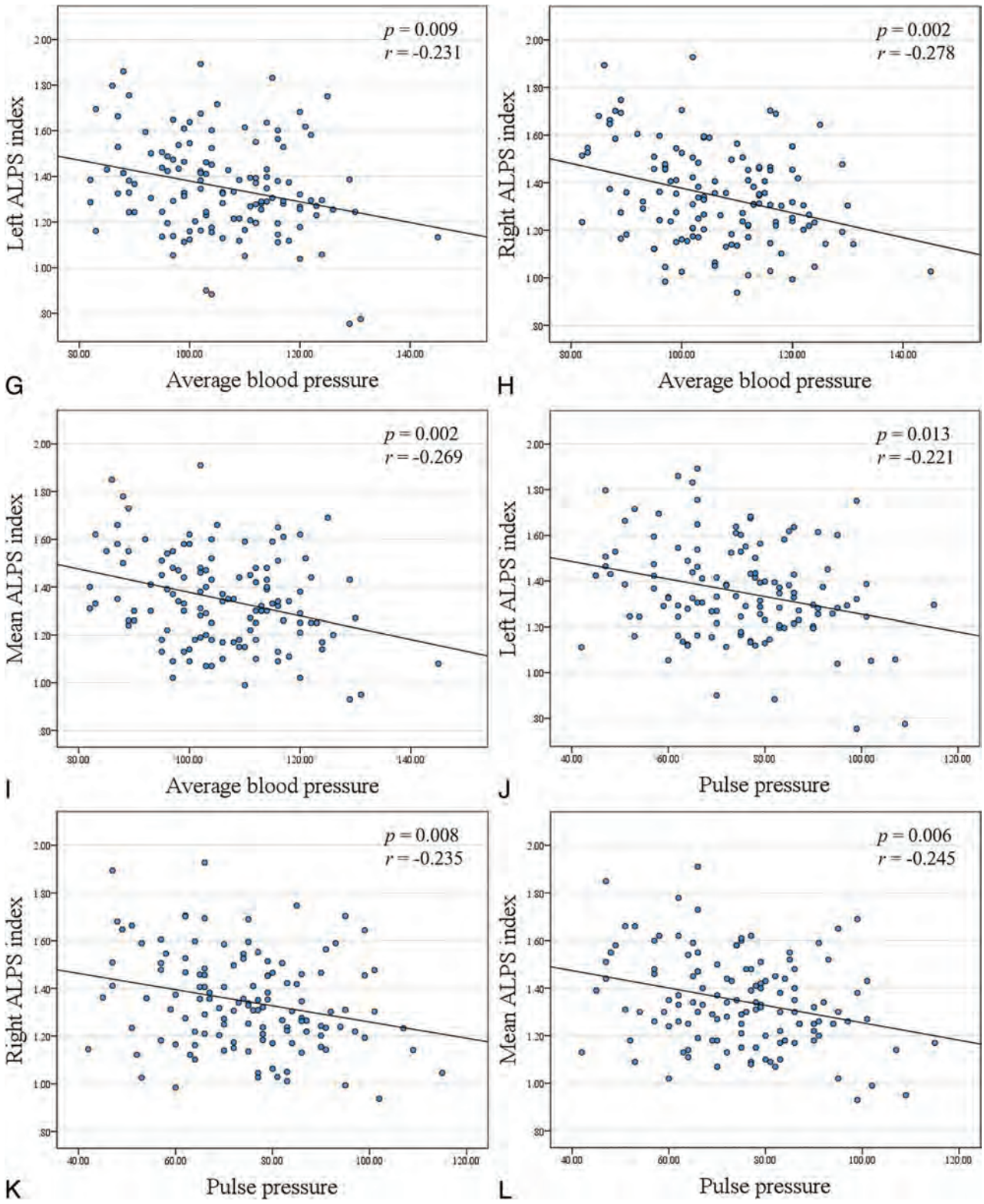

FIG 3. Continued

enters the brain along the cortical pial arteries by labeling the CSF via an injection of a fluorescent tracer into the cisterna magna CSF in mice. CSF dynamics have also been observed using intrathecal or intravenous injections of gadolinium-based contrast agents as tracers.[3,32-39] However, the invasive injection of gadolinium-based contrast agents carries risks. Intrathecal administration of high-dose gadolinium-based contrast agents may cause gadolinium deposition in the globus pallidus and dentate nucleus[40,41] or serious gadolinium encephalopathy, which includes nausea, dyspnea, subjective chills, delirium, dysarthria,

spastic pain of the lower extremities, limb ataxia, and gaze-evoked nystagmus.[42-44] Moreover, the tracking method requires several hours to track the distribution of a tracer in the brain, and monitoring glymphatic activity in real-time is challenging.

In contrast, the ALPS index is a noninvasive tool to assess the glymphatic system using DWI, which has a short acquisition time. As mentioned previously, the ALPS method is based on the hypothesis that diffusion plays an important role in fluid transport in the parenchyma. Fluid transport was believed to be caused mainly by cardiac pulsatility.[13,29] However, Smith et al[45] argued against this theory and suggested that diffusion played an important role in the transport of neurofluids. Several reports using mathematic modeling have further demonstrated the involvement of diffusion and advection in fluid transport in the parenchyma.[46,47] Martinac and Bilston[26] showed that diffusion is most likely the primary mechanism that drives fluid transport into the interstitial space. Taken together, diffusivity along the perivascular space could, at least in part, underlie glymphatic activity. Alterations of the glymphatic system in Alzheimer disease,[15,48] idiopathic normal pressure hydrocephalus,[18] diabetes,[49] and Parkinson disease[50] have been shown in living humans using the ALPS method, which is in line with the findings of studies using gadolinium-based contrast agents as tracers.[3,39,51] Additionally, Zhang et al[52] recently reported that the ALPS index is significantly associated with the glymphatic clearance function calculated by glymphatic MR imaging, following intrathecal administration of gadolinium in patients with small-vessel disease ($r = -0.772$ to -0.844, $P < .001$). The report strongly supported the clinical use of the ALPS index as a glymphatic biomarker.

This study has several limitations. First, it consisted of a relatively large number of participants compared with previous studies using the ALPS index; however, we obtained DWI data from only a single institution. Future research should include multisite data to evaluate the clinical utility of the ALPS index. In addition, given that a slight difference in the subject's head position can influence the ALPS index, we encourage investigations evaluating the influence of head motion on the calculation of the ALPS index. Second, we did not consider other physiologic statuses such as perfusion or pulsatile motion of the brain. Finally, Yokota et al[18] showed that the size of the ROI may influence the calculated ALPS index, in which larger ROIs were more effective than smaller ROIs. Thus, further studies evaluating different sizes and shapes of ROIs for calculating the ALPS index are needed.

CONCLUSIONS

Our results are consistent with a model in which HT causes glymphatic dysfunction.

ACKNOWLEDGMENTS

We acknowledge Masahiro Abe for his help in data handling and graphic assistance. Additionally, the authors would like to thank Enago (www.enago.jp) for the English language review.

Disclosures: Junko Kikuta—*RELATED*: *Grant*: Japan Society for the Promotion of Science Grants-in-Aid for Scientific grant No. 20K16737.* Toshiaki Taoka—*UNRELATED*: *Grants/Grants Pending*: Canon Medical Systems.* Akihiko Wada—*UNRELATED*: *Employment*: Juntendo University. Yoshifumi Tamura—*UNRELATED*: *Employment*: Juntendo University. Hirotaka Watada—*UNRELATED*: *Grants/Grants Pending*: Novo Nordisk Pharma, Mitsubishi Tanabe Pharma, LifesScan Japan, Dainippon Sumitomo Pharma, Kyowa Kirin, Merck Sharp & Dohme; *Payment for Lectures Including Service on Speakers Bureaus*: Mitsubishi Tanabe Pharma, Dainippon Sumitomo Pharma, Sanwa Kagaku, Takeda, Sanofi, Kowa Pharmaceuticals, Merck Sharp & Dohme, Boehringer Ingelheim, Eli Lilly, Novo Nordisk Pharma. Shigeki Aoki—*UNRELATED*: *Board Membership*: Canon; *Expert Testimony*: Ono Pharmaceutical Co; *Grants/Grants Pending*: Medi-Physics, Daiich Sankyo, GE Healthcare, Eisai, FUJIFILM Toyama Chemical Co, Guerbet, *Comments*: grant for diagnostic radiology from Medi-Physics, Daiich Sankyo, GE Healthcare, Eisai, FUJIFILM Toyama Chemical Co, Guerbet; *Payment for Lectures Including Service on Speakers Bureaus*: Bayer, Canon, FUJIFILM Toyama Chemical Co, Eisai, Guerbet, GE Healthcare, Medi-Physics, Siemens, Daiichi Sankyo, *Comments*: payment for lectures/Chair from Bayer, Canon, FUJIFILM Toyama Chemical Co, Eisai, Guerbet, GE Healthcare, Medi-Physics, Siemens, Daiichi Sankyo. *Money paid to the institution.

REFERENCES

1. Iliff JJ, Wang M, Liao Y, et al. **A paravascular pathway facilitates CSF flow through the brain parenchyma and the clearance of interstitial solutes, including amyloid beta.** *Sci Transl Med* 2012;4:147ra111 CrossRef Medline
2. Jessen NA, Munk AS, Lundgaard I, et al. **The glymphatic system: a beginner's guide.** *Neurochem Res* 2015;40:2583–99 CrossRef Medline
3. Iliff JJ, Lee H, Yu M, et al. **Brain-wide pathway for waste clearance captured by contrast-enhanced MRI.** *J Clin Invest* 2013;123:1299–1309 CrossRef Medline
4. Louveau A, Smirnov I, Keyes TJ, et al. **Structural and functional features of central nervous system lymphatic vessels.** *Nature* 2015;523:337–41 CrossRef Medline
5. Faraco G, Park L, Zhou P, et al. **Hypertension enhances Aβ-induced neurovascular dysfunction, promotes β-secretase activity, and leads to amyloidogenic processing of APP.** *J Cereb Blood Flow Metab* 2016;36:241–52 CrossRef Medline
6. Cifuentes D, Poittevin M, Dere E, et al. **Hypertension accelerates the progression of Alzheimer-like pathology in a mouse model of the disease.** *Hypertension* 2015;65:218–24 CrossRef Medline
7. Tadic M, Cuspidi C, Hering D. **Hypertension and cognitive dysfunction in elderly: blood pressure management for this global burden.** *BMC Cardiovasc Disord* 2016;16:208 CrossRef Medline
8. Kress BT, Iliff JJ, Xia M, et al. **Impairment of paravascular clearance pathways in the aging brain.** *Ann Neurol* 2014;76:845–61 CrossRef Medline
9. Plog BA, Dashnaw ML, Hitomi E, et al. **Biomarkers of traumatic injury are transported from brain to blood via the glymphatic system.** *J Neurosci* 2015;35:518–26 CrossRef Medline
10. Rasmussen MK, Mestre H, Nedergaard M. **The glymphatic pathway in neurological disorders.** *Lancet Neurol* 2018;17:1016–24 CrossRef Medline
11. Rusanen M, Kivipelto M, Levälahti E, et al. **Heart diseases and long-term risk of dementia and Alzheimer's disease: a population-based CAIDE study.** *J Alzheimers Dis* 2014;42:183–91 CrossRef Medline
12. Turana Y, Tengkawan J, Chia YC, et al. **Hypertension and dementia: a comprehensive review from the HOPE Asia Network.** *J Clin Hypertens (Greenwich)* 2019;21:1091–98 CrossRef Medline
13. Mestre H, Tithof J, Du T, et al. **Flow of cerebrospinal fluid is driven by arterial pulsations and is reduced in hypertension.** *Nat Commun* 2018;9:4878 CrossRef Medline
14. Mortensen KN, Sanggaard S, Mestre H, et al. **Impaired glymphatic transport in spontaneously hypertensive rats.** *J Neurosci* 2019;39:6365–77 CrossRef Medline
15. Taoka T, Masutani Y, Kawai H, et al. **Evaluation of glymphatic system activity with the diffusion MR technique: diffusion tensor image analysis along the perivascular space (DTI-ALPS) in Alzheimer's disease cases.** *Jpn J Radiol* 2017;35:172–78 CrossRef Medline
16. Someya Y, Tamura Y, Kaga H, et al. **Skeletal muscle function and need for long-term care of urban elderly people in Japan (the**

Bunkyo Health Study): a prospective cohort study. *BMJ Open* 2019;9:e031584 CrossRef Medline
17. Jenkinson M, Beckmann CF, Behrens TE, et al. **FSL.** *Neuroimage* 2012;62:782–90 CrossRef Medline
18. Yokota H, Vijayasarathi A, Cekic M, et al. **Diagnostic performance of glymphatic system evaluation using diffusion tensor imaging in idiopathic normal pressure hydrocephalus and mimickers.** *Curr Gerontol Geriatr Res* 2019;2019:1–10 CrossRef Medline
19. Aronow WS. **Hypertension and cognitive impairment.** *Ann Transl Med* 2017;5:259 CrossRef Medline
20. Kario K, Pickering TG. **Blood pressure variability in elderly patients.** *Lancet* 2000;355:1645–46 CrossRef Medline
21. Adler S, Martinez J, Williams DS, et al. **Positive association between blood brain barrier disruption and osmotically-induced demyelination.** *Mult Scler* 2000;6:24–31 CrossRef Medline
22. Yamamoto Y, Ihara M, Tham C, et al. **Neuropathological correlates of temporal pole white matter hyperintensities in CADASIL.** *Stroke* 2009;40:2004–11 CrossRef Medline
23. Kamagata K, Andica C, Shimada K, et al. **Effects of arterial stiffness on cerebral white matter integrity in the elderly.** In: *Proceedings of the Annual Meeting of the International Society for Magnetic Resonance in Medicine and the Society for MR Radiographers & Technologists*, Virtual; August 8–14, 2020
24. Joutel A, Corpechot C, Ducros A, et al. **Notch3 mutations in CADASIL, a hereditary adult-onset condition causing stroke and dementia.** *Nature* 1996;383:707–10 CrossRef Medline
25. Selwaness M, van den Bouwhuijsen Q, van Onkelen RS, et al. **Atherosclerotic plaque in the left carotid artery is more vulnerable than in the right.** *Stroke* 2014;45:3226–30 CrossRef Medline
26. Martinac AD, Bilston LE. **Computational modelling of fluid and solute transport in the brain.** *Biomech Model Mechanobiol* 2020;19:781–800 CrossRef Medline
27. Bewick V, Cheek L, Ball J. **Statistics review 7: correlation and regression.** *Crit Care* 2003;7:451–59 CrossRef Medline
28. Krzesinski JM. **Management of high blood pressure in peripheral arterial disease.** *Acta Chir Belg* 2005;105:560–66 CrossRef Medline
29. Iliff JJ, Wang M, Zeppenfeld DM, et al. **Cerebral arterial pulsation drives paravascular CSF-interstitial fluid exchange in the murine brain.** *J Neurosci* 2013;33:18190–99 CrossRef Medline
30. Hadaczek P, Yamashita Y, Mirek H, et al. **The "perivascular pump" driven by arterial pulsation is a powerful mechanism for the distribution of therapeutic molecules within the brain.** *Mol Ther* 2006;14:69–78 CrossRef Medline
31. Braun M, IIif J. **The impact of neurovascular, blood-brain barrier, and glymphatic dysfunction in neurodegenerative and metabolic diseases.** *Int Rev Neurobiol* 2020;154C:413–36 CrossRef
32. Gaberel T, Gakuba C, Goulay R, et al. **Impaired glymphatic perfusion after strokes revealed by contrast-enhanced MRI.** *Stroke* 2014;45:3092–96 CrossRef Medline
33. Di Chiro G, Knop RH, Girton ME, et al. **MR cisternography and myelography with Gd-DTPA in monkeys.** *Radiology* 1985;157:373–77 CrossRef Medline
34. Biceroglu H, Albayram S, Ogullar S, et al. **Direct venous spinal reabsorption of cerebrospinal fluid: a new concept with serial magnetic resonance cisternography in rabbits.** *J Neurosurg Spine* 2012;16:394–401 CrossRef Medline
35. Naganawa S, Nakane T, Kawai H, et al. **Gd-based contrast enhancement of the perivascular spaces in the basal ganglia.** *MRMS* 2017;16:61–65 CrossRef
36. Naganawa S, Nakane T, Kawai H, et al. **Age dependence of gadolinium leakage from the cortical veins into the cerebrospinal fluid assessed with whole brain 3D-real inversion recovery MR imaging.** *Magn Reson Med Sci* 2019;18:163–69 CrossRef
37. Naganawa S, Nakane T, Kawai H, et al. **Lack of contrast enhancement in a giant perivascular space of the basal ganglion on delayed flair images: implications for the glymphatic system.** *Magn Reson Med Sci* 2017;16:89–90 CrossRef Medline
38. Siebner HR, von Einsiedel HG, Conrad B. **Magnetic resonance ventriculography with gadolinium DTPA: report of two cases.** *Neuroradiology* 1997;39:418–22 CrossRef Medline
39. Ringstad G, Vatnehol SA, Eide PK. **Glymphatic MRI in idiopathic normal pressure hydrocephalus.** *Brain* 2017;140:2691–2705 CrossRef Medline
40. Kanda T, Ishii K, Kawaguchi H, et al. **High signal intensity in the dentate nucleus and globus pallidus on unenhanced T1-weighted MR images: relationship with increasing cumulative dose of a gadolinium-based contrast material.** *Radiology* 2014;270:834–41 CrossRef
41. Taoka T, Naganawa S. **Gadolinium-based contrast media, cerebrospinal fluid and the glymphatic system: possible mechanisms for the deposition of gadolinium in the brain.** *Magn Reson Med Sci* 2018;17:111–19 CrossRef Medline
42. Samardzic D, Thamburaj K. **Magnetic resonance characteristics and susceptibility weighted imaging of the brain in gadolinium encephalopathy.** *J Neuroimaging* 2015;25:136–39 CrossRef Medline
43. Arlt S, Cepek L, Rustenbeck HH, et al. **Gadolinium encephalopathy due to accidental intrathecal administration of gadopentetate dimeglumine.** *J Neurol* 2007;254:810–12 CrossRef Medline
44. Provenzano DA, Pellis Z, DeRiggi L. **Fatal gadolinium-induced encephalopathy following accidental intrathecal administration: a case report and a comprehensive evidence-based review.** *Reg Anesth Pain Med* 2019;44:721–79 CrossRef
45. Smith AJ, Yao X, Dix JA, et al. **Test of the 'glymphatic' hypothesis demonstrates diffusive and aquaporin-4-independent solute transport in rodent brain parenchyma.** *eLife* 2017;6:e677679 CrossRef Medline
46. Asgari M, de Zélicourt D, Kurtcuoglu V. **Glymphatic solute transport does not require bulk flow.** *Sci Rep* 2016;6:38635 CrossRef Medline
47. Koundal S, Elkin R, Nadeem S, et al. **Optimal mass transport with Lagrangian workflow reveals advective and diffusion driven solute transport in the glymphatic system.** *Sci Rep* 2020;10:1990 CrossRef Medline
48. Steward CE, Venkatraman VK, Lui E, et al. **Assessment of the DTI-ALPS parameter along the perivascular space in older adults at risk of dementia.** *J Neuroimaging* 2021;31:569–78 CrossRef Medline
49. Yang G, Deng N, Liu Y, et al. **Evaluation of glymphatic system using diffusion MR technique in T2DM cases.** *Front Hum Neurosci* 2020;14:300 CrossRef Medline
50. Chen HL, Chen PC, Lu CH, et al. **Associations among cognitive functions, plasma DNA, and diffusion tensor image along the perivascular space (DTI-ALPS) in patients with Parkinson's disease.** *Oxid Med Cell Longev* 2021;2021:4034509 CrossRef Medline
51. Jiang Q, Zhang L, Ding G, et al. **Impairment of the glymphatic system after diabetes.** *J Cereb Blood Flow Metab* 2017;37:1326–37 CrossRef Medline
52. Zhang W, Zhou Y, Wang J, et al. **Glymphatic clearance function in patients with cerebral small vessel disease.** *Neuroimage* 2021;238:118257 CrossRef Medline

White Matter Alterations in Spastic Paraplegia Type 5: A Multiparametric Structural MRI Study and Correlations with Biochemical Measurements

Y. Liu, Z. Ye, J. Hu, Z. Xiao, F. Zhang, X. Yang, W. Chen, Y. Fu, and D. Cao

ABSTRACT

BACKGROUND AND PURPOSE: In spastic paraplegia type 5, spinal cord atrophy and white matter signal abnormalities in the brain are the main MR imaging alterations. However, the specific mechanism remains unclear. We explored the microstructural changes occurring in spastic paraplegia type 5 and assessed the relation between MR imaging and clinical data.

MATERIALS AND METHODS: Seventeen patients with spastic paraplegia type 5 and 17 healthy controls were scanned with DTI and T1 mapping on a 3T MR imaging scanner. Fractional anisotropy, mean diffusivity, radial diffusivity, axial diffusivity, and T1 values were obtained using Tract-Based Spatial Statistics and the Spinal Cord Toolbox. Neurofilament light and myelin basic protein in the CSF were measured. The differences in MR imaging and biochemical data between patients with spastic paraplegia type 5 and healthy controls were compared using the Student *t* test.

RESULTS: A widespread reduction of fractional anisotropy values and an elevation of mean diffusivity, T1, and radial diffusivity values were found in most cervical, T4, and T5 spinal cords; corona radiata; optic radiations; and internal capsules in spastic paraplegia type 5. A variation in axial diffusivity values was shown only in C2, C6, and the corona radiata but not in the gray matter. The levels of neurofilament light and myelin basic protein were higher in those with spastic paraplegia type 5 than in healthy controls (myelin basic protein, 3507 [SD, 2291] versus 127 [SD, 219] pg/mL; neurofilament light, 617 [SD, 207] versus 265 [SD, 187] pg/mL; $P < .001$). No correlation was found between the clinical data and MR imaging–derived measures.

CONCLUSIONS: Multiparametric MR imaging and biochemical indicators demonstrated that demyelination (mainly) and axonal loss led to the white matter integrity loss without gray matter injury in spastic paraplegia type 5.

ABBREVIATIONS: AD = axial diffusivity; FA = fractional anisotropy; HC = healthy control; HSP = hereditary spastic paraplegia; MBP = myelin basic protein; MD = mean diffusivity; NFL = neurofilament light; RD = radial diffusivity; SPG5 = spastic paraplegia type 5; SPRS = Spastic Paraplegia Rating Scale

Hereditary spastic paraplegia (HSP) is a neurodegenerative disorder characterized by retrograde axonal degeneration of the corticospinal tracts.[1] Spastic paraplegia type 5 (SPG5) is a rare subtype of HSP for which treatment with cholesterol-lowering drugs can be attempted,[2] but the target of drug action remains uncertain. Recent evidence has indicated that SPG5 is caused by a recessive mutation in the oxysterol-7α-hydroxylase gene *CYP7B1*, which leads to the accumulation of neurotoxic oxysterols, especially 27-hydroxycholesterol (27-OHC), which was found to impair the viability of human cortical neurons in SPG5.[2-4] Given that axons in the white matter are known to exert essential functions in lipid transport,[5] we hypothesized that patients with SPG5 might have white matter integrity loss. An improved understanding of white matter integrity loss patterns (ie, demyelination and/or dying-back axonopathy) would be of substantial clinical relevance for enabling personalized treatment approaches for patients with SPG5.[6,7]

DTI is a robust method to detect in vivo white matter abnormalities. Specifically, radial diffusivity (RD) values can provide a quantitative evaluation of myelin sheaths, while axial diffusivity (AD) values support the assessment of axon status.[8,9] Accordingly, DTI has been used to evaluate common subtypes of HSP, such as

Received July 16, 2021; accepted after revision September 10.

From the Departments of Radiology (Y.L., J.H., F.Z., X.Y., D.C.) and Neurology and Institute of Neurology (Z.Y., W.C., Y.F.), and Key Laboratory of Radiation Biology of Fujian Higher Education Institutions (D.C.), First Affiliated Hospital, Fujian Medical University, Fuzhou, China; Department of Medical Imaging Technology (Y.L.), College of Medical Technology and Engineering, Department of Neurology and Institute of Neurology (Z.Y., W.C., Y.F.), and Fujian Key Laboratory of Molecular Neurology (W.C.), Fujian Medical University, Fuzhou, China; and Department of Biomedical Sciences (Z.X.), University of Pennsylvania, Philadelphia, Pennsylvania.

Ying Liu and Zhixian Ye contributed equally to this study.

This work was supported by a Startup Fund for Scientific Research, Fujian Medical University (2017XQ1016).

Please address correspondence to Dairong Cao, MD, Department of Radiology of The First Affiliated Hospital of Fujian Medical University, No. 20, Chazhong Rd, Taijiang District, Fuzhou, Fujian, 350005, China; e-mail: dairongcao@163.com

Indicates article with online supplemental data.

http://dx.doi.org/10.3174/ajnr.A7344

SPG4 and SPG11.[10-14] However, to date, no study has reported using DTI to assess both the brain and spinal cord of SPG5. One challenge with the application of DTI to HSPs is that physiologic motion and susceptibility artifacts in the spinal cord can challenge DTI quality. T1 mapping, which is relatively less susceptible to artifacts, can reflect myelin conditions and could potentially complement DTI to explore the myelin injury in HSP; the working principle of T1 mapping exploits the relatively faster relaxation of myelin water compared with nonmyelin water.[15] Moreover, neurofilament light (NFL) and myelin basic protein (MBP) in the CSF are promising biomarkers that can accurately reflect neuroaxonal loss and myelin damage, respectively.[16,17]

In this study, we performed multiparametric structural MR imaging, including DTI and T1 mapping, to investigate the brain and spinal cord microstructural alterations in 17 patients with genetically confirmed SPG5 and conducted biochemical measurements to verify observed trends in myelin and axonal damage. Subsequently, we explored the correlations of these indicators with clinical manifestations.

MATERIALS AND METHODS

Subject Selection

Participants were prospectively recruited into the registered cohort spastic paraplegia study (National Clinical Trials: 04006418) from 2019 to 2020. This case-control parallel cohort study received approval from the local ethical committees (The First Affiliated Hospital of Fujian Medical University). All the participants agreed to participate and signed an informed consent form.

Seventeen patients with SPG5 with genetic confirmation were included (Online Supplemental Data), and 17 age- and sex-matched healthy controls (HCs) were also recruited for imaging assessment. Eleven inpatients without neurologic diseases requiring a subarachnoid block in anesthesia served as controls for CSF biochemical evaluation (Online Supplemental Data).

Clinical and Biochemical Measurements

All participants completed neurologic examinations and CSF collection on the same day as the MR imaging examination. Disease severity was quantified with the Spastic Paraplegia Rating Scale (SPRS).[18] CSF NFL was measured using Simoa NF-light Advantage Kits (Quanterix) on a Simoa HD-1 Analyzer instrument. MBP was measured by a Human MBP DuoSet ELISA (R&D Systems).

MR Imaging Acquisition

All participants underwent an examination on a 3T MR scanner (Magnetom Skyra; Siemens) equipped with a 20-channel head-neck coil and a 24-channel spine-array coil. The following sequences were performed: 1) axial T2WI, T2-FLAIR, and sagittal 3D T1WI covering the whole brain; 2) sagittal 3D-T2WI and 3D-T1WI covering the cervical and thoracic spinal cord; 3) DTI with a single-shot echo-planar imaging sequence for both brain and spinal cord (32 and 20 different gradient directions, respectively); and 4) a T1-mapping sequence based on B_1 inhomogeneity–corrected variable flip angle methods for the spinal cord. DTI and T1 mapping consisted of 2 axial slabs in the spinal cord: cervical (C2–C7) and thoracic (T1–T5) slabs. The parameters are listed in the Online Supplemental Data.

Image Processing

MR Imaging Analysis. DWI preprocessing was performed on the basis of FSL (http://fsl.fmrib.ox.ac.uk/fsl) and the Diffusion Toolkit (DTK; http://www.trackvis.org/dtk/). The 3D T1WIs were preprocessed using the CAT12 toolbox of Statistical Parametric Mapping, Version 12 (SPM; http://www.fil.ion.ucl.ac.uk/spm/software/spm12). Spinal cord images were analyzed on the basis of the open-source software Spinal Cord Toolbox (Version 4.01; https://spinalcordtoolbox.com/) (Online Supplemental Data).[19]

Brain Image Analysis. The DTI analysis of the brain was performed with Tract-Based Spatial Statistics (TBSS; http://fsl.fmrib.ox.ac.uk/fsl/fslwiki/TBSS). Voxel-based whole-brain white matter measures (DTI metrics) were assessed with TBSS using FSL 5.0 (http://www.fmrib.ox.ac.uk/fsl).

Voxel-based morphometry analysis was performed to analyze the alterations in the gray matter using the CAT12 toolbox.

Spinal Cord Image Analysis. Atlas-based analyses of spinal cord DTI and T1-mapping data were performed. The analysis pipeline is shown in the Online Supplemental Data. The spinal cord segments that met the quality control requirements are summarized in the Online Supplemental Data.

Statistical Analysis. Statistical analyses were performed with SPSS (Version 26; IBM). The sample size was determined by the number of eligible patients willing to participate without prospective calculation. Demographic, clinical, and biochemical variables were compared between SPG5 and HCs groups by means of Student t and Pearson $\chi 2$ tests. Bonferroni adjustment was used to correct for multiple comparisons. Correlations were analyzed, counting age and sex as nuisance covariates.

TBSS statistical analysis was performed using a nonparametric permutation inference tool, FSL Randomize (http://fsl.fmrib.ox.ac.uk/fsl/fslwiki/Randomise/UserGuide). DTI metrics were compared between 2 groups using a 2-sample independent t test. A voxelwise 2-sample t test was conducted to detect the differences in the gray matter between patients with SPG5 and HCs. The total intracranial volume of each participant was entered as a covariate of no interest. Statistical inferences were made at $P < .001$ (uncorrected) and for clusters larger than $\kappa = 20$.

RESULTS

Demographic and Clinical Features

The demographic and clinical data of all participants are shown in the Table. According to the Harding criteria,[20] 16 patients had pure HSP and 1 patient had complicated HSP. All 17 patients presented with lower limb spasticity and weakness and dorsal column dysfunction. Sixteen patients had a severely reduced or nonexistent vibration sense in the lower limbs.

The CSF MBP levels and CSF NFL levels in patients with SPG5 (CSF MBP, 3507 [SD, 2291] versus 127 [SD, 219] pg/mL, $P < .001$; CSF NFL, 617 [SD, 207] versus 265 [SD, 187] pg/mL; $P < .001$) were both higher than those in the control group. However, the increased degree in MBP was much higher than that in NFL in patients with SPG5 (compared with controls, the MBP increased by 27.61 [3507/127]

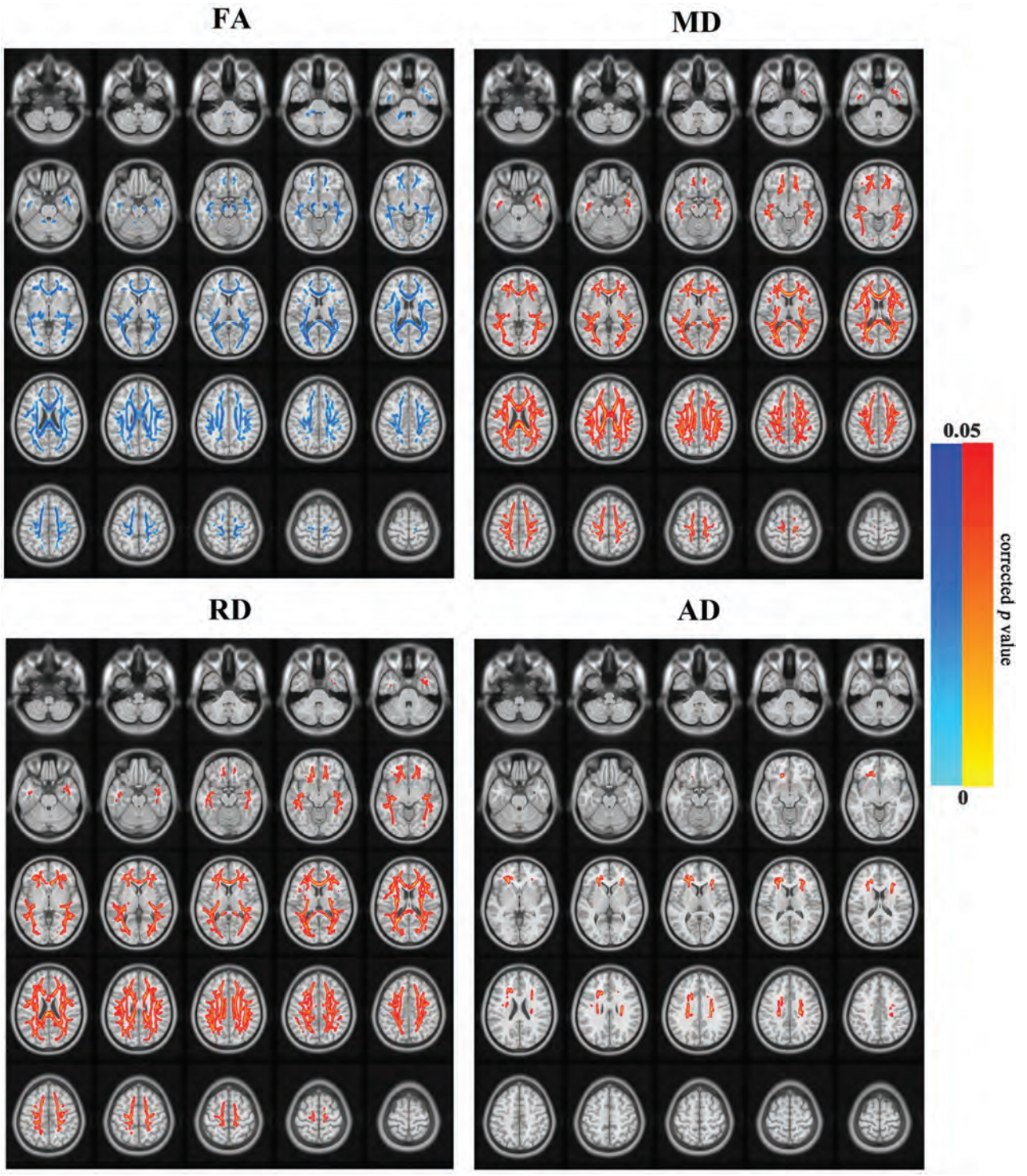

FIG 1. Images show whole-brain voxel-based analysis. Voxelwise FA, MD, RD, and AD comparisons by TBSS analysis.

folds on average, while the NFL increased only by 2.33 [617/265] in patients with SPG5). Conventional MR imaging showed no apparent signal abnormalities in the brain or spinal cord of those with SPG5 or HCs.

Brain MR Imaging Analysis

TBSS Analysis. Compared with HCs, an extensive and bilateral symmetric reduction of fractional anisotropy (FA) and an elevation of mean diffusivity (MD) and RD were found in the cerebral peduncles, optic radiation, internal capsules, corona radiata, corpus callosum, posterior thalamic radiation, cingulum, and superior and inferior longitudinal fasciculi of patients with SPG5. The areas of elevated RD and MD closely mirrored the areas featuring reduced FA. However, an elevation of AD reached a statistically significant level only in the corona radiata (Fig 1).

Demographic and clinical data of study participants[a]

Characteristic	HC[1]	HC[2]	SPG5	*P* Value[1]	*P* Value[2]
Participants[b]	17	11	17	>.99[c]	<.01[c]
Sex[b]				.99[c]	.98[c]
Men	11	8	11		
Women	6	3	6		
Age (yr)[e]	29 (SD, 10) (14–49)	39 (SD, 18) (11–69)	30 (SD, 10) (13–49)	.93[d]	.13[d]
SPRS[e]			16 (SD, 9) (2–38)		
Disease duration (yr)[e]			18 (SD, 10) (6–37)		

[a]1 = Healthy controls recruited for imaging assessment, 2 = hospitalized patients requiring subarachnoid block in anesthesia without neurologic disease enrolled as controls for CSF biochemical assessment.
[b]Data are numbers of participants.
[c]Pearson χ^2 test.
[d]Student *t* test.
[e]Data are mean (SD). Data in parentheses are ranges.

Voxel-Based Morphometry Analysis. There were no statistically significant differences in gray matter volume between patients with SPG5 and HCs with a less conservative threshold ($P < .001$, uncorrected).

Spinal Cord Analysis. Compared with HCs, patients with SPG5 had reduced FA values and elevated RD, MD, and T1 values at the C2–T5 segments in the white matter, dorsal columns, and bilateral lateral corticospinal tract. Significant differences of FA, RD, and T1 values in the white matter regions between patients with SPG5 and HCs were observed in most cervical spinal cords but not in the thoracic segments, except T4 and T5. In contrast, no evident differences of AD values were observed in most spinal cord segments, and marked reduced AD values were found only at specific segments (eg, C2 and C6) (Fig 2 and Online Supplemental Data). Notably, no significant differences in DTI metrics or T1 values were detected in spinal cord gray matter between patients with SPG5 and HCs (Online Supplemental Data).

Correlation Analysis. No correlations were found between DTI parameters and disease severity (SPRS scores) or disease duration using TBSS. DTI or T1 values at all spinal cord segments in patients with SPG5 did not correlate with the clinical data ($P > .05$, after adjustment for multiple comparisons).

DISCUSSION

This prospective study investigated microstructural alterations occurring in patients with SPG5. First, the FA values of the brain and spinal cord white matter were reduced diffusely, indicative of widespread white matter injury in SPG5. Second, the RD, AD, T1 values, and biochemical indicators (NFL and MBP) demonstrated that the white matter injury pattern of SPG5 was demyelination (mainly). Third, there were no correlations between the degree of white matter injury and the clinical data in SPG5.

Although case reports showed scattered high signal intensity in the cerebral white matter,[21,22] our patients with SPG5 demonstrated a normal appearance on conventional MR imaging (16 of 17 were pure HSP), like the "pure" phenotype HSP that has been reported without white matter abnormalities.[23,24] However, reduced FA in the brain and spinal cord revealed white matter integrity loss in patients with SPG5. Meanwhile, corticospinal tract and dorsal column involvement was consistent with the clinical symptoms: lower limb spasticity, weakness, and dorsal column dysfunction. In addition, we noted that the optic radiations were also affected in SPG5, though there were no clinical manifestations. Therefore, SPG5-specific widespread white matter defects were possibly related to the accumulation of 27-OHC[22] rather than a genetic cause of damage to a specific site. On the basis of MR imaging, we have demonstrated the clinical feasibility of treating patients with SPG5 by lowering the pathologically elevated levels of oxysterols.[25]

Reduced FA could be caused by axonal loss and/or myelin breakdown. RD and AD values derived from DTI can, respectively, indicate myelin sheath and axon status.[26] Our findings showed that RD increased in both the spinal cord and brain; AD values varied in only several cervical spinal cord segments and brain regions. These findings suggest that the white matter damage in SPG5 was more related to myelin destruction than to axonal loss. Similar to our results, an MR spectroscopy study showed an elevated mIns/Cr ratio in the occipitoparietal region in 2 patients, also indicating demyelination in SPG5.[27] Moreover, considering the limited stability of spinal cord DTI, we used the T1-mapping sequence to detect the possible myelin injury.[28] A prolonged T1-relaxation time in the spinal cord may indicate demyelination changes in SPG5 to some extent.

Furthermore, the NFL and MBP levels in the CSF were also analyzed to explore the myelin and axonal degeneration in SPG5. NFL is a component of the cytoskeleton of myelinated axons and can reflect axonal injury,[16] while the MBP holds the layers of myelin together, so quantifying MBP supports the assessment of myelin destruction.[17] Significant differences of both NFL and MBP were found between HCs and those with SPG5. Additionally, the mean MBP level in the CSF (3507 pg/mL) in our study was much higher than that in neuromyelitis optica (706 pg/mL) or multiple sclerosis (106 pg/mL);[29] the mean NFL level (617 pg/mL) was lower than that in Guillain-Barré syndrome (1308 pg/mL)[30] or multiple sclerosis (884 pg/mL).[31]

Thus, our DTI evidence and biochemical measurements together support the cautious deduction that the copresence of demyelination (mainly) and axonal loss resulted in white matter degeneration in SPG5. On the other hand, no gray matter abnormalities were found in the brain or spinal cord, in good agreement with the results of a previous MR spectroscopy study: no increased or reduced Cho/Cr ratio in the gray matter of the occipital

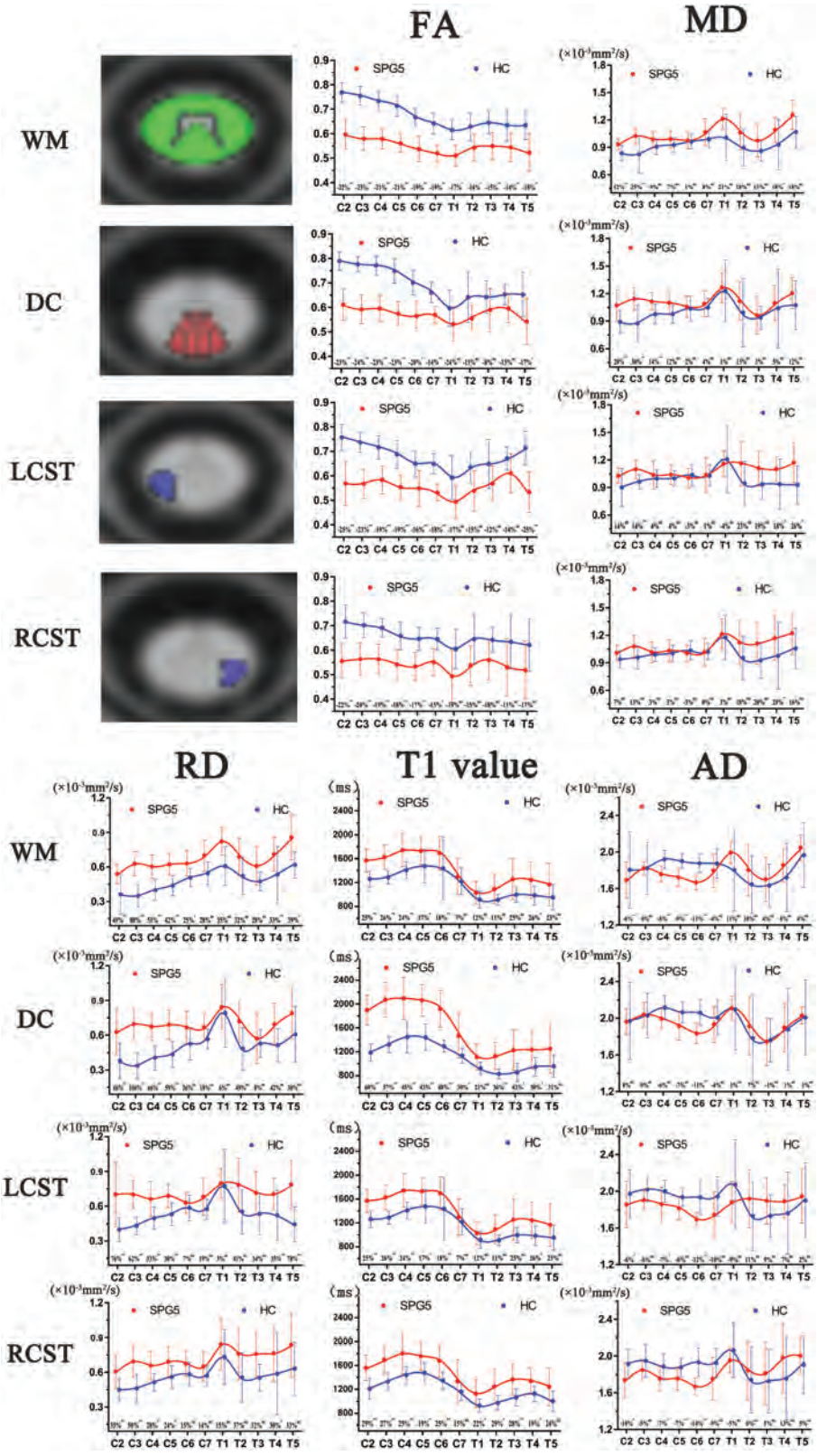

FIG 2. Analysis of DTI metrics and T1 values in 4 spinal cord regions. Percentage rates were calculated as follows: ($FA_{SPG5} - FA_{HC}$) / FA_{HC}. DC indicates dorsal column; LCST, left lateral corticospinal tract; RCST, right lateral corticospinal tract; WM, white matter.

region.[27] In brief, demyelination in both white matter and preserved gray matter in patients with SPG5 was consistent with the characteristics of pure HSP as reported in the literature[12,14,32]

We found no correlations between clinical data (disease duration or SPRS scores) and MR imaging metrics. As previously reported,[11] the ceiling effect may be a good explanation. Patients

with SPG5 in our study were disabled and had a long disease duration (the mean SPRS of our patients was 16, the mean disease duration was 18 years); even though neurodegeneration was still taking place, the correlation analyses failed to capture clinical deterioration.[33] Meanwhile, considering the slowly progressive nature of the disease, white matter injury may be compensated by neuroaxonal redundancy or adaptative neuroplasticity, which led to a discrepancy between the functional evaluation of SPG5 patients and DTI structural assessment in SPG5.[34] Additionally, cholesterol is a vital component of myelin; we assumed that abnormalities in cholesterol metabolism could influence the early development of myelin before the degeneration.

Our study had several limitations. First, the interpretations of AD, RD, and T1 values are still contested.[35] Diffusional kurtosis imaging and neurite orientation dispersion and density imaging may be the optimal MR imaging techniques to strengthen the findings of this study.[35] Second, lumbar puncture is an invasive examination; the HCs who underwent the MR imaging examinations were not the same ones who underwent the lumbar puncture to get the biochemical measurements. Third, the data reliability of thoracic spinal cord DTI may be a problem in this study, which is expected to be solved by more sequence improvement.

CONCLUSIONS

Multiparametric structural MR imaging and biochemical measurements revealed that the neurodegeneration progression of SPG5 was related to white matter integrity loss (demyelination mainly) rather than neuronopathy. Our identification of the widespread myelin damage can support the development of SPG5 treatment regimens in the future.

ACKNOWLEDGMENTS

We thank all patients with SPG5 and healthy controls participating in this study.

Disclosure forms provided by the authors are available with the full text and PDF of this article at www.ajnr.org.

REFERENCES

1. Salinas S, Proukakis C, Crosby A, et al. **Hereditary spastic paraplegia: clinical features and pathogenetic mechanisms.** *Lancet Neurol* 2008;7:1127–38 CrossRef Medline
2. Schols L, Rattay TW, Martus P, et al. **Hereditary spastic paraplegia type 5: natural history, biomarkers and a randomized controlled trial.** *Brain* 2017;140:3112–27 CrossRef Medline
3. Schule R, Wiethoff S, Martus P, et al. **Hereditary spastic paraplegia: clinicogenetic lessons from 608 patients.** *Ann Neurol* 2016;79:646–58 CrossRef Medline
4. Bjorkhem I, Leoni V, Meaney S. **Genetic connections between neurological disorders and cholesterol metabolism.** *J Lipid Res* 2010;51:2489–503 CrossRef Medline
5. Vance JE, Campenot RB, Vance DE. **The synthesis and transport of lipids for axonal growth and nerve regeneration.** *Biochim Biophys Acta* 2000;1486:84–96 CrossRef Medline
6. Tsaousidou MK, Ouahchi K, Warner TT, et al. **Sequence alterations within CYP7B1 implicate defective cholesterol homeostasis in motor-neuron degeneration.** *Am J Hum Genet* 2008;82:510–15 CrossRef Medline
7. Criscuolo C, Filla A, Coppola G, et al. **Two novel CYP7B1 mutations in Italian families with SPG5: a clinical and genetic study.** *J Neurol* 2009;256:1252–57 CrossRef Medline
8. Alexander AL, Lee JE, Lazar M, et al. **Diffusion tensor imaging of the brain.** *Neurotherapeutics* 2007;4:316–29 CrossRef Medline
9. Qiu D, Tan LH, Zhou K, et al. **Diffusion tensor imaging of normal white matter maturation from late childhood to young adulthood: voxel-wise evaluation of mean diffusivity, fractional anisotropy, radial and axial diffusivities, and correlation with reading development.** *Neuroimage* 2008;41:223–32 CrossRef Medline
10. Pan MK, Huang SC, Lo YC, et al. **Microstructural integrity of cerebral fiber tracts in hereditary spastic paraparesis with SPG11 mutation.** *AJNR Am J Neuroradiol* 2013;34:990–96 CrossRef
11. Agosta F, Scarlato M, Spinelli EG, et al. **Hereditary spastic paraplegia: beyond clinical phenotypes toward a unified pattern of central nervous system damage.** *Radiology* 2015;276:207–18 CrossRef Medline
12. Rezende TJ, de Albuquerque M, Lamas GM, et al. **Multimodal MRI-based study in patients with SPG4 mutations.** *PLoS One* 2015;10:e0117666 CrossRef Medline
13. Oğuz KK, Sanverdi E, Has A, et al. **Tract-based spatial statistics of diffusion tensor imaging in hereditary spastic paraplegia with thin corpus callosum reveals widespread white matter changes.** *Diagn Interv Radiol* 2013;19:181–86 CrossRef Medline
14. Lindig T, Bender B, Hauser TK, et al. **Gray and white matter alterations in hereditary spastic paraplegia type SPG4 and clinical correlations.** *J Neurol* 2015;262:1961–71 CrossRef Medline
15. Battiston M, Schneider T, Prados F, et al. **Fast and reproducible in vivo T1 mapping of the human cervical spinal cord.** *Magn Reson Med* 2018;79:2142–48 CrossRef Medline
16. Khalil M, Teunissen CE, Otto M, et al. **Neurofilaments as biomarkers in neurological disorders.** *Nat Rev Neurol* 2018;14:577–89 CrossRef Medline
17. Lillico R, Zhou T, Khorshid Ahmad T, et al. **Increased post-translational lysine acetylation of myelin basic protein is associated with peak neurological disability in a mouse experimental autoimmune encephalomyelitis model of multiple sclerosis.** *J Proteome Res* 2018;17:55–62 CrossRef Medline
18. Schule R, Holland-Letz T, Klimpe S, et al. **The Spastic Paraplegia Rating Scale (SPRS): a reliable and valid measure of disease severity.** *Neurology* 2006;67:430–34 CrossRef Medline
19. De Leener B, Levy S, Dupont SM, et al. **SCT: Spinal Cord Toolbox, an open-source software for processing spinal cord MRI data.** *Neuroimage* 2017;145:24–43 CrossRef Medline
20. Harding AE. **Classification of the hereditary ataxias and paraplegias.** *Lancet* 1983;1:1151–55 CrossRef Medline
21. Biancheri R, Ciccolella M, Rossi A, et al. **White matter lesions in spastic paraplegia with mutations in SPG5/CYP7B1.** *Neuromuscul Disord* 2009;19:62–65 CrossRef Medline
22. Chou CT, Soong BW, Lin KP, et al. **Clinical characteristics of Taiwanese patients with hereditary spastic paraplegia type 5.** *Ann Clin Transl Neurol* 2020;7:486–96 CrossRef Medline
23. Dong EL, Wang C, Wu S, et al. **Clinical spectrum and genetic landscape for hereditary spastic paraplegias in China.** *Mol Neurodegener* 2018;13:36 CrossRef Medline
24. Duning T, Warnecke T, Schirmacher A, et al. **Specific pattern of early white-matter changes in pure hereditary spastic paraplegia.** *Mov Disord* 2010;25:1986–92 CrossRef Medline
25. Mignarri A, Malandrini A, Del Puppo M, et al. **Treatment of SPG5 with cholesterol-lowering drugs.** *J Neurol* 2015;262:2783–85 CrossRef Medline
26. Noguerol TM, Barousse R, Amrhein TJ, et al. **Optimizing diffusion-tensor imaging acquisition for spinal cord assessment: physical basis and technical adjustments.** *Radiographics* 2020;40:403–27 CrossRef Medline
27. Roos P, Svenstrup K, Danielsen ER, et al. **CYP7B1: novel mutations and magnetic resonance spectroscopy abnormalities in hereditary spastic paraplegia type 5A.** *Acta Neurol Scand* 2014;129:330–34 CrossRef Medline

28. Hofer S, Wang X, Roeloffs V, et al. **Single-shot T1 mapping of the corpus callosum: a rapid characterization of fiber bundle anatomy.** *Front Neuroanat* 2015;9:57 CrossRef Medline
29. Takano R, Misu T, Takahashi T, et al. **Astrocytic damage is far more severe than demyelination in NMO: a clinical CSF biomarker study.** *Neurology* 2010;75:208–16 CrossRef Medline
30. Martin-Aguilar L, Camps-Renom P, Lleixa C, et al. **Serum neurofilament light chain predicts long-term prognosis in Guillain-Barre syndrome patients.** *J Neurol Neurosurg Psychiatry* 2021;92:70–77 CrossRef Medline
31. Sejbaek T, Nielsen HH, Penner N, et al. **Dimethyl fumarate decreases neurofilament light chain in CSF and blood of treatment naive relapsing MS patients.** *J Neurol Neurosurg Psychiatry* 2019;90: jnnp-2019-321321–30 CrossRef Medline
32. Aghakhanyan G, Martinuzzi A, Frijia F, et al. **Brain white matter involvement in hereditary spastic paraplegias: analysis with multiple diffusion tensor indices.** *AJNR Am J Neuroradiol* 2014;35:1533–38 CrossRef Medline
33. Servelhere KR, Casseb RF, de Lima FD, et al. **Spinal cord gray and white matter damage in different hereditary spastic paraplegia subtypes.** *AJNR Am J Neuroradiol* 2021;42:610–15 CrossRef Medline
34. Castellano A, Papinutto N, Cadioli M, et al. **Quantitative MRI of the spinal cord and brain in adrenomyeloneuropathy: in vivo assessment of structural changes.** *Brain* 2016;139:1735–46 CrossRef Medline
35. Andica C, Kamagata K, Hatano T, et al. **MR biomarkers of degenerative brain disorders derived from diffusion imaging.** *J Magn Reson Imaging* 2020;52:1620–36 CrossRef Medline

Reduced Leukoaraiosis, Noncardiac Embolic Stroke Etiology, and Shorter Thrombus Length Indicate Good Leptomeningeal Collateral Flow in Embolic Large-Vessel Occlusion

T. Hashimoto, T. Kunieda, T. Honda, F. Scalzo, L. Ali, J.D. Hinman, N.M. Rao, M. Nour, M. Bahr-Hosseini, J.L. Saver, R. Raychev, and D. Liebeskind

ABSTRACT

BACKGROUND AND PURPOSE: Acute leptomeningeal collateral flow is vital for maintaining perfusion to penumbral tissue in acute ischemic stroke caused by large-vessel occlusion. In this study, we aimed to investigate the clinically available indicators of leptomeningeal collateral variability in embolic large-vessel occlusion.

MATERIALS AND METHODS: Among prospectively registered consecutive patients with acute embolic anterior circulation large-vessel occlusion treated with thrombectomy, we analyzed 108 patients admitted from January 2015 to December 2019 who underwent evaluation of leptomeningeal collateral status on pretreatment CTA. Clinical characteristics, extent of leukoaraiosis on MR imaging, embolic stroke subtype, time of imaging, occlusive thrombus characteristics, presenting stroke severity, and clinical outcome were collected. The clinical indicators of good collateral status (>50% collateral filling of the occluded territory) were analyzed using multivariate logistic regression analysis.

RESULTS: Good collateral status was present in 67 patients (62%) and associated with independent functional outcomes at 3 months. Reduced leukoaraiosis (total Fazekas score, 0–2) was positively related to good collateral status (OR, 9.57; 95% CI, 2.49–47.75), while the cardioembolic stroke mechanism was inversely related to good collateral status (OR, 0.17; 95% CI, 0.02–0.87). In 82 patients with cardioembolic stroke, shorter thrombus length (OR, 0.91 per millimeter increase; 95% CI, 0.82–0.99) and reduced leukoaraiosis (OR, 5.79; 95% CI, 1.40–29.61) were independently related to good collateral status.

CONCLUSIONS: Among patients with embolic large-vessel occlusion, reduced leukoaraiosis, noncardiac embolism mechanisms including embolisms of arterial or undetermined origin, and shorter thrombus length in cardioembolism are indicators of good collateral flow.

ABBREVIATIONS: LCS = leptomeningeal collateral status; LVO = large-vessel occlusion

Patients with ischemic stroke caused by the large-vessel occlusions (LVOs) of embolic origin often have large initial hypoperfusion lesions, extensive subsequent infarction, and poor long-term functional outcomes.[1] To maintain perfusion to penumbral tissue in acute stroke caused by LVO, acute leptomeningeal collateral flow is vital. Leptomeningeal collaterals are pre-existing, small arteriolar anastomoses that cross-connect the distal-most arterioles within the crowns of the cerebral arterial trees and provide an alternative route for blood flow to fields supplied by the occluded artery, thus reducing hypoperfusion and infarct extent.[2]

The robustness of acute leptomeningeal collateral flow varies widely among patients with LVO ischemic stroke. However, the frequency, determinants, and outcomes of this variability have been incompletely characterized.[3] Genetic factors have been suggested as an important determinant of collateral flow in preclinical rodent stroke models[4] but have not been extensively studied in human patients. Some premorbid vascular risk profiles such as older age, prior hypertension, and metabolic syndrome have been associated with worse leptomeningeal collateral flow, but findings have been contradictory.[2,3,5-8] Recently, it has also been reported

Received May 20, 2021; accepted after revision September 20.

From the Department of Neurology and Comprehensive Stroke Center, University of California, Los Angeles, Los Angeles, California.

This work was supported by the Uehara Memorial Foundation (grant No. 201840008), the Fukuda Foundation for Medical Technology (Research Training Award), and the Japanese Society of Neurology (Overseas Training Program for Young Researchers).

Please address correspondence to Tetsuya Hashimoto, MD, PhD, Department of Neurology and Comprehensive Stroke Center, University of California, Los Angeles, Neuroscience Research Building Suite 116, 635 Charles E. Young Dr S, Los Angeles, CA 90095; e-mail: tetsuyahashimoto629@hotmail.co.jp

Indicates article with online supplemental data.

http://dx.doi.org/10.3174/ajnr.A7360

that increasing severity of leukoaraiosis, which is thought to originate from chronic arteriolosclerosis and chronically reduced deep cerebral blood flow, is associated with poor leptomeningeal collateral flow.[9,10] Additionally, factors present at the time of stroke onset have been reported to be associated with collateral flow status, including stroke etiology and mechanism,[1,11,12] blood pressure,[5] and blood glucose levels.[2,3,6] Moreover, occlusive thrombus extent and composition have been suggested to be associated with the degree of collateral robustness.[13,14] Prior research has often not clearly distinguished between LVOs of embolic and local in situ atherosclerotic origin in probing associations between collateral variability and clinical factors. Further research into the potential indicators of collateral variability in embolic LVOs will improve our understanding of the collateral system and potentially identify ways to improve clinical outcomes in embolic LVOs.

CTA, which is widely used in clinical practice, offers the possibility of evaluating acute leptomeningeal collateral status by assessing the amount of vascular enhancement in the affected brain regions distal to the occluded artery.[2,15] In the present study, we aimed to investigate the clinically available indicators of CTA-identified acute leptomeningeal collateral flow variability in embolic LVOs.

MATERIALS AND METHODS

Patients

All patients admitted to our institution with acute ischemic stroke who underwent acute reperfusion therapy, including thrombolysis using IV rtPA and/or endovascular reperfusion therapy, were prospectively registered in a single comprehensive stroke center database. For this study, patients were identified in this database, from January 2015 to December 2019, who met the following criteria: 1) had acute occlusion of the intracranial ICA terminus or MCA horizontal or insular segments seen on the initial CTA that was treated by endovascular reperfusion therapy; 2) had a single LVO; 3) had embolus of cardiac, artery-to-artery, other arterial, or undetermined origin as the identified stroke mechanism; 4) underwent NCCT and CTA on admission before acute reperfusion therapy, with evaluable leptomeningeal collateral status (LCS) and thrombus length; and 5) underwent MR imaging within 24 hours after admission, permitting robust evaluation of leukoaraiosis. Acute endovascular reperfusion therapy procedures were performed in accordance with national and institutional guidelines.

Patients with multiple intracranial occlusions were excluded because multiple occlusions may variably further compromise LCS and be a confounding factor. For the exclusion of patients with the intracranial in situ atherosclerotic mechanism of occlusion, patients were considered to have likely in situ occlusion on postprocedural angiograms under the following conditions: 1) a residual 50%–99% stenosis after endovascular treatment; or 2) evidence of intracranial dissection on reperfusion.

This study was overseen by the Research Ethics Committee of our institution, which approved the performance of the study without explicit research informed consent because it was a minimal-risk study involving only analysis of clinically acquired data. All study protocols and procedures were conducted in accordance with the Declaration of Helsinki. The de-identified data that support the findings of this study are available from the corresponding author on reasonable request for the purpose of replicating procedures and results.

Clinical Information

The following demographic and clinical characteristics were analyzed for each patient: sex; age; history of hypertension; history of diabetes mellitus; history of dyslipidemia; history of premorbid atrial fibrillation; history of smoking; history of stroke/TIA; premorbid antithrombotic medication; premorbid statin medication; body mass index; NIHSS score on emergency admission; initial systolic/diastolic blood pressure; initial glucose, Cr, and blood urea nitrogen blood levels; stroke subtype; time from last known well to imaging; occluded target vessel; and ASPECTS from admission NCCT. The stroke subtypes were determined by expert stroke neurologists in our institution using the ASCOD (A, atherosclerosis; S, small-vessel disease; C, cardiac pathology; O, other causes; and D, dissection) phenotyping scheme, including cardioembolic stroke, artery-to-artery embolic stroke secondary to extracranial carotid arterial stenosis of >50% due to atherosclerosis, artery-to-artery embolic stroke secondary to extracranial dissection, and embolic stroke of undetermined source. The degree of carotid artery stenosis was confirmed by DSA during the thrombectomy procedure using the NASCET criteria. The time of imaging was defined as the time point at which the first images were acquired for the patient after admission. The clinical outcome of each patient, measured by the mRS score at 3 months after admission, was also collected. Favorable outcome was defined as an mRS score of 0–2 at 3 months.

Imaging Protocols

Institutional NCCT and CTA scans were performed on emergency admission using Somatom Sensation 64-detector series scanners (Siemens). First, NCCT images were obtained sequentially with the following parameters: FOV, 230 mm; voltage, 120 kV; effective current, 250–350 mAs; section collimation, 1.2 mm; effective section thickness, 3 mm; and reconstruction kernels, H40s medium for brain window and H60 for bone window. Next, CTA was performed with the nonionic monomer iohexol (Omnipaque; GE Healthcare) at 350-mg iodine/mL. Contrast-enhanced image acquisition was performed after a single-bolus IV injection of 150 mL of contrast medium at a rate of 3–5 mL/s, autotriggered by the appearance of contrast in an ROI manually placed in the ascending aorta. The vessels were scanned in helical mode with the following parameters: tube voltage, 120 kV; tube current, 300 mAs; collimation, 0.6 mm; and effective section thickness, 1 mm. CTA was performed immediately after the acquisition of NCCT images. In addition, the delayed-phase contrast-enhanced image acquisition (80 seconds post-CTA contrast injection) was obtained using the same parameters used for CTA in accordance with our institution's stroke code protocol to reduce vascular nonopacification and increase the frequency of the identification of the proximal and distal ends of the occlusive thrombus.[16] In cases in which IV rtPA was administered, patients were treated after the acquisition of delayed-phase contrast-enhanced images.

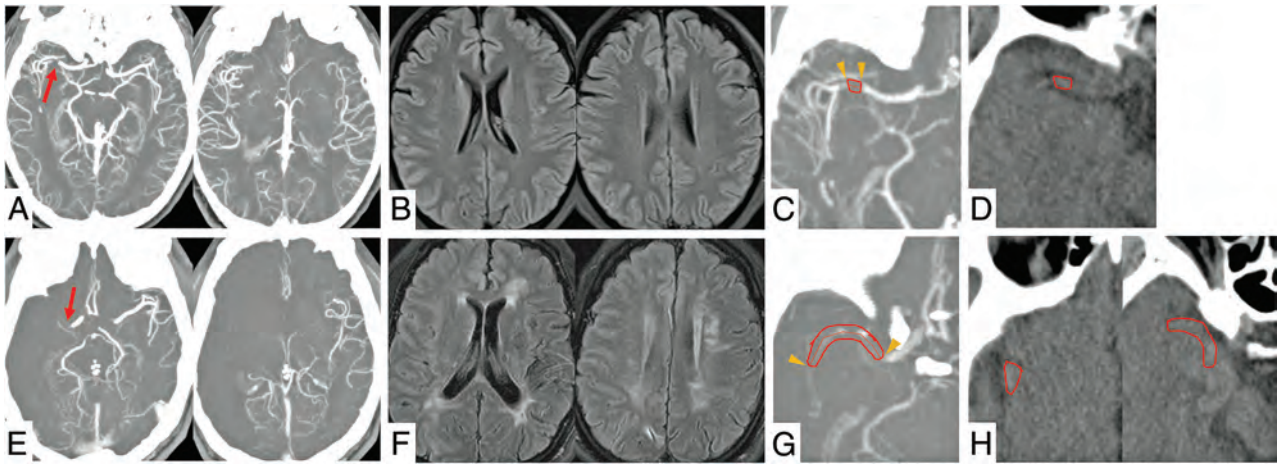

FIG 1. Exemplary cases of an imaging assessment with good (*A–D*) and poor (*E–H*) acute leptomeningeal collateral flow. *A*, CTA shows right proximal MCA occlusion (*arrow*) with a collateral score of 3. *B*, MR imaging shows mild leukoaraiosis with a total Fazekas score of 1. *C*, Delayed-phase CTA shows a short occlusive thrombus identified by the filling defect of contrast (*between arrowheads, with a tracer tool for measuring thrombus length*). *D*, NCCT shows an occlusive thrombus with the placement of a single ROI for measuring Hounsfield unit density (*outlined region*). *E*, CTA shows right proximal MCA occlusion (*arrow*) with a collateral score of zero. *F*, MR imaging shows severe leukoaraiosis with a total Fazekas score of 5. *G*, Delayed-phase CTA shows a long occlusive thrombus identified by the filling defect of contrast (*between arrowheads, with a tracer tool for measuring thrombus length*). *H*, NCCT shows an occlusive thrombus on multiple slices, with the placement of 2 ROIs for measuring Hounsfield unit density (*outlined regions*).

MR imaging was performed within 24 hours after admission on 1.5T Magnetom Avanto or 3T Magnetom Trio MR imaging scanners (Siemens). The standard MR imaging protocol included DWI (TR, 5600 ms; TE, 106 ms; FOV, 255 mm; matrix, 192 × 192; section thickness, 5 mm); FLAIR (TR, 9000 ms; TE, 89 ms; FOV, 220 mm; matrix, 320 × 216; section thickness, 5 mm); and MRA of the cervical and intracranial vessels.

Imaging Analyses

Imaging data for all patients were independently reviewed by 2 experienced stroke neurologists. Imaging analyses were performed without any knowledge of the clinical findings except for the side of the stroke lesion.

LCS was assessed on 20-mm CTA MIP images using a scale of 0–3:[15,17] 0 = absent collateral supply to the occluded vascular territory; 1 = collateral supply filling ≤50% but >0% of the occluded vascular territory; 2 = supply filling >50% but <100% of the occluded vascular territory; and 3 = 100% collateral supply of the occluded vascular territory. Rater discrepancies were settled by consensus discussions. Good LCS was defined as collateral scores of 2–3.[2,3]

Leukoaraiosis was assessed using FLAIR, and the Fazekas scale was used to categorize the degree of leukoaraiosis. This scale divides the WM into periventricular and deep regions, and each region is given a grade from 0 to 3, depending on the size and confluence of lesions on MR imaging; a higher score indicates a greater degree of leukoaraiosis. The examinations were scored in unaffected hemispheres of the present stroke using all available slices, rather than the single supraganglionic and single ganglionic slices from the original methodology.[10] Rater discrepancies were settled by consensus discussions. The total Fazekas score was obtained as a grade from 0 to 6 by summing scores from the periventricular and deep WM lesions.

For the occlusive thrombus signals on imaging, we assessed thrombus length and thrombus density on CT scans. Horos, Version 3.3.5, software (http://www.horosproject.org) was used to reconstruct 2D MPR images in the axial, coronal, and sagittal planes and measure quantitative values of length and density on DICOM images. First, the site of occlusive thrombus was identified on CTA together with the delayed-phase images. The proximal and distal ends of the thrombus were identified by the filling defect of contrast on delayed-phase images, and thrombus length was measured using a tracer tool that traced the profile of the whole thrombus within the arterial tree in the axial, coronal, and sagittal planes.[13] For thrombus involving the bifurcation, only the longest branch was used for the measurement. The longest length on any of these planes was set as the thrombus length. Next, the proximal and distal ends of the thrombus were identified in the axial plane on NCCT under the guidance of the filling defect of contrast on delayed-phase images. As support for the detection of occlusive thrombus, CTA and delayed-phase images were displayed simultaneously with the NCCT images. ROIs were manually placed on the whole thrombus on NCCT images, and the Hounsfield unit density of the thrombus was then measured by averaging all of the voxels within the ROIs. If ROIs were placed on multiple slices, the mean value (calculated by averaging all voxels within all ROIs) was used as the Hounsfield unit density of the thrombus. For the length and density of each thrombus, the results of the 2 raters were averaged. Representative cases are shown in Fig 1.

Histopathologic Analyses of Retrieved Thrombi

We investigated the histopathologic characteristics of the occlusive thrombi using specimens retrieved by thrombectomy, as reported in Liebeskind et al.[18] Fragmented pieces of retrieved thrombi were collected and fixed in a 10% phosphate-buffered formalin solution for 1 day. Formalin-fixed specimens were

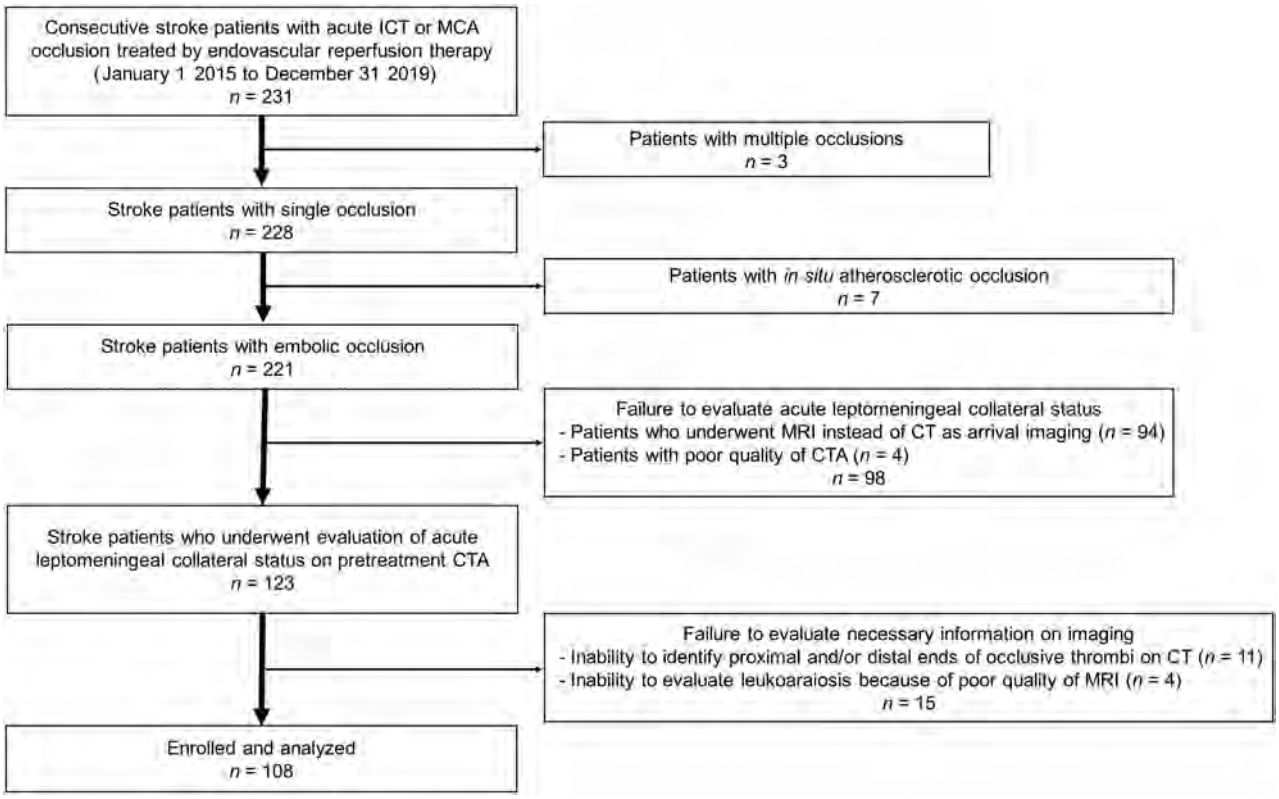

FIG 2. Flow diagram of the patients screened, enrolled, and analyzed in the study. ICT indicates internal carotid artery terminus.

embedded in paraffin, cut at 8-μm thickness, and stained with H&E. Histopathologic evaluation was performed without any knowledge of the clinical and radiographic findings. Stained slides were scanned at ×400 magnification using an Aperio ScanScope XT digital scanner (Aperio). ImageJ software (National Institutes of Health) was used to quantify the percentages of red blood cells, white blood cells, and fibrin by area. These measurements were repeated for each fragment of thrombus retrieved from the entire procedure. When multiple fragments were retrieved for analysis, the mean values across fragments were used for each constituent.

Statistical Analyses

Statistical analyses were performed using JMP 13.0 software (SAS Institute). Categoric data are expressed as numbers (percentages), and continuous data are expressed as medians (interquartile ranges). Patients' clinical and radiographic characteristics and the histopathologic characteristics of the thrombi were compared between the good LCS group (collateral scores of 2–3) and the poor LCS group (collateral scores of 0–1). For comparisons between 2 groups of patients, variables were analyzed using the Fisher exact test or Pearson χ^2 test for categoric data and the Mann-Whitney U test for continuous data, as appropriate. In the analyses, stroke subtypes were dichotomized into cardioembolic stroke and other noncardiac embolic stroke subtypes. The total Fazekas score was further examined by receiver operating characteristic curve analysis, and the cutoff value related to good LCS was calculated. A multivariate logistic regression analysis model, adjusted for sex, age, and variables with $P < .05$ in the univariate analysis, was built to assess the influence of clinical factors on good LCS. Subgroup analyses on the group of patients with cardioembolic stroke were performed in the same manner. Interrater reliability for the data before resolving disagreements, as measured by a quadratic weighted Cohen κ, was excellent, with $\kappa = 0.87$ for LCS and $\kappa = 0.81$ for the Fazekas score. For all statistical analyses, values of $P < .05$ were considered significant.

RESULTS

Patient Characteristics

Among 231 consecutive patients with acute ischemic stroke caused by ICA terminus or MCA occlusion treated by endovascular reperfusion therapy from January 1, 2015, to December 31, 2019, exclusions were for multiple occlusions (3 patients), in situ atherosclerotic occlusion (7 patients), initial MR imaging instead of CT as arrival imaging (94 patients), poor quality of CTA (4 patients), inability to visualize the full extent of thrombus (11 patients), and poor quality of MR imaging within 24 hours (4 patients) (Fig 2). Among the 108 patients fully meeting the study inclusion criteria, 49 patients (45%) were women, the median age was 76.5 years (interquartile range, 63.3-86 years), and the median NIHSS score on admission was 18 (interquartile range, 11.25–22) (detailed characteristics are listed in the Online Supplemental Data). The occluded vessels were the ICA terminus in 33 patients (31%), the horizontal segment of the MCA in 57 patients (53%), and the insular segment of the MCA in 18 patients (17%). Embolic LVO stroke subtype was most often cardioembolic (82 patients [76%]), followed by atheroembolic stroke due to extracranial carotid artery atherosclerotic stenosis (12 patients [11%]). The median time from last known well to imaging was 104 minutes (interquartile range, 62–379 minutes).

Table 1: Clinical indicators independently associated with good acute leptomeningeal collateral flow on multivariate analysis

	OR	95% CI	*P* Value
Female sex	0.59	0.17–1.93	.38
Age (for 1-year increase)	1.04	0.99–1.09	.10
NIHSS score on admission (for 1-point increase)	0.95	0.88–1.04	.29
Cardioembolic stroke subtype	0.17	0.02–0.87	.03
Reduced leukoaraiosis (total Fazekas scores of 0–2)	9.57	2.49–47.75	<.001
Thrombus length (for 1-mm increase)	0.93	0.84–1.01	.07

Table 2: Clinical indicators independently associated with good acute leptomeningeal collateral flow in patients with cardioembolic stroke on multivariate analysis

	OR	95% CI	*P* Value
Female sex	0.81	0.21–2.87	.74
Age (for 1-year increase)	1.03	0.99–1.09	.14
NIHSS score on admission (for 1-point increase)	0.95	0.86–1.04	.26
Blood glucose level (for 1-mmol/L increase)	0.87	0.64–1.13	.30
Reduced leukoaraiosis (total Fazekas scores of 0–2)	5.79	1.40–29.61	.01
Thrombus length (for 1-mm increase)	0.91	0.82–0.99	.04

Clinical Indicators of Acute Leptomeningeal Collateral Flow

Good LCS (collateral scores of 2–3) was present in 67 patients (62%) (zero, 8 patients [7%]; one, 33 patients [31%]; two, 51 patients [47%]; and three, 16 patients [15%]). Demographic and clinical characteristics of the good and poor LCS groups are shown in the Online Supplemental Data. Patients with good LCS had lower presenting NIHSS scores (15 [10–22] versus 19 [16–24.5]; $P = .001$), a lower incidence of cardioembolic stroke (69% versus 89%; $P = .04$), a lower total Fazekas score (2 [1–3] versus 4 [3–5]; $P < .001$), and shorter occlusive thrombus length (9.8 [6.7–15.6] versus 14.7 [8.7–20.2] mm; $P = .01$). There were no significant differences between the 2 groups in thrombus Hounsfield unit densities or thrombus histopathologic compositions.

In the receiver operating characteristic curve analysis, the optimal cutoff value for the total Fazekas score related to good LCS was 2 (area under the curve, 0.81; $P < .001$; sensitivity, 0.68; specificity, 0.83) (total Fazekas scores of 0–2, thirty-nine patients [36%]; and 3–6, sixty-nine patients [64%]). Of the 39 patients with total Fazekas scores of 0–2, LCS was poor in only 5 patients.

In the multivariate logistic regression analysis identifying factors independently associated with good LCS, cardioembolic stroke subtype was inversely related to good LCS (OR, 0.17; 95% CI, 0.02–0.87; $P = .03$), and reduced leukoaraiosis (total Fazekas scores, 0–2) was positively related to good LCS (OR, 9.57; 95% CI, 2.49–47.75; $P < .001$) (Table 1). Favorable clinical outcomes were achieved more frequently in patients with good compared with poor LCS (49% versus 16%; $P = .006$).

Subgroup Analyses of Patients with Cardioembolic Stroke

Of the 82 patients with cardioembolic stroke, 46 patients (56%) had good LCS (zero, 8 patients [10%]; one, 28 patients [34%]; two, 34 patients [41%]; and three, 12 patients [15%]). Compared with other patients with noncardiac embolic stroke, patients with cardioembolic stroke were older (79.5 [68.3–89.3] versus 65 [55–75] years; $P < .001$), had higher total Fazekas scores (3 [2–4] versus 2 [1–3]; $P = .03$), and had, less commonly, a good LCS (56% versus 81%; $P = .04$) (Online Supplemental Data).

Patients with cardioembolic stroke with good LCS compared with those with poor LCS had lower presenting NIHSS scores (15 [9–22] versus 19.5 [16.25–25]; $P = .002$), lower blood glucose levels (6.42 [5.83–7.39] versus 7.28 [6.26–8.26] mmol/L; $P = .02$), lower total Fazekas scores (2 [1–3.25] versus 4 [3–5]; $P < .001$), and shorter occlusive thrombus length (10.7 [7.2–14.3] versus 16.6 [9.6–20.5] mm; $P = .007$) (Online Supplemental Data). In multivariate logistic regression analysis, shorter thrombus length (OR, 0.91 per millimeter increase; 95% CI, 0.82–0.99; $P = .04$), and reduced leukoaraiosis (OR, 5.79; 95% CI, 1.40–29.61; $P = .01$) were independently related to good LCS (Table 2).

DISCUSSION

In the present study, among patients with acute ischemic stroke caused by LVOs due to embolism, good collateral robustness was present in >6 of every 10 patients. Independent indicators of good collateral flow were reduced leukoaraiosis, noncardiac embolism mechanism including embolism of arterial or undetermined origin rather than cardiac embolism, and occlusive thrombi of substantially shorter length. In addition, in patients with good collateral flow, neurologic deficits on presentation were less severe, and independent functional outcomes at 3 months were achieved 3 times more often.

Of the chronic factors in patients' premorbid vascular risk profiles, reduced leukoaraiosis was positively associated with good leptomeningeal collateral flow in embolic LVO. Our finding is in agreement with those in previous studies.[9,10] Leukoaraiosis is thought to originate from small-vessel disease, which is caused by chronically reduced CBF due to arteriolosclerosis, lipohyalinosis, and fibrinoid necrosis of the small arteries and arterioles.[19] The leptomeningeal collateral system is also composed of small arteries and arterioles. Therefore, it is possible that mechanisms causing leukoaraiosis might also affect the arterioles of the leptomeningeal collateral system.[10] On the other hand, 1 study reported that leukoaraiosis had no relationship with the extent of collaterals.[20] Our study differed from that study in an important aspect. Our cohort contained appropriate numbers of patients with severe leukoaraiosis, while almost all the patients had absent or minimal leukoaraiosis in the previous study. In contrast, age and vascular risk factors including a history of hypertension, diabetes mellitus, dyslipidemia, smoking, and obesity were not univariately associated with poor leptomeningeal collateral flow in the present study, though the severity of leukoaraiosis has been reported to be associated with several of these parameters, including older age, hypertension, diabetes mellitus, smoking, and obesity.[21,22] Our results indicate

that leukoaraiosis, as a physiologic expression of cumulative small-vessel injury from multiple risk factors, more strongly correlates with leptomeningeal impairment. Although leptomeningeal impairment may also arise, in part, from the joint effect of multiple vascular risk factors, the chronic small-vessel injury of leukoaraiosis itself and its associated chronic mild deep ischemic stress may be an important contributor to impairing pial collateral recruitment. Leukoaraiosis might, therefore, be an imaging marker of global cerebrovascular dysfunction and a determinant of leptomeningeal collateral variability.

Among the acute factors present at the time of stroke, cardioembolic stroke subtype, rather than other noncardiac embolic stroke subtypes including embolism of arterial or undetermined origin, was associated with poor leptomeningeal collateral flow. Similar findings have been demonstrated in several prior studies.[1,11,12] However, our study complements the prior studies by having excluded intracranial atherosclerotic disease and comparing cardioembolic stroke only to other noncardiac embolic strokes, most often of extracranial atherosclerotic origin. Atheroembolic stroke is preceded by arterial stenosis that develops across decades, which may promote cerebral collateral circulation because of the chronic and slowly progressive nature of cerebral large-vessel hypoperfusion.[23] In contrast, cardioembolic stroke usually has an abrupt onset without chronic cerebral large-vessel hypoperfusion, which may be associated with a paucity of collateral artery formation and recruitment.[24] In addition, compared with patients with other noncardiac embolic strokes, patients with cardioembolic stroke were older and had higher total Fazekas scores, which could also impair pial collateral recruitment caused by small-vessel injury. Thus, the underlying stroke etiology may be a determinant of leptomeningeal collateral flow.

Shorter thrombus length was another acute factor associated with good leptomeningeal collateral flow in cardioembolic stroke. Few studies have assessed the relationship between occlusive thrombus characteristics and collateral flow.[13,14] Theoretically, a longer thrombus might obstruct more orifices of arteries that provide collateral blood flow, leading to decreased pial collateral recruitment to the occluded vascular territory.[14] Conversely, collaterals may possibly influence thrombus length, and longer thrombus length may result causally from poor collateral flow because patients with poor collaterals have an increased stasis around the occlusive thrombus, leading to thrombus extension.[13] Previous studies have suggested that shorter thrombus length may be a consequence rather than a cause of good collateral flow.[13] However, further studies using time-series data are necessary to analyze the causal relationships. On the other hand, we did not identify any relationship between leptomeningeal collateral flow and the histopathologic components of the whole occlusive thrombus. In future studies investigating the relationship between collateral circulation and the histopathologic components of occlusive thrombus, we, therefore, suggest that occlusive thrombi should be analyzed, if possible, in a manner that differentially assesses the original thrombus component (which comes from a proximal source) and the new thrombus component (which forms in situ from the stasis of blood flow around the original thrombus).[13]

Good leptomeningeal collateral flow after embolic occlusion was associated with lower NIHSS scores at presentation and favorable functional outcomes at 3 months. Previous studies have also reported that more robust CTA collaterals were predicted by lower NIHSS scores and were associated with better clinical outcomes.[25,26] Poorer leptomeningeal collateral flow has been reported to be associated with both larger initial infarction size and larger follow-up infarct progression volumes, leading to poorer functional outcomes and increased mortality.[25] In addition, poorer collaterals may serve as an indicator of a worse response to reperfusion therapy and higher rates of intracranial hemorrhage after reperfusion therapy, which may partly explain the unfavorable effects of poor collaterals.[27] The findings that patients with good collaterals showed favorable outcomes stress the need to clarify the clinically useful indicators of good leptomeningeal collateral variability, to provide appropriate acute stroke treatments and improve clinical outcomes in embolic LVOs. Premorbid leukoaraiosis, underlying stroke etiology, and occlusive thrombus length may be helpful indicators of acute leptomeningeal collateral flow in clinical practice.

Some limitations of our study should be noted. This was a single-center study, and replication in other populations is desirable to demonstrate generalizability. The power to detect clinical features with less marked effects on collateral flow robustness may have been constrained by sample size, despite the relatively large, well-studied population examined in our study. In addition, the multivariate analysis model was built using variables with $P < .05$ in the univariate analysis due to the modest sample size, and some potentially relevant factors, such as an occluded vessel site, might have been excluded from the model. All our patients underwent the assessment of LCS using single-phase CTA, which may have led to the underestimation of LCS in the case of delayed filling in combination with an early acquisition phase.[28] Newer techniques, such as CTA reconstruction from CTP data and multiphase CTA, make CTA independent of the timing of contrast administration and scan acquisition and may improve the assessment of LCS.[29,30]

The criterion standard for assessing LCS is DSA.[8] However, multivessel complete DSA is not always performed, and we aimed to determine features associated with collateral extent on presentation. Although the Fazekas scale was useful to evaluate the degree of leukoaraiosis, the scale is relatively crude. Measuring quantitative volumes of WM lesions may allow more accurate evaluation of leukoaraiosis. While noncardiac rather than cardiac embolism was associated with good collateral flow, the noncardiac embolic stroke subgroup might have potentially contained a different extent of collaterals according to different stroke etiologies. We did not analyze the circle of Willis for anatomic variants, possibly a confounding factor.[2]

CONCLUSIONS

Among patients with embolic LVOs, good collateral flow is present in 62% of patients and is associated with better clinical outcomes. Reduced leukoaraiosis, a noncardiac embolism mechanism including embolism of arterial or undetermined origin rather than a cardiac embolism mechanism, and shorter thrombus length in cardioembolism are indicators of good collateral flow. These

findings suggest that chronic small-vessel injury as well as an abrupt stroke onset without chronic large-vessel hypoperfusion may reduce collateral robustness, and they also suggest that improvement of collaterals may protect against thrombus extension.

Disclosure forms provided by the authors are available with the full text and PDF of this article at www.ajnr.org.

REFERENCES

1. Guglielmi V, LeCouffe NE, Zinkstok SM, et al; on behalf of the MR-CLEAN Registry Investigators. **Collateral circulation and outcome in atherosclerotic versus cardioembolic cerebral large vessel occlusion.** *Stroke* 2019;50:3360–68 CrossRef Medline
2. van Seeters T, Biessels GJ, Kappelle LJ, et al; Dutch Acute Stroke Study (DUST) Investigators. **Determinants of leptomeningeal collateral flow in stroke patients with a middle cerebral artery occlusion.** *Neuroradiology* 2016;58:969–77 CrossRef Medline
3. Wiegers EJ, Mulder MJH, Jansen IG, et al; MR CLEAN Trial and MR CLEAN Registry Investigators. **Clinical and imaging determinants of collateral status in patients with acute ischemic stroke in MR CLEAN Trial and Registry.** *Stroke* 2020;51:1493–502 CrossRef Medline
4. Zhang H, Prabhakar P, Sealock R, et al. **Wide genetic variation in the native pial collateral circulation is a major determinant of variation in severity of stroke.** *J Cereb Blood Flow Metab* 2010;30:923–34 CrossRef Medline
5. Lima FO, Furie KL, Silva GS, et al. **The pattern of leptomeningeal collaterals on CT angiography is a strong predictor of long-term functional outcome in stroke patients with large vessel intracranial occlusion.** *Stroke* 2010;41:2316–22 CrossRef Medline
6. Menon BK, Smith EE, Coutts SB, et al. **Leptomeningeal collaterals are associated with modifiable metabolic risk factors.** *Ann Neurol* 2013;74:241–48 CrossRef Medline
7. Nannoni S, Sirimarco G, Cereda CW, et al. **Determining factors of better leptomeningeal collaterals: a study of 857 consecutive acute ischemic stroke patients.** *J Neurol* 2019;266:582–88 CrossRef Medline
8. Fujita K, Tanaka K, Yamagami H, et al. **Detrimental effect of chronic hypertension on leptomeningeal collateral flow in acute ischemic stroke.** *Stroke* 2019;50:1751–57 CrossRef Medline
9. Giurgiutiu DV, Yoo AJ, Fitzpatrick K, et al. **Severity of leukoaraiosis, leptomeningeal collaterals, and clinical outcomes after intra-arterial therapy in patients with acute ischemic stroke.** *J Neurointerv Surg* 2015;7:326–30 CrossRef Medline
10. Mark I, Seyedsaadat SM, Benson JC, et al. **Leukoaraiosis and collateral blood flow in stroke patients with anterior circulation large vessel occlusion.** *J Neurointerv Surg* 2020;12:942–45 CrossRef Medline
11. Rebello LC, Bouslama M, Haussen DC, et al. **Stroke etiology and collaterals: atheroembolic strokes have greater collateral recruitment than cardioembolic strokes.** *Eur J Neurol* 2017;24:762–67 CrossRef Medline
12. Hassler E, Kneihsl M, Deutschmann H, et al. **Relationship between stroke etiology and collateral status in anterior circulation large vessel occlusion.** *J Neurol* 2020;267:3362–70 CrossRef Medline
13. Qazi EM, Sohn SI, Mishra S, et al. **Thrombus characteristics are related to collaterals and angioarchitecture in acute stroke.** *Can J Neurol Sci* 2015;42:381–88 CrossRef Medline
14. Alves HC, Treurniet KM, Dutra BG, et al; MR CLEAN Trial Investigators. **Associations between collateral status and thrombus characteristics and their impact in anterior circulation stroke.** *Stroke* 2018;49:391–96 CrossRef Medline
15. Tan IY, Demchuk AM, Hopyan J, et al. **CT angiography clot burden score and collateral score: correlation with clinical and radiologic outcomes in acute middle cerebral artery infarct.** *AJNR Am J Neuroradiol* 2009;30:525–31 CrossRef Medline
16. Mortimer AM, Little DH, Minhas KS, et al. **Thrombus length estimation in acute ischemic stroke: a potential role for delayed contrast enhanced CT.** *J Neurointerv Surg* 2014;6:244–48 CrossRef Medline
17. Tan JC, Dillon WP, Liu S, et al. **Systematic comparison of perfusion-CT and CT-angiography in acute stroke patients.** *Ann Neurol* 2007;61:533–43 CrossRef Medline
18. Liebeskind DS, Sanossian N, Yong WH, et al. **CT and MRI early vessel signs reflect clot composition in acute stroke.** *Stroke* 2011;42:1237–43 CrossRef Medline
19. Merino JG. **White matter hyperintensities on magnetic resonance imaging: what is a clinician to do?** *Mayo Clin Proc* 2019;94:380–82 CrossRef Medline
20. Sanossian N, Ovbiagele B, Saver JL, et al. **Luekoaraiosis and collaterals in acute ischemic stroke.** *J Neuroimaging* 2011;21:232–35 CrossRef Medline
21. Zhang C, Wang Y, Zhao X, et al; Chinese IntraCranial AtheroSclerosis (CICAS) Study Group. **Factors associated with severity of leukoaraiosis in first-ever lacunar stroke and atherosclerotic ischemic stroke patients.** *J Stroke Cerebrovasc Dis* 2014;23:2862–68 CrossRef Medline
22. Lin Q, Huang WQ, Ma QL, et al. **Incidence and risk factors of leukoaraiosis from 4683 hospitalized patients: a cross-sectional study.** *Medicine (Baltimore)* 2017;96:e7682 CrossRef Medline
23. Jing Z, Shi C, Zhu L, et al. **Chronic cerebral hypoperfusion induces vascular plasticity and hemodynamics but also neuronal degeneration and cognitive impairment.** *J Cereb Blood Flow Metab* 2015;35:1249–59 CrossRef Medline
24. Tu HT, Campbell BC, Christensen S, et al; Echoplanar Imaging Thrombolytic Evaluation Trial (EPITHET) Investigators. **Pathophysiological determinants of worse stroke outcome in atrial fibrillation.** *Cerebrovasc Dis* 2010;30:389–95 CrossRef Medline
25. Souza LC, Yoo AJ, Chaudhry ZA, et al. **Malignant CTA collateral profile is highly specific for large admission DWI infarct core and poor outcome in acute stroke.** *AJNR Am J Neuroradiol* 2012;33:1331–36 CrossRef Medline
26. Liebeskind DS, Tomsick TA, Foster LD, et al. **Collaterals at angiography and outcomes in the Interventional Management of Stroke (IMS) III trial.** *Stroke* 2014;45:759–64 CrossRef Medline
27. Leng X, Fang H, Leung TW, et al. **Impact of collaterals on the efficacy and safety of endovascular treatment in acute ischaemic stroke: a systematic review and meta-analysis.** *J Neurol Neurosurg Psychiatry* 2016;87:537–44 CrossRef Medline
28. Jansen IG, Mulder MJ, Goldhoorn RB, et al; MR CLEAN Registry Investigators. **Impact of single phase CT angiography collateral status on functional outcome over time: results from the MR CLEAN Registry.** *J Neurointerv Surg* 2019;11:866–73 CrossRef Medline
29. Smit EJ, Vonken EJ, van Seeters T, et al. **Timing-invariant imaging of collateral vessels in acute ischemic stroke.** *Stroke* 2013;44:2194–99 CrossRef Medline
30. Menon BK, d'Esterre CD, Qazi EM, et al. **Multiphase CT angiography: a new tool for the imaging triage of patients with acute ischemic stroke.** *Radiology* 2015;275:510–20 CrossRef Medline

Petrobasal Vein: A Previously Unrecognized Vein Directly Connecting the Superior Petrosal Sinus with the Emissary Vein of the Foramen Ovale

S. Ide, H. Kiyosue, R. Shimada, S. Tanoue, K. Tokuyama, and Y. Asayama

ABSTRACT

BACKGROUND AND PURPOSE: The superior petrosal sinus terminates anteriorly at the cavernous sinus and posteriorly at the transverse sinus. Venous variations directly connecting the superior petrosal sinus and the emissary veins of the foramen ovale are not well-recognized. We present a connecting vein, provisionally named the petrobasal vein.

MATERIALS AND METHODS: Biplane cerebral angiography of the bilateral internal carotid arteries and the vertebral artery acquired in 267 patients was retrospectively reviewed by 2 neuroradiologists with special interest in the existence and course of the petrobasal vein.

RESULTS: The petrobasal vein was observed to lie anterior-posteriorly on the superior surface of the petrosal bone and connected to the midportion of the superior petrosal sinus and the emissary veins of the foramen ovale in 41 patients (15%) and sides (7.9%); it drained into the pterygoid plexus. The petrobasal vein was observed on VAG in 21 patients, on ICAG alone in 8 patients (9 sides), on both VAG and ICAG in 12 patients, and on ICAG in 1 patient. In the patients in whom the petrobasal vein was visualized on the ICAs, the superficial middle cerebral vein drained into a combination of the pterygoid plexus via the emissary veins of the foramen ovale and the superior petrosal sinus.

CONCLUSIONS: The petrobasal vein, an unknown vein directly connecting the superior petrosal sinus and the emissary veins of the foramen ovale and draining into the pterygoid plexus, can occasionally be identified on cerebral angiography as a variant drainage route from the cerebellum and brainstem veins and/or from the superficial middle cerebral vein. The petrobasal vein is thought to be a remnant of the primitive tentorial sinus.

ABBREVIATIONS: dAVF = dural AVF; EVFO = emissary vein of the foramen ovale; ICAG = internal carotid angiography; PBV = petrobasal vein; PTS = primitive tentorial sinus; SMCV = superior middle cerebral vein; SPS = superior petrosal sinus; VA = vertebral artery; VAG = vertebral angiography

The superior petrosal sinus (SPS) is an important venous sinus that receives venous blood from the cerebellum and brainstem, and it drains posteriorly into the transverse sinus and anteriorly into the cavernous sinus. Some variations in the SPS, including the absence of either termination to the cavernous sinus or the transverse sinus, disconnection between the anterior and posterior parts of the SPS, and absence of the SPS, have been reported.[1,2] The SPS occasionally receives a variant type of the superficial middle cerebral vein called the sphenopetrosal vein.[3,4] The emissary vein of the foramen ovale (EVFO), a major emissary vein at the middle cranial fossa, connects medially to the cavernous sinus and laterally to the middle meningeal vein.[5,6] It runs inferiorly through the foramen ovale and joins into the pterygoid plexus and/or the pharyngeal plexus. It also receives the superficial middle cerebral vein in individuals with a type of variant termination, the so-called sphenobasal vein. Blood from the SPS can drain into the cavernous sinus, and in some individuals, the SPS drains into the EVFO. There is another potential route indirectly connecting the SPS to the EVFO. The petrosquamous sinus, a rare remnant of the embryologic emissary vein, arises from the transverse sinus near the confluence with the SPS and runs anteriorly in the petrosquamous fissure or in an intraosseous canal at the most lateral part of the petrous bone to join the EVFO or the retromandibular vein through the postglenoid foramen.[7,8] It is generally thought that there is no direct connection between the SPS and the EVFO. However, we observed on cerebral angiography a previously unrecognized venous channel that directly

Received May 26, 2021; accepted after revision September 14.

From the Department of Radiology (S.I., H.K., R.S., S.T., K.T., Y.A.), Faculty of Medicine, Oita University, Oita, Japan; and Department of Radiology (S.T.), Faculty of Medicine, Kurume University, Kurume, Fukuoka, Japan.

Paper previously presented, in part, at: Annual Meeting of the Radiological Society of North America, November 27 to December 2, 2016; Chicago, Illinois.

Please address correspondence to Satomi Ide, MD, Department of Radiology, Oita University Faculty of Medicine, Idaigaoka, Hasama, Yufu, Oita, Japan; e-mail: idesat@oita-u.ac.jp

http://dx.doi.org/10.3174/ajnr.A7345

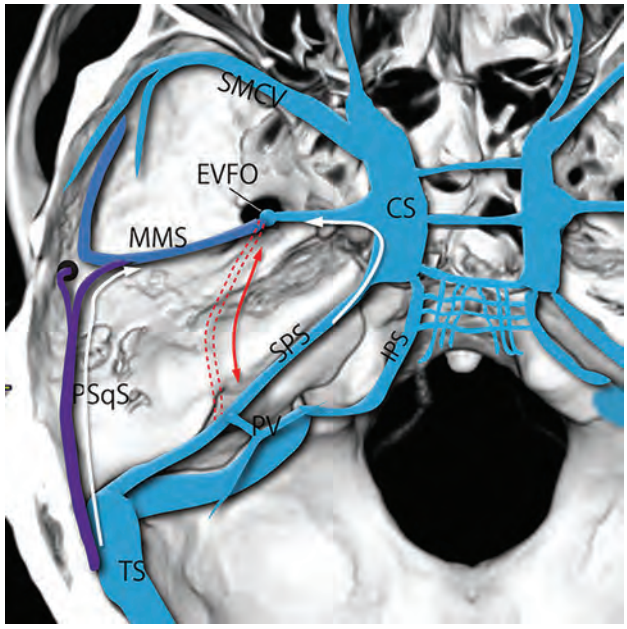

FIG 1. Schematic drawing of the potential venous pathway between the SPS and the EVFO. Two known routes include the medial route through the cavernous sinus (CS) and the lateral route through the petrosquamosal sinus (PSqS) and the middle meningeal sinus (MMS). There is another unknown route running on the superior surface of the petrosal bone connecting directly between the EVFO and the SPS (*red dotted line*). PV indicates petrosal vein; IPS, inferior petrosal; TS, tentorial sinus.

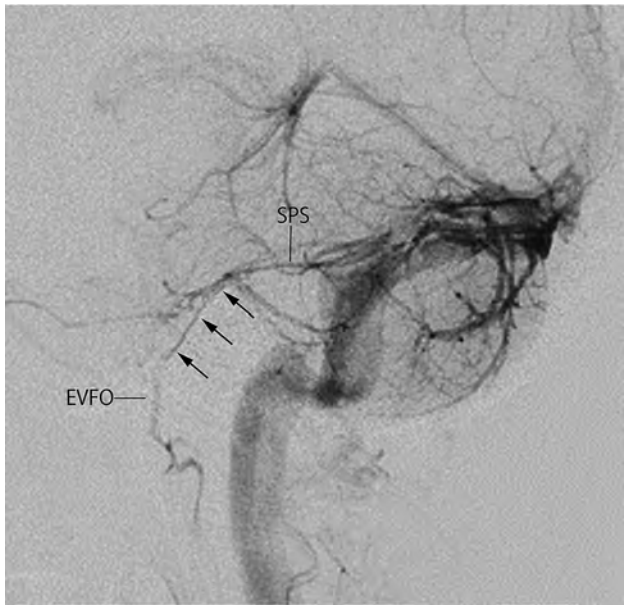

FIG 2. Lateral view on left vertebral angiography in the venous phase showing a venous channel (*arrows*) arising from the midportion of the SPS that runs anterior-inferiorly to join the EVFO. It is provisionally named the PBV.

connects the SPS to the EVFO and serves as a drainage route for normal cerebral venous blood or as a potential access route to intracranial lesions, such as dural AVFs (dAVFs) (Figs 1–3); this vein is referred to as the petrobasal vein (PBV) in this article.

MATERIALS AND METHODS

This study was approved by the local ethics review board, which waived the requirement for written informed consent due to its retrospective nature. We retrospectively reviewed cerebral angiography images acquired at our institution (Oita University Hospital) from May 2015 to January 2018. After excluding patients with lesions affecting cerebral venous drainage and/or with suboptimal angiography imaging quality mainly due to motion artifacts, 267 sets of biplane cerebral angiographic images of the bilateral internal/common carotid and vertebral arteries were retrospectively reviewed by 2 neuroradiologists with special interest in visualization and the course of the PBV. The PBV was defined as a venous structure directly connecting the midportion of the SPS and the EVFO.

3D rotational angiography in the venous phase, CT angiography, and 3D T1 contrast-enhanced MR images were also reviewed when available. 3D rotational angiography was performed for selected patients who had brain tumors to depict detailed anatomic relationships of the tumors with adjacent venous structures before an operation, who had spontaneous hemorrhage with an unknown origin, and who were suspected of having venous abnormalities, including developmental venous anomalies. The patients included 111 men and 156 women, and the average age of the patients was 57.9 years. The included patients had various underlying diseases; there were 91 patients with brain or head and neck tumors, 80 patients with cerebral aneurysms, 54 patients with cerebral artery stenosis, 17 patients with dAVFs, 12 patients with cerebral arteriovenous malformations, 7 patients with spontaneous subarachnoid or cerebral hemorrhage, and 6 patients with other diseases. All angiographic procedures, including biplane DSA and 3D rotational angiography, were performed using biplane angiography equipment (Infinix VB; Toshiba Medical). For biplane angiography, the injection volume and rate in the ICA, common carotid artery, and vertebral artery (VA) were 8–9 mL at 4–4.5 mL/s, 9–10 mL at 4.5–5 mL/s, and 6–7 mL at 3–3.5 mL/s, respectively.

For 3D rotational angiography, the injection volume and rate were 18–24 mL at 3–4 mL/s in the ICA and 18–21 mL at 3-3.5 mL/s in the VA. The raw 3D rotational angiography data were transferred to a workstation (Ziostation; Ziosoft), and 3D and multiplanar reconstruction images consisting of 0.3- to 1-mm-thick sections obtained at a 0.5-mm interval were reconstructed.

RESULTS

Visualization of the PBV

The PBV was identified on 42 sides in 41 patients (7.9% and 15%) and was identified on vertebral angiography alone in 21 patients, on carotid angiography alone in 8 patients (9 sides), and on both vertebral and internal carotid angiography in 12 patients. The PBV originated at the anterior aspect of the midportion of the SPS and ran anteriorly to join the EVFO when it was visualized on vertebral angiography (Fig 4). In patients in whom the PBV was visualized on carotid angiography, the superior middle cerebral vein (SMCV) showed a combined type of sphenobasal and sphenopetrosal vein that drained into the 2 terminations of the EVFO and the SPS; additionally, the PBV formed part of the SMCV between the EVFO and the SPS (Fig 5). Among 21 patients in whom the PBV was visualized on vertebral

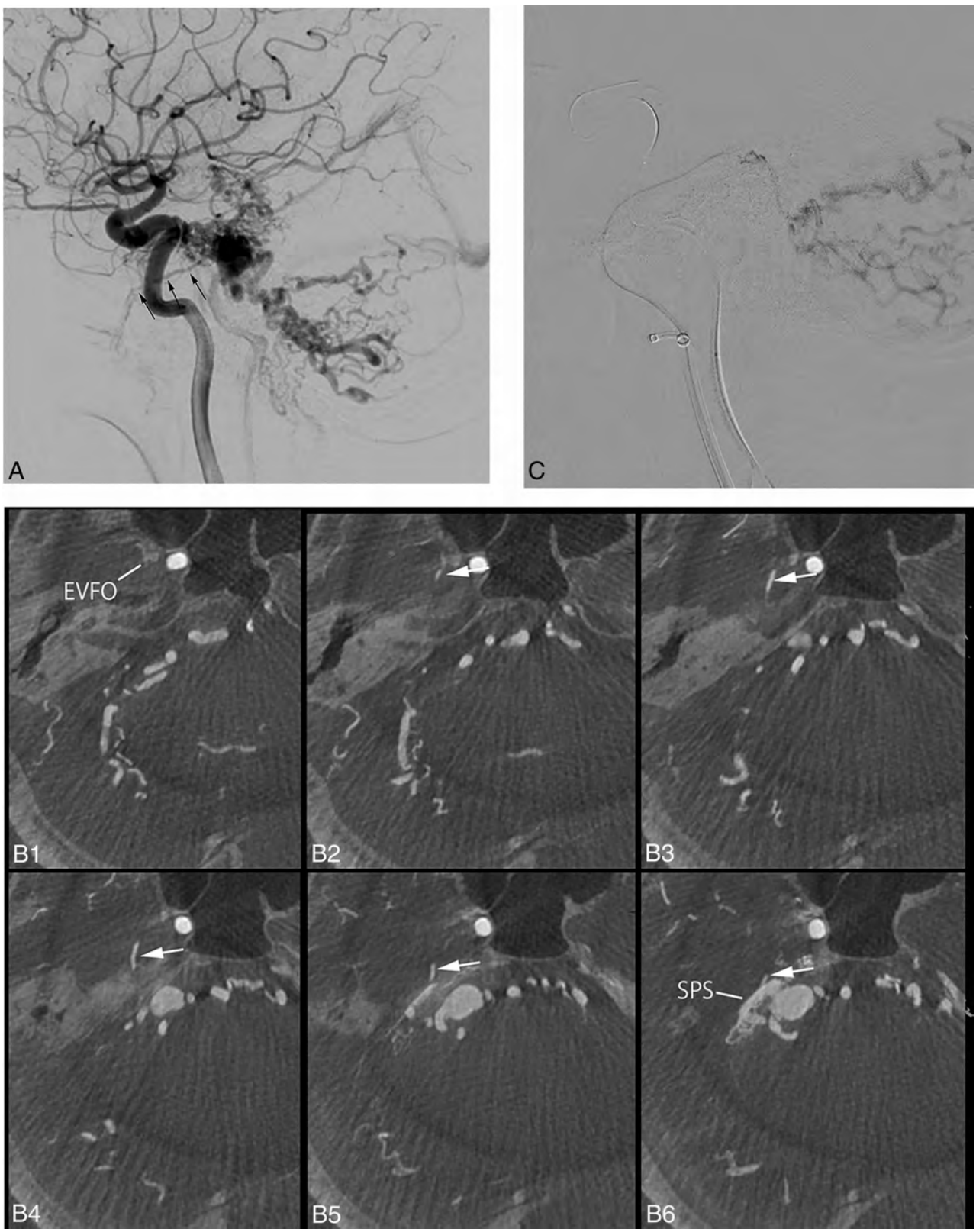

FIG 3. A case of a dAVF involving the SPS with a drainage route via the PBV. *A*, Lateral view on right internal carotid angiography shows a dAVF fed by multiple feeders from the meningohypophyseal trunk. The dAVF drains retrogradely via the various petrosal veins into the cerebellar cortical veins and the lateral mesencephalic vein. There is another drainage route via the PBV (*arrows*) into the emissary vein of the foramen rotundum. *B*, Axial MPR images based on rotational angiography of the right ICA show the dAVF involving the SPS. A drainage route (*white arrow*) via the PBV arising from the anterior aspect of the SPS to the EVFO is noted. *C*, Selective venography via a microcatheter shows transvenous introduction of the microcatheter into the petrosal vein via the PBV. Thereafter, the dAVF was completely occluded by transvenous embolization.

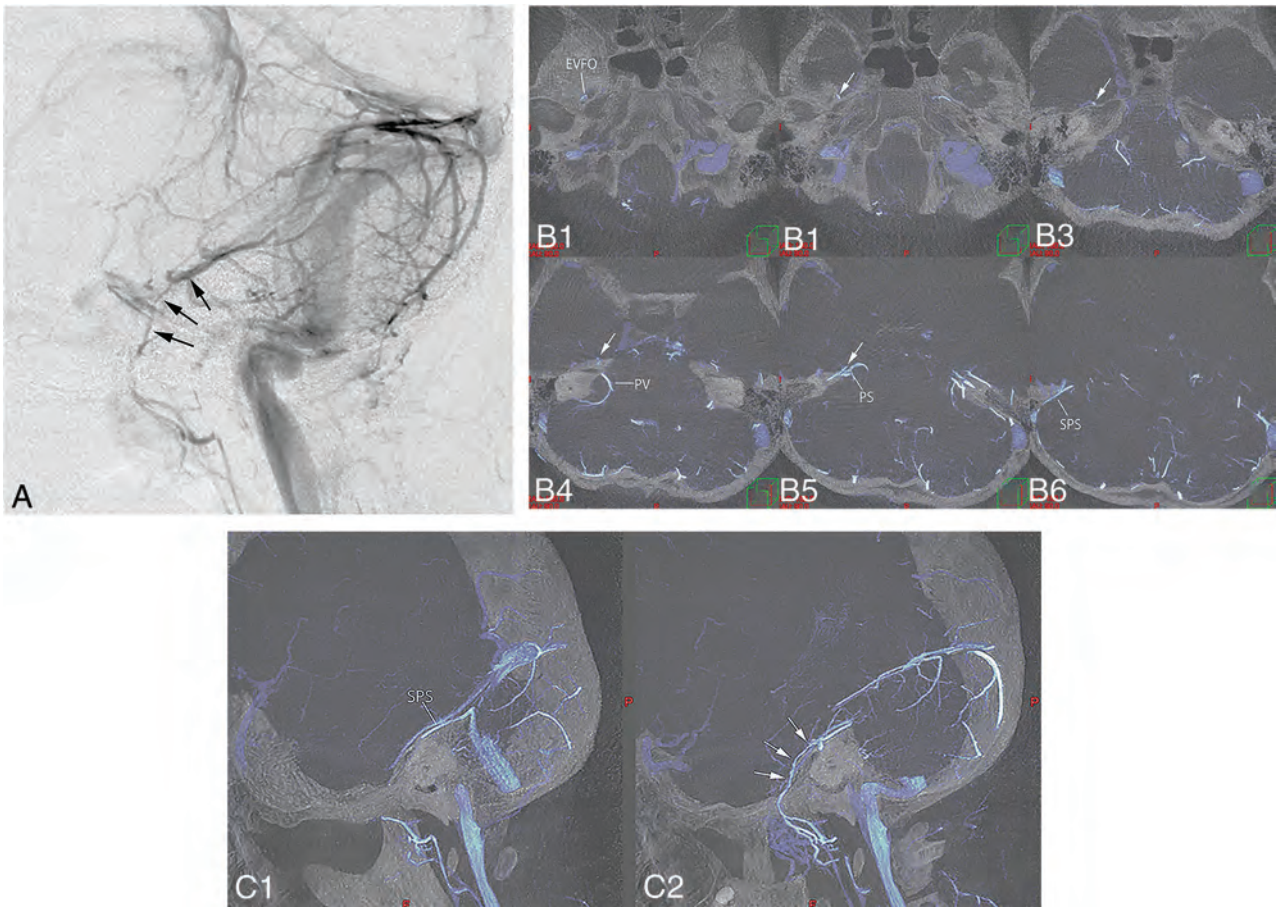

FIG 4. PBV visualized on vertebral angiography alone. *A*, Lateral view on left vertebral angiography in the venous phase shows the PBV (*arrows*) from the superior petrosal sinus at the confluence of the petrosal vein. The PBV runs anterior-inferiorly to join the emissary vein of the foramen ovale. Axial (*B*) and sagittal (*C*) MPR images based on rotational angiography of the right VA show the PBV (*arrows*) from the anterior aspect of the SPS. It runs anteriorly on the superior surface of the petrosal bone to join the EVFO.

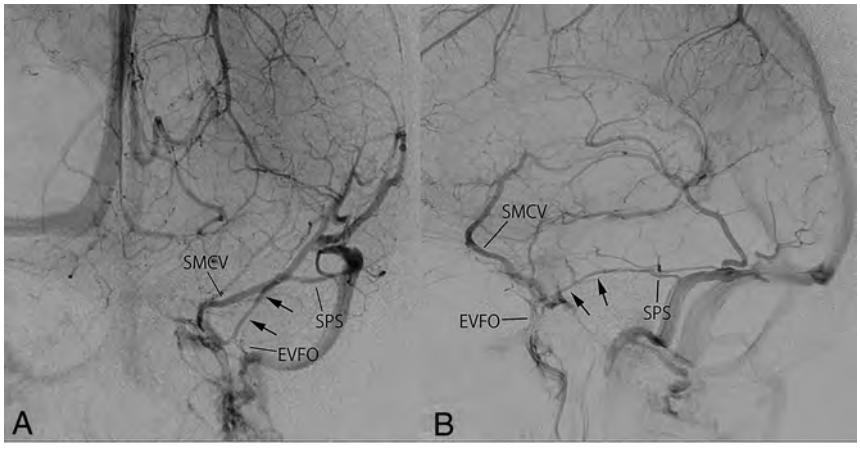

FIG 5. Internal carotid angiography showing the PBV as part of the drainage route of the superficial middle cerebral vein (combined type of the sphenobasal and the sphenopetrosal veins). Frontal (*A*) and lateral (*B*) views on left internal carotid angiography in the venous phase show the combined sphenobasal and sphenopetrosal drainage type of the SMCV. The PBV (*arrows*) composes part of the termination of the SMCV between the EVFO and the SPS. Axial (*C, next page*) and sagittal (*D, next page*) MPR images based on rotational angiography of the left ICA show the PBV (*arrows*) running anterior-posteriorly between the midportion of the SPS and the EVFO. The SMCV joins the EVFO.

angiography alone, the SMCV terminated in the cavernous sinus on 10 sides, in the EVFO in 6 patients, and in the transverse sinus in 1 patent, and the SMCV was absent in 2 patients.

Course of the PBV

The PBV lies anterior-posteriorly on the superior surface of the petrous bone and connects posteriorly to the anterior aspect of the SPS near the termination of the petrosal vein. Additionally, it runs inferiorly and anteromedially on the middle fossa to the foramen ovale to join the EVFO. The EVFO runs downward through the foramen ovale and joins the pterygoid plexus.

DISCUSSION

It is generally believed that no direct connection exists between the SPS and EVFO; however, in this study, we

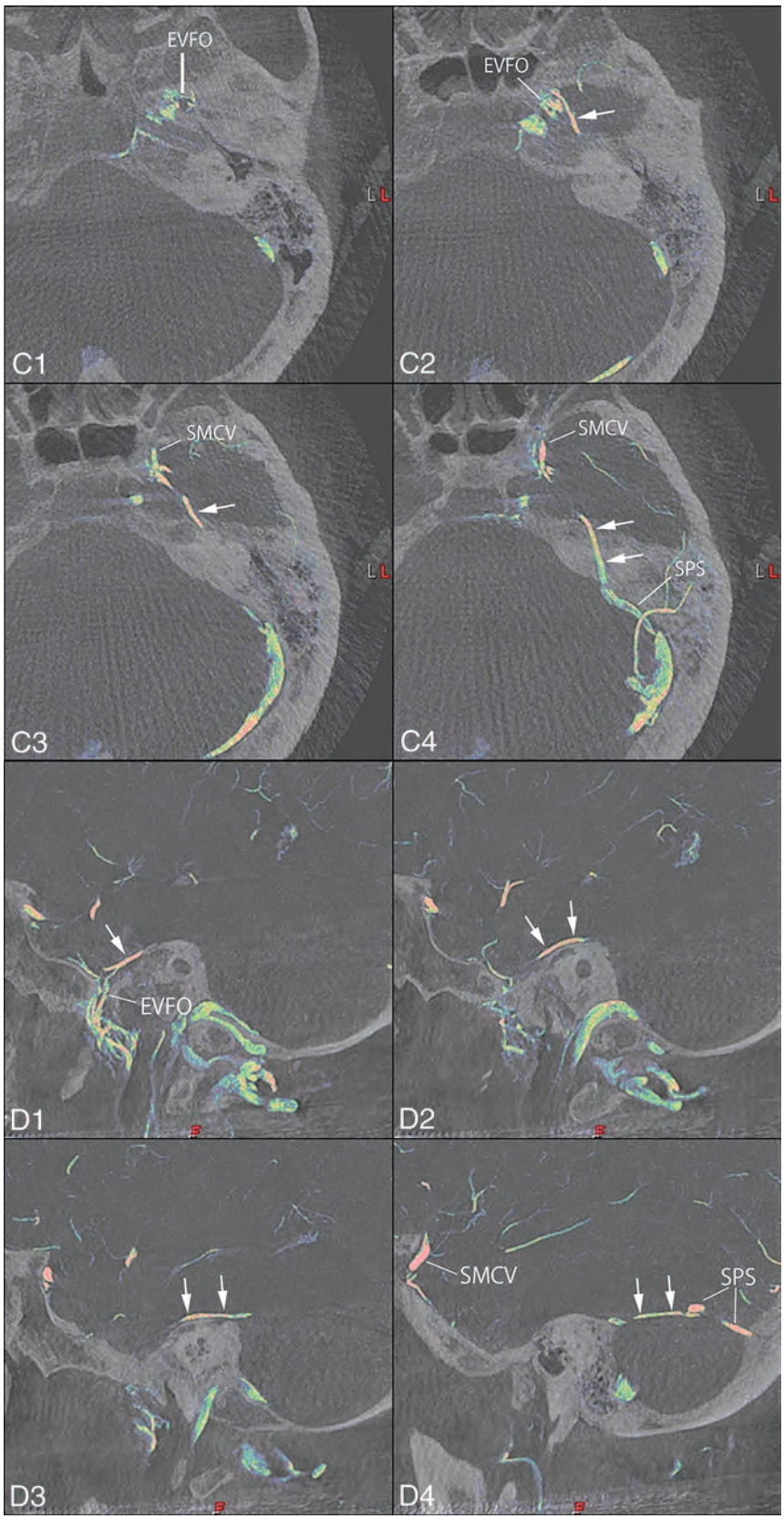

FIG 5. Continued

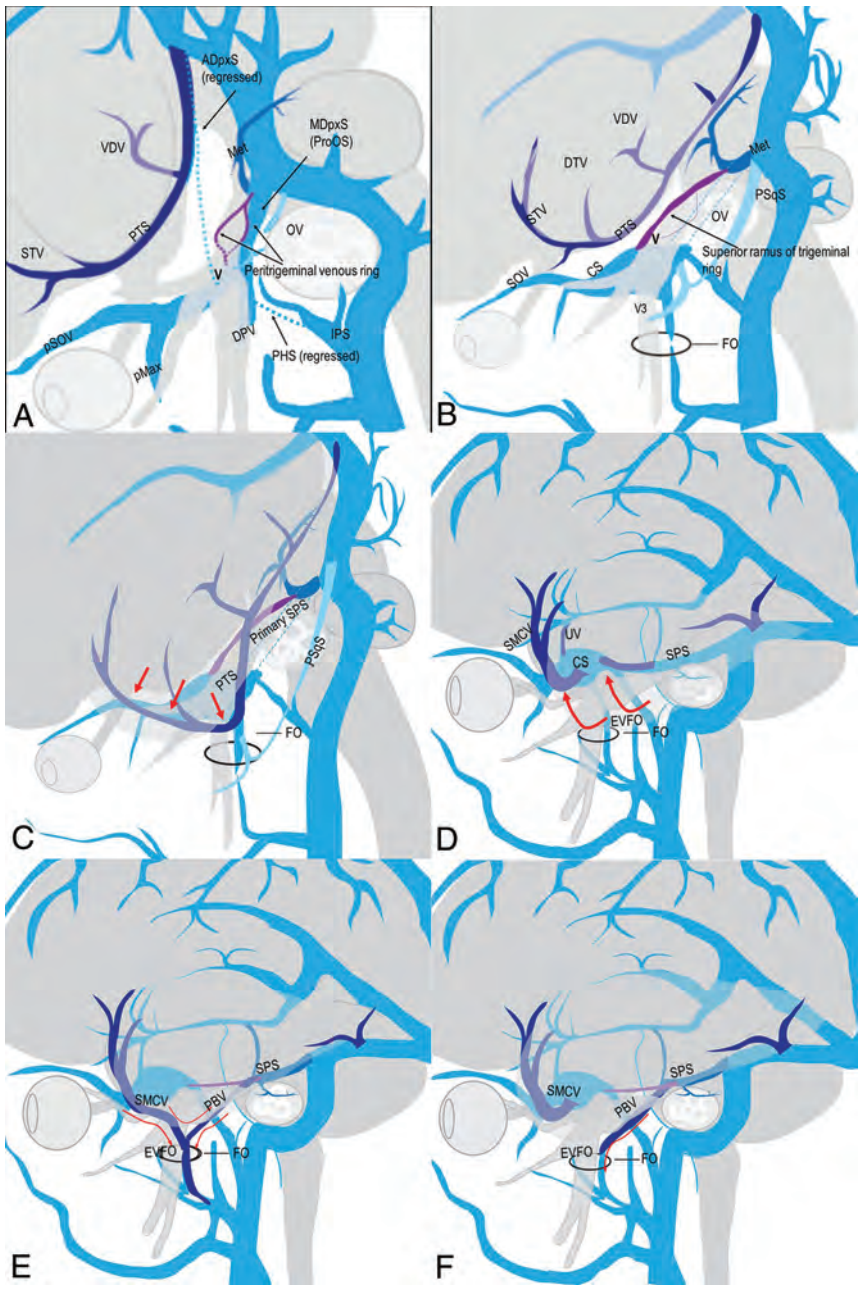

FIG 6. Schematic drawing of the embryologic development of the SPS, EVFO, and SMCV. *A*, Lateral view of an embryo at 18–26 mm in crown rump length. ADpxS indicates anterior dural plexus stem; PHS, primary head sinus; OV, otic vesicle; pSOV, primitive superior ophthalmic vein; pMax, primitive maxillary vein; DPV, dorsal pharyngeal vein; MDpxS, middle dural plexus; STV, superficial telencephalic vein; Met, metencephalic vein; IPS, inferior petrosal sinus; V, trigeminal nerve; VDV, ventral diencephalic vein. The *dotted lines* indicate regressed parts of the ADpxS and PHS. The dorsal part of the MDpxS forms the posterior part of the SPS in the future. The peritumoral venous ring surrounds the trigeminal nerve, and it connects the distal and proximal portions of the prootic sinus (proOS). *B*, View a few weeks after that shown in *A*. DTV indicates deep telencephalic vein; V3, mandibular nerve; Met, metencephalic vein; PSqS, petrosquamosal sinus; FO, foramen ovale; CS, cavernous sinus; SOV, superior ophthalmic vein. The anterior part of the MDpxS and inferior ramus of the paratrigeminal venous ring disappear, and the remnant of the superior ramus of the venous ring and the residual posterior portion of the MDpxS form the primary SPS. The DPV runs along the V3, which connects with the pterygoid venous plexus through the FO to become the EVFO. *C*, View just before or after birth. The PTS deviates inferomedially (*red arrows*) to the middle cranial fossa close to the FO secondary to further development of the temporal lobe. *D*, Common venous system type in adults. The PTS is further deviated medially (*red arrows*) and fuses to the CS, and the SMCV and uncal vein (UV) drain into the CS. The midportion of the PTS fuses to the primary SPS. A remnant of the posterior part of the PTS becomes the lateral and/or medial tentorial sinus. The metencephalic vein becomes the petrosal vein. *E*, The PBV combined with the sphenobasal vein. In this type, the anterior and midportions of the PTS remain at the middle cranial fossa and fuse to the EVFO. Venous blood from the SMCV drains into the EVFO and the SPS via the PBV. Venous blood from the SPS can also be drained via the PBV into the EVFO, depending on the pressure gradient. *F*, The PBV alone. In this type, the midportion of the PTS remains alone at the middle cranial fossa. The anterior part fuses to the CS. Venous blood from the SMCV drains into the CS. Venous blood from the SPS partially drains via the PBV into the EVFO.

found that a connection between the SPS and the EVFO, known as the PBV, can be demonstrated in 15% of patients on cerebral angiography. The PBV has been unnoticed for a long time, probably due to its small size and the fact that it overlays other veins such as the inferior temporal vein on biplane angiography. Furthermore, the PBV runs on the surface of the petrosal bone; therefore, it can be hidden by the petrosal bone in areas with hyperdensity on CT angiography unless careful attention is paid to it.

During embryologic development, the SPS and EVFO are formed through a complicated process.[8] In the early embryonic period, veins in the primitive brain initially drain by the primitive dural venous plexuses through the 3 anterior, middle, and posterior dural plexus stems into the primary head sinus. The primary head sinus also receives blood from the orbital and nasopharyngeal areas by the primitive maxillary vein and dorsal pharyngeal vein. According to the development of the brain, the anterior dural plexus stem disappears and the primary head sinus between the middle and the posterior dural plexus stem regresses due to enlargement of the trigeminal ganglion and otic vesicle; new dorsal drainage pathways develop through the transverse-sigmoid sinuses. The stem of the middle dural plexus becomes the prootic sinus. The remnant of the primary head sinus and prootic sinus forms the lateral part of the cavernous sinus and wing, the dorsal pharyngeal vein becomes the EVFO, and the emissary vein of the foramen Vesalius anastomoses with deep facial tributaries of the primitive maxillary vein.[8] The EVFO also drains the middle meningeal sinus. The posterior part of the SPS develops as a drainage route of the metencephalic vein, becoming the petrosal vein. The metencephalic vein joins the distal portion of the stem of the middle dural plexus. The primitive tentorial sinus (PTS) drains into the anastomotic dural plexus between the anterior and middle dural plexuses during the same period.

A few weeks later, a venous ring surrounding the trigeminal nerve develops, and it connects the distal portion and proximal portion of the prootic sinus (Fig 6*A*).[9] The anterior part of the middle dural plexus and inferior ramus of the peritrigeminal venous ring regresses and disappears due to further development of the trigeminal nerve and the otic vesicle. The remnant of the superior ramus of the venous ring and the residual posterior portion of the middle dural plexus stem form the primary SPS (Fig 6*B*). The PTS receives the superficial and deep telencephalic veins, and the ventral diencephalic vein (in the future, these become the SMCV and uncal vein) initially joins the anterior dural plexus stem and then drains into the transverse sinus after regression of the anterior dural plexus stem. The PTS deviates medially and stretches due to the development of the temporooccipital lobes (Fig 6*C*). Finally, it connects and fuses to the lateral portion of the primary cavernous sinus. The midportion of the PTS fuses with the primary SPS[1] and further evolves to constitute the final form of the cavernous sinus and the SPS (Fig 6*D*).

There are some variations in the termination of the SMCV due to the incomplete fusion of the PTS to the cavernous sinus and the SPS. Two types of the variations are well-known. One is the sphenobasal vein in which the SMCV drains into the EVFO and the pterygoid plexus through the foramen ovale. Another is the sphenopetrosal vein, which drains into the SPS or the transverse sinus.[3] Osborn[4] reported that a combination of the 2 major variations was occasionally observed on cerebral angiography, in which the vein drains into both the EVFO and the SPS or the transverse sinus (Fig 6*E*). In our study, all patients in whom the PBV was visualized on carotid angiography demonstrated termination of the SMCV into either the EVFO or SPS; this appears to confirm the concept that the PBV is formed by incomplete fusion of the midportion of the PTS to the SPS and the cavernous sinus (Fig 6*F*).

Regarding the clinical relevance of the PBV, the PBV itself functions as an accessory or a main drainage route from the cerebellum and brainstem via the SPS; it also composes a part of the termination of a variant of the SMCV from the cerebral hemisphere. Furthermore, it can potentially serve as a collateral pathway of the cerebellar and brainstem venous systems in patients with sinus occlusion of the SPS or the transverse-sigmoid sinus. When a dAVF is present, the SPS and adjacent venous sinuses can serve as a drainage pathway, as shown in Fig 3. Additionally, the PBV can potentially be used as a transvenous access route to the SPS via the pterygoid plexus. Furthermore, knowledge of the detailed vascular anatomy and variations of the middle cranial fossa, including the PBV, may be important for potentially gaining access to the undersurface of the temporal lobe and the trigeminal nerve to perform endovascular neuromodulation and stimulation in the diagnosis and future endovascular treatment of epilepsy and trigeminal neuralgia.[10-12]

Limitations

The PBV can be obscured by overlapping tributes on 2D angiography. We also reviewed 3D angiography, CT angiography, and 3D T1 contrast-enhanced MR images in addition to the 2D angiography when available. However, there were some cases evaluated by 2D angiography alone. We carefully reviewed angiographic images and eliminated the doubtful cases if possible. However, there is a potential risk of overdiagnosis of the PBV for such cases.

CONCLUSIONS

The PBV, an embryologic remnant of the PTS that is interposed between the SPS and EVFO, may occasionally be seen in the venous phase on carotid or vertebral angiography and may be considered a transvenous therapeutic access route in selected indications.

ACKNOWLEDGMENTS

We would like to thank Drs Hisaya Hiramatsu and Mika Kamiya for providing an interesting case.

Disclosure forms provided by the authors are available with the full text and PDF of this article at www.ajnr.org.

REFERENCES

1. Shimada R, Kiyosue H, Tanoue S, et al. **Superior petrosal sinus: hemodynamic features in normal and cavernous sinus dural arteriovenous fistulas.** *AJNR Am J Neuroradiol* 2013;34:609–15 CrossRef Medline

2. Matsushima K, Ribas ES, Kiyosue H, et al. **Absence of the superior petrosal veins and sinus: surgical considerations.** *Surg Neurol Int* 2015;6:34 CrossRef Medline
3. Tanoue S, Kiyosue H, Okahara M, et al. **Para-cavernous sinus venous structures: anatomic variations and pathologic conditions evaluated on fat-suppressed 3D fast gradient-echo MR images.** *AJNR Am J Neuroradiol* 2006;27:1083–89 Medline
4. Osborn AG. **Craniofacial venous plexuses: angiographic study.** *AJR Am J Roentgenol* 1981;136:139–43 CrossRef Medline
5. Leonel LC, de Sousa SD, Liberti EA. **Topographic and microscopic anatomical description of the emissary sinus of foramen ovale in adult humans.** *Clin Neurol Neurosurg* 2018;169:77–85 CrossRef Medline
6. Shapiro M, Raz E, Nossek E, et al. **Dural venous system: angiographic technique and correlation with ex vivo investigations.** *J Neurointerv Surg* 2021 Mar 16. [Epub ahead of print] CrossRef Medline
7. San Millán Ruíz D, Gailloud P, Yilmaz H, et al. **The petrosquamosal sinus in humans.** *J Anat* 2006;209:711–20 CrossRef Medline
8. Padget DH. **The development of cranial venous system in man from the view point of comparative anatomy.** *Contr Embryol* 1957;36:81–89
9. Butler H. **The development of certain human dural venous sinuses.** *J Anat* 1957;91:510–26 Medline
10. Rajah G, Saber H, Singh R, et al. **Endovascular delivery of leads and stentrodes and their applications to deep brain stimulation and neuromodulation: a review.** *Neurosurg Focus* 2018;45:E19 CrossRef Medline
11. Shaparin N, Gritsenko K, Garcia-Roves DF, et al. **Peripheral neuromodulation for the treatment of refractory trigeminal neuralgia.** *Pain Res Manag* 2015;20:63–66 CrossRef Medline
12. Dumot C, Sindou M. **Trigeminal neuralgia due to neurovascular conflicts from venous origin: an anatomical-surgical study (consecutive series of 124 operated cases).** *Acta Neurochir (Wien)* 2015;157:455–66 CrossRef Medline

Cerebral Veins: A New "New Frontier"

The article by Ide et al[1] in this issue of the *American Journal of Neuroradiology* has significant relevancy from both theoretic and practical perspectives.

The cerebral venous system develops through a series of complex stages, some that remain incompletely understood.[2] In the early embryo (5–8 mm), a continuous primitive venous plexus drains the brain through 3 stems (anterior, middle, and posterior). Around the 11- to 14-mm stage, lateral dural sinuses develop, which drain the brain through primitive pia-arachnoid vessels. By the 17- to 20-mm stage, posterior (sigmoid, tentorial, and marginal) sinuses are formed, while the 2 anterior components of the primitive venous plexus start to involute and form the prootic sinus (a stem of the middle dural plexus that connects to the posterior plexus via the sigmoid sinus). At the 40-mm stage, the cavernous sinuses form as medial extensions of the prootic sinus, which is continuous with the inferior petrosal sinus; laterally, the prootic sinus anastomoses with a primitive temporal emissary vein to form the petrosquamous sinus. By the 60- to 80-mm embryonic stage, while the posterior (sigmoid, transverse, tentorial) sinuses move backward to their permanent configuration, the otic capsule promotes the development of the superior petrosal sinus, while the prootic sinus remains continuous with the petrosquamous sinus. Laterally, the petrosquamous sinus and prootic sinus remnants are later destined to involute as diploic veins, which drain meningeal structures via the foramen ovale. Medially, the primitive tentorial sinus also involutes after the superior petrosal sinus has formed and is connected to the cavernous sinus. Variations may occur as a result of incomplete involution of those venous structures, lateral and medial.

Comparative anatomy among species reveals that major evolutionary variations exist in the cranial venous anatomy, especially in primates.[3] In primitive primates, cerebral venous drainage is mainly through the postglenoid emissary vein, which receives the cranio-orbital and petrosquamous sinuses in a configuration that is recognized as the orbitotemporal venous sinuses. In higher primates and humans, while the orbitotemporal sinuses persist as the middle meningeal venous network, the petrosquamous sinus generally involutes or becomes intradiploic. Remnants of the orbitotemporal sinuses are occasionally encountered in the form of a persistent petrosquamous sinus,[4] a venous sinus of Kelch,[5] which runs through the superior orbital fissure and connects the superior ophthalmic and middle meningeal veins to the transverse sinus, or a sinus of Hyrtl,[6] which connects the sphenoparietal sinus to middle meningeal veins in the foramen spinosum.

Therefore, the article by Ide et al[1] sheds new light on the embryology of the human cerebral venous system with the description of what likely represents a previously unrecognized remnant of orbitotemporal connections of the primitive prootic sinus.

Indeed, an important contribution to our understanding of human cerebrovascular embryology, this work has also considerable practical implications. Proper knowledge of venous anatomic variations may minimize misdiagnoses of vascular lesions and, more important, may help prevent surgical complications of hemorrhage, thrombosis, or venous infarction.

Similarly, the spread of infections from the middle ear to the intracranial venous system has been reported to only occur with the presence of an abnormal petrosquamous sinus.[4] The same would be expected with periorbital infections and the rare persistent sinuses of Kelch of Hyrtl. Recognition of such predisposing pathways of intracranial spread of disease may prompt earlier, more aggressive treatment.

It has been suggested by Miyachi et al[7] that emissary veins contribute to the pathophysiology of dural arteriovenous fistulas (DAVFs). Emissary veins, along with their companion emissary arteries within skull base or transdiploic foramina, may be exposed to inflammation (from adjacent infection or trauma), which may lead to angiogenic stimuli and the opening of physiologic postcapillary arteriovenous shunting, all resulting in dural sinus or cortical vein DAVFs. The emissary vein of the foramen ovale may, therefore, have a role in triggering cavernous sinus fistulas, and the petrobasal vein described in the article may further promote the extension of arteriovenous shunting to the superior petrosal sinus and possibly the tentorium (which does not receive emissary veins).

Endovascular therapy has become the preferred treatment option for DAVFs, having virtually replaced surgery or radiosurgery in most specialized centers. The transvenous approach to embolization is becoming increasingly favored over the transarterial approach, which is associated with a higher incidence of complications of cerebral ischemia or cranial neuropathy. Increasingly, more precise knowledge of the cerebral venous anatomy allows treating more complex lesions, including with the use of open surgical access when needed.[8]

Similarly, transvenous endovascular therapy of brain AVMs is increasingly used and is increasingly successful as definitive therapy in skilled hands, with expected improvements in technique and extension in indications.[9]

Another practical area to benefit from sound anatomic understanding of cerebral venous anatomy is the field of neuromodulation, which is expected to take off in major ways. Decades of experience with implantable cardiac electronic devices (cardiac defibrillators and permanent pacemakers) have definitely established the safety of intravenous wiring. More recently, technologic advances in signal transmission through increasingly miniaturized transvenous devices have opened the path to intracranial neuromodulation, considering the immediate proximity of eloquent brain regions to various venous structures. Applications of neuromodulation that are currently well underway include epilepsy monitoring, neurostimulation in various indications (including epilepsy), motor control of exoskeletons and robotic limbs in paralyzed patients, and the enabling of speech paradigms on the basis of text or even thought in patients after a stroke.[10] In the same "vein," transvenous catheter-based ablation for epilepsy is predicted to allow treating epilepsy in "the same way as cardiac disturbances."[11]

A novel treatment for communicating hydrocephalus currently under prospective multicenter evaluation involves the transvenous implantation of a miniaturized 1-way valve allowing CSF to drain directly from the cerebellopontine angle cistern into the jugular vein. This device (eShunt System; CereVasc), or some improved version of it, is expected to obviate the need for extensive surgical placement of ventriculoperitoneal shunts in many patients.[12,13]

The cerebral venous system may be currently considered the "new frontier" in neuroscience therapeutics with the convergence of major advances in technology, vascular access, and our increased understanding of the anatomy. In that regard, the article by Ide et al[1] is also a useful contribution.

REFERENCES

1. Ide S, Kiyosue H, Shamada R, et al. **Petrobasal vein: a previously unrecognized vein directly connecting the superior petrosal sinus to the emissary vein of the foramen ovale.** *AJNR Am J Neuroradiol* 2022;43:70–77 CrossRef
2. Padget DH. **The cranial venous system in man in reference to development, adult configuration, and relation to the arteries.** *Am J Anat* 1956;98:307–55 CrossRef Medline
3. Diamond MK. **Homology and evolution of the orbitotemporal venous sinuses of humans.** *Am J Phys Anthropol* 1992;88:211–44 CrossRef Medline
4. An YH, Wee JH, Han KH, et al. **Two cases of petrosquamosal sinus in the temporal bone presented as perioperative finding.** *Laryngoscope* 2011;121:381–84 CrossRef Medline
5. Couldwell M, Aysenne A, Iwanaga J, et al. **Bilateral venous sinuses of Kelch.** *Anat Cell Biol* 2021;54:395–98 CrossRef Medline
6. Tubbs RS, Loukas M, Shoja MM, et al. **Accessory venous sinus of Hyrtl.** *Folia Morphol (Warsz)* 2007;66:198–99 Medline
7. Miyachi S, Izumi T, Matsubara N, et al. **Mechanism of the formation of dural arteriovenous fistula: the role of the emissary vein.** *Interv Neuroradiol* 2011;17:195–202 CrossRef Medline
8. Bhatia KD, Lee H, Kortman H, et al. **Endovascular management of intracranial dural AVFs: transvenous approach.** *AJNR Am J Neuroradiol* 2021 Oct 14. [Epub ahead of print] CrossRef Medline
9. Mosimann PJ, Chapot R. **Contemporary endovascular techniques for the curative treatment of cerebral arteriovenous malformations and review of neurointerventional outcomes.** *J Neurosurg Sci* 2018;62:505–13 CrossRef Medline
10. Raza SA, Opie NL, Morokoff A, et al. **Endovascular neuromodulation: safety profile and future directions.** *Front Neurol* 2020;11:351 CrossRef Medline
11. Thoma C. **Epilepsy: novel transvenous catheter mapping and ablation could supersede invasive antiepileptic surgery.** *Nat Rev Neurol* 2014;10:306 CrossRef Medline
12. Heilman CB, Basil GW, Beneduce BM, et al. **Anatomical characterization of the inferior petrosal sinus and adjacent cerebellopontine angle cistern for development of an endovascular transdural cerebrospinal fluid shunt.** *J Neurointerv Surg* 2019;11:598–602 CrossRef Medline
13. **First patient treated in eShunt clinical trial.** In: *Proceedings of the Barts Research and Advanced Interventional Neuroradiology Brain Conference,* London, UK. December 13–16, 2021

L. Hacein-Bey
University of California Davis Medical School
Sacramento, California

http://dx.doi.org/10.3174/ajnr.A7359

Transcranial Doppler Velocities and Angiographic Vasospasm after SAH: A Diagnostic Accuracy Study

T.E. Darsaut, M.B. Keough, A.M. Chan, B. Farzin, J.M. Findlay, M.M. Chow, M. Chagnon, J. Zehr, G. Gevry, and J. Raymond

ABSTRACT

BACKGROUND AND PURPOSE: After aneurysmal SAH, transcranial Doppler is commonly used to monitor cerebral vasospasm. The diagnostic accuracy of transcranial Doppler flow velocity values in detecting angiographic vasospasm in patients requiring urgent endovascular intervention has not been established.

MATERIALS AND METHODS: We performed a retrospective analysis of a consecutive series of patients with aneurysmal SAH who underwent transcranial Doppler (index test) within 24 hours of conventional angiography (reference test). The judgment of 33%, 50%, and 66% degree of vessel narrowing on angiography was independently established by multiple neuroendovascular clinicians. Vessel-specific per-segment and per-patient transcranial Doppler velocities were studied using receiver operating characteristic curves, the Youden index, and minimal acceptable sensitivity models. Optimal mean flow-velocity thresholds were explored to calculate sensitivity and specificity using a per-patient judgment of vasospasm of at least 50% angiographic narrowing in any large arterial segment except A1.

RESULTS: In 221 patients, vasospasm was found in 15%, 8%, and 4% of arteries when the degree of reference angiographic luminal narrowing was 33%, 50%, and 66%, respectively. Mean flow velocities were significantly higher in vasospastic segments ($P = .001$), but per-segment exploratory analyses yielded unsound mean flow velocity thresholds. The Youden and minimal acceptable sensitivity models proposed mean flow velocity thresholds of approximately 160 cm/s for the anterior circulation and 80 cm/s for the posterior circulation in the per-patient diagnosis of angiographic vasospasm (≥50%), yielding a sensitivity of 80%–90% (95% CI, 0.77–0.96), but with a corresponding specificity of 50% (95% CI, 0.40–0.56).

CONCLUSIONS: In this study, a threshold transcranial Doppler mean flow-velocity value that would accurately diagnose ≥50% angiographic vasospasm remained elusive.

ABBREVIATIONS: MFV = mean flow velocity; ROC = receiver operating characteristic; TCD = transcranial Doppler

The use of transcranial Doppler (TCD) ultrasonography in the detection and management of patients at risk of vasospasm after intracranial aneurysm rupture has been studied by many groups since its introduction in 1982.[1-11] The appeal of this noninvasive test is that unlike conventional angiography, it can be performed daily at the bedside in the intensive care unit, alerting clinicians that medical or endovascular interventions may be indicated to prevent delayed cerebral infarction. The use of TCD monitoring has been recommended by expert societies.[12,13] The diagnostic accuracy of TCD in the diagnosis of vasospasm is important to verify because false-negative studies could result in vasospasm-related infarctions only found on CT when it is too late to intervene, and false-positives could lead to inappropriate interventions, including unnecessary premature or repeat catheter angiographies or even unnecessary angioplasty. Yet the diagnostic accuracy of TCD remains uncertain despite multiple previous studies, including 2 meta-analyses.[5,14]

There are a number of fundamental problems that became evident as the literature was reviewed. These problems have remained unsolved since the very early days of vasospasm research and include the following: 1) Although some boundaries are commonly mentioned, such as <120 (absent vasospasm)

Received June 29, 2021; accepted after revision September 14.

From the Division of Neurosurgery (T.E.D., M.B.K., A.M.C., J.M.F., M.M.C.), Department of Surgery, University of Alberta Hospital, Mackenzie Health Sciences Centre, Edmonton, Alberta, Canada; Department of Radiology (B.F., G.G., J.R.), Centre Hospitalier de l'Université de Montréal, Montreal, Quebec, Canada; and Department of Mathematics and Statistics (M.C., J.Z.), Pavillon André-Aisenstadt, Montreal, Quebec, Canada.

Please address correspondence to Jean Raymond, MD, Department of Radiology, Centre Hospitalier de l'Université de Montréal (CHUM), 1000 St-Denis St, Room D03.5462B, Montreal, Quebec, Canada H2X 0C1; e-mail: jean.raymond@Umontreal.ca

Indicates article with online supplemental data.

http://dx.doi.org/10.3174/ajnr.A7347

and >200 cm/s as indicative of severe vasospasm, no mean flow velocity (MFV) threshold value has been shown to accurately diagnose clinically significant angiographic vasospasm with a sensitivity and specificity at the arterial segment level; 2) there is no accepted definition of the degree of vessel narrowing sufficient to be considered a clinically significant angiographic vasospasm; and 3) there is no recognized method to assign a vasospasm score at the individual patient level. Other problems with previous studies include the following: limiting the analyses of performance to a particular arterial segment (often M1), failing to verify the reliability of the angiographic gold standard,[15,16] failing to clearly define the intended role of the index test, and unclear methodology.[14] The most important problem is that many reports used an angiographic threshold that was too low to define vasospasm (33% or 25% luminal diameter reduction). While the degree of luminal diameter reduction necessary for clinically relevant restrictions in blood flow is not known with certainty, it is at least 50%.[17,18] Previous studies have commonly tried to determine the sensitivity and specificity of TCD in detecting any degree of angiographic vasospasm, even though some degree of vasospasm is almost always found after substantial subarachnoid bleeding.[19] Such studies may have designated many patients with clinically irrelevant angiographic vasospasm as true-positives. A more pertinent role of TCD would be the identification of patients who may need urgent medical or endovascular intervention to reverse vasospasm or prevent infarction.

At our institution (University of Alberta Hospital), TCD is routinely used to monitor all patients with SAH during the vasospasm risk period (days 3–12 post-SAH). Furthermore, conventional angiography is also routinely performed 5–9 days after aneurysm treatment to confirm aneurysm occlusion and assess the presence of vasospasm. All patients are included in a prospective database. These data, covering 10 years of clinical practice, give us the opportunity to study anew the accuracy of TCD velocity measurement, this time not for the diagnosis of any degree of vasospasm but more specifically to detect patients who may require timely conventional angiography and possibly endovascular intervention.[20]

The main objective of this work was to study the diagnostic accuracy of various TCD flow-velocity values in the diagnosis of ≥50% angiographic vasospasm severe enough to consider conventional angiography and endovascular treatment when confirmed.

MATERIALS AND METHODS

Literature Review

The full-text English- and French-language articles included in the initial and updated meta-analyses of 2001[5] and 2018[14] on diagnostic accuracy of TCD were examined independently by 2 authors (A.M.C. and T.E.D.), and the reported degree of vessel narrowing used in each source article was extracted.

Diagnostic Accuracy Study

Institutional ethics approval was obtained for this study (Pro0080185). This work is reported according to the Standards for Reporting of Diagnostic Accuracy Studies.[21]

We attempted to address some of the shortcomings of previous studies by detailing the methodology we used, by clarifying the purported role of the index test (to detect vasospasm severe enough to justify angiography and endovascular rescue), by exploring 3 degrees of severity of vasospasm, by verifying the reliability of the reference test, by including all arterial segments (except A1) in the analysis, and by providing a definition of "vasospasm" at the individual patient level.

Patients

This retrospective study included consecutive adult (≥18 years of age) patients with nontraumatic SAH hospitalized at the University of Alberta Hospital from January 2007 to December 2017. Patients with SAH are monitored by TCD during the vasospasm risk period (days 3–12), and conventional angiography is routinely performed 5–9 days after aneurysm treatment. Conventional angiography may have been repeated in response to a concerning increase in TCD velocities or in the event of a new neurologic deficit. For the purpose of this study, each patient was represented by a single TCD-angiography pair of examinations: Patients were included when TCD MFV values were acquired on the same day as conventional angiography. Patients were excluded when the angiographic study did not include the left and right ICAs and at least 1 vertebral artery injection (see the flow chart, Fig 1). We did not record how patients were treated medically or study the effects of treatment on TCD velocities or angiographic determinations.

Transcranial Doppler (Index Test)

TCD readings (MFVs) were obtained daily or every other day starting on post-SAH day 3 and continuing until day 12 by the same dedicated sonographer (14 years of TCD experience at the beginning of this study interval) using a PMD 100 or 150 TCD system (Spencer Technologies) from 2007 to 2012, and a ST3 system (Spencer Technologies) from 2013 to 2017. Cases were not excluded when only 1 or 2 vessel segments could not be insonated ($n = 25$). One MFV value was acquired per vessel segment (ICA, M1, A1, and basilar artery), with results reviewed by a vascular neurologist and recorded in a prospectively maintained case log.

Angiographic Vasospasm (Reference Test)

Severe vasospasm was defined as ≥50% reduction in the diameter of the proximal intracranial arteries, as adjudicated by at least 14/17 (80%) interventionists independently rating catheter angiograms without knowledge of the TCD values. In a consensus session, 2 senior authors (T.E.D. and J.R.) reviewed the additionally identified cases of severe vasospasm as the number of raters agreeing on a verdict was lowered 1 reader at a time from 17/17 to 11/17 (65% of raters), while remaining blinded to TCD values. The result of this consensus session was that 14/17 readers provided the optimal collection of cases, and it was determined that only those cases would be considered correctly flagged by the triage TCD test. The reliability of the gold standard angiographic diagnosis of severe vasospasm in the same series of patients has previously been reported.[15] Briefly, for each patient, clinicians were provided with anterior-posterior projections for 3 injections (right ICA, left ICA, and vertebral artery) and asked to visually judge the degree of vessel narrowing for each arterial segment at the level of the supraclinoid ICA, M1, A1, and basilar artery (7 arterial segments). The thresholds were as follows: none/mild vasospasm:

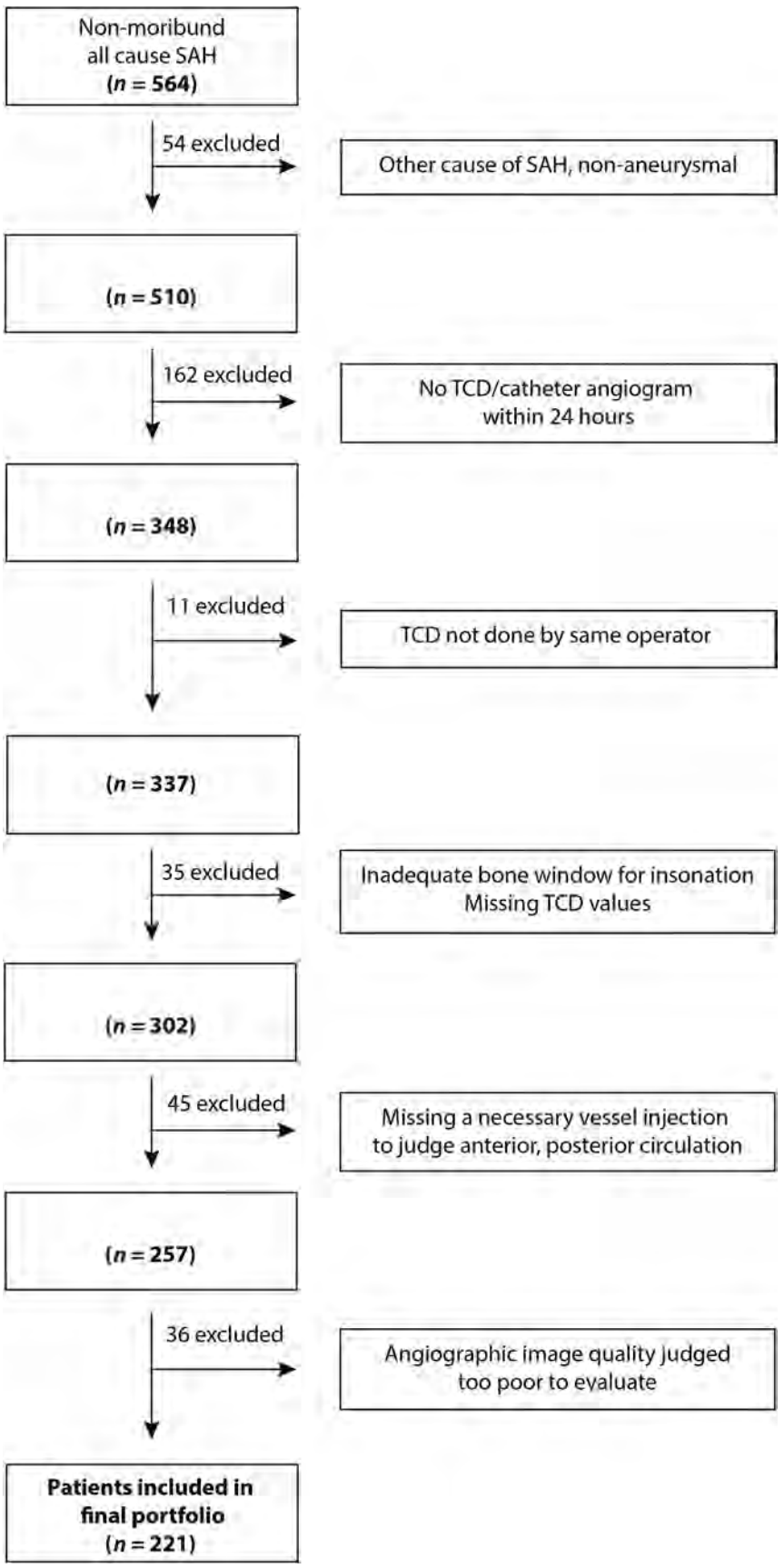

FIG 1. Flow chart of patients included in the diagnostic accuracy study.

<33% vessel narrowing; moderate vasospasm: 33%–50% vessel narrowing; severe vasospasm: >50% vessel narrowing, according to a modified scheme used at our institution.[8] Raters were not provided with any clinical information concerning the case and were blinded to the scores given by other participants. Severe vasospasm was predefined as a 50% reduction in luminal diameter, but the effects of reducing this threshold to 33% were also examined. The scores provided were based on simple visual inspection of the degree of luminal narrowing. Four clinicians were also asked to evaluate the same permuted portfolio using a 66% vessel narrowing threshold. This time 66% severe vasospasm was adjudicated when 3 of 4 raters independently agreed.[15]

Definition of TCD MFV Thresholds

MFV thresholds were studied in 3 different ways: 1) by performing receiver operating characteristic (ROC) curves and exploring the velocities corresponding to the Youden index (maximizing sensitivity and specificity); 2) by examining the sensitivity and specificity of fixed-threshold MFV values (110, 120, 130, 140, 150, 160 cm/s); and 3) by exploring the threshold velocities corresponding to a minimal sensitivity of 80%, 85%, 90%, and 95% in diagnosing 50% angiographic vasospasm.

Per-Arterial Segment and Per-Patient Analyses

The distribution and diagnostic accuracy of TCD MFV values were first studied at the level of arterial segments (each patient contributed 7 arterial segments) using means and ROC curves.

A per-patient diagnosis of vasospasm was then defined when any 1 segment (or more) excluding A1 was adjudicated at a 50% degree of narrowing. Here, TCD was conceived as a "triage test" to detect patients who might benefit from conventional angiography and endovascular interventions: A true-positive TCD verdict was then adjudicated at the patient level when any segment (except A1) reached a certain velocity, even if that velocity concerned a different segment than the one judged

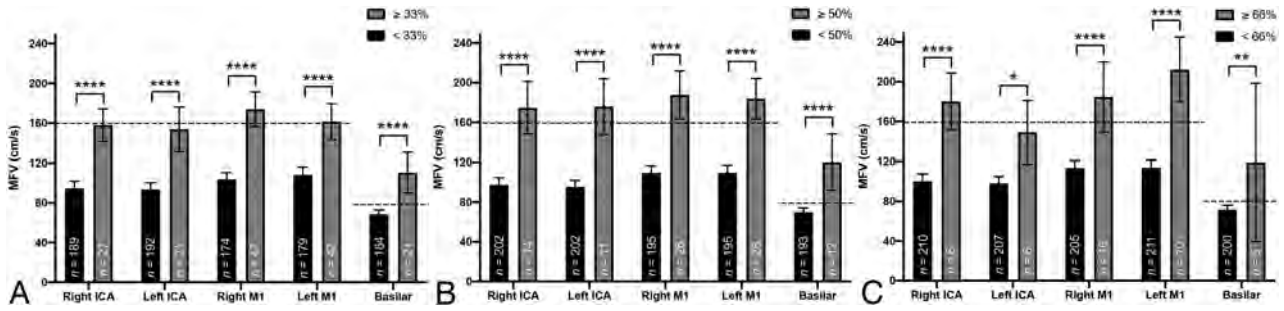

FIG 2. Mean flow velocities for patients with and without vasospasm, defined as 33% (*A*), 50% (*B*), and 66% (*C*) vessel narrowing. MFV thresholds for anterior and posterior circulation vessels are shown (*dashed lines*). Note that for all individual arterial segments, MFVs were significantly higher for spastic vessels. Four asterisks indicate $P < .0001$; 2 asterisks, $P < .01$; 1 asterisk, $P < .05$. Error bars represent 95% confidence intervals.

to be 50% narrowed by angiography. A true-negative TCD verdict was adjudicated when no segment reached that velocity and no segment on angiography was perceived to have <50% narrowing in diameter. Analyses were repeated using 2 other angiographic thresholds (33% and 66%).

Statistical Analysis

All analyses were performed by statisticians (M.C., J.Z.) using STATA, Version 16.0 (StataCorp) and SPSS, Version 26 (IBM) with a significance level set at .05.

This study used all patients who fit the selection criteria without formally calculating the sample size necessary to test a prespecified hypothesis. Mean TCD velocities for each segment in nonsevere and severe vasospasm at the 3 different thresholds were compared using the Student *t* test. For each of the 7 segments, ROC curves were generated and the MFV at which sensitivity and specificity were optimized using the Youden index was determined. Corresponding sensitivities and specificities with 95% CIs were reported. We constructed Gaussian curves for patients with and without vasospasm at each of the 3 thresholds for visual comparison of the overlap of the curves, looking for fixed sensitivity values of 80%, 85%, 90%, and 95%. To evaluate the diagnostic accuracy of various TCD flow-velocity values, we selected 4 predefined levels of sensitivity (80%, 85%, 90%, and 95%). ROC curves were generated to define threshold MFVs for the diagnosis of severe vasospasm for each of the anterior circulation (bilateral ICA and M1 segments) and posterior circulation (basilar segment) arteries. The corresponding specificities were then determined. Actual sensitivities and specificities with 95% CIs are reported. Per-patient determinations (yes/no) of a correct TCD judgment of severe vasospasm was considered when these MFV thresholds of either the anterior or posterior circulation were exceeded.

RESULTS

Literature Review

The meta-analyses on the diagnostic accuracy of TCD identified 36 source articles published between 1984 and 2013.[5,14] Two articles in Japanese were excluded, leaving 34 English- or French-language reports for full-text analysis (Online Supplemental Data). Thirty-one of the 34 (91%) articles included in the systematic reviews were diagnostic accuracy studies that compared the TCD index test with a reference test. Twenty-four of 31 (77%) diagnostic accuracy studies reported on anterior circulation velocities only, while 2 (6%) focused exclusively on posterior circulation vasospasm, with 5 (16%) reporting both.

The percentage of luminal narrowing on conventional angiography used as the reference test was ≥50% in 8/31 or 26% of articles [no threshold: 13 articles (42%); 20%–25% luminal narrowing: 8 articles (26%); 30%–33%: 2 articles (6%); 50%: 7 articles (23%); 75%: 1 article (3%)]. Reported MFV thresholds to diagnose vasospasm in the anterior circulation ranged from 90 to 180 cm/s and 60 to 95 cm/s for the posterior circulation. There were no reports regarding a per-patient judgment of vasospasm using a luminal narrowing threshold of at least 50%.

Diagnostic Accuracy Study

The flow chart of patients included in the diagnostic accuracy study is shown in Fig 1, and the characteristics of the 221 patients with SAH are available in the Online Supplemental Data.

Per-Segment Analyses

We first compared the MFVs of arterial segments with or without angiographic vasospasm, defined according to 33%, 50%, and 66% narrowing thresholds (Fig 2).

The proportion of arterial segments judged to be vasospastic decreased with increasing angiographic thresholds (15%, 8%, and 4% of segments for >33%, 50%, and 66% vessel narrowing, respectively). The MFVs of vasospastic segments were significantly higher for all segments ($P = .001$). MFVs of basilar segments were significantly lower than those of anterior circulation arterial segments ($P = .001$).

The ROC curves of the TCD MFV values in the diagnosis of 50% vasospasm for each arterial segment (without prespecifying a threshold velocity) are available in the Online Supplemental Data. The areas under the curve and the MFVs corresponding to the Youden index (which optimizes sensitivity and specificity) are summarized in Table 1.

This data-dependent method of exploring optimal velocities to diagnose angiographic vasospasm provided clinically unsound results (ie, widely discrepant threshold velocity values for the right and left ICAs [154 and 109 cm/s], and also for right and left M1 segments [157–124 cm/s]), whereas similar results would be expected.

Per-Patient Analyses

We then examined ROC curves and the sensitivity and specificity of various predefined threshold velocity values (when

Table 1: Per-arterial segment TCD MFVs corresponding to Youden index optimizing sensitivity and specificity in detecting 50% vasospasm

	MFV Threshold (cm/s)	Sensitivity (95% CI)	Specificity (95% CI)	AUC (95%CI)
Right ICA	154	0.86 (0.56–0.98)	0.86 (0.81–0.90)	0.88 (0.81–0.95)
Left ICA	109	1.0 (0.68–1.0)	0.69 (0.63–0.76)	0.90 (0.84–0.96)
Right M1	157	0.73 (0.56–0.90)	0.82 (0.76–0.87)	0.84 (0.75–0.92)
Left M1	124	0.92 (0.73–0.99)	0.65 (0.58–0.72)	0.85 (0.78–0.91)
Basilar artery	98	0.75 (0.51–0.81)	0.81 (0.76–0.87)	0.84 (0.73–0.95)

Note:—AUC indicates area under the curve.

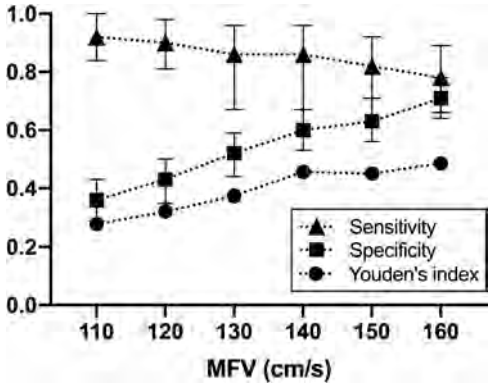

FIG 3. Sensitivity, specificity, and the Youden number at various possible mean flow velocity cutoffs for anterior circulation arterial segments. This data-driven method of analysis shows that the best MFV cutoff is close to 160 cm/s. Data for posterior circulation segments are not shown.

reached in any anterior circulation segment in the same patient) in the diagnosis of severe vasospasm at the patient level (defined as 50% narrowing in any segment). Figure 3 shows that low-velocity thresholds are sensitive but poorly specific; when velocities reach 160 cm/s (the velocities with the highest Youden number), the specificity reaches 70%, but sensitivity decreases below 80%.

The distributions of the maximal velocity found in any segment of the anterior circulation in patients categorized with or without vasospasm (any segment) according to the 3 angiographic thresholds are shown in Fig 4, along with corresponding ROC curves and areas under the curve (results for basilar segments are not shown). The overlap between patients with and without vasospasm increases with sensitivity. Optimal velocities corresponding to a minimal sensitivity of 80% (along with the corresponding specificity and 95% confidence intervals) are summarized in Table 2. Optimal MFV threshold values for a minimal sensitivity of 80% in the diagnosis of 50% angiographic vasospasm were 164 cm/s (anterior circulation segments) and 80 cm/s (basilar artery). Yet, the specificity remained low (56%–71%).

DISCUSSION

This study shows that high MFVs are closely associated with severe angiographic vasospasm. Nevertheless, TCD MFVs did not perform well when tested at the individual patient level to triage patients who showed angiographic vasospasm that might require urgent treatment: Using relatively high-threshold MFV values (such as 160 cm/s) would still unnecessarily send patients for cerebral angiography 50% of the time yet would still risk missing 10%–20% of patients with vasospasm (≥50%) sufficient enough to be at risk of cerebral infarction.

Our results differ from those of many of the studies collected in the most recent systematic review (2018), which showed TCD to be specific (90%) but not sensitive (67%).[14]

However, many of the included studies examined the performance of TCD when TCD played a different role; most used low MFV values (in the range of 120 cm/s) to identify patients with much lower gold standard angiographic thresholds for the diagnosis of vasospasm (≤25% narrowing). As revealed by the reported expected prevalence of 70% of vasospasm, these studies were designed to assess the accuracy of TCD in diagnosing any degree of vasospasm, no matter the clinical relevance.[14] We are unsure of the added value of a diagnostic test that identifies any degree of vasospasm in patients with a high pretest probability of any vasospasm (70%). The more important role for TCD in this context should rather be to accurately identify patients who could eventually be rescued with induced hypertension or endovascular treatment. Unfortunately, the clinical benefit of medical or endovascular interventions has not been rigorously verified.[22,23]

One fundamental problem is that angiographic vasospasm itself is not a well-defined disease. It is rather a test finding that is vaguely associated with delayed cerebral ischemia, but the relationship between angiographic vasospasm and clinical outcomes is uncertain. Furthermore, there is no well-accepted definition of angiographic vasospasm at the arterial segment or per-patient level, and the reliability and clinical significance of the gold standard itself is, at best, questionable.[15,16] In such circumstances, the diagnostic accuracy methodology we have used may not be the best way to assess the value of TCD monitoring in the prevention of delayed cerebral ischemia.[24] With so much uncertainty at so many levels, we need to seek a scientific way to make progress.

The problem may call for an entirely different approach regarding how diagnoses are determined. Other medical specialties confronted with uncertain threshold values have recently addressed decades-old diagnostic controversies using pragmatic trial methodology.[25] We believe progress in this field would also be possible by designing randomized trials that test the value of TCD monitoring, angiography, and endovascular intervention in the prevention of delayed cerebral ischemia after SAH.

This study has several limitations. The patients and the TCD values were prospectively collected, but angiograms were retrospectively analyzed for the purpose of this study. TCD was performed by a single expert technician (patients

examined by other technicians or neurologists were excluded). While TCD is used to monitor patients during a period at risk of vasospasm, for each patient a single examination was retained for comparison with the same-day angiogram. We did not examine various other TCD indices (such as Lindegaard ratios[26]) nor attempt to identify patients with rising MFVs across time, which could have led to different results.[8] We also did not examine the effects of diagnoses on patient outcomes.

This study assessed a snapshot comparison of TCD values and an angiographic verdict within 24 hours; it does not consider the way TCD results of each patient were judged in real-time or how they were used for clinical decisions and subsequent management.

In this analysis, we considered TCD a triage test to identify whether individual patients should undergo angiography. The gold standard angiographic criterion itself was previously shown to be poorly repeatable, and we had to arbitrarily fix a threshold (14/17 raters) to provide a final verdict necessary to proceed with a diagnostic-accuracy study.[15] We chose to call true-positive per-patient TCD verdicts whenever the TCD threshold was exceeded in any segment in the same patient—even if it was not the correct segment found narrowed on catheter angiography. This evaluation of the diagnostic accuracy of TCD could be considered too generous. Finally, the methods we used to explore the threshold velocities that would maximize sensitivity and specificity are known to overestimate the diagnostic accuracy of the index test.[21]

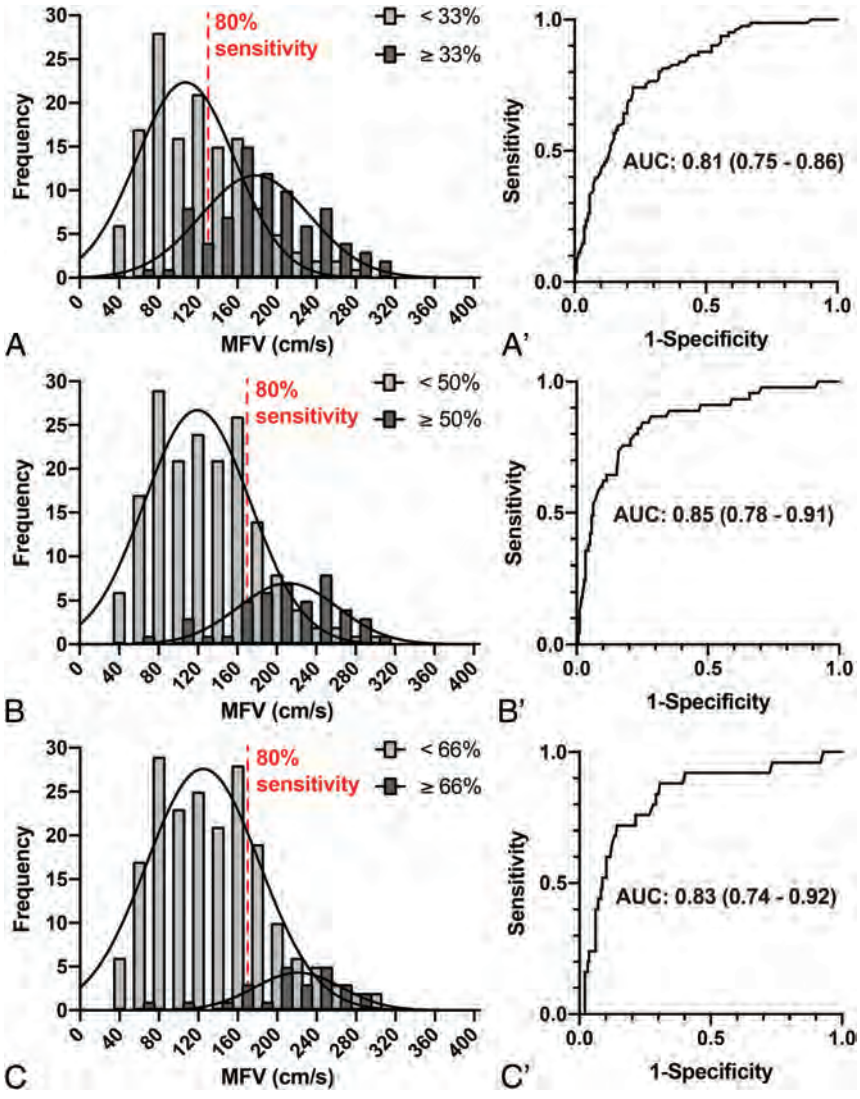

FIG 4. Per-patient analysis of the diagnostic accuracy of TCD. Distributions of the maximal mean flow velocity found in any segment of the anterior circulation with or without vasospasm according to thresholds of 33% (*A*), 50% (*B*), and C) 66%. The 80% sensitivity line is labeled. Corresponding ROC curves are presented in A', B', and C'. Note the large amount of overlap of the curves despite acceptable areas under the curve (AUCs).

CONCLUSIONS

There is a general correlation between blood flow velocity increases and angiographic vasospasm. Thus, TCD findings can alert clinicians to the possibility of vasospasm and to the need for careful patient assessment and examination for the development of neurologic findings. However, a threshold MFV value that can accurately distinguish patients with or without ≥50% angiographic narrowing remains elusive.

Disclosure forms provided by the authors are available with the full text and PDF of this article at www.ajnr.org.

Table 2: Per-patient TCD MFV thresholds for various minimal sensitivities in detecting 50% vasospasm

	Predefined MFV Threshold (cm/s)[a]			
Minimum Sensitivity	ICA or M1	Basilar Artery	Sensitivity (95% CI)	Specificity (95% CI)
80%	>164	>80	0.86 (0.72–0.94)	0.64 (0.56–0.71)
85%	>160	>61	0.90 (0.77–0.96)	0.48 (0.40–0.56)
90%	>126	>60	0.94 (0.82–0.98)	0.37 (0.30–0.45)
95%	>95	>56	0.96 (0.85–0.99)	0.24 (0.18–0.31)

[a] Severe vasospasm was determined when 1 threshold was exceeded.

REFERENCES

1. Aaslid R, Markwalder TM, Nornes H. **Noninvasive transcranial Doppler ultrasound recording of flow velocity in basal cerebral arteries.** *J Neurosurg* 1982;57:769–74 CrossRef Medline
2. Gonzalez NR, Boscardin WJ, Glenn T, et al. **Vasospasm probability index: a combination of transcranial Doppler velocities, cerebral blood flow, and clinical risk factors to predict cerebral vasospasm after aneurysmal subarachnoid hemorrhage.** *J Neurosurg* 2007;107:1101–12 CrossRef Medline
3. Krejza J, Kochanowicz J, Mariak Z, et al. **Middle cerebral artery spasm after subarachnoid hemorrhage: detection with transcranial color-coded duplex US.** *Radiology* 2005;236:621–29 CrossRef Medline
4. Lindegaard KF, Nornes H, Bakke SJ, et al. **Cerebral vasospasm after subarachnoid haemorrhage investigated by means of transcranial Doppler ultrasound.** *Acta Neurochir Suppl (Wien)* 1988;42:81–84 Medline
5. Lysakowski C, Walder B, Costanza MC, et al. **Transcranial Doppler versus angiography in patients with vasospasm due to a ruptured cerebral aneurysm: a systematic review.** *Stroke* 2001;32:2292–98 CrossRef Medline
6. Okada Y, Shima T, Nishida M, et al. **Comparison of transcranial Doppler investigation of aneurysmal vasospasm with digital subtraction angiographic and clinical findings.** *Neurosurg* 1999;45:443–49; discussion 449–50 CrossRef Medline
7. Proust F, Hannequin D, Langlois O, et al. **Causes of morbidity and mortality after ruptured aneurysm surgery in a series of 230 patients: the importance of control angiography.** *Stroke* 1995;26:1553–57 CrossRef Medline
8. Vora YY, Suarez-Almazor M, Steinke DE, et al. **Role of transcranial Doppler monitoring in the diagnosis of cerebral vasospasm after subarachnoid hemorrhage.** *Neurosurg* 1999;44:1237–47; discussion 1247–38 CrossRef Medline
9. Wardlaw JM, Offin R, Teasdale GM, et al. **Is routine transcranial Doppler ultrasound monitoring useful in the management of subarachnoid hemorrhage?** *J Neurosurg* 1998;88:272–76 CrossRef Medline
10. Weir B, Grace M, Hansen J, et al. **Time course of vasospasm in man.** *J Neurosurg* 1978;48:173–78 CrossRef Medline
11. Sebastian J, Derksen C, Khan K, et al. **Derivation of transcranial Doppler criteria for angiographically proven middle cerebral artery vasospasm after aneurysmal subarachnoid hemorrhage.** *J Neuroimaging* 2013;23:489–94 CrossRef Medline
12. Diringer MN, Bleck TP, Hemphill JC 3rd, et al; Neurocritical Care Society. **Critical care management of patients following aneurysmal subarachnoid hemorrhage: recommendations from the Neurocritical Care Society's Multidisciplinary Consensus Conference.** *Neurocrit Care* 2011;15:211–40 CrossRef Medline
13. Edmonds HL Jr, Isley MR, Sloan TB, et al. **American Society of Neurophysiologic Monitoring and American Society of Neuroimaging joint guidelines for transcranial Doppler ultrasonic monitoring.** *J Neuroimaging* 2011;21:177–83 CrossRef Medline
14. Mastantuono JM, Combescure C, Elia N, et al. **Transcranial Doppler in the diagnosis of cerebral vasospasm: an updated meta-analysis.** *Crit Care Med* 2018;46:1665–72 CrossRef Medline
15. Darsaut TE, Derksen C, Farzin B, et al. **Reliability of the diagnosis of cerebral vasospasm using catheter cerebral angiography: a systematic review and inter- and intraobserver study.** *AJNR Am J Neuroradiol* 2021;42:501–07 CrossRef Medline
16. Letourneau-Guillon L, Farzin B, Darsaut TE, et al. **Reliability of CT angiography in cerebral vasospasm: a systematic review of the literature and an inter- and intraobserver study.** *AJNR Am J Neuroradiol* 2020;41:612–18 CrossRef Medline
17. Weir B. **Vasospasm: does it cause infarction and poor outcome?** *J Neurosurg* 2020;134:1006–11 CrossRef Medline
18. Young DF. **Fluid mechanics of arterial stenoses.** *J Biomech Eng* 1979;101:157–75 CrossRef
19. Dorsch NW, King MT. **A review of cerebral vasospasm in aneurysmal subarachnoid haemorrhage, Part I: incidence and effects.** *J Clin Neurosci* 1994;1:19–26 CrossRef Medline
20. Rosenwasser RH, Armonda RA, Thomas JE, et al. **Therapeutic modalities for the management of cerebral vasospasm: timing of endovascular options.** *Neurosurg* 1999;44:975–79; discussion 979–80 CrossRef
21. Bossuyt PM, Reitsma JB, Bruns DE, et al; STARD Group. **STARD 2015: an updated list of essential items for reporting diagnostic accuracy studies.** *BMJ* 2015;351:h5527 CrossRef Medline
22. Frontera JA, Fernandez A, Schmidt JM, et al. **Defining vasospasm after subarachnoid hemorrhage: what is the most clinically relevant definition?** *Stroke* 2009;40:1963–68 CrossRef Medline
23. Wang LS, He W, Zhang HQ, et al. **Comparison of transcranial color Doppler sonography without and with contrast enhancement for detection and characterization of intracranial aneurysms.** *J Clin Ultrasound* 2012;40:535–39 CrossRef Medline
24. Rutjes AW, Reitsma JB, Coomarasamy A, et al. **Evaluation of diagnostic tests when there is no gold standard: a review of methods.** *Health Technol Assess* 2007;11:iii, ix–51 CrossRef Medline
25. Hillier TA, Pedula KL, Ogasawara KK, et al. **A pragmatic, randomized clinical trial of gestational diabetes screening.** *N Engl J Med* 2021;384:895–904 CrossRef Medline
26. Lindegaard KF, Bakke SJ, Sorteberg W, et al. **A non-invasive Doppler ultrasound method for the evaluation of patients with subarachnoid hemorrhage.** *Acta Radiol Suppl* 1986;369:96–98 Medline

Parent Artery Straightening after Flow-Diverter Stenting Improves the Odds of Aneurysm Occlusion

K. Janot, R. Fahed, A. Rouchaud, K. Zuber, G. Boulouis, G. Forestier, C. Mounayer, and M. Piotin

ABSTRACT

BACKGROUND AND PURPOSE: Intracranial stents for the treatment of aneurysms can be responsible for parent artery straightening, a phenomenon with potential consequences for aneurysmal occlusion. We aimed to evaluate parent artery straightening following flow-diverter stent placement in patients with intracranial aneurysms and explored the association between parent artery straightening and subsequent aneurysm occlusion.

MATERIALS AND METHODS: All patients treated with flow-diverter stents for anterior circulation aneurysms located downstream from the carotid siphon between January 2009 and January 2018 were screened for inclusion. Parent artery straightening was defined as the difference (α–β) in the parent artery angle at the neck level before (α angle) and after flow-diverter stent deployment (β angle). We analyzed the procedural and imaging factors associated with parent artery straightening and the associations between parent artery straightening and aneurysmal occlusion.

RESULTS: Ninety-five patients met the inclusion criteria ($n = 64/95$ women, 67.4%; mean age, 54.1 [SD, 11.2] years) with 97 flow-diverter stents deployed for 99 aneurysms. Aneurysms were predominantly located at the MCA bifurcation ($n = 44/95$, 44.4%). Parent artery straightening was found to be more pronounced in patients treated with cobalt chromium stents than with nitinol stents ($P = .02$). In multivariate analysis, parent artery straightening ($P = .04$) was independently associated with aneurysm occlusion after flow-diverter stent deployment.

CONCLUSIONS: The use of flow-diverter stents for distal aneurysms induces a measurable parent artery straightening, which is associated with higher occlusion rates. Parent artery straightening, in our sample, appeared to be more prominent with cobalt chromium stents than with nitinol stents. This work highlights the necessary trade-off between navigability and parent artery straightening and may help tailor the selection of flow-diverter stents to aneurysms and parent artery characteristics.

Flow-diverter stents are an interesting treatment option for selected patients with intracranial aneurysms.[1,2] Their efficacy to obtain aneurysm occlusion depends notably on the incident angle of blood flow through the flow-diverter stents into the aneurysm sac,[3] which directly correlates with parent artery anatomy. In patients with aneurysms located in the carotid siphon,[4] flow-diverter stents have been shown to straighten the parent artery after deployment, and the straightening may independently be associated with higher aneurysm occlusion rates. Yet, this effect has not, to date, been explored in patients with more distal aneurysms, their parent vessels being less subjected to local constraints and, in turn, a likely more important susceptibility to deformation. Indeed, vessel anatomy is constrained by the local osseous environment in the siphon, whereas vessels located in the Sylvian cisterns or more distally at the surface of the brain are more prone to anatomic changes under external or internal constraint.

In a retrospective study, we aimed to measure parent artery straightening after deployment of flow-diverter stents in patients with intracranial aneurysms located beyond the carotid siphon and to assess whether parent artery straightening is associated with aneurysm occlusion.

Received May 23, 2021; accepted after revision September 16.

From the Department of Interventional Neuroradiology (K.J., G.B.), University Hospital of Tours, Tours, France; Department of Interventional Neuroradiology (R.F., M.P.) and Research and Biostatistics Unit (K.Z.), Rothschild Foundation Hospital, Paris, France; and Department of Interventional Neuroradiology (A.R., G.F., C.M.), Dupuytren University Hospital, Limoges, France.

The data used for this work have been presented at the 2019 annual conference of the French Neuroradiology Society, as an oral communication.

Please address correspondence to Kevin Janot, MD, Department of Interventional Neuroradiology, University Hospital of Tours, 2 Boulevard Tonnellé, 37 000 Tours, France; e-mail: kevin.janot@hotmail.com

Indicates article with online supplemental data.

http://dx.doi.org/10.3174/ajnr.A7350

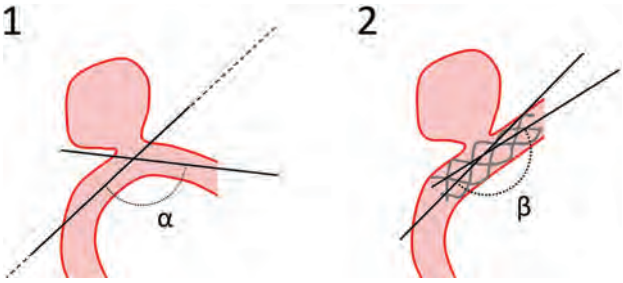

FIG 1. Measurement of parent artery straightening. Angles were measured at the intersection of 2 lines drawn from the neck center in the axis of the proximal and distal segments of the parent artery. α is the angle measured before stent placement, and β is the angle measured after stent deployment. Preoperative (1) and postoperative (2) drawings.

MATERIALS AND METHODS

Ethics

The study protocol was approved by the local ethics committee at Rothschild Foundation Hospital. In line with regulations in France where the study was conducted, the institutional review board waived the need for patients' signed consent. Patients were informed that they could refuse the use of their data.

Data Sharing

Data will be made available on reasonable request by a qualified investigator after institutional review board approval.

Population

All patients treated with flow-diverter stents for intracranial aneurysms located beyond the carotid siphon between January 2009 and January 2018 were included. At our institution, flow-diverter stents are used as an alternative to coiling or an operation for the treatment of complex aneurysms, including giant, fusiform, or wide-neck lesions. Flow-diverter stents are not used in the context of suspected mycotic lesions. Posterior circulation aneurysms, fusiform aneurysms, ruptured aneurysms, aneurysms without available images, and those treated with >1 flow-diverter stent or previously treated by stent placement were excluded.

Treatment

Endovascular treatment was performed with the patient under general anesthesia. All patients received systemic heparinization during the procedure. Four different flow-diverter stent devices were available: 2 cobalt chromium stents, the Pipeline Embolization Device (PED; Medtronic) and the Surpass FD (Stryker Neurovascular) and 2 nitinol stents, the Silk (Balt Extrusion) and the Flow-Redirection Endoluminal Device (FRED; MicroVention). Concomitant coiling was sometimes performed during the same procedure at the discretion of the operators.

Antiplatelet Therapy

In the postoperative period, all treated patients received dual-antiplatelet therapy by aspirin and clopidogrel for 3 months (except for one who received aspirin combined with ticagrelor) followed by monotherapy using aspirin alone.

Clinical and Imaging Follow-up

Patients were assessed by a first cerebral angiogram at 6–12 months and a second cerebral angiogram at 36 months, then by brain MR imaging.

Data Collection and Analysis

All clinical and imaging data were retrieved from electronic medical records. The parent artery angle was measured at the intersection of the central lines of the proximal and distal portions of the parent vessel to the center point of the parent artery facing the aneurysm neck, before and after stent deployment and at first follow-up (Fig 1). Parent artery straightening was defined as the difference between the postdeployment angle (β) and the initial angle (α). Two independent physicians blinded to the angiographic outcome of the aneurysm performed these measurements on DSA working projections. The postdeployment angle used for analyses was the mean of both raters' measurements. Discrepancies of >10° of parent artery straightening were resolved by consensus. Aneurysm occlusion was evaluated using the O'Kelly-Marotta grading scale based on the DSA images.[5]

Statistical Analysis

Continuous variables were reported as mean (SD), with extreme values and categoric variables as number and percentage. Agreement between readers for angle measurements was determined using the interclass correlation coefficient and a 95% confidence interval. For complete aneurysm occlusion, univariate, logistic regression models were used to test the association, whereas a univariate linear regression model was used for factors associated with parent artery straightening. Variables with $P < .20$ in univariable analysis were included in a multiple logistic regression model for occlusion and a multiple linear regression model for the parent artery straightening angle. Backward variable selection was used to select the independent predictors of complete occlusion and postdeployment angle. $P < .05$ was considered significant. The interaction term "parent artery straightening × stent type" may allow us to understand whether the effect of parent artery straightening varies within stent type. All statistical analyses were performed using JMP Pro 14 (SAS Institute, 1989–2019).

RESULTS

Study Cohort Characteristics

Ninety-five patients were included in the present study (64 women, 67.4%; mean age, 54.1 [SD, 11.2] years) for a total of 99 aneurysms located downstream from the carotid siphon treated with 97 flow-diverter stents, including 45 aneurysms (45.5%) previously treated with coils. All aneurysms were saccular and measured 6.1 (SD, 5.0) mm in maximal diameter and 3.9 (SD, 2.1) mm at the neck. Fifty-two aneurysms were treated using a cobalt chromium stent (PED, Surpass) (52.5%) and 47, using a nitinol stent (Silk, FRED) (47.5%). Detailed cohort characteristics are shown in Table 1.

Parent Artery Straightening

The mean postdeployment angle (β) was significantly superior to the initial angle (α) (141.6° [SD, 24.8°] versus 124.1° [SD, 64]°; $P < .001$).

Table 1: Comparison of demographic, angiographic, and treatment characteristics between complete occluded and incomplete occluded aneurysms[a]

	All Aneurysms ($n = 99$)	Complete Occlusion ($n = 64$)	Incomplete Occlusion (n = 20)	*P* Value
Age (yr) (mean)	54.1 (SD, 11.2)	53.8 (SD, 10.8)	54.3 (SD, 10.4)	.76
Sex, M/F	31 (31.3%)/68 (68.7%)	18 (28.1%)/46 (71.9%)	9 (45%)/11 (55%)	.26
Follow-up (mo) ($n = 84$)	23.9 (SD, 16.3)	24.2 (SD, 15.0)	22.9 (SD, 20.2)	.27
Previous treatment	45 (45.5%)	28 (43.8%)	13 (65%)	.16
Aneurysm location				.62
MCA	44 (44.4%)	25 (39.1%)	12 (60%)	
AcomA	27 (27.3%)	20 (31.3%)	5 (25%)	
A1	2 (2.0%)	2 (3.1%)	0	
A2	2 (2.0%)	2 (3.1%)	0	
Pericallosal	24 (24.2%)	15 (23.4%)	3 (15%)	
Aneurysm size (mm)				
Neck	3.9 (SD, 2.1)	3.6 (SD, 2.1)	4.3 (SD, 2.0)	.06
Diameter	6.1 (SD, 5.0)	6.1 (SD, 5.7)	6.5 (SD, 3.5)	.14
Concomitant coiling	15 (15.2%)	9 (14.1%)	2 (10%)	1
Flow-diverter stent				
Length (mm)	16.9 (SD, 3.9)	16.5 (SD, 3.8)	18.2 (SD, 4.3)	.42
Type				.004
Nitinol	47 (47.5%)	26 (40.6%)	16 (80%)	
Cobalt chromium	52 (52.5%)	38 (59.4%)	4 (20%)	
Angle of parent artery				
Initial angle (α)	124.1° (SD, 64.0°)	118.3° (SD, 29.8°)	122.7° (SD, 28.1°)	.58
Postdeployment angle (β)	141.6° (SD, 24.8°)	146.0° (SD, 21.8°)	135.9° (SD, 24°)	.12
Parent artery straightening ($\beta-\alpha$)	3.8° (SD, 21.6°)	27.7 (SD, 22.6)	13.3° (SD, 12.3°)	<.001

Note:—AcomA indicates anterior communicating artery; A1, proximal segment of the anterior cerebral artery; A2, distal segment of the anterior cerebral artery.
[a]Data are presented as mean (standard deviation, SD) for continuous variables and absolute number (percentage of column total) for discrete variables.

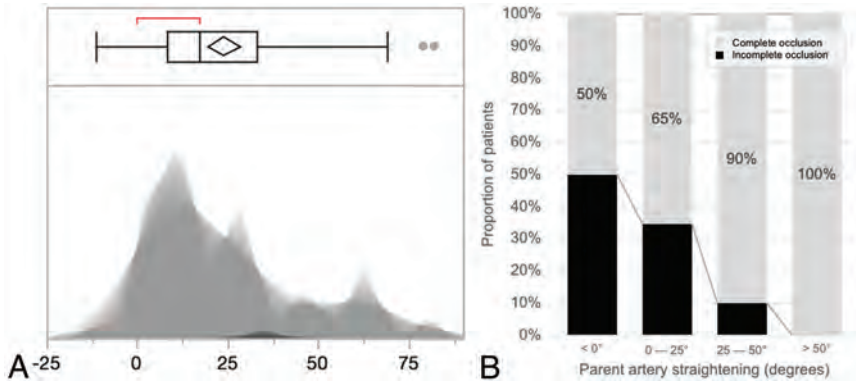

FIG 2. Distribution of angles of parent artery straightening and association with aneurysmal occlusion. *A*, Shadowgram distribution of parent artery straightening. *B*, Stacked histograms of the proportion of patients with complete occlusion in bins of increasing parent artery straightening (offset = 0, width = 25°).

The mean follow-up angle was further significantly increased compared with the postdeployment angle β (148.7°[SD, 20.3°]; $P < .001$), with a mean first DSA follow-up time of 8.5 (SD, 4.3) months. According to the criteria of Cicchetti et al,[6] interobserver agreement was considered good for all 3 measurements, with interclass correlation coefficient values of 0.64 (0.40–0.75) for the initial angle (α), 0.65 (0.46–0.78) for the postdeployment angle (β), and 0.70 (0.53–0.83) for the follow-up angle, respectively.

Parent artery straightening was common, with a median parent artery angle reduction of 17° (interquartile range, 8.25°–33°) (see Fig 2 for a complete distribution).

In univariate analysis, stent type ($P = .02$) and initial angle (α) ($P < .001$) were significantly associated with parent artery straightening. There was no association with patient sex, age, previous embolization, aneurysm location, aneurysm size, and associated coiling. The initial angle (α) ($P = .01$) and stent type ($P < .001$) remained associated independently with parent artery straightening (Online Supplemental Data). Figure 3 and the Online Supplemental Data show illustrations of parent artery straightening following flow-diverter stent placement.

Factors Associated with Aneurysm Occlusion

Fifteen patients with 15 aneurysms (15.2%) were lost during follow-up, leaving 84 aneurysms for this analysis. Complete occlusion (O'Kelly-Marotta score D) was observed in 64 aneurysms (76.2%) at follow-up, with a mean follow-up duration of 23.9 (SD, 16.3) months. In univariate analysis, cobalt chromium stents ($P = .004$) and higher parent vessel straightening ($\beta-\alpha$) ($P < .001$) were associated with complete aneurysm occlusion (Table 1). After adjustment, parent artery straightening ($P = .036$), stent type ($P = .02$), and aneurysm neck ($P < .001$) were independently associated with complete aneurysm occlusion. The interaction term between stent type and parent artery straightening was not significant ($P = .055$), meaning that there was no varying

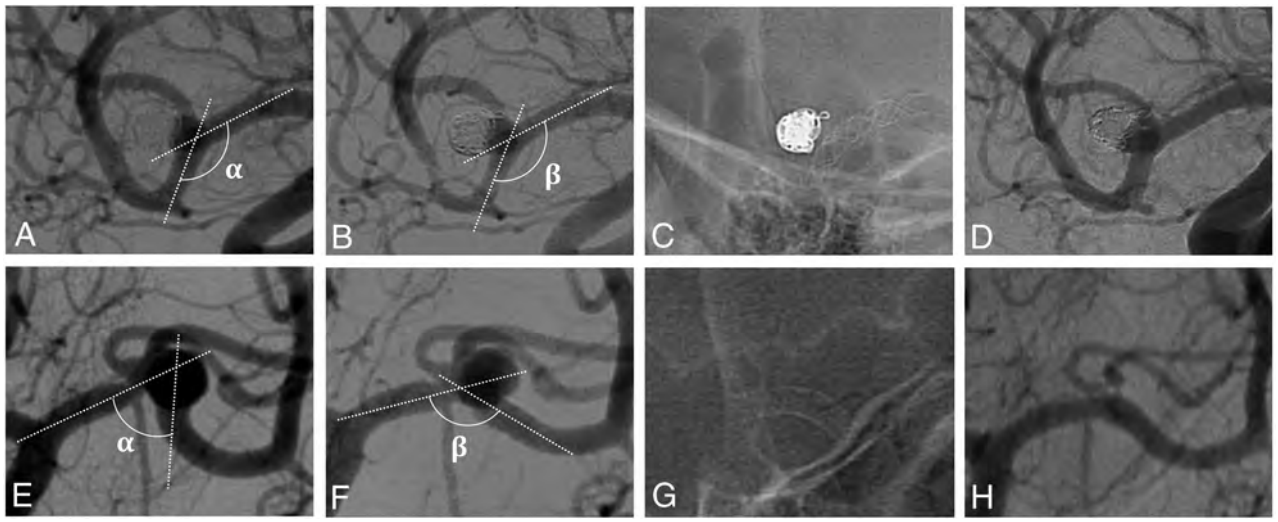

FIG 3. Comparison of vascular geometry modifications in 2 treatments of MCA aneurysms. The second flow-diverter stent deployment appears to modify the vascular anatomy (*E–G*) more than the first flow-diverter stent (*A–C*). Angiogram controls show complete aneurysm occlusion with the second flow-diverter stent (*H*) compared with the first-flow diverter (*D*) stent. *A* and *E*, Preoperative angiogram. *B* and *F*, Angiogram after stent placement. *C* and *G*, Unsubtracted view after stent deployment. *D* and *H*, First angiogram follow-up. α indicates the angle measured before stent placement; β, the angle measured after stent placement.

Table 2: Multivariable analysis of aneurysm occlusion determinants

Variables	Multivariate Analysis, aOR (95% CI)	*P* Value
Aneurysm neck (mm)	0.57 (0.38–0.87)	<.001
Stent type: chromium cobalt	2.13(1.26–11.93)	.020
Parent artery straightening	1.04° (1.01°–1.17°)	.036
Initial angle (α)	0.95°(0.91°–1.02°	.401
Parent artery straightening × stent type[a]	0.99 (0.94–1.02)	.055

Note:—aOR indicates adjusted odds ratio.
[a]Interaction term.

influence of parent artery straightening according to stent type. Detailed results are shown in Table 2.

DISCUSSION

These results suggest that flow-diverter stents deployed beyond the carotid siphon modify the anatomy by inducing straightening of the parent artery, and parent artery straightening, in turn, favors higher rates of aneurysm occlusion. This result brings additional insight into the mechanisms at play after flow-diverter stent placement during aneurysm healing. It also suggests that while the distal navigability of a flow-diverter stent is highly desired for procedural success, it may come at the cost of lower parent artery straightening and lower odds of aneurysmal occlusion in aneurysms located beyond the carotid siphon.

Previous studies have reported failure rates as high as 17% after flow-diverter treatment in distal aneurysm locations,[2] and mechanisms of occlusion failure still remain poorly understood.

Some animal studies have suggested that flow-diverter stent treatment was more effective when deployed in a straight artery than in a curved artery.[7-9] Our study also suggests that this straightening phenomenon goes on after deployment, because follow-up angles were significantly superior to immediate postdeployment angles.[4] In addition to its effects on the incident angle of blood flow into the aneurysm sac, this straightening effect could improve aneurysm occlusion through other mechanisms: It might influence the wall apposition of the flow-diverter stents,[10] and it could also improve the "scaffolding" effect for reconstruction of the aneurysmal neck[11] and promote arterial remodeling in a more favorable geometric configuration. It is, nonetheless, hypothesized that despite the flow-diverting effect, flow-diverter stents inducing important parent artery straightening may, in part, correct the geometric configuration that was involved in aneurysm development in the first place.

Hemodynamic factors indeed play an important role in the pathogenesis of cerebral aneurysms.[12] Gao et al[13] reported vascular geometric consequences of single conventional stent placement: Angular remodeling was more pronounced using the stiffer closed-cell-like flow-diverter stents. Our study demonstrates that flow-diverter stent placement in the distal artery straightens parent artery geometry like conventional stents, which has already been theoretically described in a computational fluid dynamics study.[14] The hemodynamic efficiency of a flow-diverter stent is related to several parameters, including the porosity and metal coverage of the stent, but intra-aneurysmal hemodynamic changes are also affected by the curvature of the parent artery.[14-16] When the aneurysm is developed on the convex wall of a curvature, cells of flow-diverter stents are more widely opened than when the artery is straightened, with a higher mesh density and increased flow diversion.[17]

Ishii et al[18] reported that in stent-assisted coiled aneurysms, angular change induced by stent placement may affect aneurysm recanalization rates during follow-up more than coil packing density. Also, Funakoshi et al[19,20] showed, in a cohort of 255 aneurysms, that distal aneurysms located in the ICA bifurcation, MCA, or anterior communicating artery develop in parent vessels that are not fixed by osseous structures, have characteristics such as small diameters and thin vessel walls, and can be more mobile. Progressive thrombosis is more often observed in these

distal aneurysms treated by stent-assisted coiling; aggressive coiling may appear futile in these cases.

Our results suggest that parent artery straightening could be more important with cobalt chromium flow-diverter stents than with nitinol flow-diverter stents, probably due to the mechanical properties of their respective components. Nitinol is an alloy composed of near-equal parts of nickel and titanium, which exhibit unique properties: superelasticity and shape memory. Cobalt chromium is stronger than stainless steel, so a cobalt chromium stent can have similar strength with thinner braids.[21,22] In the multivariable model, we indeed showed that cobalt chromium stents were associated with a 2-fold increase in subsequent aneurysm occlusion, and the interaction term between stent type and parent artery straightening attained near-significance ($P = .055$), implying that the degree of parent artery straightening might differ between both stents, which is substantiated by the analysis of parent artery straightening determinants. Most important, there are many other mechanical characteristics that differentiate these types of stents (such as navigability); therefore, our findings do not imply that one type of flow diverter stent is superior to the other. Indeed, our analysis was focused on aneurysms that are not constrained by osseous structures due to their distal situation. In these anatomic locations, increased navigability is a highly desirable characteristic of flow-diverter stents, and we cannot exclude a confounding by indication, which led to more distal/complex aneurysms being treated with nitinol stents in our sample.

Of interest, while software is currently being used to simulate the behavior of a stent after its deployment to help in planning treatment and choosing stent size,[23] these tools assume that the vessel is a rigid, not deformable structure. Our results suggest that this approach might be misleading, at least for arteries beyond the circle of Willis, and there is room for incorporating parent artery straightening in this software to facilitate placement and postdeployment management in more complex cases.

Our study has several limitations due to its retrospective nature and the small number of patients included. Also, the angle measurements were made on 2D angiographic images, and measurement performed on 3D acquisitions might be more precise and could have shown different results.

CONCLUSIONS

In patients with intracranial aneurysms located beyond the carotid siphon, flow-diverter stent placement induces parent artery straightening, a phenomenon found in our sample to be associated with higher rates of subsequent aneurysmal occlusion. This feature may be of importance for device-selection planning in patients scheduled for elective flow-diverter stent placement and may need to be considered in future studies investigating the efficacy of flow-diverter stents to better comprehend the healing process of aneurysms.

Disclosure forms provided by the authors are available with the full text and PDF of this article at www.ajnr.org.

REFERENCES

1. Pistocchi S, Blanc R, Bartolini B, et al. **Flow diverters at and beyond the level of the circle of Willis for the treatment of intracranial aneurysms.** *Stroke* 2012;43:1032–38 CrossRef Medline
2. Primiani CT, Ren Z, Kan P, et al. **A2, M2, P2 aneurysms and beyond: results of treatment with Pipeline embolization device in 65 patients.** *J Neurointerv Surg* 2019;11:903–07 CrossRef Medline
3. Meng H, Wang Z, Kim M, et al. **Saccular aneurysms on straight and curved vessels are subject to different hemodynamics: implications of intravascular stenting.** *AJNR Am J Neuroradiol* 2006;27:1861–65 Medline
4. Waihrich E, Clavel P, Mendes G, et al. **Influence of anatomic changes on the outcomes of carotid siphon aneurysms after deployment of flow-diverter stents.** *Neurosurgery* 2018;83:1226–33 CrossRef Medline
5. O'Kelly CJ, Krings T, Fiorella D, et al. **A novel grading scale for the angiographic assessment of intracranial aneurysms treated using flow diverting stents.** *Interv Neuroradiol* 2010;16:133–37 CrossRef Medline
6. Cicchetti DV, Shoinralter D, Tyrer PJ. **The effect of number of rating scale categories on levels of interrater reliability: a Monte Carlo investigation.** *Appl Psychol Meas* 1985;9:31–36 CrossRef
7. Darsaut TE, Bing F, Salazkin I, et al. **Flow diverters failing to occlude experimental bifurcation or curved sidewall aneurysms: an in vivo study in canines.** *J Neurosurg* 2012;117:37–44 CrossRef Medline
8. Fahed R, Raymond J, Ducroux C, et al. **Testing flow diversion in animal models: a systematic review.** *Neuroradiology* 2016;58:375–82 CrossRef Medline
9. Fahed R, Darsaut TE, Gentric JC, et al. **Flow diversion: what can clinicians learn from animal models?** *Neuroradiology* 2017;59:255–61 CrossRef Medline
10. Rouchaud A, Ramana C, Brinjikji W, et al. **Wall apposition is a key factor for aneurysm occlusion after flow diversion: a histologic evaluation in 41 rabbits.** *AJNR Am J Neuroradiol* 2016;37:2087–91 CrossRef Medline
11. Fu Y, Zhang S, Du H, et al. **Impact of vessel curvature on neointimal healing after stent implantation as assessed by optical coherence tomography.** *Medicine (Baltimore)* 2018;97:e0518 CrossRef Medline
12. Can A, Du R. **Association of hemodynamic factors with intracranial aneurysm formation and rupture: systematic review and meta-analysis.** *Neurosurgery* 2016;78:510–20 CrossRef Medline
13. Gao B, Baharoglu MI, Malek AM. **Angular remodeling in single stent-assisted coiling displaces and attenuates the flow impingement zone at the neck of intracranial bifurcation aneurysms.** *Neurosurgery* 2013;72:739–48 CrossRef Medline
14. Xu J, Wu Z, Yu Y, et al. **Combined effects of flow diverting strategies and parent artery curvature on aneurysmal hemodynamics: a CFD study.** *PLoS One* 2015;10:e0138648 CrossRef Medline
15. King RM, Chueh JY, van der Bom IM, et al. **The effect of intracranial stent implantation on the curvature of the cerebrovasculature.** *AJNR Am J Neuroradiol* 2012;33:1657–62 CrossRef Medline
16. Huang QH, Wu YF, Xu Y, et al. **Vascular geometry change because of endovascular stent placement for anterior communicating artery aneurysms.** *AJNR Am J Neuroradiol* 2011;32:1721–25 CrossRef Medline
17. Shapiro M, Raz E, Becske T, et al. **Variable porosity of the Pipeline embolization device in straight and curved vessels: a guide for optimal deployment strategy.** *AJNR Am J Neuroradiol* 2014;35:727–33 CrossRef Medline
18. Ishii A, Chihara H, Kikuchi T, et al. **Contribution of the straightening effect of the parent artery to decreased recanalization in stent-assisted coiling of large aneurysms.** *J Neurosurg* 2017;127:1063–69 CrossRef Medline
19. Funakoshi Y, Imamura H, Tani S, et al. **Progressive thrombosis of unruptured aneurysms after coil embolization: analysis of 255 consecutive aneurysms.** *J Neurointerv Surg* 2019;11:1113–17 CrossRef Medline

20. Funakoshi Y, Imamura H, Tani S, et al. **Effect of straightening the parent vessels in stent-assisted coil embolization for anterior communicating artery aneurysms.** *World Neurosurg* 2019;126:e410–16 CrossRef Medline
21. Rajah G, Narayanan S, Rangel-Castilla L. **Update on flow diverters for the endovascular management of cerebral aneurysms.** *Neurosurg Focus* 2017;42:E2 CrossRef Medline
22. Suzuki T, Takao H, Fujimura S, et al. **Selection of helical braided flow diverter stents based on hemodynamic performance and mechanical properties.** *J Neurointerv Surg* 2017;9:999–1005 CrossRef Medline
23. Piergallini L, Cagnazzo F, Conte G, et al. **Virtual simulation with Sim&Size software for Pipeline Flex Embolization: evaluation of the technical and clinical impact.** *J Neurointerv Surg* 2020;12:968–73 CrossRef

Interrater Agreement and Detection Accuracy for Medium-Vessel Occlusions Using Single-Phase and Multiphase CT Angiography

J.M. Ospel, F. Bala, R.V. McDonough, O. Volny, N. Kashani, W. Qiu, B.K. Menon, and M. Goyal

ABSTRACT

BACKGROUND AND PURPOSE: Accurate and reliable detection of medium-vessel occlusions is important to establish the diagnosis of acute ischemic stroke and initiate appropriate treatment with intravenous thrombolysis or endovascular thrombectomy. However, medium-vessel occlusions are often challenging to detect, especially for unexperienced readers. We aimed to evaluate the accuracy and interrater agreement of the detection of medium-vessel occlusions using single-phase and multiphase CTA.

MATERIALS AND METHODS: Single-phase and multiphase CTA of 120 patients with acute ischemic stroke (20 with no occlusion, 44 with large-vessel occlusion, and 56 with medium-vessel occlusion in the anterior and posterior circulation) were assessed by 3 readers with varying levels of experience (session 1: single-phase CTA; session 2: multiphase CTA). Interrater agreement for occlusion type (large-vessel occlusion versus medium-vessel occlusion versus no occlusion) and for detailed occlusion sites was calculated using the Fleiss κ with 95% confidence intervals. Accuracy for the detection of medium-vessel occlusions was calculated for each reader using classification tables.

RESULTS: Interrater agreement for occlusion type was moderate for single-phase CTA ($\kappa = 0.58$; 95% CI, 0.56–0.62) and almost perfect for multiphase CTA ($\kappa = 0.81$; 95% CI, 0.78–0.83). Interrater agreement for detailed occlusion sites was moderate for single-phase CTA ($\kappa = 0.55$; 95% CI, 0.53–0.56) and substantial for multiphase CTA ($\kappa = 0.71$; 95% CI, 0.67–0.74). On single-phase CTA, readers 1, 2, and 3 classified 33/56 (59%), 34/56 (61%), and 32/56 (57%) correctly as medium-vessel occlusions. On multiphase CTA, 48/56 (86%), 50/56 (89%), and 50/56 (89%) medium-vessel occlusions were classified correctly.

CONCLUSIONS: Interrater agreement for medium-vessel occlusions is moderate when using single-phase CTA and almost perfect with multiphase CTA. Detection accuracy is substantially higher with multiphase CTA compared with single-phase CTA, suggesting that multiphase CTA might be a valuable tool for assessment of medium-vessel occlusion stroke.

ABBREVIATIONS: EVT = endovascular treatment; LVO = large-vessel occlusion; mCTA = multiphase CTA; MeVO = medium-vessel occlusion

Medium-vessel occlusions (MeVOs) are defined as occlusions of the M2 and M3/4 segments of the MCA, A2 and A3/4 segments of the anterior cerebral artery, and P2 and P3/4 segments of the posterior cerebral artery.[1] MeVOs account for approximately 25%–40% of all acute ischemic strokes, and although they have traditionally been thought to cause only minor symptoms, MeVO strokes frequently result in disabling deficits.[2,3] This outcome has led to a paradigm shift in treatment: An increasing number of physicians now routinely offers endovascular treatment (EVT) as a stand-alone therapy instead of or in addition to intravenous thrombolysis for MeVO stroke.[4-6] Furthermore, 2 randomized trials, ESCAPE-MeVO and DISTAL, are being planned to generate level 1A evidence for EVT in MeVO stroke (personal communication: Mayank Goyal, Marios-Nikos Psychogios, oral communication). The prerequisite for conducting these trials and for appropriate treatment of MeVOs is accurate and reliable MeVO detection and distinction between MeVOs and large-vessel occlusions (LVOs). However, MeVOs are missed in up to one-third of cases.[7] Furthermore, distinguishing MeVOs from LVOs is not always straightforward because

Received August 10, 2021; accepted after revision September 22.

From the Department of Diagnostic Imaging (J.M.O., F.B., R.V.M., N.K., W.Q., B.K.M., M.G.), and Department of Clinical Neurosciences (N.K., B.K.M., M.G.), University of Calgary, Calgary, Alberta, Canada; Department of Radiology (J.M.O.), University Hospital of Basel, Basel, Switzerland; Czech National Centre for Evidence-Based Healthcare and Knowledge Translation (O.V.), Masaryk University, Brno, Czech; and Department of Neurology (O.V.), University Hospital Ostrava, Ostrava, Czech.

This study was funded, in part, by the Canadian Institutes of Health Research.

Please address correspondence to Mayank Goyal, MD, Departments of Diagnostic Imaging and Clinical Neurosciences, Foothills Medical Centre, 1403 29th St NW, University of Calgary, Calgary, Alberta, Canada, T2N2T9; e-mail: mgoyal@ucalgary.ca; @johanna_ospel; @rosevmcd; @mayank_G0

Indicates open access to non-subscribers at www.ajnr.org

Indicates article with online supplemental data.

http://dx.doi.org/10.3174/ajnr.A7361

various definitions for the borders between the M1 and M2 segments exist.[8] The same holds true for the anterior and posterior cerebral arteries. Multiphase CTA (mCTA) is a dynamic imaging method in which an arch-to-vertex CTA is obtained in a manner identical to single-phase CTA. The same contrast bolus is then used to obtain 2 additional series during the peak-venous and late-venous phases, covering only the intracranial vasculature from the skull base to the vertex (Online Supplemental Data). The delayed washout on the second and third phases in the vascular territory downstream to the occlusion may help to improve detection accuracy and interrater agreement for MeVOs.

In this study, we aimed to compare interrater agreement and detection accuracy for MeVOs using single-phase CTA and mCTA.

MATERIALS AND METHODS

Patient Sample

This study was approved by the local institutional review board at the University of Calgary. Data are from the Precise and Rapid Assessment of Collaterals Using Multi-Phase CTA in the Triage of Patients with Acute Ischemic Stroke for IV or IA Therapy (PRove-IT) study (clinicaltrials.gov identifier: NCT02184936). PRove-IT was a prospective multicenter cohort study that enrolled 595 patients who presented with symptoms of acute ischemic stroke. Patients were included if they presented to the emergency department with symptoms consistent with acute ischemic stroke, were older than 18 years of age, and had mCTA and CT perfusion performed within 12 hours of symptom onset and before recanalization therapy. Exclusion criteria were intracranial hemorrhage at baseline NCCT, previous sizeable stroke in the ipsilateral hemisphere, mRS >2 at baseline, estimated creatinine clearance of <60 mL/min, contrast material allergy or other contraindications for iodinated contrast, and estimated life expectancy of <1 year.[9] The enrollment period was July 2012 to October 2016. For this study, a sample of 120 patients (20 with no occlusion, 44 with LVO, and 56 with MeVO in the anterior and posterior circulation) was randomly chosen. The proportions of patients with MeVOs in relation to LVOs and scans without occlusions were chosen so that they approximately reflected the distribution of occlusions in the PRove-IT study.

Imaging

We exclusively used baseline CTA imaging in this study. The first CTA phase consisted of an arch-to-vertex coverage (CTA head and neck and conventional single-phase CTA). This first phase was used for the single-phase CTA reading session and was followed by skull base-to-vertex coverage for the second (peak venous) and third (late venous) phases of an mCTA acquisition. All 3 phases were available in the mCTA reading session. Detailed mCTA acquisition parameters have been published previously.[9] Axial images with 1-mm overlap and multiplanar axial, coronal, and sagittal reconstructions with 3-mm thickness, 1-mm intervals, and 1-mm overlap for the first phase were obtained, along with axial minimum intensity projections for all 3 phases with 24-mm thickness and 4-mm intervals, available for the readers.

Image Analysis

Three blinded readers (a general radiologist with 4 years of experience and 2 neuroradiologists with 7 and 2 years of experience) interpreted the images in 2 separate reading sessions. In the first session, only single-phase CTA (ie, the first CTA phase with arch-to-vertex coverage) was available. In the second session, all 3 mCTA phases were available. Readers were informed that the set of cases included patients with LVO and MeVO in the anterior and posterior circulation as well as cases without any occlusion, but they did not know the distribution of occlusions and occlusion locations. They were blinded to all other baseline imaging, follow-up imaging, and clinical information. Occlusion sites were captured as either no occlusion; intracranial internal carotid artery occlusion; M1, M2, or M3/4 segment MCA occlusion; A1, A2, or A3/4 segment anterior cerebral artery occlusion; or P1, P2, or P3/4 segment posterior cerebral artery occlusion. Detailed definitions of vessel segments and borders between them as they were used in this study are shown in the Online Supplemental Data. Besides these detailed occlusion sites, occlusions were also grouped into no occlusion versus LVOs (occlusions of the ICA, M1, A1, or P1 segments) versus MeVOs (occlusions of the M2/3/4, A2/3/4, or P2/3/4 segments). The reference standard was set by an independent core lab (M.G., interventional neuroradiologist with 24 years of neuroimaging experience), with all imaging information (baseline noncontrast head CT, mCTA, CT perfusion, and follow-up imaging) as well as clinical information being available.

Statistical Analysis

Interrater agreement for occlusion type (LVO versus MeVO versus no occlusion) and for detailed occlusion sites was assessed using the Fleiss κ for multiple raters[10] with respective optimism-corrected bootstrapped 95% confidence intervals. According to common convention, $\kappa<0$ was interpreted as poor agreement; $\kappa=0$–0.2, as slight agreement; $\kappa=0.21$–0.40, as fair agreement; $\kappa=0.41$–0.60, as moderate agreement; $\kappa=0.61$–0.80, as substantial agreement; and $\kappa=0.81$–1, as almost perfect agreement.[11] The accuracy of MeVO detection overall and for each MeVO occlusion site was calculated for each reader using classification tables. All analyses were performed in STATA, Version 15.1 (StataCorp).

RESULTS

A total of 120 cases were included in the study, among them 20 with no visible occlusion, 44 LVOs (22 intracranial ICA occlusions, 2 vertebral artery occlusions, 1 basilar artery occlusion, 18 M1 occlusions, and 1 P1 occlusion), and 56 MeVOs (21 M2 occlusions, 12 M3/4 occlusions, 5 A2 occlusions, 4 A3/4 occlusions, and 14 P2 occlusions).

Interrater Agreement

Interrater agreement for occlusion type was moderate for single-phase CTA ($\kappa=0.58$; 95% CI, 0.56–0.62) and significantly improved to excellent agreement when mCTA was used ($\kappa=0.81$; 95% CI, 0.78–0.83). Interrater agreement for detailed occlusion sites (see the Online Supplemental Data for detailed definitions) was

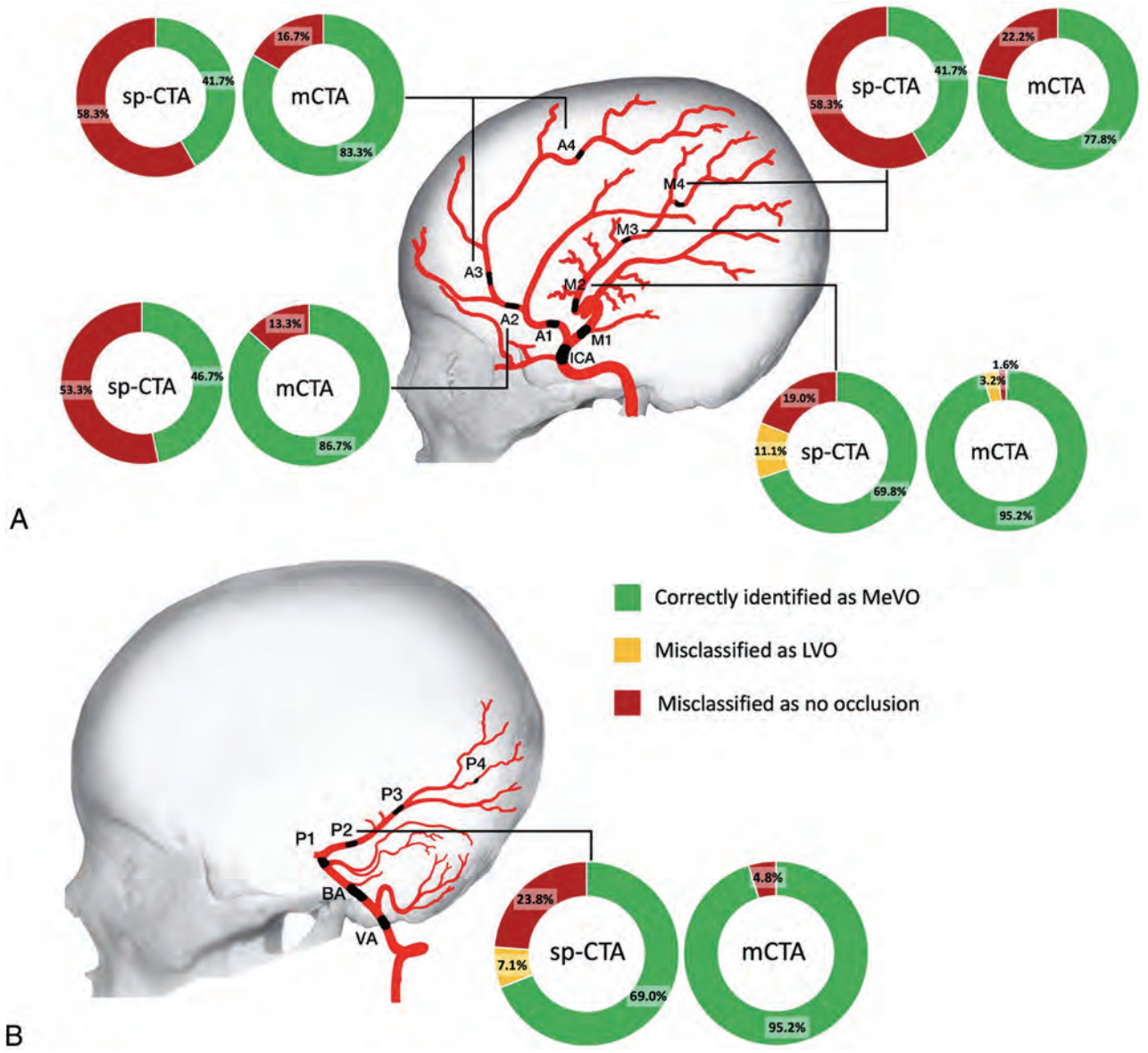

FIGURE. Proportion of MeVOs that were correctly classified as MeVOs (green), misclassified as LVOs (yellow), and misclassified as no occlusion (red) on single-phase and multiphase CTA, stratified per occlusion site. *A*, Proportions for M2, M3/4, A2, and A3/4 MeVOs. *B*, Proportions for P2 MeVOs. sp-CTA indicates single-phase CT angiography.

moderate for single-phase CTA ($\kappa = 0.55$; 95% CI, 0.53–0.56) and substantial for mCTA ($\kappa = 0.71$; 95% CI, 0.67–0.74).

Accuracy of MeVO Detection

Classification tables for the 3 readers on single-phase CTA and mCTA are shown in the Online Supplemental Data. On single-phase CTA, readers 1, 2, and 3 classified 33/56 (59%), 34/56 (61%), and 32/56 (57%) MeVOs correctly as such. Most of the misclassified MeVOs on single-phase CTA (21/23 [91%], 16/22 [73%], and 22/24 [92%]) were erroneously classified as "no occlusion," while only very few were mistaken for LVOs. On mCTA, 48/56 (86%), 50/56 (89%), and 50/56 (89%) MeVOs were classified correctly, and most misclassified MeVOs (6/8 [75%], 4/6 [67%], and 5/6 [83%]) were misclassified as no occlusion. The Figure shows the proportion of MeVOs that were correctly classified as MeVOs, misclassified as LVOs, and misclassified as no occlusion on single-phase and multiphase CTA, stratified per occlusion site.

DISCUSSION

Interrater agreement for occlusion sites in this study was moderate when using single-phase CTA and almost perfect with mCTA. The accuracy of MeVO detection for all 3 readers ranged between 57% and 61% on single-phase CTA and improved to 86%–89% with mCTA.

In the past, it was thought that MeVO strokes resulted in relatively favorable clinical outcomes due to their more distal occlusion location and smaller ischemic tissue volume compared with LVOs. However, data from large, prospective cohort studies and a pooled meta-analysis from randomized trials showed that only half of the patients with MeVOs achieve a good functional outcome at

90 days with current best medical management.[12-14] Together with the high efficacy and safety of EVT in LVO stroke, this finding has led many physicians to routinely offer EVT for MeVO stroke.[4-6]

To offer the appropriate treatment, it is, however, necessary that MeVOs are quickly and reliably identified on imaging. Missing a MeVO on baseline imaging can lead to a delayed diagnosis or misdiagnosis, which may result in a patient not receiving intravenous thrombolysis or not getting transferred to a comprehensive stroke center for EVT. It may also cause misclassification of the patient's symptoms as a stroke mimic and, as a consequence, failure to initiate appropriate stroke work-up and secondary stroke-prevention measures. Unfortunately, recent data suggest that this scenario is not an uncommon one: Fasen et al[7] retrospectively reviewed 520 single-phase CTA studies of patients with clinically confirmed acute ischemic stroke and found that M2 occlusions, which are arguably the most easily detectable MeVOs, were 5 times more likely to be overlooked compared with LVOs and were missed in up to one-third of cases. Misses were most common when non-neuroradiologists and trainees interpreted the scans.[7]

We have recently commented on the potential value of mCTA in improving MeVO detection.[15] Indeed, our study showed an excellent interrater agreement and substantially higher detection accuracy for MeVOs with mCTA compared with single-phase CTA, suggesting that mCTA could be a valuable tool for MeVO detection. Innovative mCTA display formats, such as color-coded time-variant mCTA maps or mCTA tissue-level perfusion maps, may be able to facilitate MeVO detection even further, but they are not widely available yet.[15,16]

Given the complexity in the anatomic definition of MeVOs (for example, there are different ways to define the border between the M1 and M2 segments of the MCA[8]), one may suspect that some MeVOs will be misclassified as LVOs. This is particularly problematic because establishing high-level evidence for MeVO EVT in randomized trials requires an accurate, reliable, and reproducible MeVO definition as part of the trial inclusion criteria. However, in our study, most misclassified MeVOs were not mistaken for LVOs but rather erroneously classified as no occlusion, suggesting that the problem of distinguishing MeVOs from LVOs is only a minor one and confirming that the MeVO definition that was previously suggested by our group[1] and has been used in the current study could potentially be used as a randomized trial inclusion criterion. Furthermore, detection of occlusion of any kind will lead to the correct diagnosis of acute ischemic stroke and trigger appropriate treatment with IV thrombolysis and potentially EVT; in other words, mistaking an MeVO as an LVO is not as fatal as missing it altogether.

The added radiation dose of 1.0 mSv for the 2 additional phases that are obtained in multiphase CTA slightly increases the mean effective dose for a CT-based acute ischemic stroke imaging protocol from 7.0 to 8.0 mSv, and it is generally deemed acceptable, given the severity of the condition.[9]

Limitations

This study has limitations. First, there is controversy about the exact anatomic definition of the M1 versus the M2 segment, and the situation is arguably even more complex in the anterior and posterior cerebral arteries, in which anatomy is even more variable [17] and includes variants such as an azygos anterior cerebral artery and fetal origin of the posterior cerebral artery. Nevertheless, this variability simply reflects the clinical reality, and some disagreement in distinguishing MeVOs versus LVOs is, therefore, expected. Second, we chose to compare single-phase CTA with mCTA because they are closely related in their acquisition technique, have identical contrast doses and comparable radiation doses, and can be performed without any postprocessing software.[9] We did not include other imaging modalities such as CT perfusion or MR imaging and are, therefore, not able to comment on the value of these imaging modalities for MeVO assessment. Third, not all MeVO sites were represented in this study; for example, we could not include any cases of P3 occlusion simply because they did not occur in our dataset. Fourth, the readers in this study relied exclusively on single-phase CTA and mCTA to assess occlusion sites and did not have access to any other imaging or clinical information, while in a real-world scenario, the reader will almost always have access to clinical information and baseline noncontrast CT. However, one could argue that access to this information may, if anything, have improved the readers' performance. Last, distinguishing between MeVOs and LVOs, which was part of the current study, while being critically important for randomized MeVO trials, may be only of limited usefulness in clinical practice once the safety and efficacy of MeVO EVT has been proven.

CONCLUSIONS

Interrater agreement for MeVOs is moderate when using single-phase CTA and almost perfect with mCTA. The accuracy of MeVO detection is higher with mCTA compared with single-phase CTA, suggesting that mCTA might be a valuable tool that allows reliable diagnosis of MeVO stroke.

ACKNOWLEDGMENTS

The authors are most grateful to all enrolling sites.

Disclosure forms provided by the authors are available with the full text and PDF of this article at www.ajnr.org.

REFERENCES

1. Goyal M, Ospel JM, Menon BK, et al. **MeVO: the next frontier?** *J Neurointerv Surg* 2020;12:545–47 CrossRef Medline
2. Duloquin G, Graber M, Garnier L, et al. **Incidence of acute ischemic stroke with visible arterial occlusion: a population-based study (Dijon Stroke Registry).** *Stroke* 2020;51:2122–30 CrossRef Medline
3. Saver JL, Chapot R, Agid R, et al; Distal Thrombectomy Summit Group. **Thrombectomy for distal, medium vessel occlusions: a consensus statement on present knowledge and promising directions.** *Stroke* 2020;51:2872–84 CrossRef Medline
4. Almekhlafi M, Ospel JM, Saposnik G, et al. **Endovascular treatment decisions in patients with M2 segment MCA occlusions.** *AJNR Am J Neuroradiol* 2020;41:280–85 CrossRef Medline
5. Cimflova P, Kappelhof M, Singh N, et al. **Factors influencing thrombectomy decision making for primary medium vessel occlusion stroke.** *J Neurointerv Surg* 2021 May 5 [Epub ahead of print] CrossRef Medline

6. Kappelhof M, Ospel J, Kashani N, et al**. Influence of intravenous alteplase on endovascular treatment decision-making in acute ischemic stroke due to primary medium-vessel occlusion: a case-based survey study.** *J Neurointerv Surg* 2021 May 25 [Epub ahead of print] CrossRef Medline
7. Fasen B, Heijboer RJJ, Hulsmans FH, et al. **CT angiography in evaluating large-vessel occlusion in acute anterior circulation ischemic stroke: factors associated with diagnostic error in clinical practice.** *AJNR Am J Neuroradiol* 2020;41:607–11 CrossRef Medline
8. Goyal M, Menon BK, Krings T, et al. **What constitutes the M1 segment of the middle cerebral artery?** *J Neurointerv Surg* 2016;8:1273–77 CrossRef Medline
9. Menon BK, d'Esterre CD, Qazi EM, et al. **Multiphase CT angiography: a new tool for the imaging triage of patients with acute ischemic stroke.** *Radiology* 2015;275:510–20 CrossRef Medline
10. Fleiss JL, Cohen J. **The equivalence of weighted kappa and the intraclass correlation coefficient as measures of reliability.** *Educational and Psychological Measurement* 1973;33:613–19 CrossRef
11. Hartling LH, Milne A. **Validity and inter-rater reliability testing of quality assessment instruments.** https://www.ncbi.nlm.nih.gov/books/NBK92295/table/methods.t2/. Accessed August 9, 2021
12. Lima FO, Furie KL, Silva GS, et al. **Prognosis of untreated strokes due to anterior circulation proximal intracranial arterial occlusions detected by use of computed tomography angiography.** *JAMA Neurol* 2014;71:151–57 CrossRef Medline
13. Menon BK, Hill MD, Davalos A, et al. **Efficacy of endovascular thrombectomy in patients with M2 segment middle cerebral artery occlusions: meta-analysis of data from the HERMES Collaboration.** *J Neurointerv Surg* 2019;11:1065–69 CrossRef Medline
14. Ospel JM, Menon BK, Demchuk AM, et al. **Clinical course of acute ischemic stroke due to medium vessel occlusion with and without intravenous alteplase treatment.** *Stroke* 2020;51:3232–40 CrossRef Medline
15. Ospel JM, Qiu W, Goyal M. **Missed medium-vessel occlusions on CT angiography: make it easier ... easily!** *AJNR Am J Neuroradiol* 2020;41:E73–74 CrossRef Medline
16. Ospel JM, Volny O, Qiu W, et al. **Displaying multiphase CT angiography using a time-variant color map: practical considerations and potential applications in patients with acute stroke.** *AJNR Am J Neuroradiol* 2020;41:200–05 CrossRef Medline
17. van der Zwan A, Hillen B, Tulleken CA, et al. **Variability of the territories of the major cerebral arteries.** *J Neurosurg* 1992;77:927–40 CrossRef Medline

Mechanical Thrombectomy for Treatment of Cerebral Venous Sinus Thrombosis in Vaccine-Induced Immune Thrombotic Thrombocytopenia

H.S. Chew, S. Al-Ali, B. Butler, D. Rajapakse, K. Nader, S. Chavda, and S. Lamin

ABSTRACT

SUMMARY: Reports of a rare form of cerebral venous sinus thrombosis with profound thrombocytopenia have emerged following introduction of the adenovirus-vectored coronavirus disease 2019 (COVID-19) vaccines. Between March and June 2021, seven cases of refractory vaccine-induced immune thrombotic thrombocytopenia were referred to our institution for mechanical thrombectomy. The condition of 1 patient deteriorated during interhospital transfer, and the remaining 6 underwent successful recanalization. No procedure-related adverse events were reported. At the time of this writing, 3 patients have been discharged with a good functional outcome (mRS 0–1), one required rehabilitation for mild dysarthria and vocal cord palsy (mRS 3), and 2 have died due to severe mass effect. Our anecdotal experience suggests that endovascular therapy may be safe and effective in reducing thrombus burden in selected cases of postvaccination cerebral venous sinus thrombosis.

ABBREVIATIONS: COVID-19 = coronavirus disease 2019; CVST = cerebral venous sinus thrombosis; HIT = heparin-induced thrombocytopenia; ICH = intracerebral hemorrhage; PF = platelet factor; VITT = vaccine-induced immune thrombotic thrombocytopenia

Vaccine-induced immune thrombotic thrombocytopenia (VITT), also known as thrombosis with thrombocytopenia syndrome, is a rare disorder of immune-driven thrombosis and thrombocytopenia linked to coronavirus disease 2019 (COVID-19) vaccines, which use adenoviral vectors to deliver the spike protein–producing genes. Initially reported after the AstraZeneca COVID-19 vaccination in Europe, similar cases also occurred after receipt of Janssen/Johnson & Johnson COVID-19 vaccines in the United States.[1] The condition shares a mechanism similar to that of spontaneous heparin-induced thrombocytopenia (HIT), without heparin exposure as a trigger. HIT is a highly prothrombotic condition that develops 4–10 days after heparin exposure, leading to widespread platelet activation triggered by formation of antibodies against the platelet factor (PF)-4 complex. As with HIT, individuals with VITT also produce similar antibodies that bind to platelets via the Fc γ RIIA receptors. It remains unclear which component of the vaccine is responsible for the production of anti-PF-4 antibodies.[2]

As of June 30, 2021, the UK regulators received 399 reports of major thromboembolic events following AstraZeneca COVID-19 vaccination. There is a high predilection for cerebral venous sinus thrombosis (CVST), affecting more than one-third of reported cases (142, 35.6%), with a higher incidence in younger adult groups (average, 46 years of age).[3] Review of recent cases has prompted the Joint Committee on Vaccination and Immunisation to recommend that those younger than 40 years of age in the UK be offered an alternative COVID-19 vaccine.[4]

There are no robust clinical data at the time of this writing to inform treatment of VITT. The British Society for Haematology issued guidance based on the experience of managing initial cases and alternative similar conditions. Estimates to date suggest that patients who develop CVST are more likely to have a fatal outcome with conventional treatment.[5] The aim of this case series was to report our experience with mechanical thrombectomy in the management of severe postvaccination CVST.

MATERIALS AND METHODS

Seven confirmed cases of VITT presenting with refractory CVST were referred to our institution for consideration of endovascular treatment between March 16 and June 10, 2021. Symptom onset ranged between 10 and 14 days after receiving at least 1 dose of the AstraZeneca vaccine. Systemic anticoagulation and immune-modulation therapy had been initiated before patients were accepted for intervention. Of the 6 patients with intracranial bleeds, 5 presented with reduced Glasgow Coma Score and required intubation

Received July 23, 2021; accepted after revision September 30.

From the Department of Neuroradiology, Queen Elizabeth Hospital Birmingham, Birmingham, UK.

Please address correspondence to Han Seng Chew, MD, Department of Neuroradiology, Queen Elizabeth Hospital Birmingham, Mindelsohn Way, Edgbaston, B15 2GW Birmingham, UK; e-mail: hanseng.chew@uhb.nhs.uk

Indicates open access to non-subscribers at www.ajnr.org

Indicates article with online supplemental data.

http://dx.doi.org/10.3174/ajnr.A7381

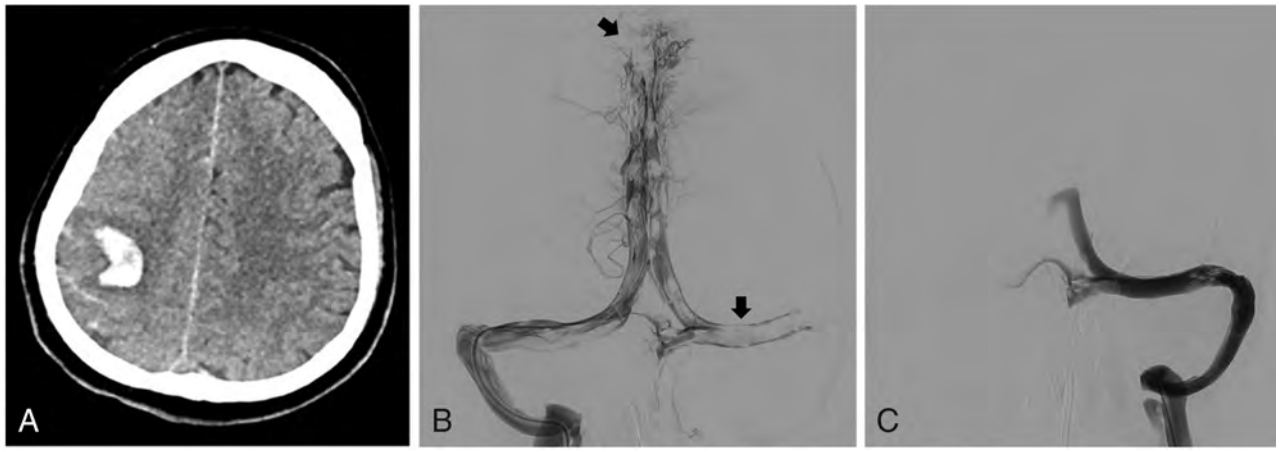

FIGURE. *A*, Axial CT of the head of patient 1 demonstrates focal ICH in the right frontal lobe with acute sulcal blood. *B*, Anterior-posterior view of a selective injection confirms extensive filling defects in the superior sagittal, left transverse, and sigmoid sinus. *C*, Complete recanalization of the left transverse and sigmoid sinuses after the final pass.

before interhospital transfer. The only patient without intracerebral hemorrhage (ICH) was accepted for treatment on the basis of evidence of clot extension on serial imaging.

Technical Details

Venous access was obtained by inserting an 8F short sheath into the right femoral vein, followed by navigating a 90-cm Neuron Max long sheath (Penumbra) to the sigmoid sinus. A large-bore reperfusion catheter was advanced into the superior sagittal sinus over a Velocity microcatheter (Penumbra). Clot extraction was performed with a 6-mm-diameter stent retriever along with concurrent suction through the reperfusion catheter at the clot face. The process was repeated until successful recanalization of the venous sinus was achieved (Figure).

The procedure was performed without reversing the anticoagulation therapy. Nearly all our patients had platelet counts lower than the safe threshold recommended for high-risk interventional procedures (50×10^9/L).[6] Several precautionary measures were taken to minimize the risk of hemorrhagic complications. The intracatheter heparin flush was switched off when the catheter system engaged the thrombus to keep the total amount of heparin infusion to a minimum. Selective ICA injection to assess cerebral capillary filling and venous drainage was not performed because this would require an additional arterial puncture. For the first 2 cases, the femoral short sheath was sutured to the skin and removed at the bedside 24 hours later to avoid groin hemorrhage. In subsequent cases, the short sheath was replaced with a Vascath catheter to facilitate plasma exchange therapy. Intrasinus thrombolysis was avoided due to the uncertain effect of thrombolytic agents in the presence of platelet-activating antibodies.

RESULTS

The mean age of patients was 40 years (range, 26–49 years). The male/female ratio was 4:3. The median interval from vaccination to admission was 12 days (range, 10–14 days). One female patient was on oral contraceptives. No other thrombotic risk factors were identified. Five patients (71%) had reduced Glasgow Coma Score at the time of referral, and three (43%) presented with mass effect and midline shift on imaging before endovascular therapy. Six of 7 patients were found to have severe thrombocytopenia ($< 50 \times 10^9$/L) on admission (range, 11–91 $\times 10^9$/L). Two patients with platelet counts lower than 20×10^9/L developed a purpuric skin rash and hematuria resembling immune thrombocytopenic purpura.

The condition of 1 patient deteriorated during interhospital transfer despite neuroprotective measures. Repeat CT imaging on arrival showed global cerebral edema far too advanced for any interventional procedures. The remaining 6 patients underwent successful endovascular therapies. Thrombectomy was performed with the patient under general anesthesia in 4 patients and local anesthesia with conscious sedation in the other 2. The mean procedural time was 100 minutes (range, 80–145 minutes). On average, 5.7 passes were made per patient (range, 4–7 passes).

Treatment Outcome

Satisfactory recanalization was achieved in all except 1 patient in whom the posterior segment of the superior sagittal sinus showed partial recanalization at the end of the procedure. No procedure-related adverse events were recorded. Two patients underwent decompressive craniectomy following endovascular treatment. In the first case, mechanical thrombectomy and decompressive craniectomy were performed in the same session because the head CT on admission demonstrated severe mass effect with midline shift. The second patient developed progressive lobar ICH and worsening mass effect, despite successful clot retrieval. Decompressive craniectomy was performed within 12 hours post-endovascular treatment. At the time of this writing, 3 (50%) patients were discharged with a good functional outcome (mRS 0–1), one (16.6%) required rehabilitation for mild dysphasia and vocal cord palsy leading to swallowing difficulty (mRS 3), and two (33.3%) died due to severe mass effect. Both patients who died following thrombectomy showed ICH with a midline shift on the initial head CT.

No reclotting of the superior sagittal sinus was identified on follow-up imaging. Recurrent transverse and sigmoid sinus

thromboses were confirmed in 2 patients. In the first case, the thrombus completely resolved on subsequent imaging. The second patient received prophylactic platelet transfusion before decompressive craniectomy and developed refractory thrombocytopenia warranting multiple sessions of plasma-exchange therapies. Repeat CT venography showed absent venous flow in the left transverse sinus and sigmoid sinus without further clot extension. Both patients made a good recovery.

DISCUSSION

VITT is a newly described syndrome characterized by thrombosis, thrombocytopenia, and markedly raised serum D-dimer levels. Symptom onset ranges from 5 to 30 days after initial exposure to adenovirus-vectored vaccines.[5,7] On the basis of the current UK data, the condition appears to affect patients of all ages and both sexes, with no clear signal of risk factors. Most developed CVST after receiving the first dose of the AstraZeneca vaccine; however, a small number of cases occurred after the second dose. Typical laboratory features included a platelet count of $<150 \times 10^9$/L, D-dimer levels of >4000 mcg/L, and low serum fibrinogen levels. Positive findings on the PF-4 antibody enzyme-linked immunosorbent HIT assay are required to confirm the diagnosis.

There is no evidence-based advice on the treatment of postvaccine CVST due to the novelty of the vaccines. The Expert Haematology Panel recommends commencing intravenous immunoglobulin and systemic anticoagulation with non-heparin-based anticoagulants in all suspected cases while awaiting a confirmatory diagnosis. Because the syndrome mimics HIT, all forms of heparin, including heparinized saline flushes, are best avoided until further evidence becomes available. Patients on treatment should have serial platelet counts to monitor disease activity and treatment response. Early use of plasma exchange is recommended in those with platelet counts lower than 30×10^9/L, who often have high levels of circulating anti-PF-4 antibodies. Repeat plasma exchange may be required if platelet recovery is slow.

Both arterial and venous thromboses at multiple organ sites have been reported. However, a significant proportion of patients with VITT developed thrombosis in the cerebral venous sinus system. This group of patients is more likely to have a poor outcome, with a tendency toward rapid progression to life-threatening hemorrhage and relevated intracranial pressure. Of 213 cases of postvaccination CVST reported to the European Medicines Agency,[8] 49% of patients in the AstraZeneca group who developed refractory CVST died compared with a 13% death rate in standard CVST.[9] A web-based survey involving all departments of neurology in Germany reported an 18.3% mortality rate among patients with CVST within 1 month from the administration of the first dose of COVID-19 vaccines.[10] In the US series, ICH occurred <48 hours after admission, and the median time from admission to death was 1 day.[1] Similar observations can be made in our cohort: All fatal cases developed intraparenchymal hemorrhage in <12 hours after the first head CT with normal findings and died within 48 hours after hospitalization.

The mechanism responsible for rapid deterioration following the onset of ICH is not fully understood. This may be partly attributed to severe thrombocytopenia associated with VITT. A recently published prospective study involving 294 patients in the UK identified the baseline platelet count and the presence of ICH as being independently associated with death.[11] A mortality rate of 73% was observed among those who presented with platelet counts below 30×10^9/L and ICH. The risk/benefit ratio of anticoagulation therapy needs to be carefully balanced in patients with severe thrombocytopenia. Switching to a low-dose anticoagulant may be appropriate when the platelet count is lower than 30×10^9/L. Platelet transfusion for correction of thrombocytopenia is likely to fuel further thrombosis and, therefore, should only be considered in life-threatening hemorrhage. The location of the thrombosis also appears to have a significant impact on patient outcomes. In our series, 3 of 4 patients who presented with complete occlusion of the superior sagittal sinus had bilateral ICH leading to fatal outcomes.

Decompressive craniectomy may be life-saving in the presence of a raised ICP and impending brain herniation.[12] In cases in which neurosurgical intervention is indicated, prophylactic platelet transfusion and reversal of systemic anticoagulation are essential in preventing a catastrophic perioperative bleed.[13] Patients should be monitored closely for signs of clot propagation following decompressive surgery.

Role of Mechanical Thrombectomy

Because most published data come from small case series, there is limited knowledge about the appropriate indications and timing of endovascular treatment in standard CVST. A systemic review of 185 cases of mechanical thrombectomy published in 2015 showed that 60% of patients had a pretreatment ICH and 40% were comatose.[9] A recently published multicenter, randomized blind-ended trial involving 67 patients between 2011 and 2016 reported that mechanical thrombectomy with standard medical care did not improve functional outcome in patients with severe CVST.[14] The investigators, however, acknowledged that future studies using different methods of patient selection and endovascular techniques may identify better patient outcomes. In the absence of convincing evidence, endovascular intervention is largely reserved for severe CVST not responding to conventional therapy.[15]

Nearly all patients in our series had developed an intracranial bleed by the time referrals were made. Within 48 hours after hospitalization, 3 died due to severe mass effect, including the one whose condition deteriorated during interhospital transfer. The sample size of this case series is too small to determine whether endovascular therapy has a positive effect on the treatment outcome of refractory CVST. Given the high probability of rapid progression to life-threatening ICH, we recommend transferring patients presenting with heavy clot burden and severe thrombocytopenia to a tertiary center for consideration of early plasma-exchange therapy and endovascular treatment when there is evidence of clinical or radiologic deterioration. For those who are clinically stable on admission, judicious use of CT/MR venography may detect silent clot propagation before the collateral pathways become overwhelmed.

Our anecdotal experience suggests that mechanical thrombectomy can be safely performed without prophylactic platelet transfusion and reversal of anticoagulation treatment. Recent

advancements in catheter-tracking technologies and stent retriever designs improve the rate of recanalization in patients with acute stroke. New-generation stent retrievers tend to be less stiff compared with older devices (eg, AngioJet; Boston Scientific), allowing the operator to complete procedures with higher degrees of recanalization within shorter timeframes. Most commercially available stent retrievers and reperfusion catheters are designed for arterial thrombectomy. Purpose-built devices with larger diameters to match the caliber of venous sinus systems may improve the recanalization rate at challenging locations such as sigmoid sinuses and jugular bulbs.

CONCLUSIONS

Management of VITT-induced CVST requires multidisciplinary care with joint input from hematology, neurology, neuroradiology, and neurosurgery. These patients are best managed at neuroscience centers with access to neurointerventional and neurosurgical expertise. There is currently insufficient data to assess the efficacy of endovascular treatment in vaccine-induced CVST due to the rarity of the condition. Mechanical thrombectomy is effective in achieving a rapid reduction in clot burden while awaiting immune-modulation therapy to neutralize platelet-activating antibodies. As new evidence emerges, treatment recommendations are expected to change. Our anecdotal experience suggests that mechanical thrombectomy is a relatively safe treatment technique with a high degree of angiographic recanalization. When appropriate expertise is available, early mechanical thrombectomy can be considered in patients with VITT with severe thrombocytopenia and heavy clot burden to alleviate raised intracranial pressure.

Disclosure forms provided by the authors are available with the full text and PDF of this article at www.ajnr.org.

REFERENCES

1. See I, Su JR, Lale A, et al. **US case reports of cerebral venous sinus thrombosis with thrombocytopenia after Ad26.COV2.S vaccination, March 2 to April 21, 2021.** *JAMA* 2021;325:2448–56 CrossRef Medline
2. Makris M, Pavord S, Lester W, et al. **Vaccine-induced immune thrombocytopenia and thrombosis (VITT).** *Res Pract Thromb Haemost* 2021;5:e12529 CrossRef Medline
3. **Coronavirus vaccine: weekly summary of Yellow Card reporting: Updated 26 November 2021.** https://www.gov.uk/government/publications/coronavirus-covid-19-vaccine-adverse-reactions/coronavirus-vaccine-summary-of-yellow-card-reporting. Accessed June 1, 2021
4. **JCVI advises on COVID-19 vaccine for people aged under 40.** https://www.gov.uk/government/news/jcvi-advises-on-covid-19-vaccine-for-people-aged-under-40. Accessed June 1, 2021
5. **Guidance from the Expert Haematology Panel (EHP) on Covid-19 Vaccine-induced Immune Thrombocytopenia and Thrombosis (VITT): 28 May 2021.** https://b-s-h.org.uk/media/19718/guidance-v20-20210528-002.pdf. Accessed June 1, 2021
6. Patel IJ, Davidson JC, Nikolic B, et al; Standards of Practice Committee, with Cardiovascular and Interventional Radiological Society of Europe (CIRSE) Endorsement. **Consensus guidelines for periprocedural management of coagulation status and hemostasis risk in percutaneous image-guided interventions.** *J Vasc Interv Radiol* 2012;23:727–36 CrossRef Medline
7. Greinacher A, Thiele T, Warkentin TE, et al. **Thrombotic thrombocytopenia after ChAdOx1 nCov-19 vaccination.** *N Engl J Med* 2021;384:2092–101 CrossRef Medline
8. Krzywicka K, Heldner MR, Sánchez van Kammen M, et al. **Post-SARS-CoV-2-vaccination cerebral venous sinus thrombosis: an analysis of cases notified to the European Medicines Agency.** *Eur J Neurol* 2021;28:3656–62 CrossRef Medline
9. Siddiqui FM, Dandapat S, Banerjee C, et al. **Mechanical thrombectomy in cerebral venous thrombosis: systematic review of 185 cases.** *Stroke* 2015;46:1263–68 CrossRef Medline
10. Schulz JB, Berlit P, Diener HC, et al. German Society of Neurology SARS-CoV-2 Vaccination Study Group. **COVID-19 vaccine-associated cerebral venous thrombosis in Germany.** *Ann Neurol* 2021;90:6273–39 CrossRef Medline
11. Pavord S, Scully M, Hunt BJ, et al. **Clinical features of vaccine-induced immune thrombocytopenia and thrombosis.** *N Engl J Med* 2021;385:1680–89 CrossRef Medline
12. Ferro JM, Bousser MG, Canhão P, et al; European Stroke Organization. **European Stroke Organization guideline for the diagnosis and treatment of cerebral venous thrombosis: endorsed by the European Academy of Neurology.** *Eur J Neurol* 2017;24:1203–13 CrossRef Medline
13. **Management of cerebral venous sinus thrombosis following Covid-19 vaccination: a neurosurgical guide.** https://www.rcseng.ac.uk/-/media/files/rcs/coronavirus/cvstguide_––1942020.pdf. Accessed June 1, 2021
14. Coutinho JM, Zuurbier SM, Bousser M, et al; TO-ACT investigators. **Effect of endovascular treatment with medical management vs standard care on severe cerebral venous thrombosis: the TO-ACT Randomized Clinical Trial.** *JAMA Neurol* 2020;77:966–73 CrossRef Medline
15. Ilyas A, Chen C, Raper DM, et al. **Endovascular mechanical thrombectomy for cerebral venous sinus thrombosis: a systematic review.** *J Neurointerv Surg* 2017;9:1086–92 CrossRef Medline

4D Flat Panel Conebeam CTA for Analysis of the Angioarchitecture of Cerebral AVMs with a Novel Software Prototype

F. Keil, A. Bergkemper, A. Birkhold, M. Kowarschik, S. Tritt, and J. Berkefeld

ABSTRACT

BACKGROUND AND PURPOSE: Time-resolved 3DRA (4D-DSA) and flat panel conebeam CTA are new methods for visualizing the microangioarchitecture of cerebral AVMs. We applied a 4D software prototype to a series of cases of AVMs to assess the utility of this method in relation to treatment planning.

MATERIALS AND METHODS: In 33 patients with AVMs, 4D volumes and flat panel conebeam CTA images were recalculated from existing 3D rotational angiography data. The multiplanar reconstructions were used to determine intranidal arteriovenous branching patterns, categorize them according to common classifications of AVM angioarchitecture, and compare the results with those from 2D-DSA.

RESULTS: 4D flat panel conebeam CTA showed angioarchitectural features equal to or better than those of 2D-DSA in 30 of 33 cases. In particular, the reconstructions helped in understanding the intranidal microvasculature. Fistulous direct arteriovenous connections with a low degree of arterial branching ($n = 22$) could be distinguished from plexiform arterial networks before the transition to draining veins ($n = 11$). We identified AVMs with a single draining vein ($n = 20$) or multiple draining veins ($n = 10$). Arteriovenous shunts in the lateral wall of the draining veins ($n = 22$) could be distinguished from cases with increased venous branching and shunts between corresponding intranidal arteries and veins ($n = 11$). Limitations were the time-consuming postprocessing and the difficulties in correctly tracing intranidal vessels in larger and complex AVMs.

CONCLUSIONS: 4D flat panel conebeam CTA reconstructions allow detailed analysis of the nidal angioarchitecture of AVMs. However, further improvements in temporal resolution and automated reconstruction techniques are needed to use the method generally in clinical practice.

ABBREVIATIONS: AV = arteriovenous; CB = conebeam; fP = flat panel; 3DRA = 3D rotational angiography

Embolization as an interventional treatment option for cerebral AVMs requires a detailed understanding and accurate classification of the angioarchitecture of the nidus and its arterial and venous environment. On the basis of angiographic findings, we can separate arterial feeders from the nidus and the draining veins. MR imaging can show the anatomic location of the AVM and help to differentiate a compact from a diffuse nidus with normal brain tissue between the malformed vessels.

Received June 11, 2021; accepted after revision September 22.

From the Institute of Neuroradiology (F.K., A. Bergkemper., J.B.), University of Frankfurt, Frankfurt, Germany; Siemens Healthcare (A. Birkhold, M.K.), Forchheim, Germany; Advanced Therapies (A. Birkhold, M.K.), Siemens Healthcare, Forchheim, Germany; and Helios Dr. Horst Schmidt Kliniken Wiesbaden (S.T.), Wiesbaden, Germany.

Please address correspondence to Fee Keil, MD, Institute of Neuroradiology, University Hospital of Frankfurt am Main, Schleusenweg 2–16, D-60528 Frankfurt am Main, Germany; e-mail: Fee.Keil@kgu.de

Indicates article with online supplemental data.

http://dx.doi.org/10.3174/ajnr.A7382

Arterial branches terminating in the nidus are distinguished from small feeders as side branches of arteries passing the nidus and supplying the brain parenchyma beyond.[1,2] Concerning the intranidal branching patterns, direct fistulous transitions between arteries and draining veins are differentiated from plexiform arterial networks before the shunt zone.[1,3] Single or multiple draining veins connected with the superficial or deep venous system are described as well as features like high flow (shunt volume), varicose enlargement, or stenosis of the draining veins. Perinidal arterial networks are regarded as separate from the nidus. Pre-, intranidal, or venous aneurysms could be associated with the AVM.[2,4-6]

Most of these angioarchitectural features are detectable by means of 2D-DSA with high spatial and temporal resolution. However, overlapping vessels on DSA projection images may obscure details of the intranidal microvasculature. Vessel overlaid on projection images can be reduced by superselective angiography after catheterization of the nidus with a microcatheter. Due

to its invasiveness and need for general anesthesia, superselective angiography is hardly applicable for pretherapeutic diagnostic purposes. In most instances, it is used during embolization procedures immediately before the injection of embolic agents,[4]

Since the A Randomised Trial of Unruptured Brain Arteriovenous Malformations (ARUBA) proved high complication rates of AVM therapy,[7] we have to ask whether our pretherapeutic understanding of AVM anatomy is good enough for planning safe and effective treatment. With increasing efficacy of embolic agents like Onyx (Covidien) for transarterial or transvenous AVM embolizations, exact visualization of the transition zone between arteries and veins in different nidal compartments becomes essential to achieve a controlled occlusion of the shunt. Accidental occlusion of arteries supplying normal brain or occlusion of the draining vein without control over the arterial part of the nidus must be avoided.[8]

There is a lack of publications concerning clear pathoanatomic descriptions of the intranidal microvasculature. Considerable disagreement between different reviewers concerning the extent and type of the nidus has been described.[9] On the basis of MR imaging and DSA, current grading systems use rather simple criteria without detailed analysis of the angioarchitecture.[10,11]

According to the described limitations of DSA and superselective angiography, we have to think about new imaging approaches: 3D rotational angiography (3DRA) and derived flat panel CT reconstructions, MR imaging, MRA, and CTA have no temporal resolution, and anatomic details may be missed due to overlapping of arteries and veins. In a pilot study, we showed that multiplanar reconstructions from time-resolved 3DRA (4D-DSA) data sets may have the potential for more detailed analysis of arteriovenous (AV) shunts.[12]

Use of a new software prototype for 4D reconstruction promised an improved visualization of the consecutive filling of arteries and veins. It was the aim of this study to analyze a variety of AVMs to determine whether 4D-DSA and flat panel conebeam CTA (4D-fPCBCTA) reconstructions with the novel software prototype could better visualize angioarchitectonic features of AVMs. Furthermore, we wanted to know whether 4D findings met the above-mentioned AVM classification criteria and to discuss the additional value for treatment planning compared with 2D-DSA.

MATERIALS AND METHODS

The novel software prototype was used to recalculate 4D-DSA volumes and 4D-fPCBCTA reconstructions from existing 3DRA data sets obtained during diagnostic angiography of patients with AVMs, which was part of our routine protocol for diagnostic work-up. The study protocol was approved by ethics committee of the Department of Medicine, University Hospital of the Goethe University.

For this retrospective study, we analyzed 38 data sets of consecutive patients with cerebral pial AVMs and indications for pretherapeutic 3DRA obtained between 2016 and 2019. All 4D reconstructions with sufficient image quality were included into this study. We excluded data sets with movement artifacts ($n = 3$) or incomplete examinations ($n = 2$).

3DRA was obtained on a modified Artis zee biplane angiography system (Siemens) using an increased 260° rotation angle of the frontal C-arm during a scan time of 12 seconds, which is intended to capture both arterial inflow and venous outflow. Acquisition consisted of 2 runs (a native run without contrast and a fill run with contrast) with 304 projection (0.85°/frame) images. In the second run, an x-ray delay of 2 seconds after automatic injection of a bolus of 20 mL of nonionic contrast material (iopromide, Ultravist 300; Bayer HealthCare) with a flow of 3 mL/s was used.

4D reconstructions (time-resolved 3D-DSA, 4D-DSA) were calculated after digital subtraction on a dedicated workstation (syngo X Workplace VD20; Siemens) with the use of a new software prototype developed by Siemens, comprising an additional postprocessing step compared with a version described in a first pilot study.[12] In this step, a physically motivated, plausibility-based flow constraint on the 4D reconstruction process required that a certain vessel segment can only be contrast-enhanced under certain conditions to reduce artifacts of incorrect/nonphysiologic vessel enhancement (due to vascular overlap).

4D-DSA uses the temporal information of 3DRA for reconstruction of 3D volumes at any given time point during the scan time. For evaluation and comparison with 2D-DSA, we used volume-rendering data sets with a display of virtual DSA images in arbitrary projections including a "working projection" showing the best feeding arteries, nidus, and draining veins (Fig 3). To reduce the overlay, we analyzed multiplanar reconstructions in 3 standard planes (coronal, sagittal, transversal) and a working projection to demonstrate intranidal, arterial, and venous branching patterns. Section thicknesses were chosen between 2.5 and 6.5 mm, depending on vessel diameters and degree of branching at the transition zone to the draining veins. The time points with the best display of intranidal vessels and veins were selected according to a cine loop of 100 reconstructed 3D volumes during the scan time. Assessment of the arterial part was favorable during the first 3 seconds; display of the veins was best at the end of the loop.

To determine the anatomic location of the AVM, we used MR imaging or fusion images between 4D-fPCBCTA reconstructions and MR imaging.[13]

We started the analysis with evaluation of 4D-fPCBCTA findings without consideration of 2D-DSA images or reports. Comparison with 2D-DSA images was performed in a second step without additional consideration of 3D-fPCBCTA reconstructions. All data sets, including 2D-DSA, were re-evaluated by a consensus by 2 reviewers.

The AVMs were characterized by following criteria:

- Anatomic location: superficial, deep, posterior fossa; sulcal, parenchymal, mixed
- Size of the nidus: $\leq 3/\leq 6$ cm / > 6 cm
- Venous drainage: superficial/deep
- Spetzler-Martin grade
- Rupture status.

Angioarchitectonic features were evaluated according to 4D volumes and 4D-fPCBCTA data:

- Arterial feeders: number, terminal, en passage, mixed

site of shunt	venous sidewall	venous sidewall	corresponding AV branches
AV-transition	fistulous	plexiform arterial network microfistulas to vein	plexiform arterial network multiple collecting veins
arterial branching	no or low	high	high
venous branching	no or low	no or low	high

FIG 1. Schematic drawing of 4D-fPCBCTA findings in cases of AVMs to characterize different types of intranidal AV shunts and intranidal branching patterns (modified according to the classification of Houdart et al[3]).

- Nidus arterial: fistulous with single or multiple direct connections to a draining vein with no or a low degree of arterial branching versus a plexiform arterial network prior to the transition into the draining vein
- Nidus venous: single-versus-several draining veins/degree of venous branching with confluent collectors
- Shunt type: sidewall/corresponding arterial and venous branches
- Draining veins: single, multiple, deep, superficial, venous stenosis, varicose enlargement, venous aneurysm
- Associated aneurysms: feeding artery/intranidal/venous.

In 5 patients treated by transarterial embolization, it was possible to compare 4D reconstructions with corresponding superselective angiograms. Due to the retrospective character of this study, the results of superselective catheterization were known to the reviewers.

RESULTS

Thirty-three 4D-DSA data sets from 33 patients, 18 men and 15 women with a mean age of 40 years (range, 18–77 years), fulfilled the inclusion criteria and were evaluable. Online Supplemental Data show the AVM characteristics.

Online Supplemental Data: AVM Characteristics

4D-fPCBCTA and 2D-DSA. Angioarchitectonic features were evaluable on 4D-fPCBCTA reconstructions in all 33 cases. Twenty-six of 33 data sets were evaluable in all aspects. In 7 cases, we had problems separating the arterial and venous portions of the shunt zone due to overlapping of the angiographic phases. With 1 exception of a patient with a very small fistulous AVM, which was difficult to detect on MPR, this problem occurred in the analysis of high-flow AVMs with several feeders and tortuous draining veins that were difficult to follow on multiplanar reconstructions. Four of the total of 7 difficult to reconstruct AVM's were Spetzler-Martin grade III and IV. However, the other AVM's with Spetzler-Martin grade III and 4 could be evaluated without particular difficulty.

Simple features such as the number and course of arterial feeders and draining veins could be detected on 2D-DSA. In 16 of 33 AVMs, intranidal angioarchitecture was adequately evaluable with 2D-DSA. In the remaining 17 cases, the reviewers found that 4D-fPCBCTA provided additional findings regarding the intranidal vasculature that was obscured on projection images. In all cases, MR imaging or fusion images of MR imaging and 4D-fPCBCTA were needed to describe the exact anatomic location of the nidus and its relationship to the surrounding brain or CSF spaces.

Terminal and En Passage Feeders. Most of the AVMs had a limited number of 1–3 arterial feeders ($n = 25$). Multiple feeders were detected in 8, and extensive perinidal networks of pial arteries, in 6 cases. Twenty AVMs were supplied by a single artery or several arteries terminating in the nidus. Feeders en passage passing the AVM with small side branches to the nidus were visible in 8, and mixed patterns, in 5 cases, mostly in cases with parenchymal AVMs (Fig 3).

Intranidal Branching Patterns and Shunt Zone. 4D-fPCBCTA reconstructions detected fistulous connections with direct transition between intranidal arteries and draining veins and a low degree of arterial branching as a dominant pattern in 22 of 33 cases. In 11 patients, we observed plexiform arterial networks before the connection to the draining veins. AV shunts in the sidewall of the draining veins without or with only a few (up to 3) confluent venous branches were dominant in 19 AVMs. Shunts between corresponding arterial and venous branches of the nidus predominated in 14 AVMs with higher degrees of arterial and venous branching.

In AVMs with a single draining vein, fistulous shunts in the sidewall were detected in 15 of 24 cases. In 8 further cases with confluent branches to a single draining vein, the shunts occurred between corresponding arterial and venous branches. In 9 AVMs, we observed several draining veins with both types of AV

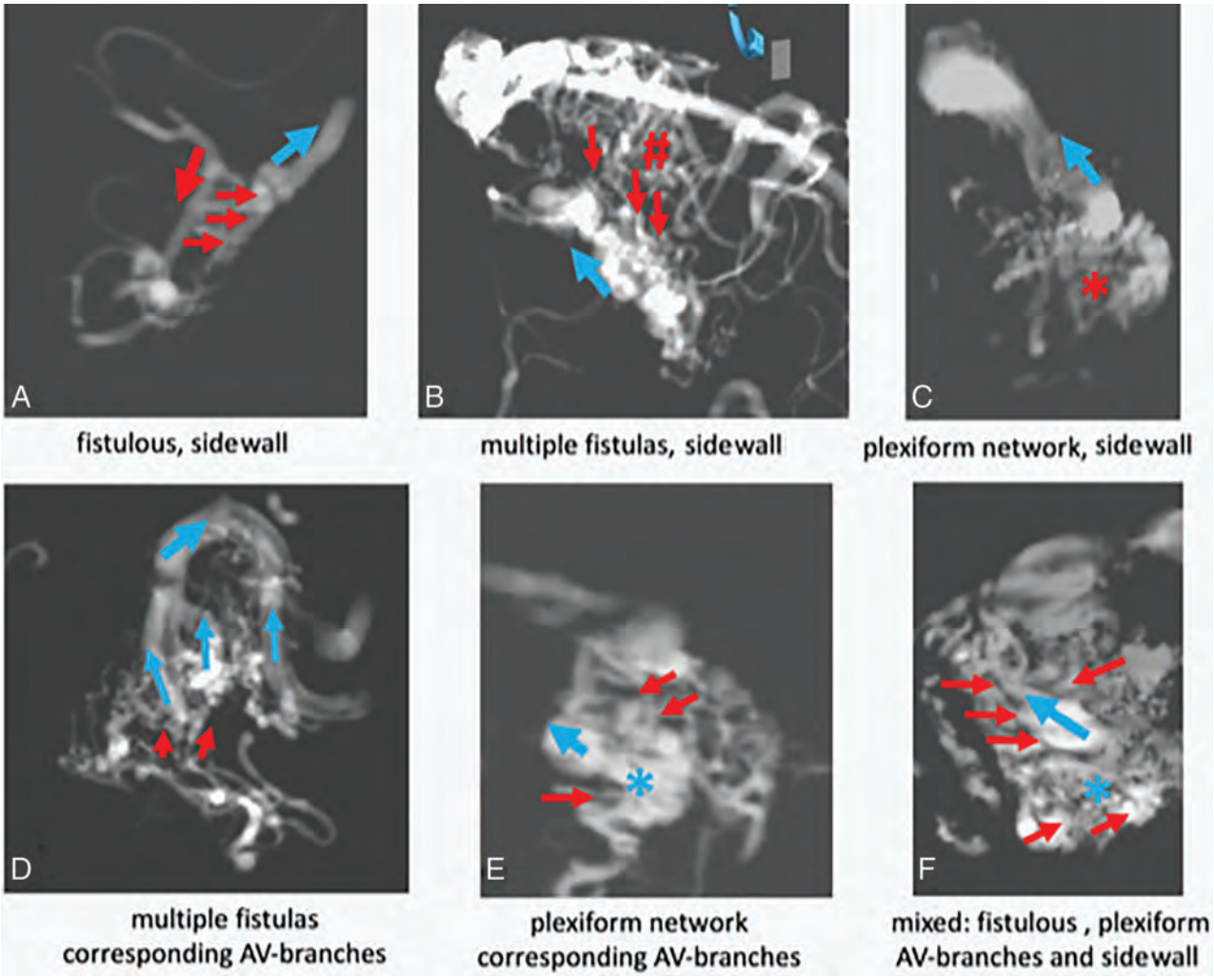

FIG 2. 4D-fPCBCTA reconstructions of the intranidal shunt zone to demonstrate different types of transitions between arterial and venous parts of the nidus in clinical cases: *A*, small AVM with several direct fistulas (*small red arrows*) between the feeding artery passing the nidus (large *red arrow*) to the sidewall of the draining vein (*blue arrow*). No arterial or venous branching. *B*, Multiple direct fistulas (*small red arrows*) to the sidewall of the tortuous draining vein (large *blue arrow*). Note the perinidal connections between the feeding arteries (*red hashtag*) in multiple fistulas, sidewall of Fig 2*B*. *C*, A plexiform arterial network (*red asterisk*) before multiple small shunts to the sidewall of the draining vein (*blue arrow*). *D*, Multiple fistulous connections between lenticulostriate arteries and corresponding branches of the thalamostriate vein in a basal ganglia AVM. *E*, A loose network of arterial branches with transition into corresponding venous branches connected to the compartmental draining vein (*blue asterisk and arrow*). *F*, A mixed pattern with multiple direct fistulas to the sidewall of the draining vein in the upper part of the nidus (*small red arrows*). A plexiform network of arterial branches with corresponding venous branches to a venous confluence (*blue asterisk*) connected to the draining vein (*blue arrow*) in the lower part of the nidus.

transitions (sidewall and confluent collecting venous branches). With the exception of 3 small fistulous AVMs with simple direct connections between the feeding arteries and veins without arterial and venous branching, mixed types between fistulous and plexiform arterial branching patterns and shunt types were observed (Table). Figure 1 shows a schematic drawing of 4D-fPCBCTA reconstructions of the different branching patterns; Fig 2 shows corresponding illustrative cases.

In 7 AVMs, different compartments with separate feeding branches and draining veins could be distinguished. Figure 3 shows a 3-compartment AVM with different branching patterns of the transitions between feeding arteries and draining veins. In this and 4 other cases, 4D-fPCTA analysis of the nidal angioarchitecture corresponded well to the findings of superselective angiograms before embolization (Fig 4).

Associated Aneurysms

AVM-associated pre- or intranidal aneurysms were detected in 5 cases (Online Supplemental Data). All aneurysms identified with 2D-DSA were also visible on 4D-DSA reconstructions. However, a targeted search is necessary to identify small intranidal aneurysms, aneurysms on the venous side, or fusiform aneurysms in the prenidal course of a feeder. Figure 4 shows a typical example with an intranidal aneurysm close to the transition between the arterial part of the nidus and the compartmental draining vein.

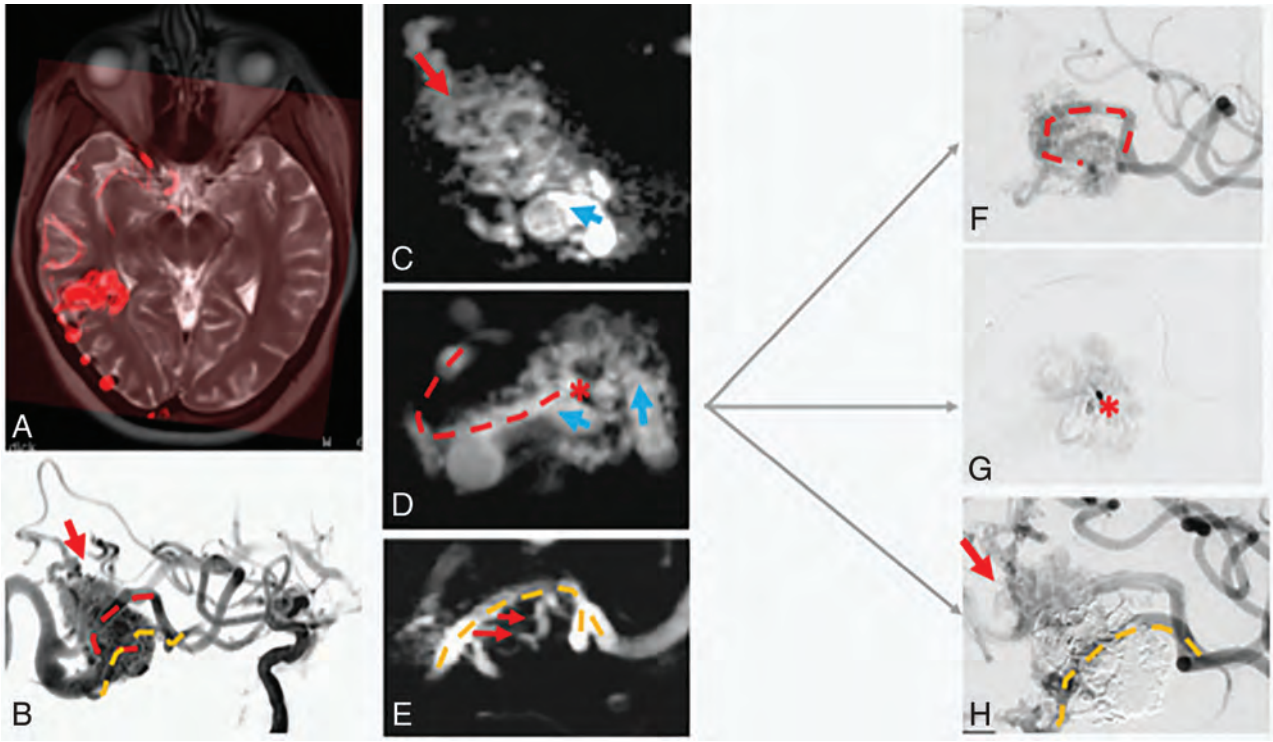

FIG 3. Angioarchitecture of the shunt zones of an AVM with a multicompartmental nidus. *A*, Fusion image between MR imaging and 4D-fPCTA shows a right, parietal, superficial AVM in a sulcus and adjacent parenchyma. *B*, 4D-volume data set presented in a virtual DSA mode with a "working projection" shows 3 main arterial feeders to the upper part of the nidus (*red arrow*) and to the middle (*red dotted line*) and lower (*orange dotted line*) compartments of the nidus. *C*, 4D-fPCBCTA reconstruction demonstrates the upper arterial feeder terminating in a plexiform arterial network before transition into the compartmental draining vein (*blue arrow*). *D*, Intranidal course of the main arterial feeder terminating in the middle compartment of the nidus (*red dotted line*, see also *B* and *F*). Intranidal arterial branching (*red asterisk*) with an arterial network and multiple small shunts in the sidewall of the draining vein (*blue arrows*). *E*, An other feeder passes the nidus (*orange dotted line*), giving off multiple side branches (*small red arrows*) connected to the arterial network of the nidus. *F*, 4D analysis corresponds well with 2D-DSA, with the main feeder terminating in the nidus (*red dotted line*). *G*, Superselective angiogram confirms the branching point to the arterial network *(red asterisk*). *H*, Occlusion of the compartment and the compartmental draining vein after injection of Onyx. The remaining nidus is fed by the upper feeder.

DISCUSSION

Our study confirmed findings from a first pilot project and showed that the application of 4D-DSA and 4D-fPCBCTA reconstructions for detailed analysis and classification of AVM is feasible. Compared with our first study,[12] the new software prototype provides an improved time-resolved visualization and facilitates separation between arterial and venous parts of the nidus. However, in complex AVM morphologies with several arterial feeders and draining veins, it was still difficult to follow the vessels and separate the arterial from the venous part of the nidus. As in any imaging approach for the analysis of AVM angioarchitecture, the 4D technique has limitations in the resolution of complex, overlapping vascular structures.

The simultaneous visualization of arteries and veins was not only a consequence of the AV shunt but also due to the overlap of the angiographic phases due to the scan time of 12 seconds and the requirement for a prolonged contrast bolus injected during >6 seconds to fill and visualize small vessels. Nevertheless, our method succeeded in selecting a suitable working projection and time of best filling of the nidus on virtual DSA reconstructions. Details of intranidal angioarchitecture could be visualized on time-resolved fPCBCTA MPRs in the working projection and in the 3 standard planes with variable section thicknesses and window settings, to reduce the complexity and overlay of vessels outside the nidus,

4D technique with the reconstruction options showed advantages over conventional angiographic imaging: It was possible to obtain most of the information from time-resolved reconstructions of a single 3DRA run. Our kind of 4D data analysis provided a more detailed display of the angioarchitecture of the nidus than previous publications dealing with less complex features like the number of arterial feeders, the size of the nidus, the presence of associated aneurysms, and the number of draining veins.[14-16] Beyond these findings, we could add more information for a detailed description of the transition between feeding arteries and the nidus, branching patterns within the shunt zone, and intranidal compartments with corresponding feeders and draining veins. Our findings met the criteria of AVM classifications and descriptions of the angioarchitecture in the literature.[1,2,6]

Thus 4D-DSA reconstructions could differentiate between arterial feeders terminating in the nidus and feeders en passage from an artery passing the AVM for supply of normal brain tissue distal to the nidus. Mixed patterns and different lengths between

the origin and target of terminal feeders suggest that there is no strong separation between the 2 entities but a continuum between single terminal feeders with a longer distance between the last visible side branch and the nidus and AVMs fed by multiple short-distance side branches of an artery passing the nidus (en passage), with the clinical consequence that embolization with fluids is more difficult and complete obliteration of the nidus less likely.[17] The presence of pial networks of collaterals between different feeding arteries has been described as perinidal angiopathy with difficulty separating the increased number and density of vessels from the nidus itself.[18]

Concerning the intranidal branching patterns, classifications distinguished between fistulous and plexiform compartments.[18] 4D-fPCBCTA with thin slices could assign nidal compartments to one of these patterns. However, we frequently detected mixed patterns, and it was difficult to distinguish tortuous intranidal branches from real networks with anastomotic channels between adjacent vessels. Pure plexiform or simple AV fistulas were rarely seen. Our findings represent rather a continuum with lower-to-higher degrees of branching and network formation before the AV shunt. Houdart et al[3] proposed a classification for AV shunts according to the branching pattern: Arteriovenous fistulas with direct connections between arteries and a draining vein were distinguished from AV fistulas with arterial branching before transition into the draining vein and AV fistulas with corresponding branches on the venous site.

This classification provides a nomenclature that is also applicable to the description of 4D-fPCBCTA findings (Fig 1 and Table).

Venous drainage into one or several draining veins was also complex and resembled normal venous anatomy in the corresponding region. In most of our cases, 4D-fPCBCTA reconstructions were helpful in identifying the course of the compartmental draining vein and the arterial inflow to the AV shunt. These findings became important for pretherapeutic planning of transvenous embolization of AVMs, demanding control of the arterial inflow and an exact definition of the venous target and shunt zone.[8]

Details of the confluence of venous branches to the main draining veins were obscured by overlay of other nidal structures or a tortuous course of the draining veins, but time-consuming analysis taking between 30 and 60 minutes gave at least an impression of venous anatomy, which was coincident with DSA findings and superselective angiography in selected cases.

We found that flow-related pathologies like associated aneurysms and venous pathologies like stenosis or varicose enlargement can be detected quite reliably by 4D-DSA, similar to findings in other studies.[14-16]

Concerning the display of all angioarchitectonic features, 4D-DSA and fPCTA provide more information compared with other angiographic imaging modalities. Thus, planning of interventional, surgical, and radiosurgical treatment may benefit from improved characterization of the nidus and the shunt zone. Conventional 2D-DSA showed most

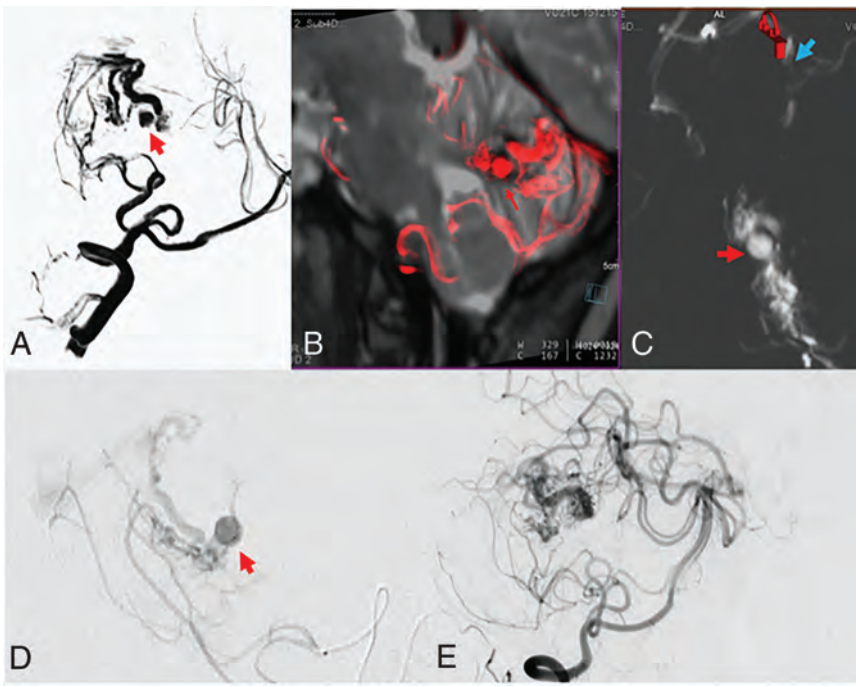

FIG 4. Posterior fossa AVM in an 18-year-old woman with cerebellar hemorrhage. *A* and *B*, Virtual DSA and sagittal reconstructions of fused images between MR imaging and 4D fPCTA show an intranidal aneurysm (*red arrows*). *C*, Axial MPRs demonstrate the origin of the aneurysms from the branches of the small nidus just proximal to the transition into the draining vein (*blue arrow*). *D*, Corresponding findings by superselective angiography. *E*, Occlusion of the aneurysm after targeted embolization. Note the diffuse nidus with a low degree of branching and dominance of single microfistulous channels.

Intranidal branching pattern and venous drainage

	Dominant Arterial Branching Pattern		Dominant Shunt Type	
Venous Drainage	Direct Fistulas	Plexiform Network	Sidewall	AV Branching
Single draining vein ($n = 24$)	17	7	15	8
Several draining veins ($n = 9$)	5	4	4	6
Total ($n = 33$)	22	11	19	14

of the findings with the advantage of better temporal resolution and separation between the angiographic phases. At the current stage of development of 4D technology, DSA projection images are still needed as complementary information. 4D with the advantage of displaying the volumes at any time point in any projection may help avoid DSA series in multiple projections or high frame rates. The main disadvantage of DSA was the overlay of vascular structures on projection images. Further prospective and multicentric studies are necessary to assess whether additional oblique 2D-DSA projections can be omitted without loss of diagnostic quality.

With the use of subtraction, soft-tissue contrast is not shown in 3D and 4D reconstructions. Therefore, display of gray and white matter gyri and sulci of the brain is not possible. Soft-tissue reconstruction algorithms for the mask are available and may also be used for C-like fPCBCT images. Currently, the resolution for soft-tissue details like the differentiation between gray and white matter is less than that with multislice CT or MR imaging. Therefore, MR imaging or fusion images between 4D-fPCBCTA and MR imaging became necessary for the exact localization of the AVM nidus and its relationship to the brain parenchyma and adjacent CSF spaces in our study.

Our study had several limitations:

1) The retrospective character with a limited number of 33 consecutive cases may be associated with a risk of bias towards certain AVM types and locations.

2) The analyses and ratings were performed with awareness of the findings of other imaging modalities. To demonstrate the validity of the new method, further prospective studies with blinded reviewers are necessary. At the current stage of software development, analyses were still time-consuming and difficult to standardize, especially in larger AVMs with complex angioarchitecture. Automated vessel-tracking algorithms and slice selection according to fused volumes between MRI and 4D-fPCTA should be developed to facilitate the determination of the AVM site and angioarchitectonic features.

3) According to our institutional rules, 3DRA in patients with AVM was only indicated if treatment was considered. This practice explains a predominance of small, ruptured AVMs in our sample, which is probably not representative.

4) In AVMs with feeders from different arterial territories, the analysis of 4D data obtained by injection of 1 feeder may not cover all compartments of the nidus. Image fusion could put the data from several 4D-DSA volumes together, with the disadvantage of increasing radiation exposure.

5) Details of the shunt zone could be confirmed by superselective angiography. In our sample, this information was only available in selected patients who underwent superselective embolization.

6) Despite suggestions to establish a standardized reporting terminology,[2] there is still a lack of validated categories for a description of angioarchitecture details. 4D-fPCBCTA reconstructions are able to display the continuum between known subtypes and may contribute to in vivo evaluation of this complex disease.

CONCLUSIONS

4D-DSA reconstructions are superior to 2D-DSA for displaying pathoanatomic details concerning angioarchitecture and classification of cerebral AVMs. At the current stage of development, DSA projection images and MR imaging are still needed as complementary diagnostic tools. Future 4D-fPCBCTA may play an important role as tool for pretherapeutic assessment of brain AVMs as well as a research tool for display of the intra- and perinidal microvasculature. Further standardization of postprocessing and improvement of fPCTA MR imaging fusion are necessary for further studies with blinded reviewers.

Disclosure forms provided by the authors are available with the full text and PDF of this article at www.ajnr.org.

REFERENCES

1. Müller-Forell W, Valavanis A. **How angioarchitecture of cerebral arteriovenous malformations should influence the therapeutic considerations.** *Minim Invas Neurosurg* 1995;38:1430–42 CrossRef Medline
2. Atkinson RP, Awad IA, Batjer HH, et al; Joint Writing Group of the Technology Assessment Committee American Society of Interventional and Therapeutic Neuroradiology; Joint Section on Cerebrovascular Neurosurgery a Section of the American Association of Neurological Surgeons and Congress of Neurological Surgeons; Section of Stroke and the Section of Interventional Neurology of the American Academy of Neurology. **Reporting terminology for brain arteriovenous malformation: clinical and radiographic features for use in clinical trials.** *Stroke* 2001;32:1430–42 CrossRef Medline
3. Houdart E, Gobin YP, Casasco A, et al. **A proposed angiographic classification for intracranial arteriovenous fistulae and malformations.** *Neuroradiologiy* 1993;35:381–85 CrossRef Medline
4. Berenstein AL, ter Brugge KG. **Clinical and Endovascular Treatment Aspects in Adults**. In: Berenstein AL, Lasjaunias P, ter Brugge KG, *Surgical Neuroangiography*. Vol 2.1. 2nd ed. Springer-Verlag; 2004
5. Yasargil MG. *Microneurosurgery, Vol 4; AVM of the Brain, History, Embryology, Pathological Considerations, Hemodynamics, Diagnostic Studies, Microsurgical Anatomy*, Thieme; 1987
6. Orlowski P, Mahmud I, Kamran M, et al. **An approach to the symbolic representation of brain arteriovenous malformations for management and treatment planning.** *Neuroradiology* 2014;56:195–209 CrossRef Medline
7. Mohr JP, Parides MK, Stapf C, et al; International ARUBA Investigators**. Medical management with or without interventional therapy for unruptured brain arteriovenous malformations (ARUBA): a multicentre, non-blinded, randomised trial.** *Lancet* 2014;383:614–21 CrossRef Medline
8. Choudhri O, Ivan ME, Lawton MT. **Transvenous approach to intracranial arteriovenous malformations: challenging the axioms of arteriovenous malformation therapy?** *Neurosurgery* 2015;77:644–52 CrossRef Medline
9. Al-Shahi R, Pal N, Lewis SC, et al; Observer Agreement Study Group**. Agreement in the angiographic assessment of arteriovenous malformations of the brain.** *Stroke* 2002;33:1501–09 CrossRef Medline
10. Spetzler RF, Ponce FA. **A 3-tier classification of cerebral arteriovenous malfromations.** *J Neurosurg* 2011;114:842–49 CrossRef Medline
11. Dumont TM, Kan P, Snyder KV, et al. **A proposed grading system for endovascular treatment of cerebral arteriovenous malformations: Buffalo score.** *Surg Neurol Int* 2015;6:3 CrossRef Medline
12. Lescher S, Gehrisch S, Klein S, et al. **Time-resolved 3D-rotational angiography display of detailed neurovascular anatomy in patients**

with intracranial vascular malformations. *J Neurointerv Surg* 2017;9:887–94 CrossRef Medline

13. Tritt S, Ommer B, Gehrisch S, et al. **Optimization of the surgical approach in AVMs using MRI and 4D DSA fusion technique.** *Clin Neuroradiol* 2017;27:443–50 CrossRef Medline
14. Lang S, Gölitz P, Struffert T, et al. **4D DSA of dynamic visualization of cerebral vasculature: a single-center experience in 26 cases.** *AJNR Am J Neuroradiol* 2017;38:1169–76 CrossRef Medline
15. Ognard J, Magro E, Caroff J, et al. **A new time-resolved 3D angiographic technique (4D-DSA): description, and assessment of its reliablity in Spetzler-Martin grading of cerbral arteriovenous malformations.** *J Neuroradiol* 2018;45:177–85 CrossRef Medline
16. Sandoval-Garcia C, Royalty K, Yang P, et al. **4D DSA a new technique for arteriovenous malformation evaluation: a feasibility study.** *J Neurointerv Surg* 2016;8:300–04 CrossRef Medline
17. Geibprasert S, Pongpech S, Jiarakongmun P, et al. **Radiologic assessment for brain arteriovenous malformations: what clinicians need to know.** *Radiographics* 2010;30:483–501 CrossRef Medline
18. Valavanis A, Pangalu A, Tanaka M. **Endovascular treatment of cerebral arteriovenous malformations with emphasis on the curative role of embolization.** *Interv Neuroradiol* 2005;11:37–43 CrossRef Medline

Symptomatic and Asymptomatic Chronic Carotid Artery Occlusion on High-Resolution MR Vessel Wall Imaging

M. Wan, L. Yan, Z. Xu, Z. Hou, K. Kang, R. Cui, Y. Yu, J. Song, F.K. Hui, Y. Wang, Z. Miao, X. Lou, and N. Ma

ABSTRACT

BACKGROUND AND PURPOSE: Chronic carotid artery occlusion remains a poorly understood risk factor for subsequent stroke, and potential revascularization is dependent on understanding the anatomy and nature of the occlusion. Luminal imaging cannot assess the nature of an occlusion, so the internal structure of the occlusion must be inferred. The present study examines the signal characteristics of symptomatic and asymptomatic carotid occlusion that may point to management differentiation.

MATERIALS AND METHODS: We prospectively recruited patients who were diagnosed with chronic carotid artery occlusion defined as longer than 4 weeks and confirmed by DSA. All patients underwent high-resolution MR vessel wall imaging examinations after enrollment. Baseline characteristics, vessel wall imaging features, and DSA features were collected and evaluated. The vessel wall imaging features included segment involvement, signal intensity, contrast enhancement, and vessel wall thickness. The symptomatic and asymptomatic chronic carotid artery occlusions were compared.

RESULTS: A total of 44 patients with 48 lesions were included in this study from February 2020 to December 2020. Of the 48 lesions, 35 (72.9%) were symptomatic and 13 (27.1%) were asymptomatic. There was no difference in baseline and DSA features. On vessel wall imaging, C1 and C2 were the most commonly involved segments (91.7% and 68.8%, respectively). Compared with symptomatic lesions, asymptomatic lesions were more often isointense (69.2%) in the distal segment ($P = .03$). Both groups had diffuse wall thickening (80% and 100%).

CONCLUSIONS: Signal characteristics between those with symptomatic and asymptomatic carotid artery occlusions differ in a statistically significant fashion, indicating a different structure of the occlusion.

ABBREVIATIONS: CCAO = chronic carotid artery occlusion; VWI = vessel wall imaging

Chronic carotid artery occlusion (CCAO) accounts for 6.5% of ischemic strokes.[1] CCAO may present as an incidental finding in asymptomatic patients, or it may present clinically as a TIA or a severe disabling stroke. The annual risk of TIA or ischemic stroke of asymptomatic CCAO is estimated to be between 2% and 8%.[2-4] The risk of stroke recurrence in symptomatic CCAO is 8% at 30 days, 10% at 1 year, and 14% at 5 years.[5]

CCAO may cause ischemic stroke due to an embolism from the occluded segment, compromised hemodynamics, and a mixture of both embolic and hemodynamic factors.[6] The role of hemodynamics in patients with symptomatic and asymptomatic CCAO has been demonstrated in previous studies.[4,7] The biology and architecture of the occluded segment of a CCAO remain unclear. Conventional imaging modalities including CTA, MRA, ultrasonography, and DSA can evaluate the structural and hemodynamic functional information of nonoccluded vessels but cannot provide sufficient information about the features of vessel segments with no substantial flow. High-resolution MR vessel

Received May 31, 2021; accepted after revision September 28.

From the Department of Interventional Neuroradiology (M.W., L.Y., Z.H., R.C., Y.Y., J.S., Z.M., N.M.) and Neurology (K.K., Y.W.), Beijing Tiantan Hospital, Capital Medical University, Beijing, China; China National Clinical Research Center for Neurological Diseases (M.W., L.Y., Z.H., K.K., R.C., Y.Y., J.S., Y.W., Z.M., N.M.), Beijing, China; Department of Neurology (Z.X.), The First Affiliated Hospital of College of Medicine, Zhejiang University, Hangzhou, China; Department of Radiology (X.L.), Chinese PLA General Hospital, Beijing, China; Department of Neurology (M.W.), Shijingshan Teaching Hospital of Capital Medical University, Beijing Shijingshan Hospital, Beijing, China; and Department of Radiology and Radiological Sciences (F.K.H.), Johns Hopkins Hospital, Baltimore, Maryland.

This work was supported by Beijing Yangfan Plan, XMLX201844, National Natural Science Foundation of China, 81730048, 81825012.

Min Wan, Long Yan, and Ziqi Xu contributed equally to this article.

Please address correspondence to Ning Ma, MD, Department of Interventional Neuroradiology, China National Clinical Research Center for Neurological Diseases, Beijing Tiantan Hospital, Capital Medical University, No. 119 South 4th Ring West Rd, Fengtai District, Beijing 100070, China; e-mail: maning_03@hotmail.com

Indicates open access to non-subscribers at www.ajnr.org

Indicates article with online supplemental data.

http://dx.doi.org/10.3174/ajnr.A7365

wall imaging (VWI) has been widely used in atherosclerotic diseases of the carotid and intracranial arteries.[8-11] VWI can determine plaque size, intraplaque hemorrhage, large lipid core, and intraluminal thrombus and can evaluate dissection flaps and subintimal plaque.[12] In addition, 3D VWI with variable flip angles can offer imaging with improved longitudinal coverage in a shorter imaging time.[13,14] VWI has been reported to be practicable and accurate in the diagnosis of CCAO.[15,16] VWI for CCAO can provide more information and direct visualization of the occluded segment, such as segment involvement, signal intensity, enhancement characteristics, and vessel wall thickness. However, few studies have focused on the characteristics of the occluded segment of CCAO on VWI.[17] Therefore, we conducted this study to assess the differing imaging characteristics between symptomatic and asymptomatic CCAO.

MATERIALS AND METHODS

Study Population

This was a prospective study, approved by the institutional review board of the hospital. Informed consent was obtained from all patients or their representatives before enrollment. Patients admitted to the Department of Interventional Neuroradiology of Beijing Tiantan Hospital and the Department of Neurology of The First Affiliated Hospital of Zhejiang University who had been diagnosed with carotid artery occlusion by sonography, CTA, or MRA were selected. Carotid artery occlusion by sonography, CTA, or MRA was defined as 100% cross-sectional truncation of the vessel lumen. "Chronic" was defined as the patient having a carotid occlusion diagnosis for >4 weeks, confirmed by DSA, with TICI grade 0.[18,19] All patients underwent DSA and VWI examinations after enrollment. The symptomatic CCAO group comprised patients who were admitted due to anterior ipsilateral ischemic events in the territory of the occluded vessel. The asymptomatic CCAO group was patients diagnosed with carotid artery occlusion incidentally during the course of routine clinical care. Ischemic events included ischemic stroke and TIA on the ipsilateral hemisphere or retinal artery. The exclusion criteria were the following: 1) contraindications to VWI or DSA examination; 2) near-occlusion or pseudo-occlusion confirmed by DSA; 3) intracranial chronic carotid artery occlusion; and 4) cardioembolic risk factors.

Data Collection

Baseline data including sex, age, body mass index, atherosclerotic risk factors, antithrombotic agents taken before and after diagnosis of CCAO, history of radiation, and time of the ischemic event onset were collected. Risk factors were defined as the following: hypertension defined as a history of hypertension or the patient taking any hypotensive drugs; diabetes mellitus defined as a history of diabetes mellitus, the patient taking any hypoglycemic agents, or a glycosylated hemoglobin level of ≥7%; hyperlipidemia defined as a history of hyperlipidemia or receiving lipid-lowering treatment; and coronary artery disease defined as a history of myocardial infarction or angina pectoris. Smoking was defined as current smokers or a smoking history. VWI and DSA features were recorded. On VWI, features of segment involvement, signal intensity of the occluded segment, contrast enhancement, and vessel wall thickness were evaluated. On DSA, the imaging features of the vascular stump and the level of the distal reconstitution were also evaluated.

Vessel Wall Imaging

VWI was performed on a 3T Magnetom Trio MR imaging scanner (Siemens) or a 3T Discovery MR750 scanner (GE Healthcare) with a head/neck coil. The 3D T1-weighted turbo spin-echo sequences on the Magnetom Trio MR imaging scanner were obtained with the following parameters: TR/TE = 760/15 ms, section partial Fourier factor = 0.75, turbo factor = 60, echo spacing = 4.52 ms, parallel imaging acceleration = 3. The FOV was 240 × 220 × 172 mm (Foot-Head × Anterior-Posterior × Right-Left), and the voxel size was 0.54 × 0.54 × 0.54 mm. The 3D T1-weighted turbo spin-echo sequences on the Discovery MR750 were obtained with the following parameters: TR/TE = 675/21 ms, echo-train length = 24, echo spacing = 7.5 ms, bandwidth = 62.50 kHz, phase and HyperSense acceleration (GE Healthcare) = 2, FOV = 180 × 180 mm (Superior-Inferior × Right-Left). The pixel size was 0.6 × 0.6 mm, and the section thickness was 0.8 mm. Other MR imaging scans included 3D TOF MRA, T2-weighted imaging, and contrast-enhanced T1-weighted imaging. Images were reconstructed using the Reformate tool in the Advantage Workstation 4.5 (GE Healthcare) or the D multiple planer reconstruction tool in the Siemens workstation.

DSA Imaging

All DSA studies were performed by 2 experienced interventional neuroradiologists with >10 years' experience each. During angiography, the bilateral common carotid arteries and bilateral vertebral arteries received contrast injections in the anterior-posterior and lateral projections, respectively.

Imaging Analysis

All MR images were reviewed separately by a neuroradiologist with 6 years' experience and a neurologist with 8 years' experience who were blinded to clinical and medical information. A third reader was used to resolve disagreements in assessing the segment involvement. We divided each ICA into 7 segments (C1–C7) according to the classification of Bouthillier et al.[20] To measure signal intensities, we placed ROIs at the occluded segment on the coronal T1-weighted turbo spin-echo sequences, with maximal size and adjacent sternomastoid muscle by the consensus decision of the 2 investigators. Signal intensity was categorized as hypointensity (less than the signal intensity of the adjacent sternocleidomastoid muscle), isointensity (equal to that of the adjacent sternocleidomastoid muscle), hyperintensity (more than that of the adjacent sternocleidomastoid muscle), and heterogeneous intensity (a mix of the above).

The occluded segment was divided into the origin segment (origin of the ICA) and the distal segment (beyond the origin of the ICA) to assess the signal intensity separately. Contrast enhancement was determined by comparing pre- and postcontrast T1-weighted images focused on the intraluminal thrombus. Vessel wall thickness was evaluated by T1-weighted turbo spin-echo sequences in the petrous ICA. The petrous ICA was divided into proximal, middle, and distal segments for measuring vessel wall thickness. Diffuse wall thickening was defined as a mean wall thickness of >1.5 mm.[21] Time intervals between the last

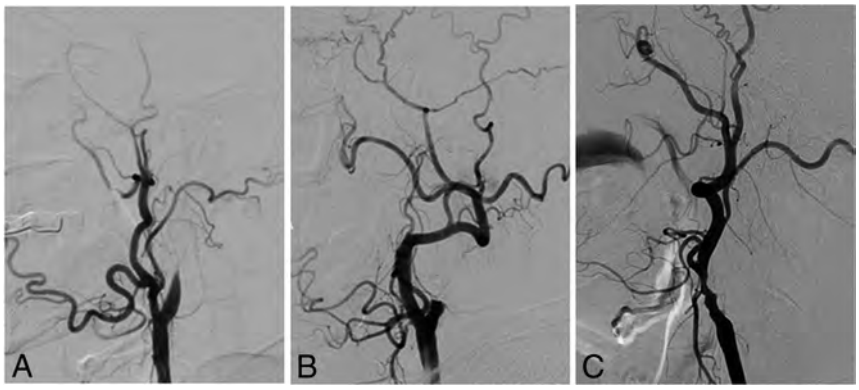

FIG 1. Stump condition: tapered stump (*A*), blunt stump (*B*), no stump (*C*)

Table 1: Baseline data of patients with asymptomatic and symptomatic CCAO

	Asymptomatic ($n = 9$)	Symptomatic ($n = 35$)	*P* Value
Male (No.) (%)	8 (88.9)	34 (97.1)	.37
Age (mean) (yr)	59 (SD, 13.35)	60.51 (SD, 11.46)	.73
Body mass index (mean)	25.30 (SD, 3.49)	24.40 (SD, 3.12)	.46
Hypertension (No.) (%)	7 (77.8)	26 (74.3)	>.99
Diabetes mellitus (No.) (%)	3 (33.3)	12 (34.3)	>.99
Hyperlipidemia (No.) (%)	7 (77.8)	28 (80.0)	>.99
Coronary artery disease (No.) (%)	1 (11.1)	3 (8.6)	>.99
Smoker (No.) (%)	4 (44.4)	15 (42.9)	>.99
Antithrombotic treatment before diagnosis of CCAO (No.) (%)	1 (11.1)	8 (22.9)	.75
Antithrombotic treatment after diagnosis of CCAO (No.) (%)	3 (33.3)	18 (51.4)	.55
History of radiation (No.) (%)	0 (0.0)	1 (2.9)	>.99
Time intervals between DSA and VWI (median) (IQR) (days)	1 (1, 2.5)	2 (1, 4)	.74

Note:—IQR indicates interquartile range.

ischemic event onset to VWI were divided into 4 stages (<7days, 7–30 days, 30–90 days, and ≥90 days). The difference in signal intensity across the 4 time points was evaluated.

DSA images were reviewed by the 2 operators. According to the contrast filling within the ICA from the common carotid artery and the shape, the morphology of the carotid stump was categorized as tapered, blunt, and no stump (Fig 1). The level of the distal collateral reconstitution was defined as the most proximal site visible at the distal end of the occlusion, divided into proximal or distal cavernous segments.

Statistical Analysis

We performed statistical analysis using SPSS software, Version 20.0 (IBM). Normal distribution measurement data were expressed as mean (SD), while skew distribution data were expressed as median and interquartile range. Counting data were expressed in frequencies and percentages. We compared baseline data of symptomatic and asymptomatic patients. DSA features and VWI features were compared between those with symptomatic and asymptomatic CCAO. The Student *t* test (normal distribution) or Mann-Whitney *U* test (skewed distribution) and the χ^2 test or Fisher exact test were used according to the situation. $P < .05$ was considered a statistically significant difference.

RESULTS

Patient Characteristics

Overall, a total of 44 patients with 48 lesions were included in this study from February 2020 to December 2020: 22 (50.0%) in Beijing Tiantan Hospital and 22 (50.0%) in The First Affiliated Hospital of Zhejiang University. Of the 44 patients, 35 (79.5%) were symptomatic and 9 (20.5%) were asymptomatic. In symptomatic patients, 32 patients had ischemic stroke (29 ipsilateral hemispheres and 3 retinal arteries) and 3 patients had experienced TIA (1 ipsilateral hemisphere and 2 retinal arteries). One (2.0%) patient had a history of radiation. Baseline characteristics are shown in Table 1; there was no difference in baseline characteristics between symptomatic and asymptomatic patients. The time intervals between DSA and VWI were 1 day (interquartile range, 1–2.5 days) in the asymptomatic group and 2 days (interquartile range, 1–4 days) in the symptomatic group ($P = .74$).

Comparison between Symptomatic and Asymptomatic CCAO

DSA showed no difference in stump morphology and the level of distal collateral reconstitution between the 2 groups (Online Supplemental Data).

On VWI, C1 and C2 were the most commonly involved segments in both symptomatic CCAO (97.1% and 68.6%) and asymptomatic CCAO (76.9% and 69.2%). Two patterns of signal intensity were detected in the origin segment (isointensity and heterogeneous intensity). There were 7 (20.0%) instances of isointensity and 27 (77.1%) of heterogeneous intensity in symptomatic CCAO (Fig 2). There were 5 (38.5%) instances of isointensity and 5 (38.5%) of heterogeneous intensity in those with asymptomatic CCAO ($P = .15$). Three patterns of signal intensity were detected in the distal segment (hyperintensity, isointensity, and heterogeneous intensity). There was a higher prevalence of isointensity (69.2%) in the asymptomatic CCAO compared with the symptomatic CCAO ($P = .03$) group. There were 14 patients (15 lesions) with contrast-enhanced scans. Nine scans in 13 patients with symptomatic CCAO were demonstrated to be contrast-enhanced, as well as 2 scans in 2 patients with asymptomatic CCAO ($P = .95$). Both patients with symptomatic, and asymptomatic CCAO had a high prevalence of diffuse thickening of the vessel wall (80% and 100% respectively).

Difference in Signal Intensity at Different Stages of Symptomatic CCAO

In symptomatic CCAO, both the origin segment and distal segment showed no difference at the following 4 stages: <7 days, 7–30 days, 30–90 days, and ≥90 days (Tables 2 and 3).

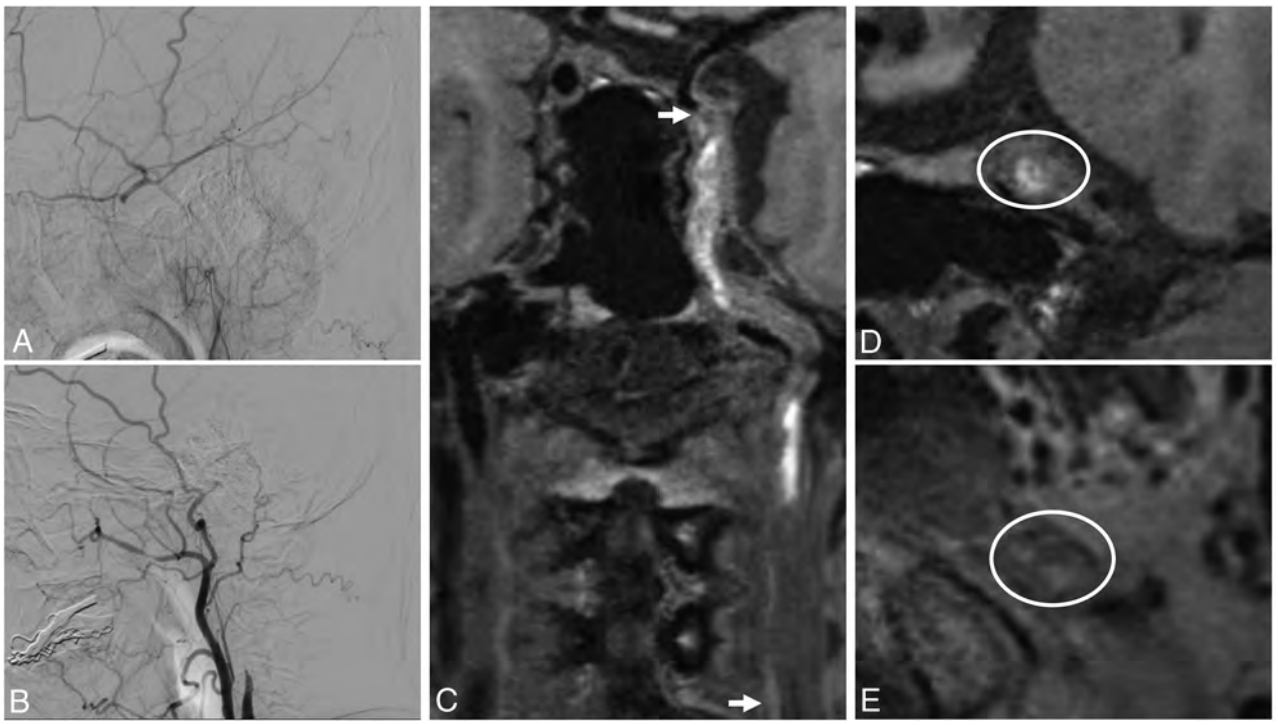

FIG 2. An adult man who presented with blurred vision for 1 month and right-limb weakness for 10 days. On DSA, the occluded segment is from C1 (*B*) to C6 (*A*). On VWI, 3D TI-weighted turbo spin-echo sequences show that the occluded segment is C1 (*arrow*) to C6 (*arrow*) (*C*). The signal intensity of the distal segment in a elliptical region-of-interest (ROI) (*D*), and the signal intensity of the origin segment is heterogeneous intensity in a elliptical ROI (*E*).

Table 2: Difference in signal intensity at the origin segment of symptomatic CCAO at different stages

	Hyperintensity ($n = 0$)	Isointensity ($n = 7$)	Hypointensity ($n = 0$)	Heterogeneous Intensity ($n = 27$)	*P* Value
<7 days (No.) (%)	0 (0.0)	0 (0.0)	0 (0.0)	5 (14.7)	.69
7–30 days (No.) (%)	0 (0.0)	4 (57.1)	0 (0.0)	16 (47.1)	
30–90 days (No.) (%)	0 (0.0)	2 (28.6)	0 (0.0)	10 (29.4)	
≥90 days (No.) (%)	0 (0.0)	1 (14.3)	0 (0.0)	3 (8.8)	

Table 3: Difference in signal intensity at the distal segment of symptomatic CCAO at different stages

	Hyperintensity ($n = 9$)	Isointensity ($n = 14$)	Hypointensity ($n = 0$)	Heterogeneous Intensity ($n = 12$)	*P* Value
<7 days (No.) (%)	2 (22.2)	1 (7.1)	0 (0.0)	2 (16.7)	.29
7–30 days (No.) (%)	2 (22.2)	6 (42.9)	0 (0.0)	8 (67.7)	
30–90 days (No.) (%)	4 (44.4)	4 (28.6)	0 (0.0)	2 (16.7)	
≥90 days (No.) (%)	1 (11.1)	3 (21.4)	0 (0.0)	0 (0.0)	

Comparison of DSA with VWI

The accuracy of VWI for the diagnosis of total CCAO was 100%. The level of occlusion differed between DSA and VWI, with a consistency rate of 27.1%. Most of the lesions were shown to be shorter on VWI than DSA, and a tiny lumen could be seen beyond the occluded segment on VWI but was considered occluded on DSA (Fig 3).

DISCUSSION

The present study demonstrates that asymptomatic CCAO lesions have a higher prevalence of isointensity compared with symptomatic CCAO lesions. The most common occluded segments in CCAO lesions were C1 and C2. Most of the CCAO lesions had diffuse thickening of the vessel wall on VWI, so VWI may provide detailed characterization of the occlusion for patients with CCAO.

VWI for the diagnosis of CCAO has been reported to have high accuracy and sensitivity using DSA as a reference.[15,22,23] A few studies have focused on the signal intensity of the occluded segment of the CCAO. Previous studies have reported a higher prevalence of heterogeneous intensity at the beginning of the occluded segment and a 47.5% presence of high signal intensity in the occluded segment.[15,17] Atherosclerosis is the major cause (about 70%) of CCAO, and most lesions are located at the origin of the ICA.[24] The deterioration of the atherosclerotic plaque

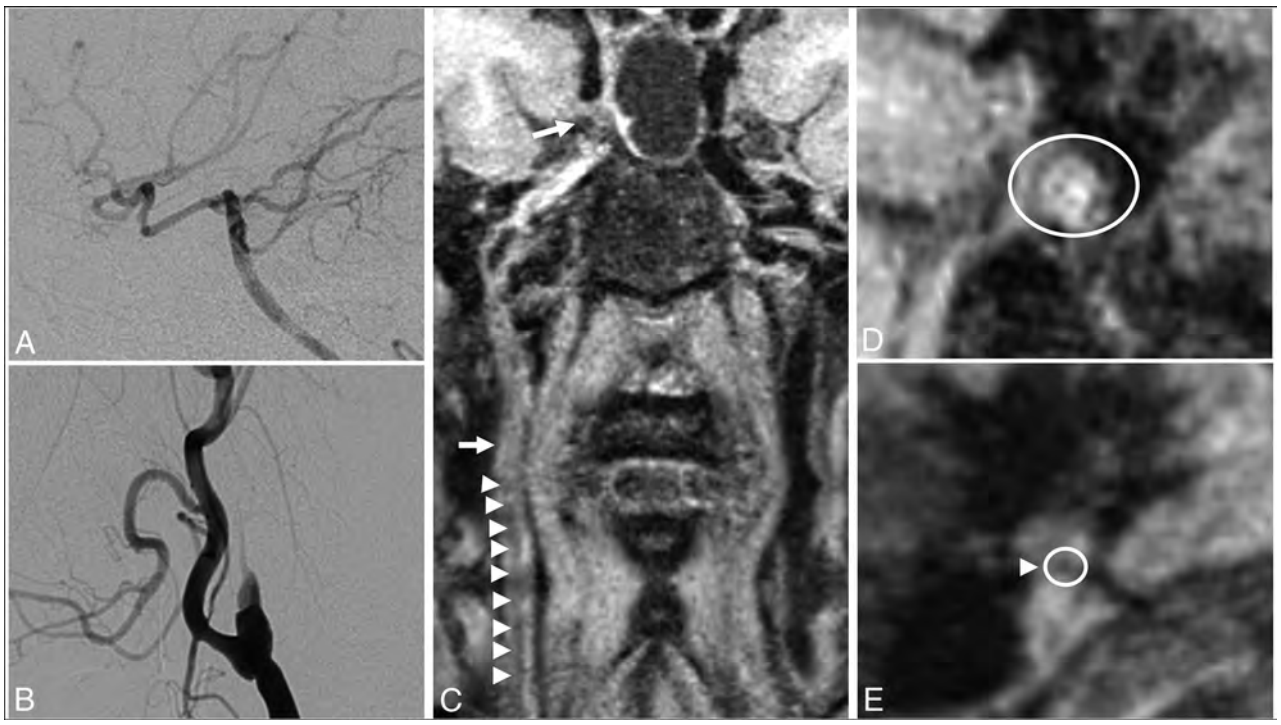

FIG 3. An adult woman who presented with dizziness for 2 months. On DSA, the occluded segment is from C1 (*B*) to C7 (*A*). On VWI, 3D T1-weighted turbo spin-echo sequences show that the occluded segment was C2 (*arrow*) to C4 (*arrow*), and C1 did not have total occlusion (*arrowheads*, *C*). The signal intensity of distal segment is isointensity in a elliptical region-of-interest (ROI) (*D*). The origin segment showed a tiny lumen (*arrowhead*), in a circular ROI which was considered an occluded segment on DSA (*E*).

leads to occlusion of the carotid artery and formation of the intraluminal thrombus within the distal segment. The signal intensities of the origin and distal segments are usually different. It is difficult to describe the whole occluded segment with uniform signal intensity. In this study, we divided the occluded segment into 2 parts to evaluate the signal intensity: the origin segment (the origin of the ICA) and the distal segment (distal C1 and above). Heterogeneous signal intensity was frequently encountered in the origin segment, but there was no difference between the 2 groups. The most common signal intensity in the distal segment was isointensity in asymptomatic lesions, which was not the case in symptomatic lesions ($P = .03$).

Cerebral hemorrhage can be chronologically divided into different stages by MR imaging: hyperacute, acute, early subacute, late subacute, and chronic stage.[25,26] Intraplaque hemorrhage of atherosclerosis on high-resolution MR imaging is also chronologically divided into fresh, recent, and old stages.[27] We proposed that the signal intensity of the distal segment may vary with time, similar to the signal intensity of cerebral hemorrhage and intraplaque hemorrhage. We selected different time intervals from the last onset of symptoms to the VWI examination in reference to cerebral hemorrhage and intraplaque hemorrhage. However, there was no difference in signal intensity at different time points. The same phenomenon has been observed in studies about intracranial large-vessel arterial occlusion.[28] The reason may be that the exact time of the CCAO is uncertain and there is spontaneous recanalization and reformation of the thrombus in the occluded segment.

In this study, all the lesions in the asymptomatic group and 80% in the symptomatic group had a diffuse thickening of the vessel wall. In a previous study, diffuse wall thickening in the petrous ICA was correlated with proximal ICA steno-occlusive disease.[29] With the increasing degree of stenosis, diffuse wall thickening became severe (present in 1.4%, 5.3%, 5.9%, and 80.4% of ipsilateral proximal ICAs, respectively, in patients with stenosis of 1%–49%, 50%–69%, 70%–99%, and total occlusion, respectively).[29] The probable cause is edema of the vessel wall due to long-term ischemia. Nutrients of the intima and inner media are supplied by diffusion from the lumen, and the adventitia is supplied by the vasa vasorum.[30] The vasa vasorum often arose directly from the lumen of the carotid artery and the arterial branching points.[31] When the carotid artery was occluded, the vessel wall lost its nutrient supply and edema occurred.

DSA remains the criterion standard for the diagnosis of vascular disease; it can evaluate structural and hemodynamic functional information but cannot provide information on the vessel wall. VWI has been widely used in atherosclerosis of the carotid artery for its sufficient black-blood effects, excellent scan efficiency, high isotropic resolution and signal-to-noise ratio, and large spatial coverage.[32,33] Compared with DSA, VWI can provide more information about the occluded segment. In this study, 72.9% of occluded segments detected by VWI were shorter than those detected by DSA. A previous study also found a similar result.[16] The tiny lumen can be observed beyond the occluded segment on VWI, but it was considered occluded on DSA. We hypothesize that this was a pseudo-occlusion caused by collapse of the vessel wall due to inadequate compensatory proximal and distal blood flow. Endovascular interventional therapy has become a major treatment for CCAO. The stump condition and

distal ICA reconstitution on DSA are important factors affecting successful recanalization.[34] It is necessary to identify the true occluded segment, and VWI may provide more information to help improve the success rate of recanalization.[16]

There were some limitations of this study. First, the MR imaging scanner was different in the 2 centers. Second, 3D T1-weighted turbo spin-echo sequences were used to evaluate occluded segments without additional flow suppression, possibly affecting the evaluation of slow blood flow in the proximal-to-distal occluded segments. Third, 9 patients included in the asymptomatic group were detected occasionally, so selection bias may exist. Due to the small sample size, the findings in the present study need to be interpreted with caution. Fourth, only a portion of patients underwent enhanced scans, possibly not fully demonstrating the characteristics of the occluded segment. Finally, the conclusion of this study needs to be confirmed by a larger amount of data research in the future.

CONCLUSIONS

VWI can provide further insight into the occluded segment of CCAO. The signal intensity was demonstrated to be different between symptomatic and asymptomatic CCAO.

Disclosure forms provided by the authors are available with the full text and PDF of this article at www.ajnr.org.

REFERENCES

1. Weimar C, Goertler M, Harms L, et al. **Distribution and outcome of symptomatic stenoses and occlusions in patients with acute cerebral ischemia.** *Arch Neurol* 2006;63:1287–91 CrossRef Medline
2. Lall A, Yavagal DR, Bornak A. **Chronic total occlusion and spontaneous recanalization of the internal carotid artery: natural history and management strategy.** *Vascular* 2021;29:733–41 CrossRef Medline
3. Hackam DG. **Prognosis of asymptomatic carotid artery occlusion: systematic review and meta-analysis.** *Stroke* 2016;47:1253–57 CrossRef Medline
4. Powers WJ, Derdeyn CP, Fritsch SM, et al. **Benign prognosis of never-symptomatic carotid occlusion.** *Neurology* 2000;54:878–82 CrossRef Medline
5. Flaherty ML, Flemming KD, McClelland R, et al. **Population-based study of symptomatic internal carotid artery occlusion: incidence and long-term follow-up.** *Stroke* 2004;35:e349–52 CrossRef Medline
6. Thanvi B, Robinson T. **Complete occlusion of extracranial internal carotid artery: clinical features, pathophysiology, diagnosis and management.** *Postgrad Med J* 2007;83:95–99 CrossRef Medline
7. Gupta A, Chazen JL, Hartman M, et al. **Cerebrovascular reserve and stroke risk in patients with carotid stenosis or occlusion: a systematic review and meta-analysis.** *Stroke* 2012;43:2884–91 CrossRef Medline
8. Underhill HR, Hatsukami TS, Cai J, et al. **A noninvasive imaging approach to assess plaque severity: the carotid atherosclerosis score.** *AJNR Am J Neuroradiol* 2010;31:1068–75 CrossRef Medline
9. Takaya N, Yuan C, Chu B, et al. **Presence of intraplaque hemorrhage stimulates progression of carotid atherosclerotic plaques: a high-resolution magnetic resonance imaging study.** *Circulation* 2005;111:2768–75 CrossRef Medline
10. de Havenon A, Mossa-Basha M, Shah L, et al. **High-resolution vessel wall MRI for the evaluation of intracranial atherosclerotic disease.** *Neuroradiology* 2017;59:1193–1202 CrossRef Medline
11. Dieleman N, Yang W, Abrigo JM, et al. **Magnetic resonance imaging of plaque morphology, burden, and distribution in patients with symptomatic middle cerebral artery stenosis.** *Stroke* 2016;47:1797–1802 CrossRef Medline
12. Hui FK, Zhu X, Jones SE, et al. **Early experience in high-resolution MRI for large vessel occlusions.** *J Neurointerv Surg* 2015;7:509–16 CrossRef Medline
13. Murata K, Murata N, Chu BC, et al; CARE-II Study Collaborators. **Characterization of carotid atherosclerotic plaques using 3-dimensional MERGE magnetic resonance imaging and correlation with stroke risk factors.** *Stroke* 2020;51:475–80 CrossRef Medline
14. Narumi S, Sasaki M, Natori T, et al. **Carotid plaque characterization using 3DT1-weighted MR imaging with histopathologic validation: a comparison with 2D technique.** *AJNR Am J Neuroradiol* 2015;36:751–56 CrossRef Medline
15. Zhang J, Ding S, Zhao H, et al. **Evaluation of chronic carotid artery occlusion by non-contrast 3D-MERGE MR vessel wall imaging: comparison with 3D-TOF-MRA, contrast-enhanced MRA, and DSA.** *Eur Radiol* 2020;30:5805–14 CrossRef Medline
16. Chai S, Sheng Z, Xie W, et al. **Assessment of apparent internal carotid tandem occlusion on high-resolution vessel wall imaging: comparison with digital subtraction angiography.** *AJNR Am J Neuroradiol* 2020;41:693–99 CrossRef Medline
17. Zhou J, Cai SF, Yuan XS, et al. **Remodeling of occluded internal carotid artery in vessel wall magnetic resonance imaging.** *Int J Neurosci* 2020 Nov 18. [Epub ahead of print] CrossRef Medline
18. Yang Y, Liu X, Wang R, et al. **A treatment option for symptomatic chronic complete internal carotid artery occlusion: hybrid surgery.** *Front Neurosci* 2020;14:392 CrossRef Medline
19. Nguyen-Huynh MN, Lev MH, Rordorf G. **Spontaneous recanalization of internal carotid artery occlusion.** *Stroke* 2003;34:1032–34 CrossRef Medline
20. Bouthillier A, van Loveren HR, Keller JT. **Segments of the internal carotid artery: a new classification.** *Neurosurgery* 1996;38:425–32; discussion 432–33 CrossRef Medline
21. Chen X, Wang J, Liu Y, et al. **Proximal internal carotid artery stenosis associates with diffuse wall thickening in petrous arterial segment of Moyamoya disease patients: a three-dimensional magnetic resonance vessel wall imaging study.** *Neuroradiology* 2019;61:29–36 CrossRef Medline
22. Zhao HL, Wang JN, Liu XS, et al. **Assessment of carotid artery atherosclerotic disease by using three-dimensional fast black-blood MR imaging: comparison with DSA.** *Radiology* 2015;274:508–16 CrossRef Medline
23. Wang Z, Lu M, Liu W, et al. **Assessment of carotid atherosclerotic disease using three-dimensional cardiovascular magnetic resonance vessel wall imaging: comparison with digital subtraction angiography.** *J Cardiovasc Magn Reson* 2020;22:18 CrossRef Medline
24. Paraskevas KI, Mikhailidis DP, Liapis CD. **Internal carotid artery occlusion: association with atherosclerotic disease in other arterial beds and vascular risk factors.** *Angiology* 2007;58:329–35 CrossRef Medline
25. Gomori JM, Grossman RI, Hackney DB, et al. **Variable appearances of subacute intracranial hematomas on high-field spin-echo MR.** *AJR Am J Roentgenol* 1988;150:171–78 CrossRef Medline
26. Gomori JM, Grossman RI, Goldberg HI, et al. **Intracranial hematomas: imaging by high-field MR.** *Radiology* 1985;157:87–93 CrossRef Medline
27. Chu B, Kampschulte A, Ferguson MS, et al. **Hemorrhage in the atherosclerotic carotid plaque: a high-resolution MRI study.** *Stroke* 2004;35:1079–84 CrossRef Medline
28. Al-Smadi AS, Abdalla RN, Elmokadem AH, et al. **Diagnostic accuracy of high-resolution black-blood MRI in the evaluation of intracranial large-vessel arterial occlusions.** *AJNR Am J Neuroradiol* 2019;40:954–59 CrossRef Medline
29. Chen X, Zhao H, Chen Z, et al. **Association between proximal internal carotid artery steno-occlusive disease and diffuse wall thickening in its petrous segment: a magnetic resonance vessel wall imaging study.** *Neuroradiology* 2017;59:485–90 CrossRef Medline

30. Bo WJ, McKinney WM, Bowden RL. **The origin and distribution of vasa vasorum at the bifurcation of the common carotid artery with atherosclerosis.** *Stroke* 1989;20:1484–87 CrossRef Medline
31. Barker SG, Causton BE, Baskerville PA, et al. **The vasa vasorum of the rabbit carotid artery.** *J Anat* 1992;180:(Pt 2):225–31 Medline
32. Xie YB, Yang Q, Xie GX, et al. **Improved black-blood imaging using DANTE-SPACE for simultaneous carotid and intracranial vessel wall evaluation.** *Magn Reson Med* 2016;75:2286–94 CrossRef Medline
33. Fan ZY, Zuehlsdorff S, Liu X, et al. **Prospective self-gating for swallowing motion: A feasibility study in carotid artery wall MRI using three-dimensional variable-flip-angle turbo spin-echo.** *Magn Reson Med* 2012;67:490–98 CrossRef Medline
34. Chen YH, Leong WS, Lin MS, et al. **Predictors for successful endovascular intervention in chronic carotid artery total occlusion.** *JACC Cardiovasc Interv* 2016;9:1825–32 CrossRef Medline

Percutaneous CT-Guided Core Needle Biopsies of Head and Neck Masses: Review of 184 Cases at a Single Academic Institution, Common and Special Techniques, Diagnostic Yield, and Safety

R.W. Jordan, D.P. Shlapak, J.C. Benson, F.E. Diehn, D.K. Kim, V.T. Lehman, G.B. Liebo, A.A. Madhavan, J.M. Morris, P.P. Morris, J.T. Verdoorn, and C.M. Carr

ABSTRACT

BACKGROUND AND PURPOSE: Percutaneous CT-guided core needle biopsies of head and neck lesions can be safely performed with vigilant planning. This largest-to-date single-center retrospective study evaluates multiple approaches with consideration of special techniques and examines the histopathologic yield.

MATERIALS AND METHODS: Retrospective review of CT-guided core biopsies of head and neck lesions from January 1, 2010, to October 30, 2020, was performed. We recorded the following: patient demographics, sedation details, biopsy needle type and size, lesion location and size, approach, patient positioning, preprocedural intravenous contrast, proceduralists' years of experience, complications, and pathology results.

RESULTS: One hundred eighty-four CT-guided core biopsies were evaluated. The initial diagnostic yield was 93% (171/184). However, of 43/184 (23%) originally "negative for malignancy" biopsies, 4 were eventually positive for malignancy via rebiopsy/excision, resulting in a 2% false-negative rate and an adjusted total diagnostic yield of 167/184 (91%). Biopsies were performed by 16 neuroradiologists with variable experience. The diagnostic yield was essentially the same: 91% (64/70) for proceduralists with ≤3 years' experience, and 90% (103/114) with >3 years' experience. The diagnostic yield was 93% (155/166) for lesions of >10 mm. The diagnostic yield per biopsy needle gauge was the following: 20 ga, 81% (13/16); 18 ga, 93% (70/75); 16 ga, 90% (64/71); and 14 ga, 91% (20/22). There were 4 asymptomatic hematomas, with none requiring intervention.

CONCLUSIONS: Percutaneous CT-guided core needle biopsies are safe procedures for superficial and deep head and neck lesions with a high diagnostic yield. Careful planning and special techniques may increase the number of lesions accessible percutaneously while minimizing the risk of complications.

ABBREVIATIONS: CNB = core needle biopsy; FNA = fine-needle aspiration; H&N = head and neck; SCC = squamous cell carcinoma

An estimated >54,000 new cases of oral cavity and pharyngeal cancer and 44,280 new cases of thyroid cancer will be diagnosed in the United States in 2021, not including head and neck (H&N) lymphomas, salivary gland tumors, and other less common malignancies.[1]

If not apparent on direct visualization, H&N lesions often require image-guided biopsy. Prior studies have shown higher diagnostic yields of image-guided core needle biopsy (CNB) versus fine-needle aspiration (FNA), including parotid, submandibular, and sublingual gland lesions, as well as cervical lymphadenopathy.[2-5] Additionally, supplementary FNA during lymph node CNB might not contribute to an actionable diagnosis in cases of lymphoma.[6]

Several standard approaches to H&N CT-guided CNB are used, including subzygomatic, paramaxillary, retromandibular, anterior, lateral, and posterior approaches.[7-13] These are illustrated in Fig 1. A recently published review of 27 CT-guided CNBs by Hillen et al[14] demonstrated the effectiveness and safety of these procedures for H&N lesions. However, large studies evaluating the diagnostic yield and safety profile of CT-guided H&N CNBs with a variety of locations and lesion sizes are lacking. In this study, we sought to review and describe our institution's experience with CT-guided CNB of H&N lesions, with emphasis on the diagnostic

Received June 11, 2021; accepted after revision September 14.

From the Division of Neuroradiology, Department of Radiology, Mayo Clinic, Rochester, Minnesota.

Paper was previously presented as a scientific presentation at: Annual Meeting of the American Society of Head & Neck Radiology, September 8–12, 2021; Virtual.

Please address correspondence to Darya Shlapak, MD, Department of Radiology, Mayo Clinic, 200 First St SW, Rochester, MN 55905; e-mail: Shlapak.darya@mayo.edu

Indicates article with online supplemental data.

http://dx.doi.org/10.3174/ajnr.A7348

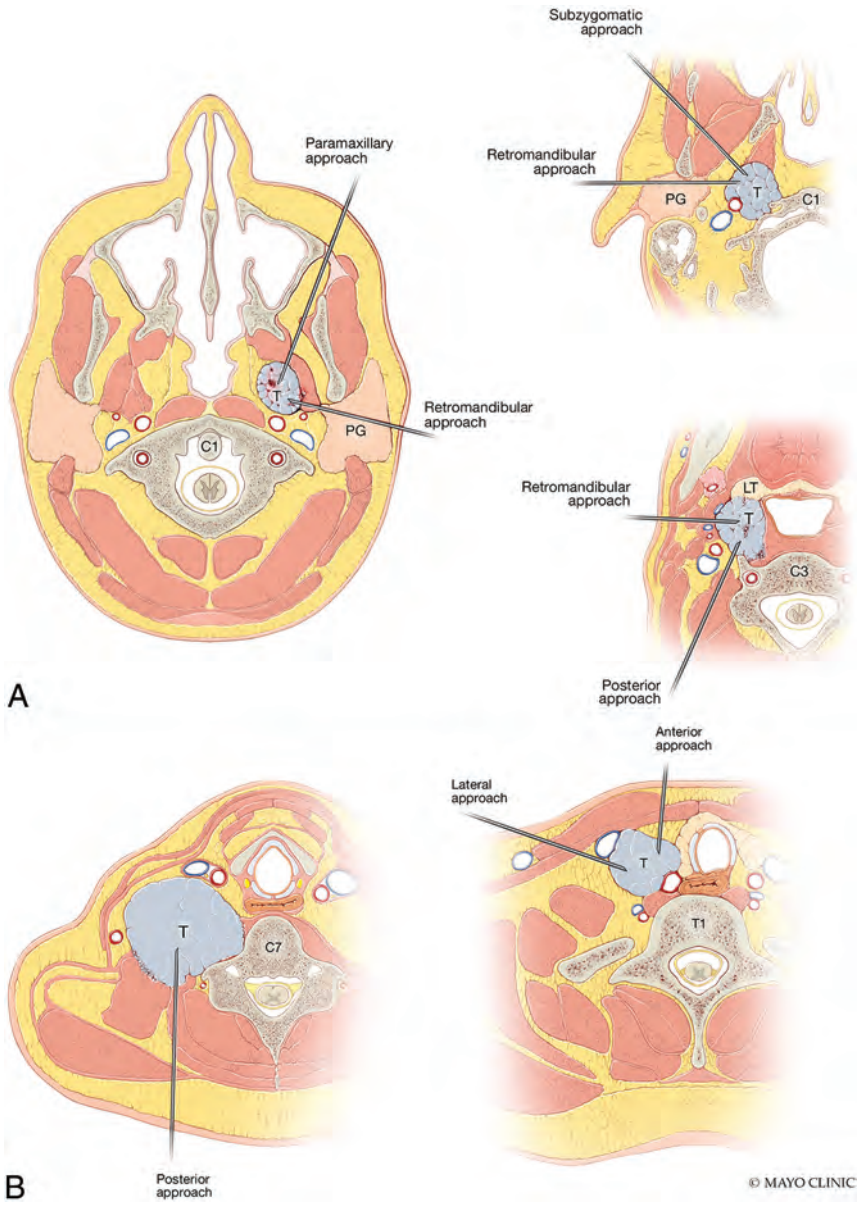

FIG 1. Common biopsy approaches to H&N lesions at different levels of the suprahyoid (***A***) and infrahyoid neck (***B***). Note that to avoid the parotid gland, one should use a retromandibular approach for more inferior retropharyngeal, parapharyngeal, pharyngeal mucosal, and masticator space lesions; more superior lesions are better accessed via paramaxillary and subzygomatic approaches. Reprinted with permission of Mayo Foundation for Medical Education and Research, all rights reserved. PG indicates parotid gland; T, tumor; LT, lingual tonsil.

and histopathologic yields and attention to target lesion and needle-gauge size, approach, safety profile, and special techniques.

MATERIALS AND METHODS

Patient Selection and Enrollment

This was a Health Insurance Portability and Accountability Act–compliant retrospective study, approved by the institutional review board. Informed consent was waived.

Our radiologic database was searched to identify all CT-guided H&N biopsies from January 1, 2010, to October 30, 2020. Search terms including "CT biopsy," "CT-guided biopsy," and "CT neuro biopsy" were autopopulated in our reporting template. This search yielded 1211 results. Inclusion criteria were biopsy with CT guidance, core biopsy, and location in the H&N. Biopsies outside the H&N (including the calvaria and spine) and FNAs were excluded. Ultimately, 184 core biopsies from 174 patients were included in the final study cohort.

Imaging and Clinical Review

Intraprocedural CT images, procedure reports, clinical follow-up notes, and pathology reports were reviewed by a neuroradiology fellow. For each biopsy case, the following data were collected (if available): patient demographics, biopsy needle gauge and brand, sedation type, biopsy approach, gantry tilt, patient positioning, anatomic space of the target lesion, maximal dimension of the lesion in the axial plane, proceduralists' years of experience, administration of pre- and intraprocedural contrast, histopathology, and complications. Intraprocedural CT images, reports, and the next patient encounter were reviewed for evaluation of procedure-related complications.

CT Imaging Parameters

A standard optimized dose protocol was used for all CT-guided core biopsies, using spiral CT with 1-second rotation time, 0.9 pitch, 120 kV(peak), 130 mAs, with an average volume CT dose index of 17.52 mGy for the planning phase. For the actual biopsy i-Sequence, 3 or 6 slices were used with 2.4- or 4.8-mm section thickness per the proceduralist's preference, with a 0.5-second rotation time, 120 kVp, 80 versus 40 mAs, and a CT dose index of 8.28 versus 4.14 mGy per scan, respectively (2.4- versus 4.8- mm section). Reduced dose protocols were used in the pediatric population. Preprocedural CT with contrast when necessary was performed according to routine neck CTA or CT soft-tissue neck protocol with iohexol contrast (Omnipaque 350 or Omnipaque 300; GE Healthcare) and "trigger of aorta," and 80-second delay, respectively.

Special Techniques

Preprocedural and Intraprocedural IV Contrast. The use of IV contrast is not uncommon for deep H&N biopsies and allows planning the safest approach to avoid major vascular structures (Fig 2*A*–*F* and Fig 3*D*). Additionally, IV contrast can make the

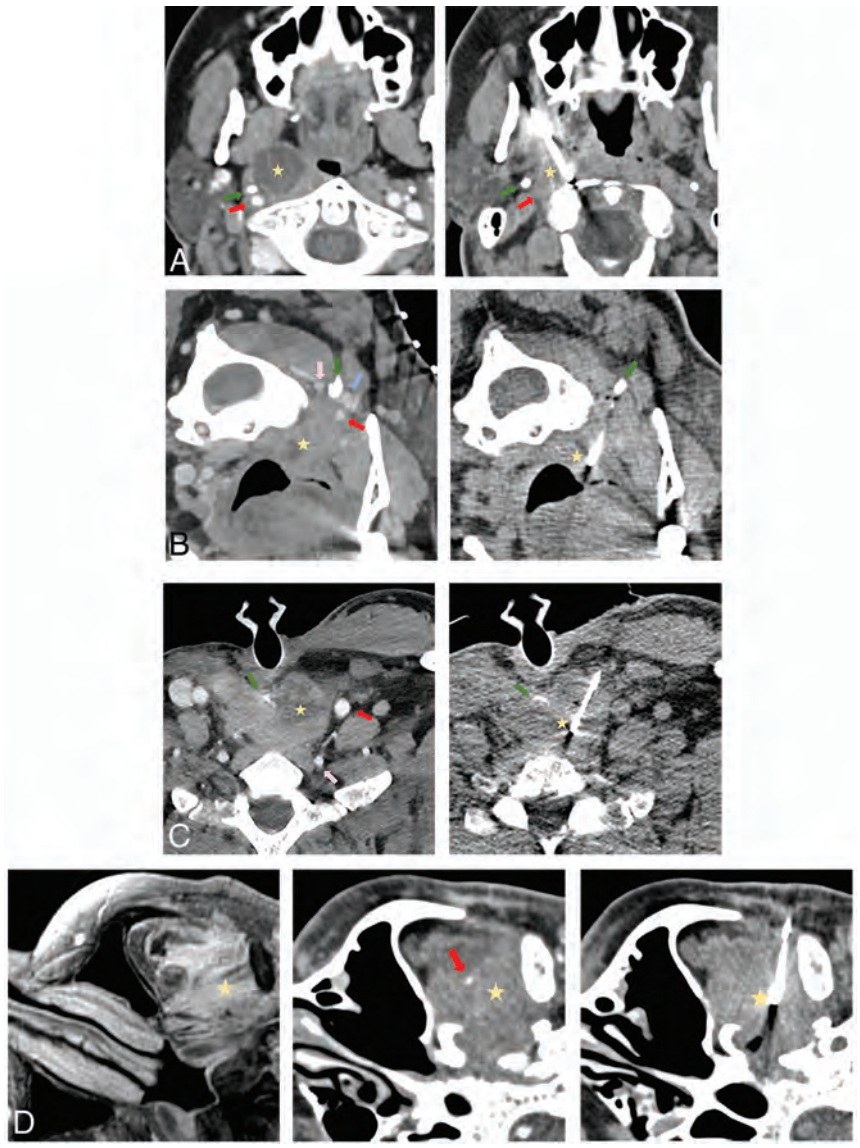

FIG 2. Common approaches used in the current series biopsy. ***A***, A paramaxillary approach targeting a 1.9-cm partially cystic right retropharyngeal lymph node (*yellow star*). *Left*, Preprocedural contrast-enhanced CT (venous phase) to better visualize the right ICA (*red arrow*) and better assess lesion margins due to peripheral enhancement. *Right*, Intraprocedural CT with a 14-ga needle trough through the lesion (part of the cystic component was initially aspirated). The styloid process (*green arrow*) is a useful landmark because it is immediately anterior to the ICA. Recurrent human papillomavirus (HPV) + SCC. This approach is commonly used to access retropharyngeal, parapharyngeal, pharyngeal mucosal, masticator, and deep parotid space lesions. ***B***, A retromandibular approach in a patient in a prone position targeting a 1.1-cm partially cystic left retropharyngeal lymph node (*yellow star*). *Left*, Contrast-enhanced CT (venous phase) to better visualize the left ICA (*red arrow*), vertebral artery (*pink arrow*), and internal jugular (IJ) vein (*blue arrow*) and highlight more solid lesion portions. *Right*, Intraprocedural CT with a 16-ga needle trough through the solid portion of the lesion. The C1 transverse process (*green arrow*) is a useful landmark because it "marks a safe pass" between the vertebral artery posterior to the needle and the ICA/IJ vein anteriorly. Recurrent HPV + SCC. This approach can be used for more inferior retropharyngeal, parapharyngeal, pharyngeal mucosal, masticator, and deep parotid lesions, as well as sublingual, submandibular, perivertebral, and carotid space lesions. ***C***, Anterior approach targeting a 3.4-cm partially cystic nodule at the tracheoesophageal groove (*yellow star*). *Left*, Preprocedural contrast-enhanced CT (venous phase) to opacify the left common carotid artery (*red arrow*) and vertebral artery (*pink arrow*) and delineate the solid component of the target lesion. *Right*, Intraprocedural CT with an 18-ga needle trough through the solid component of the lesion. A partially visualized esophageal stent (*green arrow*) is a useful landmark showing the approximate location of the infiltrated esophagus, lateral to the stent. Recurrent SCC. This approach is used with a neutral supine position for more midline anterior neck lesions such as the visceral space, level VI, and the supraclavicular lymph nodes. ***D***, A subzygomatic approach targeting an infiltrating left masticator space mass seen on MR imaging (*left image*, *yellow star*). *Middle*, Preprocedural contrast-enhanced CT (venous phase) to opacify the left internal maxillary artery (*red arrow*). *Right*, Intraprocedural CT with an 18-ga needle trough through the infiltrating lesion with the biopsy device clearly posterior to the expected location of the internal maxillary artery in correlation with the middle image. Recurrent SCC with perineural spread. By far, masticator space lesions are the most common targets for this approach.

lesion more conspicuous and help direct the biopsy toward more solid components of a cystic/necrotic mass, potentially increasing the diagnostic yield (Fig 2*B*, -*C*, and -*F*).

To our knowledge, the use of intraprocedural contrast during H&N lesion core sampling has not been reported, though intraprocedural contrast-enhanced CT was recently described for the

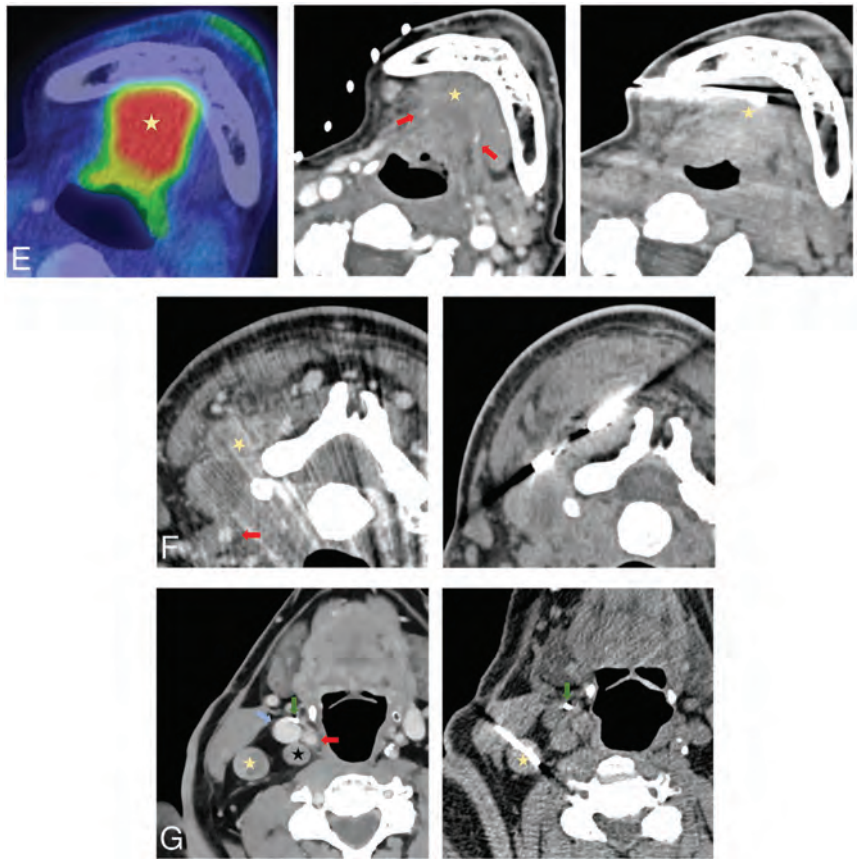

FIG 2. Continued *E*, Submandibular approach targeting diffuse soft-tissue thickening in the sublingual space, hypermetabolic on PET/CT (*left image*, *yellow star*). *Middle*, Preprocedural contrast-enhanced CT (venous phase) to localize and avoid vascular structures (*red arrows*). *Right*, Intraprocedural CT with an 8-ga needle trough through the lesion with the biopsy device clearly anterior to the expected location of the prominent vessels in correlation with the middle image. Adenoid cystic carcinoma. This approach offers access to the sublingual and submandibular spaces, level IA and IB lymph nodes, and potentially retropharyngeal/parapharyngeal lesions; however, it would require gantry tilt and/or neck manipulation. ***F***, Posterior approach with the patient in a prone position targeting the more posterior component of the bilobed 5.3-cm partially cystic mass in the left perivertebral space. *Left*, Preprocedural contrast-enhanced CT (venous phase) to localize the ICA (*red arrow*) and delineate solid components of the mass (*yellow star*). *Right*, Intraprocedural CT with a 14-ga needle trough through the solid portion of the lesion. Metastatic papillary thyroid carcinoma. Perivertebral and carotid space lesions and level V lymph nodes are most accessible with this approach, usually with the patient in a prone position. ***G***, A lateral approach targeting a right-level IIB 1.5-cm lymph node seen on the routine contrast-enhanced soft-tissue neck CT (*left image*, *yellow star*). Preprocedural contrast was not obtained because prior soft-tissue neck CT (*left image*) showed that the ICA (*red arrow*) and the IJ vein (*blue arrow*) can be well-visualized with at least a 7-mm fat plane between vessels and target lesion. Note the postoperative right carotid endarterectomy clip (*green arrow*) and an additional smaller metastatic lymph node (*black star*) too close to the vessels. *Right*, Intraprocedural CT with a 16-ga needle trough through the target. Metastatic small-cell carcinoma. This approach is commonly used to access levels II–IV and sometimes level V and the supraclavicular lymph nodes.

evaluation of the completeness of renal mass ablation.[15] While this is not a standardized technique at our institution, depending on the proximity of the critical vascular structure to the target lesion, proceduralists can choose to slowly infuse IV contrast during lesion sampling to continuously opacify and visualize adjacent vessels (Fig 4).

Gantry Tilt and/or Neck Flexion/Extension. Modern CT scanners allow gantry tilting to provide variable degrees of angle access to approach deep lesions while bypassing vascular and osseous structures, which otherwise would be difficult to avoid. Neck flexion/extension can partially compensate for gantry tilt because steep gantry tilt considerably narrows the working space for the proceduralist within the CT scanner bore (Fig 3*C*).

RESULTS

Patient Demographics and Periprocedural Details

One hundred seventy-four patients with 184 CT-guided CNB procedures were included in the final cohort. Eight patients underwent 2 biopsies, and 1 patient, 3 biopsies. The mean patient age at the time of the biopsy was 60 years (range, 2–86 years); 70 (38%) were female. All procedures were performed by a total of 16 board-certified and board-eligible fellowship-trained neuroradiologists. A trainee (resident or fellow) assisted in 95/184 (52%) cases.

Moderate sedation was administered in 145 cases (79%); general anesthesia, in 23 cases (13%); and only local anesthetic, in 16 cases (7%). A 14-ga core biopsy needle was used in 22 cases (12%); 16 ga, in 71 cases (39%); 18 ga, in 75 cases (41%); and 20 ga, in 16 cases (9%).

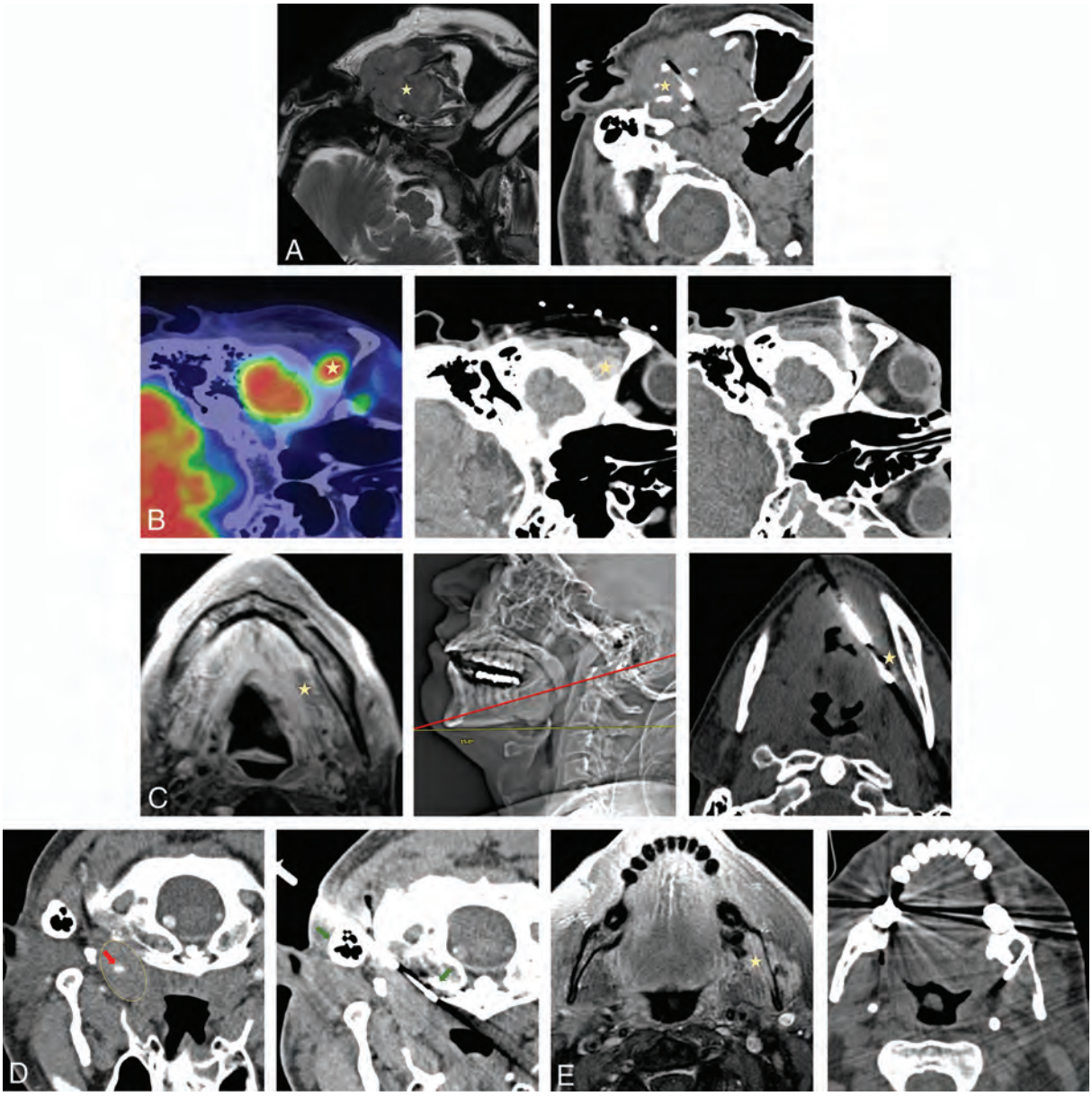

FIG 3. Less commonly used biopsy approaches. ***A***, Preauricular approach targeting a 4.2-cm expansile left mandibular lesion with an extraosseous soft-tissue component on MR imaging (*left image*, *yellow star*). No preprocedural contrast was administered given the size of the lesion and the lack of proximity of the crucial neurovascular structures. *Right*, Intraprocedural CT with a 16-ga needle trough through the lesion. Plasmacytoma. This approach is used for superficial lesions in the masticator or superficial parotid space, particularly when a zygoma is partially destructed. ***B***, A suprazygomatic approach targeting hypermetabolic on PET/CT 1.5-cm right suprazygomatic masticator mass (*left image*, *yellow star*). *Middle*, Preprocedural contrast-enhanced CT (venous phase) to delineate the lesion (*yellow star*) that enhances more than background tissues. *Right*, Intraprocedural CT with a 16-ga needle trough through the expected location of the lesion in correlation with bony landmarks and previous contrast enhancement on the middle image. Recurrent adenoid cystic carcinoma. This approach is essentially exclusively used for superficial suprazygomatic masticator space (temporal fossa) lesions. ***C***, Submental approach targeting diffusely heterogeneously enhancing on MR imaging left sublingual/floor of the mouth soft-tissue (*left image, yellow star*). *Middle*, Intraprocedural scout CT image showing patient positioning and a cranial gantry tilt of 15° (*red line*, biopsy plane after 15° gantry tilt) to bypass a mental protuberance. *Right*, Intraprocedural axial CT with a 14-ga needle trough through the expected location of the target (*yellow star*). Preprocedural contrast was not administered due to regional vasculature paucity in correlation with prior imaging. Recurrent adenoid cystic carcinoma. Sublingual space and floor of the mouth lesions can be accessed via this approach; to avoid the mental protuberance, cranial gantry tilt and/or substantial neck extension might be needed. ***D***, A retromastoid approach with the patient in the prone position targeting a 2.6-cm left retropharyngeal mass (*left image, yellow ellipse*), encasing the ICA on preprocedural limited CTA (*red arrow*). Right, intraprocedural CT with a 16-ga needle advanced between mastoid tip and the C1 anterior arch (*right image*, *green arrows*); these osseous landmarks align a safe trajectory into the lesion portion posterior to the ICA in correlation with preprocedural CTA. Recurrent human papillomavirus + SCC. This approach can be used for more lateral retropharyngeal and anterior perivertebral lesions. ***E***, A transosseous approach targeting an enhancing 2.5-cm left masticator mass expanding the mandibular canal on MR imaging (*left image*, *yellow star*). *Right*, Intraprocedural CT scan with a 16-ga needle traversing the buccal cortex of the mandibular ramus. Preprocedural contrast was not administered given lack of critical regional vasculature in correlation with MR imaging. Recurrent adenoid cystic carcinoma with inferior alveolar perineural spread. This approach can be used to access lesions along the inner cortex of the mandible and zygoma.

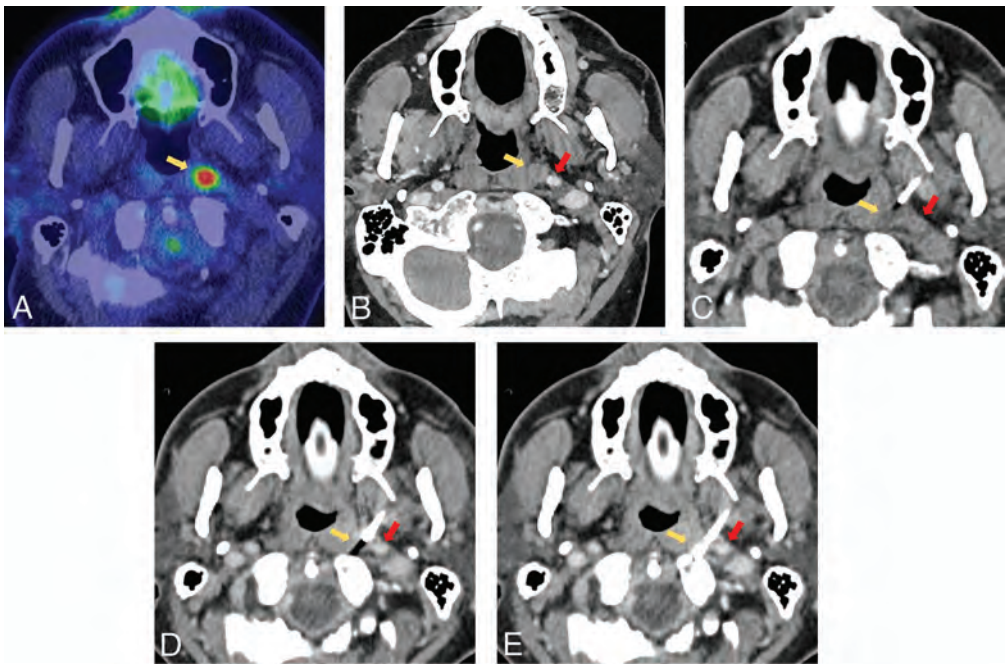

FIG 4. ***A***, PET/CT with hypermetabolic left retropharyngeal 6-mm lymph node (*yellow arrow*). ***B***, This lesion is centrally cystic/necrotic on follow-up contrast-enhanced CT (*yellow arrow*) and immediately medial to the ICA (*red arrow*). ***C***, Intraprocedural CT without contrast with an 18-ga needle advanced via a paramaxillary approach anterior to the target retropharyngeal lymph node (*yellow arrow*) and medial to the expected location of the unopacified ICA (*red arrow*). Before further needle advancement, 60 mL of Omnipaque-300 was slowly infused at a rate of 0.6 mL/s to continuously opacify the ICA (*red arrows*) for adequate visualization before (***D***) and during (***E***) lesion sampling (*yellow arrows*). Pathology reported poorly differentiated metastatic carcinoma in a patient with a history of oropharyngeal human papillomavirus + SCC.

Table 1: Biopsy approaches

Approach	No.	%
Paramaxillary[a]	43	23%
Retromandibular[a]	30	16%
Anterior[a]	24	13%
Subzygomatic[a]	21	11%
Submandibular[a]	20	11%
Posterior[a]	18	10%
Lateral[a]	14	8%
Preauricular	5	3%
Submental	4	2%
Suprazygomatic	3	2%
Retromastoid	1	1%
Transosseous	1	1%
Total	184	100%

[a] More common techniques.

A Temno Evolution core biopsy device (Merit Medical) was used in 167 cases (91%); a Mission Disposable Core Biopsy Device (Bard, BD), in 4 cases (2%); and Stryker Bone Biopsy Kit Needle (Stryker) and SuperCore Semi-Automatic Biopsy Instrument (Argon Medical Devices) were both used in 1 case each. Device type was not specified in 11 cases (6%).

Complications

Minor complications (asymptomatic hematomas) were observed in 4 (2%) cases, none requiring intervention. Manual compression was held for 10–15 minutes, and follow-up CT was performed in the procedure room before the patient was transferred to the postprocedural care unit.

Patient Positioning, Approach, and Intraprocedural Considerations

Patients were positioned supine in 139 (76%), prone in 23 (13%), and in a lateral decubitus position in 22 cases (12%). The H&N position remained relatively neutral in most cases of supine positioning, with the head usually slightly turned to the contralateral side of the lesion.

To optimize access to the target lesion, the gantry was tilted in 14/184 cases (8%). IV contrast was administered for the preprocedural CT in 114/184 cases (62%). While both protocols were used (arterial and venous phase, per proceduralist), the venous phase seemed more optimal, allowing assessment of all 3 major components of the biopsy: target lesion (particularly the solid component in cases of partially cystic/necrotic lesions) and major venous and arterial vasculature, because major arteries are usually still adequately visualized even in the venous phase.

A total of 12 different approaches were used in our cohort, listed in Table 1 along with the number of cases for each approach.

Target Lesion Details

Target lesion size measured in the longest dimension on axial images ranged from 5 to 75 mm (mean, 24 mm). Anatomic spaces of the lesions are summarized in Table 2.

Diagnostic Yield and Histopathologic Biopsy Results

Of 184 core biopsies, 13 were nondiagnostic (7%), with an initial diagnostic yield of 93%. However, of 43/184 (23%) biopsies originally negative for malignancy, 4 were eventually positive for malignancy via

Table 2: Target lesion space

Head and Neck Space	No.	%
Masticator	36	20%
Parotid	24	13%
Cervical lymph nodes[a]	23	13%
Retropharyngeal	23	13%
Sublingual	19	10%
Perivertebral	14	8%
Pharyngeal mucosal	13	7%
Visceral[b]	9	5%
Parapharyngeal	6	3%
Carotid	6	3%
Submandibular	4	2%
Other[c]	4	2%
Transpatial	3	2%
Total	184	100%

[a] Cervical lymph node levels II–VI and supraclavicular.
[b] Biopsies involving the supraglottic larynx, glottis, subglottic larynx, tracheoesophageal groove, and thyroid gland.
[c] Biopsies of the periorbital region, anterior maxilla, preauricular, postauricular, and intramuscular regions.

Table 3: Follow-up of "negative for malignancy" biopsies

Patients' Characteristics and Lesion Management	No.	%
Initially "negative for malignancy" biopsies	43/184	23%
Patients with a known malignancy	29/43	68%
Rebiopsied/excised	7/29	20%
Ultimately +malignancy	4/7	57%
Stable/resolved (mean f/u time: 32 mo, 2–120 mo)	17/29	59%
No f/u	5/29	17%
Patients without known malignancy	14/43	32%
Rebiopsied/excised	5/14	36%
Ultimately + malignancy	0/5	0%
Stable/resolved (mean f/u time: 25.6 mo, 1–72 mo)	7/14	50%
No f/u	2/14	14%
Total false-negative rate	4/184	2%
Total diagnostic yield	167/184	91%

Note:—f/u indicates follow-up.

rebiopsy/surgical excision, resulting in a 2% false-negative rate and an adjusted diagnostic yield of 167/184 (91%). The diagnostic yield was 93% (155/166) for lesions of >10 mm in the greatest axial dimension, but for lesions of ≤10 mm, the yield was only 67% (12/18).

Biopsies were performed by 16 neuroradiologists with variable experience. The diagnostic yield was essentially the same: 91% (64/70) for proceduralists with ≤3 years and 90% (103/114) with >3 years' experience. The diagnostic yield per biopsy needle gauge was as follows: 20 ga, 81% (13/16); 18 ga, 93% (70/75); 16 ga, 90% (64/71), and 14 ga, 91% (20/22). Although we as a practice try to use the largest needle size (smallest gauge) safely possible to get the most tissue, ultimately the choice of the needle gauge was up to the proceduralist, understandably resorting to thinner needles in cases of challenging anatomy (eg, retropharyngeal/carotid/parapharyngeal space and close ICA proximity), but not necessarily in cases of smaller lesions.

Histopathology results are summarized in the Online Supplemental Data. Eighty-six of 184 (47%) lesions were malignant: 23/86 (27%), reflecting primary malignancy; 36/86 (42%), local recurrence; and 27/86 (31%), metastases.

Eighty-five of 184 (46%) lesions were benign, including 43/85 (51%) reported as samples negative for malignancy containing regional tissues.

Of these 43 biopsies initially negative for malignancy, 4/43 (9%) were ultimately positive for malignancy after rebiopsy/excision. Follow-up of biopsies negative for malignancy is summarized in Table 3. Finally, of 13 nondiagnostic biopsies, 3/13 (23%) were ultimately positive for malignancy after rebiopsy/excision.

DISCUSSION

Our study of 184 CT-guided CNBs of H&N lesions represents the largest-to-date single-center retrospective review. This study confirms a very high diagnostic yield of 91% with a low false-negative rate of only 2%. These results in such a large sample with 16 operators with different experience levels are clinically important, suggesting that the described techniques would be generalizable across multiple medical centers. Additionally, on the basis of our large sample size, these procedures are clinically useful because they can be performed safely and efficiently, delivering a timely diagnosis and expediting appropriate treatment while avoiding much more invasive surgical excisional biopsies and with a much higher diagnostic yield than FNAs, especially in cases of unusual etiology.[2-4,16,17]

Our diagnostic yield of 91%, including a 2% false-negative rate, is concordant with several prior, though much smaller sample studies (each with <30 patients), which showed a diagnostic yield of 73%–100%.[12-14,18,19]

In addition to being the largest-to-date single-center cohort of CT-guided CNBs of H&N lesions, our study demonstrates a wider variety of biopsy approaches, including transosseous, and provides an extensive morphologic and histologic assessment of 184 lesions. We also describe a novel technique of intraprocedural IV contrast to improve the safety profile through continuous opacification of the adjacent vessels immediately prior to and during lesion sampling in cases of proximity of the vessels to the target lesion.

Our study, in addition to its retrospective design, has a potential limitation of selection bias for lesions that were challenging/inaccessible to excisional or ultrasound-guided biopsy, whether core or FNA. Our institution preferentially performs CT-guided core needle biopsies of H&N lesions as opposed to CT-guided aspiration, with the latter reportedly having up to an 88% concordant diagnostic yield based on the largest study of 216 patients by Sherman et al,[10] in 2004. We also preferentially perform CT-guided CNBs of the superficial H&N lesions as opposed to ultrasound-guided CNB, though Haldar et al,[5] in 2015, reported a very high diagnostic yield (96%) of ultrasound-guided CNB of 313 parotid neoplasms with only 2 samples being false-negatives (versus 44% and 3 samples, respectively, in 120 parotid ultrasound-guided FNAs).

Aiken, in 2020,[17] published a great commentary addressing a practical approach to the triage of H&N biopsies at a major academic institution, which usually starts with FNA and then shifts to core biopsy if directed by the cytopathologist's real-time feedback. We do agree that FNA will usually suffice to diagnose cervical nodal metastasis or recurrence for most

common pathologies such as SCC or thyroid carcinoma, and CNB as opposed to FNA is mostly based on our institutional preference. FNAs are, indeed, often the first step in cases of obvious cervical lymphadenopathy and are not uncommonly performed by our ear, nose, and throat group with ultrasound guidance during the patient encounter. However, cases of impalpable cervical lymphadenopathy and smaller nodes (eg, <1.5 cm) without apparent abnormal morphology on CT would go straight to CT-guided CNB to avoid discrepancies between CT and ultrasound imaging modalities and to maximize the diagnostic yield.

Further prospective studies with high volumes of CT-guided biopsies of H&N lesions could focus on direct comparison of CT-guided core biopsies with FNAs in a variety of anatomic spaces, particularly of more challenging smaller lesions of <10 mm in retropharyngeal and parapharyngeal spaces.

CONCLUSIONS

Our largest-to-date single-center retrospective study of 184 CT-guided core needle biopsies of H&N lesions confirms that these procedures can be performed safely with a high diagnostic yield by operators with variable experience. In addition to gantry tilt and preprocedural IV contrast administration for vessel and target lesion mapping, continuous intraprocedural IV contrast infusion during lesion sampling can significantly facilitate the procedure and increase the safety profile.

Disclosure forms provided by the authors are available with the full text and PDF of this article at www.ajnr.org.

REFERENCES

1. Siegel RL, Miller KD, Fuchs HE, et al. **Cancer statistics, 2021.** *CA A Cancer J Clin* 2021;71:7–33 CrossRef Medline
2. Huang YC, Wu CT, Lin G, et al. **Comparison of ultrasonographically guided fine-needle aspiration and core needle biopsy in the diagnosis of parotid masses.** *J Clin Ultrasound* 2012;40:189–94 CrossRef Medline
3. Song IH, Song JS, Sung CO, et al. **Accuracy of core needle biopsy versus fine needle aspiration cytology for diagnosing salivary gland tumors.** *J Pathol Transl Med* 2015;49:136–43 CrossRef Medline
4. Ryu YJ, Cha W, Jeong J, et al. **Diagnostic role of core needle biopsy in cervical lymphadenopathy.** *Head Neck* 2015;37:229–33 CrossRef Medline
5. Haldar S, Mandalia U, Skelton E, et al. **Diagnostic investigation of parotid neoplasms: a 16-year experience of freehand fine needle aspiration cytology and ultrasound-guided core needle biopsy.** *Int J Oral Maxillofac Surg* 2015;44:151–57 CrossRef Medline
6. Drylewicz MR, Watkins MP, Shetty AS, et al. **Formulating a treatment plan in suspected lymphoma: ultrasound-guided core needle biopsy versus core needle biopsy and fine-needle aspiration of peripheral lymph nodes.** *J Ultrasound Med* 2019;38:581–86 CrossRef Medline
7. Abrahams JJ. **Mandibular sigmoid notch: a window for CT-guided biopsies of lesions in the parapharyngeal and skull base regions.** *Radiology* 1998;208:695–99 CrossRef Medline
8. Gupta S, Henningsen JA, Wallace MJ, et al. **Percutaneous biopsy of head and neck lesions with CT guidance: various approaches and relevant anatomic and technical considerations.** *Radiographics* 2007;27:371–90 CrossRef Medline
9. McKnight CD, Glastonbury CM, Ibrahim M, et al. **Techniques and approaches for safe, high-yield CT-guided suprahyoid head and neck biopsies.** *AJR Am J Roentgenol* 2017;208:76–83 CrossRef Medline
10. Sherman PM, Yousem DM, Loevner LA. **CT-guided aspirations in the head and neck: assessment of the first 216 cases.** *AJNR Am J Neuroradiol* 2004;25:1603–07 Medline
11. Tu AS, Geyer CA, Mancall AC, et al. **The buccal space: a doorway for percutaneous CT-guided biopsy of the parapharyngeal region.** *AJNR Am J Neuroradiol* 1998;19:728–31 Medline
12. Connor SEJ, Chaudhary N. **CT-guided percutaneous core biopsy of deep face and skull-base lesions.** *Clin Radiol* 2008;63:986–94 CrossRef Medline
13. Wu EH, Chen YL, Wu YM, et al. **CT-guided core needle biopsy of deep suprahyoid head and neck lesions.** *Korean J Radiol* 2013;14:299–306 CrossRef Medline
14. Hillen TJ, Baker JC, Long JR, et al. **Percutaneous CT-guided core needle biopsies of head and neck masses: technique, histopathologic yield, and safety at a single academic institution.** *AJNR Am J Neuroradiol* 2020;41:2117–22 CrossRef Medline
15. Grewal A, Khera SS, McGahan JP, et al. **Utility of intra-procedural contrast enhanced CT in ablation of renal masses.** *AJR Am J Roentgenol* 2020;214:122–28 CrossRef Medline
16. Park YM, Oh KH, Cho JG, et al. **Analysis of efficacy and safety of core-needle biopsy versus fine-needle aspiration cytology in patients with cervical lymphadenopathy and salivary gland tumour.** *Int J Oral Maxillofac Surg* 2018;47:1229–35 CrossRef Medline
17. Aiken AH. **Image-guided biopsies in the head and neck: practical value and approach.** *AJNR Am J Neuroradiol* 2020;41:2123–25 CrossRef Medline
18. Wu EH, Chen YL, Toh CH, et al. **CT-guided core needle biopsy of deep suprahyoid head and neck lesions in untreated patients.** *Interv Neuroradiol* 2013;19:365– 69 CrossRef Medline
19. Cunningham JD, McCusker MW, Power S, et al. **Accessible or inaccessible? Diagnostic efficacy of CT-guided core biopsies of head and neck masses.** *Cardiovasc Intervent Radiol* 2015;38:422–29 CrossRef Medline

Regional Differences in Gamma-Aminobutyric Acid and Glutamate Concentrations in the Healthy Newborn Brain

S.K. Basu, S. Pradhan, S.D. Barnett, M. Mikkelsen, K.J. Kapse, J. Murnick, J.L. Quistorff, C.A. Lopez, A.J. du Plessis, and C. Limperopoulos

ABSTRACT

BACKGROUND AND PURPOSE: Gamma-aminobutyric acid and glutamate system disruptions may underlie neonatal brain injury. However, in vivo investigations are challenged by the need for special ^{1}H-MR spectroscopy sequences for the reliable measurement of the neurotransmitters in this population. We used *J*-edited ^{1}H-MR spectroscopy (Mescher-Garwood point-resolved spectroscopy) to quantify regional in vivo gamma-aminobutyric acid and glutamate concentrations during the early postnatal period in healthy neonates.

MATERIALS AND METHODS: We prospectively enrolled healthy neonates and acquired Mescher-Garwood point-resolved spectroscopy spectra on a 3T MR imaging scanner from voxels located in the cerebellum, the right basal ganglia, and the right frontal lobe. CSF-corrected metabolite concentrations were compared for regional variations and cross-sectional temporal trends with advancing age.

RESULTS: Fifty-eight neonates with acceptable spectra acquired at postmenstrual age of 39.1 (SD, 1.3) weeks were included for analysis. Gamma-aminobutyric acid (+ macromolecule) (2.56 [SD, 0.1]) i.u., glutamate (3.80 [SD, 0.2]), Cho, and mIns concentrations were highest in the cerebellum, whereas NAA (6.72 [SD, 0.2]), NAA/Cho, Cr/Cho, and Glx/Cho were highest in the basal ganglia. Frontal gamma-aminobutyric acid (1.63 [SD, 0.1]), Glx (4.33 [SD, 0.3]), Cr (3.64 [SD, 0.2]), and Cho concentrations were the lowest among the ROIs. Glx, NAA, and Cr demonstrated a significant adjusted increase with postmenstrual age (β = 0.2–0.35), whereas gamma-aminobutyric acid and Cho did not.

CONCLUSIONS: We report normative regional variations and temporal trends of in vivo gamma-aminobutyric acid and glutamate concentrations reflecting the functional and maturational status of 3 distinct brain regions of the neonate. These measures will serve as important normative values to allow early detection of subtle neurometabolic alterations in high-risk neonates.

ABBREVIATIONS: *J*-DIFF = *J*-edited difference spectrum; GABA = gamma-aminobutyric acid; GABA+ = GABA with macromolecules; Glu = glutamate; GSH = glutathione; MEGA-PRESS = Mescher-Garwood point-resolved spectroscopy; NDI = neurodevelopmental impairment; NS = not significant; PMA = postmenstrual age; TEA = term-equivalent age

Gamma-aminobutyric acid (GABA) and glutamate (Glu) are principal neurotransmitters and play a critical role in fetal and neonatal brain development.[1] Microstructural disruptions of neurotransmitter systems have been reported following preterm birth in animal and ex vivo human studies.[2,3] Subtle disruptions may play a role in neurodevelopmental impairments (NDIs) observed in surviving premature infants even without structural brain injury on conventional neuroimaging at term-equivalent age (TEA).[4] Recent advances in ^{1}H-MR spectroscopy, including *J*-edited Mescher-Garwood point-resolved spectroscopy (MEGA-PRESS), have allowed detection of the otherwise overlapped GABA and glutamate signals.[5,6] However, the application of these techniques to the neonate has been limited by technical challenges, including motion during nonsedated scans, suboptimal tissue segmentation and correction using adult algorithms, and a

Received June 14, 2021; accepted after revision September 10.

From the Department of Neonatology (S.K.B.), Developing Brain Institute (S.K.B., S.P., S.D.B., K.J.K., J.L.Q., C.A.L., C.L.), Division of Diagnostic Imaging and Radiology (C.L.), and Fetal Medicine Institute (A.J.d.P.), Children's National Hospital, Washington, DC; George Washington University School of Medicine (S.K.B., S.P., S.D.B., J.M., A.J.d.P., C.L.), Washington, DC; and Department of Radiology (M.M., J.M.), Weill Cornell Medicine, New York, New York.

The study was supported by grant funding from the National Institutes of Health–National Heart, Lung, and Blood Institute award No. 1R01HL116585; Intellectual and Developmental Disabilities Research Center award No. 1U54HD090257; National Center for Advancing Translational Sciences award Nos. UL1TR001876 and KL2TR001877; and the A. James and Alice B. Clark Foundation award. Additional support was received from internal departmental funds of Children's National Hospital in Washington, DC.

The content is solely the responsibility of the authors and does not necessarily represent the official views of the Intellectual and Developmental Disabilities Research Center, the National Center for Advancing Translational Sciences, or the National Institutes of Health.

Please address correspondence to Catherine Limperopoulos, PhD, George Washington University School of Medicine, 111 Michigan Ave, NW, Washington, DC 20010; e-mail: climpero@childrensnational.org

Indicates open access to non-subscribers at www.ajnr.org

Indicates article with online supplemental data.

http://dx.doi.org/10.3174/ajnr.A7336

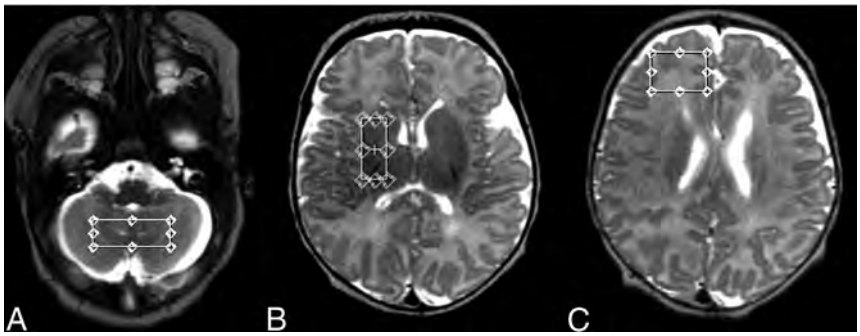

FIG 1. Voxel locations of ROIs: cerebellum (*A*), right basal ganglia (*B*), and right frontal lobe (*C*).

lower SNR from a limited voxel volume in the small neonatal brain, to name a few.[7-11]

Important knowledge gaps remain in our understanding of the normal temporal trajectory of in vivo GABA and glutamate concentrations during the critical perinatal transition and early postnatal maturation, which, in turn, limit the ability to detect abnormalities following premature birth.[11] Animal and adult human studies have characterized the temporal trajectories of brain metabolites, their regional and sex-based variations, and the influence of mode of delivery; early postnatal studies, however, are currently limited.[12-16] Conventional neonatal ^{1}H-MR spectroscopy allows measurement of NAA and Cr (markers of neuronal integrity and metabolic activity), Cho (lipid membrane component), and mIns (cytoplasmic osmotic agent). Neonatal brain injury has been associated with lower NAA,[17,18] and simultaneous GABA and glutamate measurements would allow in vivo neurotransmitter-specific interrogation of the developing brain.[7-10,19]

To fill these critical knowledge gaps, we measured in vivo GABA+ and Glx concentrations from MEGA-PRESS spectra acquired from voxels placed in 3 ROIs: namely, the cerebellum, the right basal ganglia, and the right frontal lobe in healthy neonates. The cerebellum is known to play a regulatory-inhibitory role and accounts for most GABA and glutamatergic neurons in the human brain. The cerebellum matures rapidly during late gestation, with extended neurogenesis through infancy; and its parenchymal injury is associated with NDI in preterm infants.[1] The basal ganglia are involved in sensorimotor organization and include an array of nuclei with glutamatergic and GABAergic neurons, and due to their high metabolic activity, they are vulnerable to the hypoxia-ischemia associated with premature birth.[1] Finally, the frontal lobe is evolutionarily recent, mediates cognitive and executive function, but is relatively less mature in neonates.[1]

We hypothesized that these 3 critical brain ROIs would have distinct profiles of GABA+ and Glx as well as other metabolite concentrations in healthy neonates. We also hypothesized that NAA, Cr, and Glx would increase with advancing age (postmenstrual age [PMA]), whereas Cho (and GABA+) would remain relatively stable.[10,16,19,20] We sought to investigate the influence of postnatal age (weeks of life), sex, and mode of delivery on the neurometabolic profile of the neonatal brain.

MATERIALS AND METHODS

Participants

Healthy neonates born after 36 completed weeks of gestational age were prospectively enrolled between 2018 and 2020 in observational multimodal neuroimaging cohort studies. Neonates with known genetic syndromes, central nervous system anomalies, brain injury on MR imaging, or congenital infections were excluded. Clinical data were collected through medical record review and parental questionnaires. All studies were approved by the Children's National Hospital review board and conducted in accordance with relevant guidelines and regulations. Written informed consent was obtained from the parents of each study participant.

MR Imaging and ^{1}H-MRS Acquisition

Enrolled infants underwent a TEA MR imaging during natural sleep using the feed and swaddle technique on a 3T Discovery MR750 MR imaging scanner (GE Healthcare). Anatomic images were acquired using a T2-weighted 3D Cube (GE Healthcare; 3D FSE) sequence with the following parameters: section thickness = 1 mm, section spacing = 0 mm, TR = 2500 ms, TE = 64.7–89.9 ms, flip angle = 90°, orientation = superior/inferior, number of slices = 120, matrix = 160 × 160. ^{1}H-MR spectroscopy data were acquired from voxels placed in 3 ROIs: a $20 \times 15 \times 15$ mm^3 voxel centered on the white matter of the right frontal lobe, a $20 \times 20 \times 20$ mm^3 voxel centered on right basal ganglia, and a $25 \times 15 \times 10$ mm^3 voxel placed in the middle of the cerebellum (Fig 1). The MEGA-PRESS sequence was acquired using TE = 68 ms, TR = 2000 ms, spectral width = 5000 Hz, 4096 points, and 256 signal averages. Frequency-selective editing pulses (16-ms duration) were placed at 1.9 ppm during ON and 7.5 ppm during OFF acquisitions, respectively. *J*-edited difference (*J*-DIFF) spectra were generated by subtracting the OFF spectrum from the ON spectrum (composite *J*-DIFF and OFF spectra are shown in Fig 2) for each acquisition. Eight unsuppressed water averages were acquired for concentration referencing.

^{1}H-MR Spectroscopy Data Pre- and Postprocessing

The pre- and postprocessing methods detailed previously[7] included frequency and phase correction[21] using the OFF and ON spectra to generate the *J*-DIFF spectrum. Each OFF and *J*-DIFF spectrum was analyzed using LCModel (http://www.lcmodel.com/) to measure metabolite concentrations using the unsuppressed water signal as an internal reference.[22] The LCModel outputs were visually screened for artifacts, and only those with a full width at half maximum of ≤15 Hz and an SNR of ≥3 for the OFF spectra and an SNR of ≥2 for the DIFF spectra were included for further analysis.

GABA measurements from MEGA-PRESS spectra included contribution from coedited resonances from unspecified macromolecule resonances at 3 ppm and hence are represented as GABA+.[6] Analysis in the LCModel was performed using SPTYPE = MEGA-PRESS-3 without inclusion of quantification of the macromolecule

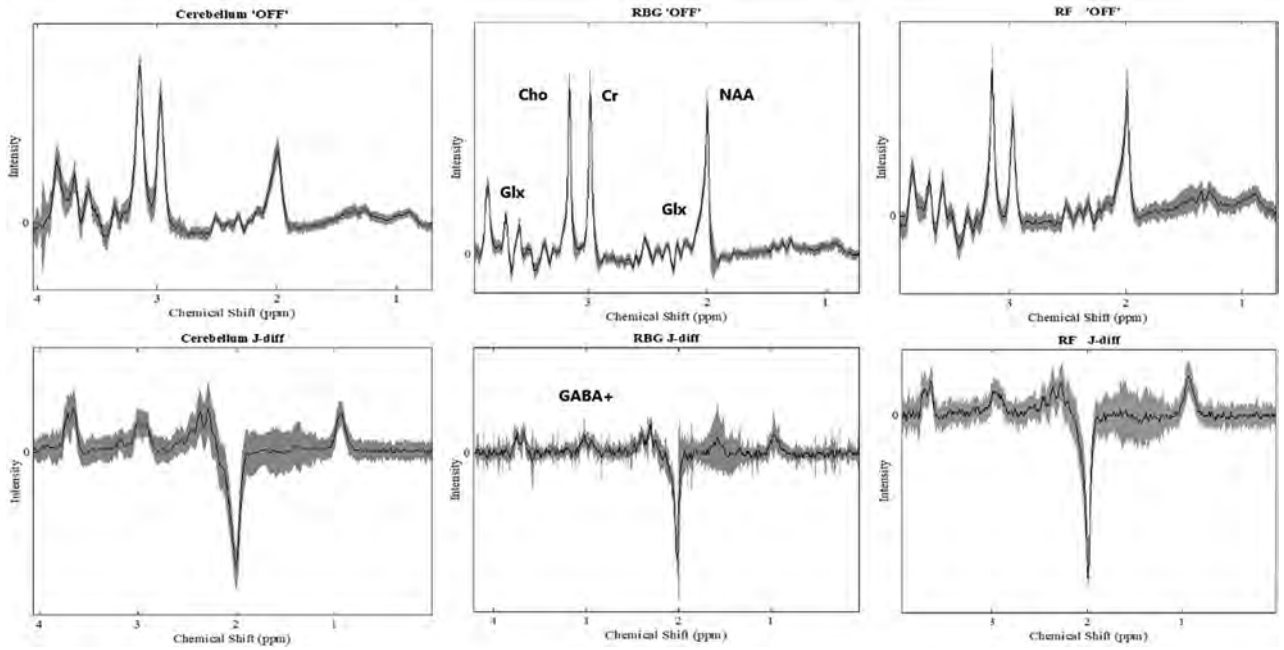

FIG 2. Composite ^{1}H-MR spectroscopy PRESS OFF and *J*-DIFF spectra for all 3 ROIs. Composite spectra from the 3 ROI voxels show the mean (*solid line*) and SD (*shaded area*) of all spectra included in the analysis. The spectra were acquired on a 3T scanner with TE = 68 ms, TR = 2000 ms, number of signal averages = 256, and the editing pulses at 1.9 and 7.5 ppm. RBG indicates right basal ganglia; RF, right frontal lobe.

peak in the analysis. Hence, the GABA+ results reported correspond 1:1 to the GABA basis function scaled to the water peak.

Concentrations of Glu, glutamine, Glx, NAA, Cho, Cr, glutathione (GSH), and mIns were measured from the OFF spectra LCModel output. All metabolite concentrations are reported in international units. We accepted Cramer-Rao lower bound confidence intervals up to 50% for NAA, Cho, and Cr and up to 100% for other metabolites due to their lower concentrations, an a priori decision consistent with previous publications.[7,19,23,24]

Tissue Segmentation and Correction for Voxel Composition

The 3D T2 Cube images were automatically segmented using Draw-EM (https://github.com/MIRTK/DrawEM) and manually corrected in ITK-SNAP (www.itksnap.org) to measure global and regional brain volumes. The Gannet code (https://github.com/richardedden/Gannet3.1) with modifications to use segmented images exported from ITK-SNAP was used to generate voxel masks and was coregistered with segmented structural images to measure the voxel tissue fractions of CSF, GM, and WM.[25] Due to the intricate cerebellar folia, we segmented the cerebellar voxel into either GM + WM or CSF (ie, 2 tissue classes). Because intrinsic differences in metabolite levels between the GM and WM remain undetermined in the neonatal population,[8] we used a composite GM + WM tissue fraction for CSF correction using the following equation:

$$Metabolite_{corrected} = M_{raw} \div (f_{GM} + f_{WM}).$$

This approach assumes that there are negligible metabolite levels in the CSF and that GM and WM contribute equally to the metabolite signal in the spectra,[8] effectively a CSF correction.

Statistical Analysis

Baseline characteristics of the cohort are presented as mean (SD) or frequency (percentage). Descriptive analyses of ^{1}H-MR spectroscopy acquisition parameters and metabolite measurements, group (sex and mode of delivery), and regional comparisons were performed using nonparametric tests (ie, median, inter-quartile range, Wilcoxon Mann–Whitney test, and Kruskal-Wallis ANOVA, respectively). Spearman correlations were performed to investigate the relationships between metabolites and gestational age at birth, PMA, and postnatal age on the day of MR imaging. Linear mixed models were used to examine differences in metabolite concentrations among the 3 ROIs, adjusted for PMA. Post hoc ROI tests were conducted using contrasts. Potential confounding from clinical variables with previously reported (sex)[7] or biologically plausible (mode of delivery)[11] associations with brain metabolites or neonatal outcomes was examined. Separate mixed-regression models were used to investigate the influence of PMA (model 1, adjusted for sex and mode of delivery) and postnatal age (model 2, adjusted for gestational age, sex, and mode of delivery) on metabolites on the day of MR imaging. Analyses were conducted using SAS 9.4 (SAS Institute). *P* values ≤ .05, two-tailed, were statistically significant. Sample size calculation and adjustment for multiple comparisons were not performed due to the descriptive nature of the study.

RESULTS

Descriptive Characteristics of the Cohort

Fifty-eight term control neonates born at a mean gestational age of 39.1 (SD, 1.3) weeks and birth weight of 3278 (SD, 464) g were included. Neonates underwent nonsedated MR imaging between 38.6 and 48.7 weeks' PMA, and their postnatal age ranged from

0.7 to 8.9 weeks. Baseline characteristics of the cohort are detailed in Table 1.

Voxel Characteristics

The median voxel volume was largest for the cerebellum (8.0 cm^3). All ROI voxels were composed <10% by CSF proportion on average, with the highest gray matter proportion (99%) in the right basal ganglia (Online Supplemental Data).

Measured Raw and CSF-Corrected Metabolite Concentrations

Of the 58 neonates included, 51 cerebellar, 36 right basal ganglia, and 48 right frontal spectra met quality inclusion criteria and raw (_r) metabolite concentration, and ratios are reported for them (Online Supplemental Data). We were able to determine tissue composition for 38/51 cerebellar, 30/36 basal ganglia, and 38/48 frontal lobe voxels and report CSF-corrected metabolite concentrations for them (Online Supplemental Data). Raw metabolite concentrations were not used for subsequent analyses (Tables 2 and 3). However, all metabolite ratios (from 51 cerebellar, 36 basal ganglia, and 48 frontal voxels) were included for regression analysis because CSF-correction factors cancel out for the ratios.

Adjusted for PMA (Table 2), cerebellar GABA+, Glu, glutamine, Cho, mIns, and GSH concentrations were the highest among the 3 ROIs, whereas NAA and Glx/Cho were the lowest. NAA concentrations and the ratio of NAA/Cho, Cr/Cho, and Glx/Cho were highest in the basal ganglia. The frontal lobe had the lowest GABA+, Glx, Cr, Cho, and GSH concentrations.

Table 1: Baseline clinical parameters ($n = 58$)[a]

Clinical Parameters	
GA at birth (wk)	39.1 (SD, 1.3)
Birth weight (g)	3278 (SD, 464)
Female sex	28 (48%)
Race	
African American	8 (15%)
White	35 (65%)
Others	11 (20%)
Singleton gestation	60 (100%)
Apgar score at 5 min (in median)	9 (9)
Vaginal delivery	31 (57%)
Maternal age (yr)	35.4 (SD, 5.6)
PMA at MR imaging (wk)	43.1 (SD, 2.4)
Postnatal age at MR imaging (wk)	3.9 (SD, 2.1)

Note:—GA indicates gestational age.
[a] Data are means and frequency. (%) unless otherwise noted.

Association of Sex, Race, and Mode of Delivery with Metabolite Concentrations

Sex, race, and mode of delivery were not associated with significant differences in metabolite concentrations. Female neonates had lower right frontal lobe GABA+ (mean, 1.57 [SD, 0.4] i.u. versus 1.74 [SD, 0.5]) i.u. concentrations compared with males, but they were not statistically significant (NS).

Correlation of Metabolite Concentrations with Age

Spearman correlations of GABA+ concentrations with PMA, gestational age at birth, and postnatal age did not demonstrate significant correlations (Spearman $\rho < 0.2$, $P =$ NS), except for positive trends in the frontal lobe with PMA ($\rho = 0.34$, $P = .08$) and postnatal age ($\rho = 0.35$, $P = .07$) (Fig 3). NAA, Cr, Glu, NAA/Cho, and Cr/Cho positively correlated with PMA (Spearman $\rho = 0.5$–0.7, $P < .01$) across all ROIs. Glx and Glx/Cho correlated positively with PMA ($\rho = 0.4$–0.5, $P < .01$) and postnatal age ($\rho = 0.3$–0.4, $P < .01$) in the basal ganglia and the frontal voxels, but not in the cerebellum. Cho concentrations in the cerebellum and frontal lobe increased with PMA with a lower slope ($\rho \sim 0.3$–0.5, $P < .03$), but not in the basal ganglia. Cho concentrations did not increase with advancing postnatal age (<.3, NS).

Relationship between Brain Metabolites and PMA and Postnatal Age

Multivariable regression analyses did not show any significant changes in GABA+ concentrations or ratios with age (Table 3). Basal ganglia Glx/Cho and NAA/Cho increased with PMA as well

Table 2: Regional difference in metabolite concentrations adjusted for PMA[a]

				Pair-Wise Comparisons (*P* Value)		
	Cerebellum	Right Basal Ganglia	Right Frontal Lobe	C vs RBG	C vs RF	RBG vs RF
Metabolites						
GABA+	2.56 (SD, 0.1)	2.25 (SD, 0.1)	1.63 (SD, 0.1)	↑.04	↑<.001	↑<.001
Glx	5.95 (SD, 0.2)	5.68 (SD, 0.3)	4.33 (SD, 0.3)	NS	↑<.001	↑<.001
NAA	3.84 (SD, 0.1)	6.72 (SD, 0.2)	4.31 (SD, 0.2)	↓<.001	↓.05	↑<.001
Cr	6.67 (SD, 0.1)	6.72 (SD, 0.2)	3.64 (SD, 0.2)	NS	↑<.001	↑<.001
Cho	3.08 (SD, 0.1)	2.33 (SD, 0.1)	1.88 (SD, 0.1)	↑<.001	↑<.001	↑<.001
Glu	3.80 (SD, 0.2)	3.78 (SD, 0.2)	3.07 (SD, 0.2)	NS	↑.006	↑.02
Gln	2.55 (SD, 0.1)	1.95 (SD, 0.2)	1.72 (SD, 0.2)	↑.005	↑<.001	NS
GSH	1.89 (SD, 0.1)	1.23 (SD, 0.1)	1.05 (SD, 0.1)	↑<.001	↑<.001	NS
mIns	8.02 (SD, 0.3)	5.10 (SD, 0.3)	6.05 (SD, 0.3)	↑<.001	↑<.001	↓.017
Metabolite ratios						
GABA+/Cho	0.85 (SD, 0.4)	0.97 (SD, 0.0)	0.86 (SD, 0.4)	↑.03	NS	NS
Glx/Cho	1.97 (SD, 0.1)	2.53 (SD, 0.1)	2.26 (SD, 0.1)	↓<.001	↓.004	↑.026
NAA/Cho	1.31 (SD, 0.0)	3.00 (SD, 0.1)	2.34 (SD, 0.0)	↓<.001	↓<.001	↑<.001
Cr/Cho	2.18 (SD, 0.0)	2.96 (SD, 0.1)	1.96 (SD, 0.0)	↓<.001	↑<.001	↑<.001
GABA+/Glx	0.45 (SD, 0.2)	0.39 (SD, 0.0)	0.41 (SD, 0.2)	NS	NS	NS

Note:—↑ indicates higher than; ↓, lower than; C, cerebellum; RBG, right basal ganglia; RF, right frontal lobe; GLN, glutamine.
[a] Metabolites are marginal means (SD, standard error, in international units) adjusted for PMA. Metabolites are the following: $n = 38$ for the cerebellum, $n = 30$ for the right basal ganglia, and $n = 38$ for the right frontal lobe. Metabolite ratios are the following: cerebellum ($n = 51$), right basal ganglia ($n = 36$), and left frontal lobe ($n = 48$).

Table 3: Association of PMA and postnatal age with metabolites adjusted for clinical factors[a]

	Age Parameter	Cerebellum (β, *P* Value)	Right Basal Ganglia (β, *P* Value)	Right Frontal Lobe (β, *P* Value)
Metabolite				
GABA+	Model 1[b]: PMA (wk)	0.02, NS	0.02, NS	0.06, .11
	Model 2[c]: postnatal age (wk)	–0.01, NS	0.10, NS	0.09, NS
Glx	PMA	0.25, .09	0.22, .003	0.3, .005
	Postnatal age	0.03, NS	0.15, .13	0.14, NS
Cr	PMA	0.29, .002	0.11, .11	0.20, <.001
	Postnatal age	0.15, NS	0.06, NS	0.14, .06
Cho	PMA	0.06, .095	0.02, NS	0.05, .016
	Postnatal age	0.03, NS	0.01, NS	0.03, NS
NAA	PMA	0.22, .002	0.23, <.001	0.36, <.001
	Postnatal age	0.14, .11	0.17, .06	0.27, .007
Metabolite ratios				
Glx/Cho	PMA	0.02, NS	0.10, .003	0.09, .02
	Postnatal age	–0.02, NS	0.08, .038	0.06, NS
GABA+/Cho	PMA	–0.01, NS	0.02, NS	0.02, NS
	Postnatal age	-0.02, NS	0.02, NS	0.03, .10
NAA Cho	PMA	0.05, .001	0.13, <.001	0.13, <.001
	Postnatal age	0.04, .04	0.08, .002	0.10, <.001
Cr/Cho	PMA	0.05, <.001	0.05, .12	0.06, <.001
	Postnatal age	0.02, .14	0.06, .13	0.05, .015
GABA+/Glx	PMA	–0.02, NS	–0.02, .11	–0.01, NS
	Postnatal age (wk)	0.00, NS	–0.01, NS	0.00, NS

[a]Metabolites are the following: $n = 38$ for the cerebellum, $n = 30$ for the right basal ganglia, and $n = 38$ for the right frontal lobe. Metabolite ratios were the following: cerebellum ($n = 51$), right basal ganglia ($n = 36$), and left frontal lobe ($n = 48$).
[b] Linear regression model 1: adjusted for PMA, sex, and mode of delivery.
[c] Linear regression model 2: adjusted for postnatal age, gestational age, sex, and mode of delivery.

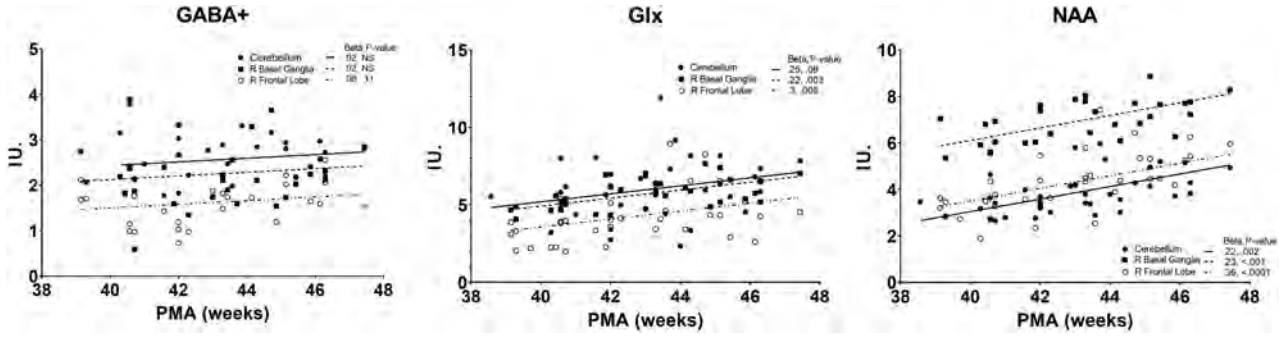

FIG 3. Temporal trajectories of metabolites with postmenstrual age. R indicates right.

as postnatal age. Glx concentrations increased with PMA (NS for the cerebellum). NAA and NAA/Cho increased with PMA across all ROIs. Cho concentrations in the frontal lobe increased with PMA, but not with postnatal age in any of the ROIs.

DISCUSSION

We report, for the first time, normative data on regional in vivo variations of GABA and glutamate concentrations and their cross-sectional temporal trajectory during the early postnatal period. We observed distinct regional metabolic profiles in relationship to PMA and postnatal age, which may reflect differential maturational states and postnatal stimulation in the healthy neonate brain.

Our normative data from 3 ROIs of 58 healthy neonates are the largest cohort reported to date and will provide references for future investigations of alterations in neonates at risk of brain injury. The previous largest study, including 25 term neonates, reported higher right frontal GABA+ concentrations compared with preterm neonates.[9] Temporal increases in basal ganglia Glx and stable GABA+ concentrations during infancy were reported in preterm neonates, without data from term controls.[19] One study including both term and preterm neonates reported higher GABA+ and Glx concentrations in the thalamus compared with anterior cingulate cortex, which lost statistical significance after tissue correction.[8]

We demonstrated that all metabolites except GABA+ positively correlated with advancing PMA, which likely reflects increasing metabolic activity of maturing neurons, dendrites, synapses, and glial cells (Fig 3). The stable GABA+ concentrations observed are consistent with those in previous animal [12,16] and clinical studies in preterm infants.[7,19] Consistent with previous studies,[16,19] Cr concentrations increased significantly with PMA, whereas Cho remained relatively stable; hence, metabolite/Cho ratios are preferable markers of metabolic changes during early postnatal life. The duration of extrauterine exposure (postnatal

age) demonstrated a significant positive correlation with basal ganglia Glx/Cho, perhaps indicating neuronal stimulation.

We found that NAA, NAA/Cho, Cr/Cho, and Glx/Cho (markers of neuronal integrity and metabolic activity) were highest in the basal ganglia, reflecting their relatively higher functional activity (Table 2). Also, the significant increase in Cr and Glx/Cho (NAA increase NS) within the basal ganglia with postnatal age (Table 3) indicates their metabolic and functional activity in response to extrauterine motor-sensory stimulation. Conversely, right frontal GABA+, Glx, and Cr concentrations were the lowest, consistent with their relative developmental immaturity in neonates. Cerebellar GABA+ and Glx concentrations were the highest, reflecting their dense neuronal composition. Cho, a marker of cell membrane turnover, was also highest in the cerebellum, perhaps inferring exuberant dendritic maturation as well as ongoing postnatal neurogenesis, as previously described in the human cerebellum. Glu, GSH (a cellular redox substrate), and mIns (cytoplasmic osmotic agent) were highest in the cell-dense cerebellum. The observed regional differences remained consistent for both raw and CSF-corrected metabolite concentrations. This finding may be due to the low CSF fraction of the voxels and that differences in gray-versus-white matter contributions to the metabolites could not be segregated.

Although not statistically significant, the lower right frontal GABA+ concentration in female neonates (Table 3) agrees with findings in a recent report in preterm infants.[7] We did not observe any significant relationship of mode of delivery with regional metabolite concentrations, perhaps due to the delay in scan time (median, 4 weeks) after birth.

Although our study findings are strengthened by nonsedated scans in a modest size cohort of healthy neonates during early postnatal life, there are several limitations. The observed correlation of metabolite concentrations with PMA or postnatal age is cross-sectional and not longitudinal. Our tissue-correction strategy was limited to the CSF content of the voxel and assumed equal gray and white matter metabolite contributions. Neonatal algorithms and segmentation maps are needed for metabolite measurements adjusted for gray matter proportion from a neonatal brain voxel because adult algorithms may not reflect the many structural and maturational changes in the neonatal brain. Our data meet the quality parameters recommended in recent expert consensus statements,[24,26,27] though one-fifth of the spectra had to be excluded due to motion or low SNR, inherent challenges with neonatal acquisitions.[11]

Regional differences in ^{1}H-MR spectroscopy acquisition parameters like voxel size and SNR (Online Supplemental Data) may also influence these measurements, though if contributing, they would affect all metabolite measurements and would be nullified for metabolite ratios. The metabolite concentrations are expressed in international units due to their dependence on acquisition parameters and are not generalizable in terms of absolute concentrations across studies using different parameters. Interpretations need to consider that GABA+ has contributions from various macromolecules, whereas Glx has contributions from glutamine. Similarly, Glu, glutamine, and GSH measurements are not optimal from an unedited PRESS acquisition at 3T due to poor spectral resolution, and adult studies have used higher magnetic field strengths, STEAM, or dedicated *J*-editing sequences. Despite these limitations, our study provides normative data and highlights regional differences and the influence of age on the metabolic milieu of the neonatal brain, which will aid in identification of alterations in disease states like neonatal encephalopathy or prematurity.

CONCLUSIONS

We report regional profiles of in vivo GABA+ and glutamate concentrations consistent with maturation and metabolic activity in the healthy neonatal brain. We also report increasing Glx, NAA, and Cr concentrations, but stable GABA and Cho concentrations during the neonatal period. The normative metabolic references may provide important, currently unavailable data that will allow detection of early metabolic and neurotransmitter alterations in neonates at high risk of NDI, even without significant structural brain injury.

ACKNOWLEDGMENT

We would like to acknowledge the contribution of the research nurses and assistants, MR imaging technicians, and other study staff whose relentless effort have made this study successful. Above all, we would like to thank all parents who have voluntarily allowed their children to undergo the MR imaging evaluations, without which this study would not have been possible.

Disclosure forms provided by the authors are available with the full text and PDF of this article at www.ajnr.org.

REFERENCES

1. Volpe JJ. *Volpe's Neurology of the Newborn*. Elsevier; 2018
2. Robinson S, Li Q, Dechant A, et al. **Neonatal loss of gamma-aminobutyric acid pathway expression after human perinatal brain injury.** *J Neurosurg* 2006;104(6 Suppl):396–408 CrossRef Medline
3. Shaw JC, Palliser HK, Dyson RM, et al. **Disruptions to the cerebellar GABAergic system in juvenile guinea pigs following preterm birth.** *Int J Dev Neurosci* 2018;65:1–10 CrossRef Medline
4. Laptook AR, O'Shea TM, Shankaran S, et al. **Adverse neurodevelopmental outcomes among extremely low birth weight infants with a normal head ultrasound: prevalence and antecedents.** *Pediatrics* 2005;115:673–80 CrossRef Medline
5. Harris AD, Saleh MG, Edden RA. **Edited ^{1}H-magnetic resonance spectroscopy in vivo: methods and metabolites.** *Magn Reson Med* 2017;77:1377–89 CrossRef Medline
6. Mullins PG, McGonigle DJ, O'Gorman RL, et al.; Cardiff Symposium on MRS of GABA. **Current practice in the use of MEGA-PRESS spectroscopy for the detection of GABA.** *Neuroimage* 2014;86:43–52 CrossRef Medline
7. Basu SK, Pradhan S, Jacobs MB, et al. **Age and sex influences gamma-aminobutyric acid concentrations in the developing brain of very premature infants.** *Sci Rep* 2020;10:10549 CrossRef Medline
8. Maria YL, Price AN, Puts NA, et al. **Simultaneous quantification of GABA, Glx and GSH in the neonatal human brain using magnetic resonance spectroscopy.** *Neuroimage* 2021;233:117930 CrossRef Medline
9. Kwon SH, Scheinost D, Lacadie C, et al. **GABA, resting-state connectivity and the developing brain.** *Neonatology* 2014;106:149–55 CrossRef Medline

10. Tomiyasu M, Aida N, Shibasaki J, et al. **In vivo estimation of gamma-aminobutyric acid levels in the neonatal brain.** *NMR Biomed* 2017;30:e3666 CrossRef Medline
11. Basu SK, Pradhan S, Du Plessis AJ, et al. **GABA and glutamate in the preterm neonatal brain: in-vivo measurement by magnetic resonance spectroscopy.** *Neuroimage* 2021;238:118215 CrossRef Medline
12. Xu G, Broadbelt KG, Haynes RL, et al. **Late development of the GABAergic system in the human cerebral cortex and white matter.** *J Neuropathol Exp Neurol* 2011;70:841–58 CrossRef Medline
13. Tkac I, Rao R, Georgieff MK, et al. **Developmental and regional changes in the neurochemical profile of the rat brain determined by in vivo ^{1}H NMR spectroscopy.** *Magn Reson Med* 2003;50:24–32 CrossRef Medline
14. O'Gorman RL, Michels L, Edden RA, et al. **In vivo detection of GABA and glutamate with MEGA-PRESS: reproducibility and gender effects.** *J Magn Reson Imaging* 2011;33:1262–67 CrossRef Medline
15. Castillo-Ruiz A, Mosley M, Jacobs AJ, et al. **Birth delivery mode alters perinatal cell death in the mouse brain.** *Proc Natl Acad Sci U S A* 2018;115:11826–31 CrossRef Medline
16. Ramu J, Konak T, Liachenko S. **Magnetic resonance spectroscopic analysis of neurometabolite changes in the developing rat brain at 7T.** *Brain Res* 2016;1651:114–20 CrossRef Medline
17. Koob M, Viola A, Le Fur Y, et al. **Creatine, glutamine plus glutamate, and macromolecules are decreased in the central white matter of premature neonates around term.** *PLoS One* 2016;11:e0160990 CrossRef Medline
18. Basu SK, Pradhan S, Kapse K, et al. **Third trimester cerebellar metabolite concentrations are decreased in very premature infants with structural brain injury.** *Sci Rep* 2019;9:1212–14 CrossRef Medline
19. Tanifuji S, Akasaka M, Kamei A, et al. **Temporal brain metabolite changes in preterm infants with normal development.** *Brain Dev* 2017;39:196–202 CrossRef Medline
20. Craddock RC, James GA, Holtzheimer PE, et al. **A whole brain fMRI atlas generated via spatially constrained spectral clustering.** *Hum Brain Mapp* 2012;33:1914–28 CrossRef Medline
21. Evangelou IE, Noeske R, Limperopoulos C. **Retrospective correction of motion induced artifacts in 1H magnetic resonance spectroscopy of the fetal brain.** In: *Proceedings of the IEEE 12th International Symposium on Biomedical Imaging (ISBI)*, Brooklyn, New York, USA. April 16–19, 2015:853–57
22. Provencher SW. **Automatic quantitation of localized in vivo 1H spectra with LCModel.** *NMR Biomed* 2001;14:260–64 CrossRef Medline
23. Kreis R. **The trouble with quality filtering based on relative Cramer-Rao lower bounds.** *Magn Reson Med* 2016;75:15–18 CrossRef Medline
24. Wilson M, Andronesi O, Barker PB, et al. **Methodological consensus on clinical proton MRS of the brain: review and recommendations.** *Magn Reson Med* 2019;82:527–50 CrossRef Medline
25. Edden RA, Puts NA, Harris AD, et al. **Gannet: a batch-processing tool for the quantitative analysis of gamma-aminobutyric acid-edited MR spectroscopy spectra.** *J Magn Reson Imaging* 2014;40:1445–52 CrossRef Medline
26. Lin A, Andronesi O, Bogner W, et al; Experts' Working Group on Reporting Standards for MR Spectroscopy. **Minimum Reporting Standards for in vivo Magnetic Resonance Spectroscopy (MRSinMRS): experts' consensus recommendations.** *NMR Biomed* 2021;34;e4484 CrossRef Medline
27. Choi IY, Andronesi OC, Barker P, et al. **Spectral editing in ^{1}H-magnetic resonance spectroscopy: experts' consensus recommendations.** *NMR Biomed* 2021;34:e4411 CrossRef Medline

Feasibility and Added Value of Fetal DTI Tractography in the Evaluation of an Isolated Short Corpus Callosum: Preliminary Results

A.-E. Millischer, D. Grevent, P. Sonigo, N. Bahi-Buisson, I. Desguerre, H. Mahallati, J.-P. Bault, T. Quibel, S. Couderc, M.-L. Moutard, E. Julien, V. Dangouloff, B. Bessieres, V. Malan, T. Attie, L.-J. Salomon, and N. Boddaert

ABSTRACT

BACKGROUND AND PURPOSE: Prognosis of isolated short corpus callosum is challenging. Our aim was to assess whether fetal DTI tractography can distinguish callosal dysplasia from variants of normal callosal development in fetuses with an isolated short corpus callosum.

MATERIALS AND METHODS: This was a retrospective study of 37 cases referred for fetal DTI at 30.4 weeks (range, 25–34 weeks) because of an isolated short corpus callosum less than the 5th percentile by sonography at 26 weeks (range, 22–31 weeks). Tractography quality, the presence of Probst bundles, dysmorphic frontal horns, callosal length (internal cranial occipitofrontal dimension/length of the corpus callosum ratio), and callosal thickness were assessed. Cytogenetic data and neurodevelopmental follow-up were systematically reviewed.

RESULTS: Thirty-three of 37 fetal DTIs distinguished the 2 groups: those with Probst bundles (Probst bundles+) in 13/33 cases (40%) and without Probst bundles (Probst bundles–) in 20/33 cases (60%). Internal cranial occipitofrontal dimension/length of the corpus callosum was significantly higher in Probst bundles+ than in Probst bundles–, with a threshold value determined at 3.75 for a sensitivity of 92% (95% CI, 77%–100%) and specificity of 85% (95% CI, 63%–100%). Callosal lipomas (4/4) were all in the Probst bundles– group. More genetic anomalies were found in the Probst bundles+ than in Probst bundles– group (23% versus 10%, $P = .08$).

CONCLUSIONS: Fetal DTI, combined with anatomic, cytogenetic, and clinical characteristics could suggest the possibility of classifying an isolated short corpus callosum as callosal dysplasia and a variant of normal callosal development.

ABBREVIATIONS: CC = corpus callosum; FA = fractional anisotropy; fDTI = fetal DTI; fMRI = fetal MR imaging; ICOFD/LCC = internal cranial occipitofrontal dimension/length of the corpus callosum; ISCC = isolated short corpus callosum; IQR = interquartile range; PB = Probst bundles; SCC = short corpus callosum

The corpus callosum (CC) is the midline commissural white matter tract that connects the 2 cerebral hemispheres. It continues to grow throughout pregnancy and even throughout infancy.[1] At the end of the first trimester, it takes on its usual curvilinear shape.[2] Improvements in fetal sonography have led to a wide range of diagnoses of callosal abnormalities, from complete callosal agenesis to partial agenesis, thick and thin corpus callosums, and hypoplasia of the corpus callosum, recently summarized as callosal dysplasia.[3] The characterization of these anomalies relies primarily on biometric criteria of length or thickness.

Short CC (SCC) represents the most frequent anomaly. Although all parts of the CC should be present by 22 weeks' gestational age, exuberant axonal growth continues until 2 months after birth[4] and final remodeling is achieved by 3 years of age.[5] Changes in developmental maturity are readily noted in the corpus callosum, and interindividual variations can be observed, particularly involving the body and isthmus.[6,7] In such cases, the prenatal anatomic integrity of these short corpus callosums cannot be assured, and prenatal counseling is, therefore, challenging.

Received July 14, 2021; accepted after revision September 27.

From the Department of Paediatric Radiology (A.-E.M., D.G., P.S., V.D., N.B.), Assistance Publique–Hôpitaux de Paris, Hôpital Necker Enfants Malades, Université de Paris, Paris France; Institut Imagine (A.-E.M., D.G., P.S., N.B.-B., I.D., V.D., N.B.), Institut National de la Santé et de la Recherche Médicale U1163, Université de Paris, Paris, France; LUMIERE Platform (A.-E.M., D.G., P.S., H.M., N.B., L.-J.S.), Paris, France; IMPC Bachaumont (A.-E.M.), Paris, France; Departments of Pediatric Neurology (N.B.-B., I.D.), Anatomical Pathology (B.B.), and Genetics (V.M., T.A.), Necker Enfants Malades University Hospital, Université de Paris, Paris, France; Departments of Gynecology and Obstetrics (J.-P.B., T.Q.) and Pediatrics (S.C.), CHI, Poissy Saint-Germain, France; Department of Pediatric Neurology (M.-L.M.), Trousseau Hospital, CHU, Trousseau, Paris; Department of Gynecology-Obstetrics (E.J.), Hospital Le Mans, Le Mans, France; Department of Gynecology-Obstetrics (L.-J.S.), Université de Paris, Paris, France; and Department of Radiology (H.M.), University of Calgary, Calgary, Alberta, Canada.

Please address correspondence to Anne-Elodie Millischer, MD, Radiology Department, Hopital Necker Enfant Malades, 149 rue de Sèvres 75015 Paris, France; e-mail: aemillischer@gmail.com

Indicates article with online supplemental data.

http://dx.doi.org/10.3174/ajnr.A7383

The prognosis in patients with callosal dysplasia is not clear. It may be associated with varying degrees of neurodevelopmental delay, which are more severe if additional brain anomalies are present. Neurodevelopmental outcome of a short CC in the fetus is uncertain, and its significance is not well-established.[8,9]

Postnatal MR imaging is widely used to characterize corpus callosal dysplasia. Among the MR imaging sequences used, DTI enables the reconstruction of normal and abnormal fiber bundles (fiber-tracking or tractography). Its application in complete or partial CC agenesis and CC hypoplasia, and a thin CC has shown the consistent presence of Probst bundles (PB).[10] These abnormal bundles, oriented anterior-posteriorly, are thought to result from the lack of transverse decussation within a dysplastic corpus callosum.[11,12]

Similar to findings in postnatal imaging, PB may also be identified using DTI tractography in the prenatal period.[13,14] This additional presence of PB can be used to differentiate CC dysplasia from other forms of isolated short corpus callosum (ISCC) without PB and normal findings on genetic testing, which might reflect variants of normal callosal development. To avoid the dilemma of which callosal biometric curves to rely on, we used the internal cranial occipitofrontal dimension/length of the corpus callosum (ICOFD/LCC) ratio to define a SCC compared with the normal index (2.35 [SD, 0.11]).[15]

Therefore, the purpose of this study was 2-fold: first, though it has already been illustrated in 16 cases previously by Kasprian et al,[16] to routinely assess the feasibility of visualizing the presence or absence of PB in fetal MR imaging (fMRI) DTI tractography on a larger cohort, and second, to assess its added value in differentiating CC dysplasia from variants of normal callosal development.

MATERIALS AND METHODS

Study Design

This study was a retrospective review in 2 tertiary level fetal medicine referral centers (Necker Hospital and Poissy Hospital, Paris, France) in a 4-year period from November 2016 to January 2020. We retrospectively analyzed all fMRI studies of fetuses referred for an SCC. The inclusion criteria were fetal imaging of a single pregnancy with a CC length below the 5th percentile according to the reference charts of Achiron and Achiron[2] for which the integrity of the morphology could not be guaranteed by the referring fetal imaging radiologists in our center. The exclusion criteria were complete agenesis of the CC, an SCC associated with other brain anomalies on MR imaging, or incomplete data.

Data were obtained from the medical records and included maternal history and prenatal history (sex, genetic testing, Toxoplasma gondii, other agents, rubella, cytomegalovirus [ToRCH serology; Bio-Rad]). Postnatal outcomes included pathologic records when termination of pregnancy was performed, follow-up of neurologic development by the Denver Developmental Screening Test,[17] and postnatal MR imaging including tractography.

fMRI Examinations

MR imaging was performed on 1.5T MR imaging units (Optima MR 450w 1.5T, GE Healthcare, or Aera 1.5T, Siemens) using a phased-array body coil. The patients were placed in a supine or lateral decubitus position. No maternal sedative or contrast agents were used.

Neuroanatomic Imaging

MR imaging protocol included 3 planes adjusted in real time and customized to the head of each fetus (coronal, sagittal, and axial) with a balanced half Fourier–acquisition single-shot turbo spin-echo HASTE sequence (TR/TE, 4000/86; matrix, 256 × 256; flip angle, 125°; signal average, 1; section thickness, 3 mm; section gap, 30%).

Anatomic Measurements

CC length was systematically evaluated using the ICOFD/LCC ratio compared with the normal index (2.35 [SD, 0.11]).[15] The length of the CC was measured in the midsagittal plane from the most anterior aspect of the genu to the most posterior aspect of the splenium. The ICOFD was measured on the same plane; the calipers were placed on the internal calvarial borders, along the same line that was used to measure the length of the CC.

For dysmorphic features, the presence or absence of an eversion of the frontal horns (Steer horn or Viking Helmet appearance) and colpocephaly was reported systematically.

Callosal thickness was systematically measured in the midcoronal plane. The corpus callosum was regarded as thick if its midpart measured >2 SDs and thin if it was <2 SDs.[2]

For the fetal DTI (fDTI) protocol, axial slices were positioned orthogonal to the fetal brainstem. The basic settings of the DTI sequence were identical for the 2 MR imaging devices used. For DTI acquisitions, an axial, single-shot, echo-planar imaging sequence was used (TR = 2200 ms, TE = 63 ms, acquisition matrix = 112 × 112 re-sampled to 256 × 256, voxel size = 1 × 1 mm, section thickness = 3–5 mm without a gap or interleaved slices). For each of the DTI scans, 15 noncolinear direction diffusion-weighted magnetic-pulsed gradients were used with a b-value = 700 s/mm^2, and 1 B_0 image without diffusion-weighting was also obtained. Fifteen slices were recorded during an overall imaging time of 2 minutes of scanning.

Fetal-Specific Postprocessing of DTI Data

For tractography, we used a deterministic linear tracking algorithm with the following cutoff values: minimum fractional anisotropy (FA) (FA threshold) = 0.10–0.15; maximum angle change (angle threshold) = 27.0°–45.0°; and minimum fiber length = 10 mm. No advanced motion correction was used.[18] Tractography was first attempted with minimum thresholds of FA = 0.15 and angle = 27°. If tractography was not satisfactory with those standard parameters, the FA threshold was lowered to 0.10 and/or the angle threshold was increased to 45°.[19]

Only 1 senior radiologist performed the fDTI analysis (A.-E.M.), a radiologist with 15 years of experience in the field of fetal MR imaging (about 380 scans/year) and neuropediatrics. To trace the fibers crossing at the CC, a polygonal ROI was drawn in the midsagittal plane of each subject, encompassing the entire CC. For the PB, the fiber trajectory was not known a priori, except in its middle portion, where it clearly showed a rostrocaudal direction in the anatomic images and in the color-coded FA maps, creating the roof of the lateral ventricles.[20] To determine

the potential connectivity of the callosal remnant in each patient with an SCC, we drew single irregular polygonal ROIs encompassing the entire remnant area in the axial plane, focused on the regions of the centra semiovale. The ROIs were drawn manually according to anatomic landmarks. The examination was considered to be uninterpretable and de facto excluded by the radiologist when fetal motion artifacts interfered with interpretation of fDTIs.

Postnatal MR imaging, when applicable, was systematically performed by an experienced radiologist blinded to the prenatal data between 0 and 12 months, to confirm the prenatal fMRI data and to exclude any other brain anomalies. Three planes of FSE T2-weighted, 3D echo-spoiled gradient echo T1-weighted, and DTI tractography scans were performed on the Optima 1.5T MR imaging unit. For each of the DTI scans, 40 noncollinear-direction diffusion-weighted magnetic-pulsed gradients were used with a b-value of 700 s/mm^2.

Genetics Analyses

All fetuses were studied by karyotyping and chromosomal microarray analysis with DNA extracted from amniotic fluid. Informed consent for genetic studies was obtained from all pregnant women. Different types of microarrays were used by the centers: Agilent 60k (Agilent Technologies) and Agilent 180k and CytoScan 750K (SNP arrays, Affymetrix). Fluorescence in situ hybridization analysis or quantitative polymerase chain reaction were performed on the fetus to confirm the detected copy number variations and on the parents to determine the fetus's inheritance. The American College of Medical Genetics and Genomics/Clinical Genome guidelines were used to assess copy number variations pathogenicity.[21]

Outcomes

Terminations of pregnancy were all performed in accordance with French laws, and pathologic assessment and postmortem examinations were systematically performed.

In cases of live birth, the neurodevelopmental outcome was evaluated by a specialist in pediatric neurology (N.B.-B.), who evaluated communication skills, daily living skills, socialization skills, and motor skills based on the international Denver Developmental Screening Test.[8,22]

Scores were considered abnormal if the standard score was <85. The mean age at follow-up was 21.5 months for PB+ and 15.2 months for PB–.

Statistical Analysis

Statistical analyses were conducted using ad hoc routines implemented in R 4.0.0 software (http://www.r-project. org). Data description was performed using median and interquartile range (IQR) for quantitative data (ICOFD/LCC ratio and thickness of the CC). Median values were compared between patients with the presence of PB (PB+) and no PB (PB–), using the nonparametric Wilcoxon rank-sum test. The pROC package (https://rdrr.io/cran/pROC/man/pROC-package.html) for receiver operating characteristic curve analysis and calculation of sensitivities and specificities assessed the diagnostic performance. A bootstrap method was used to calculate the 95% CI of the area under the receiver operating characteristic curves, sensitivities, and specificities. All tests were 2-sided, with α set at 5%.

Ethics Approval

The local (DPO-APHP, France) institutional ethics board approved the study: institutional review board registration 00011928 (CERAPH 2020–12-06).

RESULTS

The study population included 37 fMRIs with fDTI tractography performed for ISCC at a median gestational age of 30.4 weeks (range, 25–34 weeks). There were 23 male (62%) and 14 female (37%) fetuses. DTI was feasible in all but 4/37 fetuses (11%) (Online Supplemental Data).

Pathology

Eleven of 33 terminations of pregnancy were performed. These included 9 cases of PB+, which represented 69% (9/13) of all cases of PB+ in our series, and 2 cases of PB–, which represented 10% (2/20) of all cases of PB–. No additional brain anomalies were found in any of the cases at postmortem examination.

We followed 22 of 33 neonates: One of 22 had a borderline psychomotor development, 1/22 had a delayed psychomotor development, 1/22 was lost to follow-up, and 19/22 had normal psychomotor development.

DTI Tractography and PB

Among the 33 interpretable fDTI tractography studies, PB+ was seen in 13 cases (13/33) versus PB– in 20 cases, demonstrating 2 patterns in our series of ISCC (Fig 1).

When PB were absent (PB–) at fDTI (20/33), this absence of PB was confirmed for all cases on postnatal DTI in 12/12 live births and by postmortem examination in 2/2 cases of termination of pregnancy. The remaining 6/20 patients did not undergo postnatal MR imaging because the pediatric neurologist and/or parents did not think it was warranted in the setting of normal neurologic development.

Among the 13 patients with PB at fDTI (PB+), the presence of PB was confirmed in all cases on postnatal DTI in 3/3 live births and by postmortem examination in 9/9 cases of termination of pregnancy. One of 13 patients was lost to follow-up. Discrimination between the cingulum and the PB was appreciated on color-coded maps: The cingulum presented in a well-recognized inferior-superior direction, and PBs presented in a typical anterior-posterior direction, as mentioned in the literature.[16]

Neuroanatomic Description between PB+ and PB– Populations

The ICOFD/LCC ratio was significantly greater in cases of PB+, 4.7 (IQR, 4.3–6.0) versus 3.4 in cases of PB– (IQR, 3.3–3.7; $P < .001$, $P = .0007$). A threshold value of 3.75 could help distinguish between cases with or without PB with a sensitivity of 92% (95% CI, 77%–100%) and a specificity of 85% (95% CI, 63%–100%) (Fig 2).

A biconvex dysmorphic appearance (Steer horn or Viking helmet) of the frontal ventricular horns was noted in 100% (13/13) of cases of PB+ and was absent in 95% (19/20) of cases of PB– ($P < .001$).

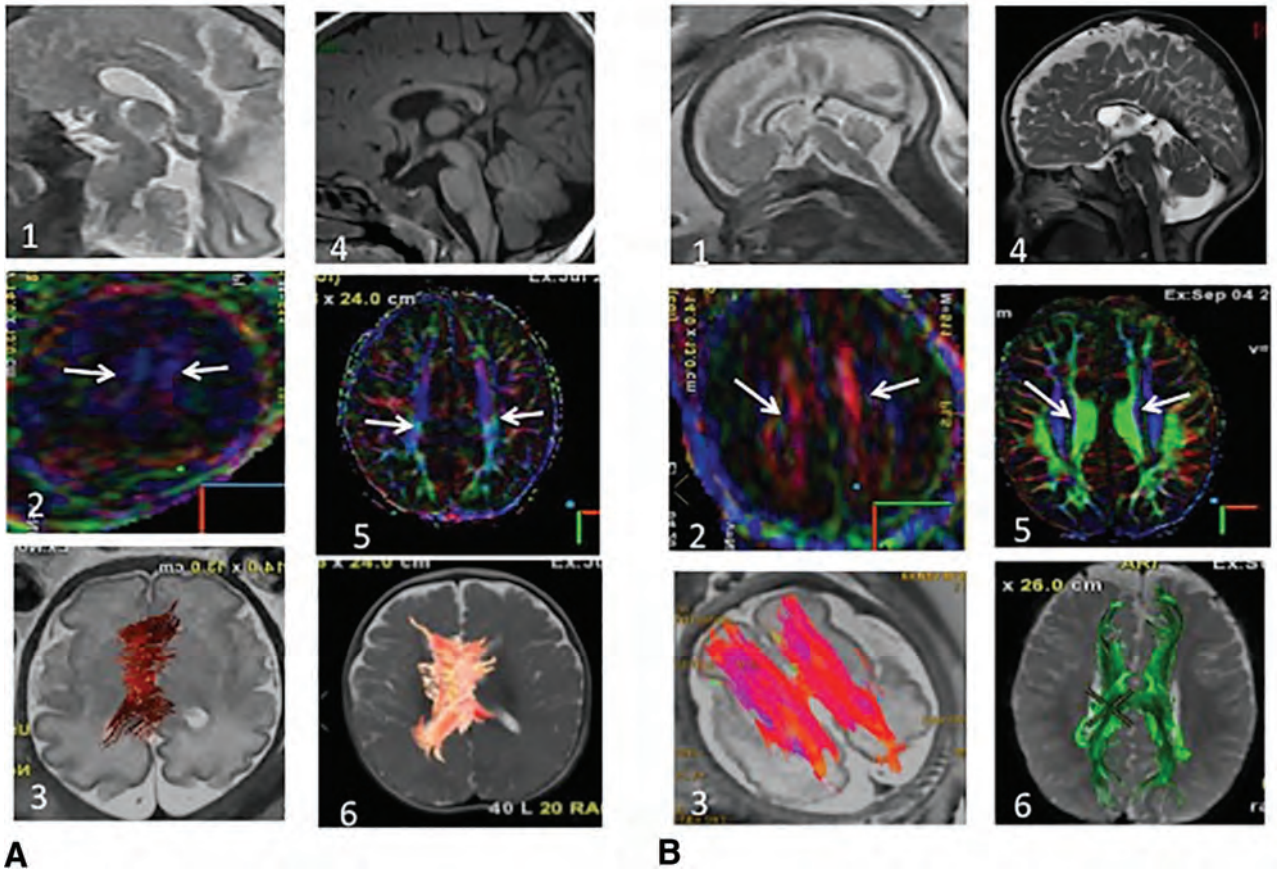

FIG 1. Fetal (30 weeks) and postnatal anatomic MR imaging and DTI (6 months) of ISCC PB– (*A*) and PB+. *A1*, Sagittal single-shot fast spin-echo T2 (SSFSET2) shows an ISCC. *A2*, DTI color-coding map shows the absence of PB, confirmed in postnatal imaging (*A3–6*). Only the cingulum is present, well-recognized by the inferior-superior direction in blue (*white arrows*), present on pre- and postnatal imaging. *B1*, Sagittal SSFSET2 shows an ISCC. *B2*, DTI color-coding map shows the presence of PB (*white arrows*), confirmed by a postnatal color-coding map (*B3–6*). PB are identified by their typical anterior-posterior orientation on the color-coding maps (*B2* and *B5*). Fiber-tracking demonstrates the typical anterior-posterior thick PB, with a remnant of the left-to-right CC (*B3* and *B6*).

Abnormal thickness of the corpus callosum was found in 23% ($n = 3/13$) of PB+ and 25% ($n = 5/20$) of PB–. No significant difference was found in the distribution of thick or thin corpus callosums related to the presence of PB, among the 2 populations (median, 1.7; IQR, 1–3, versus median, 2.2; IQR, 2–3.2; $P < .10$).

Among the 8 thick corpus callosums, postnatal MR imaging diagnosed 4 callosal lipomas, all among the 5 thick CCs in the PB– group (4/5). No lipomas were identified among the 3 cases of thick corpus callosum in the PB+ population.

Neurologic Evaluation

Among the 4 PB+ live births, the median age was 21.5 months (IQR, 15–36 months), 2/4 had a normal psychomotor development at 2.5 years and 15 months of age, respectively. One of 4 had a borderline developmental delay at 3 years, and 1 of 4 was lost to follow-up.

Among the 18 cases of PB–, the median age was 15.3 months (IQR, 3–36 months), 17/18 had a normal psychomotor development (94%), and 1 had a delayed psychomotor development thought to be secondary to trisomy 21.

No significant differences were observed between these 2 populations within the limits of the neurologic evaluation period ($P = .27$; OR, 0.14; 95% CI, 0.0014–13.82).

Genetic Anomalies

There were 5 genetic anomalies: 23% (3/13) in the PB+ group and 10% (2/20) in the PB– group ($P = .08$). In the PB+ group, we found the following: 1) A 8q21.12q21.3 duplication, 11.4 Mb, was detected in the fetus. The genomic position of this copy number variant was arr[GRCh37] 8q21.12q21.3 (79321132_90690216)x3 dn. This anomaly occurred de novo. 2) A fetus was found to have a pericentric inversion of chromosome 18, which arose de novo. The karyotype of the fetus was 46,XX,inv(18)(p11.31q21.2). 3) A de novo 14q12q21.2 deletion was detected in another fetus. The deletion was 16 Mb: arr[GRCh37] 14q12q21.2(30273044_46669990) x1dn, a mutation of Zinc finger E-box-binding homeobox 1, a case of deletion 14q12q21. 4) A case of duplication 3q21 Zinc finger E-box-binding homeobox 1 mutation was found in one fetus. 5) A case of duplication 8q211q21.3 was found in one fetus.

In the PB– group, 1 case of trisomy 21 and 1 case of mutation 18p11.31 to 18q21 were found.

DISCUSSION

To our knowledge, this is the first study that routinely reports the feasibility (about 90%) of visualizing the presence or absence of PB in fDTI tractography in a large cohort. This study demonstrates

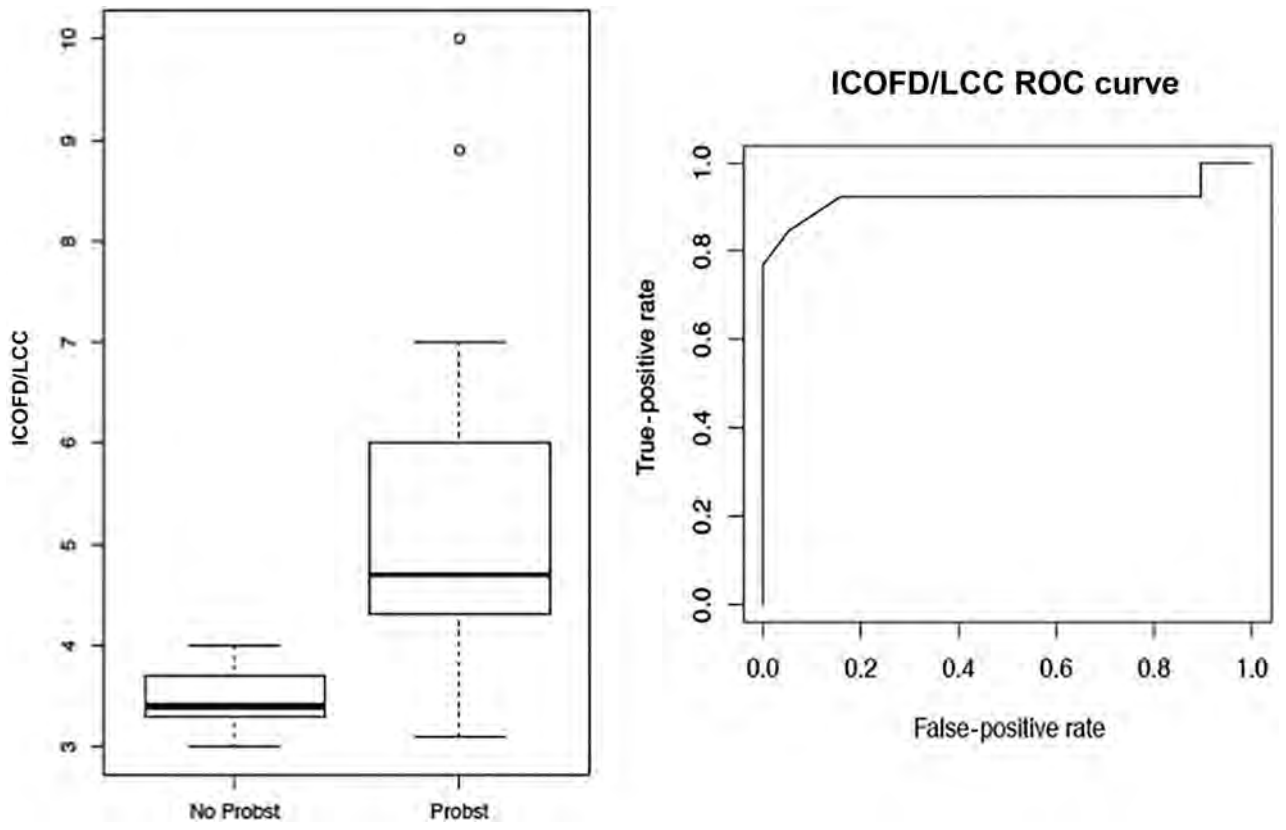

FIG 2. Length of the CC. Dimensions of the CC compared between PB+ and PB–. Boxplot and receiver operating characteristic curve (ROC) about the ICOFD/LCC ratio.

the added value in differentiating CC dysplasia from variants of normal callosal development with an objective technical tool.

Moreover, our data suggest that 3 important features are associated with the presence or absence of PB:

1) When PB are present, the ICOFD/LCC ratio recently published[15] is usually higher. Accordingly, a value of ≥3.75 was associated with the presence of PB+ in >90% of our cases. This simple and straightforward threshold could be used as a routine first-line tool to characterize fetuses with an ISCC at risk for callosal dysplasia. It is not unexpected that we noted that biconvex dysmorphic frontal ventricular horns were also present in 100% of the PB+ group. These data corroborate the anatomic knowledge regarding lateral ventricles in complete or partial agenesis of the corpus callosum, which is usually displaced from the midline by paired PB that fail to cross the hemispheres and run parallel to the midline as T2 hypointense bundles resulting in the Steer horn or Viking helmet appearance of the ventricles.[23] In our study, on re-review of all of cases of PB+, the appearance of T2-hypointense bands along the inner edge of the frontal ventricular horns was always present. These 3 signs (ICOFD/LCC ratio, dysmorphic frontal ventricular horns, and T2-hypointense bands) could, therefore, be easily used on anatomic images to suggest the presence of PB. Thus, our data show that the presence of the bull horn configuration of the lateral ventricles associated with relative shortening of the corpus callosum is associated with a high probability of finding Probst fascicles using DTI. This advanced technique, therefore, provides an objective criterion for an optimal description of the SCC.

2) Genetic anomalies are more frequent in an ISCC with PB+ (23% versus 10%). This finding correlates well with previously published data suggesting that callosal dysplasias are more often associated with genetic syndromes.[24,25] However, our results are also in line with the recent literature, which points out that the presence of PB is not necessarily associated with a poor prognosis.[26] Accordingly, neurologic follow-up was normal for most children with an ISCC and PB–, suggesting, in our preliminary study, that ISCCs with no PB are more likely to be variants of normal development of the corpus callosum. Regarding the case of trisomy 21 in PB–, the diagnosis was suspected as of the first trimester due to an increased nuchal translucency, for which the couple chose not to pursue any confirmatory prenatal cytogenetic investigations. At least on the basis of the data in our study, we believe this case confirms once again that prenatal genetic exploration is essential for the appropriate classification of ISCC.

3) In the absence of the PB, a thick corpus callosum is usually related to lipomas (4/5 in PB– versus 0/3 in PB+). An antenatal diagnosis of lipoma is often challenging and underdiagnosed because the lipomatous components are difficult to demonstrate on fMRIs and antenatal ultrasound,[27-29] whereas this entity is well-recognized in the postnatal period on MRI, showing typical hyperintensity on T1-weighted MR images (Online Supplemental Data). Indeed, Chougar et al[29] and Atallah et al[27] concluded in their fMRI series that the type and size of a lipoma influence prenatal T1 signal intensity, and the variability of the T1 intensity may also be related to fat maturation within the lipoma and

perhaps reflects changes related to gestational age. The corollary of our result in fDTI could be that in a thick corpus callosum without PB on tractography, one might suggest the possibility an "occult" callosal lipoma on fetal imaging. To our knowledge, this is the first antenatal study that highlights this feature in the diagnosis of callosal lipoma. This information can be helpful in prenatal counseling, given the excellent prognosis of callosal lipomas.

On the basis of these results, we believe a new decision tree can be proposed, taking into account the results of MR tractography and genetic studies (Online Supplementary Data). To simplify and standardize the prenatal morphologic classification system, as we proposed in our recent study[3] and according to the definitions proposed by Edwards et al,[4] we would suggest defining an ISCC with a Probst bundle as "callosal dysplasia," and "variant of normal callosal development" in cases of ISCCs without a Probst bundle and no cytogenetic anomalies. Therefore, the generally favorable prognosis of ISCC, reported by Meidan et al,[8] can be partly explained by the hypothesis that some of the conditions of fetuses and children followed in their study were true variants of normal and not callosal malformations, in other words, children with a fetal diagnosis of ISCC but without PB. However, the major prognostic element remains the association of abnormalities in the CC, Probst band or not.[30]

We must acknowledge several limitations in our study. First is the retrospective nature of our study, and the number of cases remains limited, even if this is the first study using fDTI in the investigation of ISCC. Second, the relatively high success rate may be related to the comparatively late gestational age of about 30 weeks. Moreover, it was not possible to obtain a full neurologic follow-up until 6 years of age, with a systematic postnatal MR imaging in all cases.

CONCLUSIONS

The challenge of prenatal differentiation of an ISCC as a variant of normal callosal development from callosal dysplasia can be optimized by the use of DTI tractography in fetal MR imaging. We believe that our results can encourage the systematic use of optimized fDTI tractography for the investigation of ISCCs, to assess the presence or absence of PB. Thus, in addition to the classic MR imaging with morphologic analysis, a new approach and paradigm can be proposed, considering the presence or absence of PB, while prospective studies with long-term and reproducible neurologic follow-up are necessary.

Disclosure forms provided by the authors are available with the full text and PDF of this article at www.ajnr.org.

REFERENCES

1. Nunez S, Mantilla MT, Bermudez S. **Midline congenital malformations of the brain and skull.** *Neuroimaging Clin N Am* 2011;21:429–82, vii CrossRef Medline
2. Achiron R, Achiron A. **Development of the human fetal corpus callosum: a high-resolution, cross-sectional sonographic study.** *Ultrasound Obstet Gynecol* 2001;18:343–47 CrossRef Medline
3. Mahallati H, Sotiriadis A, Celestin C, et al. **Heterogeneity in defining fetal callosal pathology: a systematic review.** *Ultrasound Obstet Gynecol* 2021;58:11–18 CrossRef
4. Edwards TJ, Sherr EH, Barkovich AJ, et al. **Clinical, genetic and imaging findings identify new causes for corpus callosum development syndromes.** *Brain* 2014;137:1579–613 CrossRef Medline
5. Garel C, Cont I, Alberti C, et al. **Biometry of the corpus callosum in children: MR imaging reference data.** *AJNR Am J Neuroradiol* 2011;32:1436–43 CrossRef Medline
6. Filippi CG, Cauley KA. **Lesions of the corpus callosum and other commissural fibers: diffusion tensor studies.** *Semin Ultrasound CT MR* 2014;35:445–58 CrossRef Medline
7. Achiron R, Lipitz S, Achiron A. **Sex-related differences in the development of the human fetal corpus callosum: in utero ultrasonographic study.** *Prenat Diagn* 2001;21:116–20 Medline
8. Meidan R, Bar-Yosef O, Ashkenazi I, et al. **Neurodevelopmental outcome following prenatal diagnosis of a short corpus callosum.** *Prenat Diagn* 2019;39:477–83 CrossRef Medline
9. Volpe P, Paladini D, Resta M, et al. **Characteristics, associations and outcome of partial agenesis of the corpus callosum in the fetus.** *Ultrasound Obstet Gynecol* 2006;27:509–16 CrossRef Medline
10. Le Bihan D. **Intravoxel incoherent motion perfusion MR imaging: a wake-up call.** *Radiology* 2008;249:748–52 CrossRef Medline
11. Tovar-Moll F, Moll J, de Oliveira-Souza R, et al. **Neuroplasticity in human callosal dysgenesis: a diffusion tensor imaging study.** *Cereb Cortex* 2007;17:531–41 CrossRef Medline
12. Benezit A, Hertz-Pannier L, Dehaene-Lambertz G, et al. **Organising white matter in a brain without corpus callosum fibres.** *Cortex* 2015;63:155–71 CrossRef Medline
13. Song JW, Gruber GM, Patsch JM, et al. **How accurate are prenatal tractography results? A postnatal in vivo follow-up study using diffusion tensor imaging.** *Pediatr Radiol* 2018;48:486–98 CrossRef Medline
14. Jakab A, Tuura R, Kellenberger C, et al. **In utero diffusion tensor imaging of the fetal brain: a reproducibility study.** *Neuroimage Clin* 2017;15:601–12 CrossRef Medline
15. Tepper R, Leibovitz Z, Garel C, et al. **A new method for evaluating short fetal corpus callosum.** *Prenat Diagn* 2019;39:1283–90 CrossRef
16. Kasprian G, Brugger PC, Schöpf V, et al. **Assessing prenatal white matter connectivity in commissural agenesis.** *Brain* 2013;136:168–79 CrossRef Medline
17. Abessa TG, Worku BN, Kibebew MW, et al. **Adaptation and standardization of a Western tool for assessing child development in non-Western low-income context.** *BMC Public Health* 2016;16:652 CrossRef Medline
18. Machado-Rivas F, Afacan O, Khan S, et al. **Tractography of the cerebellar peduncles in second- and third-trimester fetuses.** *AJNR Am J Neuroradiol* 2021;42:194–200 CrossRef Medline
19. Mitter C, Prayer D, Brugger PC, et al. **In vivo tractography of fetal association fibers.** *PLoS One* 2015;10:e0119536 CrossRef Medline
20. Mitter C, Jakab A, Brugger PC, et al. **Validation of in utero tractography of human fetal commissural and internal capsule fibers with histological structure tensor analysis.** *Front Neuroanat* 2015;9:164 CrossRef Medline
21. Riggs ER, Andersen EF, Cherry AM, et al. **Technical standards for the interpretation and reporting of constitutional copy-number variants: a joint consensus recommendation of the American College of Medical Genetics and Genomics (ACMG) and the Clinical Genome Resource (ClinGen).** *Genet Med* 2020;22:245–57 CrossRef Medline
22. Elliman AM, Bryan EM, Elliman AD, et al. **Denver developmental screening test and preterm infants.** *Arch Dis Child* 1985;60:20–24 CrossRef Medline
23. Leombroni M, Khalil A, Liberati M, et al. **Fetal midline anomalies: diagnosis and counselling, Part 1: corpus callosum anomalies.** *Eur J Paediatr Neurol* 2018;22:951–62 CrossRef Medline
24. Das S, Bhansali A, Dutta P, et al. **An unusual association of corpus callosum agenesis in a patient with acromegaly.** *BMJ Case Rep* 2010;2010;bcr012010265 CrossRef Medline

25. Paul LK, Brown WS, Adolphs R, et al. **Agenesis of the corpus callosum: genetic, developmental and functional aspects of connectivity.** *Nat Rev Neurosci* 2007;8:287–99 CrossRef Medline
26. Diogo MC, Glatter S, Prayer D, et al. **Improved neurodevelopmental prognostication in isolated corpus callosal agenesis: fetal magnetic resonance imaging-based scoring system.** *Ultrasound Obstet Gynecol* 2021;58:34–41 CrossRef Medline
27. Atallah A, Lacalm A, Massoud M, et al. **Prenatal diagnosis of pericallosal curvilinear lipoma: specific imaging pattern and diagnostic pitfalls.** *Ultrasound Obstet Gynecol* 2018;51:269–73 CrossRef Medline
28. Shinar S, Lerman-Sagie T, Telleria ME, et al. **Fetal pericallosal lipomas: clues to diagnosis in the second trimester.** *Eur J Paediatr Neurol* 2018;22:929–34 CrossRef Medline
29. Chougar L, Blondiaux E, Moutard ML, et al. **Variability of T1-weighted signal intensity of pericallosal lipomas in the fetus.** *Pediatr Radiol* 2018;48:383–91 CrossRef Medline
30. Glatter S, Kasprian G, Bettelheim D, et al. **Beyond isolated and associated: a novel fetal MR imaging-based scoring system helps in the prenatal prognostication of callosal agenesis.** *AJNR Am J Neuroradiol* 2021;42:782–86 CrossRef Medline

Quantitative Diffusion and Spectroscopic Neuroimaging Combined with a Novel Early-Developmental Assessment Improves Models for 1-Year Developmental Outcomes

H.G. Moss, L.G. Wolf, P. Coker-Bolt, V. Ramakrishnan, T. Aljuhani, M. Yazdani, T.R. Brown, J.H. Jensen, and D.D. Jenkins

ABSTRACT

BACKGROUND AND PURPOSE: Preterm infants are at risk for overt and silent CNS injury, with developmental consequences that are difficult to predict. The novel Specific Test of Early Infant Motor Performance, administered in preterm infants at term age, is indicative of later developmental gross motor and cognitive scores at 12 months. Here, we assessed whether functional performance on this early assessment correlates with CNS integrity via MR spectroscopy or diffusional kurtosis imaging and whether these quantitative neuroimaging methods improve predictions for future 12-month developmental scores.

MATERIALS AND METHODS: MR spectroscopy and quantitative diffusion MR imaging data were acquired in preterm infants ($n = 16$) at term. Testing was performed at term and 3 months using the Specific Test of Early Infant Motor Performance and the Bayley Scales of Infant and Toddler Development, Third Edition, at 12 months. We modeled the relationship of MR spectroscopy and diffusion MR imaging data with both test scores via multiple linear regression.

RESULTS: MR spectroscopy NAA ratios at a TE of 270 ms in the frontal WM and basal ganglia and kurtosis metrics in major WM tracts correlated strongly with total Specific Test of Early Infant Motor Performance scores. The addition of MR spectroscopy and diffusion separately improved the functional predictions of 12-month outcomes.

CONCLUSIONS: Microstructural integrity of the major WM tracts and metabolism in the basal ganglia and frontal WM strongly correlate with early developmental performance, suggesting that the Specific Test of Early Infant Motor Performance reflects CNS integrity after preterm birth. This study demonstrates that combining quantitative neuroimaging and early functional movement improves the prediction of 12-month outcomes in premature infants.

ABBREVIATIONS: AIC = Akaike Information Criterion; adj-R^2 = Adjusted R-squared; Bayley-III = Bayley Scales of Infant and Toddler Development, Third Edition; BG = basal ganglia; DKI = diffusional kurtosis imaging; FA = fractional anisotropy; gCC = genu of the corpus callosum; IFOF = inferior fronto-occipital fasciculus; KFA = kurtosis fractional anisotropy; PLIC = posterior limb of the internal capsule; PTR = posterior thalamic/optic radiations; sCC = splenium of the corpus callosum; STEP = Specific Test of Early Infant Motor Performance

Premature birth results in CNS dysmaturation characterized by altered microstructural WM and myelination not quantifiable on head sonography or qualitative MR imaging.[1-3] Interventions for developmental delays are typically not started until later in infancy on failure to sit or walk, squandering a period of high neuroplasticity. We developed the Specific Test of Early Infant Motor Performance (STEP) to address this need and have shown that STEP scores at term and 3 months can predict scores on the Bayley Scales of Infant and Toddler Development, Third Edition (Bayley-III) at 12 months.[4-6]

A recent consensus statement emphasized combining neuroimaging with clinical assessment for improved diagnosis of cerebral palsy.[7] In this study, we determined whether neuroimaging (MR spectroscopy or diffusion MR imaging) reflects STEP performance at term and improves the ability of STEP to predict later development. MR spectroscopy quantifies mobile intracellular metabolomics in the basal ganglia (BG) and frontal WM regions

Received June 17, 2021; accepted after revision September 27.

From the Department of Neuroscience (H.G.M., J.H.J.), Center for Biomedical Imaging (H.G.M., T.R.B., J.H.J., D.D.J.), Department of Pediatrics (L.G.W., D.D.J.), Division of Occupational Therapy (P.C.-B., T.A.), College of Health Sciences, Division of Public Health Sciences (V.R., T.A.), and Department of Radiology and Radiological Science (M.Y., T.R.B., J.H.J.), Medical University of South Carolina, Charleston, South Carolina.

This research was supported by the South Carolina Clinical & Translational Research Institute at the Medical University of South Carolina, Clinical and Translational Science Awards National Institutes of Health/National Center for Advancing Translational Sciences UL1TR000062 (to P. Coker-Bolt), and National Institutes of Health/National Institute of Neurological Disorders and Stroke F31NS108623 (to H.G. Moss).

Please address correspondence to Hunter Moss, BS, Center for Biomedical Imaging, Department of Neuroscience, Medical University of South Carolina, 173 Ashley Ave, Room 403, Charleston, SC 29425; e-mail: mossh@musc.edu

Indicates open access to non-subscribers at www.ajnr.org

Indicates article with online supplemental data.

http://dx.doi.org/10.3174/ajnr.A7370

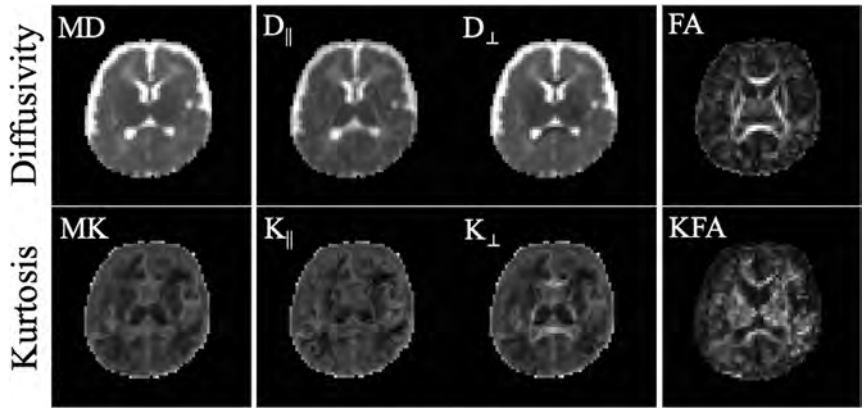

FIG 1. An axial section from a representative subject showing rotationally invariant tensor quantities calculated from the DKI analysis. The *upper row* shows the mean, axial, and radial diffusivities and fractional anisotropy (MD, $D_{\parallel}$, $D_{\perp}$, and FA, respectively). The *lower row* shows the corresponding kurtosis metrics (MK, $K_{\parallel}$, $K_{\perp}$, and KFA). Diffusivity quantifies the degree of water mobility, while kurtosis is a measure of the complexity of water diffusion within the tissue microenvironment. Kurtosis provides more detail in the sparsely myelinated infant brain. The MD, $D_{\parallel}$, and $D_{\perp}$ have units of square micrometer/millisecond with the remaining metrics being unitless. MD indicates mean diffusivity; $D_{\parallel}$, axial diffusivity; $D_{\perp}$, radial diffusivity; MK, mean kurtosis; $K_{\parallel}$, axial kurtosis; $K_{\perp}$, radial kurtosis.

affected by neonatal injury that relate to outcome.[8-12] Both diffusional kurtosis imaging (DKI)[13] and DTI[14] are diffusion MR imaging methods that quantify tissue integrity through the random movement of water molecules. Kurtosis quantifies the water movement deviation away from and not represented by the strict Gaussian distribution that DTI imposes.[13] DKI measures tissue heterogeneity (intra- or extracellular barriers)[15] and is acutely sensitive to pathologic processes.[16] While application of DKI to brain development is new,[17-21] studies in typically developing children show nonlinear relationships of kurtosis with age.[19-21] The kurtosis tensor provides higher-order CNS structural information on the organization of the microenvironment, which may directly impact development.

We hypothesized that lower metabolic or microstructural integrity identifies dysmaturation that manifests as functional developmental performance at term or 3 months by the STEP and at 12 months by the Bayley-III.[4,12] This investigation provides evidence that quantitative neuroimaging paired with early developmental assessment improves the prediction of later-stage development.

MATERIALS AND METHODS

Sample

We enrolled infants ($n = 16$) born at 24–34 weeks gestational age with institutional review board approval and parental informed consent, in accordance with the Declaration of Helsinki.

Developmental Assessments

The STEP was administered at term (37–42 weeks) and at 3 months. The STEP is composed of 10 items with a maximum total score of 30. STEP cutoff scores for low and below normal at 12 months and Bayley-III scores are ≤16 (term) and ≤22 (3 months).[6]

We assessed neurodevelopment at 12 months by the Bayley-III ($n = 15$). Below normal or low Bayley-III gross motor and cognitive scaled scores are defined as <9 and 1 SD below the mean.[22,23]

Image Acquisition and Processing

We performed MRIs at 38–44 weeks on a 3T Tim Trio scanner (Siemens) on unsedated infants, as previously described.[24] We acquired single-voxel ^{1}H-MR spectra using point-resolved spectroscopy (TR = 2000 ms, TE = 30 and 270 ms, 128 signal averages). Data were acquired using an isotropic voxel $(15\,\text{mm})^3$ in the left BG and right frontal WM (Online Supplemental Data) for TE = 30 ms and in the right frontal WM for TE = 270 ms. A single voxel $(14.37\,\text{mm})^3$ was extracted from the left BG region of a multivoxel point-resolved spectroscopy chemical shift imaging scan (TR = 1700 ms, TE = 270 ms, 16 × 16 grid, and 1 signal average). All voxels were placed (or extracted) in regions that had no apparent lesions.

The LCModel[25] (http://www.lcmodel.com/) quantified metabolite ratios to creatine using a simulated metabolite basis set[26] generated with the VeSPA software package[27] (https://github.com/vespa-mrs/vespa) with any additional metabolite ratios computed from these (Online Supplemental Data). Processed spectra were visually inspected for quality of fit, and the metabolite ratio inclusion criterion was the Cramer-Rao lower bound of <20%. For the TE = 30 ms spectra, the mean (SD) (median, minimum–maximum) of the full width at half maximum was 0.044 (0.033) (0.041, 0.014–0.114) with an SNR of 10 (3) (10, 4–14) for the BG and 0.055 (0.038) (0.043, 0.01–0.114) with an SNR of 10 (3) (9, 6–16) for the WM. For the TE = 270 ms spectra, the full width at half maximum was 0.069 (0.039) (0.060, 0.014–0.143) for the BG with an SNR of 8 (3) (8, 4–14) and 0.045 (0.032) (0.038, 0.010–0.124) for the WM with an SNR of 5 (2) (4, 2–9).

We obtained DKI data with $(2.7\,\text{mm})^3$ isotropic voxels, with TE = 99 ms, TR = 4800 ms, and $b = 0$, 1000, and 2000 s/mm^2 with 64 diffusion-encoding directions per nonzero b-value shell, 37 contiguous axial slices per image volume, and 10 additional non-diffusion-weighted images ($b = 0$ s/mm^2).

After removing image volumes and gradient directions corrupted by excessive head motion (on average, 13 [12] volumes were removed), we used the DESIGNER pipeline[28-34] (https://pydesigner.readthedocs.io/en/latest/) to perform a DKI[35] analysis, which calculated fractional anisotropy (FA), mean, axial, and radial diffusivities; and mean, axial, and radial kurtosis and kurtosis FA (KFA).[13,36-39] DKI data were fit globally to obtain the best estimates for both the diffusion and kurtosis tensors along with their associated diffusion metrics (Fig 1).

ROI Placement

Bilateral WM ROIs ($n = 8$) were manually drawn using each subject's FA image for anatomic reference in the anterior limb and posterior limb of the internal capsule (PLIC), external capsule, uncinate fasciculus, inferior fronto-occipital fasciculus (IFOF),

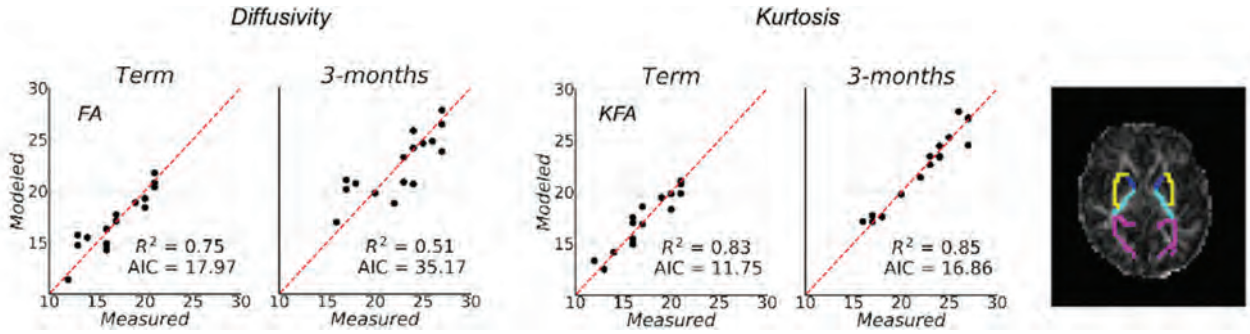

FIG 2. Plots showing measured STEP scores at term or 3 months versus modeled STEP scores using FA for diffusivity (*left columns*) or KFA for kurtosis (*right columns*) to predict STEP. KFA and FA models show the best fit to measured STEP scores primarily from combining metrics in the external capsule (yellow) and the PTR (purple). Goodness-of-fit metrics of adj-R^2 and AIC are noted with each model. While both FA and KFA predict STEP function during 3 months of development, KFA performs better in the model than FA (higher R^2 and lower AIC); for STEP at term: ΔAIC = 6.22, $P < .05$; and for STEP at 3 months: ΔAIC = 18.31, $P < .001$. All models are corrected for gestational age at birth and at MR imaging.

posterior thalamic/optic radiations (PTR), and the corpus callosum (genu/splenium [gCC]/[sCC], Online Supplemental Data). A clinical pediatric neuroradiologist verified correct ROI placement. Last, a total WM ROI was created by combining these individual ROIs.

Statistical Analysis

Multiple linear regression (SAS 3.8; SAS Institute) was performed with STEP at term or 3 months as the response variable and metabolite ratios from TE = 30 or 270 ms or DKI-derived metrics as predictor variables. Gestational age at birth and MR imaging were included in all models to account for degree of prematurity.

For the DKI metrics, STEP was modeled in two ways:

1. For a single ROI, each diffusion parameter was averaged separately over all voxels and included as an independent covariate (eg, $STEP_{term} = FA_{sCC} + KFA_{sCC}$). This approach yields a parsimonious model in which a single WM tract could be sampled with several different diffusion parameters to model prognosis in a clinical setting.
2. To assess whether global brain dysmaturity or injury is more important to functional outcome prediction, we used a single diffusion metric averaged within each ROI as the covariates in the models (eg, $STEP_{term} = FA_{sCC} + FA_{PTR} + FA_{PLIC}$). This allowed us to determine whether an individual diffusivity or kurtosis parameter in major WM tracts could improve model predictions for parsimonious sampling compatible with clinical settings.

Model Selection

We selected models for the best goodness of fit via larger adjusted R-squared (adj-R^2) and smaller Akaike Information Criterion (AIC). The difference in the AIC from full-versus-simpler models (Δ_{AIC}) was calculated with a P value, $P = \exp(-\Delta_{AIC}/2)$.[40] The model that minimized the AIC[41] and maximized the Δ_{AIC} between full and simple models with $P < .05$ was selected as the most parsimonious model.

RESULTS

Demographics

MR spectroscopy ($n = 12$ or 16) and DKI ($n = 16$) scans met our inclusion criteria. The mean age at MR imaging was 41.9 (1.5) weeks. Many infants had CNS conditions that may affect neurodevelopment (Online Supplemental Data).

MR Spectroscopy $(NAA/Cho)_{BG}$ and $(NAA/Cr)_{WM}$ at TE = 270 ms Strongly Correlate with STEP Performance

We assessed whether STEP performance represents concurrent MR spectroscopy metabolomics in the BG or frontal WM. After adjusting for gestational age at birth and MR imaging, $(NAA/Cho)_{BG}$ quantified at TE = 270 ms ($n = 12$) strongly correlated ($P = .04$) with term STEP: $\beta = 5.83$, adj-$R^2 = 0.82$, AIC = 11.32, $P_{model} < .001$; and $(NAA/Cr)_{WM}$ correlated ($P = .04$) with 3-month STEP: $\beta = 9.76$, adj-$R^2 = 0.82$, AIC = 16.11, $P_{model} < .001$. A correlation was observed with the TE = 30 ms MR spectroscopy ($n = 16$) and STEP term (adj-$R^2 = 0.77$, AIC = 16.76, $P_{model} = .02$), but unlike the compact TE = 270 ms models, it was composed of 5 WM and 2 BG metabolite ratios (Online Supplemental Data).

KFA and Inferior Fronto-Occipital Fasciculus Correlate Best with STEP Performance

We found a strong linear relationship between diffusivity or kurtosis parameters and STEP scores (Online Supplemental Data). The Online Supplemental Data provide details of the β-value estimates for each WM ROI in the model fits. Of note are FA and KFA (Fig 2): KFA showed a notable improvement over FA in predicting concurrent functional performance, though FA models included fewer ROIs (Fig 2 and Online Supplemental Data). The KFA also outperformed all the other diffusion metrics at both STEP time points. Most metric models resulted in models with adj-$R^2 > 0.70$, indicating very strong correlations.

For the ROI-centered approach, we found that many individual WM tracts had moderately strong linear relationships with STEP scores (adj-$R^2 \geq 0.60$, Online Supplemental Data). IFOF modeled the STEP term (adj-$R^2 = 0.86$, AIC = 8.86), and gCC modeled the STEP 3-month (adj-$R^2 = 0.74$, AIC = 25.38), similar to the total WM ROI (adj-$R^2 = 0.74$, AIC = 25.47) across diffusion metrics (Online Supplemental Data). Again, kurtosis metrics contributed more than diffusivity to the models (Online Supplemental Data).

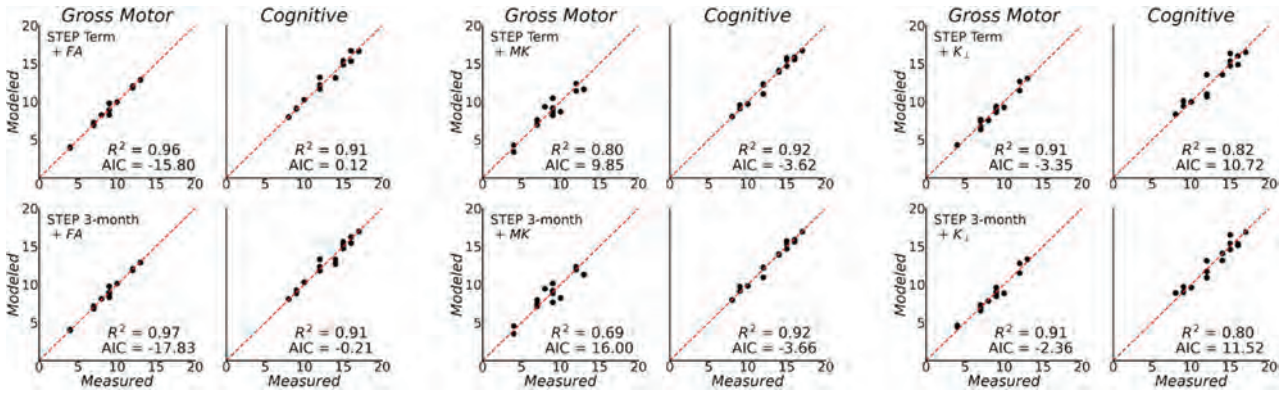

FIG 3. Measured 12-month Bayley-III gross motor (*left columns*) and cognitive scores (*right columns*) compared against the modeled Bayley scores, using an individual diffusivity (*upper rows*) or kurtosis (*lower rows*) parameter across various WM ROIs. By means of this diffusion parameter approach, FA (*left*), MK (*center*), and $K_{\perp}$ (*right*) combined with STEP strongly predict both motor and cognitive Bayley scores, adjusted for gestational age at birth and MR imaging. Other metrics also predicted future function when combined with STEP scores (see the Online Supplemental Data for details on the optimal combination of WM ROIs for each diffusion metric [β-values, highest adj-R^2 and lowest AIC]). MK indicates mean kurtosis; $K_{\perp}$, radial kurtosis.

Both MR Spectroscopy and DKI Improve STEP Prediction of Bayley-III Scores

Combining MR spectroscopy with STEP scores predicted Bayley-III motor and cognitive scores markedly better than STEP scores alone (Online Supplemental Data). For TE = 270 ms data, improved motor score prediction models were found for term STEP (Δ_{AIC} = 33.02, $P < .001$) and for 3-month STEP (Δ_{AIC} = 22.63, $P < .001$). In modeling cognitive scores with TE = 270 ms, $(NAA/Cho)_{BG}$ improved predictions beyond STEP alone (term: Δ_{AIC} = 17.09; 3 months: Δ_{AIC} = 32.05; both $P < .001$). MR spectroscopy at TE = 30 ms improved STEP predictive models of cognitive scores (term: Δ_{AIC} = 15.36; 3 months: Δ_{AIC} = 27; both $P < .001$) but included multiple metabolite ratios that detracted from a parsimonious model, unlike the TE = 270 ms models, which included a single ratio. Model β-value estimates for each metabolite ratio included are detailed in the Online Supplemental Data.

We found that FA and radial and mean kurtosis were the best diffusion metrics to combine with STEP scores in predicting Bayley-III scores (Fig 3). For gross motor scores, FA improved the STEP-alone model at term and 3 months (both $\Delta_{AIC} > 41$, $P < .001$) as did radial kurtosis (both $\Delta_{AIC} > 26$, $P < .001$). For cognitive scores, FA improved the STEP-alone model at term and 3 months (both $\Delta_{AIC} > 4$, $P < .001$), as did mean kurtosis (both $\Delta_{AIC} > 27$, $P < .001$). Other DKI-derived metrics also predicted Bayley-III scores with STEP time points. (Online Supplemental Data). Included WM ROIs and β-value estimates for each are listed in the Online Supplemental Data.

For the ROI-centered approach, various combinations of kurtosis and diffusivity metrics within individual ROIs improved the predictions of Bayley-III gross motor and cognitive scores compared with the STEP-only models. For parsimony and simplicity, models using either PTR and IFOF with STEP scores had the lowest AICs for predicting Bayley Motor scores (Fig 4) and improved the model fit over the STEP alone (at term: $\Delta_{AIC} > 30$; $P < .001$; at 3 months: $\Delta_{AIC} > 28$; $P < .001$). The gCC and external capsule with STEP scores improved prediction in Bayley cognitive scores (Online Supplemental Data) over STEP alone (at term: $\Delta_{AIC} > 18$; $P < .001$; and at 3 months: $\Delta_{AIC} > 14$; $P < .001$). Model fits and β-value estimates for each diffusion metric covariate included in the selected models for each WM ROI are provided in the Online Supplemental Data.

DISCUSSION

During early life after preterm birth, brain injuries as well as alterations in gray and WM maturation occur that influence later development of motor and cognitive skills. Influencing neuroplasticity to improve outcomes requires understanding the neuroimaging representations of brain injuries and their relation to functional movements during early infancy. Using MR spectroscopy and DKI parameters at term-age equivalent, we show that metabolomics for healthy neurons and microstructural integrity correspond to concurrent performance on the STEP early developmental assessment and that neuroimaging combined with the STEP improves prediction of future motor and cognitive scores compared with the STEP alone. Better predictive models would allow testing interventions at a very early period to optimally harness neuroplasticity. Our data highlight the potential for prognostication using the STEP and term-age quantitative neuroimaging and serve as a guide for metric selection. Our data provide proof of concept that quantitative MR imaging of the developing brain is vitally important in prognosis.

MR spectroscopy at TE = 270 ms in either the frontal WM or BG strongly related to STEP and NAA, and Cho ratios improved STEP predictive models for both gross motor and cognitive Bayley-III scores (Online Supplemental Data). However, we observed no relation or benefit with NAA or other metabolite ratios obtained from point-resolved spectroscopy sequence spectra at TE = 30 ms. This discrepancy may be due to a more reliable quantification of NAA and Cho at a long TE, in which there are fewer overlapping metabolite peaks, as has previously been reported.[26] As markers of neuronal metabolic health[42] and myelination, NAA and Cho are both complementary and additive in our models.[1,9-11] Lower concentrations of NAA in the deep gray nuclei of the BG reflect metabolic impairment, lower neuronal

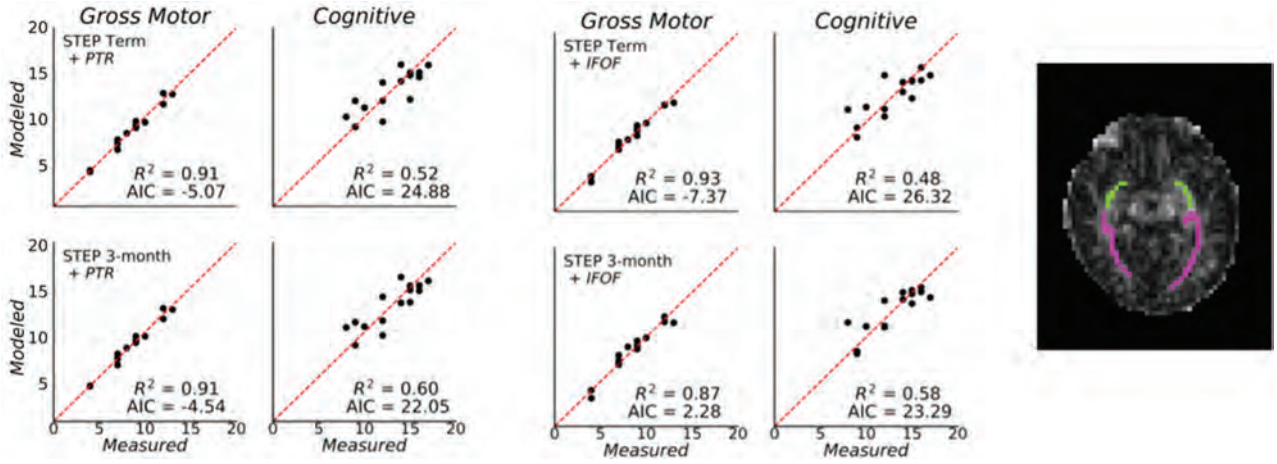

FIG 4. Measured 12-month Bayley-III gross motor (*left columns*) and cognitive scores (*right columns*) plotted against the modeled Bayley scores using STEP at term (*upper rows*) or 3 months (*lower rows*) + diffusivity and kurtosis metrics within individual WM ROIs to predict function. By means of this ROI-centered approach, the PTR and IFOF metrics combined with the STEP score result in the best predictive models, adjusted for gestational age at birth and MR imaging. Compared with STEP-alone predictive models (Online Supplemental Data), diffusivity and kurtosis in individual WM ROIs greatly improve the STEP model fit for both Bayley-III gross motor and cognitive test scores at 12 months. β-value estimates are provided in the Online Supplemental Data.

volume or density, and possibly insufficient dendritic arborization in the thalamus, responsible for sensory-input integration and regulation of voluntary movement.[43] In the WM, lower NAA is associated with decreased axonal integrity in neonatal WM disease[10,44] and worse developmental outcomes in both preterm and term infants.[9,11,12]

ROIs (IFOF, PTR, and gCC) were also strongly correlated with STEP performance (Online Supplemental Data), indicating that visuomotor and sensorimotor integration pathways are critical in the early development of motor skills. IFOF and PTR with the STEP also predicted later motor function, while the gCC and the external capsule contributed strongly to STEP prediction for later cognitive function (Fig 4 and Online Supplemental Data). The best WM tracts for prognostication from our study (IFOF, PTR, and gCC) are readily identified, and ROIs are easily placed by clinical neuroradiologists on standard anatomic MR images or ROIs registered with an appropriate WM atlas.

Most quantitative clinical investigations use diffusion tensor–derived FA that measures the directional dependence of water diffusion in a Gaussian distribution. FA increases nonlinearly with axon myelination, packing, and maturation that plateaus around 2 years of age.[19,21] However, the diffusion tensor neither accounts for non-Gaussian cellular factors nor fully characterizes microstructure across the spectrum of development. In estimating the kurtosis tensor, we captured the non-Gaussian spin displacement that corresponds to cellular and tissue heterogeneity within the WM microstructure, different from DTI.[13,16,45] Kurtosis metrics show a nonlinear relationship with age[19,21] and increase with intracellular complexity, cell density, and myelination due to further restrictions on water movement. Radial kurtosis, in particular, increases more quickly during development than its diffusivity counterpart because myelin restricts diffusion across the axon.[21] KFA is mathematically analogous to FA, but the kurtosis tensor provides complementary, more detailed directional variation on anisotropy information.[37,38] Thus, unlike FA, KFA measurements are sensitive to higher-order angular variations in WM fiber orientations,[36,38] also found in fiber-crossing regions.[37]

In our study, KFA outperformed FA in representing early function via STEP performance (Figs 2 and Online Supplemental Data), suggesting that complex WM cellular barriers or fiber-crossings are important in the early ability to move with normal tone. Although not widely used, kurtosis metrics may be better markers of WM tract injury and health in the largely unmyelinated brain of infants than diffusivity metrics such as FA. When predicting future gross motor and cognitive performance (Online Supplemental Data), however, FA provided better results, followed closely by the KFA, radial kurtosis (gross motor), and mean kurtosis (cognitive). Taken together, our data support kurtosis information possibly significantly adding to conventional FA in understanding the complexity of WM development at term age.

As a standard protocol on clinical MR imaging machines, MR spectroscopy can yield high-quality results in neonatal studies due to high water content of brain tissue and low iron deposition. MR spectroscopy can be challenging in a clinical environment in unsedated neonates. Therefore, clinicians and MR imaging technicians should attempt to schedule MR spectroscopy scans after a feeding to encourage sleep and should be cognizant of when to repeat scans (ie, motion artifacts) or modify the imaging setup (eg, better swaddling/head immobilization). Furthermore, on the basis of our findings, long-TE spectral quantification is robust (ie, a more stable baseline and less confounding peaks) in quantifying a large concentration of metabolites (namely, NAA, Cho, and Cr). Conversely, shorter-TE MR spectroscopy will have a better SNR and more information on a small concentration of metabolites compared with long-TE sequences, with a trade-off in difficulties in quantification of overlapping peak shapes.

For more advanced diffusion imaging, DKI is easily performed within 4–6-minutes by adding the b-value 2000s/mm^2 to standard DTI protocols with 30 directions per nonzero b-value. Numer-

ous open-source platforms (eg, Diffusional Kurtosis Estimator,[33] https://github.com/m-ama/DKE, DESIGNER,[28]/pyDesigner, and https://pydesigner.readthedocs.io/en/latest/) are available that provide semiautomated off-line DKI analysis.

Limitations of our study include our sample size, which precluded assessing whether brain dysmaturity or specific sites of injury were more important in neuroimaging models and any contributions of sex. Also, 12 months is a typical time for general developmental delays to manifest but is not optimal for diagnosing cerebral palsy. Another limitation is the combination of single-voxel and CSI data for the TE = 270 ms MR spectroscopy data modeling, which had slightly different TR values as well as differing spectral and shim quality. Last, MR spectroscopy voxel placement and WM ROI voxels were selected to reflect "apparently healthy" WM, but it is possible that lesions (Online Supplemental Data) may not have been readily visible during data gathering and analysis.

CONCLUSIONS

Our neuroimaging data provide proof of concept that the STEP reflects preterm brain dysfunction, dysmaturation, and/or injury. These data suggest that either MR spectroscopy or DKI can augment the STEP at term age in the prediction of long-term motor and cognitive development. If validated in a larger cohort, quantitative neuroimaging and STEP assessments may be used as surrogate end points in clinical trials and may facilitate earlier intervention for infants at high risk of developmental delays.

Disclosure forms provided by the authors are available with the full text and PDF of this article at www.ajnr.org.

REFERENCES

1. Lean RE, Han RH, Smyser TA, et al. **Altered neonatal white and gray matter microstructure is associated with neurodevelopmental impairments in very preterm infants with high-grade brain injury.** *Pediatr Res* 2019;86:365–74 CrossRef Medline
2. Back SA, Miller SP. **Brain injury in premature neonates: a primary cerebral dysmaturation disorder?** *Ann Neurol* 2014;75:469–86 CrossRef Medline
3. Duerden EG, Foong J, Chau V, et al. **Tract-based spatial statistics in preterm-born neonates predicts cognitive and motor outcomes at 18 months.** *AJNR Am J Neuroradiol* 2015;36:1565–71 CrossRef Medline
4. Coker-Bolt P, Barbour A, Moss H, et al. **Correlating early motor skills to white matter abnormalities in preterm infants using diffusion tensor imaging.** *J Pediatr Rehabil Med* 2016;9:185–93 CrossRef Medline
5. Coker-Bolt P, Woodbury ML, Perkel J, et al. **Identifying premature infants at high and low risk for motor delays using motor performance testing and MRS.** *J Pediatr Rehabil Med* 2014;7:219–32 CrossRef Medline
6. Gower L, Jenkins D, Fraser JL, et al. **Early developmental assessment with a short screening test, the STEP, predicts one-year outcomes.** *J Perinatol* 2019;39:184–92 CrossRef Medline
7. Novak I, Morgan C, Adde L, et al. **Early, accurate diagnosis and early intervention in cerebral palsy: advances in diagnosis and treatment.** *JAMA Pediatr* 2017;171:897–907 CrossRef Medline
8. Chau V, Synnes A, Grunau RE, et al. **Abnormal brain maturation in preterm neonates associated with adverse developmental outcomes.** *Neurology* 2013;81:2082–89 CrossRef Medline
9. Kreis R, Hofmann L, Kuhlmann B, et al. **Brain metabolite composition during early human brain development as measured by quantitative in vivo 1H magnetic resonance spectroscopy.** *Magn Reson Med* 2002;48:949–58 CrossRef Medline
10. Tanifuji S, Akasaka M, Kamei A, et al. **Temporal brain metabolite changes in preterm infants with normal development.** *Brain Dev* 2017;39:196–202 CrossRef Medline
11. Kendall GS, Melbourne A, Johnson S, et al. **White matter NAA/Cho and Cho/Cr ratios at MR spectroscopy are predictive of motor outcome in preterm infants.** *Radiology* 2014;271:230–38 CrossRef Medline
12. Lally PJ, Montaldo P, Oliveira V, et al. **MARBLE consortium magnetic resonance spectroscopy assessment of brain injury after moderate hypothermia in neonatal encephalopathy: a prospective multicentre cohort study.** *Lancet Neurol* 2019;18:35–45 CrossRef Medline
13. Jensen JH, Helpern JA. **MRI quantification of non-Gaussian water diffusion by kurtosis analysis.** *NMR Biomed* 2010;23:698–710 CrossRef Medline
14. Basser PJ, Mattiello J, LeBihan D. **MR diffusion tensor spectroscopy and imaging.** *Biophys J* 1994;66:259–67 CrossRef Medline
15. Jensen JH, Helpern JA, Ramani A, et al. **Diffusional kurtosis imaging: the quantification of non-Gaussian water diffusion by means of magnetic resonance imaging.** *Magn Reson Med* 2005;53:1432–40 CrossRef Medline
16. Steven AJ, Zhuo J, Melhem ER. **Diffusion kurtosis imaging: an emerging technique for evaluating the microstructural environment of the brain.** *AJR Am J Roentgenol* 2014;202:W26–33 CrossRef Medline
17. Galdi P, Blesa M, Stoye DQ, et al. **Neonatal morphometric similarity mapping for predicting brain age and characterizing neuroanatomic variation associated with preterm birth.** *Neuroimage Clin* 2020;25:102195 CrossRef Medline
18. Gao J, Li X, Li Y, et al. **Differentiating T2 hyperintensity in neonatal white matter by two-compartment model of diffusional kurtosis imaging.** *Sci Rep* 2016;6:24473 CrossRef Medline
19. Paydar A, Fieremans E, Nwankwo JI, et al. **Diffusional kurtosis imaging of the developing brain.** *AJNR Am J Neuroradiol* 2014;35:808–14 CrossRef Medline
20. Shi J, Chang L, Wang J, et al. **Initial application of diffusional kurtosis imaging in evaluating brain development of healthy preterm infants.** *PLoS One* 2016;11:e0154146 CrossRef Medline
21. Shi J, Yang S, Wang J, et al. **Detecting normal pediatric brain development with diffusional kurtosis imaging.** *Eur J Radiol* 2019;120:108690 CrossRef Medline
22. Duncan AF, Bann C, Boatman C, et al. **NICHD Neonatal Research Network: do currently recommended Bayley-III cutoffs overestimate motor impairment in infants born <27 weeks gestation?** *J Perinatol* 2015;35:516–21 CrossRef Medline
23. Vohr BR, Stephens BE, Higgins RD, et al. **NICHD Neonatal Research Network: are outcomes of extremely preterm infants improving? Impact of Bayley assessment on outcomes.** *J Pediatr* 2012;161:222–28 CrossRef Medline
24. Bentzley JP, Coker-Bolt P, Moreau NG, et al. **Kinematic measurement of 12-week head control correlates with 12-month neurodevelopment in preterm infants.** *Early Hum Dev* 2015;91:159–64 CrossRef
25. Provencher SW. **Automatic quantitation of localized in vivo 1H spectra with LCModel.** *NMR Biomed* 2001;14:260–64 CrossRef Medline
26. Moss HG, Jenkins DD, Yazdani M, et al. **Identifying the translational complexity of magnetic resonance spectroscopy in neonates and infants.** *NMR Biomed* 2019;32:e4089 CrossRef Medline
27. Soher BJ, Todd PS, Steinburg J, et al. **VeSPA: integrated applications for RF pulse design, spectral simulation and MRS data analysis.** In: *Proceedings of the Annual Meeting of the International Society for Magnetic Resonance in Medicine*, Montreal, Quebec, Canada; May 7–13, 2011
28. Ades-Aron B, Veraart J, Kochunov P, et al. **Evaluation of the accuracy and precision of the diffusion parameter EStImation with Gibbs and NoisE removal pipeline.** *Neuroimage* 2018;183:532–43 CrossRef Medline

29. Veraart J, Novikov DS, Christiaens D, et al. **Denoising of diffusion MRI using random matrix theory.** *Neuroimage* 2016;142:394–406 CrossRef Medline
30. Kellner E, Dhital B, Kiselev VG, et al. **Gibbs-ringing artifact removal based on local subvoxel-shifts.** *Magn Reson Med* 2016;76:1574–81 CrossRef Medline
31. Andersson JL, Graham MS, Zsoldos E, et al. **Incorporating outlier detection and replacement into a non-parametric framework for movement and distortion correction of diffusion MR images.** *Neuroimage* 2016;141:556–72 CrossRef Medline
32. Andersson JL, Sotiropoulos SN. **An integrated approach to correction for off-resonance effects and subject movement in diffusion MR imaging.** *Neuroimage* 2016;125:1063–78 CrossRef Medline
33. Tabesh A, Jensen JH, Ardekani BA, et al. **Estimation of tensors and tensor-derived measures in diffusional kurtosis imaging.** *Magn Reson Med* 2011;65:823–36 CrossRef Medline
34. Gudbjartsson H, Patz S. **The Rician distribution of noisy MRI data.** *Magn Reson Med* 1995;34:910–14 CrossRef Medline
35. Veraart J, Sijbers J, Sunaert S, et al. **Weighted linear least squares estimation of diffusion MRI parameters: strengths, limitations, and pitfalls.** *Neuroimage* 2013;81:335–46 CrossRef Medline
36. Glenn GR, Helpern JA, Tabesh A, et al. **Quantitative assessment of diffusional kurtosis anisotropy.** *NMR Biomed* 2015;28:448–59 CrossRef Medline
37. Hansen B, Jespersen SN. **Kurtosis fractional anisotropy, its contrast and estimation by proxy.** *Sci Rep* 2016;6:23999 CrossRef Medline
38. Hansen B. **An introduction to kurtosis fractional anisotropy.** *AJNR Am J Neuroradiol* 2019;40:1638–41 CrossRef Medline
39. Hui ES, Glenn RG, Helpern JA, et al. **Kurtosis analysis of neural diffusion organization.** *Neuroimage* 2015;106:391–403 CrossRef Medline
40. Akaike H. **Likelihood of a model and information criteria.** *J Econometrics* 1981;16:3–14 CrossRef
41. Burnham KP, Anderson DR. **Multimodel inference.** *Sociological Methods & Research* 2004;33:261–304 CrossRef
42. Urenjak J, Williams SR, Gadian DG, et al. **Proton nuclear magnetic resonance spectroscopy unambiguously identifies different neural cell types.** *J Neurosci* 1993;13:981–89 CrossRef Medline
43. Schuff N, Meyerhoff DJ, Mueller S, et al. **NAA as a marker of neuronal injury in neurodegenerative disease.** *Adv Exp Med Biol* 2006;576:241–62 CrossRef Medline
44. Moffett JR, Arun P, Ariyannur PS, et al. **NAA reductions in brain injury: impact on post-injury neuroenergetics, lipid synthesis, and protein acetylation.** *Front Neuroenergetics* 2013;5:11 CrossRef Medline
45. Gadin E, Lobo M, Paul DA, et al. **Volumetric MRI and MRS and early motor development of infants born preterm.** *Pediatr Phys Ther* 2012;24:38–44 CrossRef Medline

ACTA2-Related Dysgyria: An Under-Recognized Malformation of Cortical Development

S. Subramanian, A. Biswas, C.A.P.F. Alves, S.V. Sudhakar, K.V. Shekdar, P. Krishnan, M. Shroff, A. Taranath, F. Arrigoni, K.A. Aldinger, R.J. Leventer, W.B. Dobyns, and K. Mankad

ABSTRACT

BACKGROUND AND PURPOSE: Pathogenic variants in the *ACTA2* gene cause a distinctive arterial phenotype that has recently been described to be associated with brain malformation. Our objective was to further characterize gyral abnormalities in patients with *ACTA2* pathogenic variants as per the 2020 consensus recommendations for the definition and classification of malformations of cortical development.

MATERIALS AND METHODS: We performed a retrospective, multicentric review of patients with proved *ACTA2* pathogenic variants, searching for the presence of malformations of cortical development. A consensus read was performed for all patients, and the type and location of cortical malformation were noted in each. The presence of the typical *ACTA2* arterial phenotype as well as demographic and relevant clinical data was obtained.

RESULTS: We included 13 patients with *ACTA2* pathogenic variants (Arg179His mutation, $n = 11$, and Arg179Cys mutation, $n = 2$). Ninety-two percent (12/13) of patients had peri-Sylvian dysgyria, 77% (10/13) had frontal dysgyria, and 15% (2/13) had generalized dysgyria. The peri-Sylvian location was involved in all patients with dysgyria (12/12). All patients with dysgyria had a characteristic arterial phenotype described in *ACTA2* pathogenic variants. One patient did not have dysgyria or the characteristic arterial phenotype.

CONCLUSIONS: Dysgyria is common in patients with *ACTA2* pathogenic variants, with a peri-Sylvian and frontal predominance, and was seen in all our patients who also had the typical *ACTA2* arterial phenotype.

ABBREVIATIONS: MCD = malformation of cortical development; PMG = polymicrogyria

Heterozygous, autosomal dominant, pathogenic variants in the *ACTA2* gene encoding α-2 smooth-muscle actin that replace the arginine at protein position 179 (Arg179) with either histidine, leucine, cysteine, or serine cause a multisystemic smooth-muscle dysfunction syndrome (Online Mendelian Inheritance in Man, 613834; https://www.omim.org). Actin is found in the contractile apparatus of muscle and the cytoskeleton. There are 6 distinct isoforms (α-skeletal, α-cardiac, α-smooth, β-cytoplasmic, γ-smooth, γ-cytoplasmic actin) encoded by 6 different genes.[1] Alpha smooth-muscle actin encoded by the *ACTA2* gene constitutes the major contractile unit of the vascular smooth muscle expressed by blood vessels.[2,3] As part of this *ACTA2* syndrome, a distinctive arterial phenotype was described by Munot et al,[4] with the phenotype further expanded by D'Arco et al[5] to include brain malformative features such as a radial orientation of frontal lobe gyri, flattening of the pons, and bending and hypoplasia of the anterior corpus callosum. Following the diagnosis of an unusual malformation of cortical development (MCD) in our index patient (Online Supplemental Data, patient 9), we reviewed the neuroimaging features of patients with *ACTA2* pathogenic variants across 4 tertiary pediatric hospitals.

Received August 11, 2021; accepted after revision September 27.

From the Division of Pediatric Radiology (S.S.), Department of Radiology, UPMC Children's Hospital of Pittsburgh, Pittsburgh, Pennsylvania; Department of Diagnostic Imaging (A.B., P.K., M.S.), The Hospital for Sick Children, University of Toronto, Toronto, Ontario, Canada; Division of Neuroradiology (C.A.P.F.A.), Department of Radiology, and Department of Radiology (K.V.S.), Perelman School of Medicine at the University of Pennsylvania, The Children's Hospital of Philadelphia, Philadelphia, Pennsylvania; Department of Radiology (S.V.S., K.M.), Great Ormond Street Hospital, NHS Foundation Trust, London, UK; Department of Medical Imaging (A.T.), Women's and Children's Hospital, Adelaide, South Australia, Australia; Neuroimaging Lab (F.A.), Scientific Institute, Istituto di Ricovero e Cura a Carattere Scientifico Eugenio Medea, Bosisio Parini, Italy; Department of Pediatrics (K.A.A.), University of Washington School of Medicine, Seattle, Washington; Center for Integrative Brain Research (K.A.A., W.B.D.), Seattle Children's Research Institute, Seattle, Washington; Department of Neurology (R.J.L.), Royal Children's Hospital and Murdoch Children's Research Institute, Parkville, Victoria, Australia; Department of Pediatrics (R.J.L.), University of Melbourne, Melbourne, Victoria, Australia; and Division of Genetics and Metabolism (W.B.D.), Department of Pediatrics, University of Minnesota, Minneapolis, Minnesota.

S. Subramanian and A. Biswas share co-first authorship.

Please address correspondence to S. Subramanian, MD, UPMC Children's Hospital of Pittsburgh of University of Pittsburgh Medical Center, Pediatric Radiology, 4401 Penn Ave, Pittsburgh, PA 15224; e-mail: subramanian.subramanian2@chp.edu

Indicates article with online supplemental data.

http://dx.doi.org/10.3174/ajnr.A7364

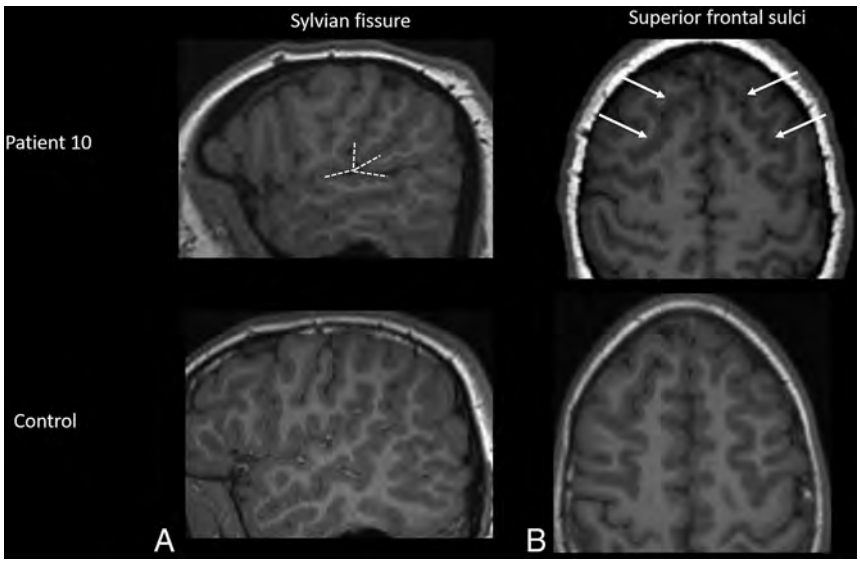

FIG 1. Peri-Sylvian and frontal dysgyria.

MATERIALS AND METHODS

Patient Population

This study included all patients with proved *ACTA2* pathogenic variants ($n = 13$) from 4 pediatric hospitals (UPMC Children's Hospital of Pittsburgh and Children's Hospital of Philadelphia; The Hospital for Sick Children, Toronto, Canada; and the Great Ormond Street Hospital, London, UK). Appropriate local research ethics board approval was obtained from each site. Patients were identified by a keyword ("*ACTA2*," "alpha actin," "MR imaging") search in their respective hospital electronic chart systems. Inclusion criteria were younger than 18 years of age and proved *ACTA2* pathogenic variants. Exclusion criteria were poor-quality imaging studies, including incomplete image acquisition and image degradation by artifacts. Patient demographics and clinical presentation were obtained from hospital electronic charts.

Image Interpretation

MR images of all patients were reviewed in consensus by 6 pediatric neuroradiologists (S.S, A.B, K.M, S.V.S, C.A.P.F.A., and F.A.) for the presence of MCDs, which were classified according to recently published international consensus recommendations.[6,7] In particular, dysgyria was diagnosed on T1-weighted and/or T2-weighted sequences if the cortex showed variable thickness and a smooth gray-white boundary but with an abnormal gyral pattern characterized by irregularities of sulcal depth and/or orientation. The location of the dysgyria was noted in each case. All patients also had MR angiograms that were used to subjectively note the presence or absence of a typical *ACTA2* arterial phenotype characterized by dilation of the proximal ICAs, abrupt caliber change with stenosis at the level of terminal ICAs, a straight course of the intracranial arteries, and absent Moyamoya-like collaterals.

RESULTS

Patient demographics and genetic and imaging findings are summarized in the Table and Online Supplemental Data. The cohort consisted of 9 females. The *ACTA2* pathogenic variants included the Arg179His mutation ($n = 11$) and the Arg179Cys mutation ($n = 2$).

Twelve of 13 patients (92%) had peri-Sylvian dysgyria, with abnormal bifurcation or trifurcation of the Sylvian fissure, which was appreciated rostrally on the sagittal sections (Fig 1*A* and Fig 2*B–E*). Ten of 13 patients had frontal dysgyria, with obliquely oriented superior frontal sulci, best appreciated in the axial plane (Fig 1*B* and Fig 2*C–E*). Two of 13 patients had generalized dysgyria in addition to the above. This was characterized by involvement of the entire cerebral cortex by an abnormal gyral pattern with variable sulcal depth and orientation (Fig 2*E*). In 10 patients, the dysgyria was associated with areas of undulated cortex that did not meet the criteria for PMG (Fig 3). Patients 3 and 13 developed seizures following a stroke, yet no other patients had epilepsy. All except 1 patient (patient 13) had the typical *ACTA2* arterial phenotype. This patient had normal intracranial imaging features (Fig 2*F*) except for a variable degree of arterial tortuosity.

DISCUSSION

We demonstrate previously under-recognized MCDs in most of our patients with the *ACTA2* pathogenic variants in the form of peri-Sylvian and frontal dysgyria. In addition, most of our patients with dysgyria had an undulating appearance of the cortex, which did not meet the criteria for PMG. We term this spectrum of malformations "*ACTA2*-related dysgyria." The typical *ACTA2* arterial phenotype was noted in all except 1 patient.

The vascular effects of *ACTA2* pathogenic variants are attributed to increased smooth-muscle cell proliferation in smaller-diameter muscular arteries and decreased contractility in larger elastic arteries.[4] Histologic specimens from patients with *ACTA2* pathogenic variants have shown large intracerebral arteries with marked intimal thickening and smooth-muscle cell proliferation; increased collagen and a relatively milder degree of smooth-muscle cell proliferation in the tunica media; as well as thickened, split, and fragmented internal elastic lamina, which showed less folding compared with that in controls.[4,8]

In the series published by D'Arco et al,[5] the abnormally oriented frontal lobe gyri were, at the time, aptly termed "abnormal radial gyration." On review of 6 cases from the article by D'Arco et al, with the addition of a further 7 cases in our series, we have termed the abnormal gyration "dysgyria," based on the latest 2020 consensus guidelines,[6,7] with this feature not only limited to the frontal lobes but also involving peri-Sylvian regions in most of our patients and generalized distribution in a minority. The peri-Sylvian dysgyria in our series was characterized by an abnormal bifurcation or trifurcation of the Sylvian fissure best appreciated on the sagittal plane. As mentioned earlier, the undulating appearance of the cortex in regions of dysgyria in our study is distinct from the appearance of PMG in that these cases lack the

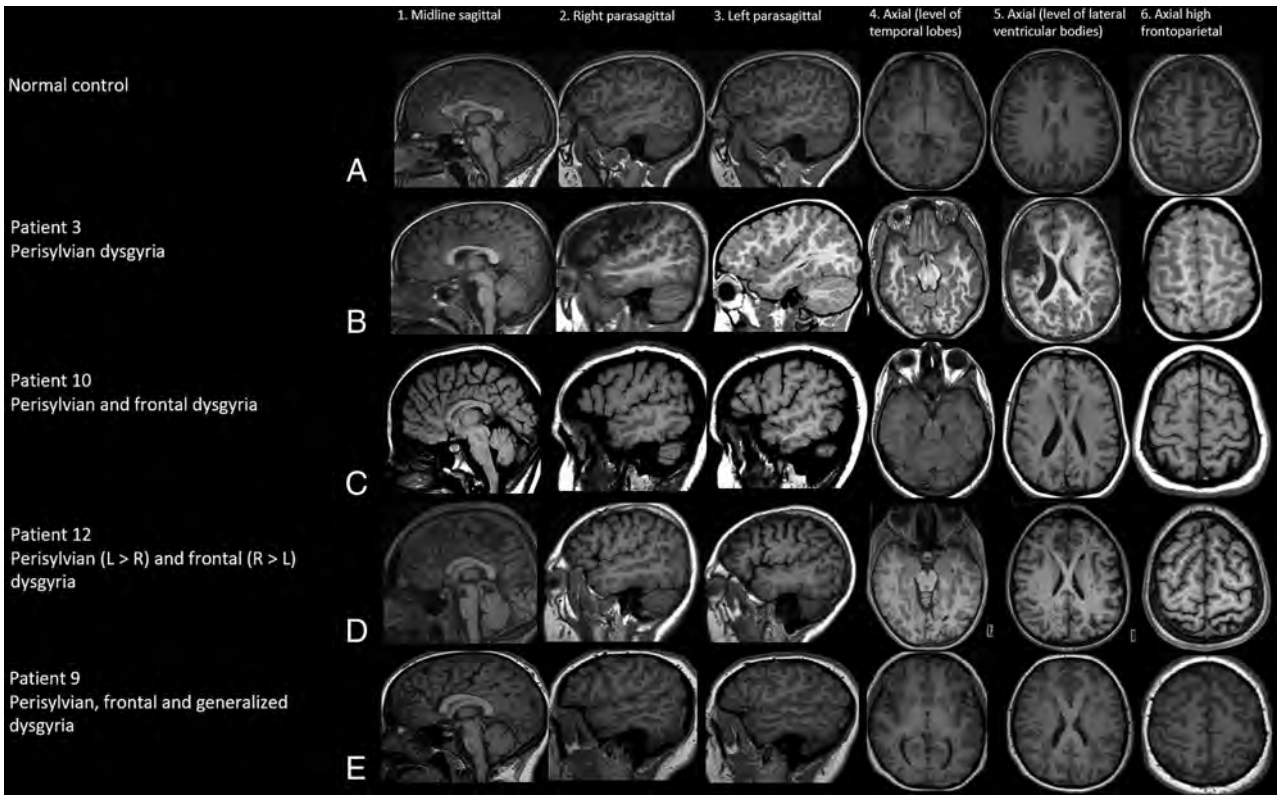

FIG 2. T1-weighted images showing the spectrum of dysgyria in *ACTA2* pathogenic variants. L indicates left; R, right.

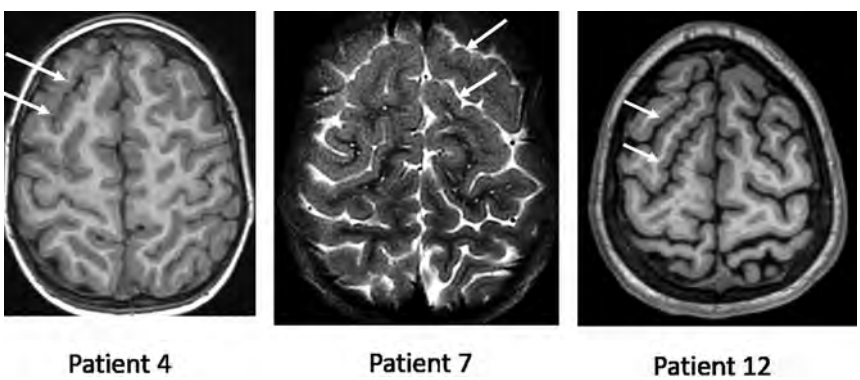

FIG 3. Undulating cortex in regions of dysgyria (*arrows*).

small microgyri at chaotic angles that have been described in classic PMG. We, therefore, use the term *ACTA2*-related dysgyria to describe our spectrum of findings.

The structural brain malformations in patients with an *ACTA2* pathogenic variant were initially attributed to either a mechanical effect from "rigid" vessels or abnormal cross-regulation between different isoforms. Before recent evidence confirming otherwise,[9-12] it was presumed that α-actin was not expressed in the brain parenchyma; therefore, it would be unlikely for *ACTA2* pathogenic variants to directly influence brain development.[5]

While rigid vessels may explain some of the features seen in *ACTA2* pathogenic variants, they do not explain the spectrum of dysgyria that we have described in this study. For instance, histologic specimens show intimal and medial thickening with a relatively spared adventitia,[4,8] explaining the luminal stenosis, but they do not explain malformations of structures extrinsic to the vascular wall. Recent studies demonstrating α-actin[9-11] and, more specifically, *ACTA2*[12] expression in the brain parenchyma shed light on potential alternate hypotheses for the presence of MCDs in these patients. In 2017, Moradi et al[11] described differing roles of α-, β-, and γ-actin in axon growth, guidance, arborization, and synaptogenesis and demonstrated that all 3 actin isoforms were expressed in motor neurons, with their respective messenger RNAs localizing within axons. Alpha-actin, in particular, was highly expressed in the axonal compartment and axonal branch points, with depletion of α-actin associated with altered filopodia dynamics, reduced filopodia length, and diminished ability to form axonal collateral branches. Another recent study demonstrated that *ACTA2* was expressed in neural stem cells of embryonic C57BL/6 mice and played an essential role in neural stem cell migration.[12]

Furthermore, several studies have shown that knockout of specific actin isoforms leads to compensatory upregulation of other isoforms so that the overall levels of actin are maintained.[11,13-16] Also, notably, no actin isoform differs from another by more than 7% at the primary amino acid level;[1] therefore,

cross-regulation between actin isoforms, especially when there is depletion of one isoform and compensatory up-regulation of other isoforms, may also play a role in *ACTA2* pathogenic variants. These observations may, therefore, help classify *ACTA2*-related dysgyria as a migrational or postmigrational disorder involving the processes of neuronal migration and organization, axonogenesis, and dendritogenesis.

The consistent distribution of dysgyria in the peri-Sylvian regions and frontal lobes is intriguing. One possible explanation may be that developing vessels perform scaffolding and a paracrine signaling function for developing neural cell populations.[17] Indeed, whole-brain MR angiography in our index patient (patient 9) revealed the presence of arterial branches coursing along the abnormally oriented sulci (Fig 4). Recent genetic insights have shown that the embryogenesis of the vascular and nervous systems are closely interlinked and that the axon growth cone and endothelial tip cell respond to growth and guidance cues in similar ways.[18-22] In addition, there is cross-talk between neural and vascular cells for the purpose of normal development, and signals from both neural and vascular tissue can influence the branching of one another.[17,23] For instance, neuronal activity has been found to influence cerebrovascular density, vessel branching, and maturation via molecular cues as well as direct cell-to-cell contact of neural cell types with endothelial cells.[17,24] Similarly, CNS vasculature patterning plays a crucial role in preventing mispositioning of neuronal precursor cells and in providing a scaffold for neuronal migration, axonal projections, and cell soma arrangements in the developing brain.[25-27] Thus, stiff and noncompliant *ACTA2*-mutant arteries may present a rigid scaffold to the developing brain, resulting in abnormal gyral patterning. Another factor that may contribute to dysgyria includes aberrant tension-induced growth of white matter, influencing folding patterns in a viscoelastic model of the brain, as described in an excellent recent review of the mechanics of cortical folding.[28] Therefore, an interplay of various factors during the

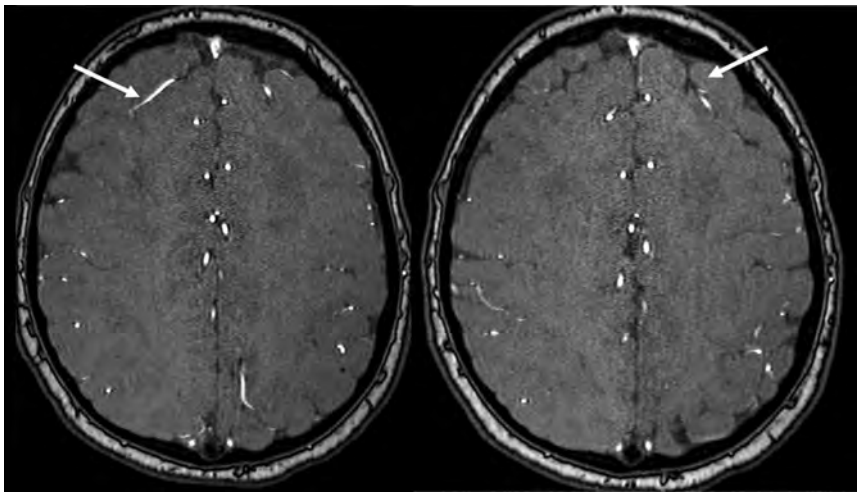

FIG 4. Anterior cerebral artery branches follow abnormal sulci (*arrows*).

Demographics, neuroimaging findings, and clinical presentation

Patient	Age	Sex	Mutation	Dysgyria			Undulating Cortex in Regions of Dysgyria	Presenting Symptom	Seizures	Typical *ACTA2* Vascular Phenotype
				Peri-Sylvian	Frontal	Generalized				
1	5 yr	M	Arg179His	+	+	+	No	Cardiac arrest in early life	No	Yes
2	4 yr	F	Arg179His	+	+	–	No	Strokelike episodes	No	Yes
3	6 yr	F	Arg179His	+	–	–	Yes	Stroke	Yes	Yes
4	13 wk	M	Arg179His	+	–	–	Yes	Aniridia	No	Yes
5	3 yr	F	Arg179His	+	+	–	Yes	Cardiac symptoms	No	Yes
6	4 yr	F	Arg179His	+	+	–	Yes	Left hemiparesis	No	Yes
7	2 mo	F	Arg179Cys	+	+	–	Yes	Anisocoria and cataract	No	Yes
8	4 yr	M	Arg179His	+	+	–	No	Congenital mydriasis	No	Yes
9	11 yr	F	Arg179His	+	+	+	Yes	Congenital mydriasis	No	Yes
10	17 yr	F	Arg179His	+	+	–	Yes	Chronic headaches	No	Yes
11	8 yr	F	Arg179His	+	+	–	Yes	Spastic quadriplegic cerebral palsy, headaches	No	Yes
12	11 yr	F	Arg179His	+	+	–	Yes	Stroke	Yes	Yes
13	7 yr	M	Arg179Cys	–	–	–	NA	None (screened as part of family)	No	No

Note:— + indicates present; –, absent; NA, not applicable.

stages of neuronal migration, axonogenesis, and vasculogenesis may each contribute to the patterns of dysgyria that we have described in this article.

CONCLUSIONS

Dysgyria is common in patients with *ACTA2* pathogenic variants and has a frontal and peri-Sylvian predominance. Although the underlying mechanisms are yet to be elucidated, recent insights suggest the potential roles of mutant α-actin in neuronal migration and axonogenesis, abnormal cross-regulation between actin isoforms, aberrant neurovascular cross-talk, and an abnormal vascular scaffold, resulting in these malformations.

Disclosure forms provided by the authors are available with the full text and PDF of this article at www.ajnr.org.

REFERENCES

1. Cheever TR, Ervasti JM. **Actin isoforms in neuronal development and function.** *Int Rev Cell Mol Biol* 2013;301:157–213 CrossRef Medline
2. Gabbiani G, Schmid E, Winter S, et al. **Vascular smooth muscle cells differ from other smooth muscle cells: predominance of vimentin filaments and a specific alpha-type actin.** *Proc Natl Acad Sci U S A* 1981;78:298–302 CrossRef Medline
3. Glukhova MA, Kabakov AE, Frid MG, et al. **Modulation of human aorta smooth muscle cell phenotype: a study of muscle-specific variants of vinculin, caldesmon, and actin expression.** *Proc Natl Acad Sci U S A* 1988;85:9542–46 CrossRef Medline
4. Munot P, Saunders DE, Milewicz DM, et al. **A novel distinctive cerebrovascular phenotype is associated with heterozygous Arg179 ACTA2 mutations.** *Brain* 2012;135:2506–14 CrossRef Medline
5. D'Arco F, Alves CA, Raybaud C, et al. **Expanding the distinctive neuroimaging phenotype of ACTA2 mutations**. *AJNR Am J Neuroradiol* 2018;39:2126–31 CrossRef Medline
6. Oegema R, Barakat TS, Wilke M, et al. **International consensus recommendations on the diagnostic work-up for malformations of cortical development.** *Nat Rev Neurol* 2020;16:618–35 CrossRef Medline
7. Severino M, Geraldo AF, Utz N, et al. **Definitions and classification of malformations of cortical development: practical guidelines.** *Brain* 2020;143:2874–94 CrossRef Medline
8. Georgescu MM, da Cunha Pinho M, Richardson TE, et al. **The defining pathology of the new clinical and histopathologic entity ACTA2-related cerebrovascular disease.** *Acta Neuropathol Commun* 2015;3:81 CrossRef Medline
9. McHugh KM, Crawford K, Lessard JL. **A comprehensive analysis of the developmental and tissue-specific expression of the isoactin multigene family in the rat.** *Dev Biol* 1991;148:442–58 CrossRef Medline
10. Tondeleir D, Vandamme D, Vandekerckhove J, et al. **Actin isoform expression patterns during mammalian development and in pathology: insights from mouse models.** *Cell Motil Cytoskeleton* 2009;66:798–815 CrossRef Medline
11. Moradi M, Sivadasan R, Saal L, et al. **Differential roles of α-, β-, and γ-actin in axon growth and collateral branch formation in motoneurons.** *J Cell Biol* 2017;216:793–814 CrossRef Medline
12. Zhang J, Jiang X, Zhang C, et al. **Actin Alpha 2 (ACTA2) downregulation inhibits neural stem cell migration through rho GTPase activation.** *Stem Cells Int* 2020;2020:4764012 CrossRef Medline
13. Crawford K, Flick R, Close L, et al. **Mice lacking skeletal muscle actin show reduced muscle strength and growth deficits and die during the neonatal period.** *Mol Cell Biol* 2002;22:5887–96 CrossRef Medline
14. Schildmeyer LA, Braun R, Taffet G, et al. **Impaired vascular contractility and blood pressure homeostasis in the smooth muscle alpha-actin null mouse.** *FASEB J* 2000;14:2213–20 CrossRef Medline
15. Perrin BJ, Ervasti JM. **The actin gene family: function follows isoform.** *Cytoskeleton (Hoboken)* 2010;67:630–34 CrossRef Medline
16. Cheever TR, Li B, Ervasti JM. **Restricted morphological and behavioral abnormalities following ablation of β-Actin in the brain.** *PLoS One* 2012;7:e32970 CrossRef Medline
17. Paredes I, Himmels P, Ruiz de Almodóvar C. **Neurovascular communication during CNS development.** *Dev Cell* 2018;45:10–32 CrossRef Medline
18. Adams RH, Eichmann A. **Axon guidance molecules in vascular patterning.** *Cold Spring Harb Perspect Biol* 2010;2:a001875 CrossRef Medline
19. Quaegebeur A, Lange C, Carmeliet P. **The neurovascular link in health and disease: molecular mechanisms and therapeutic implications.** *Neuron* 2011;71:406–24 CrossRef Medline
20. Eichmann A, Thomas JL. **Molecular parallels between neural and vascular development.** *Cold Spring Harb Perspect Med* 2013;3:a006551 CrossRef Medline
21. Tam SJ, Watts RJ. **Connecting vascular and nervous system development: angiogenesis and the blood-brain barrier.** *Annu Rev Neurosci* 2010;33:379–408 CrossRef Medline
22. Wälchli T, Wacker A, Frei K, et al. **Wiring the vascular network with neural cues: a CNS perspective.** *Neuron* 2015;87:271–96 CrossRef Medline
23. Carmeliet P. **Blood vessels and nerves: common signals, pathways and diseases.** *Nat Rev Genet* 2003;4:710–20 CrossRef Medline
24. Lacoste B, Comin CH, Ben-Zvi A, et al. **Sensory-related neural activity regulates the structure of vascular networks in the cerebral cortex.** *Neuron* 2014;83:1117–30 CrossRef Medline
25. Javaherian A, Kriegstein A. **A stem cell niche for intermediate progenitor cells of the embryonic cortex.** *Cerebral Cortex* 2009;19:i70–77 CrossRef Medline
26. Li S, Haigh K, Haigh JJ, et al. **Endothelial VEGF sculpts cortical cytoarchitecture.** *J Neurosci* 2013;33:14809–15 CrossRef Medline
27. Paredes MF, James D, Gil-Perotin S, et al. **Extensive migration of young neurons into the infant human frontal lobe.** *Science* 2016;354:aaf7073 CrossRef Medline
28. Garcia KE, Kroenke CD, Bayly PV. **Mechanics of cortical folding: stress, growth and stability.** *Philos Trans R Soc Lond B Biol Sci* 2018;373:2017321 CrossRef Medline

Imaging Features with Histopathologic Correlation of CNS High-Grade Neuroepithelial Tumors with a *BCOR* Internal Tandem Duplication

L. Cardoen, A. Tauziède-Espariat, V. Dangouloff-Ros, S. Moalla, N. Nicolas, C.-J. Roux, Y. Bouchoucha, F. Bourdeaut, K. Beccaria, S. Bolle, G. Pierron, C. Dufour, F. Doz, N. Boddaert, and H.J. Brisse

ABSTRACT

BACKGROUND AND PURPOSE: A new brain tumor entity occurring in early childhood characterized by a somatic *BCL6* corepressor gene internal tandem duplication was recently described. The aim of this study was to describe the radiologic pattern of these tumors and correlate this pattern with histopathologic findings.

MATERIALS AND METHODS: This retrospective, noninterventional study included 10 children diagnosed with a CNS tumor, either by ribonucleic acid–sequencing analysis or deoxyribonucleic acid methylation analysis. Clinical, radiologic, and histopathologic data were collected. A neuropathologist reviewed 9 tumor samples. Preoperative images were analyzed in consensus by 7 pediatric radiologists.

RESULTS: All tumors were relatively large (range, 4.7–9.2 cm) intra-axial peripheral masses with well-defined borders and no peritumoral edema. All tumors showed mild and heterogeneous enhancement and marked restriction on DWI of the solid portions. Perfusion imaging showed a relatively lower CBF in the tumor than in the adjacent normal parenchyma. Nine of 10 tumors showed areas of necrosis, with the presence of hemorrhage in 8/10 and calcifications in 4/7. Large intratumoral macroscopic veins were observed in 9/10 patients. No intracranial or spinal leptomeningeal dissemination was noted at diagnosis.

CONCLUSIONS: CNS tumors with a *BCL6* corepressor gene internal tandem duplication present as large intra-axial peripheral masses with well-defined borders, no edema, restricted diffusion, weak contrast enhancement, frequent central necrosis, hemorrhage and calcifications, intratumoral veins, and no leptomeningeal dissemination at the time of diagnosis. Knowledge of these imaging characteristics may aid in histologic, genomic, and molecular profiling of brain tumors in young children.

ABBREVIATION: ITD = internal tandem duplication

Recently, a new group of CNS tumors characterized by a genetic *BCL6* corepressor (*BCOR*) alteration and distinct histopathologic and clinical features was identified.[1] CNS tumors with an internal tandem duplication (ITD) of the *BCOR* gene, formerly included in the group of primitive neuroectodermal tumors of the CNS, form a specific molecular entity.[2]

To date, 50 cases have been reported,[1,3-13] with mainly a genomic and histopathologic description. Only 2 publications included a few MR images[6,12] but no detailed discussion of the CT and MR imaging features.

The aim of our study was to report a series of CNS tumors with a proved somatic *BCOR* ITD, to describe their radiologic patterns on CT and MR imaging, and to correlate these patterns with the histopathologic findings.

MATERIALS AND METHODS

This retrospective noninterventional study was approved by the institutional review board of the Institut Curie, with a waiver of the requirement for patient consent.

Patients

Ten children were diagnosed with a CNS tumor with a *BCOR* ITD during 2010–2019 in France, either by ribonucleic acid–sequencing

Received July 15, 2021; accepted after revision September 27.

From the Imaging Department (L.C., N.N., H.J.B.), SIREDO Oncology Center Care, Innovation and Research for Children, Adolescents and Young Adults with Cancer (Y.B., F.B., F.D.), and Department of Biopathology and Genetics (G.P.), Institut Curie, Paris, France; Department of Neuropathology (A.T.-E.), Centre Hospitalier Sainte Anne, Paris, France; Department of Neurosurgery (K.B.) and Pediatric Radiology Department (V.D.-R., C.-J.R., N.B.), Assistance Publique–Hôpitaux de Paris, Hôpital Universitaire Necker-Enfants Malades, Paris, France; Institut Imagine (V.D.-R., N.B.), Université de Paris, Unité Médicale de Recherche (UMR) 1163, Paris, France; Departments of Radiology (S.M.), Radiation Oncology (S.B.), and Paediatric and Adolescent Oncology (C.D.), Gustave Roussy, Villejuif, France; Université de Paris (V.D.-R., K.B., F.D., N.B.), Institut National de la Santé et de la Recherche Médicale, ERL UA10, Paris, France; and Université Paris Saclay (H.J.B.), Institut National de la Santé et de la Recherche Médicale, LITO U1288, Orsay, France.

Please address correspondence to Liesbeth Cardoen, MD, Institut Curie, 26, rue d'Ulm, Paris 75248, France; e-mail: liesbeth.cardoen@curie.fr

Indicates article with online supplemental data.

http://dx.doi.org/10.3174/ajnr.A7367

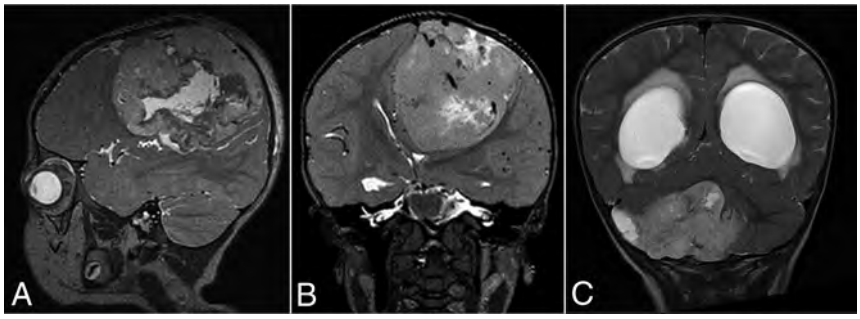

FIG 1. T2-weighted MR images showing large masses located supratentorially (*A* and *B*) and infratentorially (*C*).

analysis performed at 2 expert centers (Institut Curie in Paris and Center Léon Bérard in Lyon, France) or by deoxyribonucleic acid methylation analysis in the Neuropathology Department of Sainte-Anne Hospital (Paris, France) using the Deutsches Krebsforschungszentrum/Heidelberg University classifier.[14] Medical records were searched retrospectively for the collection of clinical, radiologic, and histopathologic data.

One patient in the cohort (patient 6) was previously included in the article by Appay et al.[5]

Histopathology

All tumor samples were evaluated by an experienced neuropathologist (9/10 were reviewed by A.T.-E., and the histopathologic findings from 1 tumor sample were previously published[5]) using hematoxylin phloxine saffron staining. For each tumor sample, we analyzed the following criteria: cellular density, the presence of necrosis, calcifications, hemorrhagic modifications, the density of the vascular network, and the presence of microvascular proliferation. The infiltrative or well-circumscribed growth pattern of the tumors was evaluated using an antibody against neurofilament (1:100, clone NF70; Dako). The density of the vascular network was evaluated using a CD34 antibody (1:40, clone QBEnd10; Dako).

Imaging

Both MR imaging and CT scans of the brain were available for 5 patients, MR images only were available for 4 patients, and only CT scans were available for 1 patient. MR imaging of the spinal axis was available for 6 patients.

MR imaging was performed at different institutions. At a minimum, the acquired sequences were T1-weighted, T2-weighted, DWI, and T1-weighted imaging after contrast media injection. The MR imaging investigation of 1 patient included unenhanced perfusion imaging a with 3D pseudocontinuous arterial spin-labeling sequence, and another patient had a dynamic susceptibility contrast-enhanced perfusion-weighted (T2*) sequence. CT images before and after iodine contrast media injection were also reviewed. The presence of calcifications was assessed either by unenhanced CT or the comparison of phase and magnitude images from SWI when available.

The preoperative images of each patient were analyzed by 7 pediatric radiologists (L.C., H.J.B., N.N., N.B., V.D.-R., C.-J.R., and S.M.), with 6, 25, 4, 20, 9, 8, and 5 years' experience, respectively, who came to a consensus regarding the findings. Images were qualitatively analyzed using the viewer of the PACS of the Institut Curie.

RESULTS

Clinical Findings

The study population included 7 girls and 3 boys. The age of the patients ranged from 1.2 years to 7.6 years with a median age of 1.8 years. The clinical symptoms at diagnosis were mainly intracranial pressure and ataxia and hemiparesis and convulsions.

Histopathologic Findings

All tumors were densely cellular and well-circumscribed from the normal brain parenchyma, as confirmed by neurofilament staining. Hemorrhagic modifications were present in 6/9 tumors. A dense branching capillary network was present in all tumors, confirmed by CD34 immunostaining, with hyalinized fibrous vessels in 2 tumors. However, no large vessels, including veins, were observed in any tumors. Only 2 tumors presented with calcifications in the viable portion of the tumor. Palisading, geographic, and calcified necrosis was observed in 6/9 tumors. Microvascular proliferation was present in only 1 tumor. Leptomeningeal involvement in 1 tumor was confirmed histopathologically.

Imaging Features

Findings are reported in the Online Supplemental Data.

All tumors were relatively large, well-defined intra-axial masses, with the largest median diameter being 6 cm (range, 4.7–9.2 cm) and the median volume being 48 cm^3 (range, 26–208 cm^3) (Fig 1).

Five tumors were located supratentorially, 2 in the frontal lobe, 2 in the temporal lobe, and 1 centered on the fornix. The 5 tumors situated infratentorially were all cerebellar hemisphere masses. Nine of 10 tumors were localized peripherally—ie, they abutted the overlying dura but showed no radiologic signs of dural invasion.

On MR imaging, tumors showed a low signal intensity on T1-weighted images and a signal intensity on T2-weighted images slightly higher than that of the normal gray matter. Nine of 10 tumors showed areas of necrosis with the presence of hemorrhage in 8/10 and calcifications in 4/7 at the border of the necrotic area and the solid portions of the tumor (Figs 2 and 3). On CT, tumor density was measured between 26 and 38 HU (versus 35 HU for normal cortical gray matter). No vasogenic edema in the surrounding white matter was observed for any tumor.

All tumors demonstrated a restriction of diffusion, with ADC values varying between 0.5 and 0.9 $\times$ $10^{-3}mm^2/s$ (Fig 4) (the ADC values measured in the normal cortical gray matter of our patients ranged between 0.8 and 1.0 $\times$ $10^{-3}mm^2/s$.

Large intratumoral macroscopic vessels connected to cortical veins were observed in 9/10 patients. All tumors showed mild and heterogeneous enhancement of the solid portion on MR imaging or CT (Fig 5). For patient n° 4, the CBF measured with arterial spin-labeling was 37 mL/min/100g and the relative CBF compared

with that of the contralateral cortical gray matter was 0.52. By T2* perfusion-weighted MR imaging, the relative CBV was 1.91 and the relative CBF was 0.87 for patient n° 6.

No intracranial or spinal leptomeningeal dissemination was noted at diagnosis.

Treatment

All patients underwent an initial operation, with macroscopic complete resection in 9/10 patients. Seven patients received adjuvant chemotherapy. Eight patients received adjuvant external radiation therapy on the tumor bed, and 6 received additional craniospinal radiation therapy.

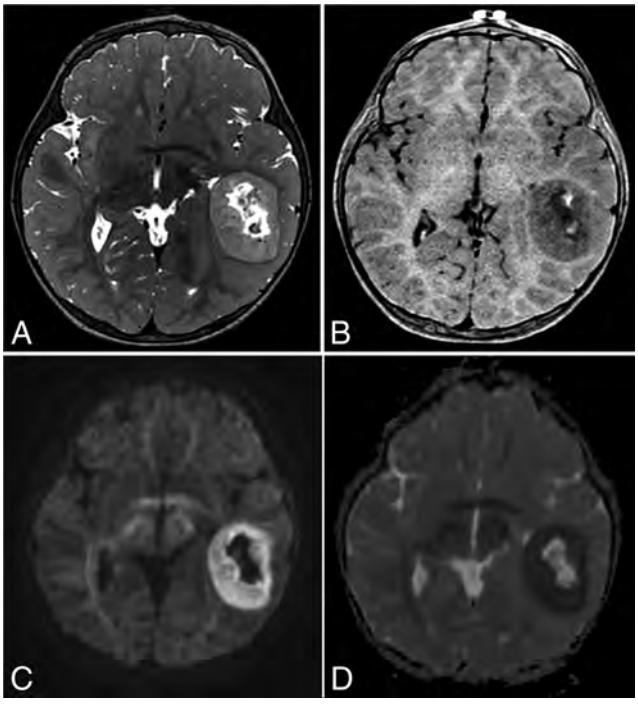

FIG 2. Characteristic MR imaging features of CNS tumors with a *BCOR* ITD. *A*, Axial T2-weighted image shows a well-defined mass, central necrosis, and no surrounding edema. *B*, Axial contrast-enhanced T1-weighted image shows poor enhancement after contrast medium administration. Axial DWI (*C*) and ADC map (*D*) show restricted diffusion of the solid portions of the tumor.

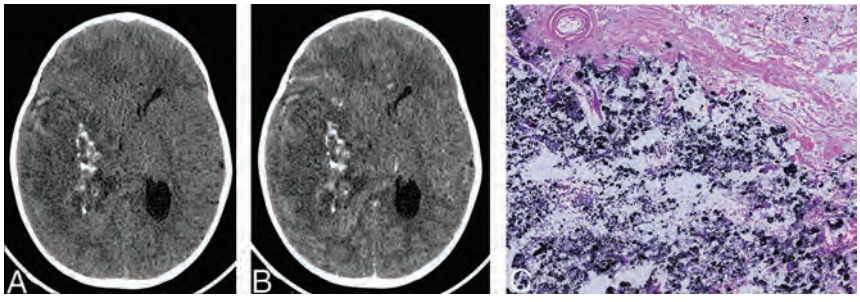

FIG 3. Axial CT images before (*A*) and after (*B*) contrast medium administration. The tumor is hypo to isodense relative to the cortex, and it exhibits weak-to-mild contrast enhancement. Intralesional calcifications are well-visualized. *C*, Visualization of several calcifications (*black stained*) (hematoxylin phloxine saffron, original magnification ×100).

Clinical/Patient Outcomes

Six patients died of their disease within 9–71 months of diagnosis (patient n° 1, 2, 3, 7, 8, 9). Three patients still have a complete response: Two patients (n° 5 and 6) had an initial complete response 19 and 51 months from diagnosis, and 1 patient (n° 4) had a second complete response 69 months from diagnosis. One patient is still being treated (n° 10).

DISCUSSION

CNS tumors with a *BCOR* ITD are a new tumor entity occurring in early childhood and are characterized by a specific genetic *BCOR* alteration and distinct histopathologic features. To the best of our knowledge, this series, though small, is the largest for which a detailed radiologic description correlated with the histopathologic characteristics is presented.

Genomic profiling of these tumors revealed a somatic ITD in the region of exon 15 of the *BCOR* gene. Somatic alterations in *BCOR* have been identified as recurrent genetic drivers in a wide spectrum of human tumor types. The same type of duplication in *BCOR* has been described in clear cell sarcoma of the kidney[15-17] and in a subset of soft-tissue undifferentiated, primitive myxoid mesenchymal tumors of infancy.[18,19]

CNS tumors with a *BCOR* ITD are compact tumors with predominantly solid growth, characterized by a combination of spindle and oval cells. The histopathologic analysis demonstrates cytologic and immunohistochemical evidence of neuroepithelial differentiation. Histologic features such as fibrillary processes, characteristics of glial differentiation, perivascular pseudorosettes, and palisading necrosis have been reported. In contrast to ependymomas however, CNS tumors with a *BCOR* ITD exhibit sparse-to-no expression of glial fibrillary acidic protein or S-100. The typical embryonal morphology as seen in embryonal tumors and evident neuronal differentiation is not observed.[1]

According to our study cohort, in CT and MR imaging, CNS tumors with a *BCOR* ITD present as relatively large intra-axial and peripheral masses with well-defined borders without peripheral edema, confirmed by pathology and in agreement with the few cases previously described.[3,6,8,12,13] An equal distribution between supratentorial and infratentorial locations was observed in our cohort, but a slight predominance of an infratentorial location has been reported in the literature.[3-9,11-13] CNS tumors with a *BCOR* ITD are located mainly in the cerebral or cerebellar hemispheres. In accordance with Ferris et al,[12] who reported that most tumors abutted the overlying dura without definite invasion, we also observed contact with the dura mater in 9 of 10 patients. This finding was not clearly described in the few previously published cases; however, this pattern was retrospectively visible in the published images.[3-5,8,13] Despite the peripheral location, no dural tail sign or thickening of the dura mater, suggesting leptomeningeal dissemination, was observed at the time of diagnosis, as previously described.[7,8,12] One patient had focal leptomeningeal

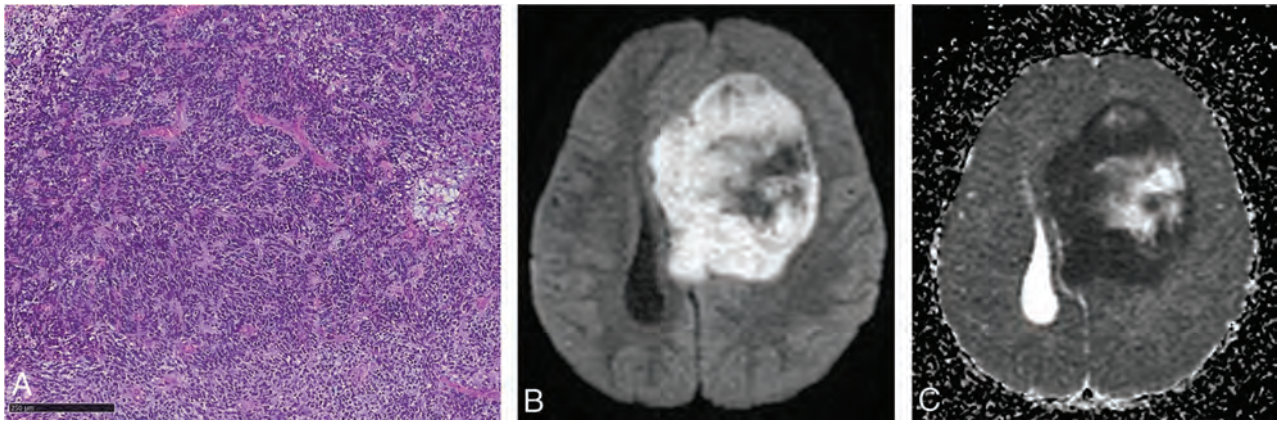

FIG 4. *A*, High cellular density of the tumor with numerous nuclei, densely packed (hematoxylin phloxine saffron, original magnification ×100). *Black scale bar* represents 250 μm. Note the corresponding diffusion-weighted image (*B*) with ADC mapping (C).

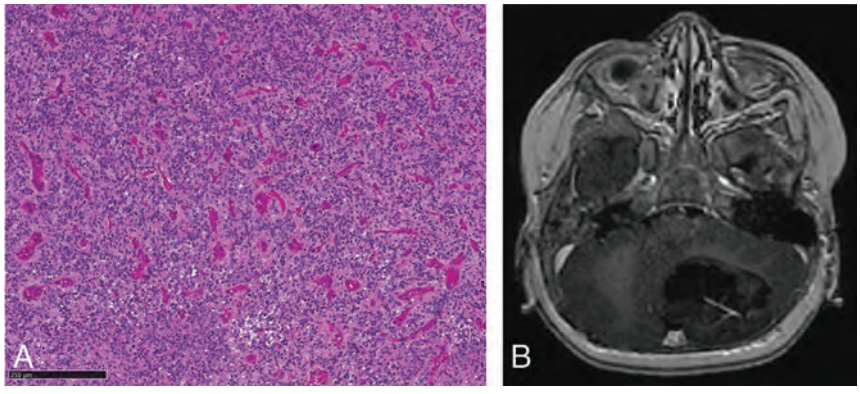

FIG 5. *A*, Rich delicate thin-walled vessels without microvascular proliferation (hematoxylin phloxine saffron, original magnification ×100). *Black scale bar* represents 250 μm. *B*, Corresponding contrast-enhanced T1-weighted MR image shows weak contrast uptake.

metastases identified on histopathologic examination, which were not visible on imaging probably because of the low sensitivity of the CT scan (no MR image was available). These imaging findings, consistent with the histopathologic findings, suggest an intraparenchymal origin of these tumors and not a mesenchymal origin as is the case of *BCOR* ITD tumors occurring in the kidney and soft tissue.

The solid portions of the tumor were hypointense on T1-weighted images and slightly hyperintense on T2-weighted images, and they showed a marked restriction on DWI related to their high cellular density. Ferris et al[12] described a more heterogeneous T2 signal, which varied from isointense to hyperintense compared with the adjacent brain. To our knowledge, the CT density of CNS tumors with a *BCOR* ITD has never been reported.

Our histopathologic results showed a high microvascular density but no microvascular proliferation for all tumors. In agreement with earlier imaging reports,[5,6,12] we also observed weak contrast enhancement of these tumors. Indeed, it has been previously reported that contrast enhancement is not a criterion for high-grade neoplasms in children.[20,21] Perfusion imaging was available in only 2 patients but demonstrated relatively low-to-intermediate CBF values compared with the adjacent normal parenchyma. This finding has not yet been reported in the radiologic literature, surprising because CBF was reported to be correlated with tumor microvascular density and histologic grade in children.[21] However, low CBF values were also reported for other high-grade tumors such as embryonal tumors with multilayered rosettes.[20] The relative CBV value for 1 patient was elevated; hence, the low CBF could be related to a long MTT in capillary vessels. These findings should be confirmed in a larger patient sample. We suggest that the relationship between perfusion and tumor neovascularization is probably multifactorial and not solely determined by vessel density and vessel wall structure.

We did not observe vasogenic edema within the surrounding white matter. This relatively uncommon finding for high-grade CNS tumors was also noted by Ferris et al[12] and Bremer et al[13] and was retrospectively visible on the available images from other published cases.[3,5,6,8] Almost all studies described areas of necrosis and blood products.[6,8,12,13] We observed calcifications located at the border of the central necrotic area and the solid peripheral portion of the tumor, a finding that had not been previously described. A possible explanation is that calcifications are more easily seen on CT and the available imaging in preceding studies was mainly MR images. Large central veins located within the mass were a feature observed in almost all our patients and have not been described to date. This finding was not correlated with pathology, probably because of tumor sampling bias.

Knowledge of these imaging features might help in the consideration of this type of tumor when facing the initial diagnosis of a brain tumor in a young child. A possible differential diagnosis is an embryonal tumor with multilayered rosettes, a rare malignant embryonal tumor occurring in the same age group that shares some features with CNS tumors with a *BCOR* ITD. Embryonal tumors with multilayered rosettes are also large tumors with

frequent calcifications, little-to-no edema, absent or weak contrast enhancement, intratumoral veins, restricted diffusion, and low CBF values in arterial spin-labeling.[20] However, in contrast to CNS tumors with a *BCOR* ITD, embryonal tumors with multilayered rosettes do not exhibit frequent central necrosis.

Primary atypical teratoid/rhabdoid tumors are another type of rare, highly malignant embryonal tumor occurring in young children. Imaging features that may distinguish them from CNS tumors with a *BCOR* ITD are the presence of peripheral cystic components, some mild-to-moderate edema, a marked enhancement of the solid portions of the tumor, and tumor dissemination within the CNS at the time of diagnosis.[22-26]

Medulloblastomas typically occur in mid-childhood (5–7 years). Most medulloblastomas occurring in early childhood belong to the sonic hedgehog group, group 3 or 4. Group 3 and 4 medulloblastomas arise from the midline (vermis and fourth ventricle) and frequently show early metastasis.[27,28] Sonic hedgehog medulloblastomas in infants with desmoplastic and nodular histologic features are located in the cerebellar hemispheres and arise from the cerebellar cortex. Sonic hedgehog medulloblastomas with extensive nodularity display a more diffuse nodular grape-like pattern on MR images than CNS tumors with a *BCOR* ITD. Moreover, sonic hedgehog medulloblastomas commonly display very strong postcontrast enhancement, which is thought to be due to leptomeningeal desmoplasia.[29]

Most ependymomas have an infratentorial intraventricular location with an extension of the tumor through the foramen of the fourth ventricle. Supratentorial ependymomas have an intraparenchymal location. They tend to be more T2-hyperintense than CNS tumors with a *BCOR* ITD, with the presence of large cysts, avid heterogeneous enhancement, and intermediate diffusion restriction.[30] Low-grade gliomas have highly variable imaging features. They generally show an increased diffusivity on ADC maps. High-grade gliomas have more irregular and infiltrative margins and exhibit peritumoral edema and more contrast uptake than CNS tumors with a *BCOR* ITD.[27]

CNS tumors with a *BCOR* ITD are aggressive tumors that require close clinical and radiologic monitoring. Despite intensive treatment, CNS tumors with a *BCOR* ITD are associated with early local recurrence and a poor outcome. Different treatments have been attempted, such as total surgical excision, focal or craniospinal radiation therapy, chemotherapy (including carboplatin, cisplatin, etoposide, cyclophosphamide, procarbazine, and temozolomide), bevacizumab, intrathecal chemotherapy (methotrexate and topotecan), and high-dose chemotherapy with autologous stem cell support. New treatment strategies are being investigated.[4,7,10]

Due to the rarity of this disease, the relatively small number of CNS tumors with a *BCOR* ITD is a limitation of our study. Because the images were evaluated retrospectively and imaging was performed at different centers, our data also show a certain degree of heterogeneity, and notably, CT and functional imaging were not available for all patients, especially perfusion imaging.

CONCLUSIONS

We described the imaging features of 10 confirmed CNS tumors with a *BCOR* ITD, and we correlated these features with the clinical and histopathologic findings. CNS tumors with a *BCOR* ITD present as large peripheral intra-axial masses with well-defined borders, no edema, restricted diffusion, weak contrast enhancement, frequent central necrosis, hemorrhage and calcifications, intratumoral veins, and no leptomeningeal dissemination at the time of diagnosis. Knowledge of these characteristics may aid in the histologic, genomic, and molecular profiling of brain tumors in young children.

ACKNOWLEDGMENTS

We thank Dr Marie Simbozel for assistance with data collection.

Disclosure forms provided by the authors are available with the full text and PDF of this article at www.ajnr.org.

REFERENCES

1. Sturm D, Orr BA, Toprak UH, et al. **New brain tumor entities emerge from molecular classification of CNS-PNETs.** *Cell* 2016;164:1060–72 CrossRef Medline
2. Louis DN, Perry A, Wesseling P, et al. **The 2021 WHO Classification of Tumors of the Central Nervous System: a summary.** *Neuro Oncol* 2021; 23:1231–51 CrossRef Medline
3. Kline CN, Joseph NM, Grenert JP, et al. **Targeted next-generation sequencing of pediatric neuro-oncology patients improves diagnosis, identifies pathogenic germline mutations, and directs targeted therapy.** *Neuro Oncol* 2017;19:699–709 CrossRef Medline
4. Paret C, Theruvath J, Russo A, et al. **Activation of the basal cell carcinoma pathway in a patient with CNS HGNET-BCOR diagnosis: consequences for personalized targeted therapy.** *Oncotarget* 2016;7:83378–91 CrossRef Medline
5. Appay R, Macagno N, Padovani L, et al. **HGNET-BCOR tumors of the cerebellum.** *Am J Surg Pathol* 2017;41:1254–60 CrossRef Medline
6. Yoshida Y, Nobusawa S, Nakata S, et al. **CNS high-grade neuroepithelial tumor with BCOR internal tandem duplication: a comparison with its counterparts in the kidney and soft tissue.** *Brain Pathol* 2018;28:710–20 CrossRef Medline
7. Paret C, Russo A, Otto H, et al. **Personalized therapy: CNS HGNET-BCOR responsiveness to arsenic trioxide combined with radiotherapy.** *Oncotarget* 2017;8:114210–25 CrossRef Medline
8. Al-Battashi A, Al Hajri Z, Perry A, et al. **A cerebellar high-grade neuroepithelial tumour with BCOR alteration in a five-year-old child.** *Sultan Qaboos Univ Med J* 2019;19:153–56 CrossRef Medline
9. Kirkman M, Pickles J, Fairchild A, et al. **Early wound site seeding in a patient with central nervous system high-grade neuroepithelial tumor with BCOR alteration.** *World Neurosurg* 2018;116:279–84 CrossRef Medline
10. Vewinger N, Huprich S, Seidmann L, et al. **IGF1R is a potential new therapeutic target for HGNET-BCOR brain tumor patients.** *Int J Mol Sci* 2019;20:3027 CrossRef Medline
11. Łastowska M, Trubicka J, Sobocińska A, et al. **Molecular identification of CNS NB-FOXR2, CNS EFT-CIC, CNS HGNET-MN1 and CNS HGNET-BCOR pediatric brain tumors using tumor-specific signature genes.** *Acta Neuropathol Commun* 2020;8:105 CrossRef Medline
12. Ferris S, Velazquez Vega J, Aboian M, et al. **High-grade neuroepithelial tumor with BCOR exon 15 internal tandem duplication: a comprehensive clinical, radiographic, pathologic, and genomic analysis.** *Brain Pathol* 2020;30:46–62 CrossRef Medline
13. Bremer J, Kottke R, Johann PD, et al. **A single supratentorial high-grade neuroepithelial tumor with two distinct BCOR mutations, exceptionally long complete remission and survival.** *Pediatr Blood Cancer* 2020;67:e28384 CrossRef Medline
14. Capper D, Jones DT, Sill M, et al. **DNA methylation-based classification of central nervous system tumours.** *Nature* 2018;555:469–74 CrossRef Medline

15. Astolfi A, Melchionda F, Perotti D, et al. **Whole transcriptome sequencing identifies BCOR internal tandem duplication as a common feature of clear cell sarcoma of the kidney.** *Oncotarget* 2015;6:40934–39 CrossRef Medline
16. Roy A, Kumar V, Zorman B, et al. **Recurrent internal tandem duplications of BCOR in clear cell sarcoma of the kidney.** *Nat Comm* 2015;6:8891 CrossRef Medline
17. Ueno-Yokohata H, Okita H, Nakasato K, et al. **Consistent in-frame internal tandem duplications of BCOR characterize clear cell sarcoma of the kidney.** *Nat Genet* 2015;47:861–63 CrossRef Medline
18. Kao YC, Sung YS, Zhang L, et al. **Recurrent BCOR internal tandem duplication and YWHAE-NUTM2B fusions in soft tissue undifferentiated round cell sarcoma of infancy: overlapping genetic features with clear cell sarcoma of kidney.** *Am J Surg Pathol* 2016;40:1009–20 CrossRef Medline
19. Santiago T, Clay MR, Allen SJ, et al. **Recurrent BCOR internal tandem duplication and BCOR or BCL6 expression distinguish primitive myxoid mesenchymal tumor of infancy from congenital infantile fibrosarcoma.** *Mod Pathol* 2018;31:374 CrossRef Medline
20. Dangouloff-Ros V, Tauziède-Espariat A, Roux CJ, et al. **CT and multimodal MR imaging features of embryonal tumors with multilayered rosettes in children.** *AJNR Am J Neuroradiol* 2019;40:732–36 Medline
21. Dangouloff-Ros V, Deroulers C, Foissac F, et al. **Arterial spin labeling to predict brain tumor grading in children: correlations between histopathologic vascular density and perfusion MR imaging.** *Radiology* 2016;281:553–66 CrossRef Medline
22. Jin B, Feng XY. **MRI features of atypical teratoid/rhabdoid tumors in children.** *Pediatr Radiol* 2013;43:1001–08 CrossRef Medline
23. Warmuth-Metz M, Bison B, Dannemann-Stern E, et al. **CT and MR imaging in atypical teratoid/rhabdoid tumors of the central nervous system.** *Neuroradiology* 2008;50:447–52 CrossRef Medline
24. Meyers SP, Khademian ZP, Biegel JA, et al. **Primary intracranial atypical teratoid/rhabdoid tumors of infancy and childhood: MRI features and patient outcomes.** *AJNR Am J Neuroradiol* 2006;27:962–71 Medline
25. Parmar H, Hawkins C, Bouffet E, et al. **Imaging findings in primary intracranial atypical teratoid/rhabdoid tumors.** *Pediatr Radiol* 2006;36:126–32 CrossRef Medline
26. Zuccoli G, Izzi G, Bacchini E, et al. **Central nervous system atypical teratoid/rhabdoid tumour of infancy. CT and MR findings.** *Clin Imaging* 1999;23:356–60 CrossRef Medline
27. Alrayahi J, Zapotocky M, Ramaswamy V, et al. **Pediatric brain tumor genetics: what radiologists need to know.** *Radiographics* 2018;38:2102–22 CrossRef Medline
28. Northcott PA, Korshunov A, Witt H, et al. **Medulloblastoma comprises four distinct molecular variants.** *J Clin Oncol* 2011;29:1408–14 CrossRef Medline
29. Mata-Mbemba D, Zapotcky M, Laughlin S, et al. **MRI characteristics of primary tumors and metastatic lesions in molecular subgroups of pediatric medulloblastoma: a single-center study.** *AJNR Am J Neuroradiol* 2018;39:949–55 CrossRef Medline
30. Yuh EL, Barkovich AJ, Gupta N. **Imaging of ependymomas: MRI and CT.** *Childs Nerv Syst* 2009;25:1203–13 CrossRef Medline

Celebrating 35 Years of the AJNR

January 1987 edition

Chemonucleation and Changes Observed on Lumbar MR Scan: Preliminary Report

Michael S. Huckman[1]
John W. Clark[1]
Thomas W. McNeill[2]
Walter W. Whisler[3]
William F. Hejna[2]
Eric J. Russell[1]
Ruth G. Ramsey[1]
David Turner[1]

This study examines the relation between the postchemonucleation clinical outcome and changes observed on the lumbar MR scan. Eight of 12 chemonucleated disks showed clinical improvement at the last follow-up, while the other four showed no improvement. In the cases that showed improvement there was a decrease in one or both dimensions of the defect in the thecal sac. Seven of eight showed an increase in the peridisk signal. Where there was no clinical improvement there were fewer decreases in the size of the defect, and three of four showed no increase in the peridisk signal.

Chemonucleation of the lumbar intervertebral disk was introduced by Smith [1] as an alternative to laminectomy for the treatment of herniated lumbar nucleus pulposus. As more recent studies have attested to the efficacy of this technique [2–8], its use has increased dramatically. With the development of sophisticated CT scanning equipment have come several studies that correlated the clinical outcome of this procedure with the radiographic changes it produces [9–11]. A description of the MR changes caused by chemonucleation has also been reported [12]. Our current study was undertaken to determine the correlation between changes in the lumbar MR examination before and after chemonucleation, and the clinical outcome.

Subjects and Methods

Eleven patients with signs and symptoms of herniated lumbar nucleus pulposus at L4–L5 or L5–S1 were entered into the study after confirmation of the diagnosis by both lumbar CT

Received May 14, 1986; accepted July 22, 1986.

Presented in part at the annual m American Society of Neuroradiology January 1986.

This work was supported by a gra Laboratories, Northbrook, IL.

[1] Department of Diagnostic Radio Presbyterian-St. Luke's Medical Cen IL 60612. Address reprint requests fo man.

[2] Department of Orthopedic Sur Presbyterian-St. Luke's Medical Cen IL 60612.

[3] Department of Neurological Sur Presbyterian-St. Luke's Medical Cen IL 60612.

AJNR 8:1–4, January/February 1987
0195-6108/87/0801-0001
© American Society of Neuroradiology

MR Imaging of the Cervical Spine: Neurovascular Anatomy

Bonnie D. Flannigan[1,2]
Robert B. Lufkin[1]
Charles McGlade[1]
James Winter[1]
Ulrich Batzdorf[3]
Gabriel Wilson[1]
Wolfgang Rauschning[4]
William G. Bradley, Jr.[5]

High-resolution surface-coil MR imaging reveals intricate anatomic detail of the cervical spinal canal and its neurovascular contents. Appreciation of the normal neurovascular anatomy provides a scientific foundation for the detection of disease. Sagittal, axial, and oblique MR images of normal subjects were correlated with comparable anatomic sections obtained with a cryomicrotome whole-organ sectioning technique. The anterior epidural venous plexus is a prominent structure in the cervical spinal canal and was consistently identified both with cryomicrotomy and with MR in sagittal and axial planes. Epidural veins can be displaced and distorted in patients with cervical disk disease. Nerve roots including dorsal and ventral rootlets were consistently identified on axial images coursing through the subarachnoid space. Oblique-plane imaging showed nerve roots "en face" in their respective foramina; this may be a useful imaging technique in the diagnosis of nerve root impingement.

This study was undertaken to define normal anatomic structures within the cervical spinal canal using MR, with particular attention to the cervical epidural veins and the cervical nerve roots. Abnormal anatomy can only be detected in comparison to normal anatomy. High-resolution MR images obtained in sagittal, axial, and oblique planes were correlated with corresponding anatomic sections obtained with a cryomicrotome whole-organ sectioning technique.

The anterior epidural cervical venous plexus is a prominent structure previously well-identified with bolus intravenous contrast CT studies. It was consistently identified on parasagittal images and also on axial images in the anterolateral recesses of the spinal canal on T1-weighted MR images. Its normal appearance should be appreciated, since distortion of this extensive venous network can occur in patients with cervical disk disease.

Axial imaging allows identification of both the ventral and dorsal nerve roots individually as they course through the subarachnoid space. Significant neural foraminal disease may be difficult to identify in the axial and sagittal plane, making MR somewhat controversial as an imaging technique in the patient with an isolated radiculopathy. Electronically activated oblique-plane imaging was used to show the nerve roots in their respective neural foramina. This may be a useful method for evaluating patients with radiculopathy.

Materials and Methods

Cervical spine examinations were performed on 30 volunteers using a flexible neck coil and a 0.3 T permanent magnet imaging system (Fonar S-3000, Melville, NY). The vertical orientation of the axis of the main magnetic field allowed the use of a solenoidal (circumferential) neck coil. Multislice imaging was performed in the axial, sagittal, and oblique planes using a spin-echo, multislice pulse sequence. Electronically activated oblique-plane imaging was performed by using an axial scout image and placing line cursors perpendicular to one neural foramen and parallel to the opposite foramen (see Fig. 6A). This enabled us to obtain images of the nerve roots on one side "en face" comparable to a 45° oblique plain radiograph.

This article appears in the January/February 1987 issue of AJNR and the April 1987 issue of AJR.

Received December 19, 1985; accepted after revision July 10, 1986.

[1] Department of Radiological Sciences, UCLA Medical Center, Los Angeles, CA 90024. Address reprint requests to B. D. Flannigan.

[2] Present address: Valley Presbyterian Hospital, 15107 Vanowen St., Van Nuys, CA 91405.

[3] Department of Neurosurgery, UCLA Medical Center, Los Angeles, CA 90024.

[4] Department of Orthopedics, University Hospital, Uppsala, Sweden.

[5] NMR Imaging of the Laboratory, Huntington Medical Research Institutes, Pasadena, CA 91109.

AJNR 8:27–32, January/February 1987
0195-6108/87/0801-0027